INVESTIGATION OF THE LOAD RATING PROCESS FOR CONCRETE BRIDGES TO REDUCE THE UNCERTAINTY IN LOAD POSTING

A Thesis

by

NUZHAT HUMAYUN KABIR

Submitted to the Office of Graduate and Professional Studies of
Texas A&M University
in partial fulfillment of the requirements for the degree of

MASTER OF SCIENCE

Chair of Committee,	Mary Beth D. Hueste
Committee Members,	Stefan Hurlebaus
	John Mander
	Stephanie Paal
	Mohammed E. Haque
Head of Department,	Robin Autenrieth

December 2019

Major Subject: Civil Engineering

ABSTRACT

The infrastructure system of the United States consists of an aging transportation system whose load carrying capacities need to be assessed. Bridges that do not have sufficient capacity to carry the legal loads are load posted. These load limits, intended to ensure public safety, impose inconvenience to travelers and significant cost to society. This thesis aims to investigate the potential for improvement in the load rating process for simple span concrete bridges, especially flat slab, and pan girder bridges. TxDOT uses the simplified load rating procedures outlined in the AASHTO Standard Specifications to load rate their bridges. These procedures are intended to be conservative and can have varying degrees of accuracy as compared to the in-situ behavior of specific bridges. Basic load rating of a group of bridges from each category was carried out to identify possible areas of refinement. An attempt to capture the expected behavior of specific bridge geometries was made through FEM modeling and experimental testing of two typical bridges. The results obtained from the field tests were compared with recommendations from AASHTO codes. The results from the field tests were used to calibrate the FEM models and the maximum load carrying capacity of the bridges were determined. The AASHTO Standard Specifications closely estimated the distribution of live load across the girders for pan girder bridges. The guidelines for concrete slab bridges with integral curbs in the Illinois Bulletin 346 (IB346) accurately predicted the moment demand for the curb section for the selected concrete slab bridge. For the selected slab bridge, it was found that the approach of Amer et al. (1999) more accurately estimated the moment demand for the interior slab sections for one-lane loading, while the approximate equations in the AASHTO LRFD Specifications (AASHTO 2017) provided a good estimate for two-lane loading.

ACKNOWLEDGEMENTS

I would like to thank my committee chair, Dr. Mary Beth Hueste, and my committee members, Dr. Stefan Hurlebaus, Dr. John Mander, Dr. Stephanie Paal, and Dr. Mohammed Haque, for their guidance and support throughout the course of this research.

I would also like to thank the post-doctoral research associate, Dr. Tevfik Terzioglu, involved in this study for his help and support throughout the duration of the project. A special thanks to Matthew Stieglitz, my fellow research assistant on this project, for his assistance, Hyeonki Hong and Hungjoo Kwon, graduate students at TAMU, for assisting with the instrumentation and load testing of the selected bridges, and the Texas A&M Transportation Institute for their support on this project.

I would like to express my sincere gratitude to my family, especially my father (Humayun Kabir) and my mother (Syeda Iffat Jahan) without whose constant support, love and encouragement this would not have been possible. I would also like to express my profound gratitude to my friends, especially Mirza Riyaz Akhter for his unfailing support and encouragement towards the end of my research.

Finally, thanks to the department, faculty and staff for providing a supportive environment for successful completion of the project.

CONTRIBUTORS AND FUNDING SOURCES

Contributors

This work was supervised by a thesis committee consisting of Dr. Mary Beth Hueste, Dr. Stefan Hurlebaus, Dr. John Mander, and Dr. Stephanie Paal of the Zachry Department of Civil and Environmental Engineering and Dr. Mohammed Haque of the Department of Construction Science. Dr. Tevfik Terzioglu, post-doctoral research associate with the Texas A&M Transportation Institute, also provided guidance for this research.

Funding Sources

Graduate study was supported by Texas Department of Transportation Research Project 0-6955, which was administered through the Texas A&M Transportation Institute.

NOMENCLATURE

AASHO	American Association of State Highway Officials
AASHTO	American Association of State Highway and Transportation Officials
ACI	American Concrete Institute
ADT	Average Daily Traffic
ADTT	Average Daily Truck Traffic
AISC	American Institute of Steel Construction
ASCE	American Society of Civil Engineers
ASD	Allowable Stress Design
ASR	Allowable Stress Rating
ASTM	American Society for Testing and Materials
CM	Concrete Multi-Girder
CS	Concrete Slab
DOT	Department of Transportation
FEM	Finite Element Method
FHWA	Federal Highway Administration
FO	Functionally Obsolete
LFD	Load Factor Design
LFR	Load Factor Rating
LLDF	Live Load Distribution Factor
LRFD	Load and Resistance Factor Design

LRFR	Load and Resistance Factor Rating
MBE	Manual for Bridge Evaluation
MCE	Manual for Condition Evaluation
NBI	National Bridge Inventory
NCHRP	National Highway Cooperative Research Program
NDE	Nondestructive Evaluation
NDT	Nondestructive Testing
RF	Rating Factor
SD	Structurally Deficient
SEI	Structural Engineering Institute
SSLO	Sub-Standard for Load Only
TxDOT	Texas Department of Transportation

TABLE OF CONTENTS

Page

LIST OF FIGURES

Page

LIST OF TABLES

Page

1. INTRODUCTION

1.1. BACKGROUND

Infrastructure plays a vital role in a nation's economy, security, and integrity. The infrastructure system of the United States consists of an aging transportation system whose load carrying capacities need to be assessed. This is carried out through the process of load rating. Prior to 1967, bridge inspections and load rating were rare processes. The Silver Bridge collapse in 1967 in West Virginia resulted in the loss of 46 lives. This led the United States (U.S.) Congress to include a section in the Federal Highway Act of 1968 calling for a national bridge inspection standard. An increased effort and diligence regarding bridge inspections was required by the new National Bridge Inspection Standards (NBIS). This led to the creation of three manuals to ensure uniformity in the state bridge inspection procedures (Lichtenstein 1993; Ryan et al. 2012).

Presently, simplified models as suggested by the American Association of State Highway and Transport Officials (AASHTO) Manual for Bridge Evaluation are adopted to evaluate a the load carrying capacity of a bridge. Bridge load carrying capacity may accurately be determined through experimental load tests and refined modeling. During field tests, vehicles with known weight are driven over the bridge at various configurations and the behavior of the bridge is studied. The load rating of the bridge is determined based on the measured response of the bridge. Refined rating, as allowed by AASHTO, may also be carried out using finite element models. Finite element models, developed using various commercial software packages, provide tools for studying bridge behavior and response to different types of loading, for bridge rating and for undertaking parametric studies. In the absence of the opportunity to conduct experimental load testing, confidence in the load rating calculations may be increased by accurately determining the input information required. The load rating calculations depend on bridge characteristics such as

span length, slab thickness, overlay thickness, additional dead loads from components, and material strength. Although this information is attainable from structural drawings, the drawings may not be readily available. Furthermore, as-built drawings may be difficult to locate for older bridges, particularly those that are off-system bridges. It would be efficient to gather this information on site during inspection. The in situ compressive strength of concrete may also be determined through non-destructive or destructive testing.

1.2. MOTIVATION AND RESEARCH OBJECTIVES

Bridges that do not have sufficient capacity to carry the legal loads are load posted. Although aimed at ensuring public safety, these load limits impose inconvenience to travelers and significant cost to society due to the time required to detour around a posted bridge. Load posting can also have significant impact on commerce, traffic, and emergency egress. These problems serve as a motivation to investigate the current load rating procedures to reduce the uncertainty and conservativeness associated with the process.

An inventory of all load posted bridges in Texas was undertaken. Based on the findings, this thesis aims to investigate simple span concrete bridges, in particular flat slab bridges and pan girder bridges. After performing a comprehensive literature review of the state-of-the-art and state-of-the-practice on load rating of existing concrete bridges, the objectives of this thesis were identified to be the following: (1) conduct basic load rating of simple-span concrete bridges and identify areas of opportunity to improve ratings, (2) develop finite element method (FEM) models of two representative concrete bridges, (3) load test two representative concrete bridges to validate and calibrate the FEM model, and (4) provide recommendations for refined load rating analysis of the selected concrete bridge types.

1.3. RESEARCH APPROACH

A thorough literature review of the state-of-the-practice was conducted to map the history of the load rating procedure. Current load rating practice adopted by TxDOT was investigated. Load rating of existing bridges is carried out using three different methods: Allowable Stress Rating (ASR), Load Factor Rating (LFR), and Load and Resistance Factor Rating (LRFR) based on the AASHTO Manual for Bridge Evaluation (AASHTO MBE 2018). The LRFR method is the most recently developed load rating method, preferred by the FHWA to load rate bridges engineered after the 1st of October, 2007 (CTC & Associates 2009). The state-of-the-art literature review identified the approach of related research in the field of load rating existing bridges and key findings.

In order to identify the areas of opportunities to improve the rating of existing bridges, a group of simple-span concrete bridges (flat slab bridges and pan girder bridges) were load rated using all the three rating methods. The effect of different bridge parameters such as number of traffic lanes, unintended end fixity, and in-situ strength of materials on the individual rating factors (RF) were examined. This helped identify potential approaches in which load posting of these bridges could be increased and/or removed.

According to the bridge attributes listed in the latest National Bridge Inventory (NBI 2016) database, two representative bridges typical of concrete slab bridges and concrete pan girder bridges were selected for finite element method (FEM) modeling and proof testing. Three-dimensional FEM models of the bridges were developed based on standard structural drawings using appropriate modeling parameters identified during the state-of-the-art review. The results from these FEM models were used to develop live load distribution factors (LLDF). The selected bridges were instrumented and subjected to the posted load during proof testing. The results from

the load test were used to determine the measured LLDFs for each bridge. The developed FEM models were verified against these experimental results and calibrated for improved accuracy. This process served to identify the impact of experimental analysis and refined analysis using FEM models on improving the load posting of a bridge.

Finally, the findings from this research were summarized and appropriate recommendations for refined load rating analysis for selected bridge types have been provided.

1.4. OUTLINE OF THESIS

The thesis is composed of nine chapters. Chapter 1 outlines the background, motivation and objectives for this research and describes the research approach. The key findings from the literature review of the state-of-the-practice and the state-of-the-art are highlighted in Chapter 2. The current load rating procedures: the ASR method, the LFR method, and the LRFR method and TxDOT's practice for load rating bridges are explained in Chapter 3. Chapter 4 presents the results from basic load rating analysis of a selected group of Texas SSLO concrete bridges using the three major load rating methods. The development of FEM model along with initial refined analysis of a representative simple span concrete multi-girder bridge, and concrete slab bridge is explained in Chapter 5 and Chapter 6, respectively. Chapter 7 and Chapter 8 describe the bridge instrumentation plan and results obtained from load testing a representative simple span concrete multi-girder bridge, and concrete slab bridge, respectively. The field test results were used to calibrate the initially developed FEM models for the two bridges. A summary of the project including conclusions and recommendations for improved load rating for the bridge types considered are presented in Chapter 9 along with suggestions for future work.

2. LITERATURE REVIEW

A comprehensive literature review of the state-of-the-practice and state-of-the-art on load rating of existing bridges was conducted. Historical and current approaches to load rating existing bridges in the U.S. are presented in the review of the state-of-the-practice. Select national and international approaches to load rating are also presented. Related research in the field of load rating existing bridges and relevant key findings are summarized in the state-of-the-art literature review.

2.1. HISTORY OF LOAD RATING OF BRIDGES

The Silver Bridge collapse in 1967 in West Virginia resulted in the addition of a section to the Federal Highway Act of 1968 calling for a national bridge inspection standard. The new National Bridge Inspection Standards (NBIS) led to the creation of three manuals to ensure uniformity in the state bridge inspection procedures (Lichtenstein 1993; Ryan et al. 2012).

The first manual, released in 1970, was the American Association of State Highway Officials (AASHO) Manual for Maintenance Inspection of Bridges (AASHO 1970), which provided guidelines for bridge load rating. The stress caused by loading was limited to the specified maximum allowable stress, calculated based on the concept of working stresses. There were different levels of rating. The Operating Rating was the absolute maximum stress where the allowable stress was restricted to 75 percent of the yield stress of the material. The Inventory Rating was the load that the bridge could be safely subjected to for an indefinite period. This corresponds to an allowable stress limited to 55 percent of the yield stress or the allowable design stress of the structure. The load ratings were evaluated based on AASHO H design loading or one of the conventional vehicle types, Type 3 Unit, the Type 3S2 Unit, and the Type 3-3 Unit. The conventional trucks are similar to the current American Association of State Highway and

Transportation Officials (AASHTO) LRFD Bridge Design Specifications (AASHTO 2017) legal loads. They are slightly lighter than the AASHTO legal loads with different loads distributed to each axle.

In 1973, AASHO became AASHTO and released three more editions of the *Manual for Maintenance Inspection of Bridges* over the next 13 years. The HS design loading was added in the 1974 *Manual for Maintenance Inspection of Bridges* (AASHTO 1974) as one of the loads required for bridge evaluation, and rating using Load Factor Design (LFD) methods was introduced. In Load Factor Rating (LFR), multiples of load or load effects are applied to the bridge. The Inventory Rating was given a higher live load factor compared to the Operating Rating. Based on the yield strength of steel and the ultimate strength of concrete, the capacity of the bridge was calculated. The rating factor (RF) for each type of bridge was determined as some variation of capacity divided by the live load effect. However, the Load Factor method of rating was only included in the appendix of the 1974 Manual, with its focus being rating bridges using working and allowable stress method.

The working stress method and load factor method for rating were equally discussed in the 1978 *Manual for Maintenance Inspection of Bridges* (AASHTO 1978). The load factor method for rating concrete bridges was introduced with the assumption that the tension reinforcement has yielded. The definition of Operating and Inventory Levels were modified to be related to the load levels that the bridge was subjected to, rather than the stresses. The three legal loads for evaluations were slightly increased and re-distributed between axles. The 1983 *Manual for Maintenance Inspection of Bridges* was identical to the 1978 version with respect to the load rating section, providing guidelines for both working stress and load factor methods for rating (AASHTO 1983; TxDOT 2013).

A new method for load rating bridges was introduced by the National Highway Cooperative Research Program (NCHRP) in 1987 called Load and Resistance Factor Rating (LRFR). This was developed through two reports: NCHRP Report 292 and NCHRP Report 301. The use of probabilistic and structural reliability methods to determine load factors for rating reinforced concrete bridges was presented in NCHRP Report 292 (Imbsen et al. 1987). The load factors for all types of bridges were developed based on the NCHRP Report 292 and incorporated into the Resistance Factor Design (LRFD) principles in the NCHRP Report 301 (Moses and Verma 1987). AASHTO accepted an all-inclusive guide with calibrated load factors for LRFD in 1993 (Kulicki 1998).

The *AASHTO Manual for Condition Evaluation of Bridges* (MCE) (AASHTO 1994) stated the LRFR method for the first time in the load rating section. A complete rewrite of the AASHTO evaluation manual, the 1994 MCE provided greater detail regarding load rating with a brief mention of LRFR directing towards its details in the *AASHTO Guide Specifications for the Strength Evaluation of Existing Steel and Concrete Bridges* (AASHTO 1994). The working stress method was given the new title Allowable Stress Rating (ASR) method while the load factor method was called Load Factor Rating (LFR) method and is the focus of the 1994 MCE. To conform with the *AASHTO LRFD Bridge Design Specifications,* the 1994 MCE used a design HS-20 truck.

A new AASHTO manual incorporating LRFR methods for load rating was developed by NCHRP Project 12-46 (Lichtenstein Consulting Engineers 2001) in 2001. This was followed by the publication of the *AASHTO Manual for Condition Evaluation and Load and Resistance Factor Rating of Highway Bridges* (AASHTO 2003). The main loading method in this manual was LRFR with procedures outlining how to calculate the load factors and a general RF equation. An appendix

with the section titled Alternate Load Rating included the ASR and LFR methods as other methods for load rating.

The first edition of the *Manual for Bridge Evaluation* (MBE) was published by AASHTO in 2008. The MBE provided an all-encompassing evaluation manual for bridges combining the 1994 MCE and the 2003 manual that superseded all previous manuals. This became the reference guide for load rating bridges in the U.S. A section was dedicated to load rating consisting of three parts: one focused on the LRFR method, one on the ASR and LFR methods, and one providing examples for each method and bridge type (AASHTO 2008).

2.2. CURRENT LOAD RATING PROCEDURES

A second edition of the MBE (2011) was released by AASHTO in 2011. Along with revisions made in 2016, this is the current standard procedure to load rate bridges in the United States. In Section 6 of the 2011 MBE, Part A describes the LRFR method while Part B describes the ASR and LFR methods. All bridges constructed after October 1, 2007 are required by the Federal Highway Administration (FHWA) to be designed using the LRFD approach. This is part of a large push by the industry to go towards the use of LRFD to design bridges and therefore, using LRFR as the accompanying load rating method (CTC & Associates 2009). This effort also requires bridges designed using Allowable Stress Design (ASD) to be re-rated using either LFR or LRFR. Bridges designed using Load Factor Design (LFD) may still be rated using LFR, although load rating using the LRFR method is preferred by the FHWA in all cases (Lwin 2006).

2.2.1. Load and Resistance Factor Rating (LRFR)

Each component of the bridge is assigned a RF based on Eqn. (2.1) and the lowest RF governs the rating of the bridge. The nominal resistance of the member is multiplied by an LRFD resistance

factor ϕ, a system factor ϕ_s, and a condition factor ϕ_c to determine the capacity for the strength limit state. The product of the condition and system factors should be greater than 0.85. The bridge RF can be calculated using the LRFR method as per the following general equation:

$$RF = \frac{C - (\gamma_{\mathrm{DC}})(DC) - (\gamma_{DW})(DW) \pm (\gamma_P)(P)}{(\gamma_{LL})(LL + IM)} \quad (2.1)$$

where:

RF = Rating Factor

C = Capacity

DC = Dead load effect due to structural components and attachments

DW = Dead load effect due to wearing surface and utilities

P = Permanent loads other than dead loads

LL = Live load effect

IM = Dynamic load allowance

γ_{DC} = LRFD load factor for structural components and attachments

γ_{DW} = LRFD load factor for wearing surfaces and utilities

γ_P = LRFD load factor for permanent loads other than dead loads = 1.0

γ_{LL} = Evaluation live load factor

Specific values for the dead load factors, γ_{DC} and γ_{DW}, and live load factor, γ_{LL}, are chosen based on the limit state as shown in Table 2.1. Strength I is the primary limit state used for LRFR method. However, the limit state evaluated is dependent on the rating procedure. LRFR includes

three different rating procedures for bridges: (1) Design Load Rating, (2) Legal Load Rating, and (3) Permit Load Rating.

Table 2.1. Load Factors for Load rating at Various Limit States (adapted from AASHTO MBE 2018)

Bridge type	Limit State	Dead Load γ_{DC}	Dead Load γ_{DW}	Design Load	
				Inventory	Operating
				γ_{LL}	γ_{LL}
Reinforced Concrete	Strength I	1.25	1.50	1.75	1.35
	Service I	1.00	1.00	-	-

2.2.1.1. Design Load Rating

The Design Load Rating uses the HL-93 load model, which includes an HS20 truck and a lane load (AASHTO 2017), and has two levels of rating: (1) Inventory Rating Level, and (2) Operating Rating Level. The Inventory RF is smaller than the Operating RF since the Inventory Rating Level applies a higher live load factor (γ_{LL}). The absolute maximum load that can safely cross the bridge at one time is given by the *Operating RF* as a multiple of HL-93 load. The *Inventory RF* is the multiple of HL-93 loads that still allows the bridge to be in service for an indefinite period. If both the Inventory and Operating RFs are greater than 1.0, the bridge does not need to be posted. If the Operating RF is greater than 1.0 and the Inventory RF is less than 1.0, the bridge may likely need to be posted for its safe load. If both the Inventory and Operating RFs are less than 1.0, the bridge should be posted and evaluated for a Legal Load Rating.

2.2.1.2. Legal Load Rating

The AASHTO LRFD Bridge Design Specifications (AASHTO 2017) provide load configurations that are legal throughout the country, called Type 3, Type 3S2, and Type 3-3 trucks, and NRL, SU4, SU5, SU6, and SU7 Specialized Hauling Vehicles. These create smaller effects compared to the HL-93 loading. Truck configurations that produce an RF greater than 1.0 are safe to travel on

the bridge, while configurations that produce an RF less than 1.0 must be posted. The LRFR live load factor, γ_{LL}, for Design Load Ratings is 1.75 for Inventory and 1.35 for Operating Level. Table 2.2 provides γ_{LL} for the Legal Load Ratings based on the truck configuration being evaluated and the Average Daily Truck Traffic (ADTT) on the bridge as provided in the AASHTO MBE.

Table 2.2. Generalized Live Load Factors for Routine Commercial Traffic and Specialized Hauling Vehicles (adapted from AASHTO 2011)

Traffic Volume (One Direction)	Load Factor for Type 3, Type 3S2, Type 3-3, and Lane Loads	Load Factor for NRL, SU4, SU5, SU6, and SU7 Vehicles
Unknown	1.80	1.60
ADTT ≥ 5000	1.80	1.60
ADTT = 1000	1.65	1.40
ADTT ≤ 100	1.40	1.15

Note: MBE allows interpolation between ADTT values.

2.2.1.3. Permit Load Rating

The Permit Load Rating determines whether a certain load greater than the defined AASHTO or state legal loads can travel safely across the bridge. The bridge is evaluated for a specific truck configuration based on a permit request. Permits are of two types: (1) Routine Permits allow unlimited trips for a specified period, and (2) Special Permits are valid for a single trip or a limited number of trips. If the bridge has an RF greater than 1.0 when evaluated for the specific permit request, it is rated as safe for that vehicle. The LRFR live load factor is different compared to the Design or Legal Load Ratings. Table 2.3 tabulates the live load factor which depends on the ADTT for the bridge. These factors are higher and thus will reduce the RF of the bridge.

Table 2.3. Permit Live Load Factors Currently in the AASHTO MBE (adapted from AASHTO 2011)

Permit Type	Frequency	Loading Conditions	Distribution Factor	ADTT (one direction)	Load Factor by Permit Weight	
					Up to 100 kips	≥ ≥ 150 kips
Routine or Annual	Unlimited Crossings	Mix with traffic (other vehicles may be on the bridge)	Two or more lanes	> 5000	1.80	11.30
				= 1000	1.60	11.20
				< 100	1.40	11.10
					All Weights	
Special or Limited Crossing	Single-Trip	Escorted with no other vehicles on the bridge	One lane	N/A	1.15	
	Single-Trip	Mix with traffic (other vehicles may be on the bridge)	One lane	> 5000	1.50	
				= 1000	1.40	
				< 100	1.35	
	Multiple-Trips (less than 100 crossings)	Mix with traffic (other vehicles may be on the bridge)	One lane	> 5000	1.85	
				= 1000	1.75	
				< 100	1.55	

Note: MBE allows interpolation between ADTT values.

2.2.1.4. LRFR Load Factors

NCHRP Project 12-33 (Kulicki 1998) developed the LRFR dead and live load factors for the Design Load Rating. These factors were derived using reliability indices, close to a target reliability, in a design and analysis specification developed by the study. This target reliability is indirectly related to the probability of failure of the structure. NCHRP project 12-46 (Moses 2001) used the same approach involving reliability indices to determine the necessary live load factors for Legal Load Rating and Permit Load Rating to keep the target reliability the same.

The live load factors obtained from these studies were examined by the NCHRP project 12-78 (Mlynarski et al. 2011) and are currently used in the MBE. 1500 bridges of different ages, materials and design were rated using the LRFR and LFR methods, and these ratings were analyzed and compared in this study. Based on the results of this project, new live load factors were proposed for the AASHTO MBE (AASHTO 2011) in the NCHRP Report 700 (Mlynarski et al. 2011). Mlynarski et al. (2011) stated that the bridges that were analyzed showed that the live load

factors correspond to a reliability index of 3.5 as opposed to 2.5 used to calculate most of the MBE live load factors. New live load factors were developed using the characteristics of the selected bridges and a reliability index of 2.5. Table 2.4 and Table 2.5 provide the updated live load factors in comparison to the original factors. The RFs calculated for the LRFR method using these smaller live load factors were higher for the selected bridges. MBE also provides details regarding how to calculate site-specific live load factors in its commentary, however these apply to heavier trucks than those used in the calibration process.

Table 2.4. Live Load Factors for Routine Commercial Traffic and Specialized Hauling Vehicles Proposed in NCHRP Report 700 (adapted from Mlynarski et al. 2011)

Traffic Volume (One Direction)	Load Factor for Type 3, Type 3S2, Type 3-3 and Lane Loads	Load Factor for NRL, SU4, SU5, SU6, and SU7 Vehicles
Unknown	~~1.80~~ 1.45	~~1.60~~ 1.45
ADTT ≥ 5000	~~1.80~~ 1.45	~~1.60~~ 1.45
ADTT = 1000	~~1.65~~ 1.30	~~1.40~~ 1.30
ADTT ≤ 100	~~1.40~~ 1.20	~~1.15~~ 1.15

Table 2.5. Live Load Factors for Permit Vehicles Proposed in NCHRP Report 700 (adapted from Mlynarski et al. 2011)

Permit Type	Frequency	Loading Conditions	Distribution Factor	ADTT (one direction)	Load Factor by Permit Weight	
					Up to 100 kips	1≥ 150 kips
Routine or Annual	Unlimited Crossings	Mix with traffic (other vehicles may be on the bridge)	Two or more lanes	> 5000	~~1.80~~ 1.45	11.30
				= 1000	~~1.60~~ 1.25	11.20
				< 100	~~1.40~~ 1.05	11.10
					All Weights	
Special or Limited Crossing	Single-Trip	Escorted with no other vehicles on the bridge	One lane	N/A	1.15	
	Single-Trip	Mix with traffic (other vehicles may be on the bridge)	One lane	> 5000	~~1.50~~ 1.25	
				= 1000	~~1.40~~ 1.15	
				< 100	~~1.35~~ 1.10	
	Multiple-Trips (less than 100 crossings)	Mix with traffic (other vehicles may be on the bridge)	One lane	> 5000	~~1.85~~ 1.60	
				= 1000	~~1.75~~ 1.50	
				< 100	~~1.55~~ 1.45	

The preferred method by the FHWA (Mertz 2015) of load rating bridges is the Load and Resistance Factor Rating which is explained in Part A of the AASHTO MBE (AASHTO 2011). The MBE recommended closing a bridge if the RF is less than 0.3. For bridges with RF between 0.3 and 1.0, the posting load safe to cross the bridge is given by Equation (2.2).

$$\text{Safe Posting Load} = \frac{W}{0.7}(RF - 0.3) \tag{2.2}$$

where:

RF = Legal load rating factor

W = Weight of rating vehicle

2.2.2. Allowable Stress Rating (ASR) and Load Factor Rating (LFR)

Allowable Stress Rating (ASR) and Load Factor Rating (LFR) are explained in Part B of the MBE. The design truck for evaluation is the HS-20 truck and if the bridge has an RF greater than 1.0, all AASHTO and state legal loads can safely pass the bridge. The general equation to obtain the RF is provided in Equation (2.3).

$$RF = \frac{C - A_1 D}{A_2 L(1 + I)} \tag{2.3}$$

where:

RF = Rating Factor for the live load carrying capacity

C = Capacity of the member

D = Dead load effect on the member

L = Live load effect on the member

I = Impact factor to be used with the live load effect

A_1 = Factor for dead loads

A_2 = Factor for live load

The dead load factor, A_1, and the live load factor, A_2, are 1.0 for both the Inventory Level and Operating Level for the ASR method. However, the capacity for the Inventory Level and Operating Level are different based on the allowable stress. The allowable stress is limited to a fraction of the yield or ultimate strength and is smaller for the Inventory Level rating. The procedure to calculate the capacity for various materials and levels for the ASR method is outlined in the MBE.

The dead load factor, A_1, is 1.3 and the live load factor, A_2, is 2.17 for Inventory Level ratings and 1.3 for Operating Level ratings for the LFR method. Here, the capacity of the member is the same for both levels, however the Operating Level has higher RF due to the smaller live load factor. AASHTO Standard Specifications (AASHTO 2002) outlines the procedure to calculate the capacity of different materials and components of the bridge.

2.2.3. Nondestructive Testing for Bridge Load Rating

The 'Nondestructive Load Testing' section in the AASHTO MBE (AASHTO 2011) explains the technique of using either diagnostic test or proof test for load rating a bridge. In diagnostic testing, the bridge is subjected to a load close to the rated capacity. While proof test uses a load greater than the rating to determine if the bridge can safely carry the increased load. The test RF, calculated using the LRFR method, is multiplied by an adjustment factor, K. Factors such as the calculated member strains based on the test vehicle, the member strains observed during the load test, and the ability of the test results to be extrapolated to performance at higher loads influences the

adjustment factor. Proof test results can only be used to find the Operating Level ratings. The RF at Operating Level, RF_O obtained from proof test results is calculated as,

$$RF_O = \frac{OP}{L_R(1 + IM)} \tag{2.4}$$

where:

OP = Operating level capacity

L_R = Comparable unfactored live load due to the rating vehicle

IM = Dynamic load allowance

The Operating Level capacity, OP, can be determined as,

$$OP = \frac{k_O L_p}{X_{pA}} \tag{2.5}$$

where:

k_O = 1.0 if the proof load test reached the target load and 0.88 if the proof load test was terminated because of distress in the bridge

L_p = Actual maximum proof live load applied to the bridge

X_{pA} = Target live load factor found using the procedure in Section 8.8.3.3.2 of the MBE (AASHTO 2011)

Load testing is an expensive and time-consuming process which can be inefficient to run for just one bridge. As a result, various states adopt LRFR, LFR and ASR approaches to load rate their bridges and use load testing to load rate critical bridges (Hearn 2014).

2.2.4. Material Properties for Bridge Load Rating

Many bridges do not have original structural/construction plans and as a result the true material strength of its constituents may be unknown. The AASHTO MBE documents the strength of common materials used during a given period of construction. This information is documented for the different load rating methods.

2.2.4.1. LRFR Material Properties

The strength based on the year of construction is provided for different types of materials in Table 2.6 through Table 2.9 for the LRFR method. These tables were obtained from the AASHTO MBE (AASHTO 2011) and other material strengths can also be found in Section A of the MBE.

Table 2.6. Minimum Compressive Strength of Concrete by Year of Construction (adapted from AASHTO 2011)

Year of Construction	Compressive Strength, f'_c, ksi
Prior to 1959	2.5
1959 and later	3.0

Table 2.7. Yield Strength of Reinforcing Steel (adapted from AASHTO 2011)

Type of Reinforcing Steel	Yield Strength, f_y, ksi
Unknown steel constructed prior to 1954	33
Structural grade	36
Billet or intermediate grade, Grade 40, and unknown steel constructed during or after 1954	40
Rail or hard grade, Grade 50	50
Grade 60	60

Table 2.8. Tensile Strength of Prestressing Steel (adapted from AASHTO 2011)

Year of Construction	Tensile Strength, f_{pu}, ksi
Prior to 1963	232
1963 and Later	250

Table 2.9. Minimum Mechanical Properties of Structural Steel by Year of Construction (adapted from AASHTO 2011)

Year of Construction	Minimum Yield Point or Minimum Yield Strength, F_y, ksi	Minimum Tensile Strength, F_u, ksi
Prior to 1905	26	52
1905 to 1936	30	60
1936 to 1963	33	66
After 1963	36	66

2.2.4.2. LFR and ASR Material Properties

The strength based on the year of construction is provided for different types of materials in Table 2.10 and Table 2.11 for the LFR and ASR methods. These tables were obtained from the AASHTO MBE (AASHTO 2011) and other material strengths can also be found in Section B of the MBE.

Table 2.10. Allowable Unit Stresses for Concrete (adapted from AASHTO 2011)

Year Built	Compressive Strength, f'_c, psi
Prior to 1959	2500
1959 and later	3000

Table 2.11. Allowable Unit Stresses (psi) for Reinforcing Steel (adapted from AASHTO 2011)

Type of Reinforcing Steel	Inventory Rating	Operating Rating	Yield
Unknown steel constructed prior to 1954	18,000	25,000	33,000
Structural grade	20,000	27,000	36,000
Billet or intermediate grade, Grade 40, and unknown steel constructed during or after 1954	20,000	28,000	40,000
Rail or hard grade, Grade 50	20,000	32,500	50,000
Grade 60	24,000	36,000	60,000

Tables 6B.6.2.1-1 and 6B.6.2.1-4 of the MBE (AASHTO 2011) documents the yield strength of other steel members not specified in accordance with the year built. The maximum strength of welds, bolts and rivets can be obtained from Table 10.56A in the AASHTO Standard Specifications (AASHTO 2002). The yield strength of a bridge may also be determined by testing steel coupons as recommended in Section 6B.6.3.1 of the MBE (AASHTO 2011). However, the yield strength would equal to the mean test value minus 1.65 times the standard deviations and this value should be used to calculate the capacity.

2.2.5. Additional Load Rating Practices

2.2.5.1. National Bridge Inventory

Public bridges with spans greater than 20 ft in all states are required by the FHWA to be load rated (United States Government 2004). Characteristics of different bridges such as span length, bridge width, number of lanes, average annual daily traffic (AADT), etc., along with their rating information are stored in the public database called the National Bridge Inventory (NBI 2016).

The Interstate Highway System are subjected to weight limits according to Title 23 of the United States Code (Government 1958) and the guidance pamphlet "*Bridge Formula Weights*"

summarizes these limits, most recently revised by the FHWA in May 2015. A formula based on the distance between the outer axles and number of axles in a group was derived to determine the allowable gross weight on any group of two or more consecutive axles on an Interstate Highway System bridge. The maximum gross weight allowed on an Interstate Highway System bridge was set to be 80,000 lbs by the FHWA, unless calculated to be lower (FHWA 2015). A limit of 20,000 lbs per axle and 34,000 lbs per tandem axle is also set by Title 23 of the United States Code (Government 1958).

2.2.5.2. Live Load Distribution Factors - LRFD

Moment capacities of a bridge usually govern when compared to the shear capacities and as a result moment based live load distribution factors (LLDFs) are discussed in this report. Equations for determining the LLDFs (moment or shear based) can be found in the AASHTO LRFD Bridge Design Specifications (AASHTO 2017). Section 4 of the AASHTO LRFD Specifications (AASHTO 2017) outlines the process to calculate the LRFD moment based LLDFs for interior beams (Table 2.12). These may depend on the girder spacing, span length, and transverse stiffness for different types and cross-section of the bridge. The LRFD moment based LLDFs for exterior beams are determined using the lever rule. The deck of the bridge is assumed to be hinged at the interior girder adjacent to the exterior girder whose LLDF is being calculated and the truck is located such that the wheel nearest the exterior girder is located 2 ft. from the barrier or curb. The exterior girder LLDF is determined from is reaction (Barth 2015).

The 1990 NCHRP Project 12-26 (Zokaie et al. 1991) first developed the equations and guidelines for the LRFD LLDFs. Wheel loads were applied to average bridges, developed from data collected from bridge inventories, representing a variety of bridge types. The effect of

geometric variations on the moment and shear based LLDFs was studied. The formulas for LLDFs were developed through three levels of analysis: simplified analysis, graphical analysis, and finite element analysis. The simplified formulas developed were compared with analytical methods and finite element methods (FEM). These formulas, after minor adjustments, are the ones that are included in the *AASHTO LRFD Bridge Design Specifications* (Mertz 2007).

Table 2.12. Moment Live Load Distribution Factors per Lane for Interior Beams in Concrete Bridges (adapted from AASHTO 2017)

Type of Superstructure	Applicable Cross Section from Table 4.6.2.2.1-1 (AASHTO 2017)	Distribution Factors	Range of Applicability
Concrete Deck or Filled Grid, Partially Filled Grid, or Unfilled Grid Deck Composite with Reinforced Concrete Slab on Steel or Concrete Beams; Concrete T-Beams; T- and Double T-Sections	a, e, k, and also i, j if sufficiently connected to act as a unit	One Design Lane Loaded: $0.06 + \left(\frac{S}{14}\right)^{0.4}\left(\frac{S}{L}\right)^{0.3}\left(\frac{K_g}{12.0Lt_s^3}\right)^{0.1}$ Two or More Design Lanes Loaded: $0.075 + \left(\frac{S}{9.5}\right)^{0.6}\left(\frac{S}{L}\right)^{0.2}\left(\frac{K_g}{12.0Lt_s^3}\right)^{0.1}$	$3.5 \le S \le 16.0$ $4.5 \le t_s \le 12.0$ $20 \le L \le 240$ $N_b \ge 4$ $10{,}000 \le K_g \le 7{,}000{,}000$
		Use lesser of the value obtained from the equation above with $N_b = 3$ or the lever rule	$N_b = 3$

2.2.5.3. Live Load Distribution Factors - LFR and ASR

Newmark in 1938 Newmark (1938) first introduced the simplified equations for calculating the LLDFs for the LFD method. These factors take the form of *S/D*, where *S* is the girder spacing and *D* is a factor dependent on the bridge type being analyzed. Deck stiffness, span length, or skew is not considered in this formula. These factors are considered in the LRFD LLDFs. As a result, for bridge characteristics beyond a certain range the LFD distribution factors could be conservation and less accurate (Hueste et al. 2015). Figure 2.1 provides the LFD distribution factors.

Kind of Floor	Bridge Designed for One Traffic Lane	Bridge Designed for Two or more Traffic Lanes
Concrete:		
On steel I-Beam stringers[f] and prestressed concrete girders	S/7.0 If S exceeds 10' use footnote f.	S/5.5 If S exceeds 14' use footnote f.
On concrete T-Beams	S/6.5 If S exceeds 6' use footnote f.	S/6.0 If S exceeds 10' use footnote f.
On timber stringers	S/6.0 If S exceeds 6' use footnote f.	S/5.0 If S exceeds 10' use footnote f.
Concrete box girders[h]	S/8.0 If S exceeds 12' use footnote f.	S/7.0 If S exceeds 16' use footnote f.
On steel box girders	See Article 10.39.2.	
On prestressed concrete spread box Beams	See Article 3.28.	

[f]In this case the load on each stringer shall be the reaction of the wheel loads, assuming the flooring between the stringers to act as a simple beam.

Figure 2.1. *S/D* Distribution Factors (reprinted from AASHTO 1996)

2.3. STATE-OF-THE-ART LITERATURE

2.3.1. Field Testing of Bridges

One of the common practices for bridge load rating is field testing. Vehicles with known weight are driven over the bridge at various configurations and the behavior of the bridge is studied. The load rating of the bridge is determined based on the measured response of the bridge.

Experimental load testing on a bridge is of two types: diagnostic and proof testing. The bridge is subjected to a load closer to its rated capacity in a diagnostic test. The corresponding response is used to develop a numerical model to help estimate the maximum allowable load.

Conversely, in a proof test the bridge is subjected to incremental loads until the targeted load or a limit state is reached. Thus, the operating capacity of the bridge is determined (Chajes 1997).

In a 2012 study (Jones and Shenton 2012), the University of Delaware Center for Innovative Bridge Engineering, evaluated the effective width of slab bridges specific to the state of Delaware and developed an improved formula to calculate the slab effective width of these bridges. This was done by carrying diagnostic load tests on a set of six slab bridges. The live load distribution factor applied to a slab is influenced by its effective width, which consequently alters the live load effect on the bridge and hence its Rating Factor (RF). A typical load test consisted of strain transducers mounted at the mid-span on the underside of the slab, spaced at approximately every two feet. Loaded Dump trucks, whose axle weights and axle spacing were pre-measured, were driven slowly across each bridge and the strains recorded. The trucks were driven at different transverse positions along the bridge. In some tests, multiple trucks were driven together across the bridge. The effective width was determined for each type of truck pass.

With the measured data from the field tests, the plots of the longitudinal strain vs. the transverse position of the sensor were generated for each bridge. Using the area under the curve of the generated plots, new plots that had a constant strain with the same area under the curve as the original plot were made. The effective width was found to be one half the width of the constant strain plot. The multi-presence factor from the AASHTO LRFD effective width equations was removed after carrying out some calculations. Then the normalized AASHTO LRDF effective width was plotted against the aspect ratio (length divided by width) of the bridge. In addition, the new field measured normalized effective widths were graphed against their aspect ratio on the same plot. Based on these plots new equations were developed by fitting the equations of the new

curves to the same form as given in AASHTO. These are presented in Table 2.13 and compared with the current AASHTO LRFD effective width equations.

Table 2.13. Comparison of Delaware Effective Width Equations for Slab Bridges with AASHTO LRFD Bridge Design Specifications (adapted from Jones and Shenton 2012)

	AASHTO LRFD	University of Delaware Study
Effective Width (in.) per lane for one lane loaded	$E = 10.0 + 5.0\sqrt{L_1 W_1}$	$E = 10.0 + 5.8\sqrt{L_1 W_1}$
Effective width (in.) per lane for multiple lanes loaded	$E = 84.0 + 1.44\sqrt{L_1 W_1} \leq \frac{12.0 W_1}{N_L}$	$E = 84.0 + 2.06\sqrt{L_1 W_1} \leq \frac{12.0 W_1}{N_L}$

where,

E = Equivalent or effective width (in.)

L_1 = Modified span length taken equal to the lesser of the actual span length or 60.0 ft

W_1 = Modified edge-to-edge width of the bridge taken to be equal to the lesser of the actual width or 60.0 ft for multilane loading, or 30.0 ft for single-lane loading

W = Physical edge-to-edge width of the bridge (ft)

N_L = Number of design lanes

The live load distribution factors (LLDF) for the loaded area of the slab bridge decreases if the effective width is increased, as suggested by this study. This decreases the live load effect on that region, thereby increasing the RF for that region and the overall RF for the bridge. These new formulae have been included in the rating software of the Delaware Department of Transportation. Which, as a result, has improved posting restrictions of over fifty bridges in Delaware (Arndt et al. 2017; Jones and Shenton 2012).

In his paper, Amer et al. (1999) used the grillage analogy method to identify the main parameters influencing the equivalent width of slab bridges, compared the equivalent widths of slab bridges defined in the standard AASHTO and LRFD Specifications with those based on field tests and analyses, and proposed a simple design formula for the effective width of solid slab bridges. The authors define the equivalent width as the ratio of total area under the moment distribution curve to the maximum moment. The main parameters affecting the equivalent width of slab bridges were identified by investigating twenty-seven cases using the grillage analogy. The main parameters considered in this study were the span length, bridge width, slab thickness, edge beam, and number of lanes. A parametric study was carried out using AASHTO HS-20 standard truck. The truck was located in the longitudinal direction to obtain the maximum bending moments. It was found, through the limited study, that variation of slab thickness and bridge width had very little effect on the equivalent width. However, the edge beam depth was found to significantly affect the equivalent width of the slab bridge. Increasing the moment of inertia of the edge beam increased the edge beam moment. This reduced the maximum moment intensity in the slab, consequently increasing the equivalent width. Based on the parametric studies, Amer et al. (1999) proposed the following equation to calculate the equivalent width (m) over which the truck load is assumed to be uniformly distributed:

$$E = 2.10 + 0.23L \leq \frac{W}{N_L} \tag{2.6}$$

where:

E = Equivalent width (m)

L = Span length (m)

W = Bridge width (m)

N_L = Number of design lanes.

This equation is limited to spans up to 12.19 m (40 ft) and slab thickness up to 0.36 m (14 in.). The effect of any edge beam, if present, is taken into account by multiplying Eqn. (2.6) with the factor C_{edge} defined as:

$$C_{edge} = 1.0 + 0.5(d_1 - 0.15) \geq 1.0 \tag{2.7}$$

where:

d_1 = Edge beam depth above slab thickness (m)

Three field tests were carried out to validate the proposed equivalent width equation. The field measured strains were multiplied by the slab section modulus and elastic modulus of the concrete to calculate the moments. Then, the same principle was used to determine the field measured equivalent width for the slab bridges. The equivalent widths determined using the proposed equation agreed with those determined using field measurements and grillage analogy.

Washer (1998) discussed the use of non-destructive testing for load rating of highway bridges. A bridge is instrumented with accelerometers, strain gauges, and deflection gauges that are used to record the structural response to an applied load. This response is then analyzed to determine the capacity of the bridge. However, Washer (1998) noted that bridge instrumentation

can be a time consuming and disruptive procedure that could be eliminated by remote measurement systems. Remote non-contact deflection measurements can be precisely obtained using a frequency modulated laser. Scanning from a single point over large sections is achieved by fitting the laser with servo-controlled motors, thus requiring no targets for measurements. This is the design principle of the laser radar system. A wireless bridge monitoring system using a network of microwave transponders and a controller has also been developed by the non-destructive evaluation (NDE) research program of the Federal Highway Administration (FHWA). Data, such as strain, rotation, deflection and vibration, are collected by the transponder and downloaded to the local controller, thereby eliminating the long wire runs from the instruments to the data acquisition system and any associated noise (Washer 1998).

Catbas et al. (2012) proposed a novel approach for structural health monitoring of bridges using computer vision techniques. Together with operating traffic image and traditional sensor data, this methodology can be extended to determine load rating of bridges. After consultation with bridge engineers, the Sunrise Bridge in Fort Lauderdale, Florida was selected for monitoring due to its typical condition, material, and geometric characteristics. This 1989 movable bridge has double bascule leaves carrying three lanes of traffic. Strain gauges, accelerometers, and tiltmeters were installed across the bridge to monitor its response to operating traffic. A video camera was installed at the bridge entrance to capture images of the vehicles during operation. These image data were matched with sensor data to record the bridge response for a given type of vehicle and to extract the unit influence line (UIL). Two UILs were developed, one corresponding to a fully loaded bus and another to an empty bus. These UILs could then be used to estimate the upper and lower bounds for the load rating of a bridge. An FEM model of the bridge, using shell elements, frames, rigid links, and solid elements, was developed in SAP2000. The results from the model

were used to validate the load rating from operational traffic and UILS, both of which showed excellent correlation.

Ji and Zhang (2012) created a method to measure displacements of civil structures using a digital camera, recording planar targets placed on vibrating structures. The computational connection between real space and the image plane was determined using computer vision. Point reconstruction rules were used to quantify the structural displacement at the location of the target. The displacement measurement method consists of three steps: camera calibration, object tracking, and point reconstruction. A fully calibrated camera is needed to detect all intrinsic and extrinsic camera parameter geometric data. The intrinsic parameters specify the optical and geometric attributes of the camera. Extrinsic parameters are used to transform the pixel coordinate system of the image into a pre-specified object coordinate system. In this study three different experiments have been carried out to validate the suggested technique. In the first experiment, a fixed planar pattern on a shake table was measured. In the second, the same pattern was placed at the end of a cantilever beam to measure the displacement during free vibration. In the last experiment, the dynamic displacement of a girder bridge was measured (Ji and Zhang 2012).

Miller et al. (1994) conducted a destructive test on a decommissioned reinforced concrete slab bridge. The bridge had a skew angle of 30 degrees, two lanes and severely deteriorated shoulders. It was incrementally loaded to a maximum load of 720 kips (3200 kN) by means of a hydraulic loading system, designed to simulate the HS20-44 truck loading. During the various stages of the incremental loading process, behavioral changes were observed in the bridge response that may be attributed to the boundary conditions. Shear failure initiated in the deteriorated shoulders over the piers and the crack propagated through the slab. At the maximum load of 720 kips, which is equivalent to 10 HS20 trucks, the slab failed in punching shear. This failure load

was found to be significantly lower than that predicted by the AASHTO Guide Specifications (AASHTO 1989) suggesting that the shoulder deterioration affected the failure mode. Bridge design load (demand) and capacity were computed via three methods: effective strip model, linear finite element analysis, and nonlinear finite element analysis. Core samples from the bridge were tested to determine the material properties for concrete and steel and these values were used in the analytical models. It was found that the effective strip model gave highly conservative estimates of bridge capacity. The flexural demand obtained from linear finite element analysis was 45 percent lower than that determined from the effective strip model, because of its capability to account for load distribution mechanisms in the slab such as slab action and effect of skew. Nonlinear finite element analysis yielded a demand approximately similar to that obtained from the linear finite element analysis due to bridge failure prior to the onset of nonlinear behavior. However, due to the consideration of factors such as slab action, membrane action, cracking, effect of skew, boundary effects, and actual material responses, nonlinear finite element analysis is expected to provide improved results.

Lantsoght et al. (2016) field tested a reinforced concrete slab bridge to failure, followed by laboratory testing of three beams sawn from the bridge. This research was carried out because, in the Netherlands, several existing reinforced concrete slab bridges were found to be unsatisfactory under shear assessment. The example bridge has five spans supported over four cross-beams cast integrally onto the piers and a skew angle of 18 degrees. During the field test, two spans were loaded with the tandem load outlined in the *Eurocode 1: Actions on Structures* (CEN 2011). Although flexural distress was observed in the first span, failure due to flexure was not achieved. This may be due to the integral nature of the bridge whereby the moment capacity of the span is higher through the effect of support moments, rather than assuming hinge supports. In the second

span, flexural failure was achieved for increased applied load. It was found that the CEN (2011) estimated the flexural capacity of the bridge satisfactorily, however the shear capacity of the bridge was higher than that predicted by the CEN (2011).

Santini-Bell et al. (2013) conducted a case study highlighting the advantages of a bridge rating procedure incorporating three-dimensional structural modeling, structural health monitoring, and non-destructive testing during the design phase. They installed strain gauges on the girders of Powder Mill Pond Bridge in Massachusetts, which is a three-span, continuous composite steel-girder bridge with a reinforced concrete deck, during fabrication. Prior to opening the bridge to traffic, it was subjected to pseudo-static loading and the results were used to calibrate a baseline structural model. The three-dimensional structural model for bridge management and experimental load rating was developed in SAP2000. It consisted of frame elements and shell elements representing the steel girders and concrete deck, respectively. The load rating factor (RF) was calculated using the AASHTO LRFR method and was found to be lower than that obtained from the three-dimensional finite element model. Two scenarios for girder section loss were simulated in the model, one for an external girder and one for an internal girder. Girder RFs for the two scenarios were first calculated assuming section loss over the entire length and then assuming section loss over the damaged area only. In the AASHTO LRFR procedure, the girder RFs were calculated assuming section loss over the entire girder length. The resulting RFs were again observed to be lower than those obtained from the cases modeled. Thus, the authors called for adjustments in the overall process of bridge design, inspection, and rating to incorporate instrumentation and modeling to accurately rate bridges.

2.3.2. Investigation of Material Properties

Pucinotti (2015) outlined the results of numerous destructive and non-destructive tests performed on the historic National Museum of Reggio Calabria in Italy for concrete strength assessment. Laboratory tests were carried out on cores extracted from selected structural elements to determine the compressive strength of concrete. These results were compared to the estimated concrete compressive strength based on non-destructive testing. The three non-destructive methods highlighted in this paper are the rebound method, the ultrasonic pulse velocity method, and the combined method (SonReb). A correlation curve was developed for each indirect method and the results calibrated with laboratory test results of concrete cores. It was found that satisfactory results were obtained from the ultrasonic pulse velocity method when compared with the results from the destructive tests. However, the author observed that the accuracy of the assessment of the in-situ compressive strength increased when combined methods are engaged.

Although material testing of the samples gives more accurate strength values, recent research has shown that strength properties of concrete and steel can accurately be inferred from nondestructive test data (Huang et al. 2011; Schindler 2005). Huang et al. (2011) explored using ultrasonic pulse velocity (UPV) and rebound number (RN) for predicting the concrete compressive strength of existing structures. While the RN gave information about the concrete strength at the surface of the concrete, the UPV test reflects interior concrete properties. The authors developed a probabilistic model to predict the compressive strength of concrete using information from rebound hammer and UPV tests. The water-cement ratio and the age of the concrete were taken into the account in their formulation; results showed the concrete compressive strength was modeled well when compared to other regression models.

Breysse (2012) reviewed past models to estimate the concrete strength based on non-destructive evaluation methods. The quality and efficiency of the strength estimation depended on the sensitivity of concrete strength to the NDT measurement, the variation of the measured NDT values in relation with range of variation of concrete strength being investigated, and the magnitude of error in the measurement. Several empirical models to establish a relation between NDT measurements and the concrete strengths have also been proposed in the past. However, it was observed that the model error was considerably small when compared to the measurement error. It was also shown that combining NDT measurement techniques whose quality of measurement are of the same order could produce effective concrete strength measurements. Analysis of datasets from laboratory tests show that combining rebound hammer test and ultrasonic pulse velocity gave good quality measurement of the concrete strength.

2.3.3. Modeling and Analysis

Finite element models, developed using various commercial software packages, provide tools for studying bridge behavior and response to different types of loading, for bridge rating and for undertaking parametric studies. Several studies are described below.

Hueste et al. (2015) investigated the practicability of spreading out precast slab beams using 4 in. thick precast concrete panel (PCP) spanning in between as stay-in-place forms topped with a minimum 4 in. thick cast-in-place reinforced concrete deck. Design guidelines for this type of spread slab beam bridge system were developed. The feasibility of the spread slab beam bridge was confirmed by testing a full-scale specimen of the bridge at the Texas A&M University Riverside Campus. The bridge was instrumented with load cells, spring potentiometers, and accelerometers, and tested under service loads. Similarly, a spread slab beam bridge on US 69 in

Grayson County, Texas was instrumented, and field tested. The measured bridge response was used to verify two computational models, grillage method and FEM, to examine the load sharing behavior for a range of bridge geometries. The grillage method is the most basic computational modeling approach in which the deck and girders are assumed to be a mesh of beam elements in orthogonal directions. The grillage model of the two bridges were developed in SAP2000 using longitudinal frame elements for the slab beams and transverse beams to distribute the applied deck loads. Three-dimensional FEM models of the two bridges using solid brick elements were developed using two commercial software, Abaqus (Dassault Systemes 2013) and CSiBridge (Computers and Structures 2015). The FEM models were found to provide more accurate deflections and live load distribution factors (LLDFs). Using the developed modeling approach and parameters, parametric studies were conducted and shear and moment LLDFs for the design of spread slab beam bridges were developed.

Davids et al. (2013) developed a finite element model for load rating flat slab bridges. The slab moments predicted from the finite element model were compared to the results from live load testing of an in-service instrumented flat-slab bridge. It was found that the finite element model gave conservative predictions of the slab moments when compared to the live load tests. Fourteen flat slab bridges were load rated with the developed finite element model and the equivalent strip method – a simplified method of analysis for flat slab bridges prescribed by AASHTO. Despite the conservatism of the developed finite element model, it predicted higher rating factors when compared to the equivalent strip method. This study showed that a significant amount of flat slab bridges with low rating factors according to the AASHTO equivalent strip method may have the potential for increased rating factors.

Sanayei et al. (2016) presented a comparison of three approaches used to load rate a concrete-steel composite bridge based on the LRFR approach. The three approaches included: (1) the conventional design office load rating technique using a simplified line girder analysis, (2) modified conventional load rating based on input from measurements from diagnostic load tests, and (3) a finite element modeling approach that accounted for the 3D structural system behavior. In the three-span continuous composite concrete slab on steel girder bridge, that was part of this investigation, it was consistently found that the load rating of the girders based on non-destructive diagnostic tests and the FEM model were greater compared to the load rating based on the conventional method.

Yousif and Hindi (2007) compared the AASHTO LRFD LLDFs with those obtained from a FEM model that was developed for simple span slab-on-girder concrete bridges. A thorough investigation of the LLDFs prescribed by AASHTO LRFD Specifications (AASHTO 2004) with regards to span length, slab thickness, girder spacing, and longitudinal stiffness was conducted. Finite element models for a wide range of bridges were developed in SAP2000. Several models were investigated to determine an accurate representation of the superstructure. The selected model idealizes the bridge as a two-dimensional system (Figure 2.2). The model uses four-node quadrilateral shell elements with six degrees of freedom (DOF) at each node to represent the bridge deck, and two-node space frame elements with six DOF at each node to represent the girders and end diaphragm beams. Hinges and rollers were used to model the simply supported span of the bridge. The models were subjected to vehicular load and standard lane load as prescribed by AASHTO LRFD Specifications (AASHTO 2004). Each bridge was loaded in one-lane, two-lane, and three-lane loading scenarios. It was concluded that the AASHTO LRFD LLDFs are conservative compared to the analysis results from the finite element models.

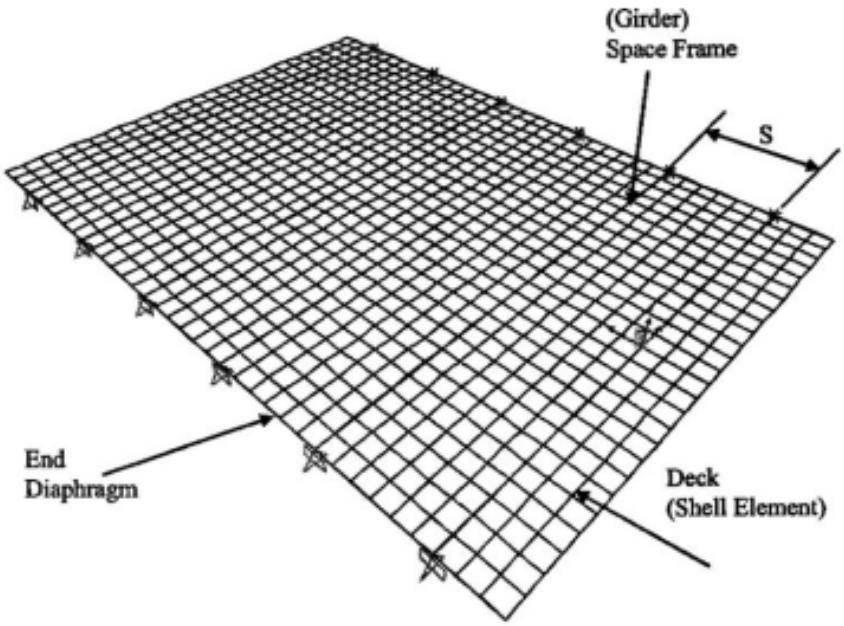

Figure 2.2: Finite-element model using SAP2000 (reprinted from Yousif and Hindi 2007)

Suksawang and Nassif (2007) carried out a parametric study to determine the effect of bridge parameters on the LLDFs. Five steel I-girder bridges were modeled and analyzed using ABAQUS (Dassault Systemes 2013) software. A comparison between two different idealizations (shell-shell and shell-beam) resulted in the selection of a shell-beam (SB) model (Figure 2.3) due to reduced computation time. In this model, the concrete deck is represented by four-node shell elements with six degrees of freedom while two-node beam elements with six degrees of freedom represent the steel girders. A rebar element was used to model the reinforcing bars in the concrete deck. All material properties were based on laboratory testing results of identical samples. The connectivity between the shell and beam elements was modeled using multiple-point constraint (TIE MPC) and the end supports were modeled using roller-pin boundary conditions. The bridge response obtained from the analysis of the FEM models was compared with field test results of the

five bridges. It was found that the LLDFs were sensitive to girder spacing and stiffness. After a thorough comparison of the various LLDF equations and verification against field test results, simpler yet accurate equations for LLDFs were proposed. These equations are of the traditional *S*-over form and independent of the girder stiffness.

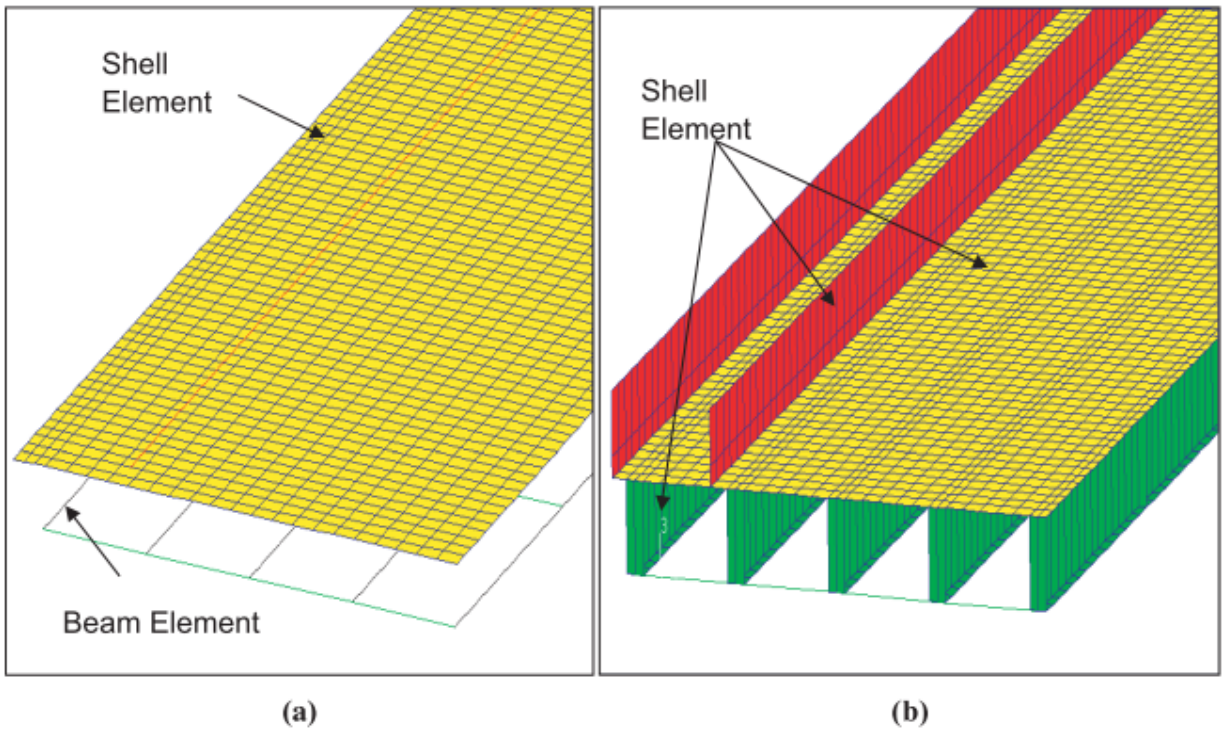

Figure 2.3: Finite-element models: (a) shell-beam model; (b) shell-shell model (reprinted from Suksawang and Nassif 2007)

Barth and Wu (2006) studied the ultimate load behavior of slab-on-steel girder bridges using three-dimensional nonlinear finite element analysis. The bridge model was created in ABAQUS (Dassault Systemes 2013) with four-node shell elements representing the girders, slab and stiffeners, one-dimensional strain theory elements representing the steel reinforcement in the concrete slab, and two-node Timoshenko beam element representing cross frames. Multiple point

constraint (MPC) beams modeled the full composite action between the deck and girders. The finite element model was validated against ultimate test results from two concrete composite steel plate girder bridges and a four-span continuous composite steel bridge. In the model, concrete behavior was represented by two methods: smeared concrete cracking and concrete damaged plasticity. It was found that the ultimate behavior of the simple span bridges was efficiently captured by the smeared crack model, while that of the continuous span bridge was captured reasonably well by the concrete damaged plasticity model.

2.4. LOAD POSTED BRIDGE INVENTORY - TEXAS

The number of load posted bridges in Texas and their distribution across the various bridge classifications is tabulated in Table 2.14. In this table, the first two condition classifications are used by the FHWA to catalog posted bridge conditions. Structurally deficient (SD) bridges have reduced load carrying capacity due to critical deformations and/or deteriorations and functionally obsolete (FO) bridges fail to satisfy the initial standard design criteria. A third classification, sub-standard for load only (SSLO), was defined by TxDOT. SSLO bridges are not structurally deficient or functionally obsolete but have a load carrying capacity below the legal limit. This type of bridge is the perfect candidate for improvement of load postings and is further investigated in this thesis. On-system bridges are maintained by TxDOT as they are part of a designated highway system. On the other hand, off-system bridges are maintained by a county or a city government body.

Table 2.14. Load Posted Bridges in Texas by Condition Classification

Condition Classification	On-System	Off-System	Total
Structurally Deficient (SD)	39	473	512
Functionally Obsolete (FO)	58	572	630
Sub-Standard for Load Only (SSLO)	78	891	969
Total	175	1936	2111

The selected bridge types for further study in this thesis were concrete slab bridges and concrete multi-girder bridges. Out of a total of 969 Texas SSLO bridges, 25 percent are comprised of concrete bridges. This further breakdowns to 42 on-system simple-span concrete slab bridges and 59 off-system simple-span concrete slab bridges. Simple-span concrete multi-girder bridges constitute 15 percent of the concrete SSLO bridges. These bridges are listed in Table 2.5.

Table 2.15. SSLO Bridge Inventory in Texas

Material/Design	Bridge Type	No. of Bridges		Total
		On System	Off System	
Steel	Stringer/Multi-beam or Girder	14	243	257
Concrete	Slab	42	59	101
Concrete	Stringer/Multi-beam or Girder	2	35	37
Steel Continuous	Stringer/Multi-beam or Girder	6	103	109
Prestressed	Other	0	68	68
Concrete Continuous	Slab	4	38	42

3. CURRENT LOAD RATING PROCEDURES

3.1. ALLOWABLE STRESS RATING (ASR) AND LOAD FACTOR RATING (LFR)

The older methods to load rate existing bridges, ASR and LFR, are discussed in Part B of the AASHTO MBE. The general equation to obtain the RF, is shown in Eqn. (3.1).

$$RF = \frac{C - A_1 D}{A_2 L(1 + I)} \tag{3.1}$$

where:

RF = Rating Factor for the live load carrying capacity

C = Capacity of the member

D = Dead load effect on the member

L = Live load effect on the member

I = Impact factor to be used with the live load effect

A_1 = Factor for dead loads

A_2 = Factor for live load

One difference between the old methods and the LRFR method is that the latter has different levels of lad rating. ASR and LFR methods analyze the bridge subjected to either the design truck load or one of the legal loads. The design truck in these methods correspond to the HS-20 truck configuration. If the RF for the bridge under the design truck is greater than 1.0, the bridge can carry all AASHTO and state legal loads.

3.2. LOAD AND RESISTANCE FACTOR RATING

Each component of the bridge is assigned an RF based on Eqn. (3.2) and the lowest RF governs the rating of the bridge. The general equation to obtain the bridge RF using the LRFR method is shown in Eqn. (3.2).

$$RF = \frac{C - (\gamma_{DC})(DC) - (\gamma_{DW})(DW) \pm (\gamma_P)(P)}{(\gamma_{LL})(LL + IM)} \quad (3.2)$$

where:

RF = Rating Factor

C = Capacity

DC = Dead load effect due to structural components and attachments

DW = Dead load effect due to wearing surface and utilities

P = Permanent loads other than dead loads

LL = Live load effect

IM = Dynamic load allowance

γ_{DC} = LRFD load factor for structural components and attachments

γ_{DW} = LRFD load factor for wearing surfaces and utilities

γ_P = LRFD load factor for permanent loads other than dead loads = 1.0

γ_{LL} = Evaluation live load factor

The load rating procedure is represented in the form of a flowchart in the AASHTO MBE (AASHTO MBE 2018) as shown in Figure 3.1. The design truck for the LRFR method is the HL-93 load model. This includes the HS-20 truck along with a lane load (AASHTO 2014). The first step of the rating procedure is design load rating. Here the inventory rating and operating rating

for the bridge under the design truck is evaluated. The number of HL-93 loads that can safely travel the bridge for an indefinite time period is determined from the inventory RF. The absolute maximum load that can traverse the bridge once, in terms of the number of HL-93 loads, is determined using the operating RF.

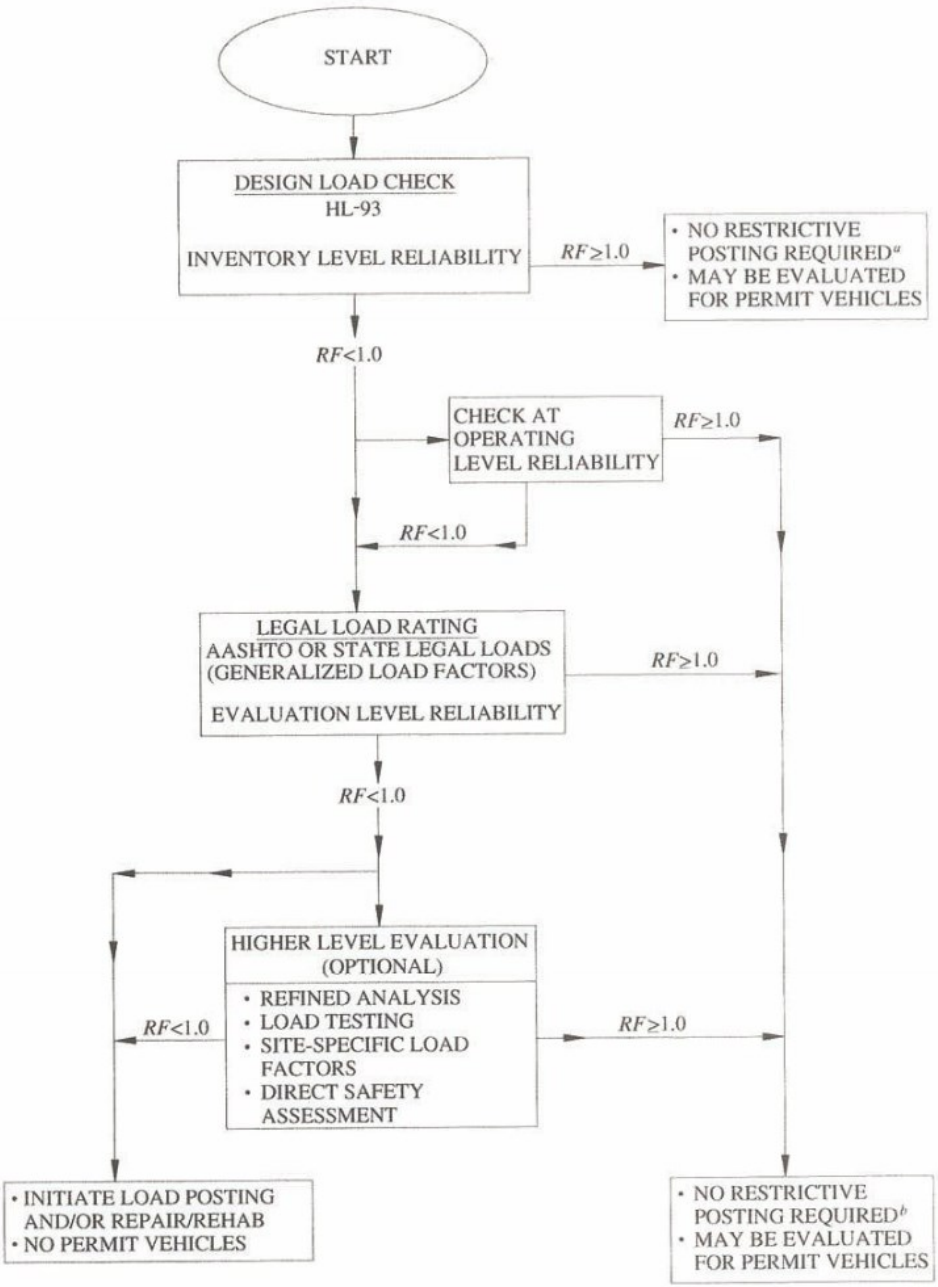

Figure 3.1. AASHTO MBE Load Rating Procedure Flowchart (reprinted from AASHTO MBE 2018)

3.3. TxDOT PRACTICES

All bridges designed after October 1, 2007 are required by the FHWA to be designed in accordance to the LRFD method. The LRFR method is currently used by TxDOT to load rate all existing bridges designed using the LRFD guidelines. However, the load posted bridges in Texas were built prior to 2007. Hence, TxDOT analyzes these bridges using the ASR or LFR approach. All on-system bridges are analyzed using the LFR approach by TxDOT while off-system bridges could be analyzed using either ASR or LFR. H-20 and HS-20 design trucks are used to analyze the bridges and the load posing for the bridges are determined using one of three flowcharts. On-system bridges are rated using the flowchart provided in Figure 3.2. The flowchart in Figure 3.3 is used to load rate off-system bridges. Concrete bridges with no structural plans are load rated using the flowchart provided in Figure 3.4. TxDOT adopts a simplified load posting procedure to determine the posting for the bridge as shown in Figure 3.5. Please note that Item 58 corresponds to the Deck Condition Rating in the NBI, Item 59 the Superstructure Condition Rating in the NBI, Item 60 the Substructure Condition Rating in the NBI, and Item 62 the Culvert Condition Rating.

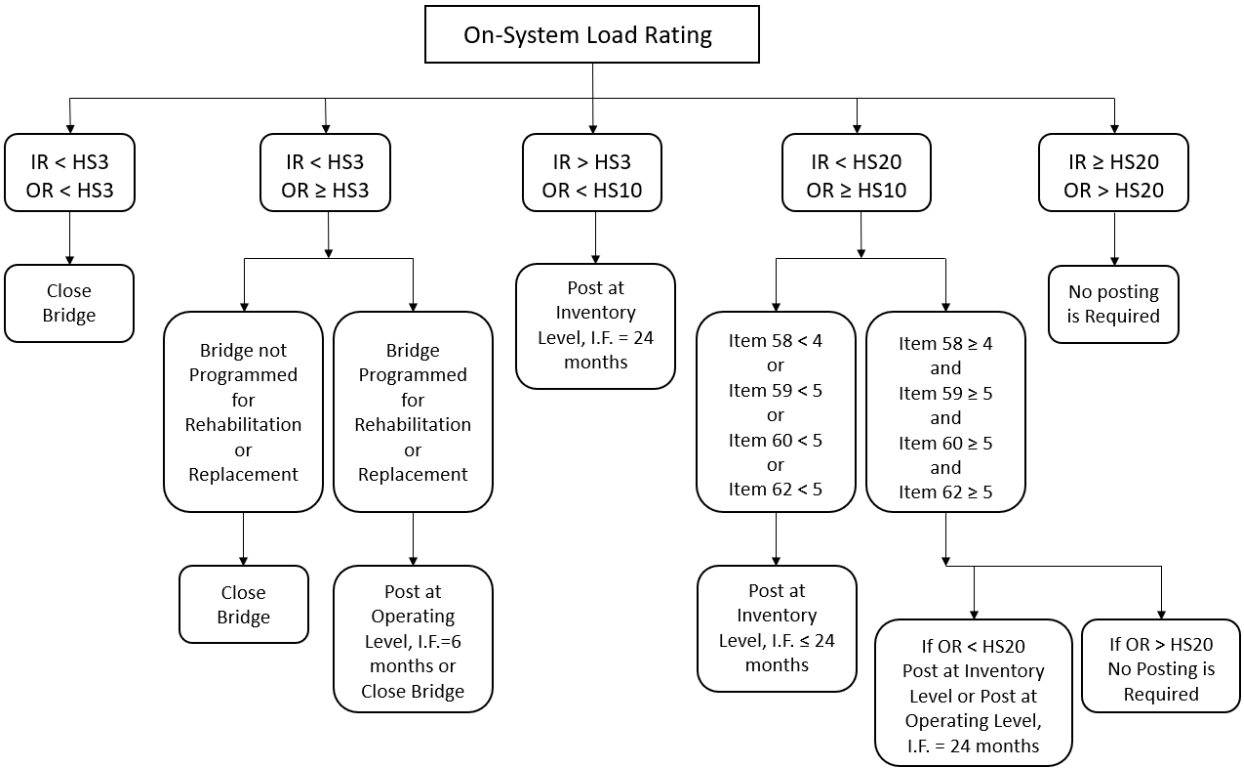

Figure 3.2. TxDOT On-System Load Rating Flowchart (adapted from TxDOT (2018a))

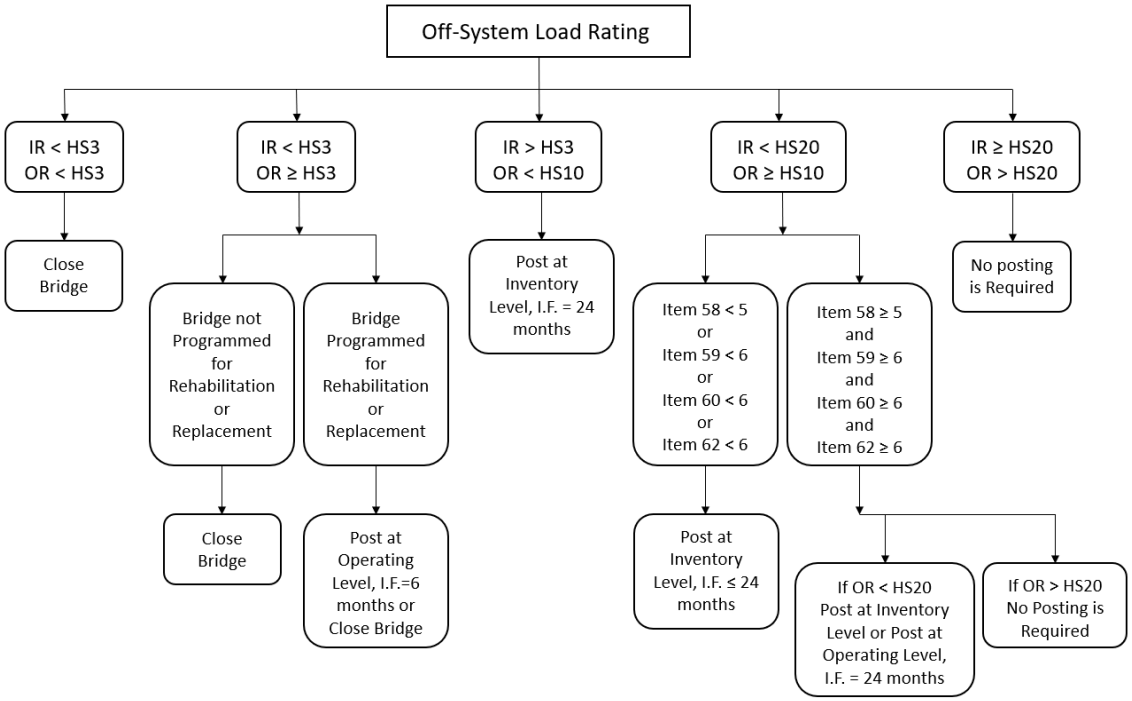

Figure 3.3. TxDOT Off-System Load Rating Flowchart (adapted from TxDOT (2018a))

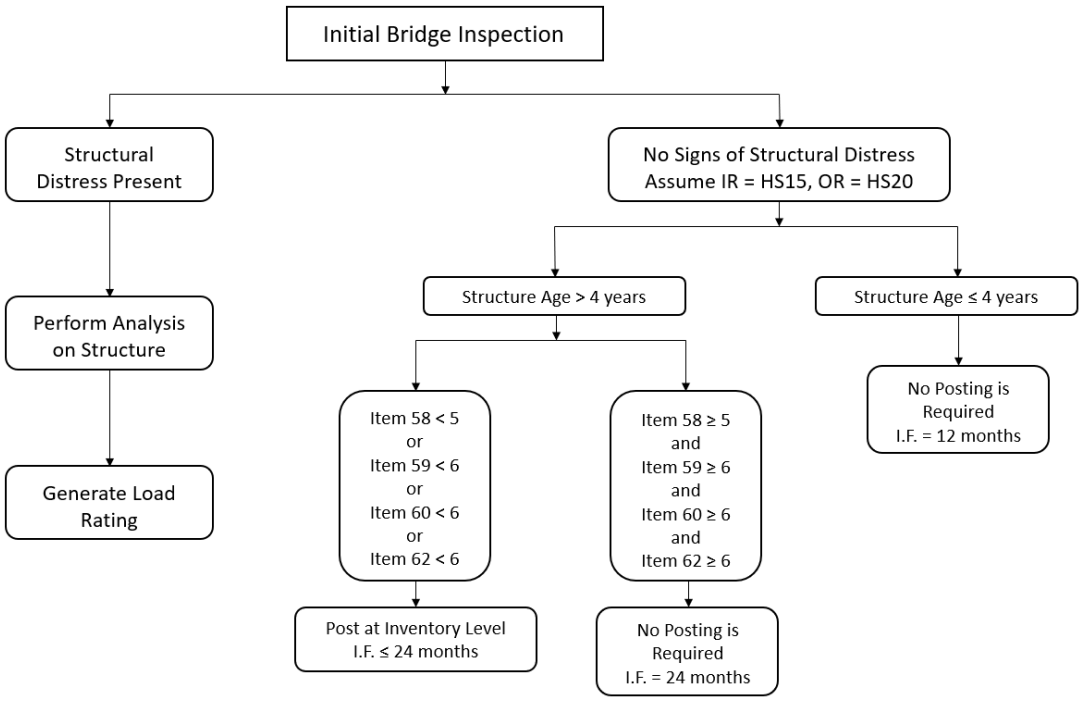

Figure 3.4. TxDOT Load Rating Flowchart for Concrete Bridges and Bridge Decks with No Plans (adapted from TxDOT (2018a))

SIMPLIFIED LOAD POSTING PROCEDURE

This procedure is appropriate for computing posting loads equivalent to the inventory rating. Approximations are involved which make this procedure unacceptable at load levels higher than the Inventory Rating.

The posting load in pounds is the product of the RATING MULTIPLIER and the INVENTORY RATING in tons for the standard "H" truck. In selecting the RATING MULTIPLIER from the table use the longest simple span length or 80% of the longest continuous span length, whichever gives the longest span length for the bridge. If the resulting span length is 160' or greater, then the bridge should receive an analysis more exact than this procedure.

The recommended posting increments are listed below. Round off to the nearest increment listed.

Post axle and gross load for span lengths 40' and greater. Post axle load only for span lengths 39' and less. Weight limit signs should conform to the Texas Manual on Uniform Traffic Control Devices. The recommended signs are R12-2Tb or R12-4Tb except if the axle load is noted "*" use signs R12-2Tc or R12-4Tc.

EXAMPLE 1
35' Simple Span Slab & Girder Bridge, H14 Rating
Axle = 14 x 1,450 = 20,300 lbs.
Post 21,000 tandem axle (Signs R12-2Tc)

EXAMPLE 2
120' Pony Truss, H7 Rating
Axle = 7 x 1,450 = 10,100 lbs.
Gross = 7 x 2,300 = 16,100 lbs.
Post 10,000 lbs. Axle or tandem and 16,000 lbs. Gross (sign R12-4Tb)

EXAMPLE 3
30'-40'-30' Continuous Slab Bridge with
25' slab approach spans, H10 Rating.
0.80 x 40' = 32'>25' = Use 32' span
Axle = 10 x 1,480 = 14,800 lbs.
Post 15,000 lbs. Axle or tandem (Sign R12-2Tb)

EXAMPLE 4
25' Simple Span Timber Bridge, H2 Rating
Axle = 1,550 x 2 = 3,100 lbs.
Recommendation: Close bridge until repair increases capacity.

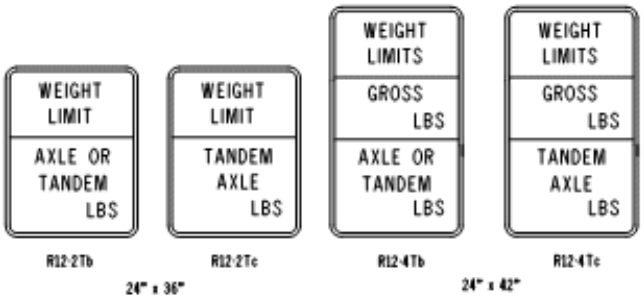

SPAN	RATING MULTIPLIER	
	AXLE OR TANDEM	GROSS
FEET	LBS. H-TON	LBS. H-TON
≤ 20	1,600	
25	1,550	
30	1,500	
35	1,450	
40	1,450	3,100
45	1,450	2,950
50	1,450	2,800
60	1,450	2,600
70	1,450	2,500
80	1,450	2,450
90	1,450	2,400
100	1,450	2,350
120	1,450	2,300
140	1,450	2,250
160	1,450	2,200

LOAD INCREMENTS FOR AXLE OR TANDEM LBS.	LOAD INCREMENTS FOR GROSS LBS.
5,000	8,000
7,500	10,000
10,000	12,000
12,500	14,000
15,000	16,000
17,500	20,000
21,000*	24,000
24,000*	28,000
28,000*	32,000
32,000*	36,000
	40,000
	44,000
	48,000
	52,000
	60,000
	68,000
	76,000

*Axle load exceeds 20,000 lbs. Single axle limit, therefore post for tandem axle (Signs R12-2Tc or R12-4Tc).

Figure 3.5. TxDOT Simplified Load Posting Procedure Guide (reprinted from TxDOT 2018a)

In Table 3.1 and Table 3.2, the condition ratings, operating ratings and inventory ratings of the superstructure for the selected SSLO concrete bridges as determined by TxDOT from the inspections are summarized. The tables also include the rating method used and the corresponding operating and inventory level HS-20 RFs. The tonnage rating provided in the table is calculated by multiplying the RF by 20. The rating of a bridge may be controlled by the deck, superstructure or substructure. In this thesis, the main focus was on the rating process of the superstructure. It should be noted that for some of the bridges listed in the following tables, the substructure governed the rating.

A number of these SSLO bridges listed have an operating RF close to 1.0 (as high as 0.99) or greater than 1.0. If the condition rating of the different components is greater than or equal to 6 (Satisfactory), then from Figure 3.2 and Figure 3.3 these postings are not required. However, these bridges may be posted to continue with the earlier posting based on the bridge inspection engineer's discretion.

Table 3.1. TxDOT Superstructure Load Ratings and Condition Ratings for Selected SSLO Concrete Slab Bridges (adapted from NBI 2016)

ID	On/Off System	Condition Rating			TxDOT Rating Method	Controlling Component	Tonnage Rating (US Tons)		HS20 RF	
		Deck	Superstr.	Substr.			Inv.	Oper.	Inv.	Oper.
CS-1	Off	6	6	5	ASR	Substructure	15	20	0.74	0.99
CS-2	Off	4	4	4	N/A	Assumed Superstructure	15	20	0.74	0.99
CS-3	Off	5	5	6	N/A	Assumed Substructure	15	20	0.74	0.99
CS-4	On	6	6	6	LFR	Superstructure	10	16	0.48	0.78
CS-5	On	7	7	7	LFR	Superstructure	8	14	0.41	0.69
CS-6	Off	6	6	5	N/A	Assumed Superstructure	15	20	0.74	0.99
CS-7	Off	6	5	6	LFR	Superstructure	7	10	0.33	0.50
CS-8	On	6	6	6	LFR	Substructure	10	18	0.50	0.91
CS-9	On	6	6	7	LFR	Superstructure	9	18	0.43	0.88
CS-10	On	8	6	7	LFR	Superstructure	10	17	0.52	0.85
CS-11	On	6	6	6	LFR	Superstructure	10	16	0.48	0.78
CS-12	On	6	6	6	LFR	Superstructure	8	18	0.40	0.88
CS-13	On	7	7	6	LFR	Superstructure	10	23	0.52	1.13
CS-14	On	7	7	6	LFR	Superstructure	11	19	0.55	0.94
CS-15	On	7	7	6	LFR	Superstructure	11	19	0.55	0.94
CS-16	On	7	7	6	LFR	Superstructure	11	19	0.55	0.94
CS-17	On	7	7	7	LFR	Superstructure	9	19	0.47	0.96
CS-18	On	7	7	6	LFR	Superstructure	9	15	0.44	0.74
CS-19	On	6	6	6	LFR	Superstructure	10	19	0.50	0.96
CS-20	Off	7	7	5	N/A	Assumed Superstructure	15	20	0.74	0.99
CS-21	Off	6	6	5	N/A	Assumed Superstructure	15	20	0.74	0.99
CS-22	Off	7	7	7	N/A	Assumed Superstructure	10	15	0.50	0.74
CS-23	Off	6	6	5	N/A	Assumed Superstructure	15	20	0.74	0.99

Condition Ratings:
0 = Failed Condition
1 = "Imminent" Failure Condition
2 = Critical Condition
3 = Serious Condition
4 = Poor Condition
5 = Fair Condition
6 = Satisfactory Condition
7 = Good Condition
8 = Very Good Condition
9 = Excellent Condition

N/A means that TxDOT did not perform load ratings for this bridge and it is therefore most likely posted based on precedent.

Table 3.2. TxDOT Superstructure Load Ratings and Condition Ratings for Selected SSLO Concrete Multi-Girder Bridges (adapted from NBI 2016)

ID	On/Off System	Condition Rating			TxDOT Rating Method	Controlling Component	Tonnage Rating (US Tons)		HS20 RF	
		Deck	Superstr.	Substr.			Inv.	Oper.	Inv.	Oper.
CM-1	On	7	6	6	LFR	Superstructure	8	11	0.40	0.55
CM-2	On	7	7	7	LFR	Assumed Superstructure	10	17	0.50	0.83
CM-3	Off	7	5	5	ASR	Assumed Superstructure	15	20	0.74	0.99
CM-4	Off	7	7	5	ASR	Assumed Superstructure	15	20	0.74	0.99
CM-5	Off	7	7	5	ASR	Assumed Superstructure	14	20	0.72	0.99
CM-6	On	6	7	6	LFR	Superstructure	18	25	0.90	1.23
CM-7	Off	6	5	6	N/A	Assumed Superstructure	11	15	0.55	0.74
CM-8	Off	6	6	5	ASR	Substructure	14	19	0.69	0.94
CM-9	Off	7	7	5	N/A	Assumed Superstructure	15	20	0.74	0.99
CM-10	Off	7	7	5	N/A	Assumed Superstructure	15	20	0.74	0.99
CM-11	Off	6	6	7	ASR	Assumed Superstructure	15	25	0.77	1.27
CM-12	Off	7	7	6	N/A	Assumed Superstructure	15	20	0.74	0.99
CM-13	Off	7	7	5	LFR	Superstructure	13	23	0.66	1.13
CM-14	Off	7	7	8	N/A	Assumed Superstructure	20	27	0.99	1.35

Condition Ratings:
0 = Failed Condition
1 = "Imminent" Failure Condition
2 = Critical Condition
3 = Serious Condition
4 = Poor Condition
5 = Fair Condition
6 = Satisfactory Condition
7 = Good Condition
8 = Very Good Condition
9 = Excellent Condition

N/A means that TxDOT did not perform load ratings for this bridge and it is therefore most likely posted based on precedent.

4. BASIC LOAD RATING FOR SSLO CONCRETE BRIDGES

4.1. SIMPLE-SPAN CONCRETE SLAB BRIDGES

4.1.1. Introduction

Twenty-three concrete slab bridges were selected from the inventory of SSLO concrete slab bridges in Texas for basic load rating evaluation. Table 4.1 summarizes these bridges along with their main characteristics.

The maximum span length corresponds to the simply supported span that governs the rating calculations. Half of the bearing length at each end of the span is deducted from the span length to determine the center-to-center bearing span length of the bridge. The deck width, slab thickness, and wearing surface thickness are obtained from the structural drawings, if available, or from field measurements recorded in the TxDOT inspection reports. The yield strength of steel reinforcement and the compressive strength of concrete are properties extracted from the rating calculations provided in the inspection records of the bridges. The skew is defined as the angle between the line normal to the centerline of the roadway and the centerline of the pier cap or abutment as shown in Figure 4.1. The skew angle affects the moment and shear demands.

There are two types of concrete slab bridges, one with structural curbs and one without structural curbs. According to the TxDOT Rate Spreadsheet User Guide (TxDOT 2001), the bridges denoted as “FS slabs” have structural curbs. These curbs contribute to the load carrying capacity of the bridge and hence are considered in the rating calculations. Illinois Bulletin 346 (Jenson et al. 1943) documents the analysis procedure for bridge with integral curbs and/or beams that is adopted by TxDOT in rating these bridges. All other concrete slab bridges are considered

to have non-structural curbs and/or beams. It should be noted that complete information regarding all the bridges was not available, especially for the off-system bridges.

Table 4.1. Characteristics of the Selected SSLO Simple-Span Concrete Slab Bridges

ID	On/Off System	Year Built	Max. Span Length (ft)	Deck Width (ft)	Yield Strength (ksi)	Compressive Strength (ksi)	Slab Thickness (in.)	Wearing Surface Thickness (in.)	Skew Angle (deg.)
CS-1	Off	1920	18	26.8	33*	2.5	15.75	1.0	0
CS-2	Off	1930	19.5	21.4	30	2.5	19.0	0.5	0
CS-3	Off	1935	22	22.8	33	2.5	19.25	4.0	0
CS-4	On	1943	23	46.0	40*	3.0*	15.5	2.0	45
CS-5	On	1946	25	46.3	33	3.0*	12.0	1.25	0
CS-6	Off	1947	23	25.3	33	2.5	10.0	12.0	0
CS-7	Off	1947	25	25.3	33	3.0*	10.0	14.0	0
CS-8	On	1947	25	25.3	33	3.0*	12.0	6.0	0
CS-9	On	1948	25	21.3	33	2.5	11.0	3.0	0
CS-10	On	1949	25	44	33	3.0*	16.0	6.0	30
CS-11	On	1949	25	44	33	3.0*	16.0	6.0	30
CS-12	On	1950	25	21.3	33	3.0*	11.0	3.0	0
CS-13	On	1951	25	21.3	38*	2.5	11.0	2.5	0
CS-14	On	1951	25	25.4	40*	3.0*	11.0	0.5	0
CS-15	On	1951	25	25.3	40*	3.0*	11.0	0.5	0
CS-16	On	1951	25	25.3	40*	3.0*	11.0	0.5	0
CS-17	On	1952	25	21.3	33	3.0*	11.0	2.0	0
CS-18	On	1952	25	36.3	33	3.0*	11.0	1.5	45
CS-19	On	1953	25	35.3	33	2.5	11.0	0.5	0
CS-20	Off	1955	20	21.8	33	2.5	12.0	4.0	0
CS-21	Off	1960	25	25.3	33	3.0	14.0	-	45
CS-22	Off	1962	20	33.8	33	3.0	11.0	5.0	99
CS-23	Off	1970	25	31.0	36	3.0	15.0	5.0	30

Notes:
1. Steel yield strength is the value used by TxDOT for load rating calculations, which typically matches the value given un the TxDOT Bridge Inspection Manual (TxDOT 2018a) and the AASHTO MBE (AASHTO MBE 2018), unless mill certificate is available.
2. *Material strengths taken from the TxDOT load rating calculations.

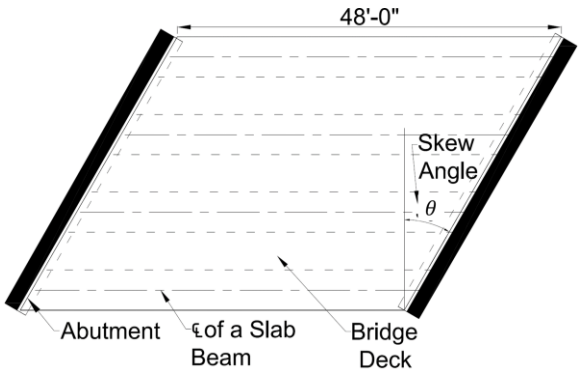

Figure 4.1. Skewed bridge (reprinted from Terzioglu et al. 2017)

4.1.2. Basic Load Rating Analysis

4.1.2.1. General

Each concrete slab bridge was rated using the three methods defined in MBE: Allowable Stress Rating (ASR), Load Factor Rating (LFR), and Load and Resistance Factor Rating (LRFR). The three rating methods follow a similar general procedure. For calculating the flexure rating factors, the following steps are used.

1. The live load moments, obtained from Table E6A-1 and Table C6B-1 of the MBE (AASHTO MBE 2018), are distributed over an equivalent width of the slab to determine the maximum live load moment demands for the bridge based on the design load.
2. The dead load moments are also found by calculating an equivalent distributed load over the design width of the slab.
3. The bending moment capacities of the reinforced concrete section are calculated using the appropriate AASHTO capacity limits. The compression reinforcement is not considered in these calculations to adhere to TxDOT practice and for simplified calculations.
4. Load rating is conducted based on the three load rating procedures (ASR, LFR, and LRFR) at the inventory and operating levels.

Article 5.14.4.1 of the AASHTO *LRFD Bridge Design Specifications* (AASHTO LRFD Specifications) (AASHTO 2017) states that slab bridges designed for flexure in accordance with Article 4.6.2.3 of the AASHTO LRFD Specifications may be satisfactory for shear. However, to provide a more complete overview of the rating process, shear rating information have been included in this report.

For calculating the shear rating factors, the following steps are used.

1. The live load shears, obtained from Table E6A-1 and Table C6B-1 of the MBE (AASHTO MBE 2018), are distributed over an equivalent width of the slab to determine the maximum live load shear demands for the bridge based on the design load.
2. The dead load shears are also found by calculating an equivalent distributed load over the design width of the slab.
3. The shear capacities of the reinforced concrete section are calculated using the appropriate AASHTO capacity limits. The concrete slabs were noted to have no shear reinforcement. Hence, the shear capacity of the reinforced concrete section comprises of only the concrete capacity.
4. Load rating is conducted based on the three load rating procedures (ASR, LFR, and LRFR) at the inventory and operating levels.

4.1.2.2. Allowable Stress Rating and Load Factor Rating

The ASR and LFR calculations follow the requirements outlined in the AASHTO *Standard Specifications for Highway Bridges* (AASHTO Standard Specifications) (AASHTO 2002). The distribution width for the ASR and LFR methods is calculated according to Article 3.24.3.2 of the Standard Specifications as:

$$E = 4 + 0.06S \tag{4.1}$$

where:

S = Effective span length (ft)

The skew of the bridge is accounted for by reducing the effective span length of the bridge by a factor of cosθ, where θ is the skew angle. If the longitudinal tensile reinforcement for the skewed bridge runs parallel to the roadway, then the area of tensile reinforcement is reduced by a factor of $\cos^2\theta$. This is in accordance with Article 3.2.6 of the AASHTO Standard Specifications, which state that the loads must be resolved in the longitudinal and transverse directions.

In the ASR calculations, the stress limits for concrete and steel are defined. Table 6B.5.2.4.1-1 of MBE provides the maximum allowable bending unit stresses in concrete at inventory and operating levels along with the modular ratio, for a given range of concrete ultimate strength. If the ultimate strength of concrete is unknown, the allowable unit stress can be obtained from Table 6B.5.2.4-1 of MBE based on the age of the structure. Similarly, the allowable unit stresses in tension for reinforcing steel at inventory and operating levels are provided in Table 6B.5.2.3-1 of MBE, based on grade of steel and year of construction. The nominal moment capacity of the section is calculated by assuming linear elastic behavior at these stress limits and satisfying force equilibrium. Any compression steel provided within the section is neglected to abide by TxDOT practice and for simplified calculations. The flexural demand for the bridge is calculated at the midspan of the bridge, which is assumed to be the critical section for both dead load and live load. The load factor for dead load and live load demands at both inventory and operating levels is 1.0.

The concrete slab bridges were observed to have no shear reinforcement. As a result, the shear capacity of the reinforced concrete section is based on the concrete capacity. The allowable shear stress, v_C, is calculated as per Article 8.15.5.2.1 of the AASHTO Standard Specifications as:

$$v_C = 0.9\sqrt{f'_c} + 1{,}100\rho_w\left(\frac{Vd}{M}\right) \tag{4.2}$$

The shear demands for dead and live loads are calculated at the critical shear location, which is defined in Article 8.15.5.1.4 of the AASHTO Standard Specifications to be at a distance of the effective depth *d* from the face of the support. The load factors for dead and live demands in ASR are the same for both moment and shear calculations.

The flexural nominal capacity calculations for reinforced concrete sections in LFR are carried out based on Article 8.16.3.2 of the Standard Specifications. In these calculations, the compression reinforcement, if provided, is not considered in the capacity calculations to adhere to TxDOT practice and for simplified calculations. The calculations are carried out with the assumption that the tensile steel has yielded. This assumption is verified after determining the neutral axis depth of the section. The flexural demand for the bridge is calculated at the critical section for both dead load and live load. This was assumed to be at the midspan of the bridge for the project calculations following TxDOT practice. The load factor for dead load demands at both inventory and operating levels is 1.3 while that for live load demands is 2.17 at inventory level and 1.3 at operating level.

The shear capacity of the section is calculated according to Article 8.16.6.2.1 of the AASHTO Standard Specifications. Shear reinforcement was not provided for the considered concrete slab bridges. Therefore, only the concrete section contributes towards the shear capacity of the bridge. The shear demands, for both dead, and live loads, are calculated at the critical section

of the bridge, as defined in Article 8.16.6.1.2 of the Standard Specifications. The loads factors for dead and live demands in LFR are the same for both moment and shear calculations.

The RF for both LFR and ASR at the inventory and operating levels are calculated using Eqn. (3.1). The controlling RFs are multiplied by the weight of the design truck to determine the allowable gross truck weight.

There are two types of concrete slab bridges in Texas: one where the curb/parapet is not integral with the concrete slab, and the other, referred to as Flat-Slab (FS) bridges, with integral curb/parapet and/or beams. These flat slab bridges were designed using the simplified procedures described in the Illinois Bulletin 346 (Jenson et al. 1943). Therefore, TxDOT adopts the Illinois Bulletin 346 (Jenson et al. 1943) formulation to account for the contribution of structural curbs and beams to the bridge capacity. For these FS bridges, calculating the RFs of the slab section using the equivalent strip approach could be too conservative because the structural curbs and/or beams attract significant moment, which is not considered in the calculation of the effective width.

4.1.2.3. Illinois Bulletin 346 Method

Concrete slab bridges have been used across the United States since 1910 (Hunt 2009) due to their simple and economical design for short span bridges. TxDOT also refers to concrete slab bridges as flat-slab (FS) bridges when they have integral curbs and/or beams. Concrete slab bridges were one of the main design and construction types between 1945 and 1965. A modified version of these constant depth slab bridges with monolithically poured curbs/parapets were called “Type FS” bridges in the TxDOT standard drawings. These integrated structural curbs/parapets were designed based on the simplified guidelines established from the findings of the research conducted at the University of Illinois (Jenson et al. 1943). It was found that by adopting integrated structural curbs

(Type FS) that acts as an edge girder, the slab could be designed thinner than standard concrete slab bridges, making FS bridges more economical. High monolithic structural curbs in FS bridges also act as parapet and were found to be relatively simple to construct.

Several analytical and experimental research findings related to the design of FS bridges in Illinois were provided in a series of documents starting with Illinois Bulletin 346, and hence the method of analysis for FS bridges is termed "Illinois Bulletin 346 Method" (IB346). The specialty of FS bridges is the additional load carrying capacity offered by structural curbs. These structural curbs are usually 18 in. in height with #9 or #11 reinforcement (TxDOT 2001). In addition to slab bridges with structural curbs, slab bridges with reinforced edge beams were also rated using the IB346 method. TxDOT has adopted the IB346 method in lieu of the AASHTO strip method to load rate FS bridges. The AASHTO Standard Specifications (AASHTO 2002) also references the IB346 method in Section 3.24 for the distribution of loads and design of concrete slabs.

The structural curbs in FS bridges are large in size with significant reinforcement compared to non-structural curbs that may not be constructed monolithic with the bridge. The IB346 report (Jenson et al. 1943) provides a simplified design methodology based on experimental evaluation of the actual behavior of several types of FS bridges. Experimental tests were conducted on a wide range of FS bridges such as ones with no curbs, ordinary curbs, heavy curbs, and ordinary curbs with handrails to study the sensitivity of relative stiffness of the curb and slab. These structures were eventually tested to failure under uniformly distributed loads as well as concentrated loads replicating the dead and vehicle live load patterns to produce maximum moments. IB346 experimental results and simplified design methodology for various FS bridges are based on the design conditions and theory developed in Illinois Bulletin 315 (Jenson 1939). The theory in IB315 considers vertical support offered by the edge beams and the torsional stiffness of the edge

curbs/beams are neglected. Also, the slab is assumed to be of constant thickness neglecting any crowning on the roadway.

In the simplified analysis method, the cross-section of an FS bridge is divided into two parts: the slab and the edge curb/beam. FS bridges are assumed to be simply supported. The total moment resisted by the slab and the curb is obtained by static moments plus fractional increase in the live load moment. The total static bending moment resisted by the curb and slab in a FS simply supported bridge is given as:

$$M_{static} = m\frac{Pa}{4} + \frac{pba^2}{8} + 2\frac{qa^2}{8} \tag{4.3}$$

where:

m = Number of rear wheel loads (e.g., m = 4 for a two-lane bridge)

P = Magnitude of real wheel load including an allowance for impact

p = Load per unit area between inside faces of curb

b = Width of roadway between inside faces of curb

a = Span of bridge from center-to-center of bearing areas

q = Load per unit length along curb; includes dead load of curb and live load (if any)

The value of 2 in the third term of Eqn. (4.3) is used when exactly same curbs are present on both sides of the roadway. Based on the analysis in IB315, the moment in the curb is given as a fraction of each term in Eqn. (4.3) as:

$$M_{curb} = C_1\frac{Pa}{4} + C_2\frac{pba^2}{8} + C_3\frac{qa^2}{8} \tag{4.4}$$

where:

$$C_1 = \left(\frac{12}{2.5 + G}\right)\frac{\left(4 - \frac{v}{a}\right)}{\left(4 + 28\left(\frac{v}{a}\right)\right)}$$

$$C_2 = \frac{0.5\left(\frac{a}{b}\right)}{0.47G + \sqrt[3]{1.15 + \left(\frac{a}{b}\right)^3}}$$

$$C_3 = \frac{\sqrt[3]{1.15 + \left(\frac{a}{b}\right)^3}}{0.47G + \sqrt[3]{1.15 + \left(\frac{a}{b}\right)^3}}$$

$$G = \frac{ah^3}{12I}$$

G = Dimensionless stiffness factor, ratio of slab stiffness to curb stiffness

I = Moment of inertia of curb gross section outside the roadway width, ft^4

h = Slab thickness, ft

v = Axle width, center-to-center of truck tires (6 ft)

Therefore, the total average moment per unit width b resisted by the slab alone is the difference between Eqn. (4.3) and Eqn. (4.4)

$$M_{slab} = (m - 1.5C_1)\frac{Pa}{4b} + (1 - 2C_2)\frac{pa^2}{8} + (2 - 2C_3)\frac{qa^2}{4b} \qquad (4.5)$$

The curb component is considered as an L-shaped section comprising of the curb and adjoining slab of width $4h$. The bending moment resisted by this composite section is calculated as:

$$M_{L-curb} = M_{curb} + 4hM_{slab} \tag{4.6}$$

In summary, the bending moment resisted by each composite curb and slab component is calculated as:

$$M_{slab-DL} = (1 - C_{3A})\frac{q_A a^2}{8b} + (1 - C_{2A} - C_{2B})\frac{pa^2}{8} + (1 - 1C_{3B})\frac{q_B a^2}{8b} \tag{4.7}$$

$$M_{slab-LL} = (1 - C_{3A})\frac{(q_A)_{LL} a^2}{8b} + (m - \frac{3}{4}C_{1A})\ \frac{Pa}{4b} + (1 - C_{3B})\frac{(q_B)_{LL} a^2}{8b} \tag{4.8}$$

$$M_{L-curbA-DL} = C_{2A}\frac{pba^2}{4} + C_{3A}\frac{(q_A)_{DL} a^2}{8} + 4h(M_{slab})_{DL} \tag{4.9}$$

$$M_{L-curbA-LL} = C_{1A}\frac{Pa}{4} + C_{3A}\frac{(q_A)_{LL} a^2}{8} + 4h(M_{slab})_{LL} \tag{4.10}$$

In the above equations, the subscript *A* corresponds to the left curb and subscript *B* corresponds to the right curb. Eqns. (4.9) and (4.10) can be re-written by changing the subscript *A* to *B* for the other curb.

The capacity shall be calculated for each component (curb, beam, and slab portions) for bridges that have integral beams and curbs (such as FS bridges in Texas). Figure 4.2 shows typical cross-sections for each component in an FS bridge. The curb capacity is calculated by considering an effective slab width of $4h$ as part of the curb. The flexural capacity of this L-shaped section is due to the compression steel reinforcement, concrete compression stress block, and tension steel reinforcement. The slab capacity is calculated per foot width using the procedure outlined in Article 8.16.3.2 of the AASHTO Standard Specifications. The edge beam capacity is also

calculated by considering an effective slab width of $4h$ as part of the beam. The compressive reinforcement in the beam is neglected.

Using the same rating procedure and coefficients as discussed for the ASR and LFR methods, each component is rated for inventory and operating levels. Inventory rating of the overall superstructure is the minimum of the inventory RFs of individual components. Operating rating of the overall superstructure is the weighted average with the curb and slab rating considered proportionate to their tributary width (TxDOT 2018a).

4.1.2.4. Load and Resistance Factor Rating

The LRFR calculations follow the requirements outlined in the AASHTO LRFD Specifications (AASHTO 2017). The dead load moments and shears were calculated over a design strip width of one foot. The live load moments and shears are distributed over the equivalent strip width E (ft) defined in AASHTO LRFD Specifications Article 4.6.2.3, where Eqn. (4.11) corresponds to a single-lane loaded situation while Eqn. (4.12) is for a multi-lane loaded condition.

$$E = 10.0 + 5.0\sqrt{L_1 W_1} \tag{4.11}$$

$$E = 84.0 + 1.44\sqrt{L_1 W_1} \leq \frac{12.0W}{N_L} \tag{4.12}$$

where:

L_1 = Modified span length (ft), minimum of actual span or 60 ft

W_1 = Modified edge-to-edge width of bridge, minimum of actual width or 60 ft for multi-lane loading, or 30 ft for single-lane loading (ft)

W = Actual edge-to-edge width of bridge (ft)

N_L = Number of design lanes

Article 4.6.2.3 of the AASHTO LRFD Specifications accounts for skew by reducing the longitudinal force effects by a factor of r, defined as:

$$r = 1.05 - 0.25\tan\theta \leq 1.00 \tag{4.13}$$

The flexural resistance of the rectangular section is calculated as per Article 5.7.3.2.3 of the AASHTO LRFD Specifications while the nominal shear capacity is calculated according to Article 5.8.3.3.

The AASHTO MBE Table 6A.4.2.2-1 defines the load factors for inventory and operating design loads for reinforced concrete bridges at the Strength I limit state. The RFs for LRFR are then calculated at the inventory and operating levels using Eqn. (3.2). The allowable gross truck weight is calculated by multiplying the governing RFs with the weight of the design truck.

4.1.3. Calculated Load Rating Results

The main focus of the basic load rating analysis is the rating of the superstructure. The 23 selected simple-span concrete slab bridges were rated using each of the three rating methods.

4.1.3.1. Flexure Analysis

The flexure RFs for the design loads for each rating method are summarized in Table 4.2 and graphically presented in Figure 4.3. It can be seen from the results that the RF corresponding to the LRFR method is consistently lower than those corresponding to the ASR and LFR methods. This may be because equivalent strip approach, which was deemed conservative for FS bridges, is used for the LRFR calculations. Two of the 23 bridges, CS-3 and CS-5, were found to have both

HS-20 inventory and operating RFs above 1.0, while ten of the bridges have HS-20 operating RFs above 1.0. Bridges CS-2, CS-6 and CS-20 to 23 are off-system bridges with no structural drawings. TxDOT practice for rating such bridges is to use the flow charts provided in the Bridge Inspection Manual TxDOT (2018a). For on-system bridges the flowchart shown Figure 3.2 is followed, for off-system bridges the flowchart shown in Figure 3.3 is applied, and for concrete bridges with no plans the flowchart shown in Figure 3.4 is used.

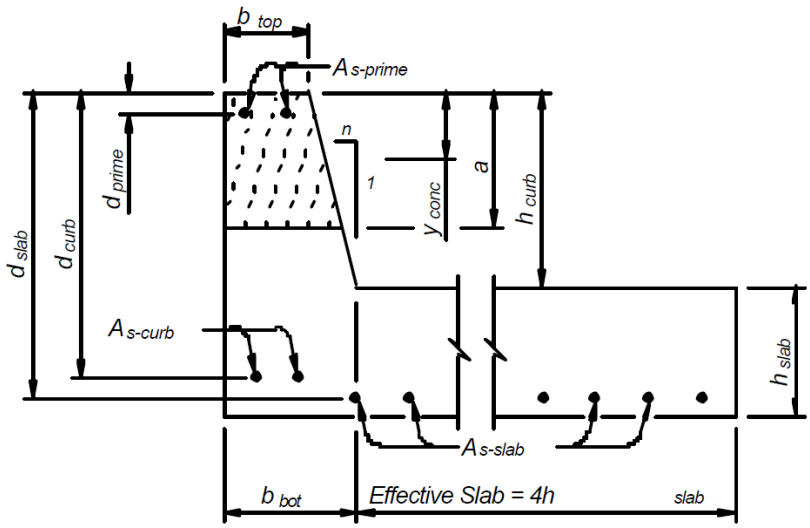

(a) Typical Curb Cross-Section for Capacity Calculations

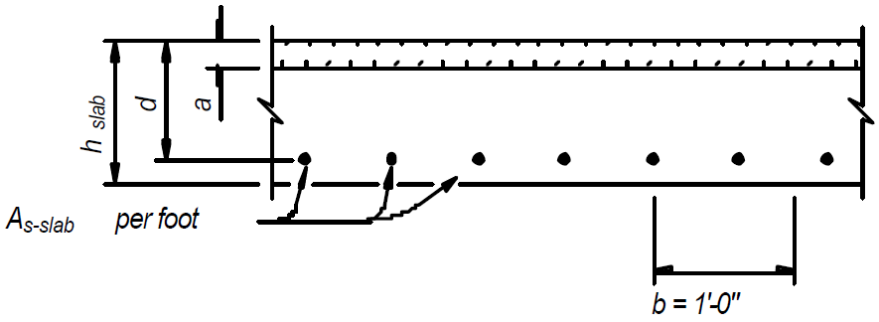

(b) Typical Slab Cross-Section for Capacity Calculations

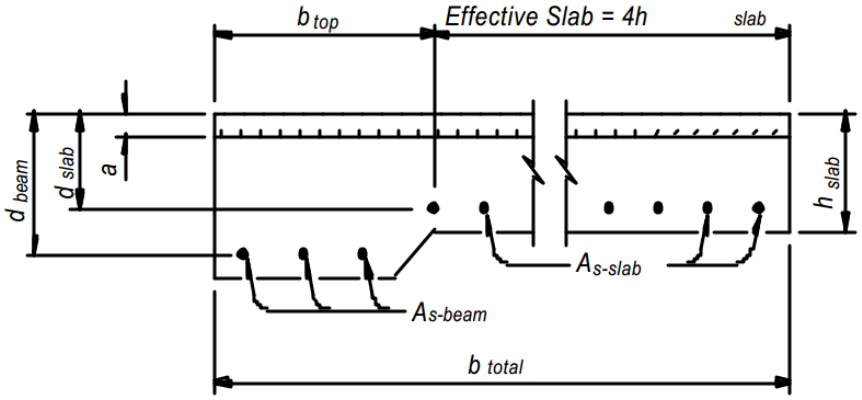

(c) Typical Beam Cross-Section for Capacity Calculations

Figure 4.2. Typical Components for FS Bridges (adapted from TxDOT 2001)

Table 4.2. Flexure RFs for CS Bridges

Bridge ID	FS Bridge	Inventory RF			Operating RF		
		ASR	LFR	LRFR	ASR	LFR	LRFR
CS-1		0.90	0.84	0.75	1.45	1.39	0.98
CS-2		-	-	-	-	-	-
CS-3		1.22	1.16	1.02	2.01	1.93	1.33
CS-4	x	0.37	0.51	0.72	0.68	0.86	0.94
CS-5	x	0.30	1.01	0.19	1.65	1.74	0.25
CS-6		-	-	-	-	-	-
CS-7	x	0.00*	0.26	0.32	0.44	0.51	0.41
CS-8	x	0.16	0.55	0.24	0.86	1.09	0.31
CS-9	x	0.15	0.45	0.14	0.67	0.95	0.18
CS-10	x	0.45	0.91	0.49	1.87	1.87	0.63
CS-11	x	0.45	0.91	0.49	1.87	1.87	0.63
CS-12	x	0.25	0.45	0.14	0.76	0.97	0.19
CS-13	x	0.16	0.54	0.13	0.67	1.16	0.17
CS-14	x	0.31	0.57	0.12	0.93	1.10	0.15
CS-15	x	0.31	0.56	0.12	0.92	1.10	0.15
CS-16	x	0.31	0.56	0.12	0.92	1.10	0.15
CS-17	x	0.28	0.47	0.13	0.79	0.99	0.17
CS-18	x	0.12	0.16	0.08	0.29	0.27	0.11
CS-19	x	0.28	0.86	0.31	1.05	1.44	0.40
CS-20		-	-	-	-	-	-
CS-21		-	-	-	-	-	-
CS-22		-	-	-	-	-	-
CS-23		-	-	-	-	-	-
Average		0.35	0.63	0.32	1.05	1.20	0.42
Std. Dev.		0.29	0.26	0.27	0.51	0.45	0.35

Note:
1. "-" Denotes bridges rated using procedure outlined in the TxDOT Bridge Inspection Manual (TxDOT 2018a) when structural drawings are not available.
2. * RF calculated to be negative due to high dead load demands.

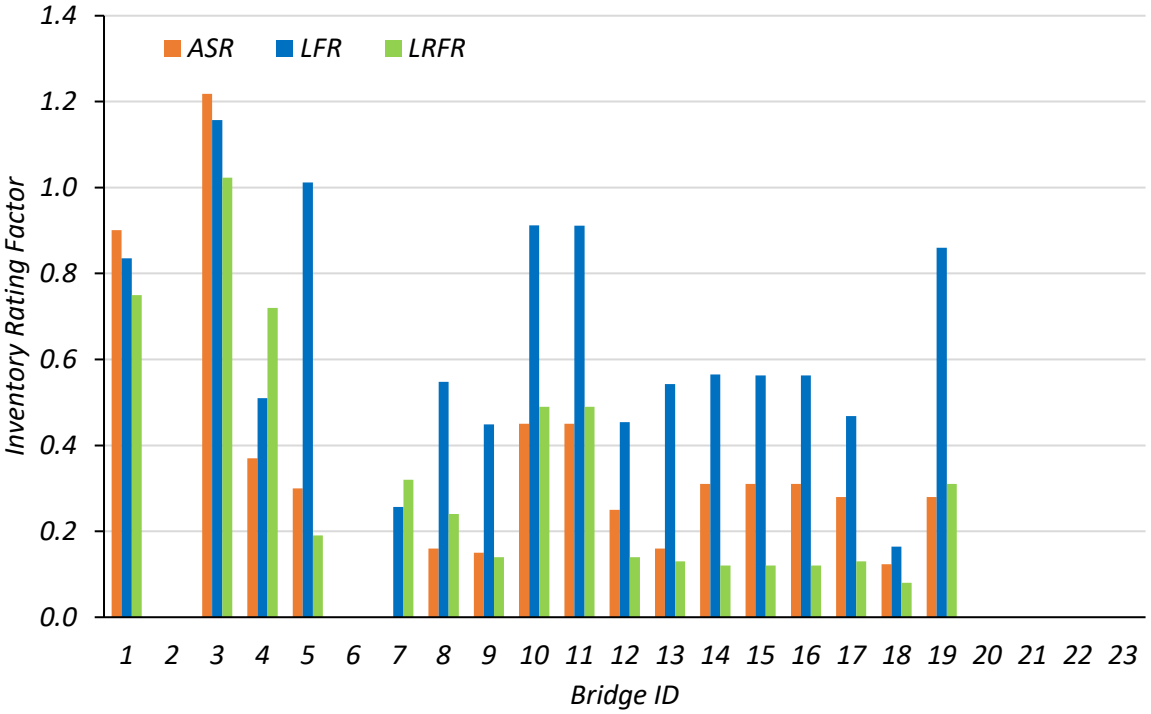

(a) Inventory RFs

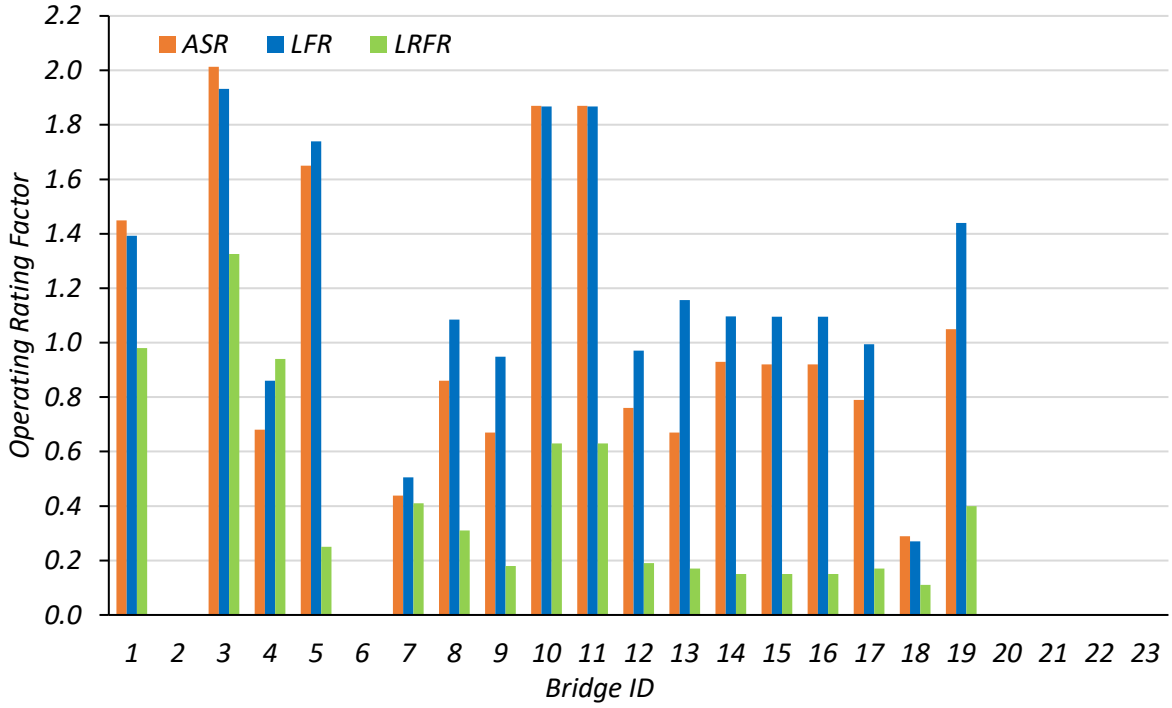

(b) Operating RFs

Figure 4.3. Flexure RFs for CS bridges

4.1.3.2. Shear Analysis

The shear RFs calculated for the selected CS bridges are shown in Table 4.3 and Figure 4.4. Again, some bridges could not be rated, due to the lack of available drawings, particularly for off-system bridges. The LRFR method resulted in higher shear inventory and operating RFs for all the bridges.

Table 4.3. Shear RFs for CS Bridges

Bridge ID	FS Bridge	Inventory RF			Operating RF		
		ASR	LFR	LRFR	ASR	LFR	LRFR
CS-1		2.78	2.48	2.57	2.78	4.13	3.33
CS-2		-	-	-	-	-	-
CS-3		2.93	2.66	2.78	2.93	4.44	3.60
CS-4	x	3.81	3.35	1.66	3.81	5.59	2.15
CS-5	x	1.36	1.25	0.86	1.36	2.09	1.11
CS-6		-	-	-	-	-	-
CS-7	x	0.61	0.72	0.72	0.61	1.21	0.93
CS-8	x	1.16	1.14	0.83	1.16	1.89	1.07
CS-9	x	0.96	0.94	0.55	0.96	1.58	0.72
CS-10	x	2.16	1.98	1.48	2.16	3.31	1.92
CS-11	x	2.16	3.31	1.48	2.16	1.98	1.92
CS-12	x	1.09	1.05	0.62	1.09	1.75	0.81
CS-13	x	0.98	0.95	0.54	0.98	1.59	0.71
CS-14	x	1.19	1.10	0.66	1.19	1.85	0.86
CS-15	x	1.19	1.11	0.66	1.19	1.85	0.85
CS-16	x	1.19	1.11	0.66	1.19	1.85	0.85
CS-17	x	1.13	1.07	0.61	1.13	1.79	0.79
CS-18	x	1.85	1.65	0.64	1.85	2.75	0.82
CS-19	x	1.23	1.14	0.83	1.23	1.91	1.07
CS-20		-	-	-	-	-	-
CS-21		-	-	-	-	-	-
CS-22		-	-	-	-	-	-
CS-23		-	-	-	-	-	-
Average		1.63	1.59	1.07	1.63	2.45	1.38
Std. Dev.		0.83	0.82	0.68	0.83	1.17	0.88

Note:
1. "-" Denotes bridges without structural drawings.

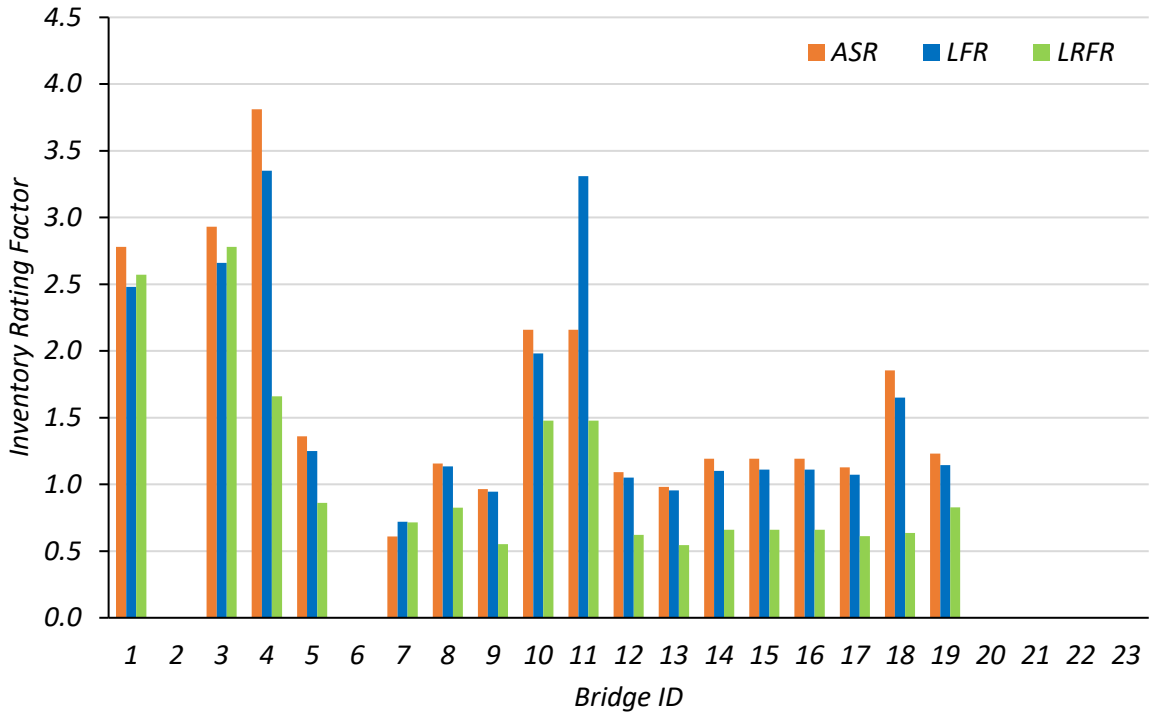

(a) Inventory RFs

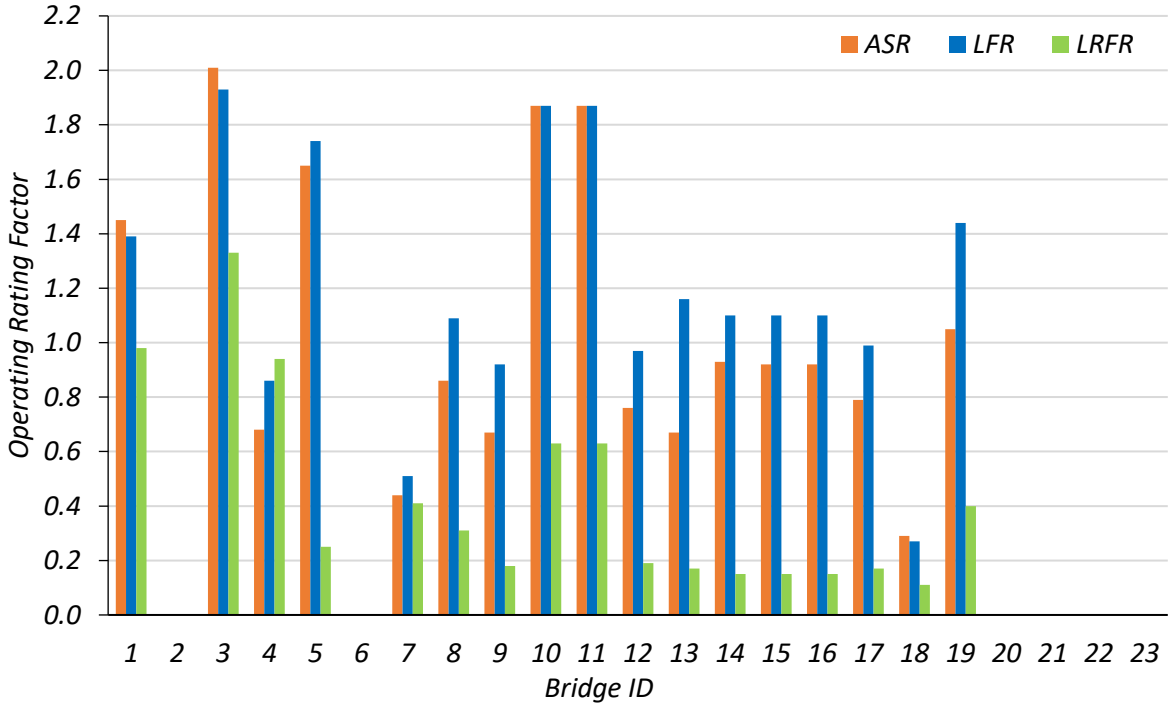

(b) Operating RFs

Figure 4.4. Shear RFs for CS Bridges

4.1.3.3. Comparison of Flexure and Shear RFs for CS Bridge

The calculated flexure RFs and shear RFs for the selected CS bridges are compared to determine the controlling RF for each bridge. Table 4.4 and Figure 4.5 show the inventory and operating flexure and shear RFs found using the same rating method TxDOT uses in analysis. For every CS bridge, the flexure RF controlled the rating at both the inventory and operating level.

Table 4.4. Comparison of Flexure and Shear RFs for CS Bridges

ID	TxDOT Rating Method	Inventory HS20 RF		Operating HS20 RF	
		Flexure	Shear	Flexure	Shear
CS-1	LFR	0.84	2.48	1.39	4.13
CS-2	-	-	-	-	-
CS-3	LFR	1.16	2.66	1.93	4.44
CS-4	LFR	0.51	3.35	0.86	5.59
CS-5	LFR	1.01	1.25	1.74	2.09
CS-6	-	-	-	-	-
CS-7	LFR	0.26	0.72	0.51	1.21
CS-8	LFR	0.55	1.14	1.09	1.89
CS-9	LFR	0.45	0.94	0.95	1.58
CS-10	LFR	0.91	1.98	1.87	3.31
CS-11	LFR	0.91	3.31	1.87	1.98
CS-12	LFR	0.45	1.05	0.97	1.75
CS-13	LFR	0.54	0.95	1.16	1.59
CS-14	LFR	0.57	1.10	1.10	1.85
CS-15	LFR	0.56	1.11	1.10	1.85
CS-16	LFR	0.56	1.11	1.10	1.85
CS-17	LFR	0.47	1.07	0.99	1.79
CS-18	LFR	0.16	1.65	0.27	2.75
CS-19	LFR	0.86	1.14	1.44	1.91
CS-20	-	-	-	-	-
CS-21	-	-	-	-	-
CS-22	-	-	-	-	-
CS-23	-	-	-	-	-
Avg.		0.63	1.59	1.20	2.45
Std. Dev.		0.26	0.82	0.45	1.17

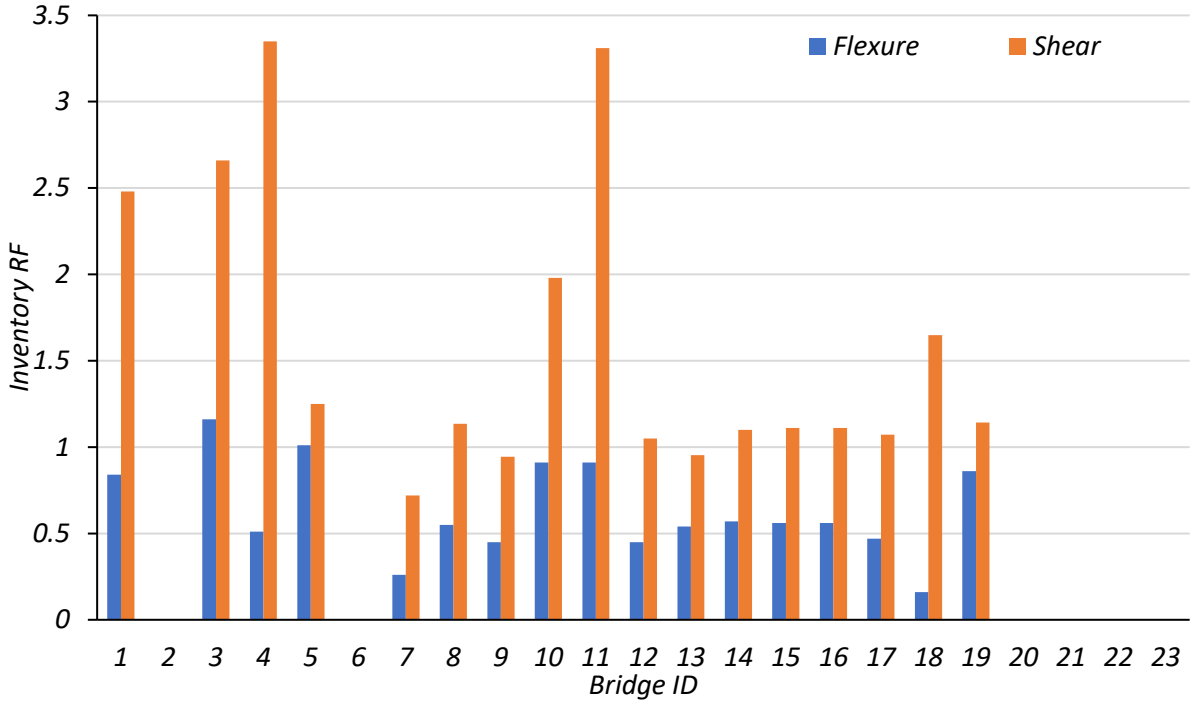

(a) Inventory RFs

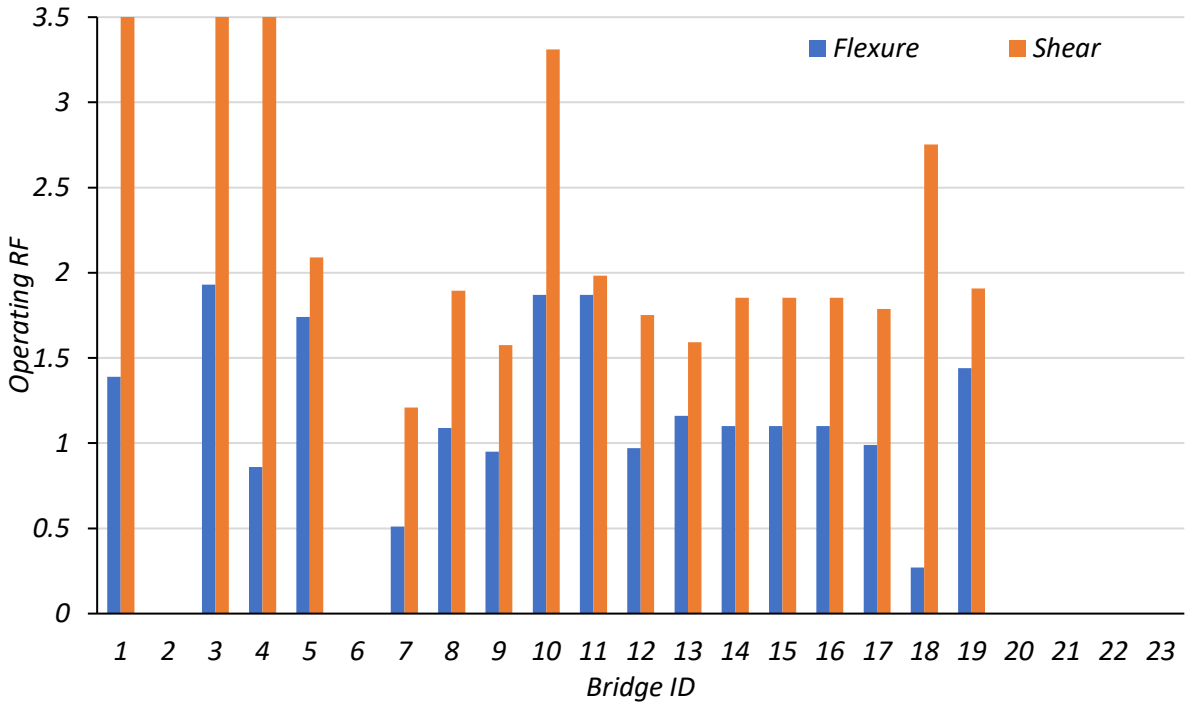

(b) Operating RFs

Figure 4.5. Comparison of Flexure and Shear RFs for CS Bridges

4.1.4. Check of CS Bridge Calculations

After conducting the rating analysis of each bridge, a check was conducted to confirm that the load rating process followed the AASHTO MBE and TxDOT practices. The calculated RFs for the CS bridges were compared to the TxDOT's ratings by changing the input characteristics of each bridge to match the TxDOT inputs for the same rating method. A tolerance of five percent against the TxDOT rating factor was adopted. Any difference within five percent may be attributed to slight rounding differences or other features. Table 4.5 provides the RFs TxDOT obtained for each selected bridge, the rating method used by TxDOT, and the ratio of the calculated RF to the TxDOT RF using the same rating method.

The inventory RF for bridge CS-7 is 11 percent lower than that calculated by TxDOT because this RF corresponds to a single design lane while the bridge operating RF corresponds to two design lanes. The calculated RF was determined for two design lanes to match the number the number of lanes reported in the NBI. Bridge CS-18 also has inventory and operating RFs greater than the five percent tolerance. This is because the input characteristics used in the original rating calculations are not clear. The TxDOT ratings for this bridge are not taken from TxDOT Rate Spreadsheet calculations, but are the values provided in the NBI. Through this exercise, the calculated ratings were found to be close to the TxDOT ratings, thus confirming the process used in the rating calculations.

Table 4.5. RFs for CS Bridges with Adjusted Characteristics

Bridge ID	Rating Method	Revised Calculations for HS20 RF		Revised Calculations RF/ TxDOT RF	
		Inventory	Operating	Inventory	Operating
CS-1	LFR	0.88	1.47	1.00	1.00
CS-2	Flowchart	-	-	-	-
CS-3	LFR	1.21	2.01	1.00	1.00
CS-4	LFR	0.52	0.87	1.00	1.00
CS-5	LFR	0.43	0.72	1.03	1.03
CS-6	Flowchart	-	-	-	-
CS-7	LFR	0.27	0.51	0.79	1.01
CS-8	LFR	0.54	1.07	1.00	1.00
CS-9	LFR	0.45	0.94	1.00	1.00
CS-10	LFR	0.52	0.87	0.97	0.98
CS-11	LFR	0.52	0.87	0.98	0.98
CS-12	LFR	0.46	0.97	1.00	1.00
CS-13	LFR	0.54	1.14	1.00	1.00
CS-14	LFR	0.57	0.96	1.01	1.00
CS-15	LFR	0.57	0.96	1.00	1.00
CS-16	LFR	0.57	0.96	1.00	1.00
CS-17	LFR	0.47	0.98	1.00	1.00
CS-18	LFR	0.47	1.48	1.06	1.95
CS-19	LFR	0.51	0.98	1.00	1.01
CS-20	Flowchart	-	-	-	-
CS-21	Flowchart	-	-	-	-
CS-22	Flowchart	-	-	-	-
CS-23	Flowchart	-	-	-	-
Average		0.56	1.04	0.99	1.06
Std. Dev.		0.20	0.33	0.05	0.22

Note:
1. "Flowchart" refers to the method of rating off-system bridges without structural drawings using the TxDOT Bridge Inspection Manual (TxDOT (2018a) (refer to Figure 3.4).

4.1.5. Comparison of Calculated Ratings with TxDOT Ratings

After confirming the rating process, the original calculated RFs were compared to the RFs that TxDOT documents in the NBI (NBI 2016). Bridges CS-2, CS-6, and CS-20 through CS-23 were load rated following the procedure outlined in the TxDOT Bridge Inspection Manual (TxDOT 2018a) and shown in Figure 3.4. Table 4.6 and Figure 4.6 present the flexure RFs obtained by TxDOT, the rating method used, and the calculated RFs.

Fourteen out of the 23 selected CS bridges were found to have operating ratings greater than or equal to the TxDOT's rating, of which nine of them also had inventory ratings greater than or equal to that of TxDOT's rating. Three out of the bridges with lower design-level ratings than TxDOT's had both inventory and operating ratings lower than that of TxDOT's while five had inventory ratings lower than that of TxDOT's. Three of these bridges resulted in a ratio of 0.99 of the calculated RF to TxDOT's RF, indicating the ratings are almost the same.

Table 4.6. Comparison of Flexure RFs for CS Bridges to TxDOT RFs

ID	Calculated HS20 RF		TxDOT HS20 RF		Rating Method	Calculated/TxDOT	
	Inventory	Operating	Inventory	Operating		Inventory	Operating
CS-1	0.84	1.39	0.89	1.48	LFR	0.94	0.94
CS-2	-	-	0.75	1.00	Flowchart	-	-
CS-3	1.16	1.93	1.21	2.01	LFR	0.96	0.96
CS-4	0.51	0.86	0.52	0.87	LFR	0.98	0.99
CS-5	1.01	1.74	0.42	0.70	LFR	2.41	2.48
CS-6	-	-	0.75	1.00	Flowchart	-	-
CS-7	0.26	0.51	0.34	0.51	LFR	0.76	1.00
CS-8	0.55	1.09	0.55	1.07	LFR	1.01	1.01
CS-9	0.45	0.95	0.45	0.94	LFR	1.01	1.01
CS-10	0.91	1.87	0.54	0.89	LFR	1.70	2.11
CS-11	0.91	1.87	0.53	0.89	LFR	1.72	2.11
CS-12	0.45	0.97	0.46	0.97	LFR	1.00	1.01
CS-13	0.54	1.16	0.55	1.15	LFR	1.00	1.01
CS-14	0.57	1.10	0.57	0.96	LFR	0.99	1.15
CS-15	0.56	1.10	0.57	0.96	LFR	0.99	1.15
CS-16	0.56	1.10	0.57	0.96	LFR	0.99	1.15
CS-17	0.47	0.99	0.47	0.99	LFR	1.00	1.01
CS-18	0.16	0.27	0.44	0.76	LFR	0.37	0.36
CS-19	0.86	1.44	0.51	0.97	LFR	1.69	1.49
CS-20	-	-	0.75	1.00	Flowchart	-	-
CS-21	-	-	0.75	1.00	Flowchart	-	-
CS-22	-	-	0.50	0.75	Flowchart	-	-
CS-23	-	-	0.75	1.00	Flowchart	-	-
Avg.	0.63	1.20	0.60	0.99		1.15	1.23
Std. Dev.	0.26	0.45	0.19	0.28		0.46	0.51

Note:
1. Flowchart refers to the method of rating off-system bridges without structural drawings using the TxDOT Bridge Inspection Manual (TxDOT 2018a) (refer to Figure 3.4).

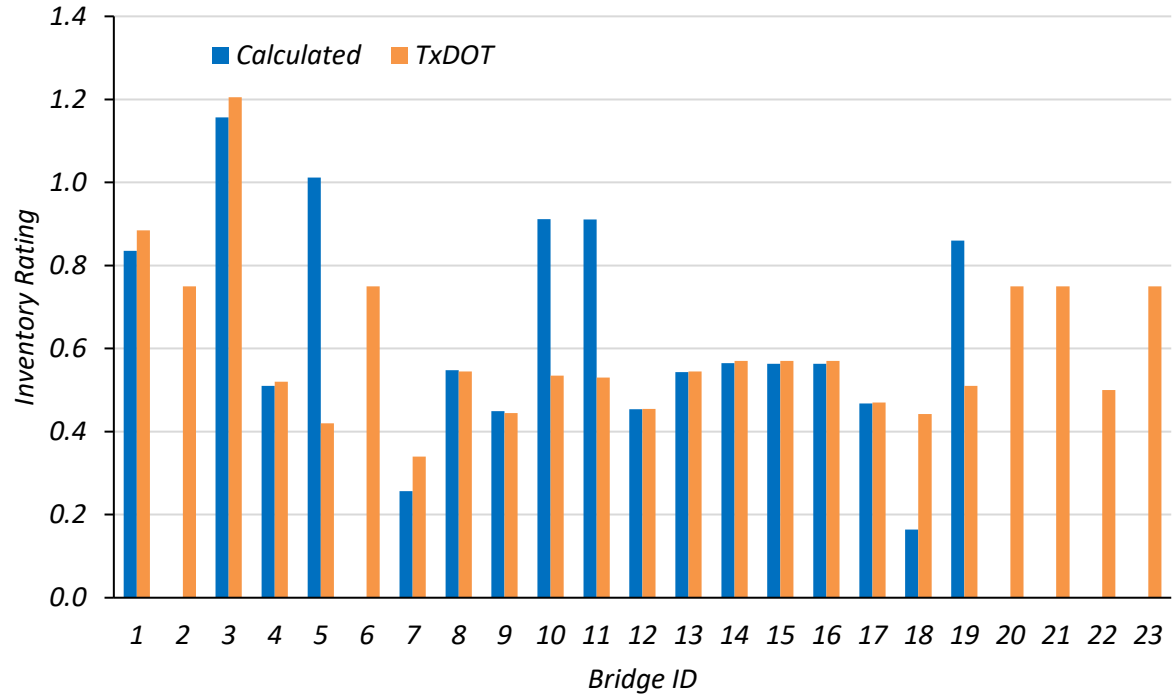

(a) Inventory RFs

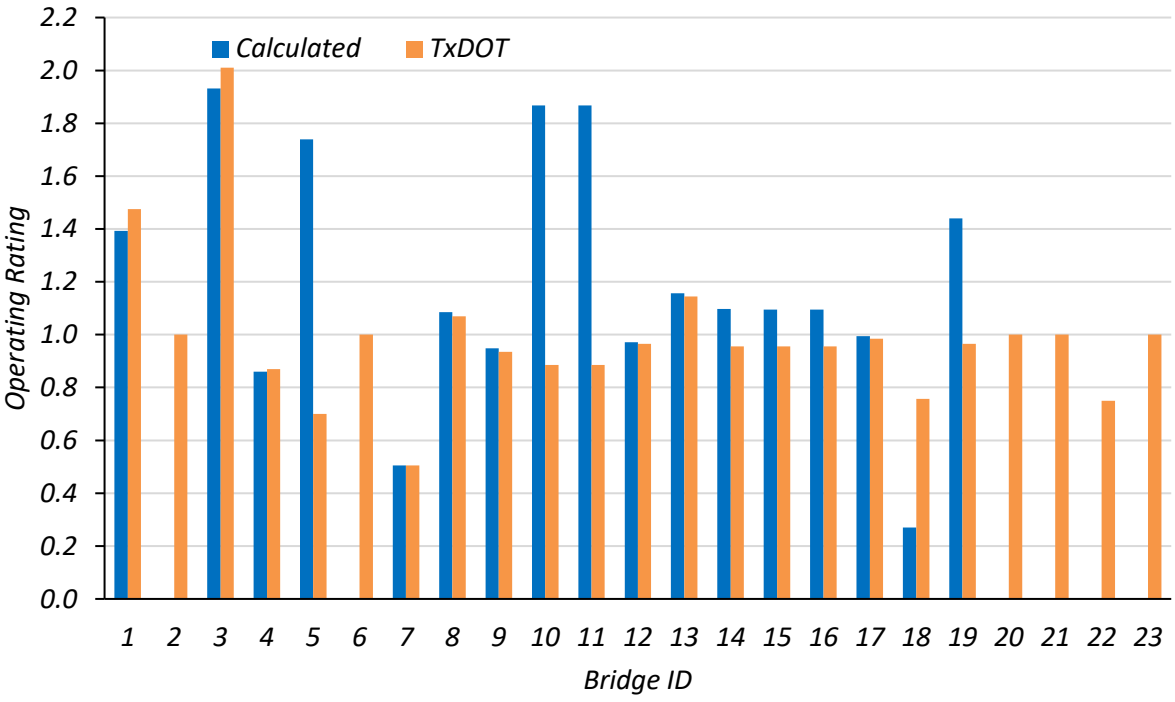

(b) Operating RFs

Figure 4.6. Calculated RF vs. TxDOT RF for Flexure of CS Bridges

Table 4.7 summarize the major reasons for differences between the calculated RFs and the TxDOT RFs. The dead load components include the self-weight of any curbs, parapets and beams along with the slab self-weight. It also accounts for the weight of the asphalt layer. The skew effect considers the reduction in the effective span by a factor of cosine of the skew angle. The tensile reinforcement within the slab and the reinforcement detail within the curb (if present and integral to the bridge) is considered based on available structural drawings of the bridge. Illinois Bulletin 346 approach is used to load rate concrete slab bridges with integral curbs.

Table 4.7. Reasons for Differences Between Calculated and TxDOT Flexure RFs for CS Bridges

Bridge ID	Reasons for Difference in Rating Factor					
	Dead Load Components	Skew Effect	Slab Tensile Reinforcement	Curb Reinforcement	Curb Reinforcement Cover	Illinois Bulletin 346
CS-1	x					
CS-2						
CS-3	x					
CS-4		x				
CS-5						x
CS-6						
CS-7	x		x	x	x	
CS-8			x	x	x	
CS-9			x	x	x	
CS-10		x	x			
CS-11		x	x			
CS-12			x		x	
CS-13			x		x	
CS-14			x	x	x	
CS-15			x	x	x	
CS-16			x	x	x	
CS-17			x	x	x	
CS-18		x				x
CS-19						x
CS-20						
CS-21						
CS-22						
CS-23						

4.1.6. Conclusion

The selected simple-span concrete slab bridges were analyzed according to the AASHTO MBE, AASHTO Standard Specifications, and AASHTO LRFD Specifications. The LFR method resulted in higher flexure RFs followed by the ASR and LRFR methods. The difference between the calculated RFs and the TxDOT RFs for each bridge was examined. Based on the analysis performed on these bridges, possible areas for improvement to load posting are identified and elaborated upon in Section 4.3 of this thesis.

4.2. SIMPLE SPAN CONCRETE MULTI-GIRDER BRIDGES

4.2.1. Introduction

Fourteen concrete multi-girder (CM) bridges were selected from the inventory of SSLO concrete multi-girder bridges in Texas. These bridges along with their main characteristics are summarized in Table 4.7. It should be noted that all selected bridges have two traffic lanes.

A concrete pan girder bridge consists of girders running along the longitudinal direction at specific spacings. Figure 4.7 shows a typical cross-section of such a bridge. The "slab + beam depth" is the total depth from the top of the slab to the bottom of the beam. This is either 24 in. or 33 in. for the selected bridges that are classified as concrete pan girder bridges. The girders for all the selected bridges were spaced at 36 in. center-to-center. All the information regarding the bridges was obtained from either the TxDOT inspection data or from the structural drawings where available. Similar to the concrete slab (CS) bridges, complete information regarding all the bridges could not be obtained, especially for the off-system bridges.

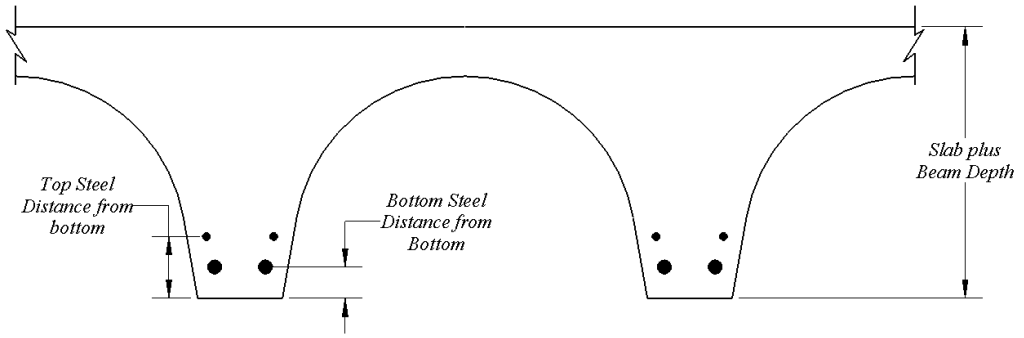

Figure 4.7. Typical Cross-section of Concrete Pan Girder Bridge (adapted from TxDOT (2001))

Table 4.8. Selected SSLO Concrete Simple-Span Multi-girder Bridges and Characteristics

ID	On/Off System	Year Built	Max Span Length (ft)	Deck Width (ft)	Yield Strength (ksi)	Compressive Strength (ksi)	Slab + Beam Depth (in.)	Spacing of Girders (in.)	Number of Girders	Wearing Surface Thickness (in.)
CM-1	On	1940	30	30.5	33	2.5	24	36	5	0.5
CM-2	Off	1942	30	35.5	33	2.5	24	36	12	0.5
CM-3	Off	1950	29	21.7	33	2.5	24	36	8	2
CM-4	Off	1950	29	21.7	33	2.5	24	36	8	1.5
CM-5	Off	1950	29	21.625	33	2.5	24	36	8	2
CM-6	On	1957	30	24.7	40*	3.0*	24	36	9	1.5
CM-7	Off	1957	40	31.2	33	2.5	33.5	36	11	3
CM-8	Off	1960	29	21.7	33	3.0	24	36	8	3
CM-9	Off	1960	30.3	24.7	33	3.0	-	36	9	-
CM-10	Off	1960	30.3	32.9	33	3.0	-	36	11	3
CM-11	Off	1960	40	48.1	33	3.0	33	36	17	-
CM-12	Off	1975	30.3	24.8	36	3.0	24	36	9	3
CM-13	Off	1982	40	28.3	40*	3.0	33	36	9	-
CM-14	Off	2000	30	32	36	3.0	-	36	11	3

Notes:
1. Steel yield strength is the value used by TxDOT for load rating calculations, which typically matches the value given in the TxDOT Bridge Inspection Manual (TxDOT 2018a) and the AASHTO MBE (AASHTO MBE 2018), unless mill certificate is available.
2. *Material strengths taken from TxDOT's load rating calculations.

4.2.2. Basic Load Rating Analysis

4.2.2.1. General

Each of the selected concrete multi-girder bridges was rated using the three methods defined in MBE: Allowable Stress Rating (ASR), Load Factor Rating (LFR), and Load and Resistance Factor Rating (LRFR), provided sufficient information was available. The following steps are used.

1. The live load moments and shears are extracted from the MBE (AASHTO MBE 2018) Table (MBE 2018 Tables E6A-1 and C6B-1).

2. The appropriate live load distribution factors are determined. The live load distribution factors, along with the appropriate impact factor, are applied to the live load moments and shears to calculate the maximum live load moments and shears applied to the bridge for the load being analyzed.
3. The dead load moments and shears from the pan girders and wearing surface are calculated over the corresponding effective widths.
4. The bending moment and shear capacities of the pan girder are calculated with the assumption of a tee beam. The compression reinforcement is not considered in these calculations for consistency with TxDOT practice and for simplified calculations.
5. Load rating is carried out for the three load rating procedures (ASR, LFR, and LRFR) at the operating and inventory levels.

4.2.2.2. Allowable Stress Rating and Load Factor Rating

The procedure outlined in the AASHTO Standard Specifications (AASHTO 2002) is followed to carry out the ASR and LFR calculations. The effective width is defined according to Article 8.10.1.1 of the AASHTO Standard Specifications. The dead load moments and shears are calculated over this effective width. Table 3.23.1 of the AASHTO Standard Specifications provides the live load distribution factor for multi-girder bridges considering concrete on concrete T-beam bridges.

The flexural demand is calculated at the midspan of the bridge and the appropriate load factors are applied. The load factors are presented in Table 4.9. For the ASR method, the load factor for dead load and live load demands at both inventory and operating levels is 1.0. For the

LRF method, the load factor for dead load demands at both inventory and operating levels is 1.3 while that for live load demands is 2.17 at inventory level and 1.3 at operating level.

The stress limits for concrete and steel are defined for the ASR method. The allowable bending unit stresses in concrete along with the modular ratio at inventory and operating levels are provided in Table 6B.5.2.4.1-1 of MBE, for a given range of concrete ultimate strength. This information can also be obtained from Table 6B.5.2.4-1 of MBE based on year of construction when ultimate strength of concrete is unknown. The allowable unit stresses in tension for reinforcing steel at inventory and operating level are provided in Table 6B.5.2.3-1 of MBE, based on grade of steel and year of construction. Linear elastic behavior at these stress limits is assumed and force equilibrium is satisfied while calculating the moment capacity of the section at the allowable stress limit. In these calculations, the compression steel is not considered to be consistent with TxDOT practice and to simplify the calculations.

The nominal flexural capacity calculations for concrete multi-girder bridges are carried out based on Article 8.16.3.3 of the AASHTO Standard Specifications. The pan girders in the selected SM bridges generally have two layers of tensile reinforcement. The adjusted centroid of the reinforcement layers is used to calculate the nominal moment capacity for the LFR method. The calculations are carried out with the assumption that the neutral axis lies within the compression flange. Once this assumption is verified, the section is the treated as a rectangular reinforced beam with width equal to the effective flange width.

The shear demands for dead and live loads are calculated at the critical shear location for the bridges, which is defined in Article 8.15.5.1.4 of the AASHTO Standard Specifications to be at a distance d from the face of the support. The load factors for dead and live demands for ASR ratings are the same for both moment and shear calculations (see Table 4.9).

The concrete pan girder bridges with structural drawings were noted to have shear reinforcement in the form of stirrups. Therefore, the shear capacity of the reinforced concrete section is calculated considering the contribution from both the concrete web and the stirrups as per Articles 8.15.5.2.1 and 8.15.5.3 of the AASHTO Standard Specifications as:

$$v = v_C + v_S = 0.95\sqrt{f'_c} + \frac{A_v f_S}{b_w S_v} \tag{4.14}$$

where:

A_v = Area of shear reinforcement (in^2)

b_w = Web width (in.)

S_v = Spacing of shear reinforcement in direction parallel to the longitudinal reinforcement (in.)

Finally, the RFs for both LFR and ASR at the inventory and operating levels are calculated for both flexure and shear according to Eqn. (3.1). The controlling RFs are multiplied by the weight of the design truck to determine the allowable gross truck weight.

4.2.2.3. Load and Resistance Factor Rating

The requirements provided in the AASHTO LRFD Specifications (AASHTO 2017) are followed for the LRFR calculations. The effective width for pan girders bridges is defined in Article 4.6.2.6.1 of the AASHTO LRFD Specifications as the spacing between the girders. The flexural demand for both dead and live load is calculated at the midspan of the bridge. The live load demands are calculated for the HL-93 design truck. The live load flexure and shear distribution factors are obtained from Table 4.6.2.2.2b-1 and Table 4.6.2.2.3a-1 of the AASHTO LRFD Specifications, respectively, considering a cast-in place concrete tee beam structure. These live

load distribution factors along with the impact factor are applied to the live load demands. The moment capacity is calculated similar to that for a reinforced rectangular concrete section with the assumption that the neutral axis lies within the compression flange (Article 5.7.3.2.2, AASHTO LRFD Specifications). This assumption is verified during the capacity analysis.

The load factor is 1.25 for dead load demands due to structural components and attachments, and 1.50 for dead load demands due to wearing surface and utilities. The load factor for live load demands is 1.75 at inventory level and 1.35 at operating level as shown in Table 4.9. Finally, the RFs for the girders are calculated at the Strength I limit state for both inventory and operating levels. The governing RFs are multiplied with the weight of the design truck to determine the allowable gross weight for the bridge.

Table 4.9. Load Factors for Rating Methods

Rating Method	Dead Load Factor (A_1)		Live Load Factor (A_2)	
	Inventory	Operating	Inventory	Operating
ASR	1.0	1.0	1.0	1.0
LFR	1.3	1.3	2.17	1.3
LRFR	1.25/1.50	1.25/1.50	1.75	1.35

4.2.3. Calculated Load Rating Results

4.2.3.1. Flexure Analysis

Only five of the selected CM bridges had sufficient information available to conduct load rating analysis. These bridges were load rated using each of the three rating methods and the results are presented in Table 4.10 and Figure 4.8. Three out of the fourteen CM bridges (CM-6, CM-13 and, CM-14) had drawings available, while bridge CM-1 had some details available within TxDOT's rating calculations. Load rating calculations for Bridge CM-5 were carried out based on

information gathered from the standard drawing for this bridge type provided on the TxDOT website titled 'CG 30'-4" Spans' (TxDOT 2005). It can be seen that when using the LFR method, Bridges CM-6 and CM-13 have operating RFs greater than 1.0, while Bridges CM-6 and CM-14 have both inventory and operating RFs greater than 1.0.

Table 4.10. Interior Girder Flexure RFs for CM Bridges

Bridge ID	Inventory RF			Operating RF		
	ASR	LFR	LRFR	ASR	LFR	LRFR
CM-1	0.46	0.50	0.28	0.87	0.83	0.36
CM-5	0.38	1.17	0.71	0.76	1.96	0.93
CM-6	0.52	0.99	0.55	0.98	1.65	0.71
CM-13	0.14	0.65	0.43	0.48	1.09	0.55
CM-14	0.46	1.46	0.80	0.90	2.44	1.04
Average	0.39	0.95	0.55	0.80	1.59	0.72
Std. Dev.	0.13	0.35	0.19	0.17	0.58	0.25

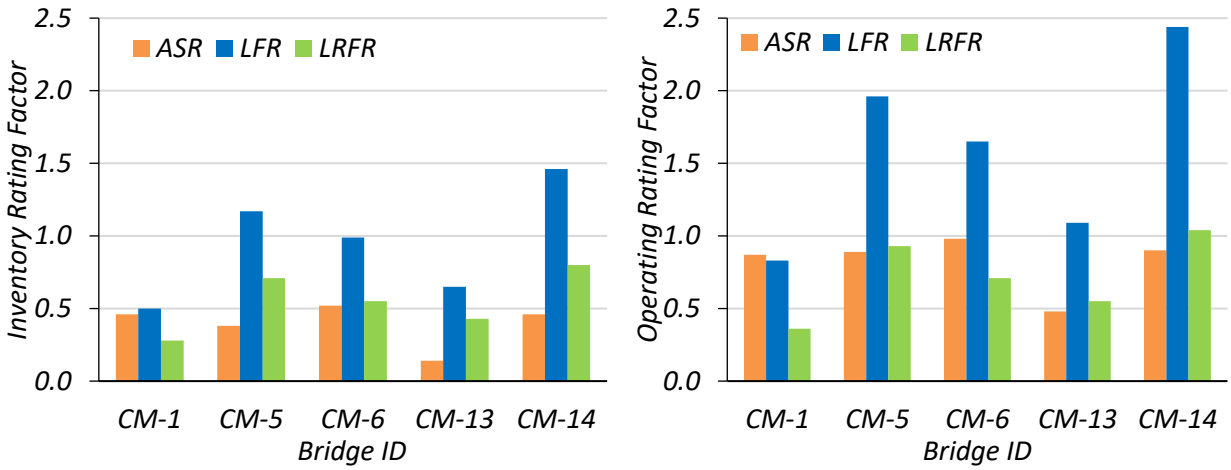

(a) Inventory RFs *(b) Operating RFs*

Figure 4.8. Interior Girder Flexure RFs for CM Bridges

4.2.3.2. Shear Analysis

Four out of the five CM bridges had sufficient information to carry out load rating using the three rating methods. Table 4.11 and Figure 4.9 show the shear RFs for the CM bridges.

Table 4.11. Shear RFs for CM Bridges

Bridge ID	Inventory RF			Operating RF		
	ASR	LFR	LRFR	ASR	LFR	LRFR
CM-5	1.49	1.18	0.60	1.84	1.97	0.78
CM-6	1.5	1.34	0.66	1.91	2.23	0.85
CM-13	1.58	1.43	0.59	2.01	2.39	0.76
CM-14	2.82	2.37	1.28	3.78	3.96	1.65
Average	1.83	1.58	0.78	2.35	2.64	1.01
Std. Dev.	0.58	0.46	0.29	0.83	0.78	0.37

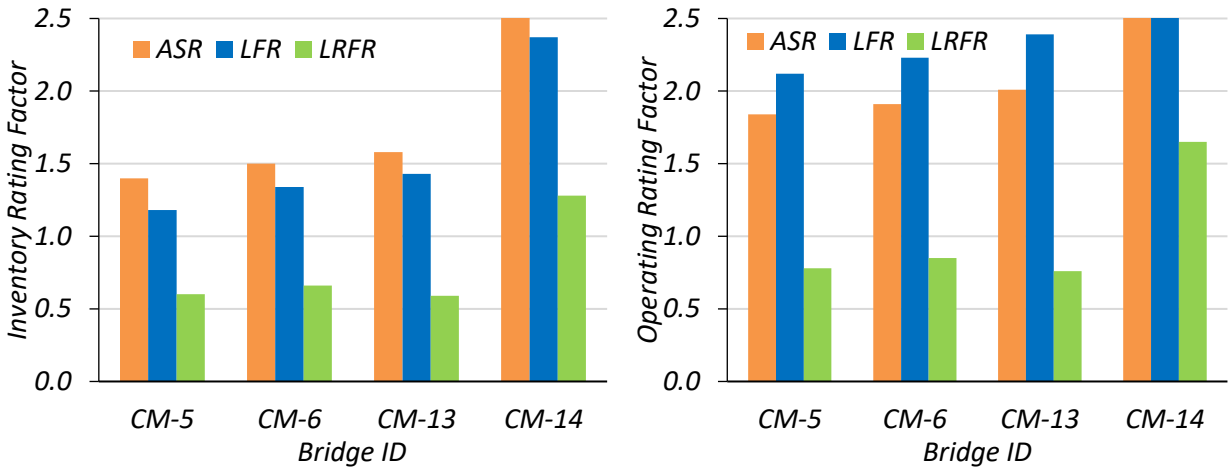

(a) Inventory RFs *(b) Operating RFs*

Figure 4.9. Interior Girder Shear RFs for CM Bridges

4.2.3.3. Comparison of Flexure and Shear RFs for CM Bridges

The calculated flexure RFs and shear RFs for the selected CM bridges are compared to determine the controlling RF for each bridge. The RFs for only four of the CM bridges could be compared. Table 4.12 and Figure 4.10 show the inventory and operating flexure and shear RFs found using the same rating method TxDOT uses in analysis. For every CM bridge, the flexure RF controlled the rating at both the inventory and operating level.

Table 4.12. Comparison of Flexure and Shear RFs for CM Bridges

Bridge ID	TxDOT Rating Method	Inventory HS20 RF		Operating HS20 RF	
		Flexure	Shear	Flexure	Shear
CM-5	LFR	1.17	1.18	1.96	1.97
CM-6	LFR	0.99	1.34	1.65	2.23
CM-13	LFR	0.65	1.43	1.09	2.39
CM-14	LFR	1.46	2.37	2.44	3.96

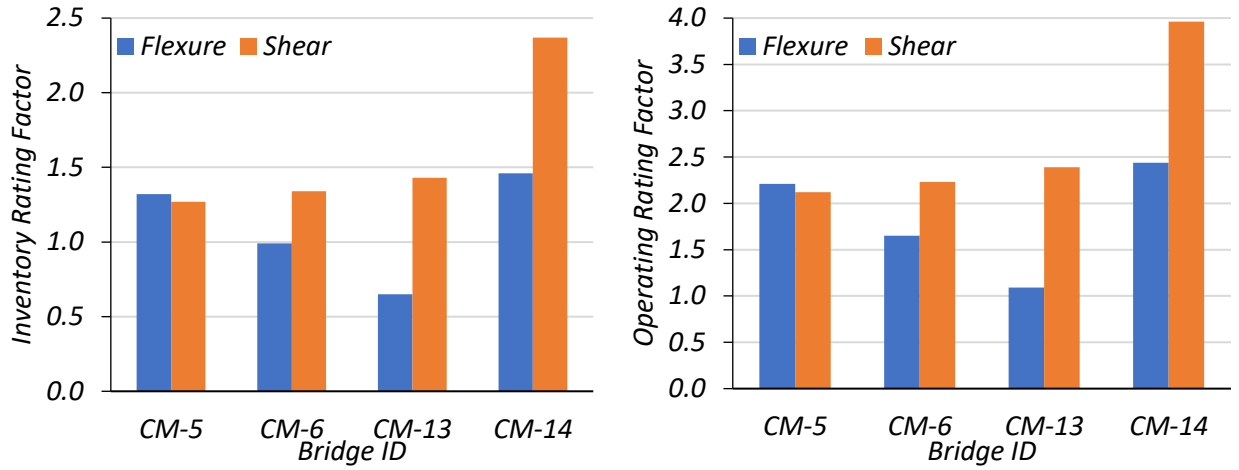

(a) Inventory RFs *(b) Operating RFs*

Figure 4.10. Interior Girder Flexure and Shear RFs for CM Bridges

4.2.4. Comparison of Calculated Ratings with TxDOT Ratings

The calculated flexure RFs for each concrete multi-girder bridge are compared to those provided by TxDOT in the NBI (NBI 2016). Table 4.13 and Figure 4.11 present the flexure RFs obtained by TxDOT, the rating method used, and the ratio of calculated RF to TxDOT's RF. It can be seen that the calculated flexure RFs closely match with the TxDOT RFs for Bridge CM-1, Bridge CM-6, and Bridge CM-13. The flexure RFs for Bridge CM-14 were found to be higher than that determined by TxDOT.

Table 4.13. Comparison of Flexure RFs for CM Bridges to TxDOT RFs

ID	Calculated HS20 RF		HS20 RF (TxDOT)		TxDOT Rating Method	Calculated/TxDOT	
	Inventory	Operating	Inventory	Operating		Inventory	Operating
CM-1	0.50	0.83	0.50	0.83	LFR	0.99	1.00
CM-5	1.17	1.96	0.72	1.00	LFR	1.63	1.96
CM-6	0.99	1.65	1.00	1.66	LFR	1.00	1.00
CM-13	0.65	1.09	0.68	1.14	LFR	0.96	0.96
CM-14	1.46	2.44	1.00	1.35	LFR	1.46	1.81
Avg.	0.95	1.59	0.78	1.20		1.21	1.35
Std. Dev.	0.35	0.58	0.19	0.29		0.28	0.44

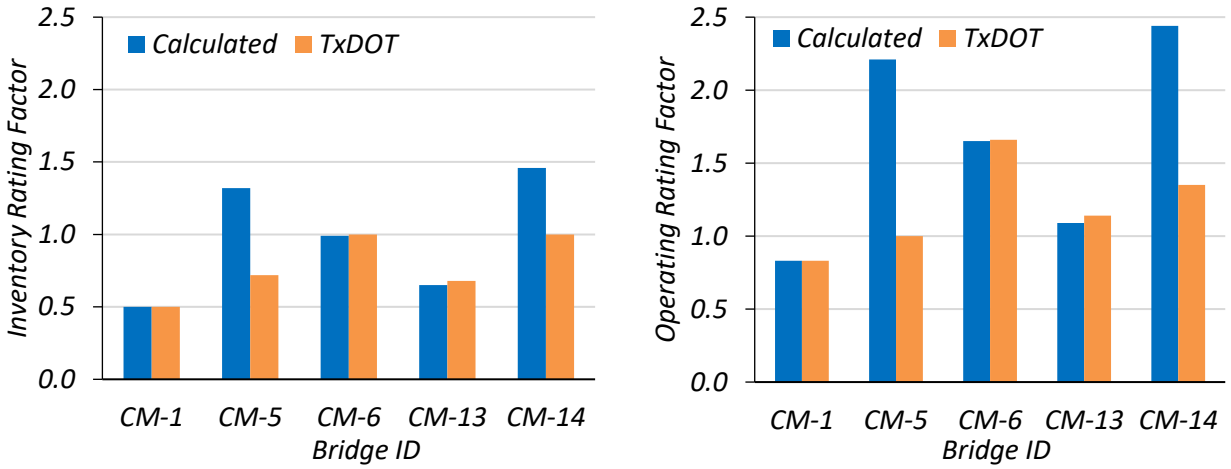

(a) Inventory RFs

(b) Operating RFs

Figure 4.11. Calculated RF vs. TxDOT RF for Flexure of CM Bridges

4.2.5. Conclusion

The selected simple-span concrete multi-girder bridges were analyzed according to the AASHTO MBE, AASHTO Standard Specifications, and AASHTO LRFD Specifications. The LFR method resulted in higher flexure RFs. The difference between the calculated RFs and TxDOT's RFs for each bridge was examined and confirmed. Based on the analysis performed on these bridges, possible areas for improvement to load posting are identified and elaborated upon in Section 4.3.

4.3. AREAS OF POSSIBLE IMPROVEMENT FOR CONCRETE BRIDGES

4.3.1. Refined Analysis

The capacity of the concrete slab bridges was calculated assuming one-way slab action. However, the bridges meet the requirements of two-way analysis. Each bridge has a span-to-width ratio less than or equal to 1.5 and both longitudinal and transverse reinforcement are present. Analyzing concrete slab bridges as two-way slabs can provide more realistic capacity estimation.

Yield line analysis can also be used to evaluate the actual ultimate capacity of a concrete slab bridge. While linear elastic analysis can only predict the first yield at the section, yield line analysis provides more realistic ultimate capacity prediction for slabs. The only concern with yield line analysis is that it may estimate a higher, or at best equal, capacity to the true load carrying capacity. Therefore, it requires experience to be able to establish reasonable or valid yield line mechanisms. In addition, knowledge of reinforcement distribution is necessary at the start of the analysis. However, this method can be very useful for analyzing existing structures (Park and Gamble 2000). The full, distributed strength capacity of the concrete slab, the global collapse of the slab instead of the failure of an effective width component, is considered in yield line analysis (Middleton 2007). Pirayeh Gar et al. (2014) demonstrated using experimental tests that the capacity of bridge deck slabs may be satisfactorily estimated by yield line theory.

The load rating methods outlined in the AASHTO manuals are simplified with assumptions resulting in conservative outcomes. Refined analysis using FEM could help increase the load rating of some of these bridges by accurately capturing the actual behavior of the bridge superstructure. However, developing finite element models takes a considerable amount of time and special care is needed while determining the model parameters. Analyzing every load posted bridge using FEM

would be a time-consuming process. However, if a number of typical bridges were analyzed using finite element models, a practice could possibly be developed for similar bridges based on representative models. FEM analysis can eliminate inherit conservatisms in approximate methods and provide higher RFs by simulating the actual bridge behavior in a more accurate manner.

Refined analysis was not explored in the basic load rating task, but will be examined in detail in Chapters 7 and 8 of the thesis.

4.3.2. Number of Lanes

For narrow two-lane bridges, reducing the number of design lanes can be an area of possible improvement. This approach has already been utilized by TxDOT in number of cases for other bridge types and could be considered for concrete FS slab bridges. Calculating live load demands for one-lane loaded case would result in a smaller live load moment and therefore higher RF values. The Illinois Bulletin 346 calculations utilizes the number of lanes in determining the number of wheels over the design width. This affects the live load moment corresponding to the design truck. In the LRFR calculations, the number of lanes limits the upper bound for the effective width of concrete slab bridges under multi-lane loaded conditions.

The effect of reducing the number of design lanes is shown in Table 4.14 for bridges CS-14 and CM-6. A single live load lane is assumed for both bridges. The RF for CS-14 was improved by 84 percent of the originally calculated while the RF for CM-6 improved by 8 percent, at inventory level.

Table 4.14. Improvements to Ratings Based on Reduced Design Lanes

Bridge ID	Rating Method	Two-lanes loaded HS20 RF		One-lane loaded HS20 RF		One-lane loaded RF / Two-lanes loaded RF	
		Inventory	Operating	Inventory	Operating	Inventory	Operating
CS-14	LFR	0.57	1.10	1.05	3.80	1.84	3.45
CM-6	LFR	0.99	1.65	1.07	1.79	1.08	1.08

4.3.3. Accurate Material Information

The yield strength of steel is one of the key parameters in the calculation of RFs. This information can be obtained from mill test results available for steel based on the year of construction. For example, during the inspection conducted in 2017, Bridge CS-14 was noted to have mill test data available. Accordingly, the yield strength of reinforcement was taken to be 40 ksi. This increased the rating of the bridge significantly, removing the need for load posting.

Another method for determining the yield strength of reinforcement in existing bridges is to conduct tensile tests on specimens obtained from the bridges. A trend could be studied by testing sufficient samples from bridges built during a certain period and, if applicable, applied to bridges constructed during that period. This may help increase the rating of a specific bridge type with certain characteristics.

The effect of increased material strengths was studied on three sample bridges: CS-14, CS-16, and CM-6. The yield strength for CS-14 and CS-16 bridges was assumed to be 40 ksi, an approximate increase of 20 percent from 33 ksi. The yield strength for CM-6 was assumed to be 50 ksi, an approximate increase of 25 percent from 40 ksi. Table 4.15 shows the results in the form of a ratio of revised RF to initially calculated RF. This process improved the RF for CS-14 by 28 percent of the originally calculated and improved the RF for CS-16 by 29 percent of the originally calculated, at inventory level. The RF for CM-6 improved by 32 percent at inventory level.

Table 4.15. Improvements to Ratings Based on Improved Yield Strength

Bridge ID	Rating Method	TxDOT HS20 RF		Calculated HS20 RF		Revised Calculated HS20 RF		Revised Calculated RF/ Calculated RF	
		Inv.	Oper.	Inv.	Oper.	Inv.	Oper.	Inv.	Oper.
CS-14	LFR	0.57	0.96	0.57	1.10	0.73	1.40	1.28	1.27
CS-16	LFR	0.57	0.96	0.56	1.10	0.72	1.40	1.29	1.27
CM-6	LFR	1.00	1.66	0.99	1.65	1.31	2.19	1.32	1.33

4.3.4. Live Load Distribution Factors

The AASHTO Standard Specifications and the AASHTO LRFD Specifications define the effective width for concrete slab bridges with empirical equations. The effective width of the slab affects the live load distribution factor and therefore the RF.

In 2012, researchers at the University of Delaware conducted load tests for a selection of concrete slab bridges and determined their actual effective width, with the goal of developing new effective width formulas to be used in Delaware (Jones and Shenton 2012). In this study, a diagnostic load test was conducted for six slab bridges without integral curbs in the State of Delaware and equations for the effective slab width developed. Table 4.16 compares the developed equations with the current AASHTO LRFD effective width equations.

The inverse of the effective width in feet is equal to the LLDF for a one-foot longitudinal strip of a slab bridge (Illinois DOT 2012; Virginia DOT 2011; Wisconsin DOT 2017). Increasing the effective width, as the Delaware study suggested, will decrease the LLDF for the loaded strip of a slab bridge. This will decrease the live load effect on that strip, therefore increasing the RF for that strip and the controlling RF for the bridge. DelDOT has included these new effective width formulas in their rating software and as a result has removed or improved posting restrictions on over fifty bridges in the state of Delaware (Arndt et al. 2017; Jones and Shenton 2012).

Table 4.16. Comparison of Effective Width Equations for Slab Bridges (adapted from Jones and Shenton 2012)

Approach	Effective width (in.) per lane for one lane loaded	Effective width (in.) per lane for multiple lanes loaded
AASHTO LRFD	$E = 10.0 + 5.0\sqrt{L_1 W_1}$	$E = 84.0 + 1.44\sqrt{L_1 W_1} \leq \frac{12.0 W_1}{N_L}$
Delaware study	$E = 10.0 + 5.8\sqrt{L_1 W_1}$	$E = 84.0 + 2.06\sqrt{L_1 W_1} \leq \frac{12.0 W_1}{N_L}$

where:

E = Equivalent or effective width (in.)

L_1 = Modified span length taken equal to the lesser of the actual span length or 60.0 ft

W_1 = Modified edge-to-edge width of the bridge taken to be equal to the lesser of the actual width or 60.0 ft for multilane loading, or 30.0 ft for single-lane loading

W = Physical edge-to-edge width of the bridge (ft)

N_L = Number of design lanes

4.3.5. Partial Fixity at Supports

Although designed as simply supported systems, unintended partial fixity may occur at the supports. This can be attributed to the bearing detail at the supports and/or friction between the bottom surface of the bridge and the bearing surface. The presence of partial fixity may be verified through field testing. Chajes (1997) conducted a non-destructive experimental load test on a three-span, load posted, slab-on-steel girder bridge. The 1940 bridge was designed as a non-composite structure with three simply supported spans. The test results indicated substantial restraint at the bearing supports. The presence of partial fixity would induce negative moments at the supports and these regions should then be checked when determining the controlling RFs.

5. FEM ANALYSIS OF SIMPLE-SPAN CONCRETE MULTI-GIRDER BRIDGE

In Chapter 4, a detailed review and synthesis of the population of load-posted bridges in Texas was conducted, and 14 simple-span concrete multi-girder (CM) bridges were selected from the inventory of SSLO concrete multi-girder bridges in Texas for basic load rating evaluation. This basic load rating analysis helped to identify several areas of opportunity for refined load rating analysis. Refined load rating analysis investigates the effect of the identified parameters using three-dimensional finite element models that can more accurately capture the actual bridge behavior. The main objective of FEM analysis of the simple-span concrete multi-girder bridge is to accurately capture the distribution of live load between girders.

5.1. INTRODUCTION

A typical load posted simple-span concrete multi-girder bridge was selected as a representative case study to further investigate the identified objectives. Table 5.1 lists some of the key parameters for the selected bridge to be modeled, and for the average SSLO simple-span concrete multi-girder bridge in Texas. In this table, the *Operating HS-20 RF* represents the multiple of HS-20 truck loads that is the absolute maximum load that can safely travel on the bridge at once. The posting evaluation represents the degree to which the operating rating of the bridge is below the maximum legal load. A "5" indicates the operating rating is equal to or above the legal load. Values of 0-4 represent varying ranges for which the operating rating is below the legal load, with "4" being within 10% of the legal load and "0" being 40% or greater below the legal load.

A three-dimensional FEM model was developed using the commercial software package CSiBridge, which has the capability to model and analyze complex bridge superstructures while

also providing user-friendly pre- and post-processing tools for bridge structures. The following sections provide the geometric and material properties of the selected simple-span concrete multi-girder bridge, a description of the FEM modeling approach, and summarize the analysis results.

Table 5.1 Selected SSLO CM Bridge and Average Characteristics

ID	Route Prefix	Year Built	ADT	Max. Span Length (ft)	Deck Width (ft)	Condition Rating			Operating HS-20 Rating Factor	Posting Eval.
						Deck	Super-structure	Sub-structure		
Avg.	-	1964	-	34	28	7	7	6	0.99	5
CM-5	4	1950	150	29	22	7	7	5	0.99	5

–: Not applicable
Route Prefix: 3=On-System
Condition Ratings: 6=Satisfactory, 7=Good
Posting Evaluation: 3=10-19.9% below legal load, 4=0.1-9.9% below legal load

Modal analysis was conducted to obtain modal properties including modal frequencies and mode shapes. The model was also analyzed with HS-20 truck and designated HL-93 load simulations to obtain deflection profiles, moment, and shear results. The deflection and modal analyses were conducted for comparison to the measured behavior of the bridge in the future field tests. The deflection values and modal characteristics will allow for calibration of the FEM model based on field test results. The main bridge characteristic of interest for the moment and shear analyses is the LLDFs. A comparison of the LLDFs found using the FEM model will be carried out with those determined from field testing, and those found using the procedures outlined in the AASHTO Standards Specifications (AASHTO 2002) and AASHTO LRFD Specifications (AASHTO 2017). LLDFs can be calculated as the moment or shear force of an individual girder divided by the sum of moments or shear forces in all of the girders for a one-lane-loaded case as given in Eqn. (5.1).

$$g = m\frac{F_{girder}}{F_{total}} \tag{5.1}$$

where:

g = Live load distribution factor

F_{girder} = Moment or shear force in the individual girder

F_{total} = Total moment or shear force on the entire section for one-lane loading

m = Multiple presence factor per the AASHTO LRFD Specifications (AASHTO 2017), 1.2 for one-lane loading and 1.0 for two-lane loading.

5.2. DESCRIPTION OF THE BRIDGE

The selected Bridge CM-5 is made up of eight pan girders each 24 in. deep. The bridge has a total length of 30 ft. The simply supported bridge is 21 ft 7.5 in. wide and has a center-to-center of bearing span length of 29 ft. The steel yield strength and the 28-day concrete compressive strength are taken as 33 ksi and 2.5 ksi, respectively, according to the AASHTO MBE (AASHTO 2018) guidelines. The bridge carries two lanes, one in each direction, and has an average daily traffic of 150 vehicles. These properties are tabulated in Table 5.2.

Table 5.2 Geometric and Material Properties for Bridge CM-5

Characteristic	Measurement
Total Length	30'-0"
Controlling Span Length	29'-0"
Deck Width	21'-7.5"
Roadway Width	21'-0"
Girder Spacing	3'-0"
Slab + Beam Depth	2'-0"
Steel Yield Strength	33 ksi
Slab Thickness	8 in.
28-day Concrete Compressive Strength	2.5 ksi
Number of Lanes	2

Bridge CM-5 has a deck condition rating of 7 (Good), a superstructure condition rating of 7 (Good), and a substructure condition rating of 5 (Fair). The concrete pan girders control the rating of the bridge, which has an inventory gross loading of 26 US tons and an operating gross loading of 36 US tons. The bridge is posted for a 24,000-pound tandem axle. Figure 5.1 shows a longitudinal section detail and Figure 5.2 shows an elevation view and an underside view of Bridge CM-5.

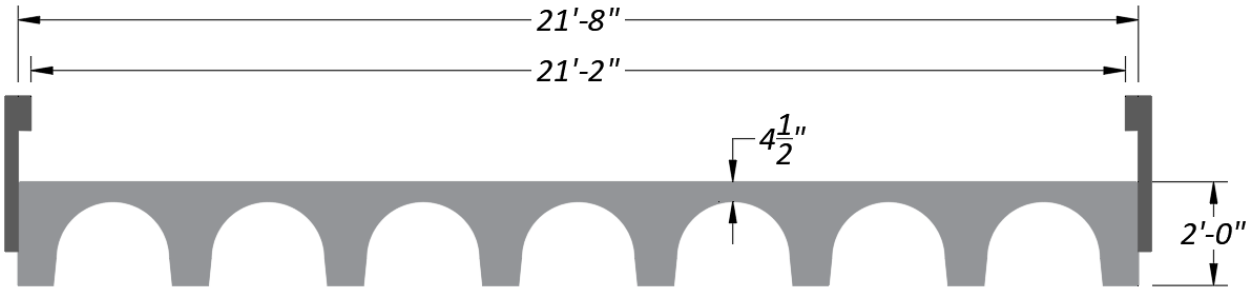

Figure 5.1. Bridge CM-5 Longitudinal Section (adapted from TxDOT 2018b)

(a) Elevation view

(b) Underside view

Figure 5.2. Photographs of Bridge CM-5

5.3. FEM MODEL DEVELOPMENT

A three-dimensional linear FEM model of the selected simple-span concrete pan girder bridge was developed using the commercial CSiBridge software (Computers and Structures 2019). The bridge geometry was modeled based on information provided in the structural design drawings (TxDOT 2005) and preliminary field measured geometries. The geometric information relevant to the development of the FEM model for Bridge CM-5 was presented in the previous sections of this chapter. The following subsection describes the FEM modeling approach, finite element types, and material properties. The next subsection presents the results of the mesh sensitivity study and selection of mesh size. The last subsection provides details about boundary conditions, which is critical for accurately capturing the behavior of the bridge.

5.3.1. Bridge Model Description

A realistic model of the bridge superstructure requires appropriate finite element types, boundary conditions, and a sufficiently refined mesh. There is ample information providing recommendations about FEM modeling for various concrete bridge superstructures (Hueste et al. (2015), Davids et al. (2013)). Based on the recommendations provided in the literature and engineering judgement, a three-dimensional linear finite element model of Bridge CM-5 was developed using the commercial software CSiBridge (Computers and Structures 2019). Due to the absence of structural drawings for this specific bridge, the bridge geometry is modeled according to the standard drawing provided on the TxDOT website titled ‘CG 30'-4" Spans’ (TxDOT 2005). The standard drawing called for nine pan girders. It was found during a preliminary field visit that the bridge actually has eight girders. The slab in this bridge did not extend beyond the edge girders as was shown in the standard drawing. Due to complications in modeling the semi-circular profile

of the pan girders, a tri-linear geometry was adopted for each girder. The geometry of the tri-linear model was determined by keeping the depth (24 in.) and bottom width of the girder web (8.25 in.) the same as shown in the standard drawing. All other dimensions of the pan girder were modified until the gross section moment of inertia (I_{xx}) matched the original value with an approximate 5% tolerance. The bridge superstructure was modeled using 3-D eight-node linear solid brick elements. The reinforcement was not modeled because the linear elastic model is analyzed under service level loads only, and the superstructure is expected to remain in the linear elastic range. Figure 5.3 shows the finite element model for Bridge CM-5.

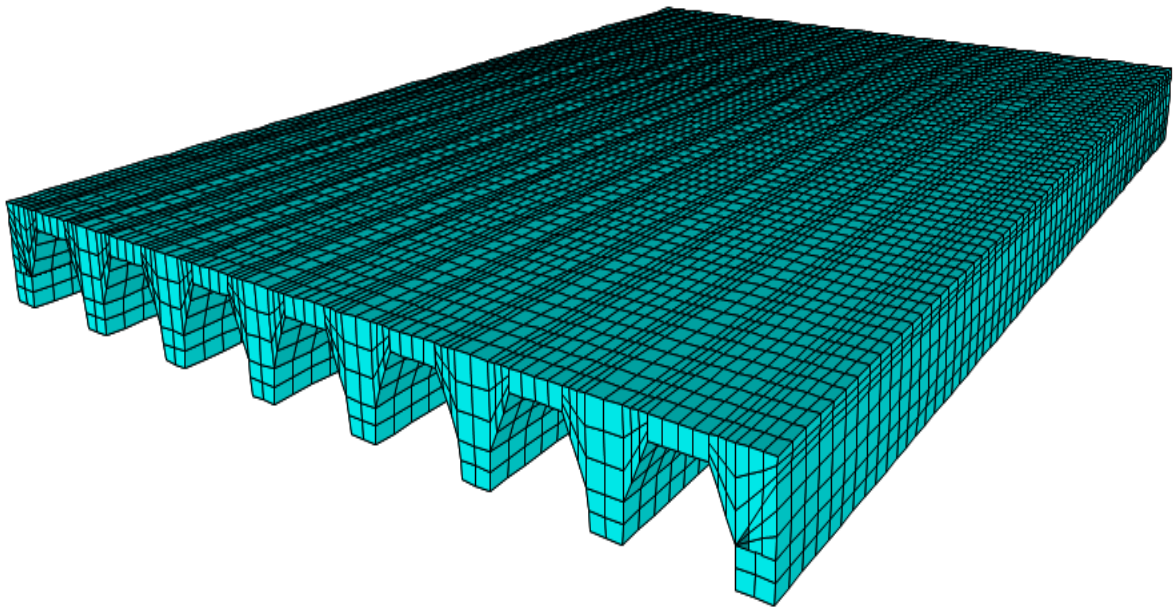

Figure 5.3 FEM Model of Bridge CM-5 (6 in. mesh)

In the absence of any record of the specified material strengths for Bridge CM-5, the steel yield strength and the 28-day concrete compressive strength are taken in accordance with the

AASHTO MBE guidelines (AASHTO 2018). Table 5.3 lists the material properties adopted for the FEM model.

Table 5.3 Material Properties for Bridge CM-5

Bridge	28-Day Concrete Compressive Strength (ksi)	Modulus of Elasticity (ksi)	Concrete Unit Weight (pcf)
CM-5	2.5	3031	150

The modulus of elasticity, E_c, for concrete was calculated using Eqn. (5.2), as stated in the AASHTO LRFD Specifications (AASHTO 2014). This equation is valid for normal weight concrete with unit weights between 0.09 and 0.155 kcf and design compressive strength up to 15.0 ksi.

$$E_c = 33{,}000 K_1 w_c^{1.5} \sqrt{f_c'} \tag{5.2}$$

where:

E_c = Elastic modulus of concrete, ksi

K_1 = Correction factor for source of aggregate, to be taken as 1.0 unless determined by physical test

w_c = Unit weight of concrete, kcf

f_c' = Compressive strength of concrete, ksi

5.3.2. Mesh Sensitivity Analysis

A mesh sensitivity study was undertaken for several models with different mesh sizes (4 in., 6 in., 12 in., and 18 in.) in order to determine the optimal mesh size for the three-dimensional linear finite element model of Bridge CM-5. The effect of different mesh sizes on the calculated shear

force, moment, and bending stress was examined. Figure 5.4 shows these different mesh sizes when applied to Bridge CM-5.

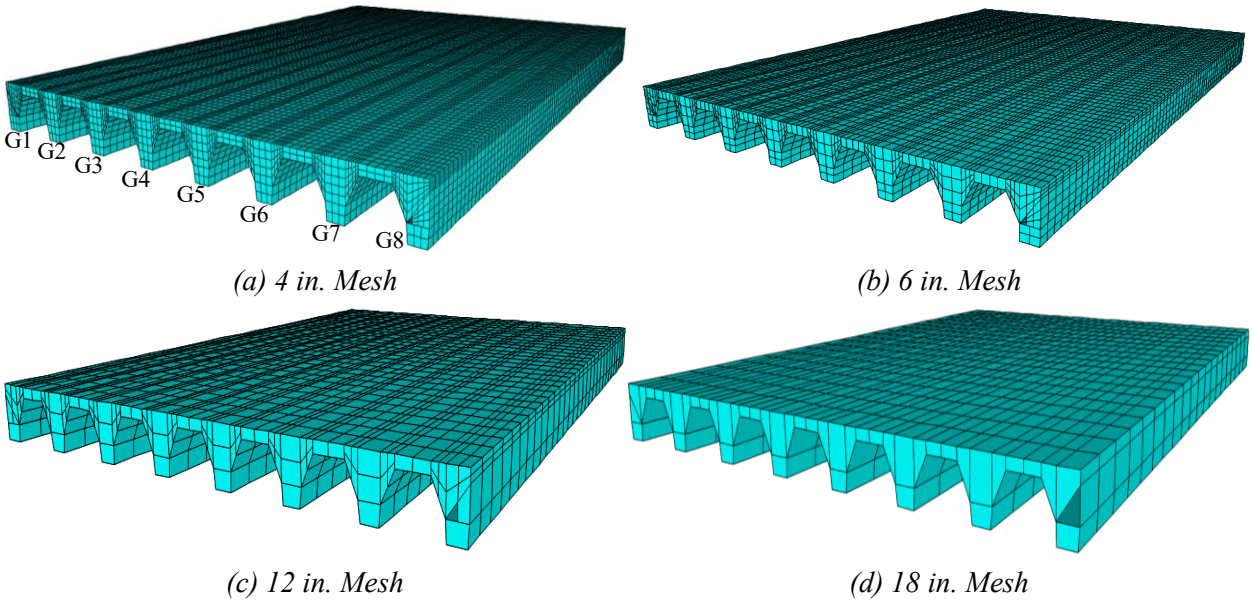

(a) 4 in. Mesh *(b) 6 in. Mesh*

(c) 12 in. Mesh *(d) 18 in. Mesh*

Figure 5.4. FEM Models Showing Different Mesh Sizes for Bridge CM-5

The FEM results for shear force, bending moment, and stress for the Bridge CM-5 models are listed in Table 5.4. All the results correspond to the case of a single HS-20 truck pass through the right lane, 2 ft from the centerline of the bridge (Path 2 in Figure 5.11). The accuracy of the results increases with decreasing mesh size. However, reducing the mesh size to 4 in. does not significantly increase the accuracy when compared to the results obtained from the model with a mesh size of 6 in. Hence, a 6 in. mesh size was chosen to be used for Bridge CM-5. With this mesh size and discretization points, an accurate FEM model of the bridge with an efficient computation time was created in CSiBridge. The final meshed CSiBridge model used for analysis of Bridge CM-5 is shown in Figure 5.5.

Table 5.4 FEM Results for CM-5 with Different Mesh Sizes

Mesh Size (in.)	Maximum Moment in Girder 3 (kip-ft)	Maximum Shear in Girder 3 (kip)	Maximum Stress in Girder 3 (ksi)
4	52.56	9.35	0.366
6	52.55	9.12	0.366
12	52.56	8.64	0.366
18	52.35	8.22	0.366

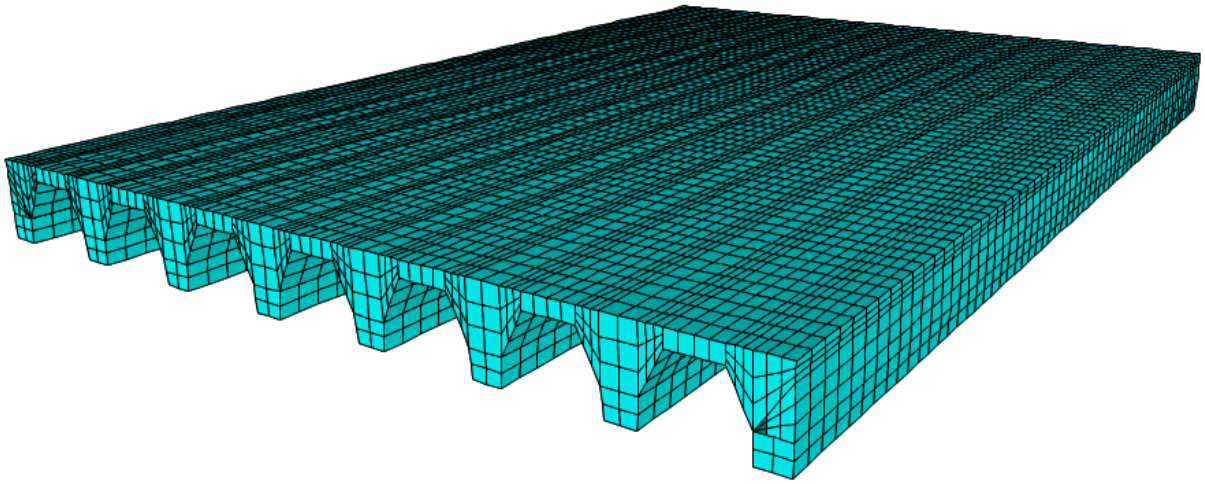

Figure 5.5. Selected CSiBridge Model (6 in. mesh)

5.3.3. Boundary Conditions

In the absence of more accurate information, the boundary conditions at the supports were modeled as simply supported with pins and rollers. One end of each girder was modeled with roller supports while the other end was modeled with pin supports. The roller support releases all three rotational degrees of freedom as well as two translational degrees of freedom in the horizontal plane (two orthogonal in-plane directions parallel to the bridge superstructure), and fully restrains the translational degree of freedom in the vertical direction (perpendicular to the plane of the bridge superstructure). The pin support releases all three rotational degrees of freedom and restrains all three translational degrees of freedom.

Accurately modeling the boundary conditions may have a significant effect on the overall behavior of the bridge. Although the boundary conditions are initially modeled as simply supported, the level of restraint will be assessed based on experimental results during the next task. Unintended partial fixity may develop at the supports due to the bearing detail at the supports and/or friction between the bottom surface of the bridge and the bearing surface.

5.4. BASIC VERIFICATION OF FEM MODELS

Some basic loading conditions were simulated to verify that the CSiBridge model was providing expected results. These basic checks were conducted by investigating maximum deflections under uniform distributed dead load, and maximum moments and shears under HS-20 truck and HL-93 loading.

The characteristics of the HS20 design truck as specified in AASHTO LRFD Specifications (AASHTO 2017) is shown in Figure 5.6. The total load in the front axle is 8 kips and is 14 ft away from the middle axle, which has a total load of 32 kips. The rear axle has a total load of 32 kips and may be spaced between 14 ft and 30 ft from the middle axle, depending on which creates the maximum force effect being investigated. An alternative loading scheme consisting of a uniformly distributed load of 0.64 kip/ft and a concentrated load of 18 kips when checking moment or 26 kips when checking shear is also considered in AASHTO Standard Specifications (AASHTO 2002).

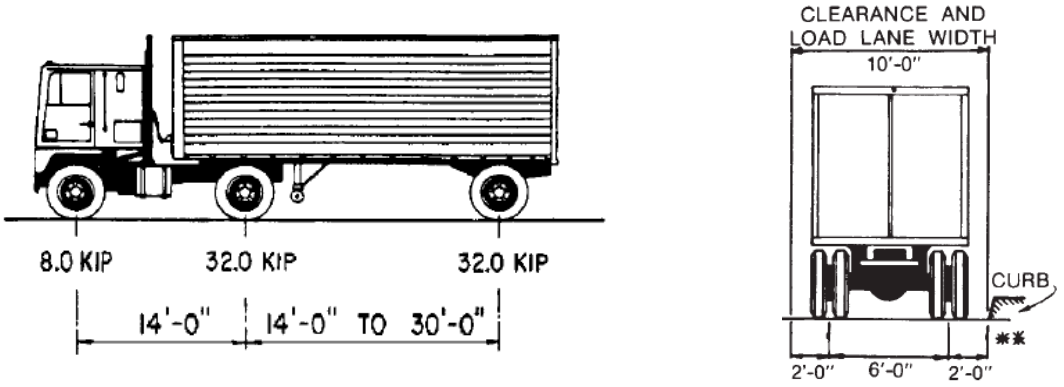

(a) Truck Axle Loadings and Longitudinal Spacings *(b) Truck Transverse Spacing*

Figure 5.6. HS-20 Truck Loading (reprinted from AASHTO 2002; AASHTO 2017)

The designated HL93 loading consisting of the design truck or design tandem coincident with design lane load is shown in Figure 5.7. The design lane load consists of 0.64 kip/ft uniformly distributed load over a 10 ft width. Two 25-kip axle loads spaced 4 ft apart longitudinally and the wheel lines 6 ft apart transversely, constitute the design tandem load. The design truck or design tandem is used depending on which will create the maximum force effect on the span.

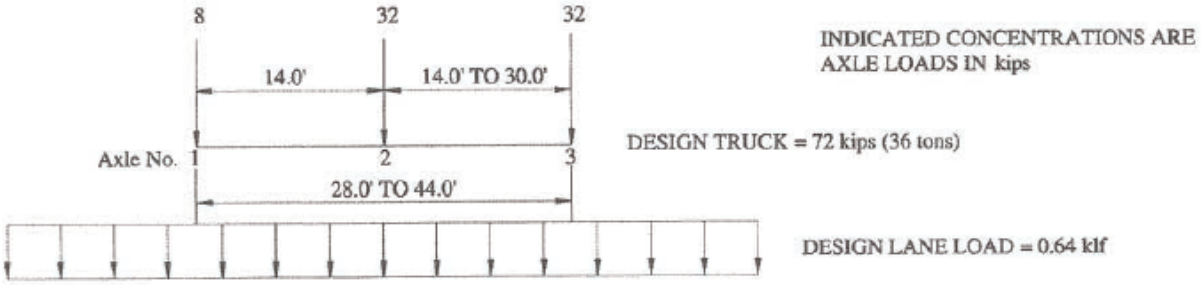

(a) Design Truck and Lane Load

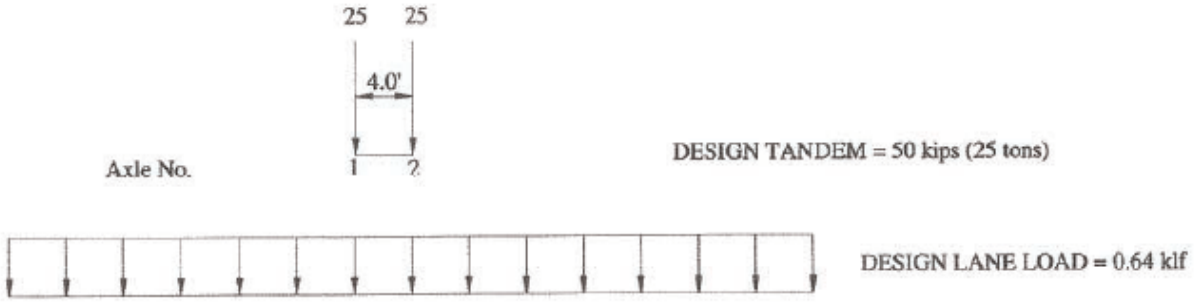

(b) Design Tandem and Lane Load

Figure 5.7. Designated HL-93 Load Model (reprinted from AASHTO MBE 2018)

5.4.1. Verification of Maximum Deflection

The maximum deflection for the bridge superstructure under uniform distributed dead load was verified against the deflections obtained from basic structural analysis. The estimated deflections for an interior girder obtained from FEM analysis were compared to the calculated deflections. The equivalent distributed load was calculated as the sum of the weight of the girder, the deck, and wearing surface. The total uniform distributed weight can be found as,

$$w = w_g + w_{ws} = 1.272 \text{ kip/ft} \tag{5.3}$$

in which:

w_g = weight of girders (including slab) = 0.408 kip/ft

$$w_{ws} = (\gamma_{ws})(t_{ws})(s) = 0.864 \text{ kip/ft} \quad (5.4)$$

where:

γ_c = unit weight of concrete = 0.15 kip/ft^3

s = spacing of the pan girders (ft)

w_{ws} = weight of wearing surface (kip/ft)

γ_{ws} = unit weight of the wearing surface = 0.144 kip/ft^3

t_{ws} = thickness of the wearing surface (ft)

The midspan deflection of the pan girder bridge can be calculated using Eqn. (5.5) for a simply supported beam under uniformly distributed load.

$$\Delta = \frac{5wL^4}{384E_cI} = 0.413 \text{ in.} \quad (5.5)$$

where:

I = Moment of inertia of an interior pan girder section = 18,501 in^4

E_c = Modulus of elasticity of concrete = 3031 ksi

Table 5.5 shows the deflections calculated using each method and the percent difference relative to the calculated deflection. The CSiBridge deflections are within two percent of the calculated deflection.

Table 5.5. Dead Load Deflection Comparison for Bridge CM-4

Bridge ID	CSiBridge Deflection (in.)	Calculated Deflection (in.)	Percent Difference (%)
CM-5	0.420	0.413	1.69

5.4.2. Verification of Absolute Maximum Moment

To verify that the truck loadings were modeled correctly, the live load moments were compared to the live load moments obtained from basic structural analysis. The model was analyzed under HS-20 truck and HL-93 loading. The calculations for obtaining the maximum moment due to moving loads in a simple span are presented in the following sections.

5.4.2.1. Maximum Moment due to HS-20 Design Truck Loading

The maximum moment for a simple span bridge under HS-20 truck loading is obtained when a the rear and middle axleas are 14 ft apart. Three cases arise for the HS-20 truck loading based on the bridge span length as explained below.

1. The first case applies for bridges with spans less than 24 ft. In this case, the rear axle is located at midspan to result in maximum moment at the center span, which is calculated using Eqn. (5.6).

$$M = \frac{PL}{4} = 8L \tag{5.6}$$

2. This case applies for bridges with spans between 24 ft and 34 ft. Here, the rear axle and the middle axle are positioned on the the bridge in order to produce the maximum moment. A generic loading diagram for such a scenario is presented in Figure 5.8(a) and the actual position for maximum moment is shown in Figure 5.8(b).

The support reaction corresponding tto the maximum moment location is calculated using Eqn. (5.7).

$$R_A = 32\left(\frac{L-x}{L}\right) + 32\left(\frac{L-x-14}{L}\right) = 64 - \frac{64x}{L} - \frac{448}{L} \tag{5.7}$$

The maximum moment is obtained at the location of one of the axles (Eqn. (5.8)).

$$M_{at\ x} = R_A \cdot x \tag{5.8}$$

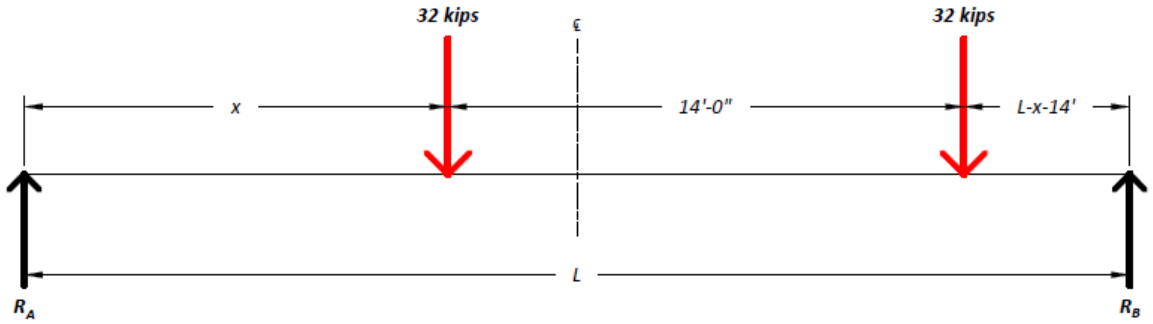

(a) Diagram of Loading Scheme

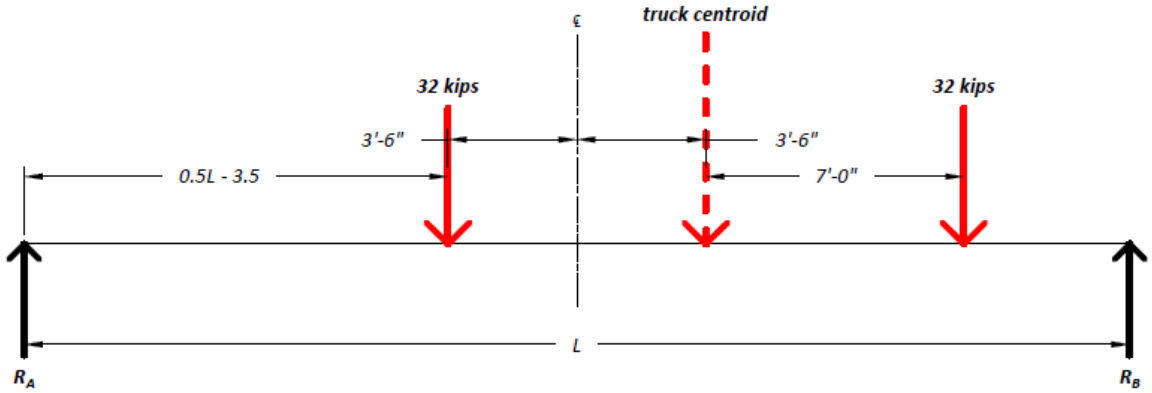

(b) Location of Axles for Maximum Moment

Figure 5.8. Positioning of HS-20 Truck for Maximum Moment for Case 2

Equating the first derivative of the moment equation to zero would help compute the distance x where the maximum moment is obtained (Eqn. (5.9)).

$$x = \frac{L}{2} - 3.5 \tag{5.9}$$

Thus, the absolute maximum moment for Case 2 HS-20 loading scenario can be calculated using Eqn. (5.10). It should be noted that the maximum moment occurs under one of the axles only if the axle and the resultant load group are equidistant from the bridge centerline.

$$M_{max} = (16L) - 224 + \frac{784}{L} \tag{5.10}$$

3. This case applies to bridges with spans greater than 34 ft. In this case, the HS-20 truck is positioned on the bridge to produce the maximum moment. A generic loading diagram for such a scenario is presented in Figure 5.9(a) and the actual position for maximum moment is shown in Figure 5.9(b) which corresponds to the middle axle located at a distance of $x +$ 14 ft from the support. The support reaction corresponding tto the maximum moment location is calculated using Eqn. (5.11).

$$R_A = 32\left(\frac{L-x}{L}\right) + 32\left(\frac{L-x-14}{L}\right) + 8\left(\frac{L-x-28}{L}\right) = 72 - \frac{72x}{L} - \frac{672}{L} \tag{5.11}$$

The maximum moment is obtained at the location of one of the axles (Eqn. (5.12)).

$$M_{at\ (x+14)} = (R_A \cdot x) + (R_A - 32) \times 14 \tag{5.12}$$

Equating the first derivative of the moment equation to zero would help compute the distance x where the maximum moment is obtained (Eqn. (5.13)).

$$x = \frac{L}{2} - 11.67 \tag{5.13}$$

Thus, the absolute maximum moment for Case 3 HS-20 loading scenario can be calculated using Eqn. (5.14). It should be noted that the maximum moment occurs under the middle axle only if the axle and the resultant load group are equidistant from the bridge centerline.

$$M_{max} = (18L) - 280 + \frac{392}{L} \tag{5.14}$$

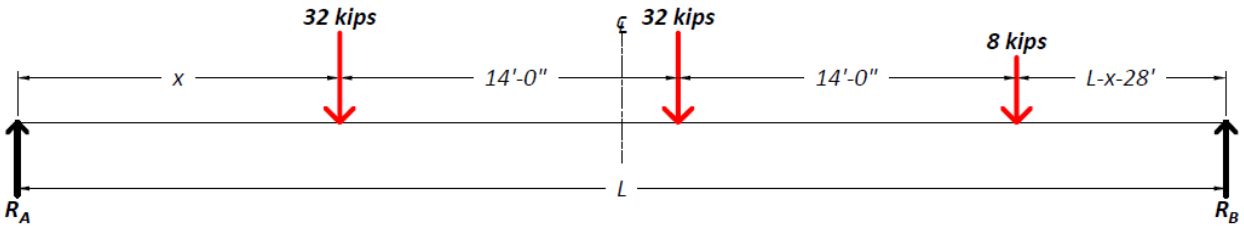

(a) Diagram of loading scheme

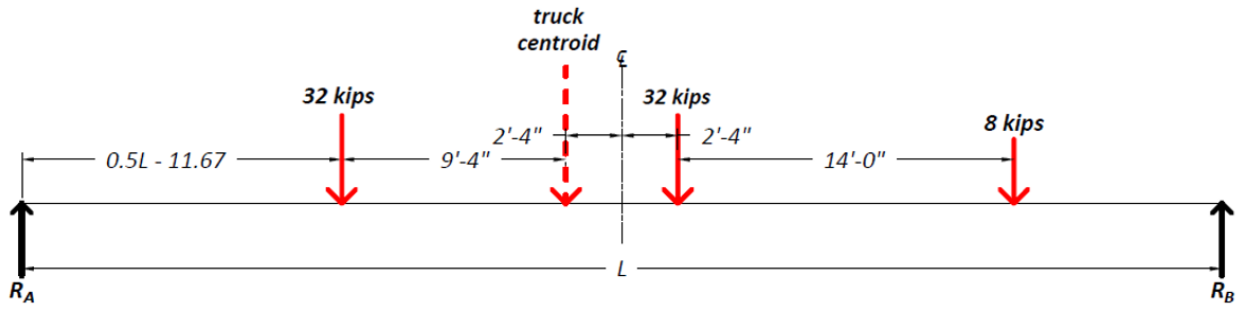

(b) Location of axles for maximum moment

Figure 5.9. Positioning of HS-20 Truck for Maximum Moment for Case 3

5.4.2.2. Maximum Moment due to Designated HL-93 Loading

The HL93 loading model is comprised of the HS-20 design truck or the design tandem along with the uniformly distributed lane load. The following explains the maximum moment calculation for a simple span bridge for the two loading types.

1. Figure 5.10(a) shows the HL93 loading comprised of the HS-20 truck and the lane load. The absolute maximum moment occurs at the middle axle location. The support reaction corresponding to the maximum moment location is calculated using Eqn. (5.15).

$$R_A = 32\left(\frac{L-x}{L}\right) + 32\left(\frac{L-x-14}{L}\right) + 8\left(\frac{L-x-28}{L}\right) = 72 - \frac{72x}{L} - \frac{672}{L} \quad (5.15)$$

The maximum moment is obtained according to Eqn. (5.16).

$$M_{at\,(x+14)} = \left(72 - \frac{72x}{L} - \frac{672}{L}\right)x + \left(40 - \frac{72x}{L} - \frac{672}{L}\right) \times 14 + 0.32L(x+14) - 0.32(x+14)^2 \quad (5.16)$$

Equating the first derivative of the moment equation to zero would help compute the distance x where the maximum moment is obtained (Eqn. (5.17)).

$$x = \frac{L^2 + 197L - 5250}{2L + 450} \quad (5.17)$$

The maximum moment in bridge can be calculated by substituting Eqn. (5.17) into Eqn. (5.16).

2. Figure 5.10(b) shows the HL93 loading comprised of the tandem truck and the lane load. The absolute maximum moment occurs at one of the axle locations. The support reaction corresponding to the maximum moment location is calculated using Eqn. (5.18).

$$R_A = \left[50 - \frac{50x}{L} - \frac{100}{L}\right] + 0.32L \quad (5.18)$$

The maximum moment is obtained according to Eqn. (5.19).

$$M_{at\,x} = \left(50 - \frac{50x}{L} - \frac{100}{L}\right)x + 0.32Lx - 0.32x^2 \quad (5.19)$$

Equating the first derivative of the moment equation to zero would help compute the distance x where the maximum moment is obtained (Eqn. (5.20)).

$$x = \frac{4L^2 + 625L - 1250}{8L + 1250} \tag{5.20}$$

The maximum moment in bridge can be calculated by substituting Eqn. (5.20) into Eqn. (5.19).

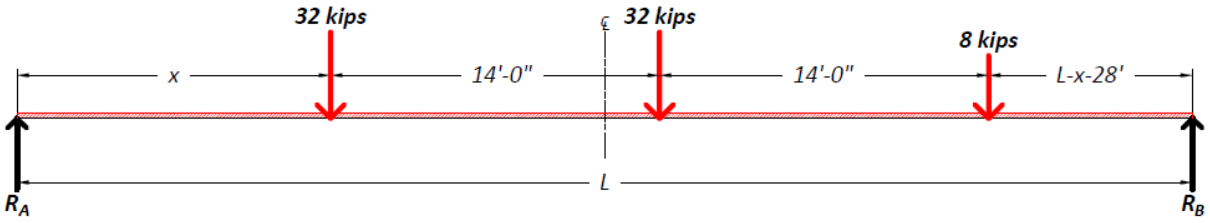

(a) Diagram of Loading Scheme

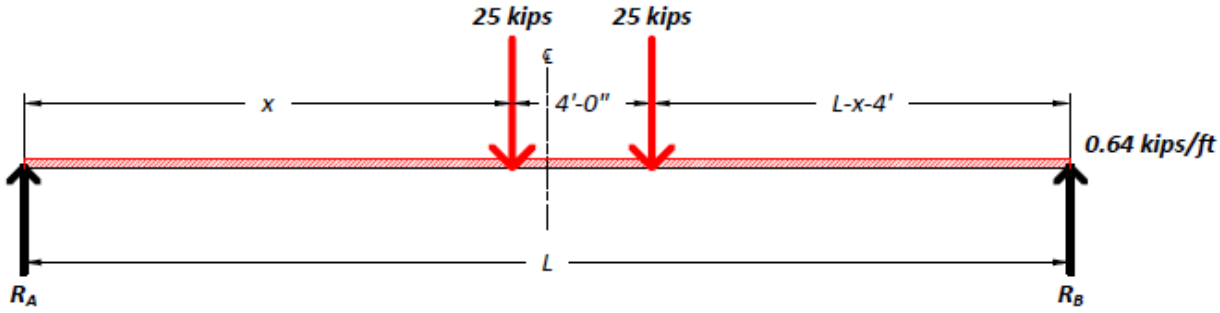

(b) Location of Axles for Maximum Moment

Figure 5.10. Positioning of HL-93 Tandem for Maximum Moment

Bridge CM-5 is less than 34 ft in span and thus Case 2 applies for the HS-20 truck moment calculation. Table 5.6 shows the calculated live load moments, the CSiBridge moments, and the percent difference between them. The CSiBridge live load moments matched up very closely to the expected live load moments.

Table 5.6. Live Load Moment on the Comparison for Bridge CM-5

Bridge ID	Applied Load	CSiBridge 1-Lane Moment on Total Section (kip-ft)	Expected 1-Lane Moment on Total Section (kip-ft)	Percent Difference (%)
CM-5	HS-20	281.6	282.1	0.18
	HL-93	398.35	398.4	0.01
Note: All calculated moments are without the application of the impact factor				

5.4.3. Verification of Maximum Shears

To verify that the structural supports have been modeled correctly, maximum shears corresponding to the live loads were verified against the shear forces obtained from basic structural analysis. Sep-by-step loading is employed by CSiBridge for moving load analysis. The step size of the moving load was adjusted so that the first step with the rear axle of the truck on the bridge positioned the rear axle 2 ft away from the support. The resulting support reactions were obtained from the FEM model and compared with those calculated using classical structural analysis methods. Table 5.7 shows the support reactions calculated using each method and the percent difference between them. The CSiBridge support reactions matched up very closely to the calculated reactions.

Table 5.7. Live Load Shears Comparison for the Bridge CM-5

Bridge ID	Applied Load	CSiBridge 1-Lane Shear on Total Section (kip)	Expected 1-Lane Shear on Total Section (kip)	Difference (%)
CM-5	HS-20	46.9	47.2	0.57
	HL-93	54.4	54.6	0.29
Note: All calculated shears are without the application of the impact factor.				

5.5. SIMULATING VEHICLE LOADS

The truck loads and lane loads were placed transversely on Bridge CM-5 as per the AASHTO Standard Specifications (AASHTO 2002) and AASHTO LRFD Specifications (AASHTO 2017). Bridge CM-5 has two lanes each 10.85 ft wide.

A linear static moving load analysis was performed with each truck moving along the length of the bridge in approximately one-foot increments. It should be noted that although it would be an unlikely event, for the two-lane-loaded cases both trucks traveled along the bridge in the same direction in order to produce the maximum possible effect on the bridge.

5.5.1. Simulating HS-20 Truck Loading

For a one-lane-loaded case based on the Standard Specifications, the truck was placed so that the exterior wheel line was 2 ft away from the edge of the barrier (Path 1). Due to the narrow lane width, the only other loading scenario considered was placing the interior wheel line 2 ft from the centerline of the bridge (Path 2). For a two-lane-loaded case, one truck was positioned in Path 1 and a second truck was positioned in Path 2. This created two separate one-lane-loaded cases and one two-lane-loaded case. Figure 5.11 shows the different HS-20 truck loading cases along the transverse section of Bridge CM-5. The red and blue arrows represent the wheel lines of the truck and the black dashed line is the centerline (CL) of the bridge.

5.5.2. Simulating HL-93 Loading

For loading based on the LRFD Specifications, the tandem configuration and lane load were added to the already created load cases. The tandem configuration was used for HL-93 loading as it controls over the truck configuration for short span bridges less than 40.5 ft long. The design tandem was placed transversely in the same manner as described for the HS-20 truck. The lane

load was placed immediately adjacent to the edge of the barrier for Path 1. For Path 2, the lane load was placed immediately adjacent to the centerline of the bridge. For the two-lane-loaded case, the lane load was kept adjacent to the centerline of the bridge in the second lane. Figure 5.12 shows the different HL-93 loading cases along the transverse section of Bridge CM-5. The red and blue arrows represent the wheel lines of the truck, the red and blue cross hatched regions represent the lane load distributed over the lane width and the black dashed line is the centerline (CL) of the bridge.

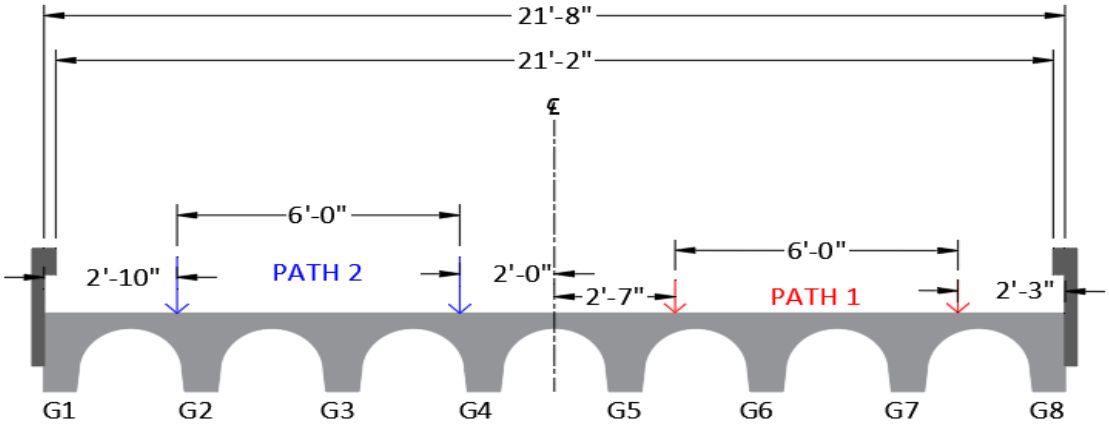

Figure 5.11. HS-20 Truck Loading Cases for Bridge CM-5

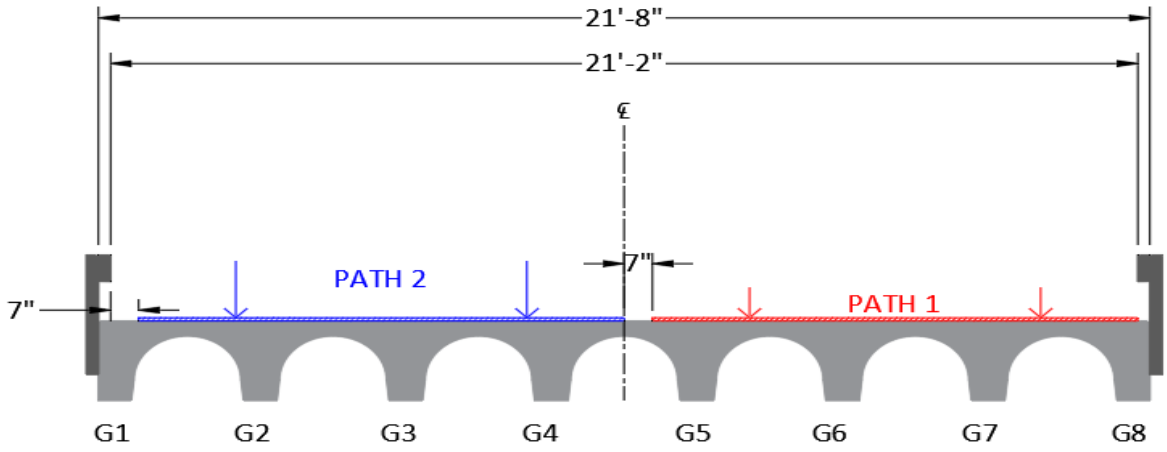

Figure 5.12. HL-93 Loading Cases for Bridge CM-5

5.6. FEM RESULTS

Bridge CM-5 was analyzed using the FEM software CSiBridge under the loading scenarios provided in Figure 5.11 and Figure 5.12. Girder displacement profiles were obtained for both one-lane-loaded and two-lane-loaded cases. Modal analysis was conducted to determine estimated modal frequencies and mode shapes. Live load moment and shear values were also extracted and analyzed to compare the expected LLDFs with the LLDFs prescribed in AASHTO Standard Specifications (AASHTO 2002) and AASHTO LRFD Specifications (AASHTO 2017).

5.6.1. Modal Properties

The first longitudinal bending mode and the first torsional mode constitute the first two modes of Bridge CM-5. The frequency for the longitudinal bending mode was determined to be 9.42 Hz and that for the torsional mode was 11.58 Hz. The contours of the longitudinal bending mode shape along with the normalized amplitudes along the span of the bridge are shown in Figure 5.10(a). Figure 5.10(b) shows the contours of the torsional mode shape along with the normalized amplitudes transverse to the span.

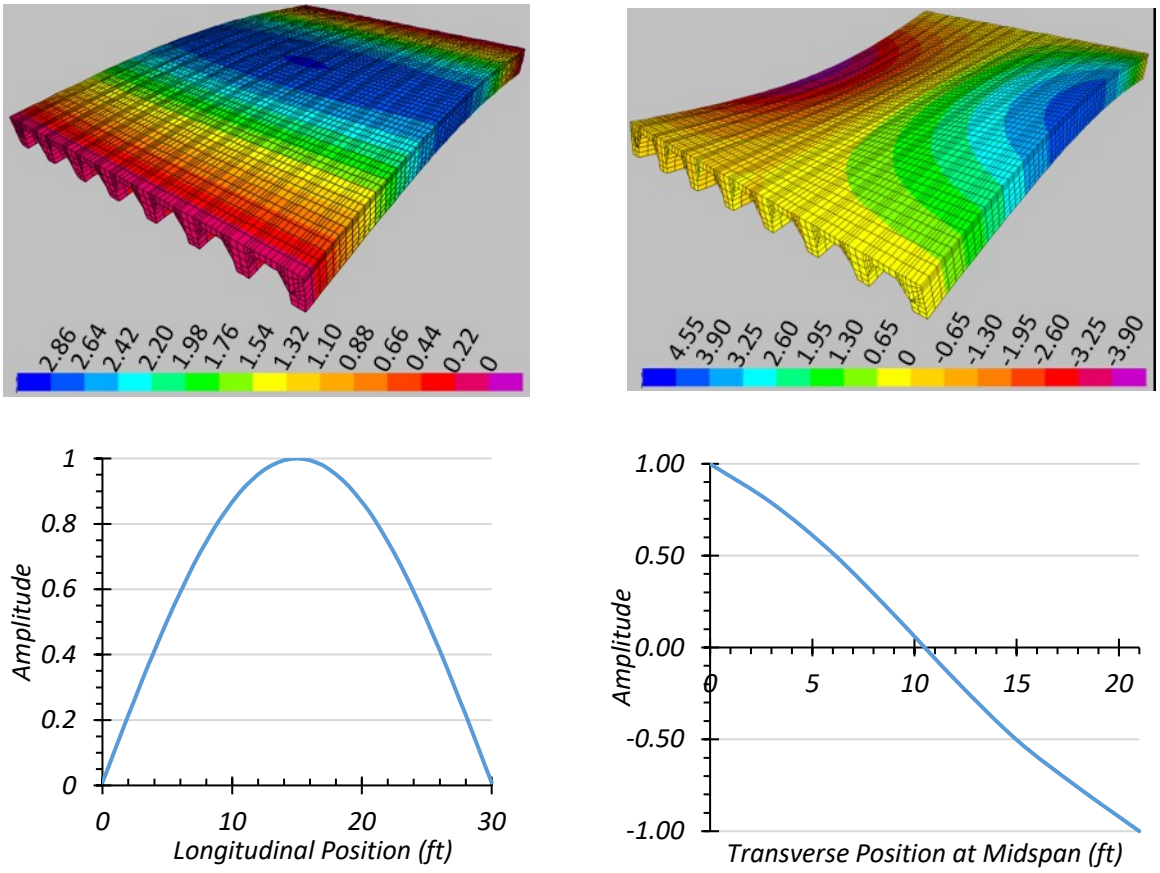

(a) Longitudinal Bending Mode (f=9.42 Hz) *(b) Torsional Mode (f=11.58 Hz)*

Figure 5.13. First Two Mode Shapes of Bridge CM-5

5.6.2. HS-20 Live Load Analysis

Bridge CM-5 was subjected to the design HS-20 truck load as defined in the AASHTO Standard Specifications (AASHTO 2002). The paths defined in Figure 5.11 were prescribed in CSiBridge for analysis. The following sections discuss the deflections, bending moment, and shear values obtained from the FEM model.

5.6.2.1. Deflection Results

The estimated girder deflection profiles and contours along the span for one-lane HS-20 loading along Path 1 and Path 2 are shown in Figure 5.14. The maximum deflections under HS-20 loading for each loaded path is tabulated in Figure 5.13. The maximum deflection under one-lane HS-20 loading was observed at the edge girders, with 0.19 in. at Girder G1 under Path 1 loading.

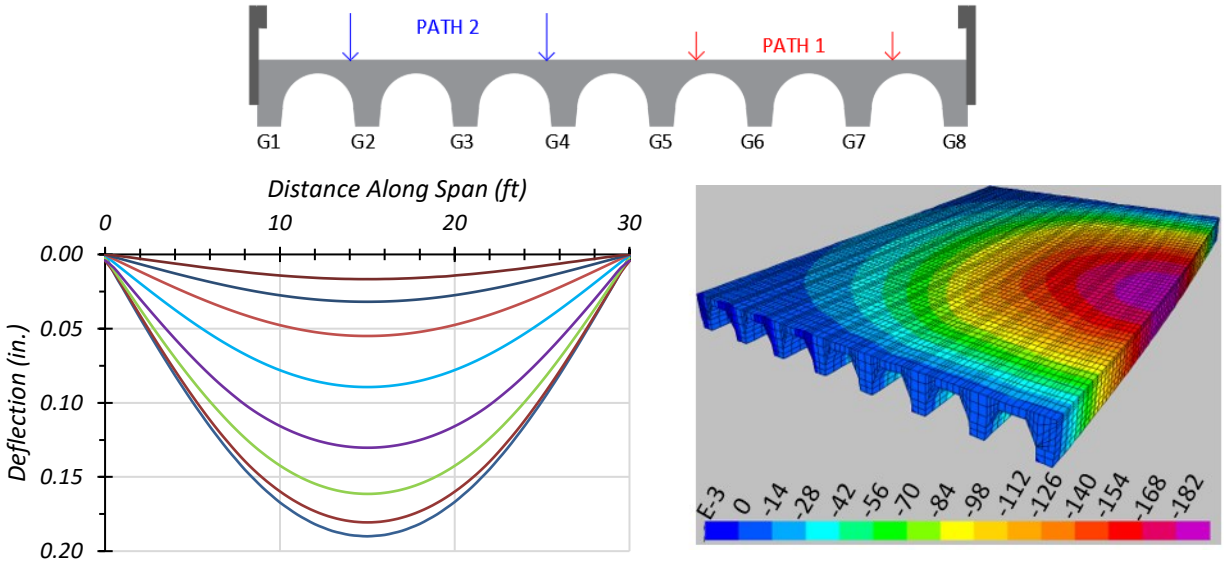

(a) Path 1

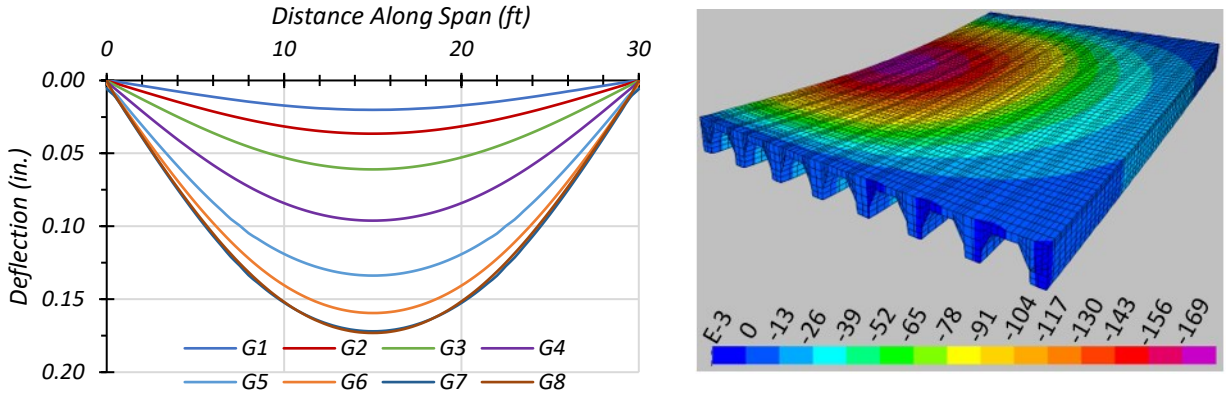

(b) Path 2

Figure 5.14. Deflection Profiles under HS-20 Loading

Table 5.8. Maximum Deflections under HS-20 Loading

Loading	G1	G2	G3	G4	G5	G6	G7	G8
Path 1	0.190	0.181	0.161	0.130	0.089	0.055	0.032	0.017
Path 2	0.020	0.036	0.061	0.096	0.134	0.159	0.172	0.173
Note: G = girder, paths indicate transverse loading positions as shown, deflections have inch units								

5.6.2.2. Moment Results

The moments corresponding to each girder and the corresponding LLDFs for the one-lane and two-lane HS-20 loading paths are shown in Figure 5.15. The corresponding maximum moments for each girder and path are listed in Table 5.9. Maximum Moments under HS-20 Loading. The estimated moment results from the FEM model were used to calculate the moment LLDFs. A comparison of the estimated moment LLDFs obtained from the FEM model and those calculated using the approximate equations in the AASTHO Standard Specifications (AASHTO 2002) is provided in Table 5.10. Governing Moment LLDF Values for HS-20 Loading. The AASHTO moment LLDF is slightly conservative for the interior girder with $g^m_{AASHTO}/g^m_{FEM} = 1.02$ and very conservative for the exterior girder with $g^m_{AASHTO}/g^m_{FEM} = 1.33$ for a one-lane HS-20 loading scenario. For the two-lane HS-20 loading case, the AASHTO prediction is unconservative with g^m_{AASHTO}/g^m_{FEM} ratio of 0.87 for the interior girder, while being conservative for the exterior girder with $g^m_{AASHTO}/g^m_{FEM} = 1.27$.

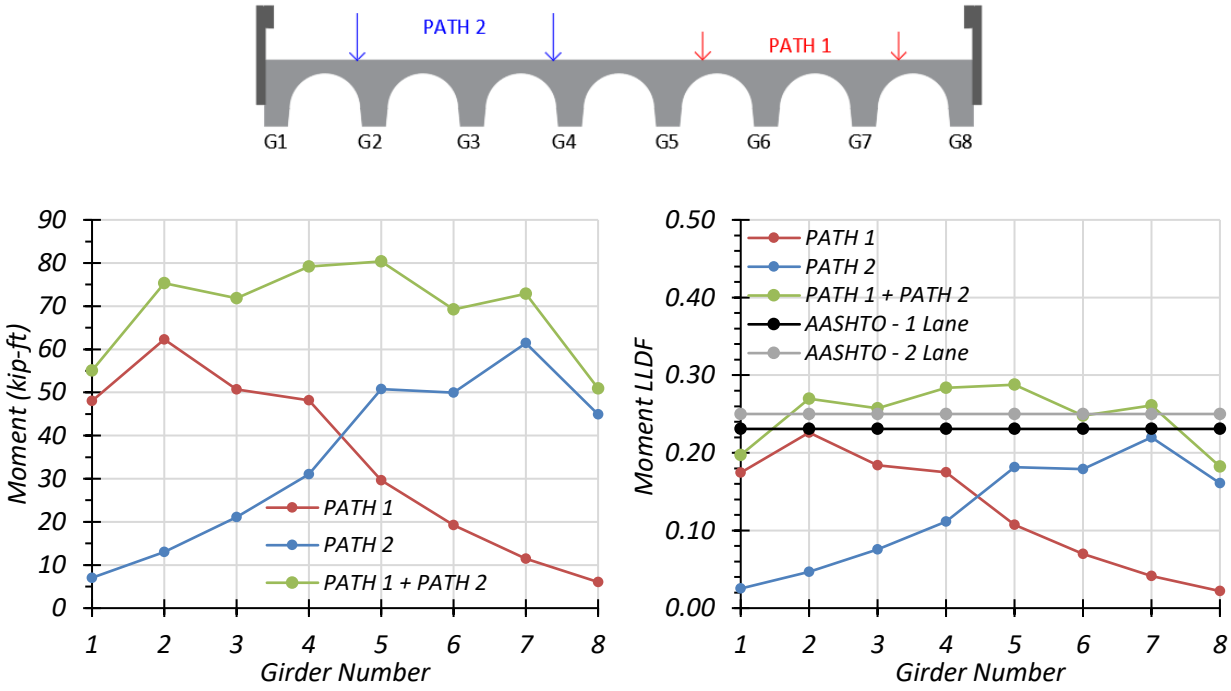

(a) Moment *(b) Moment LLDF*

Figure 5.15. Moment Results under HS-20 Loading

Table 5.9. Maximum Moments under HS-20 Loading

Loading	G1	G2	G3	G4	G5	G6	G7	G8
Path 1	48.03	62.30	50.71	48.14	29.62	19.25	11.44	6.04
Path 2	7.03	13.03	21.13	31.07	50.75	49.99	61.42	44.89
Path 1 + Path 2	55.06	75.33	71.84	79.21	80.37	69.24	72.86	50.93
Note: G = girder, paths indicate transverse loading positions as shown, moments have kip-ft units								

Table 5.10. Governing Moment LLDF Values for HS-20 Loading

Loading	Girder Location	AASHTO (g^m_{AASHTO})	FEM (g^m_{FEM})	g^m_{AASHTO}/g^m_{FEM}
One-lane	Interior	0.231	0.226	1.02
	Exterior	0.231	0.174	1.33
Two-lane	Interior	0.250	0.288	0.87
	Exterior	0.250	0.197	1.27

5.6.2.3. Shear Results

The shear forces in each girder and the corresponding shear LLDFs for the one-lane and two-lane HS-20 loading paths are shown in Figure 5.16. The corresponding maximum support reactions for each girder and path are listed in Table 5.11. Maximum Shears under HS-20 Loading A comparison of the estimated shear LLDFs, calculated from the FEM support reactions, and those calculated using the approximate equations in the AASTHO Standard Specifications (AASHTO 2002) is provided in Table 5.12. Governing Shear LLDF Values for HS-20 Loading. The AASHTO shear LLDF is conservative for the exterior girder with $g^v_{AASHTO}/g^v_{FEM} = 1.38$, while being unconservative for the interior girder with $g^v_{AASHTO}/g^v_{FEM} = 0.84$, for a one-lane HS-20 loading scenario. Similarly, for the two-lane HS-20 loading case, g^v_{AASHTO}/g^v_{FEM} has an unconservative value of 0.75 for the interior girder and a conservative ratio of 1.42 for the exterior girder.

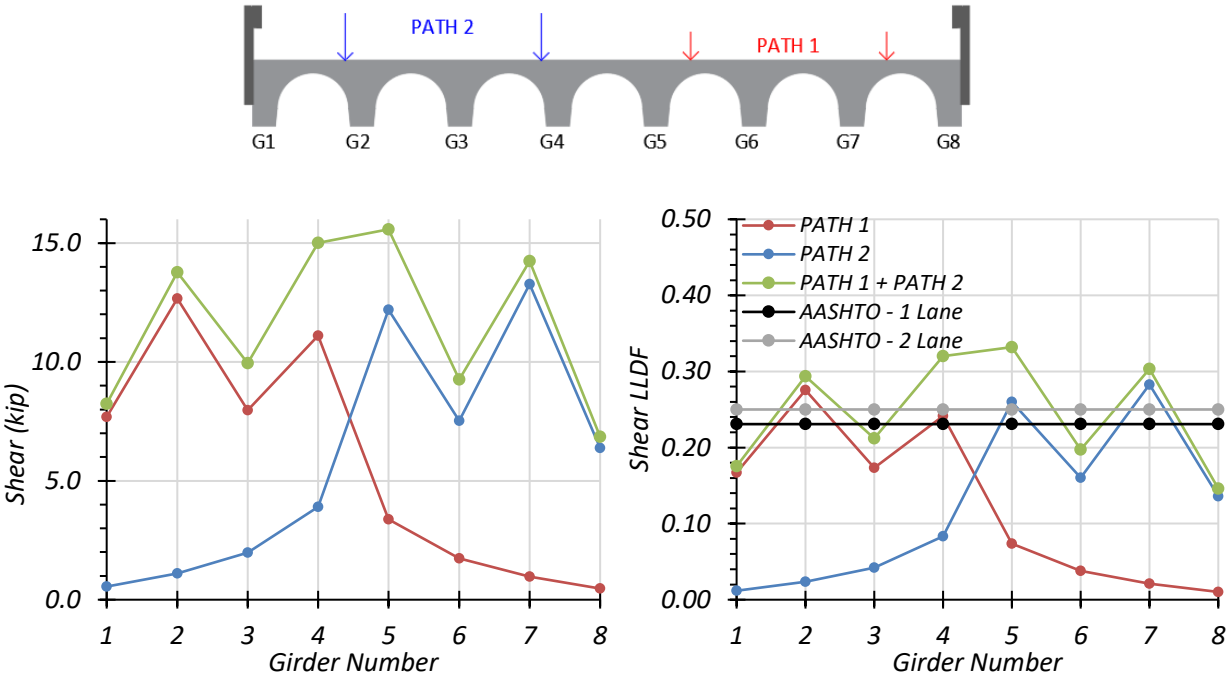

(a) Shear *(b) Shear LLDF*

Figure 5.16. Shear Results under HS-20 Loading

Table 5.11. Maximum Shears under HS-20 Loading

Loading	G1	G2	G3	G4	G5	G6	G7	G8
Path 1	7.68	12.67	7.97	11.11	3.38	1.73	0.97	0.47
Path 2	0.55	1.10	1.98	3.91	12.20	7.53	13.27	6.39
Path 1 + Path 2	8.24	13.77	9.95	15.01	15.58	9.26	14.24	6.85
Note: G = girder, paths indicate transverse loading positions as shown, shears have kip units								

Table 5.12. Governing Shear LLDF Values for HS-20 Loading

Loading	Girder Location	AASHTO (g^v_{AASHTO})	FEM (g^v_{FEM})	g^v_{AASHTO}/g^v_{FEM}
One-lane	Interior	0.23	0.28	0.84
	Exterior	0.23	0.17	1.38
Two-lane	Interior	0.25	0.33	0.75
	Exterior	0.25	0.18	1.42

5.6.3. HL-93 Live Load Analysis

Bridge CM-5 was subjected to the HL-93 design loading as defined in the AASHTO LRFD Specifications (AASHTO 2017). The paths defined in Figure 5.12 were prescribed in CSiBridge for analysis. The following sections discuss the deflections, bending moment, and shear values obtained from the FEM model.

5.6.3.1. Deflection Results

The estimated girder deflection profiles and contours along the span for one-lane HL-93 loading along Path 1 and Path 2 are shown in Figure 5.17. The maximum deflections under HL-93 loading for each loaded path is tabulated in Table 5.13. The maximum deflection under one-lane HL-93 loading was observed at the edge girders, with 0.248 in. at Girder G1 under loading Path 1.

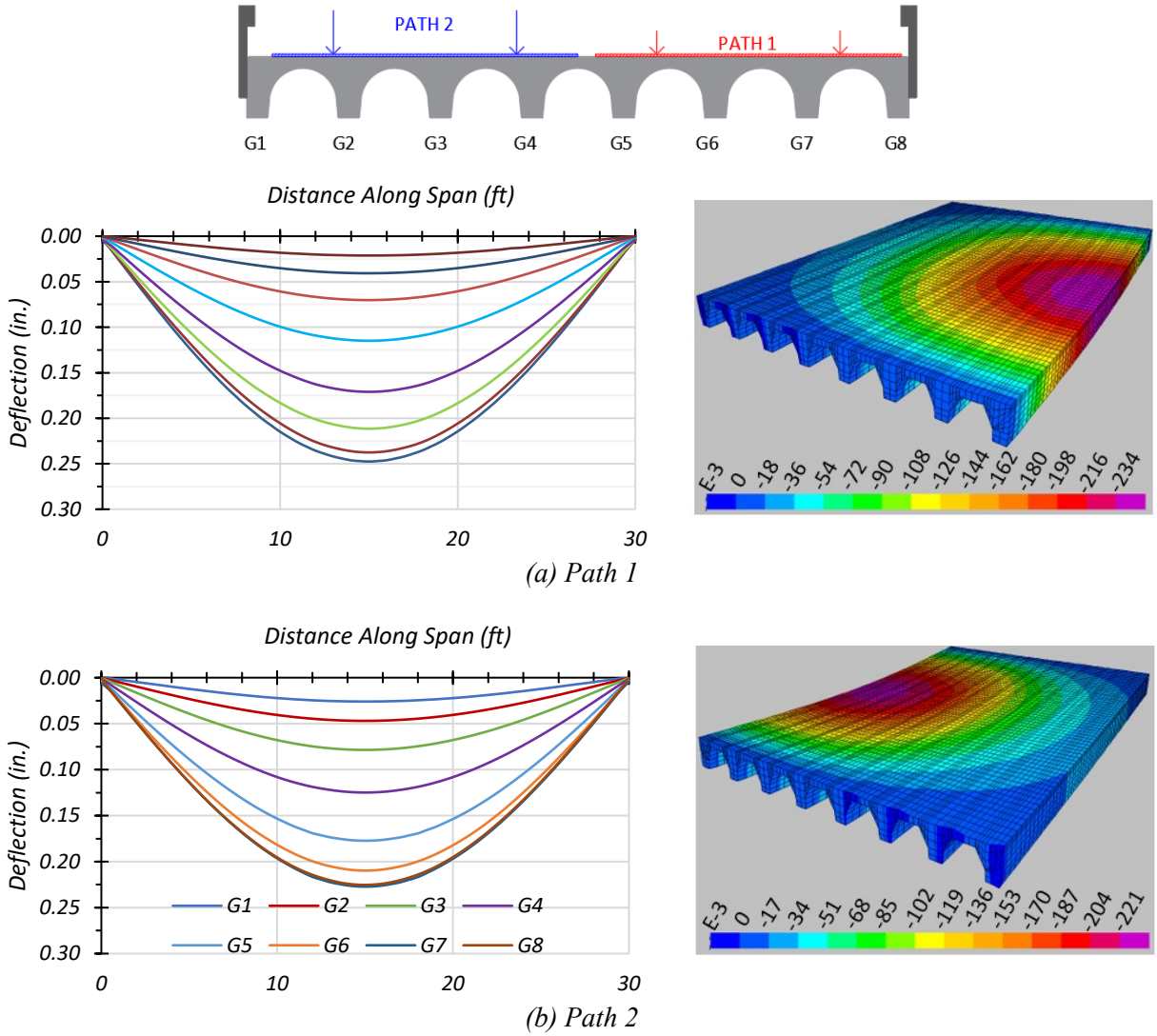

Figure 5.17. Deflection Profiles under HL-93 Loading

Table 5.13. Maximum Deflections under HL-93 Loading

Loading	G1	G2	G3	G4	G5	G6	G7	G8
Path 1	0.248	0.238	0.212	0.171	0.115	0.070	0.041	0.021
Path 2	0.026	0.047	0.079	0.125	0.177	0.210	0.227	0.225
Note: G = girder, paths indicate transverse loading positions as shown, deflections have inch units								

5.6.3.2. Moment Results

The moments corresponding to each girder and the corresponding LLDFs for the one-lane and two-lane HL-93 loading paths are shown in Figure 5.18. The corresponding maximum moments for each girder and path are listed in Table 5.14. The estimated moment results from the FEM model were used to calculate the moment LLDFs. A comparison of the estimated moment LLDFs obtained from the FEM model and those calculated using the approximate equations in the AASHTO LRFD Specifications (AASHTO 2017) is provided in Table 5.15. AASHTO LRFD approximate LLDF values were calculated using two different methods: (1) using the simplified stiffness parameter, (2) using the more accurate analytical stiffness parameter. Both methods gave almost the same LLDFs as shown in Figure 5.18. The AASHTO LRFD moment LLDF is very conservative for the interior girder with $g^m_{AASHTO}/g^m_{FEM} = 1.49$ and conservative for the exterior girder with $g^m_{AASHTO}/g^m_{FEM} = 1.29$ for a one-lane HL-93 loading scenario. For the two-lane HL-93 loading case, the AASHTO LRFD prediction is very conservative with g^m_{AASHTO}/g^m_{FEM} ratio of 1.43 for the interior girder and 1.57 for the exterior girder.

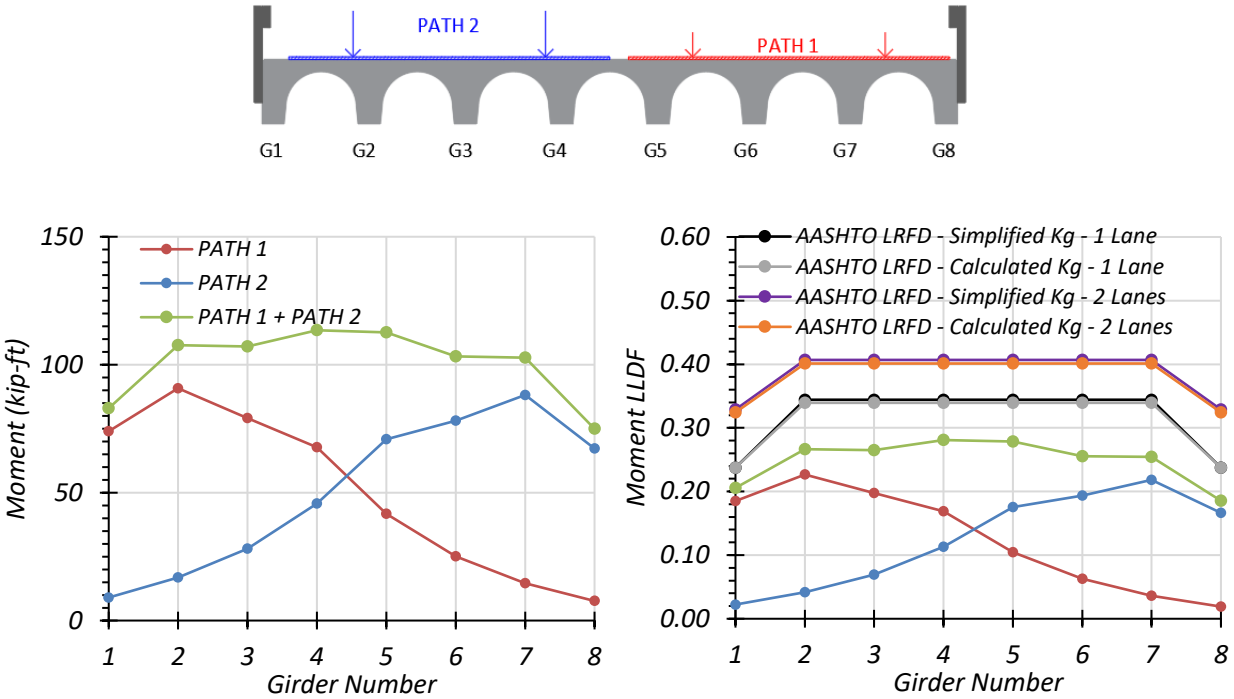

(a) Moment *(b) Moment LLDF*

Figure 5.18. Moment Results under HL-93 Loading

Table 5.14. Maximum Moments under HL-93 Loading

Loading	G1	G2	G3	G4	G5	G6	G7	G8
Path 1	74.03	90.78	79.04	67.70	41.77	25.06	14.55	7.64
Path 2	9.00	16.79	28.04	45.75	70.81	78.15	88.17	67.28
Path 1 + Path 2	83.03	107.57	107.08	113.45	112.58	103.21	102.72	74.92
Note: G = girder, paths indicate transverse loading positions as shown, moments have kip-ft units								

Table 5.15. Governing Moment LLDF Values for HL-93 Loading

Loading	Girder Location	AASHTO (g^m_{AASHTO})	FEM (g^m_{FEM})	g^m_{AASHTO}/g^m_{FEM}
One-lane	Interior	0.37	0.23	1.49
	Exterior	0.27	0.19	1.29
Two-lane	Interior	0.40	0.28	1.43
	Exterior	0.32	0.21	1.57

5.6.3.3. Shear Results

The shear forces in each girder and the corresponding shear LLDFs for the one-lane and two-lane HL-93 loading paths are shown in Figure 5.18. The corresponding maximum support reactions for each girder and path are listed in Table 5.16. A comparison of the estimated shear LLDFs, calculated from the FEM support reactions, and those calculated using the approximate equations in the AASHTO LRFD Specifications (AASHTO 2017) is provided in Table 5.17. The AASHTO LRFD shear LLDF is conservative for the exterior girder with $g^v_{AASHTO}/g^v_{FEM} = 1.36$, in comparison to the FEM results, while $g^v_{AASHTO}/g^v_{FEM} = 2.20$ for the interior girder, for a one-lane HL-93 loading scenario. For the two-lane HL-93 loading case, g^v_{AASHTO}/g^v_{FEM} has a value of 1.44 for the interior girder and 1.53 for the exterior girder.

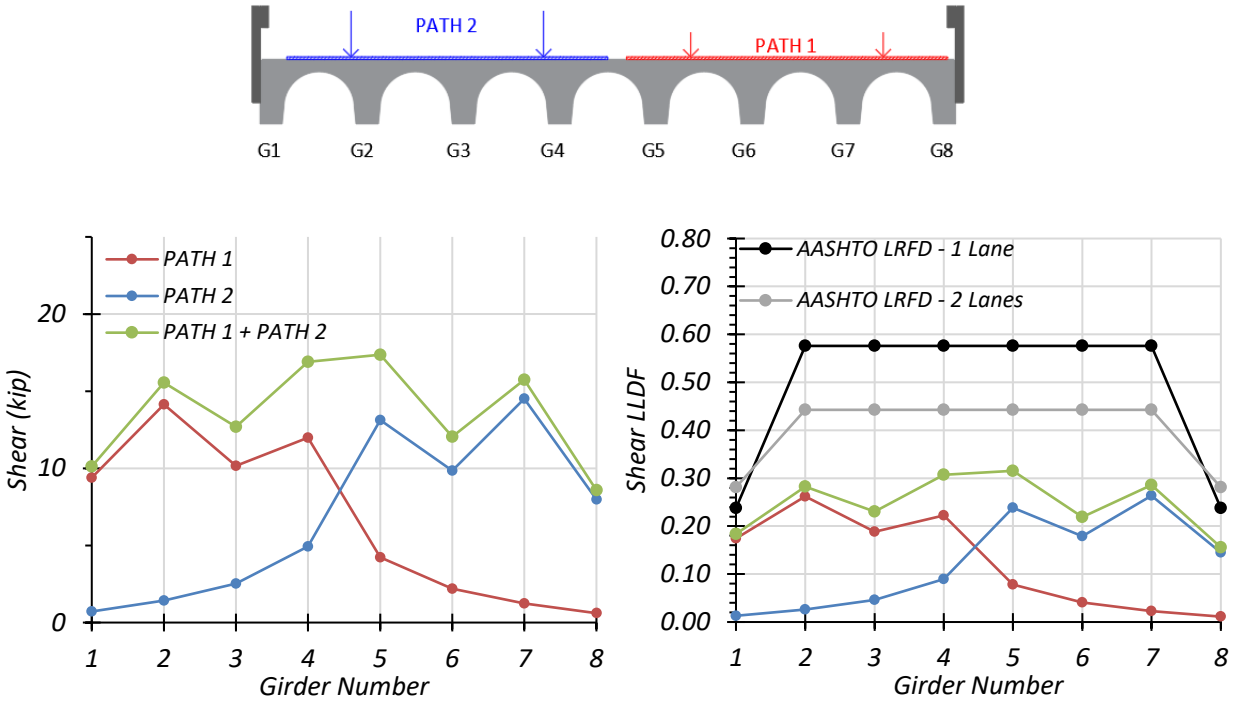

(a) Shear *(b) Shear LLDF*

Figure 5.19. Shear Results with HL-93 Loading

Table 5.16. Maximum Shears with HL-93 Loading

Loading	G1	G2	G3	G4	G5	G6	G7	G8
PATH 1	9.39	14.14	10.16	11.98	4.23	2.20	1.24	0.61
PATH 2	0.72	1.42	2.53	4.92	13.13	9.86	14.51	7.97
PATH 1 + PATH 2	10.11	15.56	12.69	16.91	17.36	12.05	15.75	8.58
Note: G = girder, paths indicate transverse loading positions as shown, shears have kip units								

Table 5.17. Governing Shear LLDF Values for HL-93 Loading

Loading	Girder Location	AASHTO (g^v_{AASHTO})	FEM (g^v_{FEM})	g^v_{AASHTO}/g^v_{FEM}
One-lane	Interior	0.576	0.262	2.20
	Exterior	0.238	0.174	1.36
Two-lane	Interior	0.443	0.307	1.44
	Exterior	0.281	0.184	1.53

5.7. SUMMARY

Finite element analysis of the selected simple-span concrete multi-girder bridge, Bridge CM-5, was conducted for various vehicular load configurations. Live load moment and shear values were extracted and analyzed to compare the expected LLDFs with the LLDFs prescribed in the AASHTO Standard Specifications (AASHTO 2002) and AASHTO LRFD Specifications (AASHTO 2017).

In general, the AASHTO Standard Specifications moment LLDF is accurate, and slightly conservative for one-lane loading scenarios for Bridge CM-5. The governing g_{AASHTO}/g_{FEM} ratio for flexure is above 1.0 for both interior and exterior girders. However, the g_{AASHTO}/g_{FEM} ratio for flexure are 0.87 and 1.27 for interior and exterior girders for the two-lane-loaded scenario. A similar trend is also observed for the AASHTO shear LLDF. The g_{AASHTO}/g_{FEM} ratio for shear with 0.84 and 1.38 for interior and exterior girders for one-lane loading, and 0.75 and 1.42 for two-lane loading. This result will not significantly affect the load rating of this bridge type.

The current AASHTO LRFD moment and shear LLDF equations provide highly conservative LLDF values for Bridge CM-5. The AASHTO LRFD moment LLDFs values obtained using the simplified stiffness parameter and calculated stiffness parameter are similar. For the two-lane-loaded case, the governing g_{AASHTO}/g_{FEM} ratio for flexure is 1.43 and 1.57 for interior and exterior girders, respectively. A similar trend is also observed for the AASHTO LRFD shear LLDFs with g_{AASHTO}/g_{FEM} ratio of 1.44 and 1.53 for the interior and exterior girders, respectively. Using more accurate LLDFs for HL-93 loading cases would likely help increase LRFR ratings.

6. FEM ANALYSIS OF SIMPLE-SPAN CONCRETE SLAB BRIDGE

In Chapter 4, a detailed review and synthesis of the population of load-posted bridges in Texas was conducted, and 23 simple-span concrete slab (CS) bridges were selected from the inventory of SSLO simple-span concrete slab bridges in Texas for basic load rating evaluation. This basic load rating analysis helped to identify several areas of opportunity for refined load rating analysis. Refined load rating analysis investigates the effect of the identified parameters using three-dimensional finite element models that more accurately captures the actual bridge behavior. The main objectives of FEM analysis of the simple-span concrete slab bridge can be summarized as: (1) create a model of the bridge superstructure to accurately capture the two-way action in the slab, (2) investigate the actual equivalent strip width, over which the vehicular loads are distributed, and (3) to evaluate the effect of integral curbs to the load distribution across the slab width.

6.1. INTRODUCTION

A typical load posted simple-span concrete slab (CS) bridge was selected as a representative case study to further investigate the identified objectives. Table 6.1 lists some of the key parameters for the selected bridge to be modeled, and for the average SSLO simple-span concrete slab bridge in Texas. In this table, the *Operating HS-20 RF* represents the multiple of HS-20 truck loads that is the absolute maximum load that can safely travel on the bridge. The posting evaluation represents the degree to which the operating rating of the bridge is below the maximum legal load. A "5" indicates the operating rating is equal to or above the legal load. Values of 0-4 represent varying ranges for which the operating rating is below the legal load, with "4" being within 10% of the legal load and "0" being 40% or greater below the legal load.

A three-dimensional FEM model was developed using the commercial software package CSiBridge, which has the capability to model and analyze complex bridge superstructures while also providing user-friendly pre- and post-processing tools for bridge structures. The following sections provide the geometric and material properties of the selected simple-span concrete slab bridge, a description of the FEM modeling approach, and summarize the analysis results.

Table 6.1 Selected SSLO Concrete Slab Bridge and Characteristics

ID	Route Prefix	Year Built	ADT	Max. Span Length (ft)	Deck Width (ft)	Condition Rating			Operating HS-20 Rating Factor	Posting Eval.
						Deck	Super-structure	Sub-structure		
Avg.	-	1949	795	22	28	6	6	6	0.98	4
CS-9	3	1948	30	25	21	6	6	7	0.94	2

–: Not applicable
Route Prefix: 3=On-System
Condition Ratings: 6=Satisfactory, 7=Good
Posting Evaluation: 3=10-19.9% below legal load, 4=0.1-9.9% below legal load

The model was analyzed with HS-20 truck and designated HL-93 load simulations to obtain modal properties, deflection profiles, moment, and shear results. The deflection and modal analyses were conducted for comparison to the measured behavior of the bridge in the future field tests. The deflection values and modal characteristics allow for calibration of the FEM model based on field test results. The equivalent strip width over which the vehicular loads are distributed is calculated using the bending moment and shear results. A comparison of the equivalent strip widths found using the FEM model will be carried out with those determined from field testing, and those found using the procedures outlined in the AASHTO Standard Specifications (AASHTO 2002) and AASHTO LRFD Specifications (AASHTO 2017).

6.2. DESCRIPTION OF THE BRIDGE

The selected Bridge CS-9 is denoted as "FS Slab" type. According to the TxDOT Rate Spreadsheet User Guide (TxDOT (2001), such slabs have structural curbs, which contribute to the load carrying capacity of the bridge. Hence, these curbs are considered in the FEM model.

The selected bridge has a total length of 75 ft consisting of three simply supported spans. Each span is 21 ft 4 in. wide and has a center-to-center of bearing span length of 25 ft. The integral curbs are trapezoidal in shape with a bottom width of 1 ft 0.5 in. and a top width of 8 in. and a height of 1 ft 6 in. The steel yield strength and the 28-day concrete compressive strength are taken as 33 ksi and 2.5 ksi, respectively, according to the values listed in the AASHTO MBE (AASHTO MBE 2018). The bridge carries two lanes, one in each direction, and has an average daily traffic of 30 vehicles. These properties are tabulated in Table 6.2.

Table 6.2 Geometric and Material Properties for Bridge CS-9

Characteristic	Measurement
Total Length	75'-0"
Controlling Span Length	25'-0"
Deck Width	21'-4"
Roadway Width	20'-0"
Curb Height	1'-6"
Curb Top Width	0'-8"
Curb Bottom Width	1'-5"
Steel Yield Strength	33 ksi
Slab Thickness	11 in.
28-day Concrete Compressive Strength	2.5 ksi
Number of Lanes	2

Bridge CS-9 has a deck condition rating of 6 (Satisfactory), a superstructure condition rating of 6 (Satisfactory), and a substructure condition rating of 6 (Satisfactory). The concrete slab controls the rating of the bridge, which has an inventory gross loading of 16 US tons and an

operating gross loading of 33.7 US tons. The bridge is posted for a 28,000-pound tandem axle. Figure 6.1 shows a transverse section detail and Figure 6.2 shows an elevation view and an underside view of Bridge CS-9.

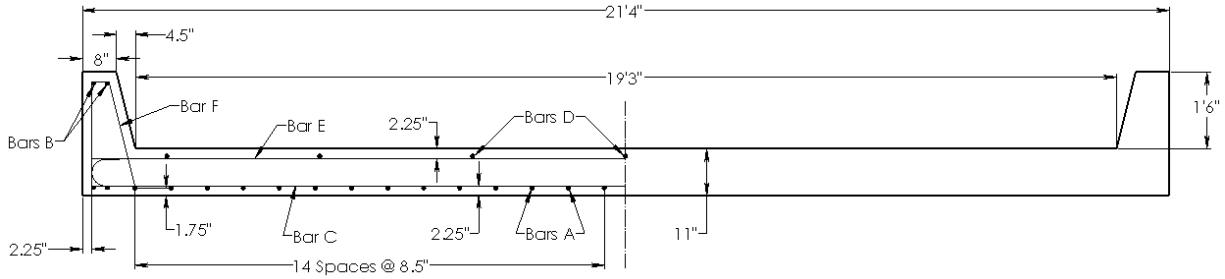

Figure 6.1. Bridge CS-9 Transverse Section (adapted from TxDOT 2018b)

(a) Elevation View

(b) Underside View

Figure 6.2. Photographs of Bridge CS-9

6.3. APPROXIMATE ANALYSIS METHODS FOR SLAB TYPE BRIDGES

6.3.1. Equivalent Strip Width Methods

The AASHTO Standard Specifications (AASHTO 2002) Article 3.24.3.2 predicts the wheel load distribution width *E* (ft) for both single-lane-loaded and multi-lane loaded cases as:

$$E = 4 + 0.06\mathrm{S} \tag{6.1}$$

where:

E = Slab width over which a wheel load is distributed (ft)

S = Effective span length (ft)

The live load moments and shears are distributed over the equivalent strip width *E* (in.) defined in AASHTO LRFD Specifications Article 4.6.2.3, where Eqn. (6.2) corresponds to a single-lane-loaded situation while Eqn. (6.3) is for a multi-lane-loaded condition.

$$E = 10.0 + 5.0\sqrt{L_1 W_1} \tag{6.2}$$

$$E = 84.0 + 1.44\sqrt{L_1 W_1} \leq \frac{12.0W}{N_L} \tag{6.3}$$

where:

E = Equivalent width for a truck load (in.)

L_1 = Modified span length (ft), minimum of actual span or 60 ft

W_1 = Modified edge-to-edge width of bridge, minimum of actual width or 60 ft for multi-lane loading, or 30 ft for single-lane loading (ft)

W = Actual edge-to-edge width of bridge (ft)

N_L = Number of design lanes

Amer et al. (1999) used the grillage analogy method to identify the main parameters influencing the equivalent width of slab bridges, compared the equivalent widths of slab bridges defined in the standard AASHTO Standard and AASHTO LRFD Specifications with those based on field tests and analyses, and proposed a simple design formula for the effective width of solid slab bridges. The main parameters considered in this study were the span length, bridge width, slab thickness, edge beam, and number of lanes. A parametric study was carried out using the AASHTO HS-20 standard truck. Based on the parametric studies, Amer et al. (1999) proposed the following equation to calculate the equivalent width *E* (ft) over which the truck load is assumed to be uniformly distributed:

$$E = 6.89 + 0.23L \leq \frac{W}{N_L} \tag{6.4}$$

where:

E = Equivalent width for a truck load (ft)

L = Span length (ft)

W = Bridge width (ft)

N_L = Number of design lanes

This equation is limited to spans up to 40 ft (12.2 m) and slab thickness up to 14 in. (360 mm). The effect of any edge beam, if present, is considered by multiplying Eqn. (6.4) with the factor C_{edge} defined as:

$$C_{edge} = 1.0 + 0.5\left(\frac{d_1}{3.28} - 0.15\right) \geq 1.0 \quad (6.5)$$

where:

d_1 = Edge beam depth above slab thickness (ft)

In 2012, researchers at the University of Delaware were tasked by the Delaware Department of Transportation (DelDOT) to load test a selection of slab bridges and determine their actual effective width, with the goal of developing new effective width formulas to be used in Delaware (Jones and Shenton 2012). In this study, a diagnostic load test was conducted on six slab bridges in the State of Delaware. Longitudinal strain versus transverse transducer location plots were developed for each bridge using the data collected from the field tests. The area under the curve of these plots was used to convert the plot to one that had a constant strain with the same area under the graph. From this new plot, the measured effective width was found as one half of the width of the constant strain graph. A schematic representation of the idealized strain distribution and effective width is shown in Figure 6.3.

The following equations for equivalent width were proposed, where Eqn. (6.6) corresponds to the equivalent width for a single-lane loaded situation and Eqn. (6.7) corresponds to a multi-lane loaded scenario:

$$E = 10.0 + 5.8\sqrt{L_1 W_1} \quad (6.6)$$

$$E = 84.0 + 2.06\sqrt{L_1 W_1} \leq \frac{12.0 W_1}{N_L} \quad (6.7)$$

where:

E = Equivalent or effective width for truck load (in.)

L_1 = Modified span length (ft) taken equal to the lesser of the actual span length or 60 ft

W_1 = Modified edge-to-edge width (ft) of the bridge taken to be equal to the lesser of the actual width or 60 ft for multilane loading, or 30 ft for single-lane loading

W = Physical edge-to-edge width of the bridge (ft)

N_L = Number of design lanes

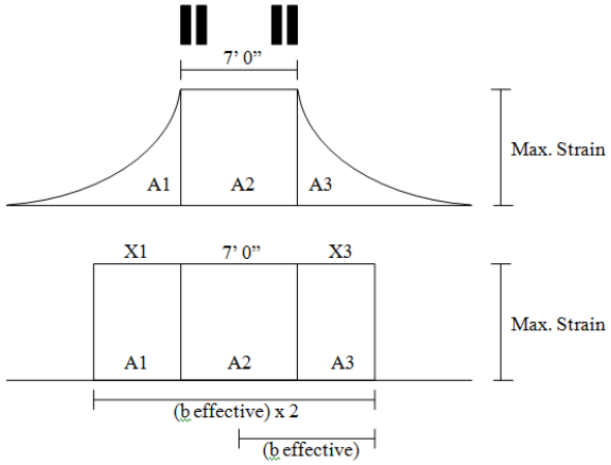

Figure 6.3. Schematic Representation of Strain Distribution and Effective Width (reprinted from Jones and Shenton 2012)

6.3.2. Illinois Bulletin Method

A modified version of these constant depth slab bridges with monolithically poured curbs/parapets were called "Type FS" bridges in the TxDOT standard drawings. These integrated structural curbs/parapets were designed based on the simplified guidelines established from the findings of the research conducted at the University of Illinois (Jenson et al. 1943). It was found that by adopting integrated structural curbs (Type FS) that acts as an edge girder, the slab could be

designed thinner than standard concrete slab bridges, making FS bridges more economical. Several analytical and experimental research findings related to the design of FS bridges in Illinois were provided in a series of documents starting with Illinois Bulletin 346, and hence the method of analysis for FS bridges is termed "Illinois Bulletin 346 Method" (IB346).

In the simplified analysis method, the cross-section of an FS bridge is divided into two parts: the slab and the edge curb/beam. The total static live load moment resisted by the curb and slab in a FS simply supported bridge is given as:

$$M_{static} = m\frac{Pa}{4} \tag{6.8}$$

where:

m = Number of rear wheel loads (e.g., m = 4 for a two-lane-loaded bridge)

P = Magnitude of real wheel load (impact factor not included for comparison with other methods)

a = Span of bridge from center-to-center of bearing areas

The live load moment in the curb is assumed to be reduced by 25 percent when the loads are shifted transversely. Therefore, the moment resisted by each curb can be calculated as:

$$M_{curb} = \frac{m}{2}0.75C_1\frac{Pa}{4} \tag{6.9}$$

where:

C_1 = Dimensionless coefficient that is defined by empirical equation as:

$$C_1 = \left(\frac{12}{2.5 + G}\right)\frac{\left(4 - \frac{v}{a}\right)}{\left(4 + 28\left(\frac{v}{a}\right)\right)}$$

in which:

$$G = \frac{ah^3}{12I}$$

G = Dimensionless stiffness factor, ratio of slab stiffness to curb stiffness

I = Moment of inertia of curb gross section outside the roadway width (ft^4)

h = Slab thickness (ft)

v = Axle width, center-to-center of truck tires (6 ft)

Therefore, the total live load moment resisted by the slab alone is the difference between total moment on the bridge and two curbs.

$$M_{slab} = M_{total} - 2M_{curb} \tag{6.10}$$

The average live load moment per unit width of slab can then be calculated as:

$$M_{slab,avg} = \frac{M_{slab}}{b} \tag{6.11}$$

where:

b = Width of roadway between curbs (ft)

6.4. FEM MODEL DEVELOPMENT

A three-dimensional linear FEM model of the selected simple-span concrete slab bridge was developed using the commercial CSiBridge software (Computers and Structures 2019). The bridge

geometry was modeled based on information provided in the structural design drawings. The next subsection describes the FEM modeling approach, finite element types, and material properties. The following subsection presents the results of the mesh sensitivity study and selection of mesh size. The last subsection provides details about boundary conditions, which is critical for accurately capturing the behavior of the bridge.

6.4.1. Bridge Model Description

A realistic model of the bridge superstructure requires appropriate finite element types, boundary conditions, and a sufficiently refined mesh. There is ample information providing recommendations about FEM modeling for various concrete bridge superstructures (Davids et al. 2013; Hueste et al. 2015; Miller et al. 1994). Based on the recommendation found in the literature, a three-dimensional linear finite element model of Bridge CS-9 was developed. The bridge geometry is modeled exactly as in the actual bridge drawings, including the integral curbs, without any simplification based on information gathered from structural drawings and inspection reports. The bridge superstructure including the curbs were modeled using 3D eight-node linear solid brick elements. The slab and curb reinforcement were not modeled because the linear elastic model will be analyzed under service level loads only and the superstructure is expected to remain in the linear elastic range. Figure 6.4 shows the finite element model for Bridge CS-9.

In the absence of any record of the specified material strengths for Bridge CS-9, the steel yield strength and the 28-day concrete compressive strength are taken in accordance with the AASHTO MBE guidelines (AASHTO 2018). Table 6.3 lists the material properties adopted for the FEM model.

The modulus of elasticity, E_c, for concrete was calculated using Eqn. (6.12), as stated in the AASHTO LRFD Specifications (AASHTO 2014). This equation is valid for normal weight concrete with unit weights between 0.09 and 0.155 kcf and design compressive strength up to 15.0 ksi.

$$E_c = 33{,}000 K_1 w_c^{1.5} \sqrt{f_c'} \tag{6.12}$$

where:

E_c = Elastic modulus of concrete, ksi

K_1 = Correction factor for source of aggregate, to be taken as 1.0 unless determined by physical test

w_c = Unit weight of concrete, kcf

f_c' = Compressive strength of concrete, ksi

Table 6.3 Material Properties for Bridge CS-9

Bridge	Concrete Strength (f_c') (psi)	Modulus of Elasticity (E_c) (ksi)	Concrete Unit Weight (w_c) (pcf)
CS-9	2.5	3031	150

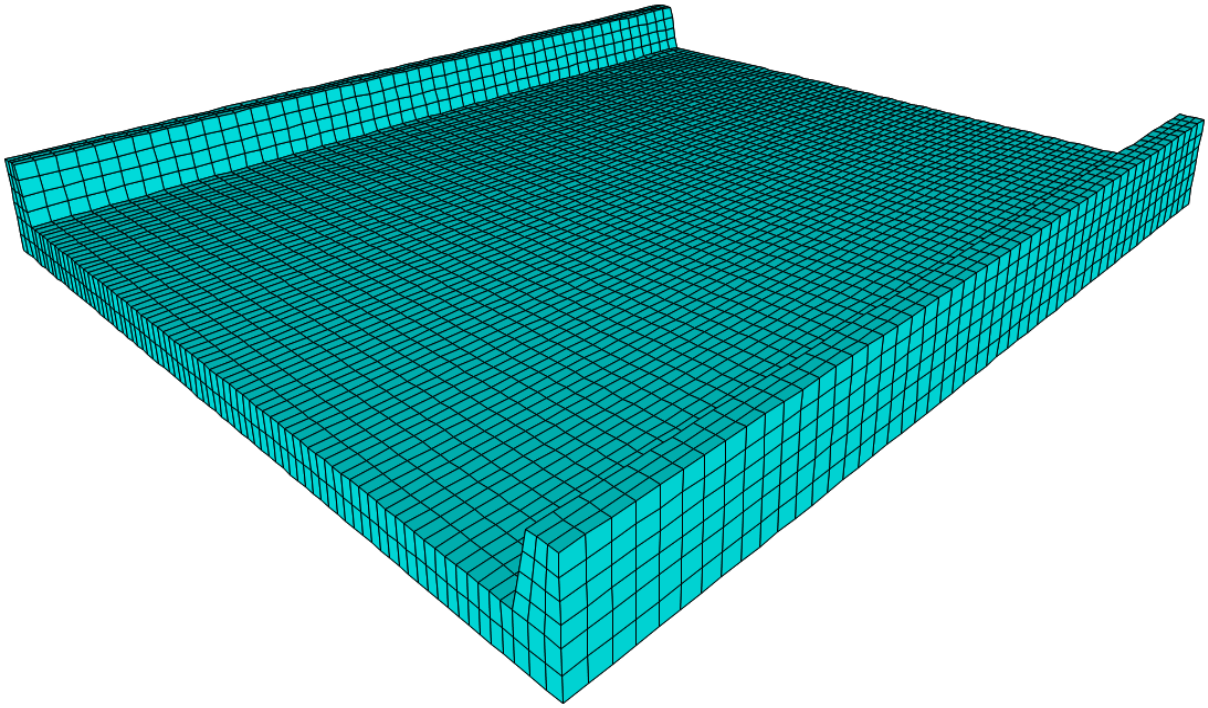

Figure 6.4 FEM Model of Bridge CS-9 (6 in. mesh)

6.4.2. Mesh Sensitivity Analysis

A finite element mesh was generated for the model with consistently spaced nodes. A mesh sensitivity study was undertaken for several models with different mesh sizes (4 in., 6 in., 12 in., and 18 in.) in order to determine the optimal mesh size for the three-dimensional linear finite element model of Bridge CS-9. The effect of different mesh sizes on the calculated shear force, moment, and bending stress was examined. Figure 6.5 shows these different mesh sizes when applied to Bridge CS-9.

The FEM results for shear force, bending moment, and stress for Bridge CS-9 model are listed in Table 6.4. All the results correspond to the case of a single HS-20 truck pass through the right lane, 2 ft from the centerline of the bridge (Path 2 in Figure 6.6). The accuracy of the results increases with decreasing mesh size from 18 in. to 12 in. However, reducing the mesh size to 4 in.

does not significantly increase the accuracy when compared to the results obtained from the model with a mesh size of 6 in. Hence, a 6 in. mesh size was chosen to be used for Bridge CS-9. With these mesh size and discretization points, an accurate FEM model of the bridge with an efficient computation time was created in CSiBridge.

Table 6.4 FEM Results for CS-9 with Different Mesh Sizes (CSiBridge)

Mesh Size (in.)	Maximum Moment (kip-ft)	Maximum Shear (kip)	Maximum Stress (ksi)
4	197.33	15.36	0.277
6	200.00	16.00	0.277
12	199.36	15.36	0.277
18	195.76	14.72	0.269

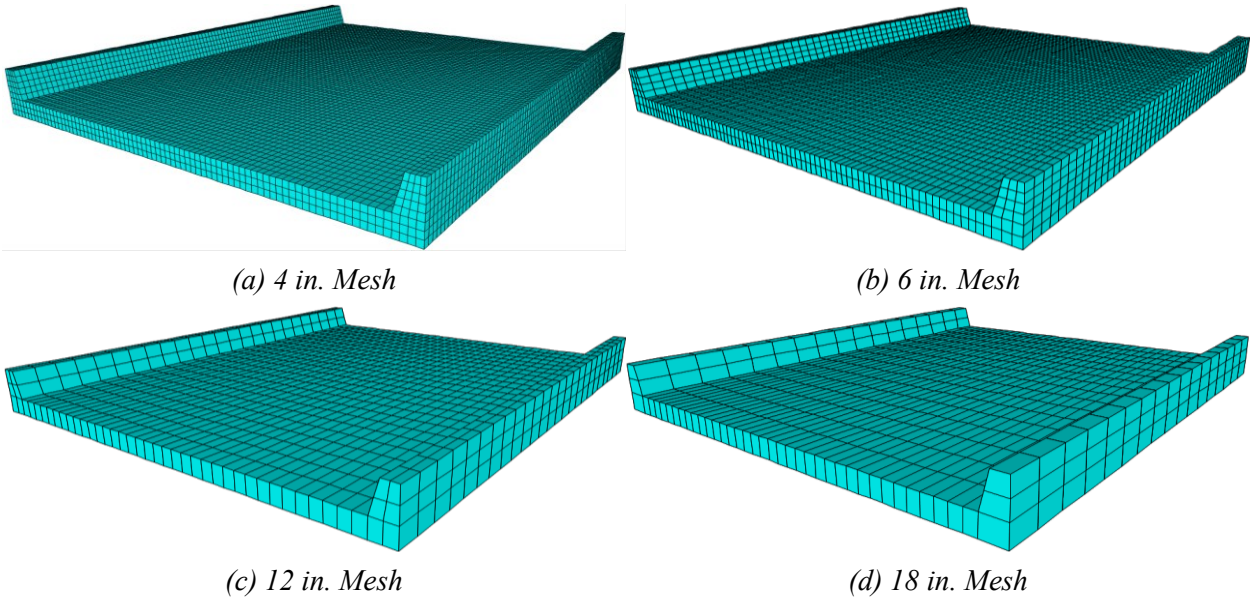

(a) 4 in. Mesh *(b) 6 in. Mesh*

(c) 12 in. Mesh *(d) 18 in. Mesh*

Figure 6.5. FEM Models Showing Different Mesh Sizes for Bridge CS-9

6.4.3. Boundary Conditions

In the absence of more accurate information, the boundary conditions at the supports were modeled as simply supported with pins and rollers. One end of the slab bridge was modeled with roller supports while the other end was modeled with pin supports. The roller support releases all three

rotational degrees of freedom as well as two translational degrees of freedom in the horizontal plane (two orthogonal in-plane directions parallel to the bridge superstructure), and fully restrains the translational degree of freedom in the vertical direction (perpendicular to the plane of the bridge superstructure). The pin support releases all three rotational degrees of freedom and restrains all three translational degrees of freedom.

Accurately modeling the boundary conditions may have a significant effect on the overall behavior of the bridge. Although the boundary conditions are initially modeled as simply supported, the level of restraint will be assessed based on experimental results from the next task. Unintended partial fixity may develop at the supports due to the bearing detail at the supports and/or friction between the bottom surface of the bridge and the bearing surface.

6.5. BASIC VERIFICATION OF FEM MODELS

Some basic loading conditions were simulated to verify that the CSiBridge model was providing expected results. These basic checks were conducted by investigating maximum deflections under uniform distributed dead load, and maximum moments and support reactions under the HS-20 truck and HL-93 loading.

The characteristics of the HS-20 design truck as specified in the AASHTO LRFD Specifications (AASHTO 2017) are shown in Figure 5.6. The total load in the front axle is 8 kips and is 14 ft away from the middle axle, which has a total load of 32 kips. The rear axle has a total load of 32 kips and may be spaced between 14 ft and 30 ft from the middle axle, depending on which creates the maximum force effect being investigated. An alternative loading scheme consisting of a uniformly distributed load of 0.64 kip/ft and a concentrated load of 18 kips when

checking moment or 26 kips when checking shear is also considered in AASHTO Standard Specifications (AASHTO 2002).

The designated HL-93 loading consisting of the design truck or design tandem coincident with the design lane load is shown in Figure 5.7. The design lane load consists of 0.64 kip/ft uniformly distributed load over a 10 ft width. Two 25-kip axle loads spaced 4 ft apart longitudinally and 6 ft apart transversely, constitute the design tandem load. The design truck or design tandem is used depending on which will create the maximum force effect on the span.

6.5.1. Verification of Maximum Deflection

The maximum deflection for the bridge superstructure under uniform distributed dead load was verified with the deflections obtained from theoretical structural analysis. The estimated deflections for the slab bridge obtained from FEM analysis were compared to the calculated deflections. The equivalent distributed load was calculated as the sum of the weight of the slab, the deck and wearing surface. The total uniform distributed weight can be found as,

$$w = w_s + w_{ws} + 2w_{CURB} = 4.02 \text{ kip/ft} \tag{6.13}$$

in which:

w_s = weight of slab = 2.65 kip/ft

w_{CURB} = weight of curb = 0.34 kip/ft

$$w_{ws} = (\gamma_{ws})(t_{ws})(b) = 0.69 \text{ kip/ft} \tag{6.14}$$

where:

γ_c = unit weight of concrete = 0.15 kip/ft^3

b = clear slab width between curbs (ft)

w_{ws} = weight of wearing surface (kip/ft)

γ_{ws} = unit weight of the wearing surface = 0.144 kip/ft^3

t_{ws} = thickness of the wearing surface (ft)

The midspan deflection of the concrete slab bridge can be calculated using Eqn. (6.15) for a simply supported beam under uniformly distributed load.

$$\Delta = \frac{5wL^4}{384E_cI} = 0.116 \text{ in.} \tag{6.15}$$

where:

I = Moment of inertia of transverse section = 100,702 in^4

E_c = Modulus of elasticity of concrete = 3031 ksi

Table 6.5 shows the deflections calculated using each method and the percent difference between them. The CSiBridge deflections are closely matched to the calculated deflections.

Table 6.5. Dead Load Deflection Comparison for Bridge CS-9

Bridge ID	CSiBridge Deflection (in.)	Calculated Deflection (in.)	Percent Difference (%)
CS-9	0.121	0.116	4.31

6.5.2. Verification of Absolute Maximum Moment

To verify that the truck loadings were modeled correctly, the live load moments were compared to the live load moments obtained from theoretical influence line analysis. The model was analyzed under HS-20 truck load and HL-93 loading. In Chapter 5, calculations for obtaining the maximum moment due to moving loads in a simple span are presented in Section 5.4.2. Table 6.6 shows the

calculated live load moments, the CSiBridge moments, and the percent difference between them. Again, the model provides a close match to the expected values.

Table 6.6. Live Load Moment on the Comparison for Bridge CS-9

Bridge ID	Applied Load	CSiBridge 1-Lane Moment on Total Section (kip-ft)	Expected 1-Lane Moment on Total Section (kip-ft)	Percent Difference (%)
CS-9	HS-20	200.00	200.00	0
	HL-93	310.63	302.56	2.67
Note: All calculated moments are without the application of the impact factor				

6.5.3. Verification of Maximum Shear Forces

To verify that the structural supports have been modeled correctly, maximum shears corresponding to the live loads were verified against the shear obtained from basic structural analysis. Sep-by-step loading is employed by CSiBridge for moving load analysis. The step size of the moving load was adjusted so that the first step with the rear axle of the truck on the bridge positioned the rear axle 1 ft away from the support. The resulting support reactions were obtained from the FEM model and compared with those calculated using classical structural analysis methods. Table 6.7 shows the support reactions calculated using each method and the percent difference between them. The CSiBridge shear forces match very closely with the calculated shear forces.

Table 6.7. Live Load Support Reactions Comparison for Bridge CS-9

Bridge ID	Applied Load	CSiBridge 1-Lane Shear on Total Section (kip)	Expected 1-Lane Shear on Total Section (kip)	Percent Difference (%)
CS-9	HS-20	43.5	43.5	0.0
	HL-93	51.5	52.00	1.0
Note: All calculated shears are without the application of the impact factor.				

6.6. SIMULATING VEHICLE LOADS

The truck loads and lane loads were placed transversely on Bridge CS-9 as per the AASHTO Standard Specifications (AASHTO 2002) and AASHTO LRFD Specifications (AASHTO 2017). Bridge CS-9 has two lanes each 9.625 ft wide.

A linear static moving load was applied with each truck moving along the length of the bridge in approximately 1 ft increments. It should be noted that although it would be an unlikely event, for the two-lane-loaded cases, both trucks traveled along the bridge in the same direction in order to produce the maximum possible load effect on the bridge.

6.6.1. Simulating HS-20 Truck Loading

For a one-lane-loaded case based on the Standard Specifications, the truck was placed so that the exterior wheel line was 2 ft from the nominal face of the curb, which is 2'-10" from the edge of the bridge (Path 1). Due to the narrow lane width, the only other loading scenario considered was where the interior wheel line was 1'-10" from the centerline of the bridge (Path 2). For a two-lane-loaded case, one truck was positioned in Path 1 and another truck in Path 2. This created two separate one-lane-loaded cases and one two-lane-loaded case. Figure 6.6 shows the different HS-20 truck loading cases across the transverse section of Bridge CS-9. The red and blue arrows represent the wheel lines of the truck and the black dashed line is the centerline (CL) of the bridge.

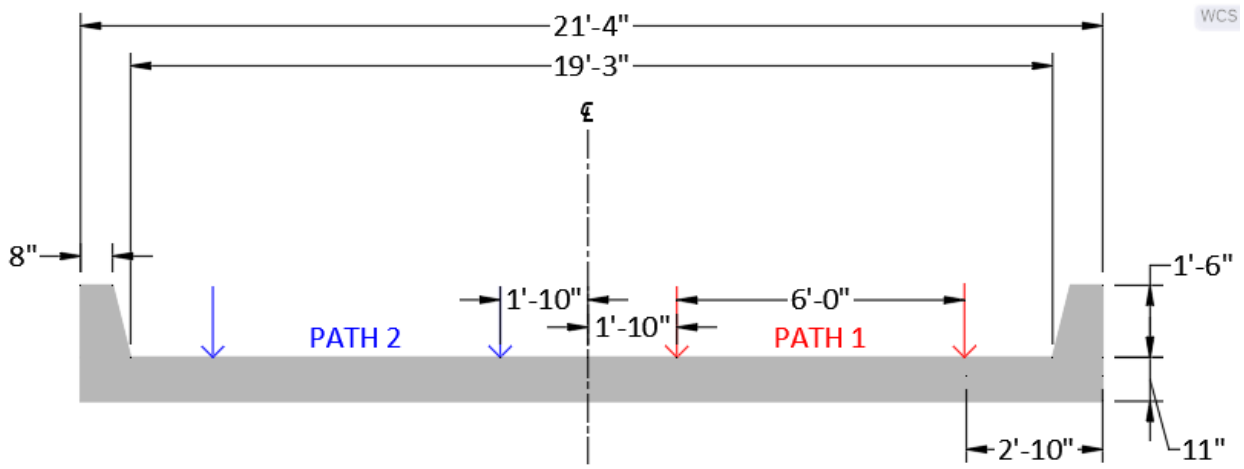

Figure 6.6. HS-20 Truck Loading Cases for Bridge CS-9

6.6.2. Simulating HL-93 Loading

For loading based on the LRFD Specifications, the tandem configuration and lane load were added to the already created load cases. The tandem configuration was used for HL-93 loading as it controls over the truck configuration for short span bridges less than 40.5 ft long. The design tandem was placed transversely in the same manner as described for the HS-20 truck. The lane load was placed immediately adjacent to the edge of the barrier for both Path 1 and Path 2. Because the lanes are less than 10 ft wide, the lane load was distributed over the lane width of 9 ft – 7.5 in. Figure 6.7 shows the different HL-93 loading cases across the transverse section of Bridge CS-9. The red and blue arrows represent the wheel lines of the truck, the red and blue cross hatched regions represent the lane load distributed over the lane width and the black dashed line is the centerline (CL) of the bridge.

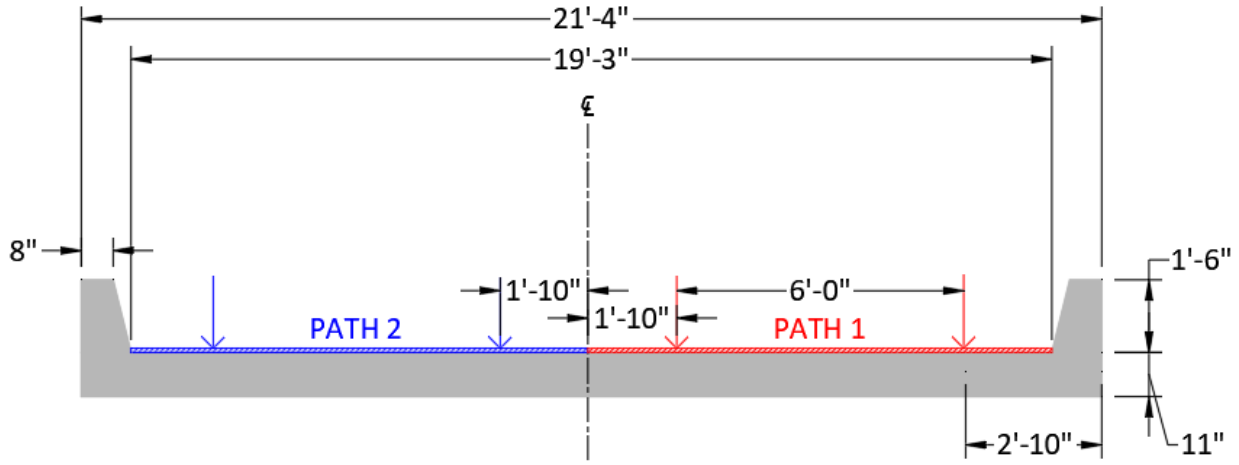

Figure 6.7. HL-93 Loading Cases for Bridge CS-9

6.7. FEM RESULTS

Bridge CS-9 was analyzed using the FEM software CSiBridge under the loading scenarios provided in Figure 6.6 and Figure 6.7. Slab displacement profiles were obtained for loading along both paths. Modal analysis was conducted to determine estimated modal frequencies and mode shapes. Live load moment and shear values were also extracted and analyzed to compare the expected LLDFs with the LLDFs prescribed in AASHTO Standard Specifications (AASHTO 2002) and AASHTO LRFD Specifications (AASHTO 2017).

6.7.1. Modal Properties

The first longitudinal bending mode and the first torsional mode constitute the first two modes of Bridge CS-9. The frequency for the first longitudinal bending mode was determined to be 10.11 Hz and that for the first torsional mode was 12.11 Hz. The contours of the first longitudinal bending mode shape along with the normalized amplitudes along the span of the bridge are shown in Figure 6.8(a). Figure 6.8(b) shows the contours of the first torsional mode shape along with the normalized amplitudes transverse to the span.

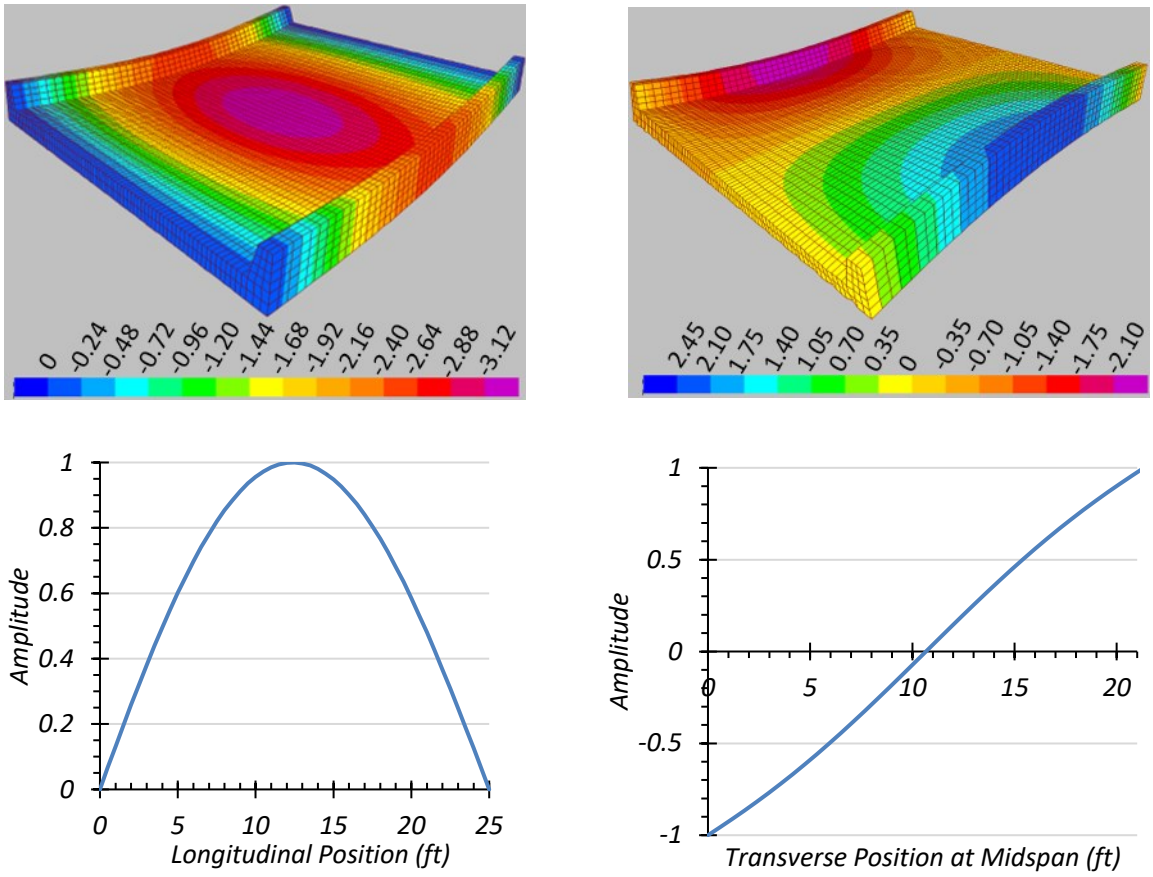

a) Longitudinal Bending Mode (f=10.11 Hz) *b) Torsional Mode (f=12.11 Hz)*

Figure 6.8. First Two Mode Shapes of Bridge CS-9

6.7.2. HS-20 Live Load Analysis

Bridge CS-9 was subjected to the design HS-20 truck load as defined in the AASHTO Standard Specifications (AASHTO 2002).The paths defined in Figure 6.6 were prescribed in CSiBridge for analysis. The slab bridge was divided into 10, 20 and 38 transverse sections and the corresponding bending moment and LLDFs compared. The exterior transverse sections for each group consisted of the two curbs, each 12.5 in. wide at the base of the curb. The clear roadway width of 19 ft 3 in. was divided into 8, 18, and 36 interior transverse sections for 10, 20 and 38 groups, respectively.

The LLDF for each transverse section was defined to be the ratio of the corresponding bending moment of the section to the total bending moment of the whole bridge section due to one-lane loading. Similarly, the LLDFs for the curbs were calculated as the ratio of the curb bending moment to the total bending moment due to one-lane loading. The bending moment and corresponding LLDFs for the various groups were compared as shown in Figure 6.9. Table 6.8 tabulates the maximum moment for each transverse section in each group. The results corresponding to 20 transverse sections (12.8 in. elements) provide sufficient refinement in the transverse direction to capture the transverse distribution of vehicle load. Hence, results corresponding to 20 transverse sections are presented in the following subsections. The equivalent width for the interior slab portion between curbs, was calculated as the inverse of per foot share of the maximum LLDF occurring within the interior slab portion.

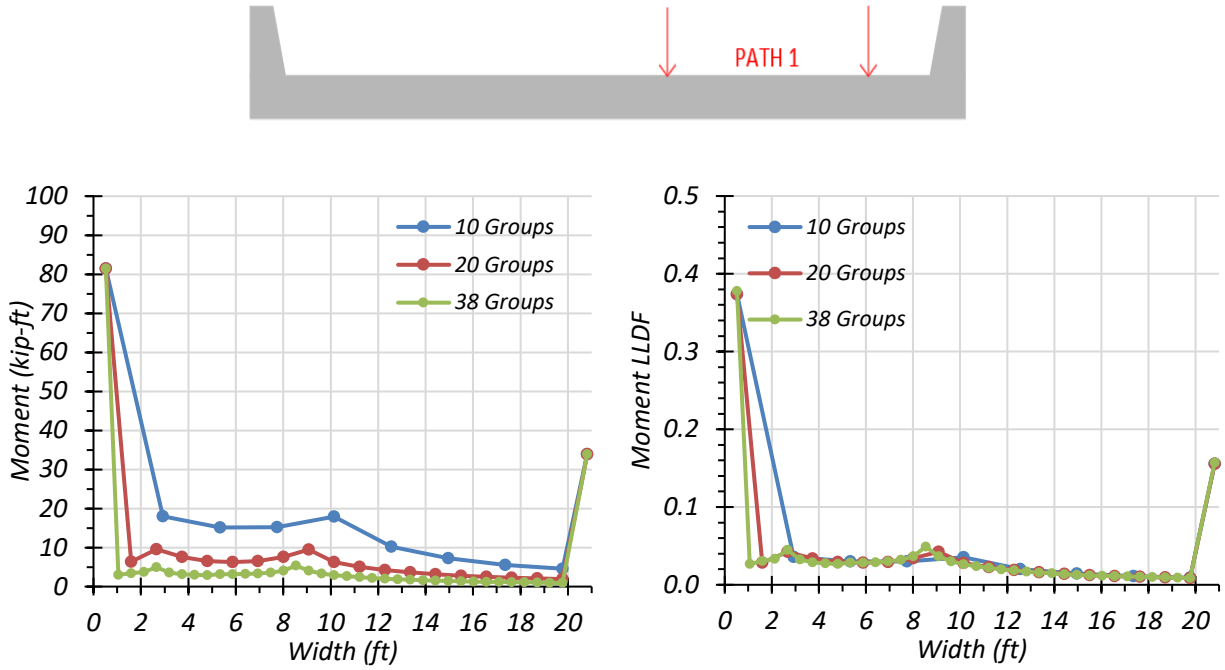

(a) Moment *(b) Moment LLDF*

Figure 6.9. Comparison of Bending Moment Results for Different Number of Sections

Table 6.8. Maximum Moments under HS-20 Loading for Different Number of Transverse Sections

Group	S1	S2	S3	S4	S5	S6	S7	S8	S9	S10	S11	S12	S13	S14	S15	S16	S17	S18	S19	S20
10	81.5	18.0	15.1	15.2	17.9	10.2	7.2	5.5	4.6	33.9										
20	81.5	6.4	9.5	7.6	6.5	6.3	6.6	7.6	9.5	6.3	5.0	4.2	3.6	3.2	2.7	2.5	2.3	2.1	1.9	33.9
38	81.5	3.0	3.4	3.7	4.9	3.6	3.2	3.0	3.0	3.2	3.2	3.2	3.3	3.6	4.1	5.4	4.1	3.3	2.9	2.6
	S21	**S22**	**S23**	**S24**	**S25**	**S26**	**S27**	**S28**	**S29**	**S30**	**S31**	**S32**	**S33**	**S34**	**S35**	**S36**	**S37**	**S38**		
	2.4	2.2	2.0	1.9	1.8	1.6	1.5	1.4	1.3	1.3	1.2	1.2	1.1	1.1	1.0	1.0	0.9	33.9		
Note: Moments have kip-ft units and load is along Path 1.																				

6.7.2.1. Deflection Results

The estimated slab deflection profiles and contours along the span for one-lane loading along Path 1 and Path 2 are shown in Figure 6.10. The maximum deflections under HS-20 loading for each loaded path is tabulated in Table 6.9. The maximum deflection under one-lane HS-20 loading was observed to be 0.12 in. for both Path 1 and Path 2.

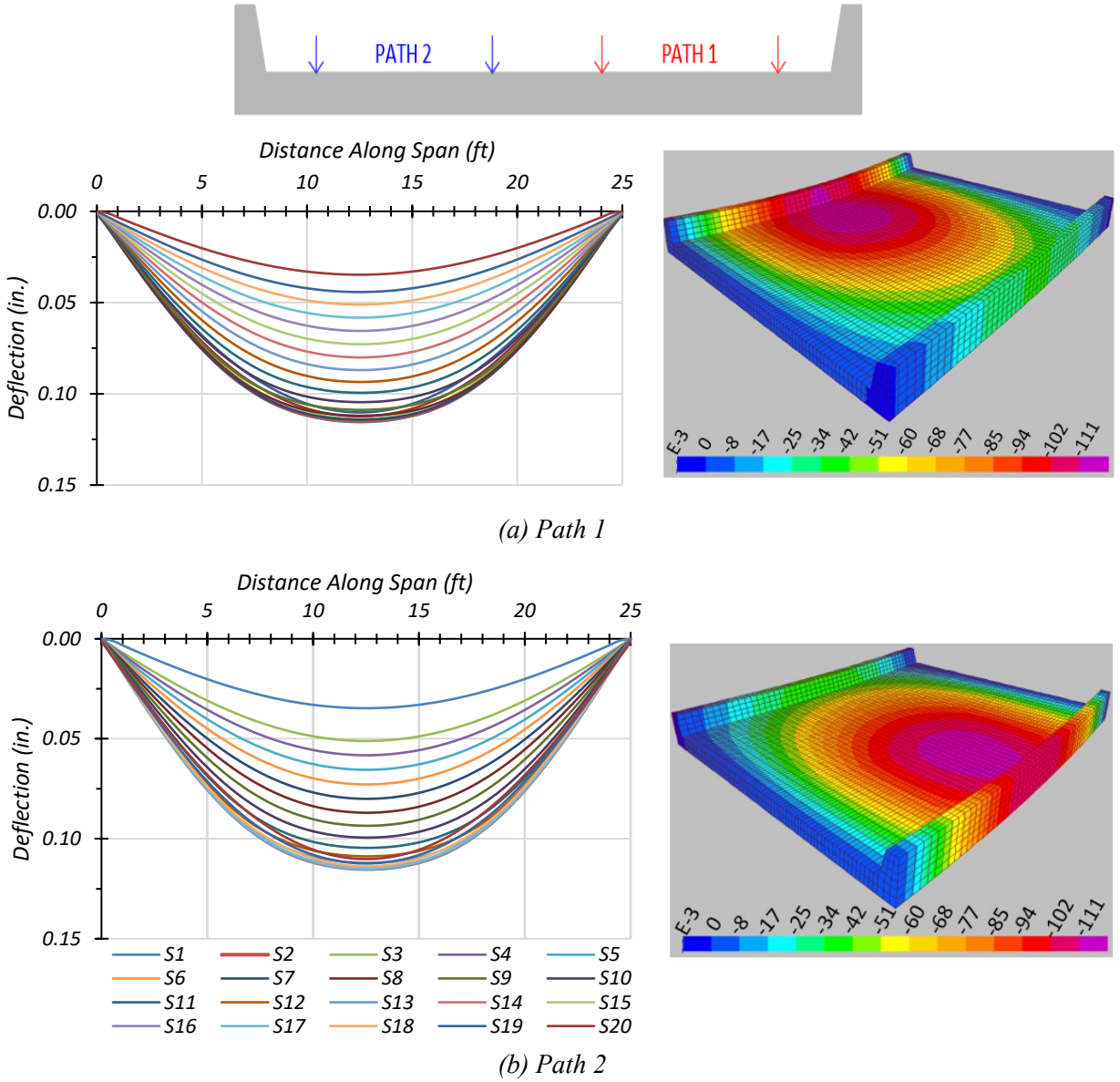

Figure 6.10. Deflection Profiles with HS-20 Loading

Table 6.9. Maximum Deflections with HS-20 Loading

Loading	S1	S2	S3	S4	S5	S6	S7	S8	S9	S10	S11	S12	S13	S14	S15	S16	S17	S18	S19	S20
Path 1	0.11	0.11	0.11	0.11	0.12	0.12	0.11	0.11	0.11	0.10	0.10	0.09	0.09	0.08	0.07	0.07	0.06	0.05	0.04	0.03
Path 2	0.03	0.04	0.05	0.06	0.07	0.07	0.08	0.09	0.09	0.10	0.10	0.11	0.11	0.11	0.12	0.12	0.11	0.11	0.11	0.11
Note: S = transverse section, paths indicate transverse loading positions as shown, deflections have inch units																				

6.7.2.2. Moment Results

The moments corresponding to each transverse section and the corresponding LLDFs for the one-lane and two-lane HS-20 loading paths are shown in Figure 6.11. The corresponding maximum moments for each transverse section and path are listed in Table 6.10. The estimated moment results from the FEM model were used to calculate the equivalent widths for the slab portion and LLDFs for the curbs. Equivalent width for the slab portion is calculated as the inverse of the maximum LLDF of one-foot slab sections. A comparison of the estimated equivalent width for the interior slab portion obtained from the FEM model for the two-lane-loaded scenario and those calculated using the approximate equations in the AASHTO Standard Specifications (AASHTO 2002) and AASHTO LRFD Specifications (AASHTO 2017) is provided in Table 6.11. Comparison with studies such as Amer et al. (1999) and Jones and Shenton (2012) was also carried out as shown in Figure 6.12 based on the two-lane-load case. All the equivalent widths were found to be conservative in comparison to the FEM results.

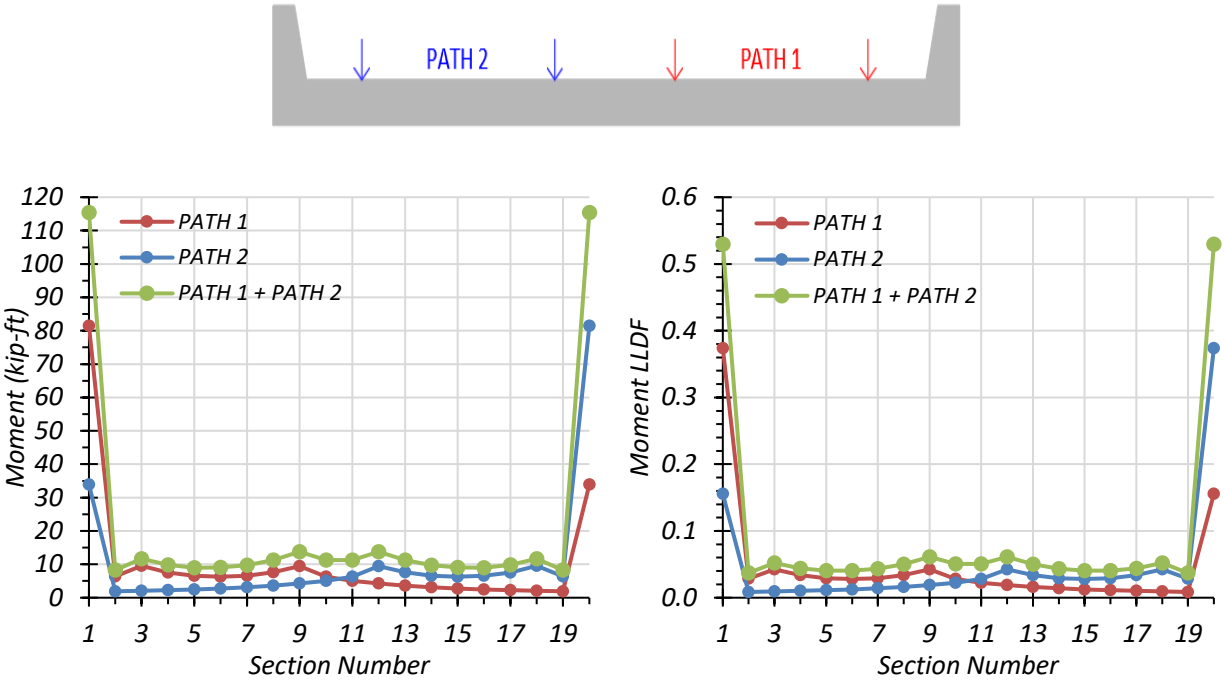

(a) Moment *(b) Moment LLDF*

Figure 6.11. Moment Results with HS-20 Loading

Table 6.10. Maximum Moments with HS-20 Loading

Loading	S1	S2	S3	S4	S5	S6	S7	S8	S9	S10	S11	S12	S13	S14	S15	S16	S17	S18	S19	S20
Path 1	81.5	6.4	9.5	7.6	6.5	6.3	6.6	7.6	9.5	6.3	5.0	4.2	3.6	3.2	2.7	2.5	2.3	2.1	1.9	33.9
Path 2	33.9	1.9	2.1	2.3	2.5	2.7	3.2	3.6	4.2	5.0	6.3	9.5	7.6	6.6	6.3	6.5	7.6	9.5	6.4	81.5
Path 1 + Path 2	115.4	8.3	11.6	9.9	9.0	9.1	9.7	11.3	13.7	11.3	11.3	13.7	11.3	9.7	9.1	9.0	9.9	11.6	8.3	115.4
Note: S = section, paths indicate transverse loading positions as shown, moments have kip-ft units																				

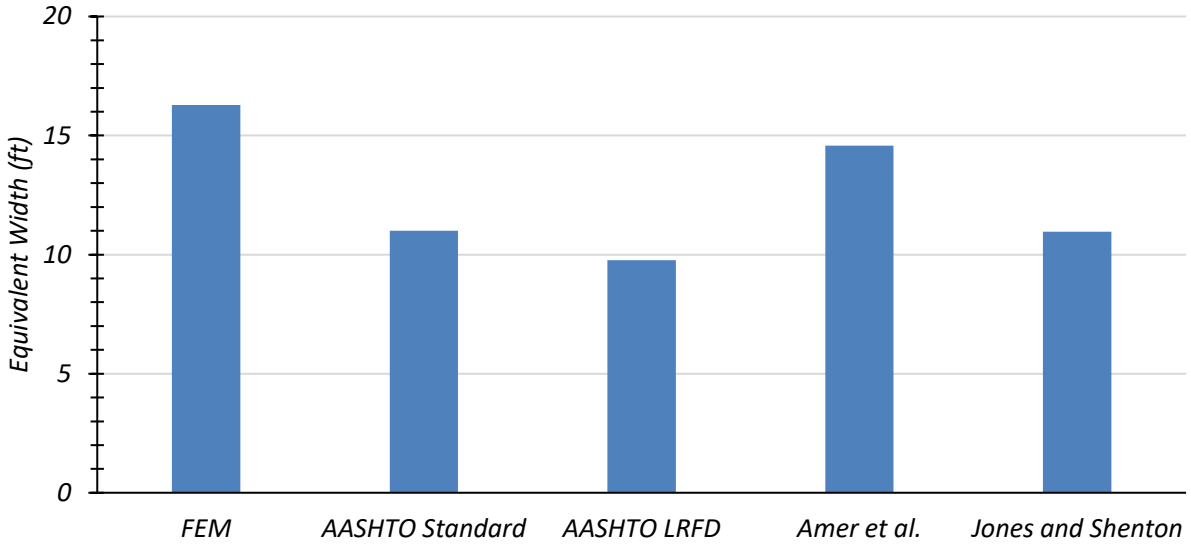

Figure 6.12. Comparison of Equivalent Width with Various Models for HS-20 Loading

Table 6.11. Governing Moment Equivalent Width (ft) for HS-20 Loading for Interior Slab

Loading	FEM (E^m_{FEM})	AASHTO (E^m_{AASHTO})	AASHTO LRFD (E^m_{LRFD})	Amer et al. (E^m_{Amer})	Jones and Shenton ($E^m_{Jones\ \&\ Shenton}$)
One-lane	23.5	11.0	10.5	14.6	12.0
Two-lane	16.3	11.0	9.8	14.6	11.0

Table 6.12 compares the curb moment and the interior slab moment per foot width from the FEM model with the respective moments obtained using the simplified analysis method outlined in IB346. The bending moment obtained from IB346 tends to be highly unconservative for the slab portion while it is slightly unconservative for the curb, for a one-lane-loaded case. For a two-lane-loaded case, the bending moment obtained from IB346 is highly unconservative for the slab and conservative for the curb.

Table 6.12. Comparison of FEM Moment with HS-20 Loading with IB346

Loading	Component	FEM Moment	IB346 Moment	IB/FEM
One-lane	Curb	81.5	80.7	0.99
	Slab	8.9	2.4	0.27
Two-lane	Curb	115.4	161.4	1.40
	Slab	12.8	4.8	0.37
Note: Curb moment have kip-ft units and slab moment have kip-ft/ft units.				

6.7.2.3. Shear Results

The shear forces in each transverse section and the corresponding shear LLDFs for the one-lane and two-lane HS-20 loading paths are shown in Figure 6.13. The corresponding maximum moments for each section and path are listed in Table 6.13. The estimated shear results from the FEM model were used to calculate the equivalent widths for the slab portion and LLDFs for the curbs. A comparison of the estimated equivalent width for the interior slab portion obtained from the FEM model and those calculated using the approximate equations in the AASHTO Standard Specifications (AASHTO 2002) and AASHTO LRFD Specifications (AASHTO 2017) is provided in Table 6.14. Comparison with studies such as Amer et al. (1999) and Jones and Shenton (2012) was also carried out. All the equivalent widths were found to be conservative in comparison to the FEM results.

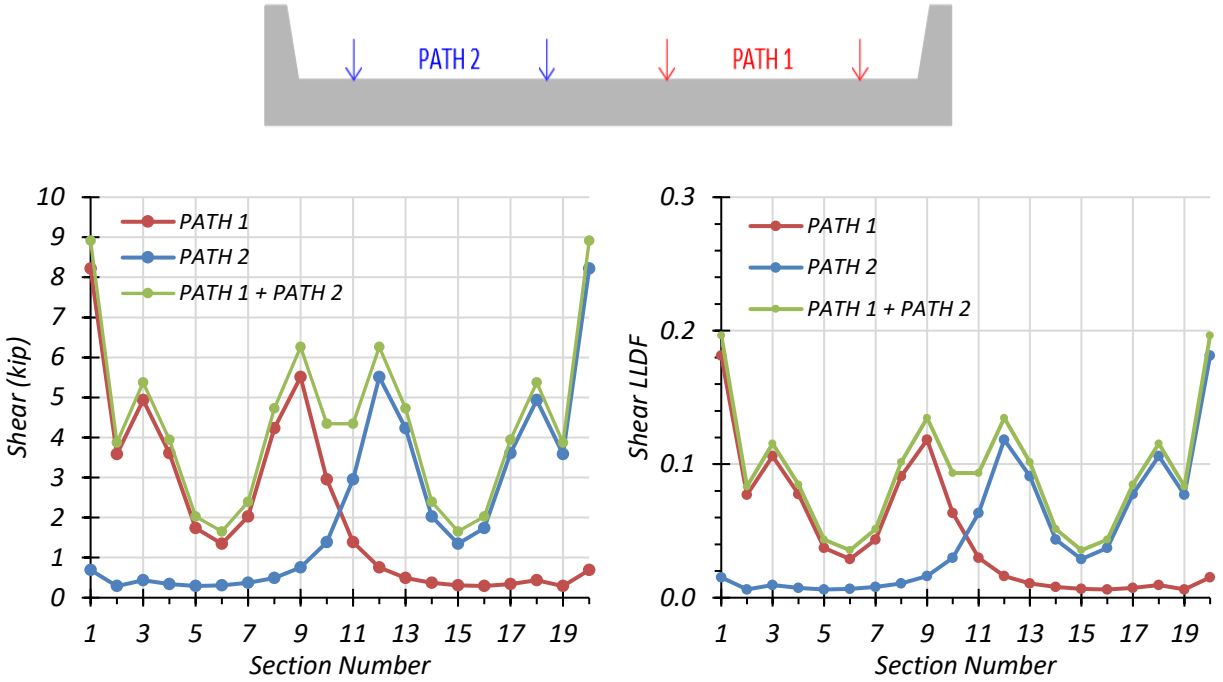

(a) Shear *(b) Shear LLDF*

Figure 6.13. Shear Results with HS-20 Loading

Table 6.13. Maximum Shears with HS-20 Loading

Loading	S1	S2	S3	S4	S5	S6	S7	S8	S9	S10	S11	S12	S13	S14	S15	S16	S17	S18	S19	S20
Path 1	8.2	3.6	4.9	3.6	1.7	1.3	2.0	4.2	5.5	3.0	1.4	0.8	0.5	0.4	0.3	0.3	0.3	0.4	0.3	0.7
Path 2	0.7	0.3	0.4	0.3	0.3	0.3	0.4	0.5	0.8	1.4	3.0	5.5	4.2	2.0	1.3	1.7	3.6	4.9	3.6	8.2
Path 1 + Path 2	8.9	3.9	5.4	3.9	2.0	1.7	2.4	4.7	6.3	4.3	4.3	6.3	4.7	2.4	1.7	2.0	3.9	5.4	3.9	8.9
Note: S = section, paths indicate transverse loading positions as shown, shears have kip units																				

Table 6.14. Governing Shear Equivalent Width (ft) for HS-20 Loading for Interior Slab

Loading	FEM (E^v_{FEM})	AASHTO (E^v_{AASHTO})	AASHTO LRFD (E^v_{LRFD})	Amer et al. (E^v_{Amer})	Jones and Shenton ($E^v_{Jones\ \&\ Shenton}$)
One-lane	8.4	11.0	10.5	14.6	12.0
Two-lane	7.4	11.0	9.8	14.6	11.0

6.7.3. HL-93 Live Load Analysis

Bridge CS-9 was subjected to the HL-93 design loading as defined in the AASHTO LRFD Specifications (AASHTO 2017). The paths defined in Figure 6.7 were prescribed in CSiBridge for analysis. The following sections discuss the deflections, bending moment and shear values obtained from the FEM model.

6.7.3.1. Deflection Results

The estimated girder deflection profiles and contours along the span for one-lane HL-93 loading along Path 1 and Path 2 are shown in Figure 6.14. The maximum deflections under HL-93 loading for each loaded path is tabulated in Table 6.15. The maximum deflection under one-lane HL-93 loading was observed to be 0.174 in. for both Path 1 and Path 2.

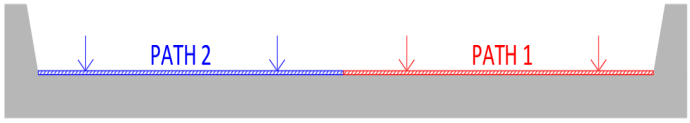

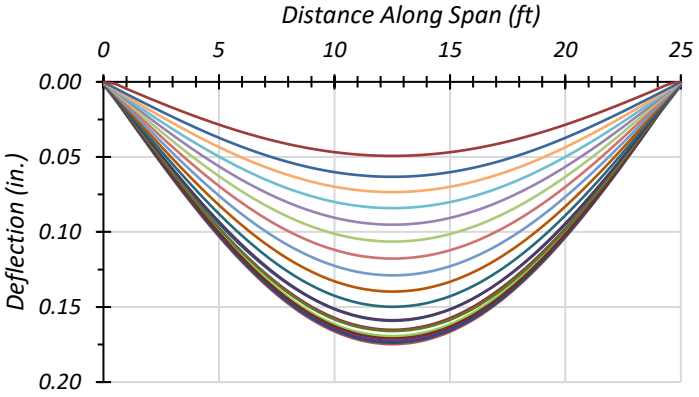

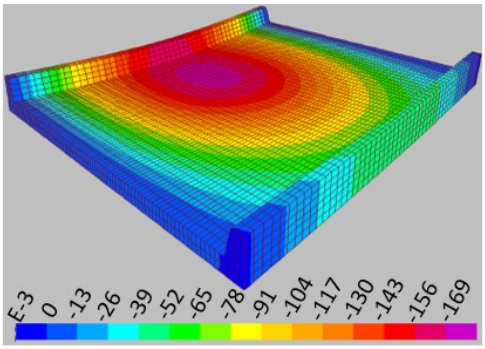

(a) Path 1

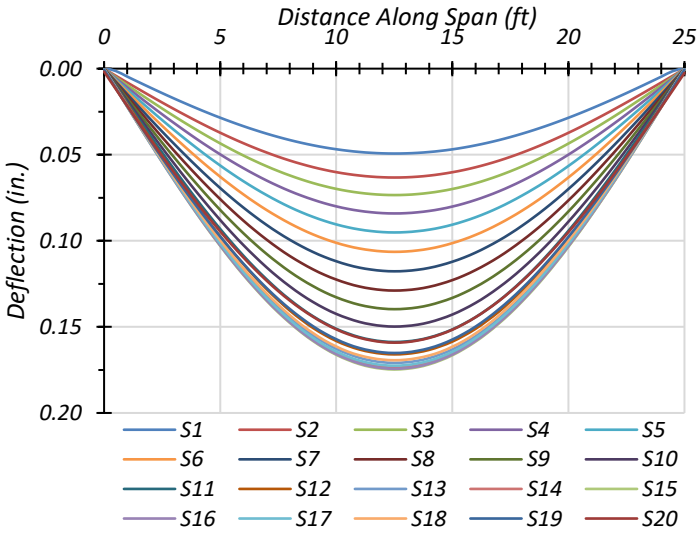

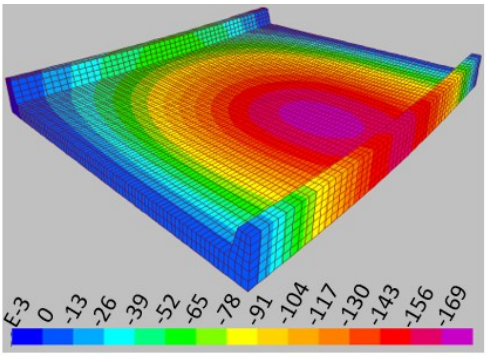

(b) Path 2

Figure 6.14. Deflection Profiles with HL-93 Loading

Table 6.15. Maximum Deflections with HL-93 Loading

Loading	S1	S2	S3	S4	S5	S6	S7	S8	S9	S10	S11	S12	S13	S14	S15	S16	S17	S18	S19	S20
Path 1	0.16	0.17	0.17	0.17	0.17	0.17	0.17	0.17	0.17	0.16	0.15	0.14	0.13	0.12	0.11	0.10	0.08	0.07	0.06	0.05
Path 2	0.05	0.06	0.07	0.08	0.10	0.11	0.12	0.13	0.14	0.15	0.16	0.17	0.17	0.17	0.17	0.17	0.17	0.17	0.17	0.16
Note: S = transverse section, paths indicate transverse loading positions as shown, deflections have inch units																				

6.7.3.2. Moment Results

The moments corresponding to each transverse section and the corresponding LLDFs for the one-lane and two-lane HL-93 loading paths are shown in Figure 6.15. The corresponding maximum moments for each section and path are listed in Table 6.16. The estimated moment results from the FEM model were used to calculate the equivalent widths for the slab portion and LLDFs for the curbs. A comparison of the estimated equivalent width for the interior slab portion obtained from the FEM model and those calculated using the approximate equations in the AASHTO Standard Specifications (AASHTO 2002) and AASHTO LRFD Specifications (AASHTO 2017) is provided in Table 6.17. Comparison with studies such as Amer et al. (1999) and Jones and Shenton (2012) was also carried out as shown in Figure 6.16 based on the two-lane-load case. All the equivalent widths were found to be conservative in comparison to the FEM results.

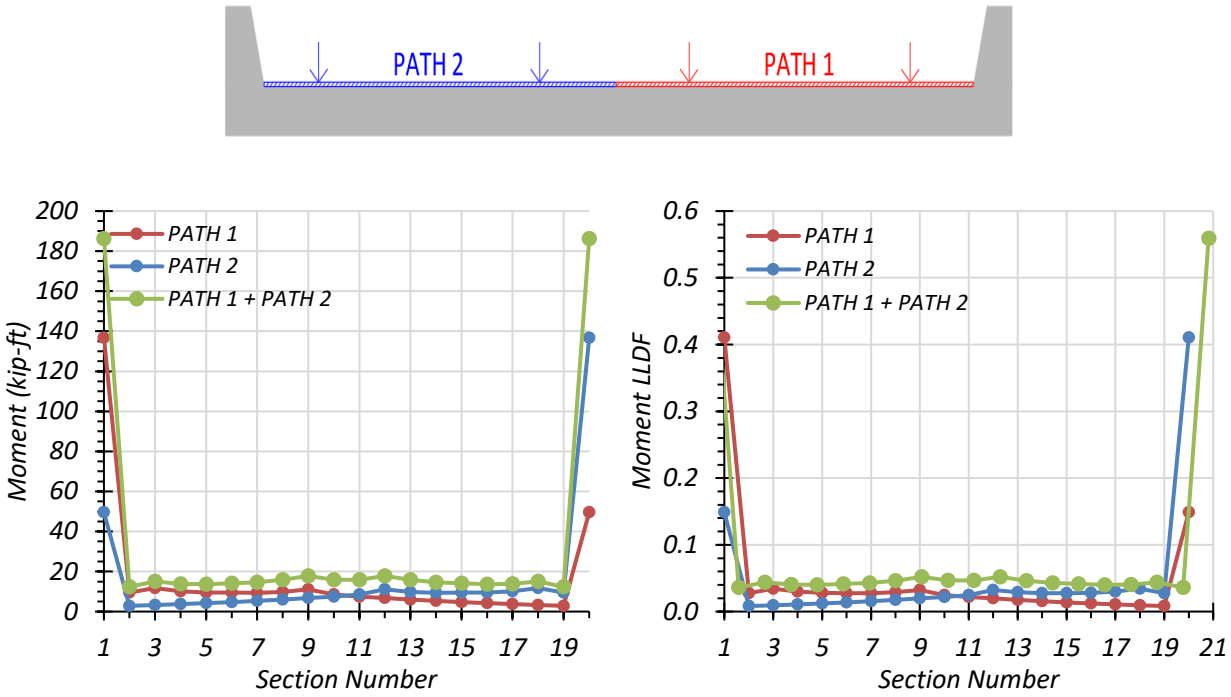

(a) Moment *(b) Moment LLDF*

Figure 6.15. Moment Results with HL-93 Loading

Table 6.16. Maximum Moments with HL-93 Loading

Loading	S1	S2	S3	S4	S5	S6	S7	S8	S9	S10	S11	S12	S13	S14	S15	S16	S17	S18	S19	S20
Path 1	136.7	9.5	11.8	10.2	9.5	9.4	9.4	9.8	11.1	8.5	7.5	6.7	6.0	5.3	4.7	4.2	3.7	3.3	2.9	49.6
Path 2	49.6	2.9	3.3	3.7	4.2	4.7	5.3	6.0	6.7	7.5	8.5	11.1	9.8	9.4	9.4	9.5	10.2	11.8	9.5	136.7
Path 1 + Path 2	186.2	12.3	15.0	13.9	13.7	14.2	14.7	15.8	17.8	15.9	15.9	17.8	15.8	14.7	14.2	13.7	13.9	15.0	12.3	186.2
Note: S = section, paths indicate transverse loading positions as shown, moments have kip-ft units																				

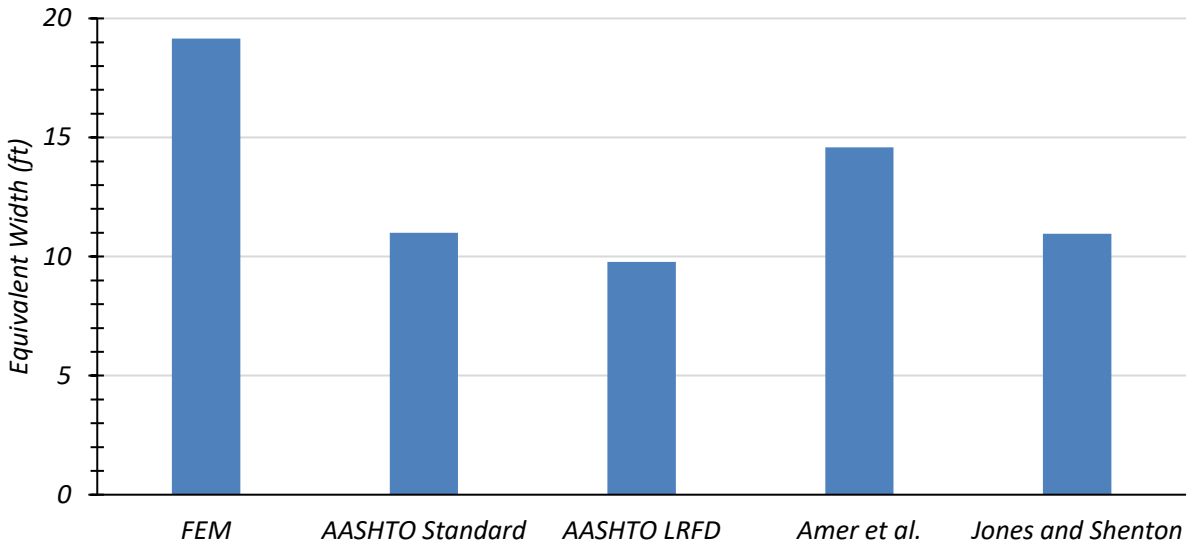

Figure 6.16. Comparison of Equivalent Width with Various Models for HL-93 Loading

Table 6.17. Governing Moment Equivalent Width (ft) for HL-93 Loading for Interior Slab

Loading	FEM (E^m_{FEM})	AASHTO (E^m_{AASHTO})	AASHTO LRFD (E^m_{LRFD})	Amer et al. (E^m_{Amer})	Jones and Shenton ($E^m_{Jones\ \&\ Shenton}$)
One-lane	29	11.0	10.5	14.6	12.0
Two-lane	19.2	11.0	9.8	14.6	11.0

6.7.3.3. Shear Results

The shear forces in each transverse section and the corresponding shear LLDFs for the one-lane and two-lane HL-93 loading paths are shown in Figure 6.17. The corresponding maximum moments for each section and path are listed in Table 6.18. The estimated shear results from the FEM model were used to calculate the equivalent widths for the slab portion and LLDFs for the curbs. A comparison of the estimated equivalent width for the interior slab portion obtained from the FEM model for two-lane-loaded case and those calculated using the approximate equations in the AASHTO Standard Specifications (AASHTO 2002) and AASHTO LRFD Specifications (AASHTO 2017) is provided in Table 6.19. Comparison with studies such as Amer et al. (1999)

and Jones and Shenton (2012) was also carried out. The AASHTO LRFD Specifications (AASHTO 2017) was slightly unconservative for both the one-lane and two-lane-loaded scenario while the AASHTO Standard Specifications (AASHTO 2002), Amer et al. (1999), and Jones and Shenton (2012) equivalent widths were unconservative for both scenarios.

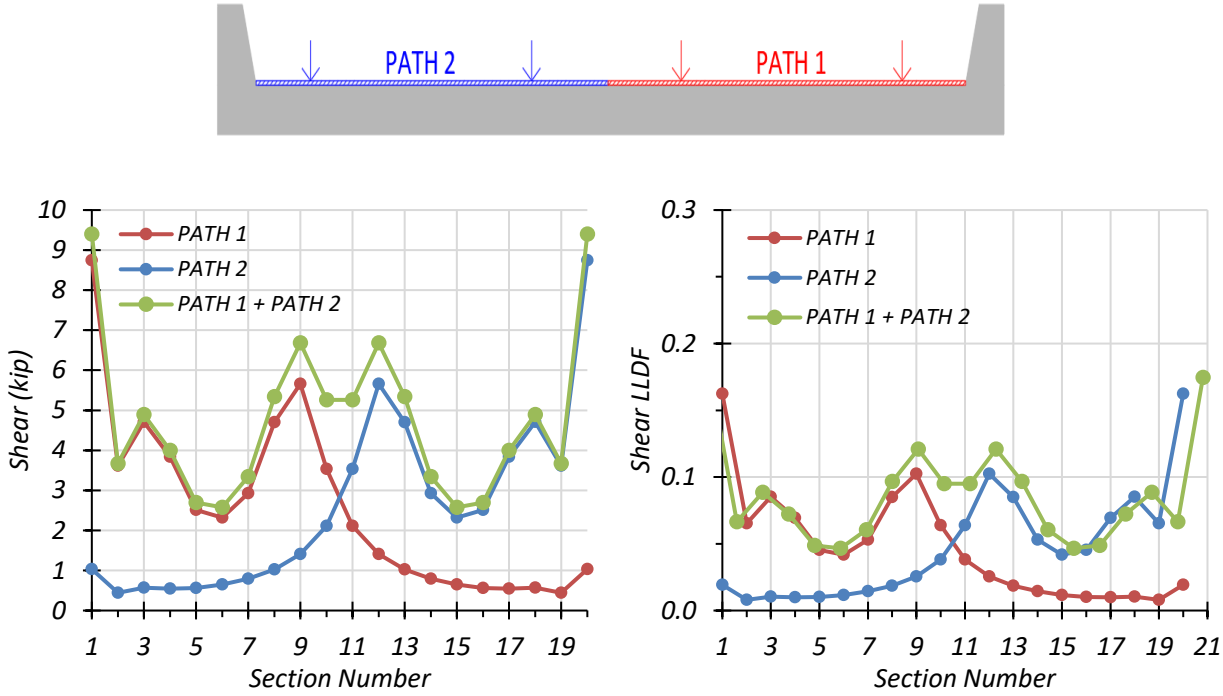

(a) Shear *(b) Shear LLDF*

Figure 6.17. Shear Results with HL-93 Loading

Table 6.18. Maximum Shears with HL-93 Loading

Loading	S1	S2	S3	S4	S5	S6	S7	S8	S9	S10	S11	S12	S13	S14	S15	S16	S17	S18	S19	S20
Path 1	8.7	3.6	4.7	3.8	2.5	2.3	2.9	4.7	5.7	3.5	2.1	1.4	1.0	0.8	0.6	0.6	0.5	0.6	0.4	1.0
Path 2	1.0	0.4	0.6	0.5	0.6	0.6	0.8	1.0	1.4	2.1	3.5	5.7	4.7	2.9	2.3	2.5	3.8	4.7	3.6	8.7
Path 1 + Path 2	9.4	3.7	4.9	4.0	2.7	2.6	3.3	5.3	6.7	5.3	5.3	6.7	5.3	3.3	2.6	2.7	4.0	4.9	3.7	9.4
Note: S = section, paths indicate transverse loading positions as shown, shears have kip units																				

Table 6.19. Governing Shear LLDF Values for HL-93 Loading

Loading	FEM (E^v_{FEM})	AASHTO (E^v_{AASHTO})	AASHTO LRFD (E^v_{LRFD})	Amer et al. (E^v_{Amer})	Jones and Shenton ($E^v_{Jones\ \&\ Shenton}$)
One-lane	9.8	11.0	10.5	14.6	12.0
Two-lane	8.3	11.0	9.8	14.6	11.0

6.8. SUMMARY

Finite element analysis of the selected simple-span concrete slab bridge, CS-9, was conducted for various vehicular load configurations. The equivalent strip width over which the vehicular loads are distributed was calculated using the bending moment and shear results. A comparison of the equivalent strip widths found using the FEM model was carried out with those determined using the procedures outlined in the AASHTO Standard Specifications (AASHTO 2002) and AASHTO LRFD Specifications (AASHTO 2017).

The equivalent widths for the interior slab portion of Bridge CS-9 calculated as per AASHTO Standard Specifications (AASHTO 2002) and AASHTO LRFD Specifications (AASHTO 2017) are conservative in comparison to the equivalent widths obtained from the FEM bending moment results, for all loading scenarios. This trend is also observed with the equivalent widths proposed by Amer et al. (1999) and Jones and Shenton (2012). However, the equivalent widths obtained from the FEM shear force results are unconservative when compared with those corresponding to AASHTO Standard Specifications (AASHTO 2002), AASHTO LRFD Specifications (AASHTO 2017), Amer et al. (1999), and Jones and Shenton (2012) for all loading scenarios. A comparison of the bending moments for the curb and slab portion obtained from the FEM with the ones calculated using the simplified approach outlined in Illinois Bulletin 346 (Jenson et al. 1943) showed that for both one-lane loading and two-lane loading the FEM curb moment was very similar and the FEM slab moment was higher.

7. EXPERIMENTAL TESTING OF BRIDGE CM-5

7.1. INTRODUCTION

In Chapter 4, basic load rating evaluation of 14 simple-span concrete multi-girder (CM) bridges was conducted and an FEM model of a typical load posted CM bridge was developed using the commercial software package CSiBridge. The selected simple-span concrete multi-girder bridge, CM-5, was load tested in the field. The purpose of the load test was to capture the actual in situ behavior of the bridge, such as the presence of partial fixity at the ends and the measured live load distribution between girders. The results from the field tests were used to calculate the experimental live load distribution factors for the individual bridge girders. The FEM model was also updated to include field measurements, nondestructive measures of concrete strength, and any observed end fixity to more accurately model the bridge.

Several nondestructive evaluation methods were used to identify the concrete compressive strength and the layout of the reinforcing bars. The results of NDE tests were used to update the FEM model of the bridge to represent the actual concrete compressive strength and reinforcement layout if it is different than the reinforcement details provided in the structural drawings. Due to the absence of structural drawings for this specific bridge, the measured bridge geometry and reinforcement details were compared to the standard drawing for this bridge type provided on the TxDOT website titled ‘CG 30'-4" Spans’ (TxDOT 2005).

In addition to conventional measuring devices, such as string potentiometers, strain gauges, and accelerometers; two cameras mounted on a tripod were also used to record the bridge response during each load test. An image analysis algorithm was used to determine the displacements from the unloaded bridge image and loaded bridge image. A thorough investigation of the field test

results along with the results from the updated and calibrated FEM model are then used to determine a refined load rating for the bridge.

7.2. GENERAL DESCRIPTION OF BRIDGE CM-5

Bridge CM-5 has a deck condition rating of 7 (Good), a superstructure condition rating of 7 (Good), and a substructure condition rating of 5 (Fair). The flexural resistance of the concrete pan girders controls the rating of the bridge, which has an inventory rating of 26 US tons and an operating rating of 36 US tons. The bridge is posted for a 24,000-pound tandem axle. Figure 7.1 shows a longitudinal section detail. Figure 7.2 shows photographs of an elevation view and an underside view of Bridge CM-5.

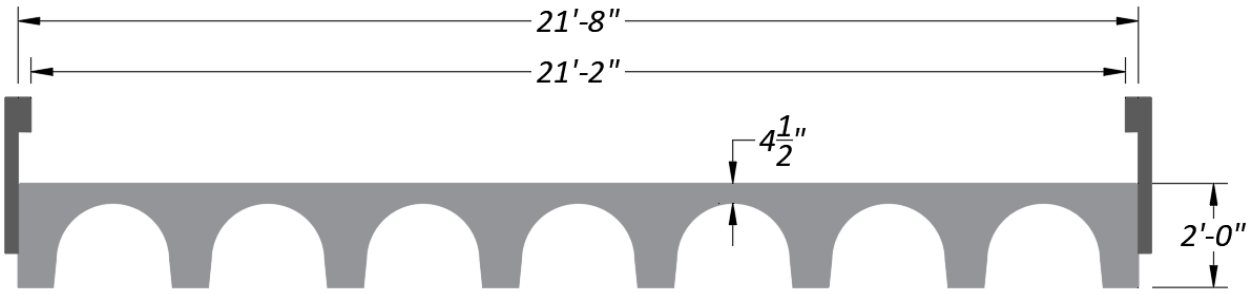

Figure 7.1. Longitudinal Section of Bridge CM-5 (adapted from TxDOT 2018b)

(a) Elevation view

(b) Underside view

Figure 7.2. Photographs of Bridge CM-5

7.3. IN-SITU MEASUREMENTS AND OBSERVATIONS

The as-built geometric details were measured to confirm the values given in the standard structural drawings. The bridge was measured to be 30 ft in length and the total roadway width was measured to be 21 ft 7 in. wide. The abutments were measured to be approximately 28 ft 4 in. apart. The bridge has eight pan girders and the external girders were measured to be 24 in. deep. The exterior girders were measured to be 7 in. wide at the bottom of the web while the interior girders were measured to be 6-7/8 in. wide at the bottom of the web.

7.3.1. Nondestructive Evaluation Results

The in-situ concrete compressive strength of Bridge CM-5 was determined onsite using rebound number test and Ultrasonic Pulse Velocity (UPV) test. The UPV test uses the speed taken for an ultrasonic pulse to pass through a known concrete thickness to determine the compressive strength. The compressive strength of concrete was determined onsite through rebound number test using two different instruments – Original Schmidt Hammer and Silver Schmidt Hammer. The surface over which these tests were conducted was first ground using an angle grinder with a masonry grinding wheel. The surface was further smoothened with the help of a grinding stone. An indicator solution of phenolphthalein in ethanol was applied to the clean surface to check for carbonation of concrete. Concrete carbonation can affect the result obtained from these tests. If the indicator solution did not turn purple, the surface was further grounded to reach the non-carbonated layer. Ten rebound number readings were obtained for both Schmidt Hammers by pushing against the surface. As per the Original Schmidt Hammer operating instructions, the highest and lowest rebound numbers were removed and the average of the remaining eight rebound numbers was calculated. The Silver Schmidt Hammer was developed in accordance with the ASTM

C805/C805M-18 (2018) guidelines. The average rebound number for the Original Schmidt Hammer was calculated to be 45.4. This corresponds to a concrete compressive strength of approximately 7 ksi using the conversion curve in Figure 7.3. In this test, the hammer was pushed vertically down.

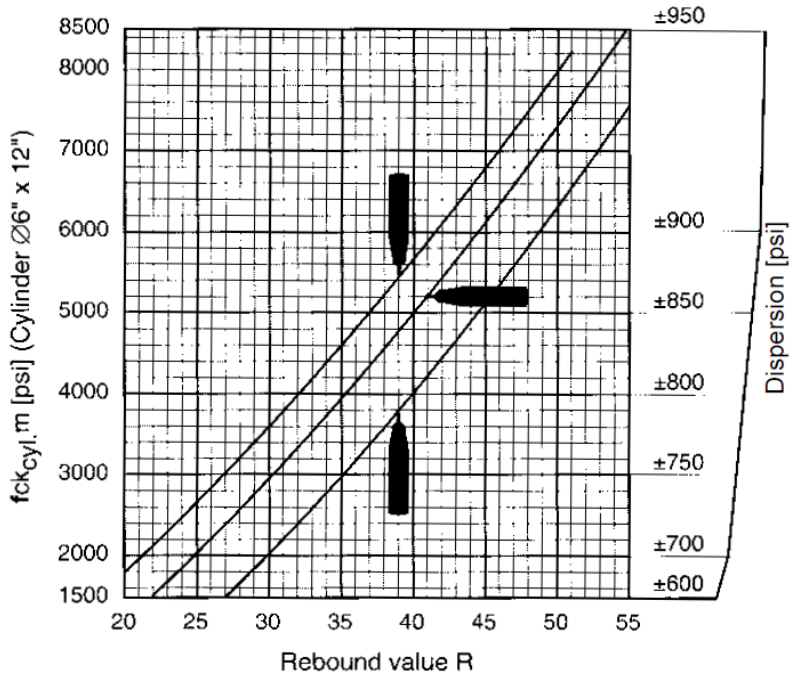

Figure 7.3. Original Schmidt Hammer Conversion Chart (reprinted from Proceq)

The Silver Schmidt Hammer uses the same principle and directly gives the compressive strength of concrete, when within the range of the instrument. This test was carried out three times and yielded different compressive strength values of 8.1 ksi, 7.0 ksi, and 7.8 ksi. The average of these values is approximately 7.6 ksi. Figure 7.8 provides the conversion chart used for Silver Schmidt Hammer rebound values.

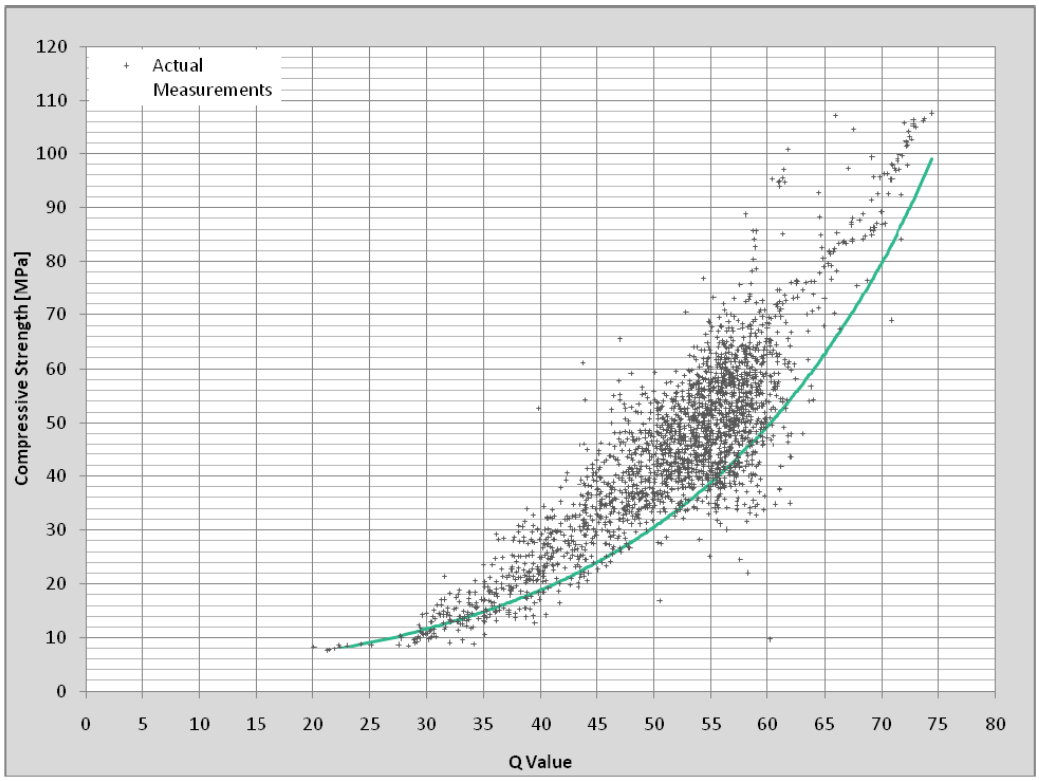

Figure 7.4. Silver Schmidt Hammer Conversion Chart (reprinted from Proceq)

Ultrasonic Pulse Velocity (UPV) test was also used to determine the compressive strength of concrete onsite. In this test, an ultrasonic pulse was passed through the concrete slab between the pan girders and the time taken for it to travel through the thickness was measured. The concrete depth was measured to be 7.25 in. The test was repeated three times and the travel times for the pulse were measured to be 48.8 µs, 44.4 µs, and 46.8 µs with an average travel time of 46.6 µs. This corresponds to an average wave velocity of 3952 m/s. Using the equation provided by Trtnik et al. (2009), the compressive strength of concrete was calculated from the average wave velocity to be 1.63 ksi. This measured compressive strength of concrete is smaller than the other NDE measurements. This may be due to interference from the reinforcement during the measurement. Huang et al. (2011) remarked that UPV alone does not provide an accurate measure of the

compressive strength of concrete and suggests using a combination of the wave speed and rebound number, known as SonReb. The concrete compressive strength was calculated to be 6.6 ksi, using the average wave velocity and the rebound number obtained from the Original Schmidt Hammer test using equations provided in Huang et al. (2011).

Table 7.1 summarizes the concrete compressive strength results obtained with the NDE tests.

Table 7.1. Concrete Compressive Strengths from NDE Tests

Test	Concrete Compressive Strength (ksi)
Schmidt Hammer Test	7.0
Silver Schmidt Hammer Test	7.6
UPV*	1.6
SonReb	6.6
*The measured wave velocity was inaccurate due to possible interference of reinforcement.	

The SonReb test provides the smallest measured value for the compressive strength of concrete (6.6 ksi). However, this measurement uses the average wave velocity measured using UPV test, which was found to be incorrect because of the small compressive strength (1.63 ksi) calculated using the measured velocity. Hence, the smallest compressive strength measured using the Original Schmidt Hammer Test and Silver Schmidt Hammer Test is used (7 ksi). As a result, this compressive strength and the corresponding estimated modulus of elasticity was adopted for the concrete in the updated FEM models.

Information regarding the steel reinforcement, such as spacing and cover, was also determined on site using Ground Penetrating Radar (GPR). The spacing of the transverse slab reinforcement was found to be irregular, ranging from 9 in. and 13 in. with an average spacing of approximately 10.8 in. A single layer of longitudinal reinforcement was located at 3 in. and another

layer at 21 in. from the bottom of the girder. This information could not be verified due to the absence of structural drawings for Bridge CM-5.

7.4. DATA ACQUISITION AND INSTRUMENTATION FOR BRIDGE CM-5

The bridge instrumentation plan was developed to capture the maximum response of the bridge subjected to the different vehicle loading scenarios. The instruments used to measure the response of the bridge included strain gauges, string potentiometers, and accelerometers, which were connected to the data acquisition system to digitally record the measured data.

7.4.1. Instrumentation Plan for Bridge CM-5

The instrumentation plan for Bridge CM-5 along with the cross-sectional views are shown in Figure 7.5. The labeling system used in the instrumentation plan is explained in Figure 7.6. The instrumentation labels for the data acquisition system are tabulated in Table 7.2. The measured bridge response is used to identify the actual bridge behavior and live load distribution, and any potential areas of opportunity to increase or remove the load posting. Several goals were identified in determining the instrumentation types and locations.

- The data collected from the strain gauges are used to determine the neutral axis position of the girders and any unintended partial fixity of the girders at the supports.
- The midspan deflection data collected by the string potentiometers are used to infer experimental moment LLDFs to compare with the estimated values from the FEM model of Bridge CM-5 and the AASHTO LLDFs.
- The accelerometers collect vibration data used to compute the dynamic properties of the bridge.

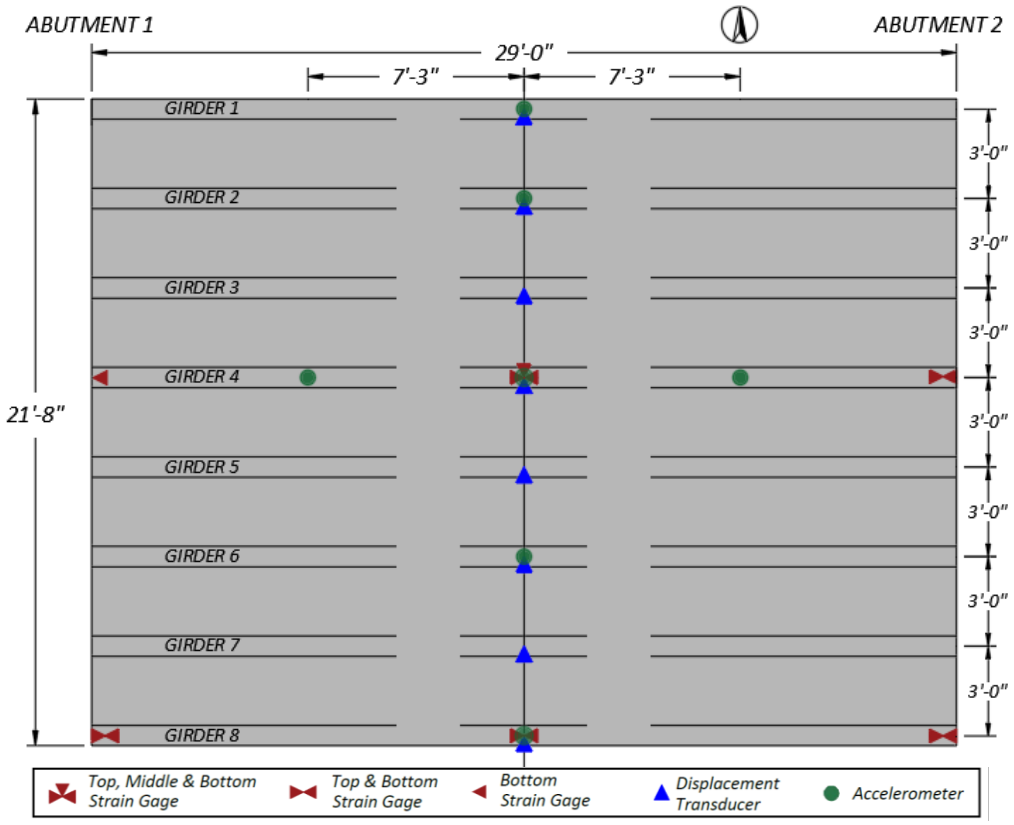

(a) Plan View

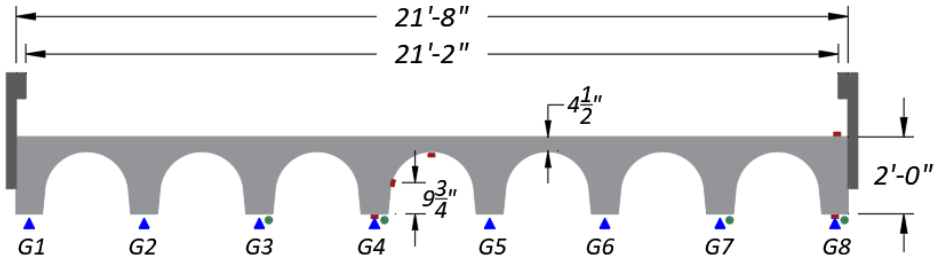

(b) Midspan Section

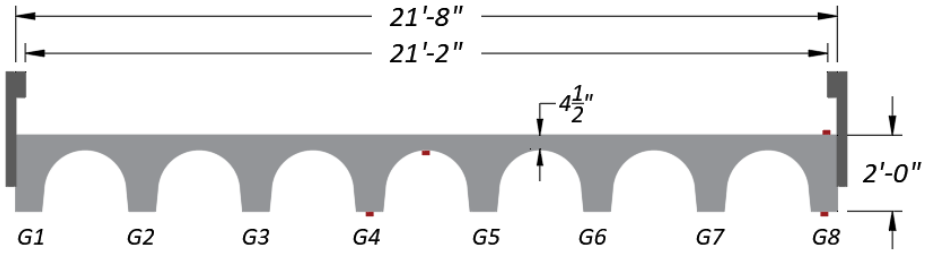

(c) End Section

Figure 7.5. Instrumentation Plan for Bridge CM-5

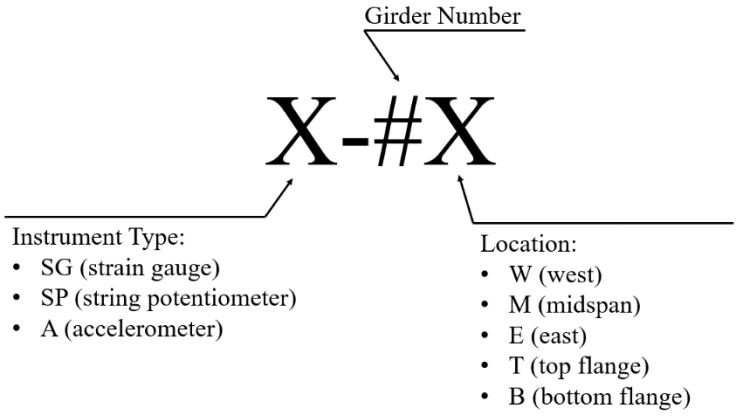

Figure 7.6. Instrumentation Labeling System Used for Bridge CM-5

Table 7.2. Instrumentation Labels for Bridge CM-5

DAQ Box	Channel	Label	Type	DAQ Box	Channel	Label	Type
Strain Book	CH1	SG-8WT	PL-60	WBK 16-3	CH25	SP-2M	SM1-2
	CH2	SG-8WB	PL-60		CH26	SP-1M	SM1-2
	CH3	SG-8MT	PL-60		CH27	-	
	CH4	SG-8MB	PL-60		CH28	-	
	CH5	SG-8ET	PL-60		CH29	-	
	CH6	SG-8EB	PL-60		CH30	-	
	CH7	SG-4Mm	PL-60		CH31	-	
	CH8	SG-4WB	PL-60		CH32	-	
WBK 16-1	CH9	SG-4MT	PL-60	WBK 18	CH57	A-8M	4507 IEPE
	CH10	SG-4MB	PL-60		CH58	A-6M	4507 IEPE
	CH11	SG-4ET	PL-60		CH59	A-4M	4507 IEPE
	CH12	SG-4EB	PL-60		CH60	A-2M	4507 IEPE
	CH13	-			CH61	A-4W	4507 IEPE
	CH14	-			CH62	A-4E	4507 IEPE
	CH15	-			CH63	A-1M	4507 IEPE
	CH16	-			CH64	-	
WBK 16-2	CH17	-					
	CH18	-					
	CH19	SP-8M	SM1-2				
	CH20	SP-7M	SM1-2				
	CH21	SP-6M	SM1-2				
	CH22	SP-5M	SM1-2				
	CH23	SP-4M	SM1-2				
	CH24	SP-3M	SM1-2				

Notes:
1. Refer to Figure 7.6 for explanation of the labeling system used.
2. ‘m’ refers to the location at the mid-height of the pan girder.

7.4.2. Data Acquisition System and Instrument Details

7.4.2.1. Data Acquisition System

A total of 24 strain gauges (at 12 measurement locations using half-bridge circuits), eight string potentiometers, and seven accelerometers were installed on Bridge CM-5. Twenty-seven channels in the data acquisition system were used. The strain gauges and string potentiometers were connected via cables to the main box (Measurement Computing StrainBook) and WBK16 extension module boxes. The accelerometer data were collected by the additional WBK18 extension module box. The data acquisition system' main box and extension modules are shown in Figure 7.7(a).

Strainbook WBK16 WBK18

(a) Main Data Acquisition Box and Extension Modules (MCC 2014)

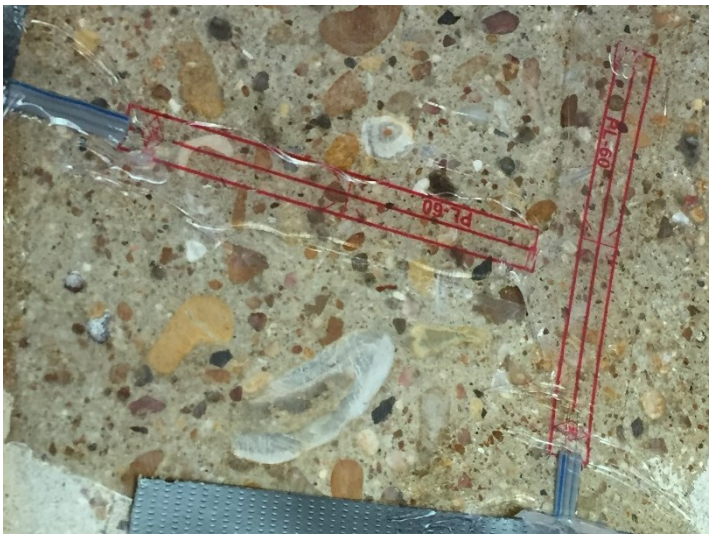

(b) Tokyo Measuring Instruments Lab PL-60-11-3LJCT Strain Gauges

(c) Celesco SM1-2 String Potentiometer

(d) Brüel & Kjær IEPE Accelerometer

Figure 7.7. Data Acquisition System and Instrumentation

7.4.2.2. Strain Gauges

A pair of strain gauges was installed at 12 measurement locations on the bridge to capture the strain profile at midspan and at the ends of the selected interior girder and exterior girder. The strain gauge type used in Bridge CM-5 was Tokyo Measuring Instruments Lab PL-60-11-3LJCT strain gauge (Figure 7.7(b)). The main gauge was installed in the longitudinal direction while the

temperature compensation gauge was installed transverse to the main gauge. Figure 7.8 shows a close-up of the installation of the concrete strain gauges. Strain gauges were installed along the bottom of the girder at six different locations on two girders. Gauges were also installed on top of the slab at three locations along an exterior girder. Gauges were installed at midspan and at an average of 6 in. from the bearing centerline at each abutment for both an exterior and an interior girder. The strains obtained from these gauges were used to determine the location of the neutral axis of the girder sections and identify the presence of partial end fixity at the supports.

Figure 7.8. Close-Up of Strain Gauge Installation

7.4.2.3. String Potentiometers

Eight string potentiometers were installed at the midspan of each girder to record the midspan deflections during the vehicular load tests. Celesco SM1-2 string potentiometers (Figure 7.7(c)) having a 2.5 in. stroke were used at all eight locations.

7.4.2.4. Accelerometers

A total of seven Brüel & Kjær IEPE accelerometers (Figure 7.7(d)) were installed; five accelerometers at midspan of every other girder and two accelerometers at quarter spans along an interior girder to record the dynamic vibrations of the bridge during the dynamic load tests. The recorded vibrations were used to obtain the frequencies and the mode shapes of the bridge. The piezoelectric accelerometers are light, compact, and sensitive having resonance frequency of 18 kHz which is much higher than the bridges natural frequency.

7.5. LOAD TESTING PROCEDURE FOR BRIDGE CM-5

A comprehensive test program was conducted to evaluate the performance and behavior of Bridge CM-5. The test program consisted of two parts: (1) static load tests, which consisted of stop location tests and crawl speed tests, and (2) dynamic load tests. The nondestructive vehicular load testing of Bridge CM-5 was conducted on April 18, 2019.

7.5.1. Test Vehicle

The vehicle used for the load testing was a Sterling LT 9500 dump truck, provided by the TxDOT Caldwell Office. The dump truck was loaded with base material to match the rear tandem axle weight to the posted load limit (posted at 24,000-pound tandem axle). The truck axle configuration along with its empty and loaded weights are shown in Figure 7.9.

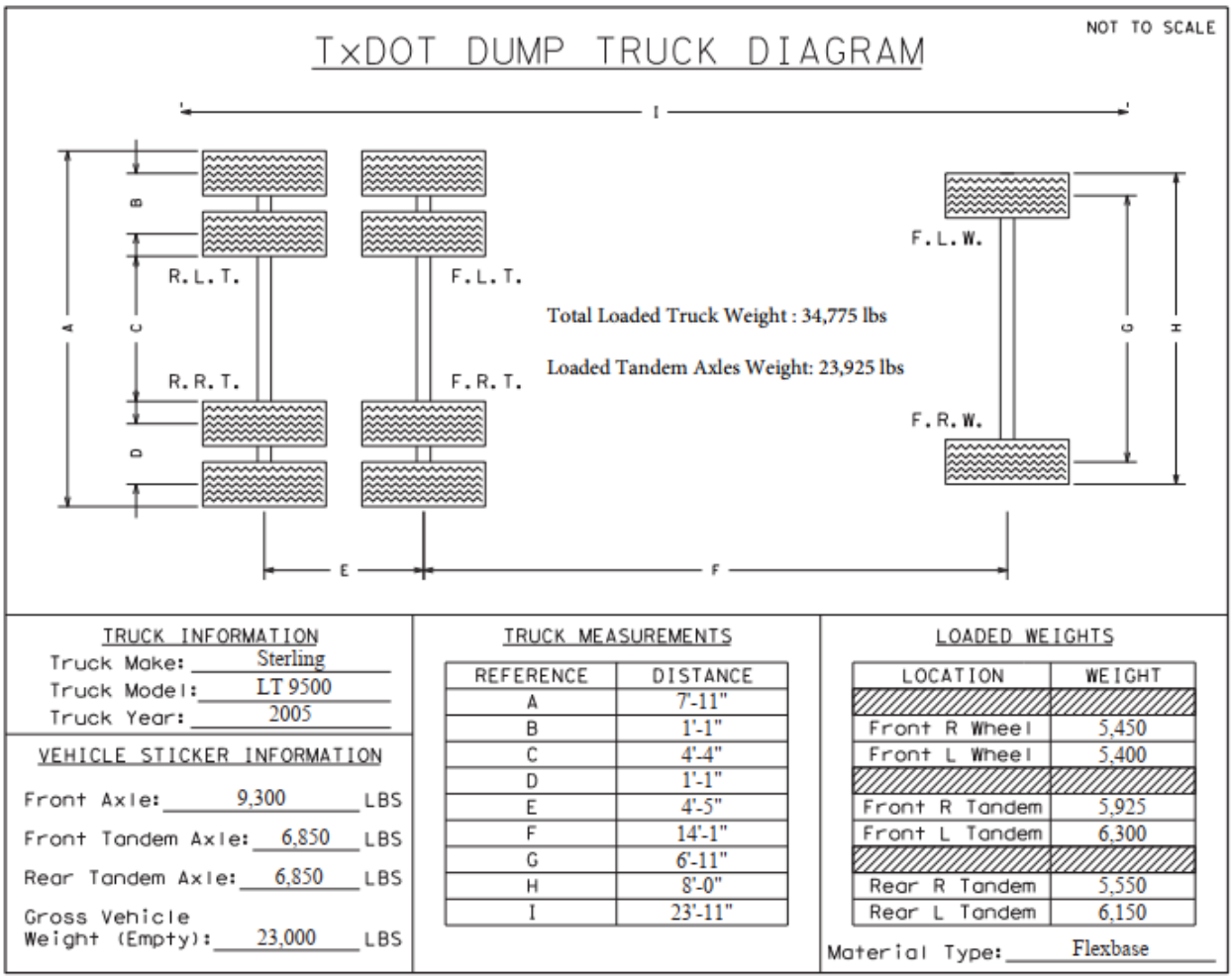

Figure 7.9. Wheel Weights and Spacing of the Loaded Dump Truck Used

7.5.2. Vehicle Positioning

Three transverse paths were defined across the bridge to create critical transverse loading positions for exterior and interior girders. The minimum allowable clearances from the barrier and centerline of the bridge, as outlined in AASHTO Standard Specifications (AASHTO 2002) and AASHTO LRFD Specifications (AASHTO 2017), were adhered to when defining the paths. Figure 7.10 shows a schematic of the loading paths across the transverse section of Bridge CM-5. Path 1 corresponds to the location where the centerline of the adjacent rear tires of the dump truck was located 2 ft from the face of the bridge guardrail. Path 2 is defined along the second lane where

the centerline of the adjacent rear tires is located 2 ft from the centerline of the bridge. A third path was defined along the centerline of the bridge, called Middle Path, where the dump truck ran along the center of the bridge.

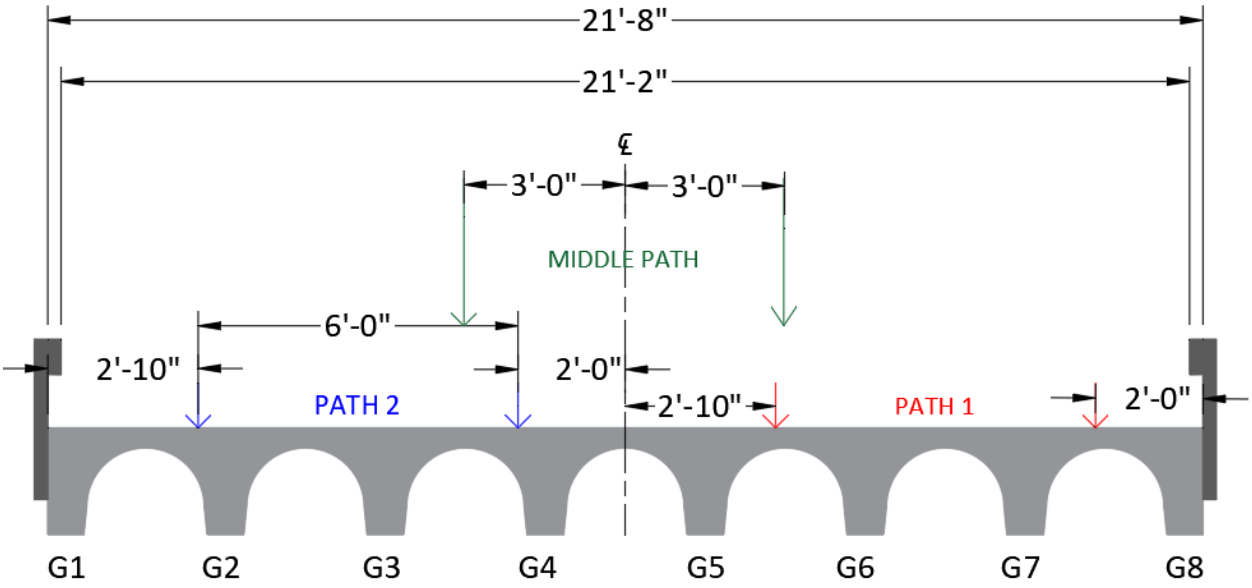

Figure 7.10. Test Paths for Bridge CM-5

7.5.3. Test Protocol

Bridge CM-5 was subjected to static, crawl speed, and dynamic tests. Impact tests were also conducted to capture the dynamic properties of the bridge. Table 7.3 lists the test protocol carried out for proof testing of Bridge CM-5. In the following sections, details regarding each test are outlined.

Table 7.3. Test Protocol for Bridge CM-5

Test Number	Load Position	Test Type
1	Path 1	Static – Stop Location
2	Path 1	Static – Crawl Speed
3	Path 1	Dynamic (31 mph)
4	Path 1	Dynamic (41 mph)
5	Path 2	Static – Stop Location
6	Path 2	Static – Crawl Speed
7	Path 2	Dynamic (30 mph)
8	Path 2	Dynamic (40 mph)
9	Middle Path	Static – Stop Location
10	Middle Path	Static – Crawl Speed
11	Middle Path	Dynamic (29 mph)
12	Middle Path	Dynamic (40 mph)
13	North	Sledgehammer
14	Middle Path	Sledgehammer
15	South	Sledgehammer

7.5.3.1. Static Tests

The static load tests conducted on Bridge CM-5 were of two types: (1) Stop Location Test, and (2) Crawl Speed Test. For each stop location test along Path 1, Path 2, and the Middle Path, reference data was recorded prior to the bridge being loaded. The truck was positioned on the bridge such that the maximum bending moment would be obtained in the girder closest to the wheel line. This was achieved when the two rear tandem axles of the truck were located equidistant from the centerline of the bridge. Due to the short span of Bridge CM-5, the front axle of the truck was off the bridge for each static test. Once the truck was positioned and the engine was turned off, data for the loaded bridge was recorded.

Reference files were recorded for each crawl speed test along the same paths prior to the truck moving over the bridge. The data was recorded while the truck passed over the entire span of the bridge at an idle speed of 2-3 mph.

7.5.3.2. Dynamic Tests

Prior to each dynamic test, reference files for the unloaded bridge were recorded. The truck was accelerated up a pre-determined speed and then passed over the entire span of the bridge while maintaining the speed. The corresponding data was recorded. The dynamic tests were carried out at two different speeds. The first test for each path was conducted for a speed of 30 mph and the second test was carried out for a speed of 40 mph. The speed limit for the road on which the bridge was located was noted to be 45 mph.

7.5.3.3. Impact Tests

To obtain information related to the dynamic properties of Bridge CM-5, a sledge hammer was used to strike the top of the bridge deck at three different transverse positions at midspan to excite different modes of the bridge. The recorded vibration data was used to determine the dynamic properties of the bridge. The tests were carried out at three midspan locations (north side of the bridge, transverse center of the bridge, and south side of the bridge).

7.5.4. Test Operations

The testing schedule for Bridge CM-5 spanned from April 16, 2019 to April 18, 2019. This includes all instrumentation installation, load testing, and instrumentation removal.

The clearance height to the underside of the bridge was approximately 8 ft. Thus, there was no need for scaffolding. All instrumentation was installed on the underside of the bridge during the first two days with the help of step ladders. The installation locations were marked as per the instrumentation plan. An angle grinder, with masonry grinding wheel, was used to grind an approximately 4 in. by 4 in. area at locations where the strain gauges were to be installed. The surface was made smooth with the help of 150 and 220 grit sandpapers and then cleaned with

acetone. The surface was repeatedly cleaned with acetone applied to paper towels, until a clean tip was no longer discolored by the scrubbing. Liberally applying acetone brings the surface pH back to an optimum alkalinity of 7.0 to 7.5 pH, ideal for bonding of the glue. Any microscopic gaps or cracks on the concrete surface were filled with the application of an epoxy. Once the epoxy cured, the surface was sandpapered and cleaned with acetone as previously described. The strain gauges were installed onto the surface with the help of suitable adhesive after the surface had dried.

For string potentiometer installation, eight wooden posts were hammered into the stream bed and the string potentiometers were screwed onto the posts. Metal hooks were installed on the bottom of each pan girder at midspan and fishing wires were attached from the hooks to the string potentiometers. Accelerometers were also attached to the metal plates glued onto the pan girders. Figure 7.11 shows the installed instrumentation for Bridge CM-5.

The nondestructive load tests were conducted on April 18, 2019. The designated paths were marked on the bridge with washable spray paint. The DAQ system was set up and the cables from all instrumentation attached to the DAQ boxes. The dump truck was loaded approximately to the posted load limit at the TxDOT Caldwell Maintenance Office (Figure 7.12 (a)). The 15 tests listed in the test protocol were carried out and the corresponding data recorded. Figure 7.12 (b) shows the set-up for Test 5. After the completion of all tests, all the instruments were removed.

(a) Installed Strain Gauges

(b) Installed Accelerometer

(c) Installed String Potentiometers

Figure 7.11. Installed Instrumentation for Bridge CM-5

(a) Dump Truck Weighing Operation

(b) Static Test along Path 2

Figure 7.12. Testing of Bridge CM-5

7.6. TEST RESULTS FOR BRIDGE CM-5

The data recorded during the diagnostic tests were processed, analyzed, and filtered for noise, if required. Strain gauge data were used to determine the strain profile and stresses within the section. String potentiometers recorded the deflections across the bridge, from which the LLDF for each girder was calculated. The dynamic properties of the bridge, such as natural frequencies and mode shapes, were obtained from the data recorded by the accelerometers. An image analysis algorithm was used to determine the deflections from the videos of each test. These results are provided in the following sections.

7.6.1. Static Load Tests on Bridge CM-5

The stop location test and crawl speed test were the two static tests conducted on Bridge CM-5. During the stop location test, the truck was positioned on the bridge such that the maximum bending moment would be obtained in the girder closest to the wheel line. During crawl speed test, the truck passed over the entire span of the bridge at a crawl speed of approximately 2-3 mph.

7.6.1.1. Strain Measurements

The strain gauge data for each test were compiled. For the stop location test, the maximum strain occurring at each strain gauge location was obtained. For the crawl speed test, the maximum bottom strain in the girder closest to the location of the truck and the corresponding time at which this occurred was first obtained. All other strain values were extracted for that specific time. It should be noted that the tensile strains are taken to be positive and the compressive strains are negative. The neutral axis location for each girder was determined from the strain profile at midspan.

Note that the strain values obtained from the bottom strain gauge attached at the midspan of Girder G4 are very high and seem to indicate an issue with the gauge, possibly due to existing cracks in the concrete surface. These values have been shown in the following graphs with a green dot but not used for calculating neutral axis depth. Using the assumption that plane sections remain plane, a linear trend was adopted between the top strain (below the slab) and mid height strain at Girder G4 and this line was extended to determine the neutral axis depth at midspan of Girder G4 (shown as a dashed green line in the following graphs).

7.6.1.1.1. Interior Girder 4 -Path 1 Loading

Strain profiles corresponding to the top and bottom strains for the interior Girder G4 under static tests along Path 1 are provided in Figure 7.13. The strain profiles at the west and east ends of Girder G4 are shown in Figure 7.13(a) for the stop location test and Figure 7.13(c) for the crawl speed test. It can be seen that the bottom strain at both the west and east ends of Girder G4 are compressive for the stop location test and crawl speed test, indicating some degree of end fixity present. The bottom strains obtained from the crawl speed test were slightly less than those obtained from the stop location test. This may be due to the truck stop location not being exactly at the moment critical position.

The strain profiles at the midspan of Girder G4 are shown in Figure 7.13(b) for the stop location test and Figure 7.13(d) for the crawl speed test. The neutral axis depth at midspan was found to be 10.40 in. from the bottom of Girder G4 using the strain profile obtained from the stop location test and 10.65 in. from the bottom of Girder G4 using the strain profile obtained from the crawl speed test. The neutral axis depth calculated using the strain profile obtained from the crawl speed test is slightly higher than the one obtained from the stop location test.

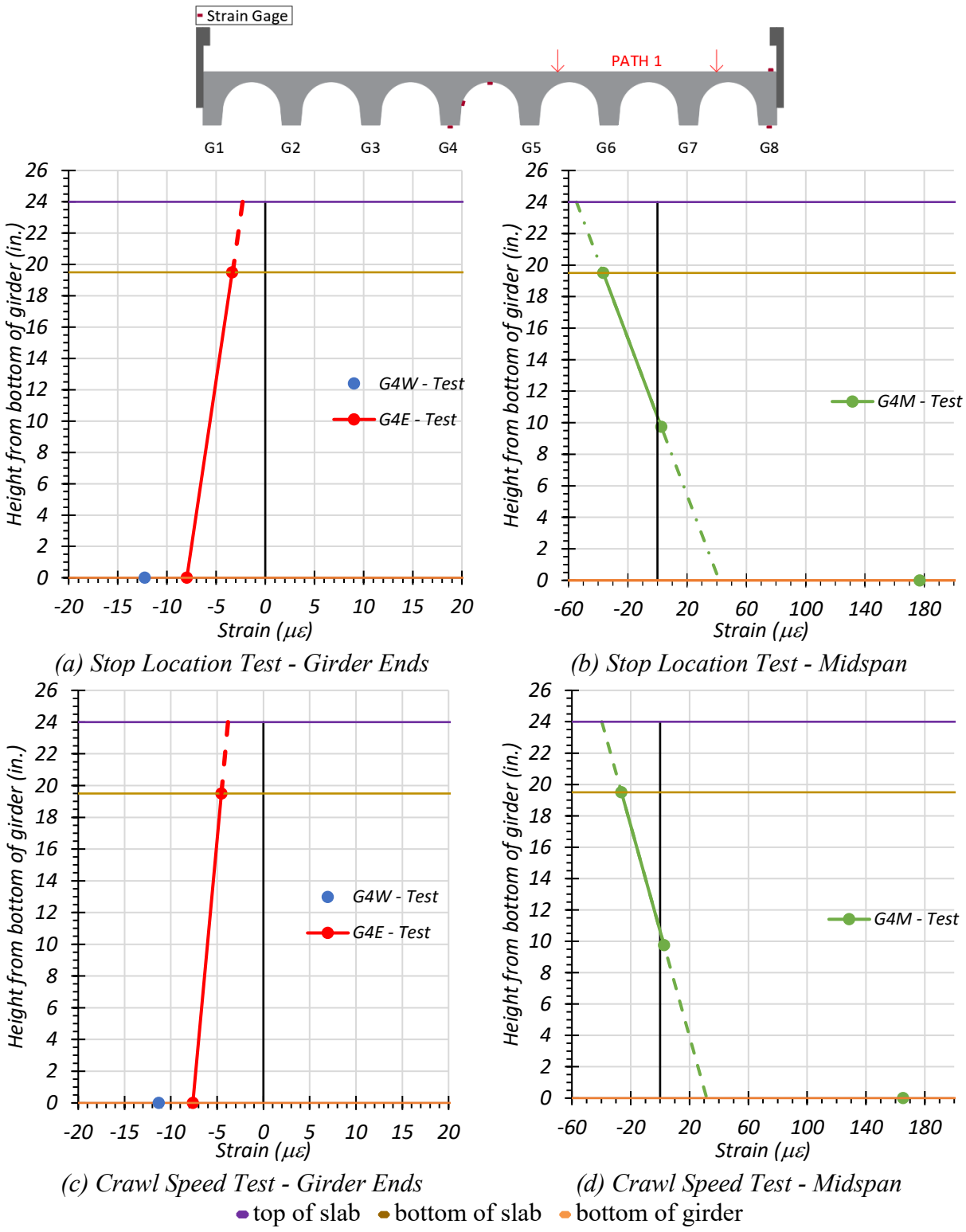

Figure 7.13. Static Strains for Interior Girder 4 – Path 1

7.6.1.1.2. Interior Girder 4 – Path 2 Loading

Strain profiles corresponding to the top and bottom strains for the interior Girder G4 under static tests along Path 2 are provided in Figure 7.14.

The strain profile at the west and east ends of G4 is shown in Figure 7.14(a) for the stop location test and Figure 7.14(c) for the crawl speed test. The bottom strain for both the west and east ends of Girder G4 are compressive for the stop location test and crawl speed test, indicating some degree of end fixity present. The bottom strains obtained from the crawl speed test is slightly less. This may be due to the truck stop location not being exactly at the moment critical position.

The strain profile at midspan of G4 is shown in Figure 7.14(b) for the stop location test and Figure 7.14(d) for the crawl speed test. The neutral axis depth at midspan was found to be 9.37 in. from the bottom of Girder G4 using the strain profile obtained from the stop location test and 10.23 in. from the bottom of Girder G4 using the strain profile obtained from the crawl speed test. The neutral axis depth calculated using the strain profile obtained from the crawl speed test is slightly higher than that obtained from the stop location test. This could be due to the stop location test being slightly different from the moment critical position for absolute maximum moment.

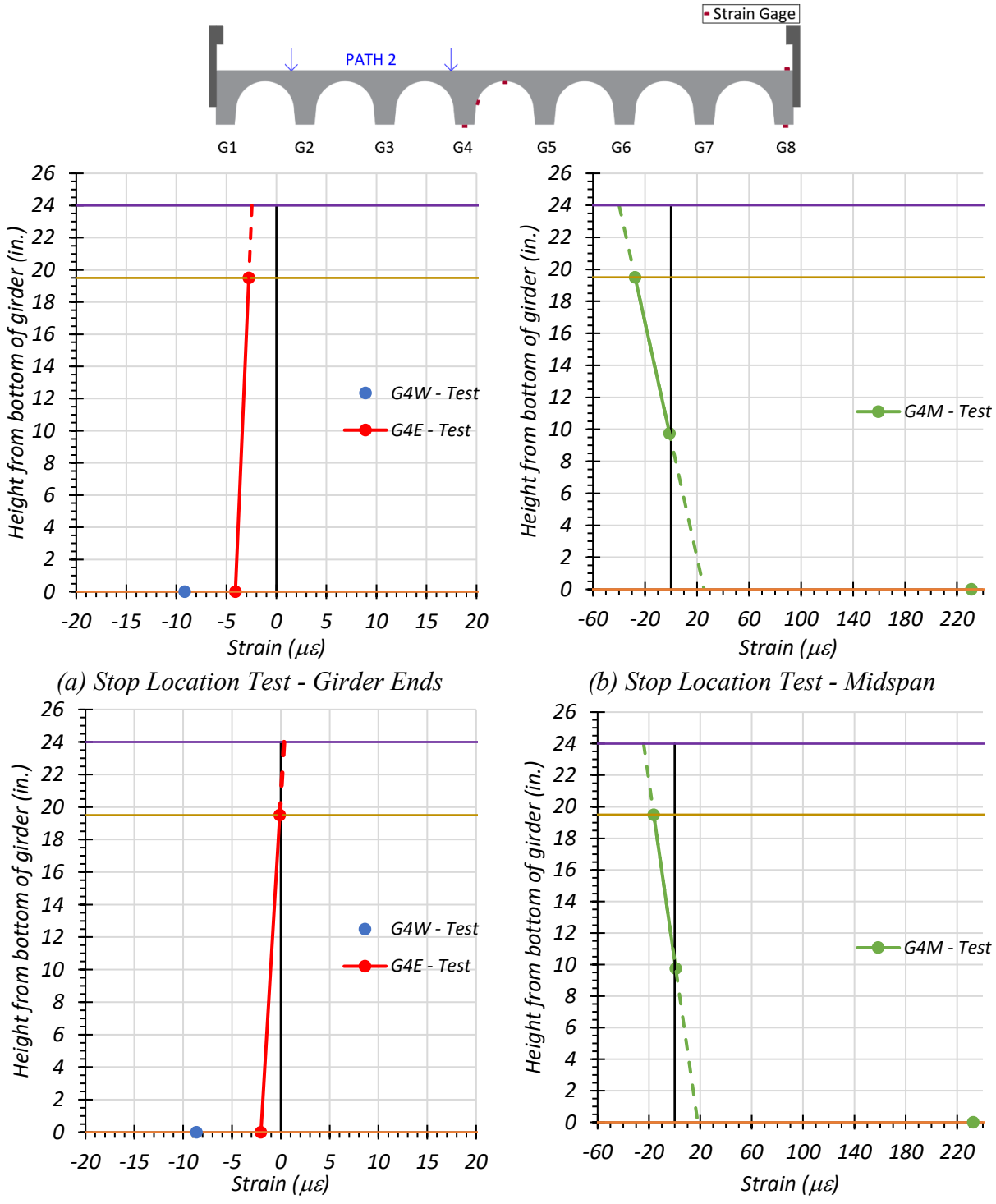

(a) Stop Location Test - Girder Ends

(b) Stop Location Test - Midspan

(c) Crawl Speed Test - Girder Ends

(d) Crawl Speed Test - Midspan

Figure 7.14. Static Strains for Interior Girder 4 – Path 2

7.6.1.1.3. Interior Girder 4 – Middle Path Loading

Strain profiles corresponding to the top and bottom strains for the interior Girder G4 under static tests along the Middle Path are provided in Figure 7.15.

The strain profiles at the west and east ends of G4 are shown in Figure 7.15(a) for the stop location test and Figure 7.15(c) for the crawl speed test. It can be seen that the bottom strain at both the west and east ends of Girder G4 are compressive for the stop location test and crawl speed test, indicating some degree of end fixity present. The bottom strains obtained from the stop location test and crawl speed test are very similar.

The strain profiles at the midspan of G4 are shown in Figure 7.15(b) for the stop location test and Figure 7.15(d) for the crawl speed test. The neutral axis depth at midspan was found to be 10.01 in. from the bottom of Girder G4 using the strain profile obtained from the stop location test and 10.24 in. from the bottom of Girder G4 using the strain profile obtained from the crawl speed test. The neutral axis depth calculated using the strain profile obtained from the crawl speed test is slightly higher than the one obtained from the stop location test. This also could be due to the stop location test being slightly different from the moment critical position for absolute maximum moment.

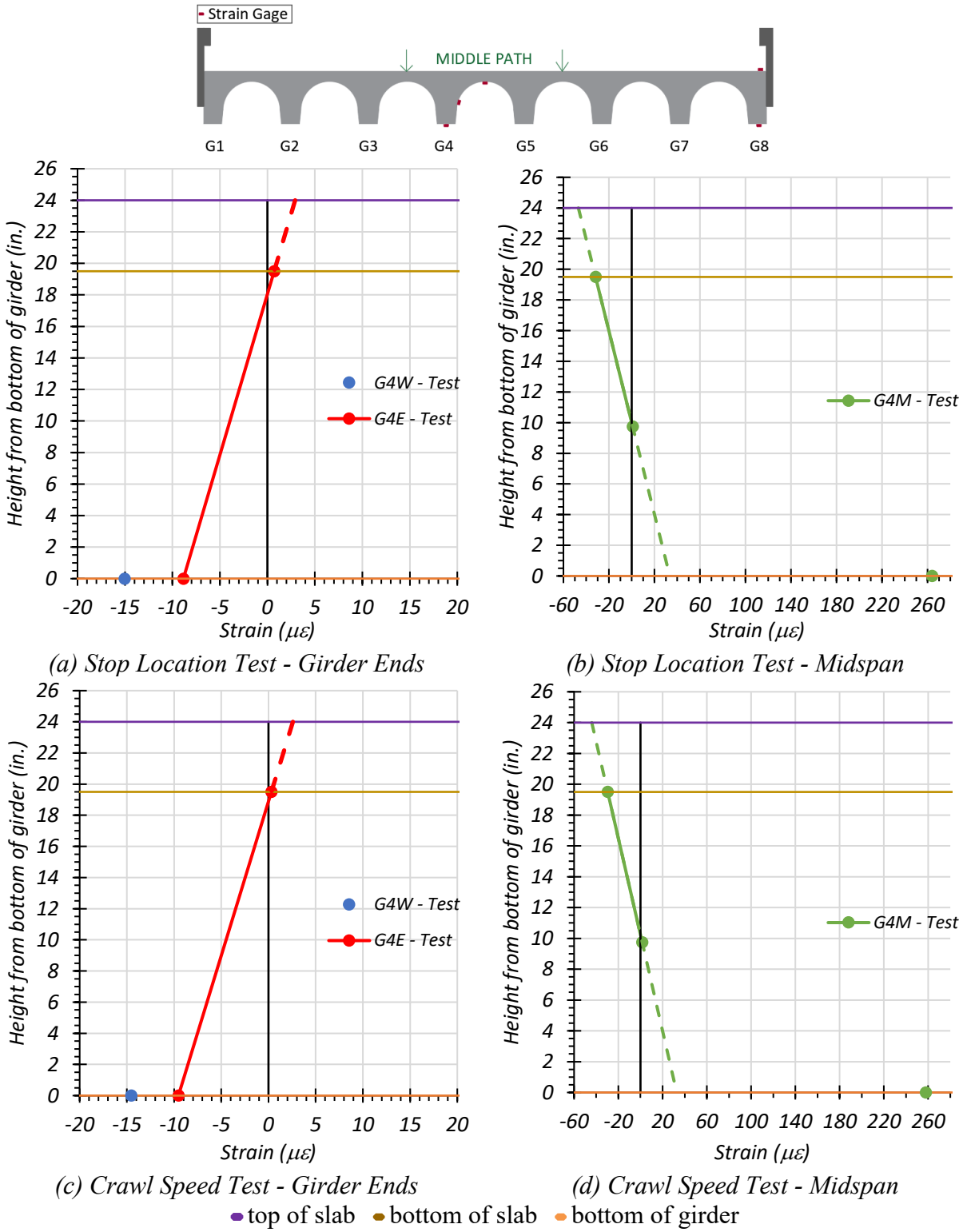

(a) Stop Location Test - Girder Ends

(b) Stop Location Test - Midspan

(c) Crawl Speed Test - Girder Ends

(d) Crawl Speed Test - Midspan

Figure 7.15. Static Strains for Interior Girder 4 – Middle Path

7.6.1.1.4. Exterior Girder 8 – Path 1 Loading

Strain profiles corresponding to the top and bottom strains for the exterior Girder G8 under static tests along Path 1 are provided in Figure 7.16.

The strain profiles at the west and east ends of G8 are shown in Figure 7.16(a) for the stop location test and Figure 7.16(c) for the crawl speed test. The bottom strains for the west end of Girder G8 are compressive for both the stop location test and crawl speed test, indicating some degree of end fixity present. For both the stop location test and crawl speed test, the bottom strains at the east end of Girder G8 are small negative values (< 5 με). This indicates the absence of significant partial restraint at this end. The bottom strains obtained from the crawl speed test were slightly higher than those obtained from the stop location test for the west end of Girder G8. The difference in strain values for the stop location test and crawl speed test may be due to the truck stop location not being exactly at the moment critical position.

The strain profiles at the midspan of Girder G8 are shown in Figure 7.16(b) for the stop location test and Figure 7.16(d) for the crawl speed test. The neutral axis depth at midspan was found to be 15.02 in. from the bottom of Girder G8 using the strain profile obtained from the stop location test and 14.37 in. from the bottom of Girder G8 using the strain profile obtained from the crawl speed test. The neutral axis depth calculated using the strain profile obtained from the crawl speed test is slightly higher than the one obtained from the stop location test. This also could be due to the stop location test being slightly different from the moment critical position for absolute maximum moment.

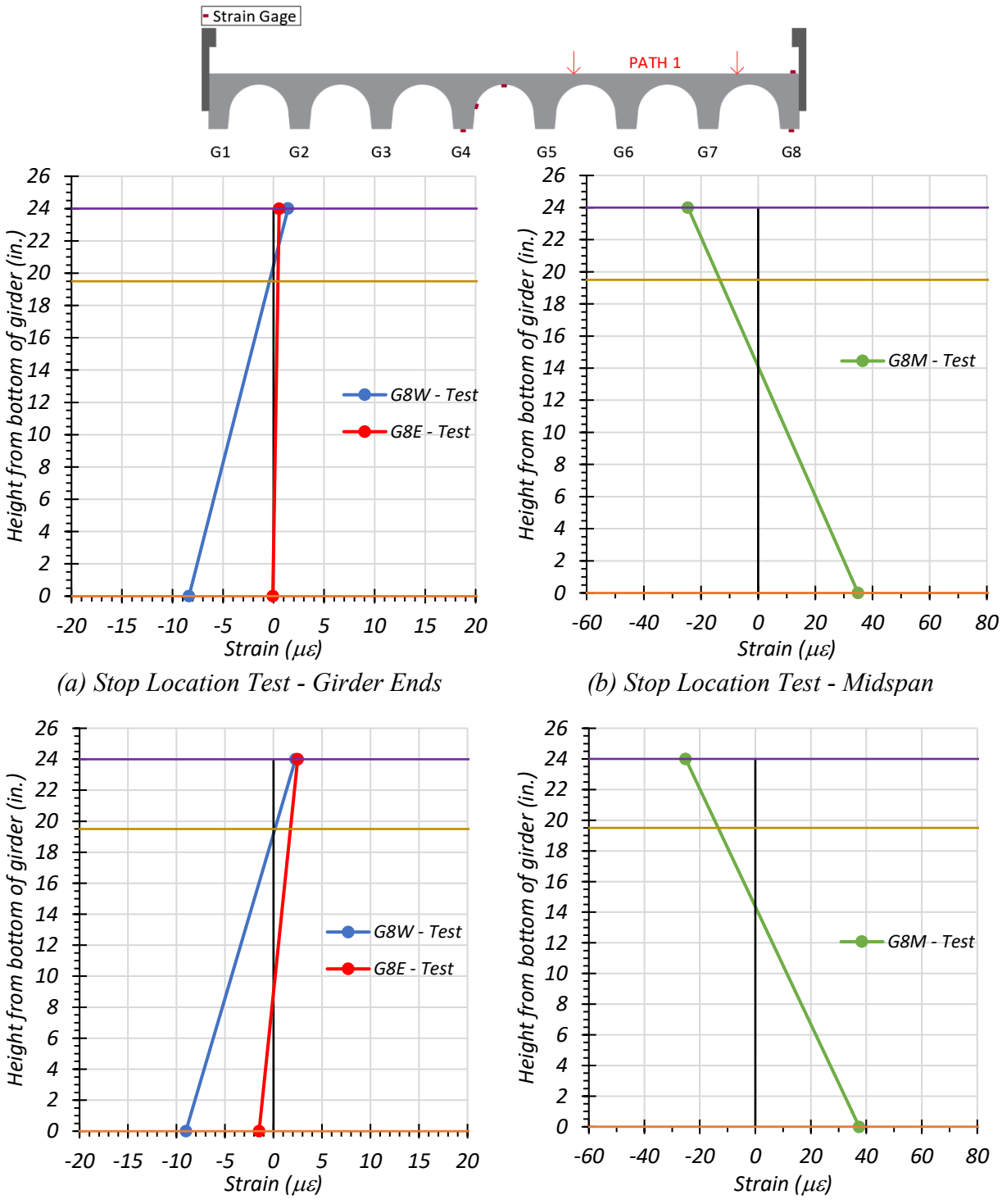

Figure 7.16. Static Strains for Exterior Girder 8 – Path 1

7.6.1.1.5. Exterior Girder 8 – Path 2 Loading

Strain profiles corresponding to the top and bottom strains for the exterior Girder G8 under static tests along Path 2 are provided in Figure 7.17.

The strain profiles at the west and east ends of Girder G8 are shown in Figure 7.17(a) for the stop location test and Figure 7.17(c) for the crawl speed test. The bottom strains for both the west and east ends of Girder G8 were positive, indicating the absence of significant partial restraint. The bottom strains at both ends for the stop location test and crawl speed test are very similar.

The strain profiles at the midspan of Girder G8 are shown in Figure 7.17(b) for the stop location test and Figure 7.17(d) for the crawl speed test. The neutral axis depth at midspan was found to be 19.06 in. from the bottom of Girder G8 using the strain profile obtained from the stop location test and 17.96 in. from the bottom of Girder G8 using the strain profile obtained from the crawl speed test. The neutral axis depth calculated using the strain profile obtained from the crawl speed test is slightly higher than the one obtained from the stop location test. This also could be due to the stop location test being slightly different from the moment critical position for absolute maximum moment.

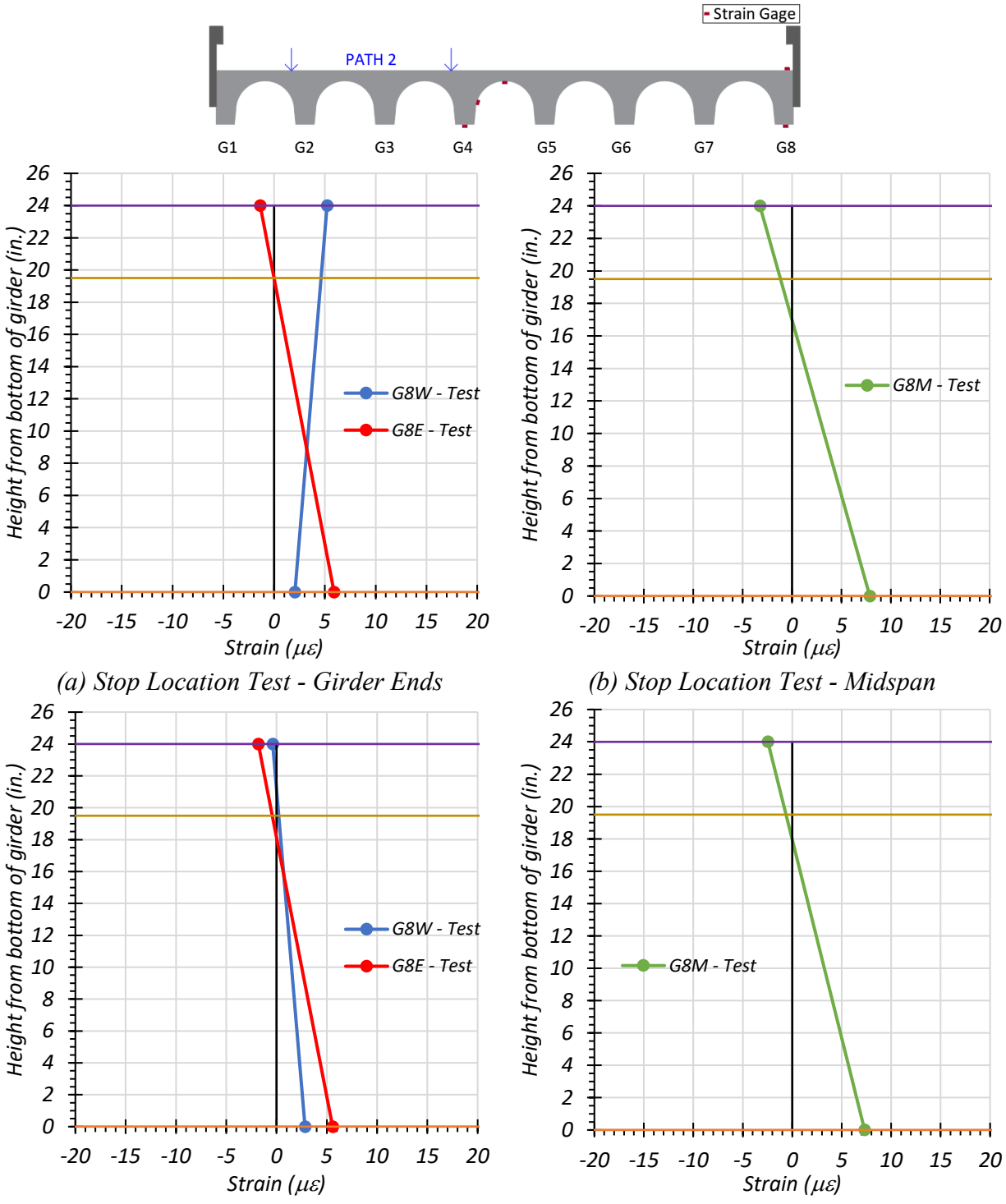

Figure 7.17. Static Strains for Exterior Girder 8 – Path 2

7.6.1.1.6. Exterior Girder 8 – Middle Path Loading

Strain profiles corresponding to the top and bottom strains for the exterior Girder G8 under static tests along the Middle Path are provided in Figure 7.18.

The strain profiles at the west and east ends of Girder G8 are shown in Figure 7.18(a) for the stop location test and Figure 7.18(c) for the crawl speed test. The bottom strains for both the west and east ends of Girder G8 were positive, indicating the absence of significant partial restraint. The bottom strain at the west end for the crawl speed test was higher than that obtained from the stop location test. The bottom strain at the east end for the crawl speed test was smaller than that obtained from the stop location test.

The strain profiles at the midspan of Girder G8 are shown in Figure 7.18(b) for the stop location test and Figure 7.18(d) for the crawl speed test. The neutral axis depth at midspan was found to be 14.73 in. from the bottom of Girder G8 using the strain profile obtained from the stop location test and 14.5 in. from the bottom of Girder G8 using the strain profile obtained from the crawl speed test. The neutral axis depth calculated using the strain profile obtained from the crawl speed test is slightly higher than the one obtained from the stop location test. This also could be due to the stop location test being slightly different from the moment critical position for absolute maximum moment.

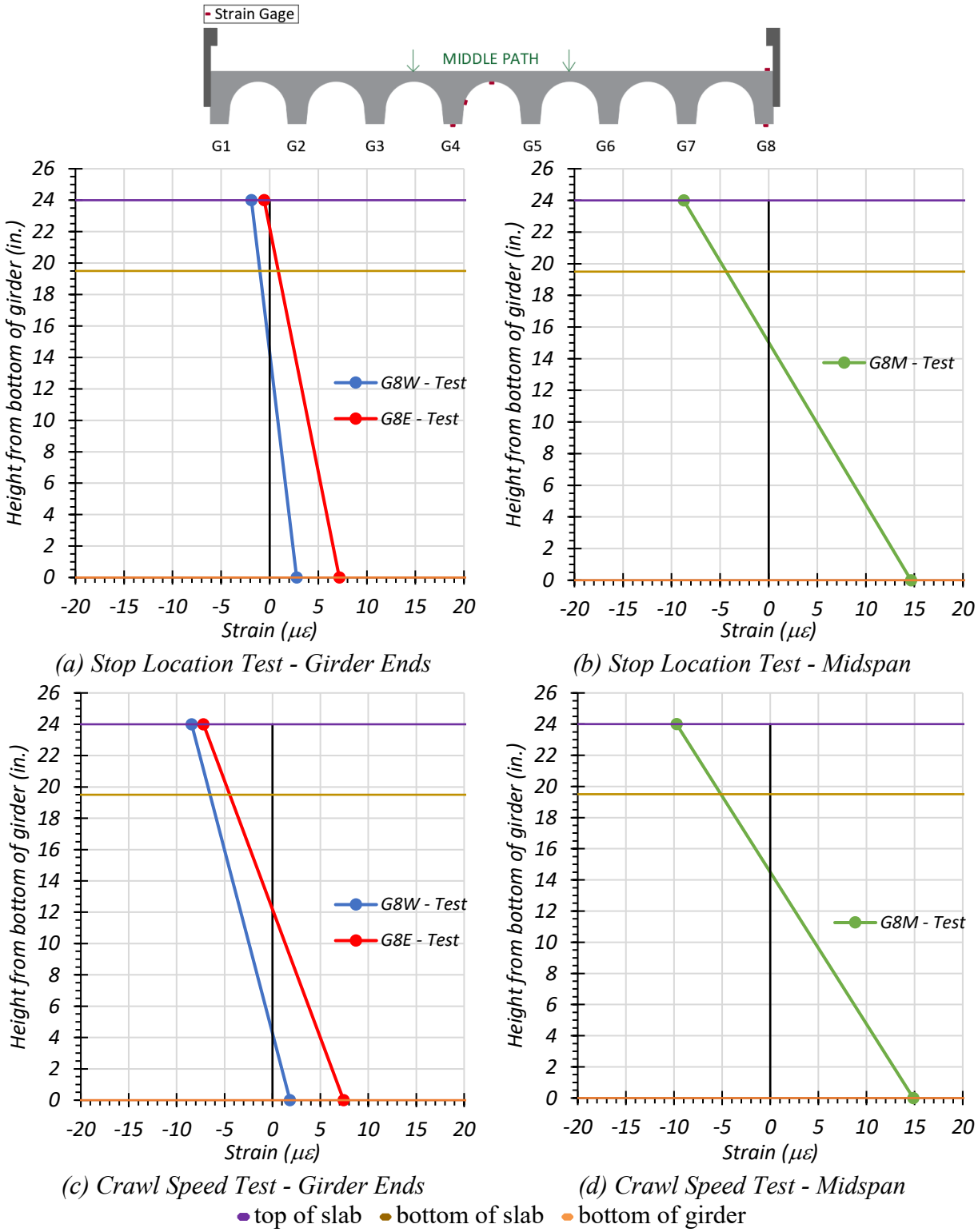

(a) Stop Location Test - Girder Ends

(b) Stop Location Test - Midspan

(c) Crawl Speed Test - Girder Ends

(d) Crawl Speed Test - Midspan

Figure 7.18. Static Strains for Exterior Girder 8 – Middle Path

7.6.1.1.7. Comparison of Measured Strain Results

Theoretical calculations to determine the neutral axis depth for a cracked and uncracked concrete section were carried out for both an exterior and interior girder. A typical transverse section, along with the reinforcement information from the standard drawings, is provided in Figure 7.19. A single layer of bottom reinforcement consisting of 2-#11 bars was considered based on the GPR measurements taken during the test. The girders were spaced at 3 ft center-to-center. The AASHTO Standard Specifications define the effective flange width as the minimum of a quarter of the span length, the center to center spacing of the girders, and 12 times the slab thickness. Thus, the effective width of the interior girder was taken to be 3 ft and that of the exterior girder was 1'-9.5". The modulus of elasticity for concrete was calculated using the following equation valid for normal weight concrete with unit weights between 0.09 and 0.155 kcf and design compressive strength up to 15.0 ksi as per Article 8.7 in the AASHTO Standard Specifications (AASHTO 2002).

$$E_c = 33{,}000 K_1 {w_c}^{1.5} \sqrt{f_c'} \tag{7.1}$$

where:

E_c = Elastic modulus of concrete, ksi

K_1 = Correction factor for source of aggregate, to be taken as 1.0 unless determined by physical test

w_c = Unit weight of concrete, kcf

f_c' = Compressive strength of concrete, ksi

The modulus of elasticity for concrete was calculated to be 5072 ksi based on the measured f_c' of 7 ksi. The theoretical position of the neutral axis depth was determined to be 15.21 in. from the bottom of the interior girder and 14.05 in. from the bottom of the exterior girder for an uncracked concrete section. For a cracked concrete section, the neutral axis depth was calculated to be 19.91 in. from the bottom of the interior girder and 18.87 in. from the bottom of the exterior girder.

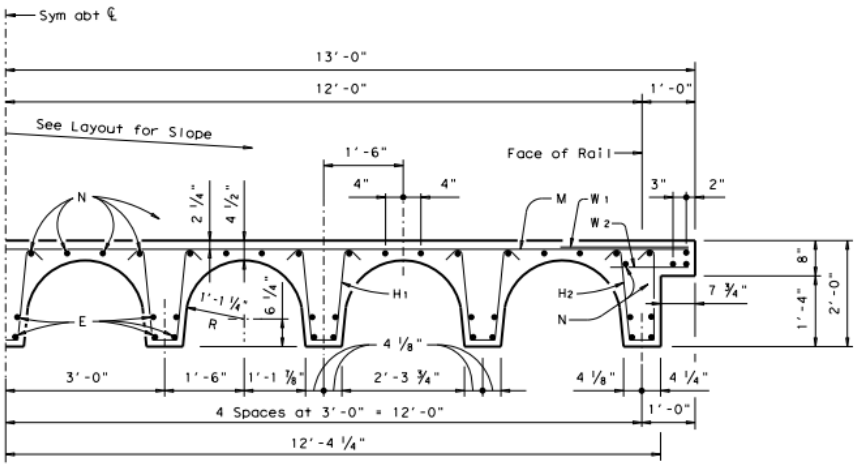

TABLE OF ESTIMATED QUANTITIES
CG-30-24

Bar	No.	Size	Length	Weight
EA	36	#11	30'- 0"	5,738
H1	273	# 4	4'-10"	881
H2	78	# 4	4'- 9"	247
K	48	# 4	5'- 3"	168
LA	4	# 5	24'- 5"	102
MA	37	# 5	25'- 9"	994
NA	42	# 5	30'- 0"	1,314
P	18	# 5	4'- 2"	78
W1	72	# 5	2'- 8"	200
W2	72	# 5	1'- 6"	113
Reinforcing Steel			Lb	9,835
Class "S" Concrete			CY	31.5

Figure 7.19. Transverse Section Typical to Pan Girder Bridges (reprinted from TxDOT 2005)

Table 7.4 lists the midspan neutral axes corresponding to all the different tests. Figure 7.20 compares the neutral axes obtained from the static tests with the FEM neutral axis for both Girder G8 and Girder G4. The neutral axes determined from the tests are closer to the theoretical uncracked neutral axis for both Girder G4 and Girder G8.

Table 7.4. Measured Neutral Axis Locations for All Static Load Tests

Test	G4 Neutral Axis Location (in. from bottom of girder)	G8 Neutral Axis Location (in. from bottom of girder)
Path 1 – Stop Location	10.40	15.02
Path 1 – Crawl Speed	10.65	14.37
Path 2 – Stop Location	9.37	19.06
Path 2 – Crawl Speed	10.23	17.96
Middle Path – Stop Location	10.01	14.73
Middle Path – Crawl Speed	10.24	14.50
Theoretical Uncracked	14.05	15.21
Theoretical Cracked	19.91	18.87

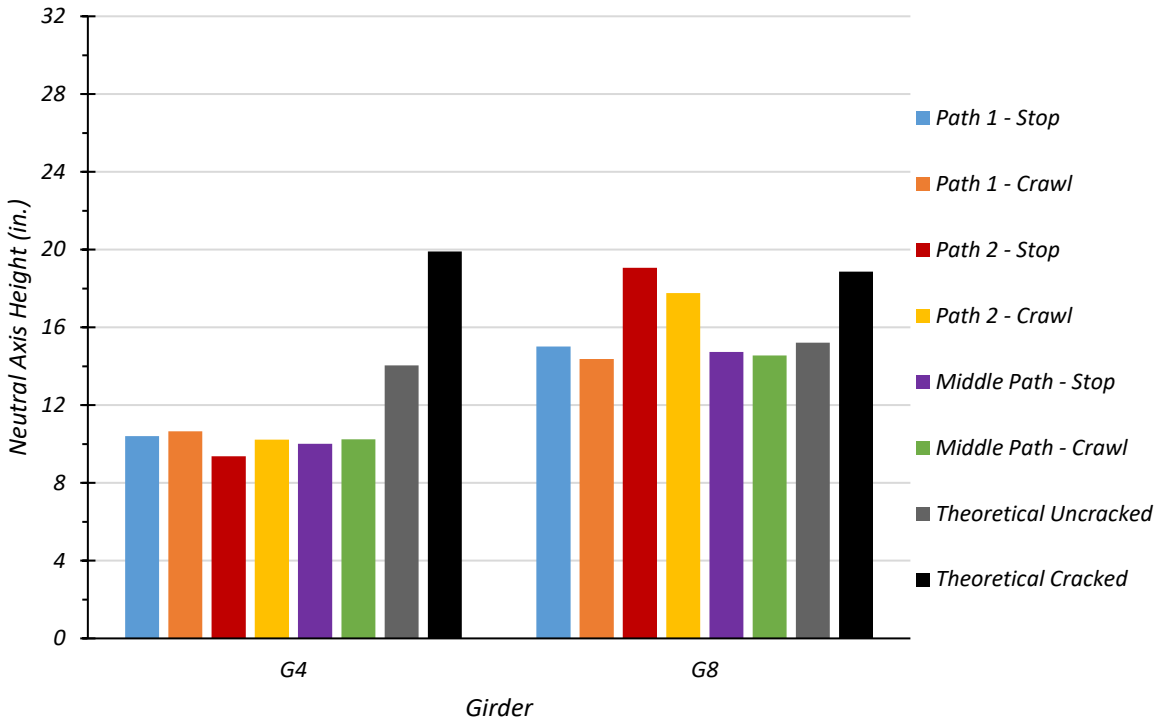

Figure 7.20. Test Neutral Axis Locations at Midspan

7.6.1.2. Deflection Measurements and LLDFs

All the instrumentation for the bridge was installed the afternoon before the test day. Heavy rainfall was encountered that night and the water level rose. The string potentiometers which were driven into the bed stream were covered with plastic bags for protection. However, some string

potentiometers may have been exposed to water. This may be one of the reasons why the string potentiometers at Girder G2 and Girder G4 show lower displacements for all static tests. The measured deflections for all girders and the corresponding LLDFs are presented in this section.

7.6.1.2.1. Path 1 Loading

The deflection for each girder was recorded over a period of time for each test. The maximum downward deflection for each girder was obtained. The corresponding LLDF for each girder was calculated using Eqn. (7.2).

$$LLDF = \frac{\Delta_i I_i}{\sum \Delta_i I_i} \tag{7.2}$$

where:

$LLDF$ = Live load distribution factor

Δ_i = Maximum vertical deflection of girder *i,* in.

I_i = Cracked moment of inertia of girder *i*, in^4

The measured deflection for all girders along with the LLDFs for the stop location test and crawl speed test along Path 1 are provided in Table 7.5. For both the stop location test and crawl speed test, the maximum exterior girder deflection was observed in Girder G8 and the maximum interior girder deflection was observed in Girder G6. This was due to the close proximity of these girders to the wheel lines. The corresponding LLDF for Girder G8 was 0.184 for the stop location test and 0.191 for the crawl speed test. Girder G6 had an LLDF of 0.218 for the stop location test and 0.222 for the crawl speed test.

A comparison of the LLDFs calculated from the test data and those calculated using the approximate equations in the AASTHO Standard Specifications (AASHTO 2002) and AASHTO LRFD Specifications (AASHTO 2017) with the simplified and analytical stiffness parameter is provided in Table 7.6. The AASHTO standard LLDF is slightly conservative with a ratio of 1.26 for Girder G8 and 1.06 for Girder G6 with respect to the test LLDF obtained for the stop location test. The AASHTO LRFD LLDF is more conservative with a ratio of 1.29 for Girder G8 and 1.58 for Girder G6 with respect to the test LLDF obtained for the stop location test.

Figure 7.21(a) and (c) show stop location test and crawl speed test measured deflections for each girder, respectively. A comparison of the test LLDFs with those calculated from the standard specifications are shown in Figure 7.21 (b) and (d) for stop location test and crawl speed test, respectively.

Table 7.5. Experimental Deflections and LLDFs for Path 1 Loading

Girder	G1	G2	G3	G4	G5	G6	G7	G8
Stop Location Test Disp. (in.)	0.006	0.002	0.014	0.016	0.034	0.041	0.040	0.037
Stop Location Test LLDF	0.032	0.012	0.076	0.088	0.180	0.218	0.210	0.184
Crawl Speed Test Disp. (in.)	0.004	0.003	0.014	0.015	0.033	0.041	0.041	0.038
Crawl Speed Test LLDF	0.019	0.013	0.074	0.079	0.180	0.222	0.221	0.191

Note: 1 – G = girder, Disp. = Displacement
2 – LLDF values are based on the midspan deflections.

Table 7.6. LLDF Comparison with AASHTO for Path 1 Loading

Test and Girder Type	AASHTO Standard Specs ($g^m_{AASHTO\_Std}$)	AASHTO LRFD Simplified ($g^m_{AASHTO\_S}$)	AASHTO LRFD K_g Calculated ($g^m_{AASHTO\_K}$)	Test (g^m_{test})	$g^m_{AASHTO\_Std}/g^m_{test}$	$g^m_{AASHTO\_S}/g^m_{test}$	$g^m_{AASHTO\_K}/g^m_{test}$
Stop Location Interior	0.231	0.344	0.339	0.218	1.06	1.58	1.56
Stop Location Exterior	0.231	0.238	0.238	0.184	1.26	1.29	1.29
Crawl Speed Interior	0.231	0.344	0.339	0.222	1.04	1.55	1.53
Crawl Speed Exterior	0.231	0.238	0.238	0.191	1.21	1.25	1.25

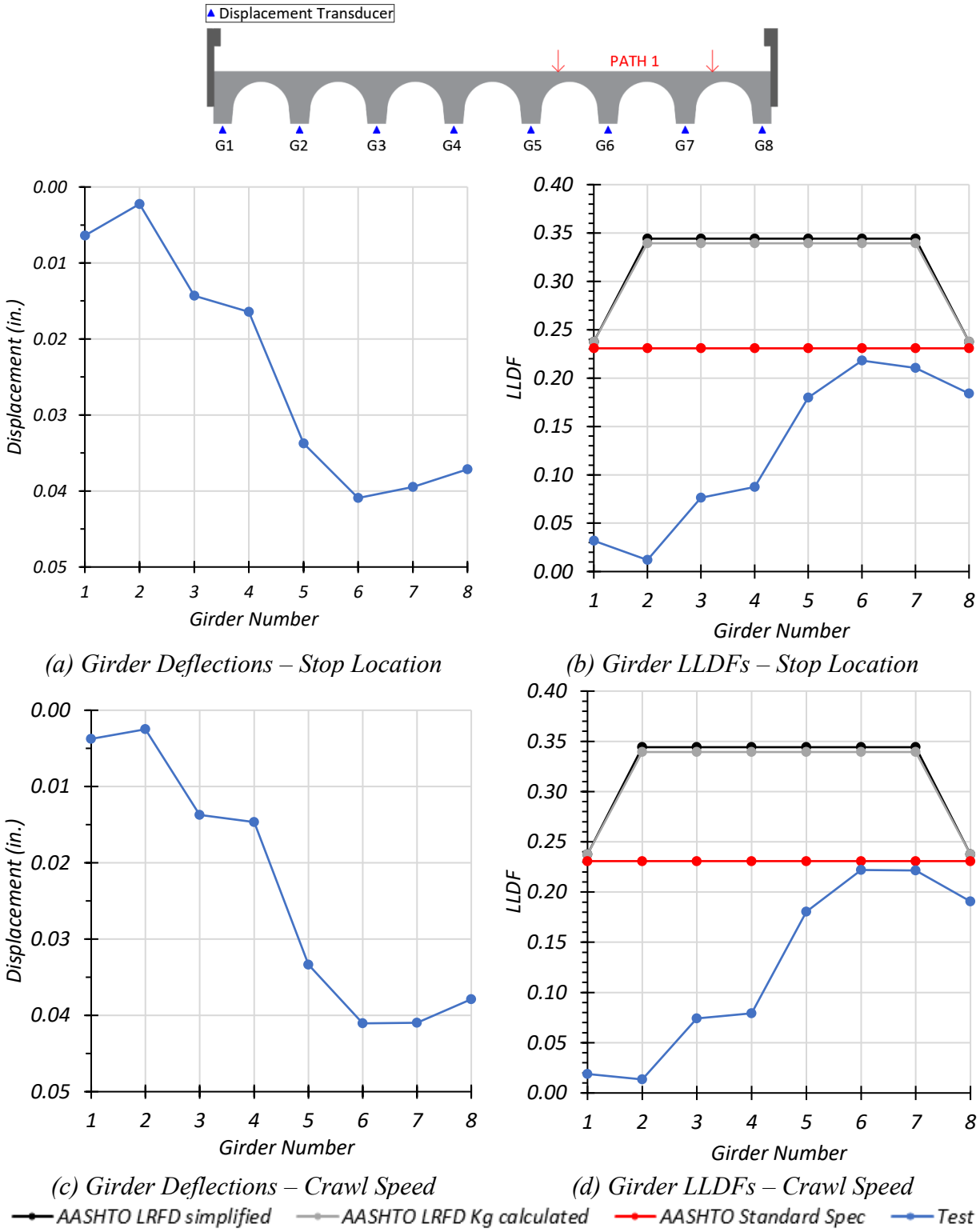

(a) Girder Deflections – Stop Location

(b) Girder LLDFs – Stop Location

(c) Girder Deflections – Crawl Speed

(d) Girder LLDFs – Crawl Speed

Figure 7.21. Static Deflection Results for Path 1 Loading

7.6.1.2.2. Path 2 Loading

The measured deflections for all girders along with the LLDFs for the stop location test and crawl speed test along Path 2 are provided in Table 7.7. For both the stop location test and crawl speed test, the maximum exterior girder deflection was observed in Girder G1 and the maximum interior girder deflection was observed in Girder G3. This was due to the close proximity of these girders to the wheel lines. The corresponding LLDF for Girder G1 was 0.164 for the stop location test and 0.187 for the crawl speed test. Girder G3 had an LLDF of 0.224 for the stop location test and 0.221 for the crawl speed test.

A comparison of the LLDFs calculated from the test data and those calculated using the approximate equations in the AASTHO Standard Specifications (AASHTO 2002) and AASHTO LRFD Specifications (AASHTO 2017) with the simplified and analytical stiffness parameter is provided in Table 7.8. The AASHTO standard LLDF is slightly conservative with a ratio of 1.41 for Girder G1 and 1.03 for Girder G3 with respect to the test LLDF obtained for the stop location test. The AASHTO LRFD LLDF is more conservative with a ratio of 1.45 for Girder G1 and 1.54 for Girder G3 with respect to the test LLDF obtained for the stop location test.

Figure 7.22(a) and (c) show static and crawl tests measured deflections for each girder, respectively. A comparison of the test LLDFs with those calculated from the standard specifications are shown in Figure 7.22(b) and (d) for static and crawl tests, respectively.

Table 7.7. Experimental Deflections and LLDFs for Path 2 Loading

Girder	G1	G2	G3	G4	G5	G6	G7	G8
Stop Location Test Disp. (in.)	0.030	0.032	0.038	0.024	0.026	0.015	0.006	0.003
Stop Location Test LLDF	0.164	0.186	0.224	0.141	0.149	0.086	0.034	0.016
Crawl Speed Test Disp. (in.)	0.033	0.031	0.036	0.022	0.023	0.014	0.005	0.003
Crawl Speed Test LLDF	0.187	0.187	0.221	0.135	0.141	0.083	0.030	0.015
Note: 1 – G = girder, Disp. = Displacement 2 – LLDF values are based on the midspan deflections.								

Table 7.8. LLDF Comparison with AASHTO for Path 2 Loading

Test and Girder Type	AASHTO Standard Specs ($g^m_{AASHTO\_Std}$)	AASHTO LRFD Simplified ($g^m_{AASHTO\_S}$)	AASHTO LRFD K_g Calculated ($g^m_{AASHTO\_K}$)	Test (g^m_{test})	$g^m_{AASHTO\_Std}/g^m_{test}$	$g^m_{AASHTO\_S}/g^m_{test}$	$g^m_{AASHTO\_K}/g^m_{test}$
Stop Location Interior	0.231	0.344	0.339	0.224	1.03	1.54	1.51
Stop Location Exterior	0.231	0.238	0.238	0.164	1.41	1.45	1.45
Crawl Speed Interior	0.231	0.344	0.339	0.221	1.05	1.56	1.53
Crawl Speed Exterior	0.231	0.238	0.238	0.187	1.24	1.27	1.27

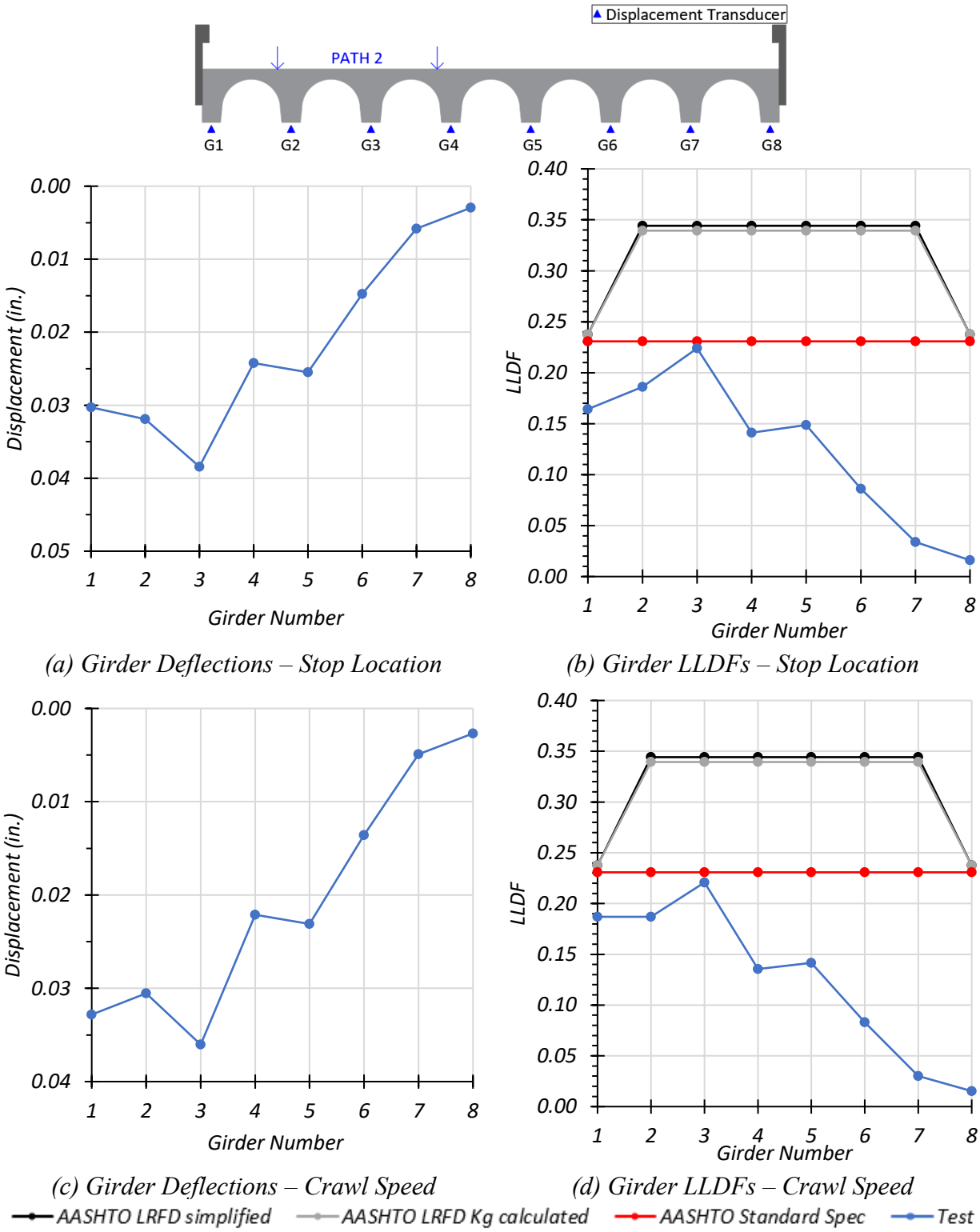

(a) Girder Deflections – Stop Location

(b) Girder LLDFs – Stop Location

(c) Girder Deflections – Crawl Speed

(d) Girder LLDFs – Crawl Speed

Figure 7.22. Static Deflection Results for Path 2 Loading

7.6.1.2.3. Middle Path Loading

The measured deflection for all girders along with the LLDFs for the stop location test and crawl speed test along the Middle path are provided in Table 7.9. For both the stop location test and crawl speed test, the maximum exterior girder deflection was observed in Girder G1 and the maximum interior girder deflection was observed in Girder G5. This was due to the close proximity of these girders to the wheel lines. The corresponding LLDF for Girder G1 was 0.076 for the stop location test and 0.069 for the crawl speed test. Girder G5 had an LLDF of 0.195 for the stop location test and 0.197 for the crawl speed test.

A comparison of the LLDFs calculated from the test data and those calculated using the approximate equations in the AASTHO Standard Specifications (AASHTO 2002) and AASHTO LRFD Specifications (AASHTO 2017) with the simplified and analytical stiffness parameter is provided in Table 7.10. The AASHTO standard LLDF is highly conservative with a ratio of 2.84 for Girder G1 and slightly conservative with a ratio of 1.20 for Girder G5 with respect to the test LLDF obtained for the stop location test. The AASHTO LRFD LLDF is highly conservative with a ratio of 2.92 for Girder G1 and 1.78 for Girder G5 with respect to the test LLDF obtained for the stop location test.

Figure 7.23(a) and (c) show static and crawl tests measured deflections for each girder, respectively. A comparison of the test LLDFs with those calculated from the standard specifications are shown in Figure 7.23(b) and (d) for static and crawl tests, respectively.

Table 7.9. Experimental Deflections and LLDFs for Middle Path Loading

Girder	G1	G2	G3	G4	G5	G6	G7	G8
Stop Location Test Disp. (in.)	0.015	0.016	0.033	0.026	0.036	0.030	0.018	0.013
Stop Location Test LLDF	0.076	0.085	0.179	0.141	0.195	0.163	0.097	0.064
Crawl Speed Test Disp. (in.)	0.013	0.015	0.030	0.025	0.035	0.028	0.019	0.012
Crawl Speed Test LLDF	0.069	0.084	0.172	0.143	0.197	0.159	0.109	0.065
Note: 1 – G = girder, Disp. = Displacement 2 – LLDF values are based on the midspan deflections.								

Table 7.10. LLDF Comparison with AASHTO for Middle Path Loading

Test and Girder Type	AASHTO Standard Specs ($g^m_{AASHTO\_Std}$)	AASHTO LRFD Simplified ($g^m_{AASHTO\_S}$)	AASHTO LRFD K_g Calculated ($g^m_{AASHTO\_K}$)	Test (g^m_{test})	$g^m_{AASHTO\_Std}/g^m_{test}$	$g^m_{AASHTO\_S}/g^m_{test}$	$g^m_{AASHTO\_K}/g^m_{test}$
Stop Location Interior	0.231	0.344	0.339	0.195	1.20	1.78	1.76
Stop Location Exterior	0.231	0.238	0.238	0.076	2.84	2.92	2.92
Crawl Speed Interior	0.231	0.344	0.339	0.197	1.18	1.76	1.74
Crawl Speed Exterior	0.231	0.238	0.238	0.069	3.12	3.21	3.21

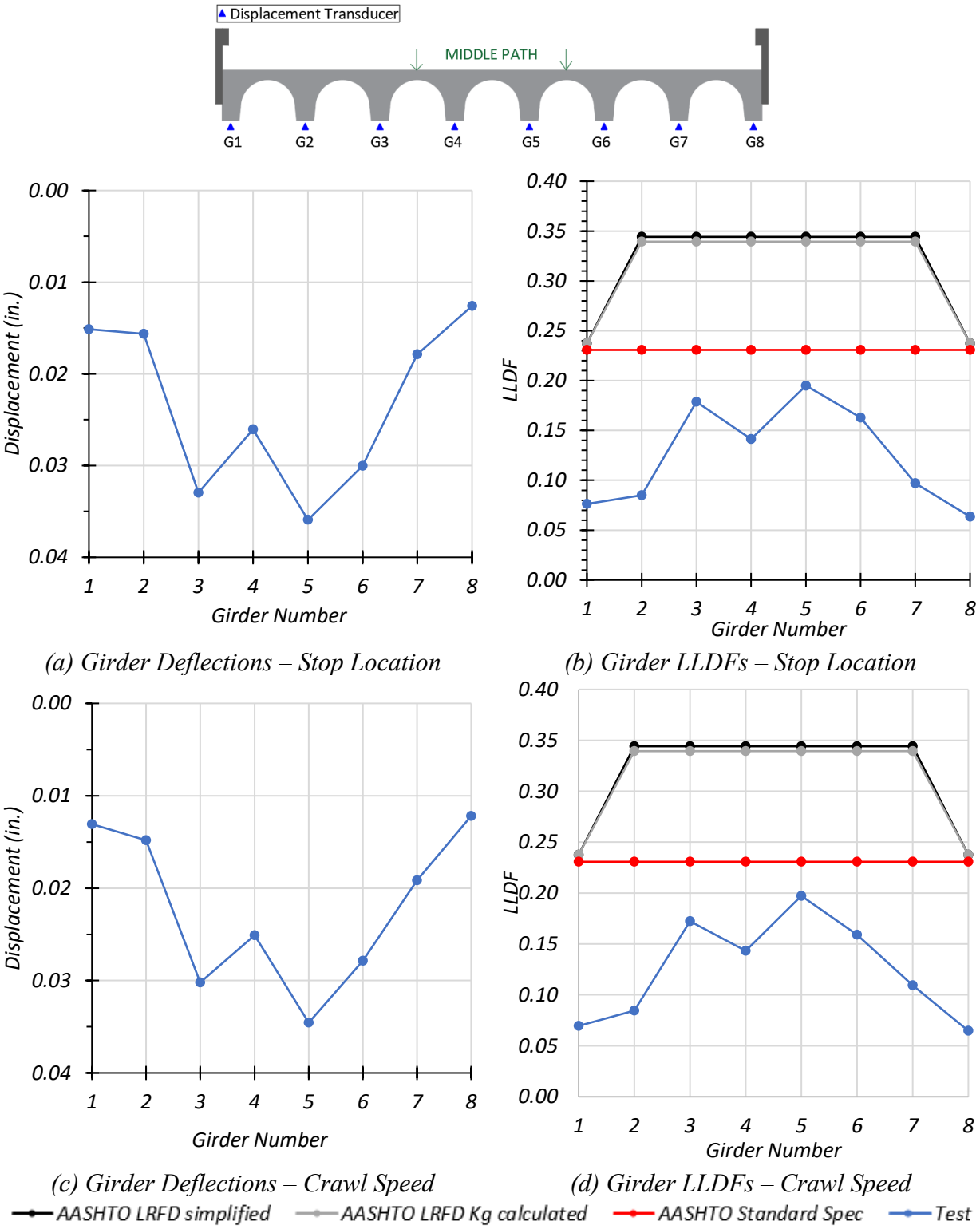

(a) Girder Deflections – Stop Location

(b) Girder LLDFs – Stop Location

(c) Girder Deflections – Crawl Speed

(d) Girder LLDFs – Crawl Speed

Figure 7.23. Static Deflection Results for Middle Path Loading

7.6.1.2.4. Comparison of Results based on Deflection Measurements

The maximum LLDF for the exterior Girder G8 under stop location test along Path 1 was found to be 0.184. This increased to 0.191 for the same girder during the crawl speed test along Path 1. The maximum LLDF for the exterior Girder G1 under stop location test along Path 2 was found to be 0.164. This increased to 0.187 for the same girder during the crawl speed test along Path 2. The maximum LLDF for the exterior Girder G1 under stop location test along the Middle Path was found to be 0.076. This decreased to 0.069 for the same girder during the crawl speed test along the Middle Path. Figure 7.24 provides a bar chart showing the maximum deflection and LLDF for each loading path. The critical LLDF for the exterior girder was noted to be 0.191 corresponding to the crawl speed test along Path 1.

Similar observations were noted for the interior girders. The maximum LLDF for the interior Girder G6 under stop location test along Path 1 was found to be 0.218. This increased to 0.222 for the same girder during the crawl speed test along Path 1. The maximum LLDF for the interior Girder G3 under stop location test along Path 2 was found to be 0.224. This decreased to 0.221 for the same girder during the crawl speed test along Path 2. The maximum LLDF for the interior Girder G5 under stop location test along the Middle Path was found to be 0.195. This increased to 0.197 for the same girder during the crawl speed test along the Middle Path. Figure 7.24 provides a bar chart showing the maximum deflection and LLDF for each loading path. The critical LLDF for the exterior girder was noted to be 0.224 corresponding to the stop location test along Path 2.

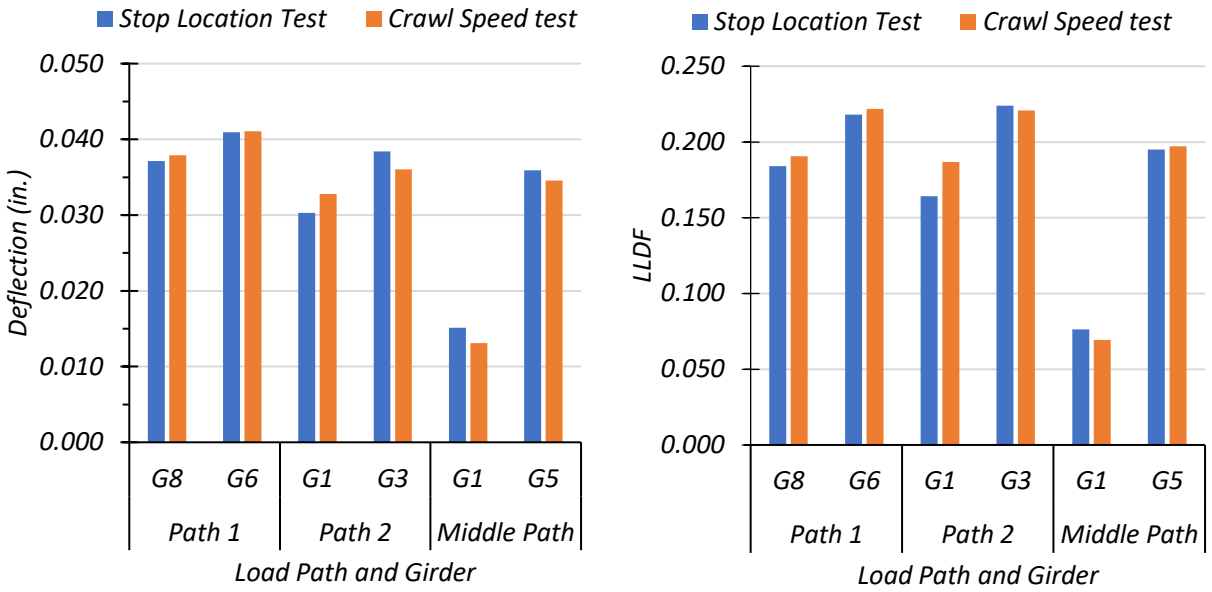

(a) Deflection *(b) LLDF*

Figure 7.24. Comparison of Maximum Deflections and LLDFs for Static Tests

Table 7.11 compares the LLDFs for the controlling interior and exterior girders with the AASHTO LLDFs for both the stop location test and crawl speed test. The AASHTO Standard Specifications provide LLDFs which are conservative for both the controlling interior and exterior girders. However, the LLDFs recommended by the AASHTO LRFD Specifications were slightly more conservative.

Table 7.11. LLDF Comparison with AASHTO for Controlling Load Paths

Test and Girder Type	AASHTO Standard Specs ($g^m_{AASHTO\_Std}$)	AASHTO LRFD Simplified ($g^m_{AASHTO\_S}$)	AASHTO LRFD K_g Calculated ($g^m_{AASHTO\_K}$)	Test (g^m_{test})	$g^m_{AASHTO\_Std}/g^m_{test}$	$g^m_{AASHTO\_S}/g^m_{test}$	$g^m_{AASHTO\_K}/g^m_{test}$
Stop Location G3	0.231	0.344	0.339	0.224	1.03	1.54	1.51
Stop Location G8	0.231	0.238	0.238	0.184	1.26	1.29	1.29
Crawl Speed G3	0.231	0.344	0.339	0.221	1.05	1.56	1.53
Crawl Speed G8	0.231	0.238	0.238	0.191	1.21	1.25	1.25

Note: 1 – Girder G8 is the controlling exterior girder under Path 1 loading.
2 – Girder G3 is the controlling interior girder under Path 2 loading.

7.6.2. Dynamic Load Tests on Bridge CM-5

In the following sections, results from the dynamic load tests are presented.

7.6.2.1. Dynamic Amplification

Amplification of strain from the static test to the dynamic test for the different paths are presented in the following subsections.

7.6.2.1.1. Maximum Girder Strains

The dynamic amplification of strains for Girder G4 and Girder G8 were obtained by comparing the dynamic test results with the static stop location results. Plots of the strain profiles for Girder G4 and Girder G8 obtained from the static tests and dynamic tests for Path 1, Path 2, and Middle are shown in Figure 7.25, Figure 7.26, and Figure 7.27, respectively. Figure 7.28 compares the dynamic strains for Girder G4 and Girder G8 with the static values.

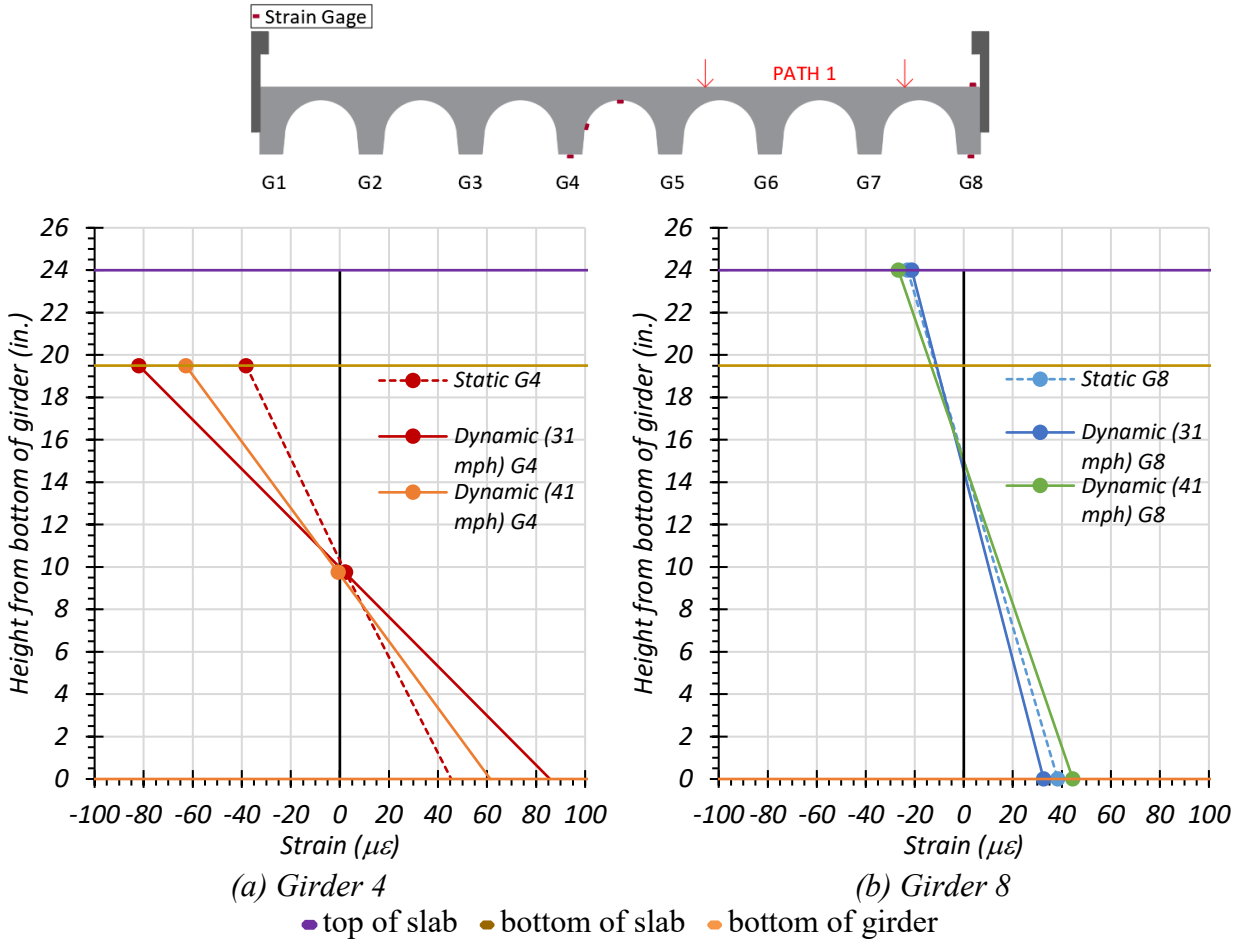

(a) Girder 4 *(b) Girder 8*

Figure 7.25. Maximum Strains for Static and Dynamic Tests for Path 1 Loading

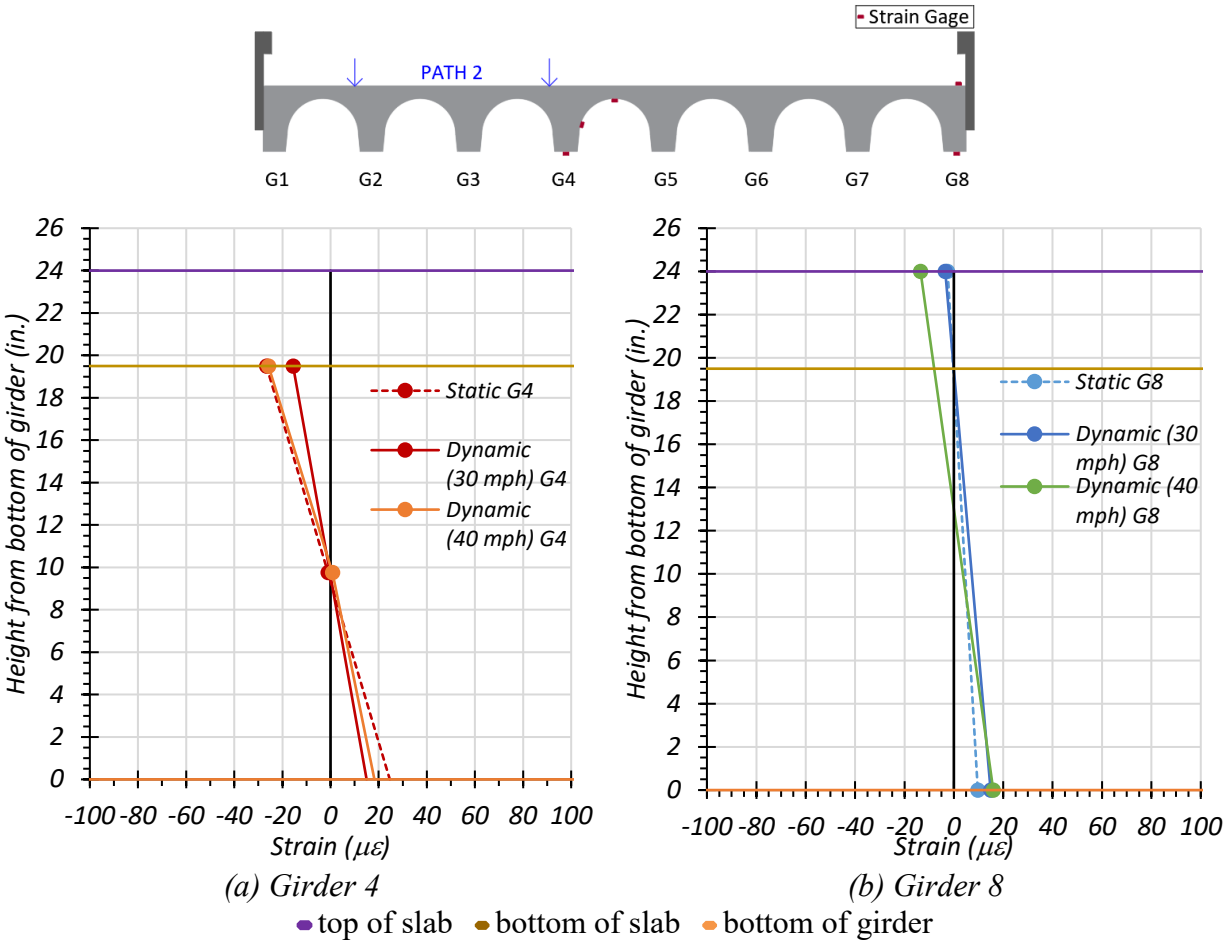

Figure 7.26. Maximum Strains for Static and Dynamic Tests for Path 2 Loading

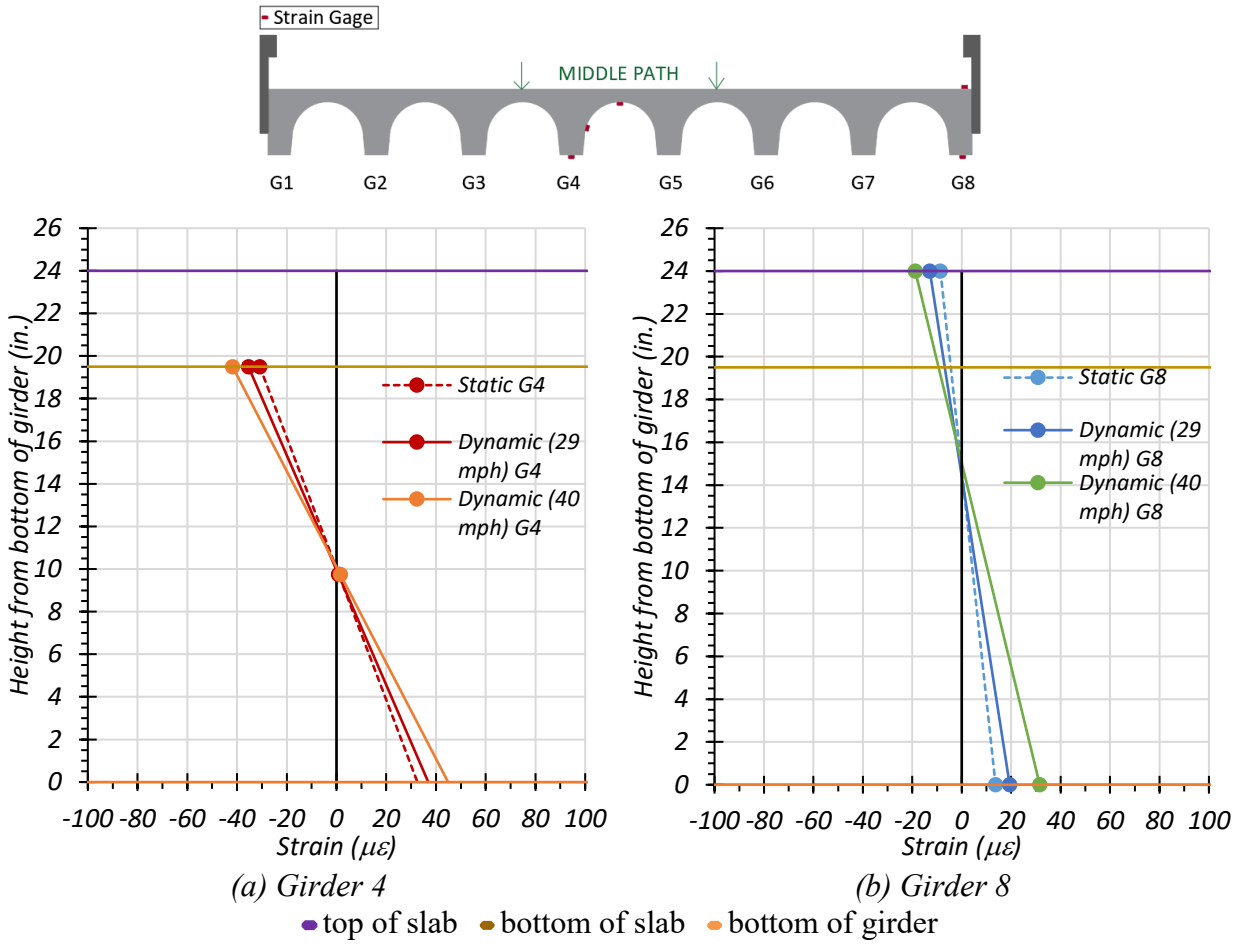

Figure 7.27. Maximum Strains for Static and Dynamic Tests for Middle Path Loading

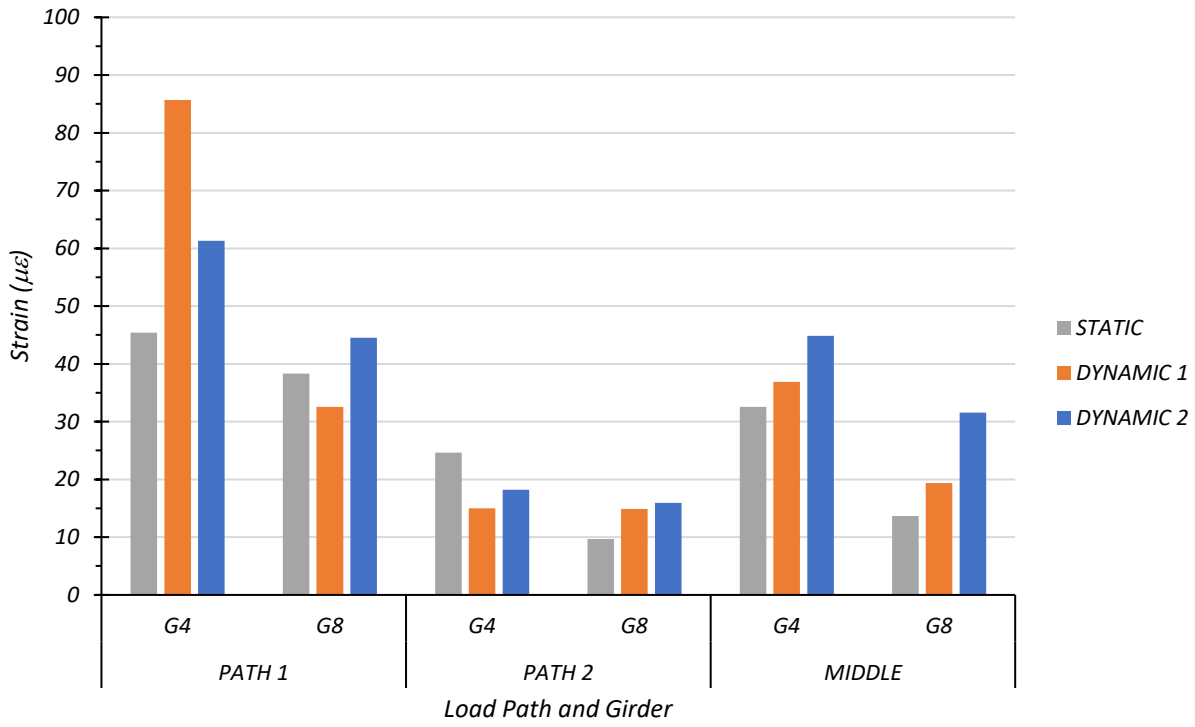

Note:

- *Path 1: Dynamic 1 = 31 mph, Dynamic 2 = 41 mph*
- *Path 2: Dynamic 1 = 30 mph, Dynamic 2 = 40 mph*
- *Middle Path: Dynamic 1 = 29 mph, Dynamic 2 = 40 mph*

Figure 7.28. Comparison of Maximum Strains for Static and Dynamic Tests

The average dynamic impact factor for the exterior girder was found to be 49 percent while that for the interior girder was calculated to be 18 percent for Bridge CM-5. These were calculated based on the maximum bottom strains recorded during testing. AASHTO Standard Specifications calls for a dynamic impact factor of 30 percent and AASHTO LRFD Specifications stipulates this to be 33 percent. Thus, for Bridge CM-5 the dynamic impact factor is higher than that specified by AASHTO for the exterior girder. However, it is lower for the interior girders.

7.6.2.1.2. Maximum Girder Deflections

Dynamic amplification can also be obtained by comparing the dynamic deflections with the static deflections. Deflection time history plots for each girder for Static test and Dynamic 1, and Dynamic 2 tests are provided in Figure 7.29, Figure 7.30, and Figure 7.31 for Path 1, Path 2 and Middle path respectively. It should be noted that the static data was recorded for a shorter time period compared to the two dynamic data. The maximum deflection for each girder under static and dynamic tests for Path 1, Path 2 and Middle path is tabulated in Table 7.12. Figure 7.32 compares the dynamic deflections for each girder with the static deflections. Figure 7.33 shows the measured deflections for each dynamic load case as a ratio to the stop location deflection.

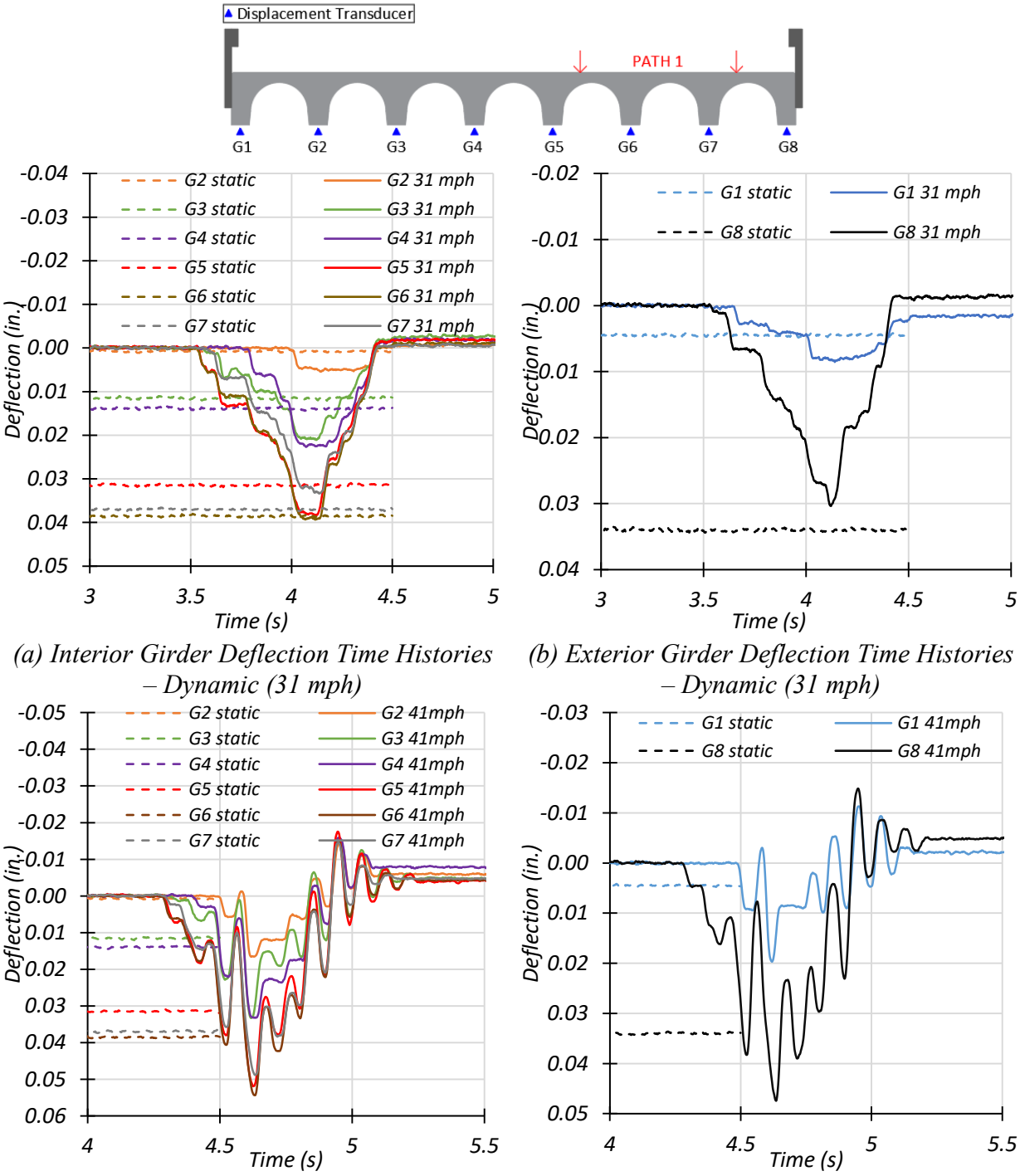

(a) Interior Girder Deflection Time Histories – Dynamic (31 mph)

(b) Exterior Girder Deflection Time Histories – Dynamic (31 mph)

(c) Interior Girder Deflection Time Histories – Dynamic (41 mph)

(d) Exterior Girder Deflection Time Histories – Dynamic (41 mph)

Figure 7.29. Midspan Deflections for Static and Dynamic Tests for Path 1 Loading

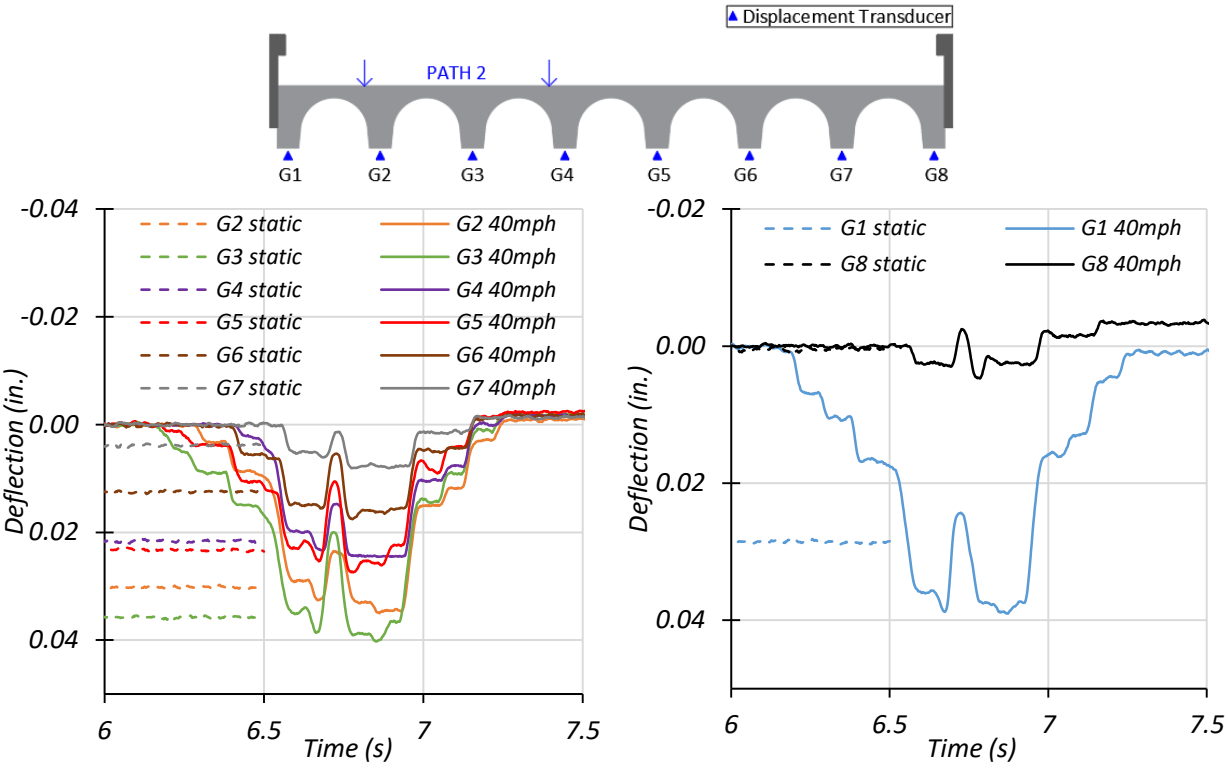

(a) Interior Girder Deflection Time Histories – Dynamic (30 mph)

(b) Exterior Girder Deflection Time Histories – Dynamic (30 mph)

(c) Interior Girder Deflection Time Histories – Dynamic (40 mph)

(d) Exterior Girder Deflection Time Histories – Dynamic (40 mph)

Figure 7.30. Midspan Deflections for Static and Dynamic Tests for Path 2 Loading

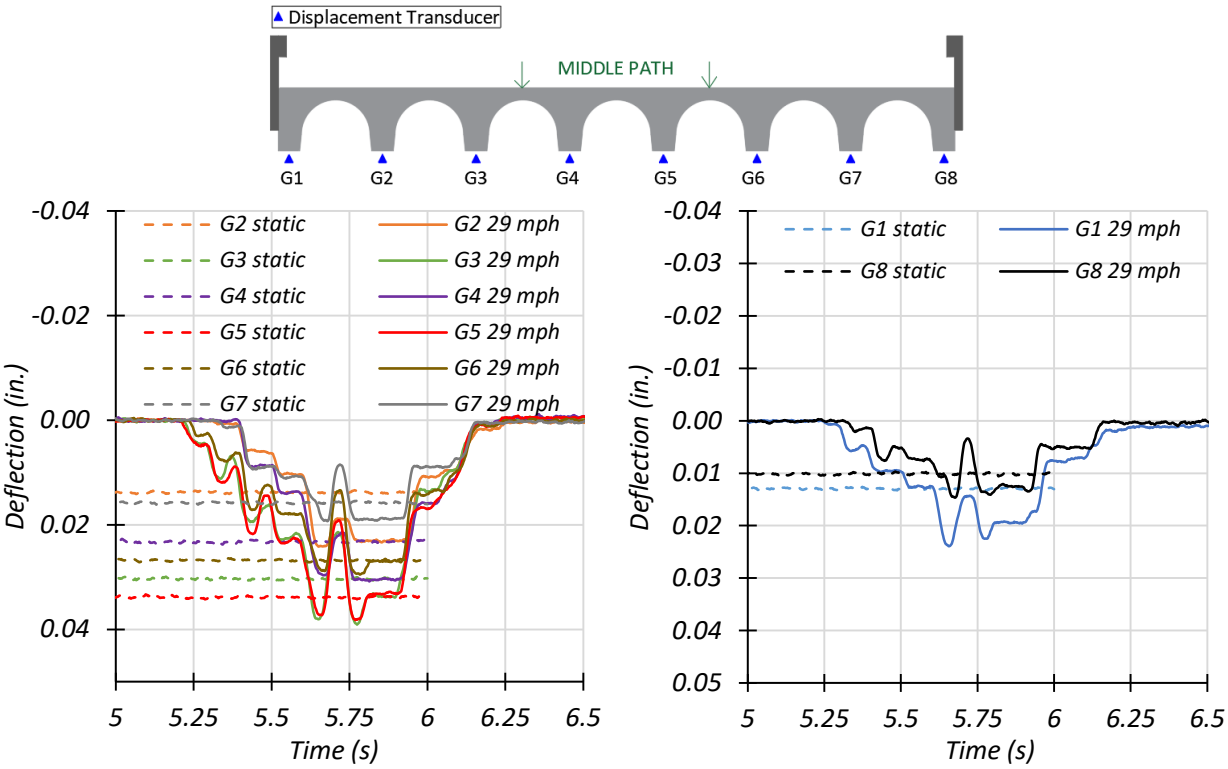

(a) Interior Girder Deflection Time Histories – Dynamic (29 mph)

(b) Exterior Girder Deflection Time Histories – Dynamic (29 mph)

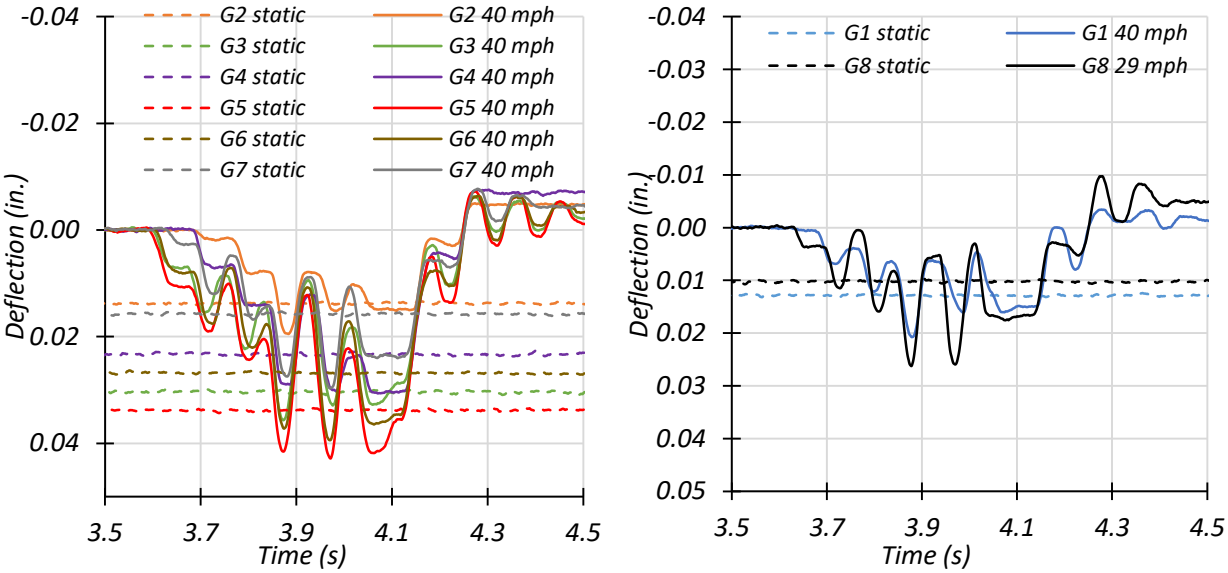

(c) Interior Girder Deflection Time Histories – Dynamic (40 mph)

(d) Exterior Girder Deflection Time Histories – Dynamic (40 mph)

Figure 7.31. Midspan Deflections for Static and Dynamic Tests for Middle Loading

Table 7.12. Maximum Midspan Deflections for Static and Dynamic Tests

	Loading	G1	G2	G3	G4	G5	G6	G7	G8
Girder Displacement (in.)	Path 1 Static	0.006	0.002	0.014	0.016	0.034	0.041	0.040	0.037
	Path 1 Dynamic (31 mph)	0.010	0.006	0.022	0.024	0.039	0.040	0.034	0.031
	Path 1 Dynamic (41 mph)	0.018	0.017	0.032	0.033	0.052	0.055	0.049	0.048
	Max. Path 1 Amplification						35%		30%
Girder Displacement (in.)	Path 2 Static	0.030	0.032	0.038	0.024	0.026	0.015	0.006	0.003
	Path 2 Dynamic (30 mph)	0.040	0.036	0.041	0.025	0.028	0.018	0.009	0.005
	Path 2 Dynamic (40 mph)	0.046	0.042	0.049	0.031	0.031	0.020	0.011	0.009
	Max. Path 2 Amplification	50%		28%					
Girder Displacement (in.)	Middle Static	0.015	0.016	0.033	0.026	0.036	0.030	0.018	0.013
	Middle Dynamic (29 mph)	0.025	0.025	0.040	0.032	0.039	0.030	0.020	0.015
	Middle Dynamic (40 mph)	0.021	0.020	0.037	0.032	0.044	0.041	0.031	0.027
	Max. Middle Path Amplification	62%				22%			

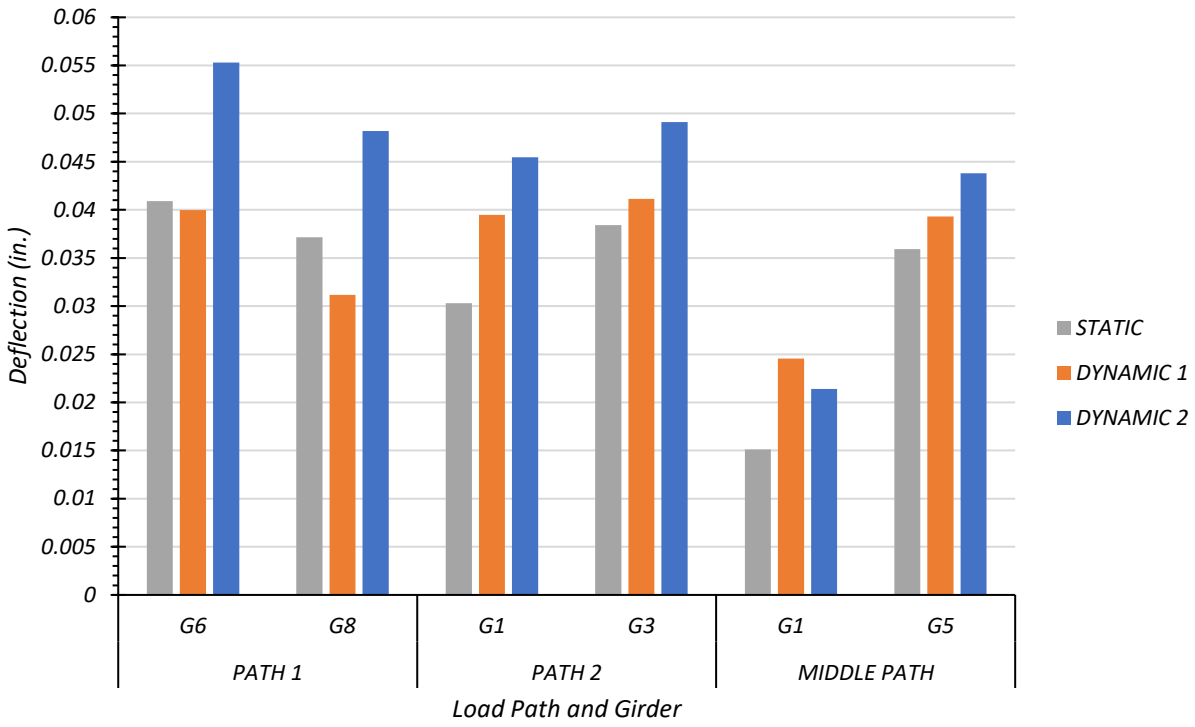

Note:

- *Path 1: Dynamic 1 = 31 mph, Dynamic 2 = 41 mph*
- *Path 2: Dynamic 1 = 30 mph, Dynamic 2 = 40 mph*
- *Middle Path: Dynamic 1 = 29 mph, Dynamic 2 = 40 mph*

Figure 7.32. Static and Dynamic Deflection Comparison for Critical Girders

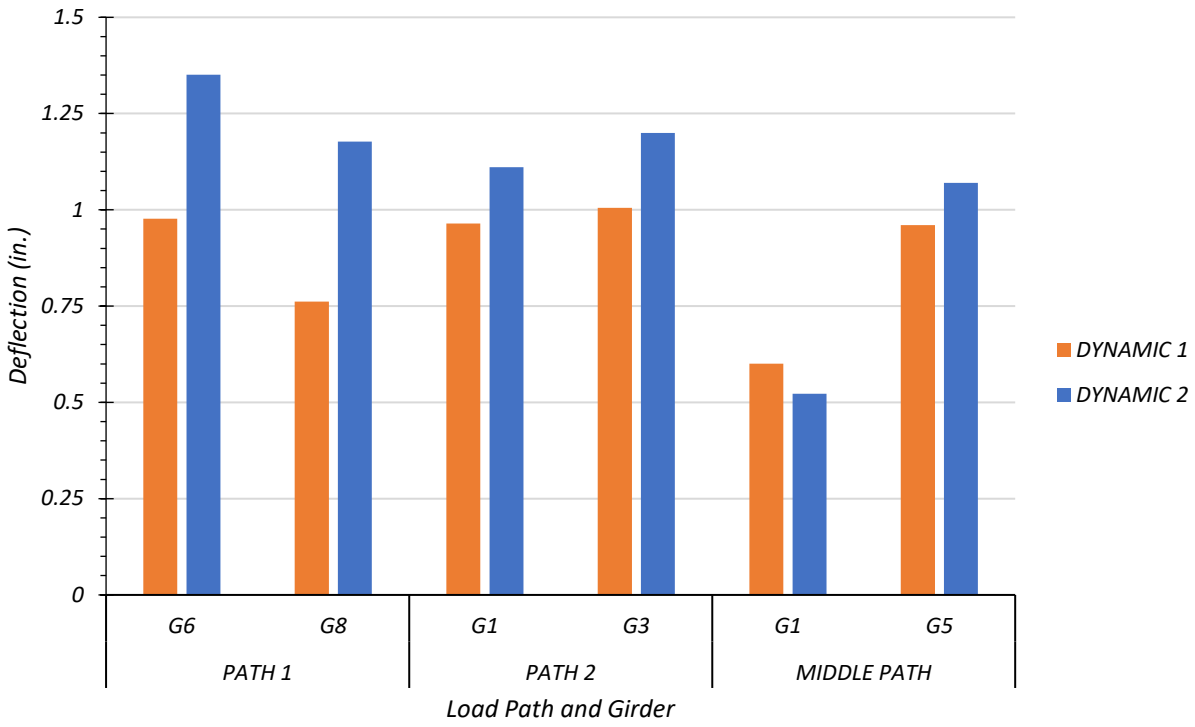

Note:

- *Path 1: Dynamic 1 = 31 mph, Dynamic 2 = 41 mph*
- *Path 2: Dynamic 1 = 30 mph, Dynamic 2 = 40 mph*
- *Middle Path: Dynamic 1 = 29 mph, Dynamic 2 = 40 mph*

Figure 7.33. Maximum Midspan Dynamic Deflections to Static Deflections Ratios

The average dynamic impact factor for the exterior girder was found to be 47 percent while that for the interior girder was calculated to be 28 percent for Bridge CM-5. These were calculated based on the maximum deflections recorded during testing. AASHTO Standard Specifications calls for a dynamic impact factor of 30 percent and AASHTO LRFD Specifications stipulates this to be 33 percent. Thus, for Bridge CM-5 the dynamic impact factor is higher than that specified by AASHTO for the exterior girder. However, it is lower for the interior girders.

The maximum deflection obtained for an interior girder during the static test, dynamic 1 test and dynamic 2 test along Path 1 was for Girder 6. The deflection reduced by 2 percent for the dynamic 1 test while it increased by 35 percent for dynamic 2 loading when compared to the static

test results. The maximum deflection obtained for an exterior girder during the static test, dynamic 1 test and dynamic 2 test along Path 1 was for the Girder 8. The deflection reduced by 16 percent for the dynamic 1 test while it increased by 35 percent for dynamic 2 loading when compared to the static test results.

The maximum deflection obtained for an interior girder during the static test, dynamic 1 test and dynamic 2 test along Path 2 was for Girder 3. The deflection increased by 7 percent for the dynamic 1 test and by 28 percent for dynamic 2 loading when compared to the static test results. The maximum deflection obtained for an exterior girder during the static test, dynamic 1 test and dynamic 2 test along Path 2 was for the Girder 1. The deflection increased by 30 percent for the dynamic 1 test and by 50 percent for dynamic 2 loading when compared to the static test results.

The maximum deflection obtained for an interior girder during the static test, dynamic 1 test and dynamic 2 test along the Middle Path was for Girder 5. The deflection increased by 9 percent for the dynamic 1 test and by 22 percent for dynamic 2 loading when compared to the static test results. The maximum deflection obtained for an exterior girder during the static test, dynamic 1 test and dynamic 2 test along the Middle Path was for the Girder 8. The deflection increased by 21 percent for the dynamic 1 test and by 115 percent for dynamic 2 loading when compared to the static test results.

7.6.2.2. Dynamic Characteristics of Bridge

The data recorded by the accelerometers for the dynamic tests and impact (sledgehammer) tests were filtered, using a low pass filter (cut-off frequency of 2 Hz) and analyzed to determine the dynamic characteristics of the bridge. Using the Fast Fourier transform (FFT) approach, the first three natural frequencies of the bridge were determined to be 11.84 Hz, 16.60 Hz, and 25.15 Hz.

The mode shape across the longitudinal and transverse section for each natural frequency was developed using the corresponding amplitude and phase angle for each accelerometer measurement. Because the bridge has an even number of girders, the accelerometer common to both the longitudinal section and transverse section is located at Girder G4, 15 ft longitudinally and 12.44 ft transversely. The mode shape along the longitudinal section and transverse section for the first natural frequency is shown in Figure 7.34. Figure 7.35 provides the mode shape along the longitudinal section and transverse section for the second natural frequency. The mode shape along the longitudinal section and transverse section for the third natural frequency is shown in Figure 7.36.

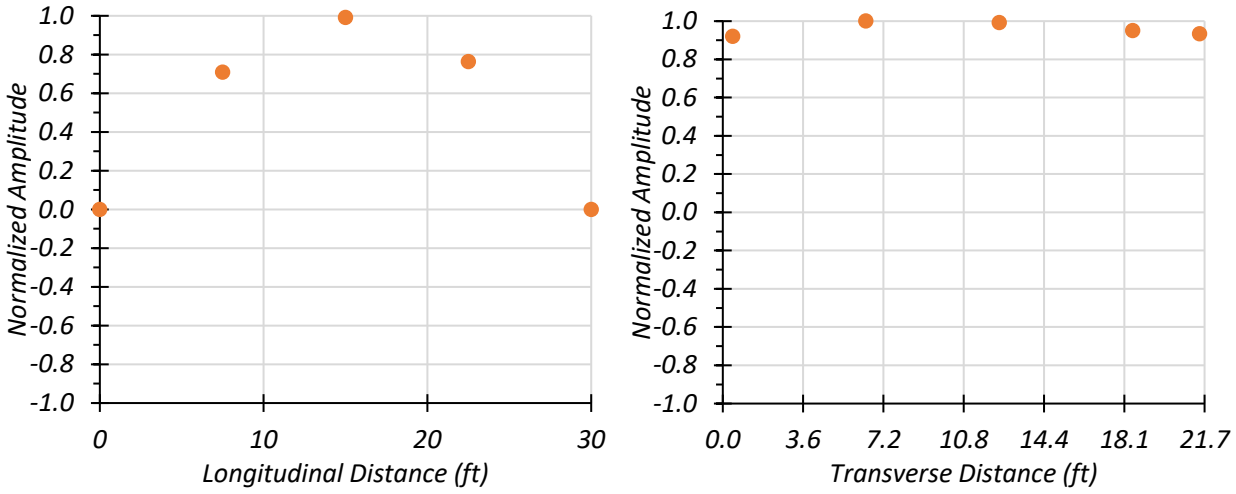

(a) Longitudinal Section *(b) Transverse Section*

Figure 7.34. Measured Mode Shape 1 for Bridge CM-5 (f_1 = 11.84 Hz)

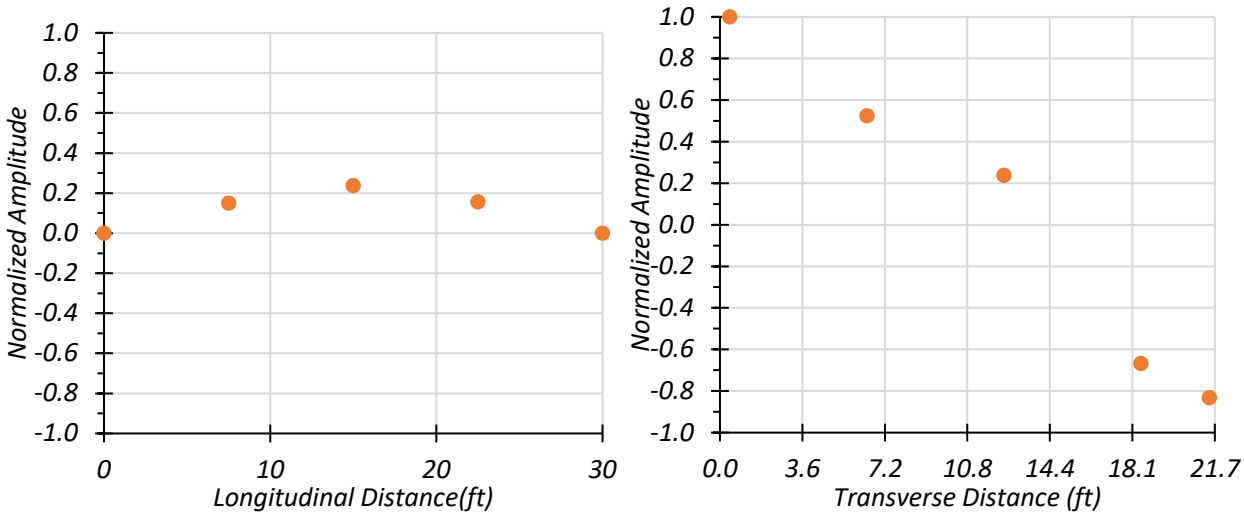

(a) Longitudinal Section *(b) Transverse Section*

Figure 7.35. Measured Mode Shape 2 for Bridge CM-5 (f_2 = 16.60 Hz)

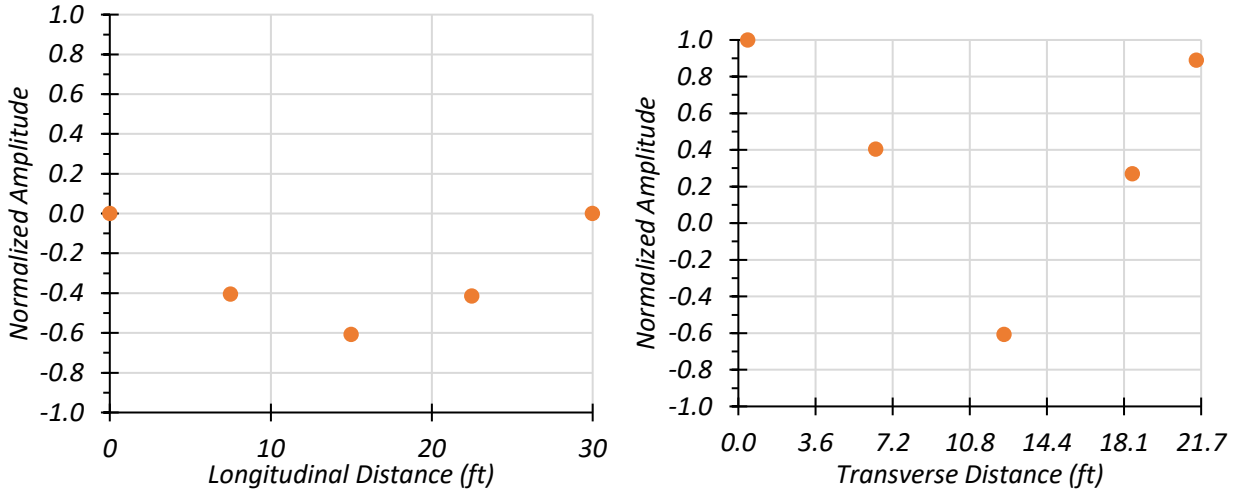

(a) Longitudinal Section *(b) Transverse Section*

Figure 7.36. Measured Mode Shape 3 for Bridge CM-5 (f_3 = 25.15 Hz)

7.6.3. Computer Vision

The possibility of determining deflection from video recordings of the bridge during a truck pass was evaluated during the testing of Bridge CM-5. Two cameras, a Sony HDR-CX405 handheld video camera and an iPhone X, were mounted on tripods and set up on either side of the bridge.

The iPhone X was located at the South end of the bridge near Girder G8 while the handheld video camera was mounted at the opposite side near Girder G1. These were used to record the bridge during each test. The video resolution of the handheld video camera was 1440 pixels by 1080 pixels and it recorded at 30 frames per second (fps). The video resolution of the iPhone was 3840 pixels by 2160 pixels and it recorded at a rate of 60 fps.

A frame-by-frame analysis of the selected sub-window of the area of interest was carried out using an image analysis algorithm written in MATLAB. The location of the sub-window on the bridge was selected such that it covered an area of high contrast. A sensitivity analysis was carried out for different sub-window sizes for the Dynamic Test at 31 mph along Path 2. The results from the different sub-window sizes are presented in Table 7.13. Although 200 x 200 pixels provided a smaller displacement close to the recorded string potentiometer displacement (0.0390 in.), the computation time associated with this window size was high. The deflections obtained using a 75 x 100 pixels sub-window and 50 x 50 pixels sub-window were the same. Because the computation time associated with the 50 x 50 pixel sub-window was less, this window size was selected for Bridge CM-5.

Table 7.13 Computer Vision Displacement for CM-5 with Different Sub-window Sizes

Window Size (pixels x pixels)	Displacement (in.)
200 x 200	0.0412
100 x 100	0.0423
75 x 75	0.0423
50 x 50	0.0418
100 x 75	0.0428
75 x 100	0.0418

Furthermore, all signals were filtered to remove the noise associated with the data such as unintended vibration of the cameras. Depending on the level of noise, a high pass, a low pass or a

band pass filter may be used. However, for this particular bridge all videos were filtered using a lowpass Butterworth filter. A sensitivity analysis was also carried out for this filter by changing the order of the filter and the cut-off frequencies for each load test presented here. A Fast Fourier Transform (FFT) was carried out to plot the magnitude vs. frequency response of the unfiltered computer vision data to determine the range of the cut-off frequency.

The three tests for which computer vision was performed include: (1) Test 2 – Path 1 – Crawl Test, (2) Test 3 – Path 1 – Dynamic at 31 mph, and (3) Test 7 – Path 2 – Dynamic at 30 mph.

The time history plot of deflection obtained from the computer vision analysis was plotted along with the corresponding deflection obtained from the string potentiometer to compare the results. The results from the sensitivity study of the Butterworth Filter for the Crawl Speed Test along Path 1 is presented in Table 7.14. Using a cut-off frequency of 1.0 Hz and a filter of order 5, the results are within 2.5 percent of the error margin when compared with the string potentiometer result. The image of the bridge taken with the iPhone, along with the sub-window used to determine the deflection of the exterior Girder G8 during the crawl speed test along Path 1 is shown in Figure 7.37. Figure 7.38 shows the time history plot for the exterior Girder G8 during the crawl test along Path 1. Since this is a crawl speed test where the truck slowly passed over the bridge, an average deflection was calculated for the period of time the truck was on the bridge. The average deflection obtained from the computer vision analysis was found to be 0.0348 in. while the string potentiometer recorded an average deflection of 0.0356 in. The deflection obtained from computer vision was 2.2 percent lower than that obtained from the string potentiometer. This difference may be due to the associated parallax error. At the end of the test, the camera shook slightly and thus the computer vision results do not return to zero after the truck got off the bridge.

Table 7.14. Butterworth Filter Sensitivity Study for Path 1 Crawl Speed Test

Order of Butterworth Filter	Cut-off Frequency (Hz)	Computer Vision Deflection (in.)	String Potentiometer Deflection (in.)	% Difference
4	0.5	0.03477	0.03561	2.36
4	0.8	0.03479		2.30
4	1.0	0.03480		2.27
5	1.0	0.03482		2.22
10	1.0	0.03460		2.84

Figure 7.37. Image and Sub-window for Girder 8 during Path 1 Crawl Speed Test

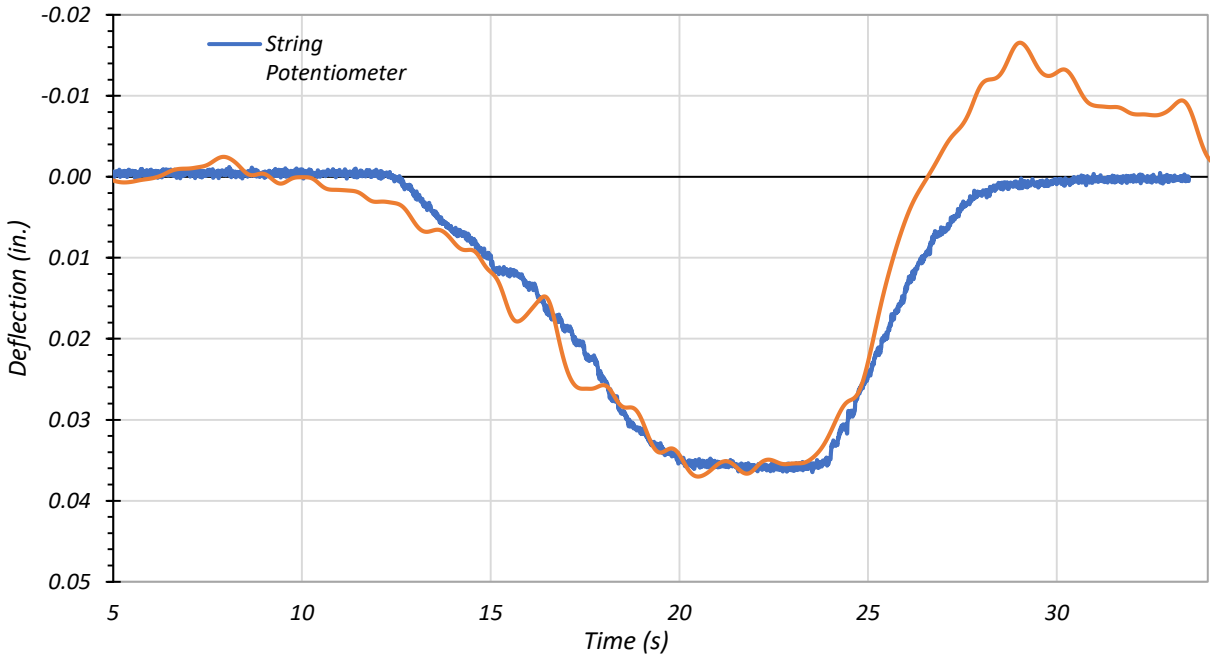

Figure 7.38. Girder 8 Midspan Deflections for Path 1 – Crawl Test

A sensitivity study of the Butterworth Filter was also carried out for the Dynamic Test along Path 1 at 31 mph and the results are presented in Table 7.15. Using a cut-off frequency of 1.0 Hz and a filter of order 15 for the image data obtained from the iPhone camera, the results are within 2 percent of the error margin when compared with the string potentiometer result. The time history deflection plot for G8 during the dynamic test at 31 mph along Path 1 is presented in Figure 7.39. The maximum deflection obtained from the computer vision analysis was found to be 0.0373 in. while the string potentiometer recorded the maximum deflection to be 0.0304 in. The deflection obtained from computer vision was 1.7 percent higher than that obtained from the string potentiometer.

Table 7.15. Butterworth Filter Sensitivity Study for Path 1 Dynamic Test at 31 mph

Order of Butterworth Filter	Cut-off Frequency (Hz)	Computer Vision Deflection (in.)	String Potentiometer Deflection (in.)	% Difference
5	1.0	0.03290	0.03035	8.40
10	1.0	0.03192		5.17
15	1.0	0.03085		1.65
15	5.0	0.03727		22.8
15	2.5	0.03782		24.6

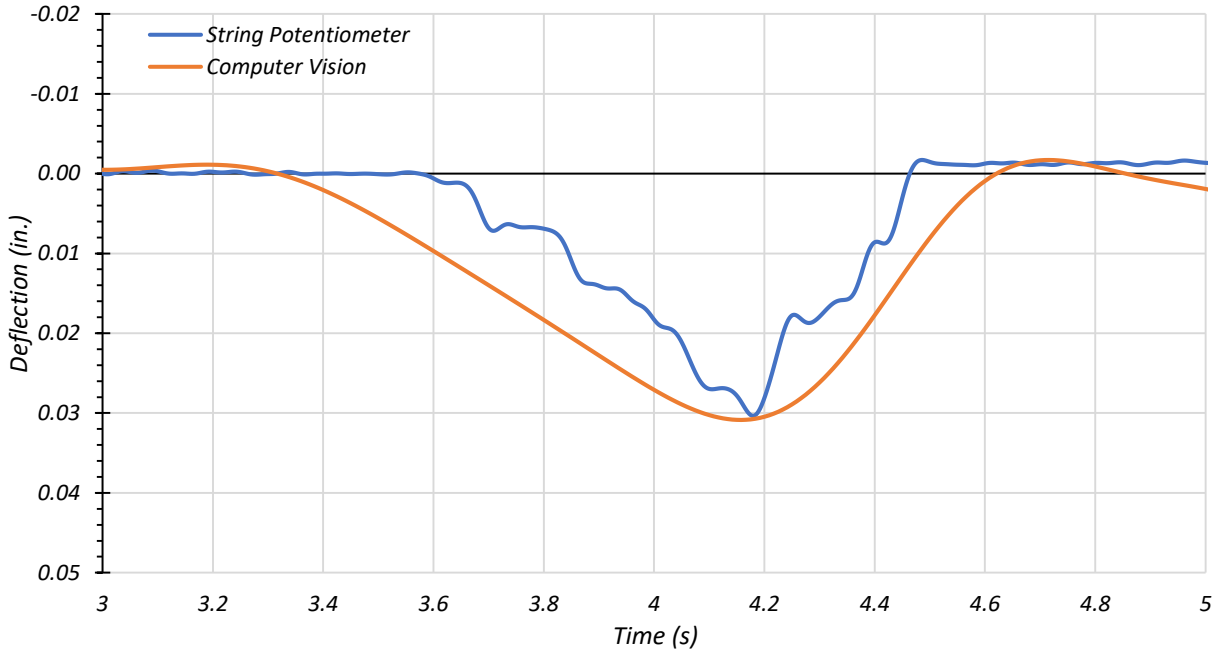

Figure 7.39. Girder 8 Midspan Deflections for Path 1 – Dynamic Test at 31 mph

The results from the sensitivity study of the Butterworth Filter for the Dynamic Test at 30 mph along Path 2 is presented in Table 7.16. Using a cut-off frequency of 2.0 Hz and a filter of order 10 for the image data obtained from the handheld video camera, the results are within 1 percent of the error margin when compared with the string potentiometer result. Figure 7.40 shows the time history plot for the exterior Girder G1 during the dynamic test at 30 mph along Path 2. The maximum deflection obtained from the computer vision analysis was found to be 0.0392 in.

while the string potentiometer recorded the maximum deflection to be 0.0390 in. The deflection obtained from computer vision was 0.6 percent lower than that obtained from the string potentiometer.

Table 7.16. Butterworth Filter Sensitivity Study for Path 2 Dynamic Test at 30 mph

Order of Butterworth Filter	Cut-off Frequency (Hz)	Computer Vision Deflection (in.)	String Potentiometer Deflection (in.)	% Difference
4	0.5	0.03152	0.03900	19.2
4	1.0	0.04061		4.13
4	1.5	0.03986		2.21
10	1.0	0.04019		3.05
10	2.0	0.03922		0.56

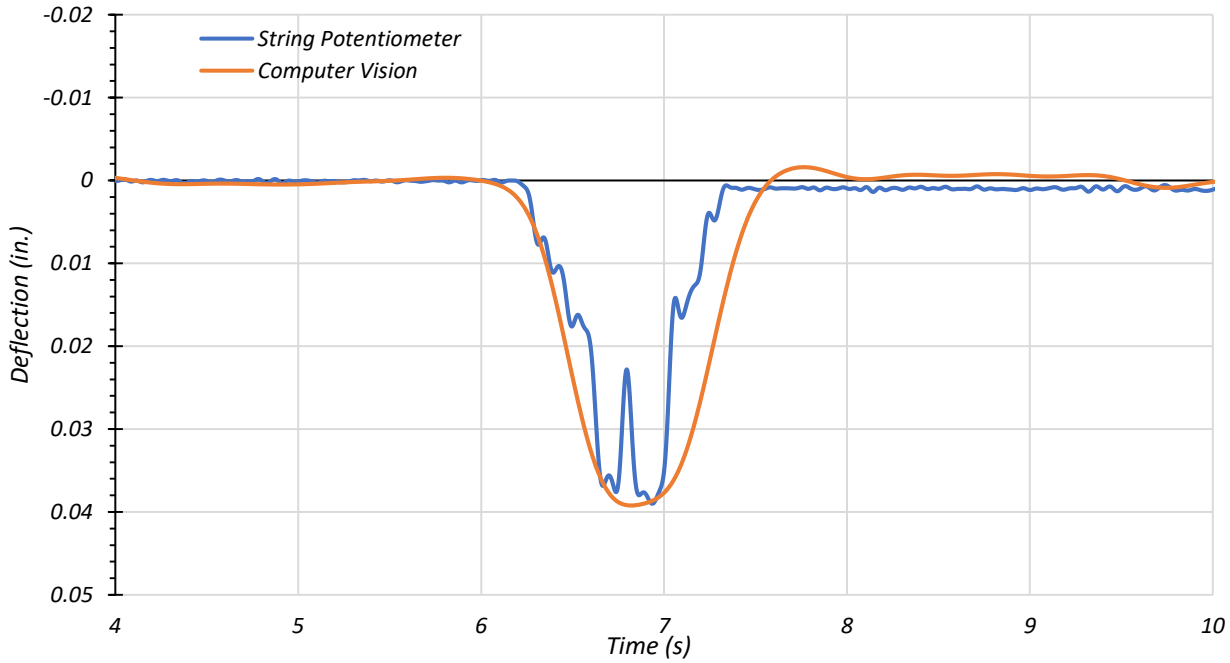

Figure 7.40. Girder 1 Midspan Deflections for Path 2 – Dynamic Test at 30 mph

In this section, several selected results obtained from the computer vision analysis are presented. The aim of this analysis was to determine the feasibility of this approach to determine the deflection of the bridge under vehicular loading from a video/image as compared to

measurements using string potentiometers. The deflections associated with this bridge are very small (multiple of 1/100 of an inch). This may be the reason for some of the variations observed in the percentage difference. Moreover, the parallax error associated with the position of the camera may also add to the variations observed. However, this approach seems to provide reasonable deflection measurements for this bridge.

7.7. FEM MODEL UPDATE AND CALIBRATION

In the following section, details regarding the FEM model update and calibration are presented.

7.7.1. General

The original FEM model for Bridge CM-5 was revised to determine appropriate modeling parameters based on comparison to test data. The FEM model update was carried out in two steps: (1) material property update based on NDE tests, and (2) end fixity update based on model calibration.

7.7.2. Updated FEM Model

The concrete compressive strength for Bridge CM-5 was determined to be 7 ksi from the NDE tests as explained in Section 7.3.1. This is higher than the initial f_c' taken to be 4 ksi. The modulus of elasticity (MOE) for Bridge CM-5 was increased by 10 percent because (1) tangent stiffness is higher than the secant stiffness, where MOE is calculated based on secant stiffness, and (2) empirical equations typically provide lower bound values to be conservative. The modulus of elasticity for concrete increased from 3834 ksi to 5579 ksi. The FEM model was updated to incorporate the measured f_c' and the measured bridge geometries noted in Section 7.3. The pan girder bottom width was reduced from 8.35 in. to 7 in. The boundary conditions of the updated

model were kept the same as the initial FEM model in which both ends of each girder was modeled with roller supports. The results obtained from this updated FEM model are compared with the experimental results in the following sections.

Table 7.17. Selected FEM Results for Updated FEM Model

Model	Modal Frequency (Hz)		Midspan Deflection (in.)		Strain (με)									
					West Top		West Bot		Mid Top	Mid Bot	East Top		East Bot	
	1st	2nd	G4	G8	G4	G8	G4	G8	G8	G8	G4	G8	G4	G8
Original	9.9	17.8	0.06	0.09	-1.2	-6.6	-12.6	28.5	-43.3	67.2	-2.6	-6.2	0.0	17.4
Updated	11.7	14.8	0.05	0.06	-3.7	-7.6	0	-0.4	-44.2	68.3	-3.6	-7.3	0.0	17.9
Field Test	11.8	16.6	0.04	0.03	-	-3.8	-11.2	-4.8	-33.0	38.3	-3.2	-5.2	-5.7	3.2

7.7.3. Model Calibration Process

The updated FEM model for Bridge CM-5 was calibrated for cracked concrete properties and end fixity at the abutments. The model developed from this process can capture the true behavior of the bridge more accurately.

During the installation of the instrumentations, it was noted that the interior pan girders were cracked in the web. The updated FEM model was calibrated to incorporate cracked concrete properties by (1) reducing the modulus of elasticity and (2) using non-linear material properties. The modulus of elasticity was reduced by a factor equal to the ratio of the cracked moment of inertia and gross moment of inertia of the section. This was calculated to be 0.386 for the exterior girder and 0.336 for the interior girder. Three cases were considered for the reduced modulus of elasticity approach. The first case used the respective reduced modulus of elasticity for the interior

girders and exterior girders with simply supported end conditions. The second case used the same properties as the first except with pin-pin end conditions. The third case used reduced modulus of elasticity for the interior girders while using the gross modulus of elasticity for the exterior girders for pin-pin end conditions. Another option used to consider the cracked behavior of concrete was the nonlinear Mander model for concrete (Mander et al. 1988). Two different values for concrete tensile strength were considered: 10% of measured concrete compressive strength and 1% of measured concrete compressive strength. These analyses were carried out for simply supported end conditions, pin-pin end conditions and roller-roller end conditions.

Four input parameters were identified for calibrating the above material-calibrated FEM model of Bridge CM-5 to determine the true end fixities. These were (1) west end of all interior girders, (2) west end of both exterior girders, (3) east end of all interior girders, and (4) east end of both exterior girders. The vertical translational degree of freedom was fully restrained for all girders. Horizontal springs were introduced at the bottom of the girders and at nodes at the top of the concrete slab. The horizontal spring stiffness was modified to provide partial fixities at the ends. Roller supports were considered to be the lower bound for the horizontal spring stiffness and pin supports were the upper bound. The corresponding upper and lower bound spring stiffness were determined. The effect of each input parameter on the analysis results was studied by gradually varying one parameter at a time. The results from this parametric study is presented in the following sections.

7.7.4. Calibrated FEM Model Results

In this section, the influence of changing each input parameter identified earlier on the analysis results is presented. The calibration of the model was carried out based on experimental results

obtained for the static test carried out on Bridge CM-5, provided in Table 7.18. It should be noted that Girder 8 results are obtained from the Path 1 stop location test and that Girder 4 results come from the Middle Path stop location test.

Table 7.18. Experimental Results for Calibration of Bridge CM-5

Modal Frequency (Hz)		Midspan Deflection (in.)		Strain (με)									
				West Top		West Bot		Mid Top	Mid Bot	East Top		East Bot	
1st Mode	2nd Mode	G4	G8	G4	G8	G4	G8	G8	G8	G4	G8	G4	G8
11.8	16.6	0.04	0.03	-	-3.8	-11.2	-4.8	-33.0	38.3	-3.2	-5.2	-5.7	3.2

7.7.4.1. Modulus of Elasticity

The modulus of elasticity (MOE) was modified to account for the cracks observed in the pan girders. The end supports were also modified to study the cumulative effect. These results are summarized and presented in Table 7.19.

Table 7.19. Effect of Modulus of Elasticity Value on Selected FEM Results

Case	West end Fixity	East end Fixity	Modal Frequency (Hz)		Midspan Deflection (in.)		West Curvature		East Curvature	
			1st Mode	2nd Mode	G4	G8	G4	G8	G4	G8
Test			11.8	16.6	0.04	0.03	-	0.36E-06	0.10E-06	0.35E-06
1(a)	Pin	Roller	7.13	12.86	0.15	0.18	2.10E-06	0.53E-06	2.00E-06	0.47E-06
1(b)	Pin	Pin	10.99	12.17	0.06	0.09	0.40E-06	1.07E-06	0.44E-06	0.96E-06
1(c)	Pin	Pin	10.99	12.17	0.06	0.09	5.89E-06	6.23E-06	5.61E-06	1.25E-06
2(a)	Pin	Pin	18.96	21.00	0.02	0.03	9.22E-06	6.23E-06	2.67E-06	1.30E-06
2(b)	Pin	Roller	12.30	22.19	0.04	0.06	1.54E-06	0.50E-06	1.44E-06	0.43E-06
2(c)	Roller	Roller	12.53	15.45	0.04	0.06	0.35E-06	0.36E-06	0.18E-06	0.32E-06
2(d)	Roller	Roller	12.53	15.45	0.04	0.06	0.20E-06	0.34E-06	0.18E-06	1.09E-06

Case 1(a) & 1(b): Both exterior and interior girders with reduced MOE
Case 1(c): Interior girders with reduced MOE, exterior girders with gross MOE
Case 2(a) – 2(c): Nonlinear Mander model for concrete with $f_t = 0.10f_c'$
Case 2(d): Nonlinear Mander model for concrete with $f_t = 0.01f_c'$

The nonlinear Mander model with $f_t = 1\% f_c'$ for concrete provided agreeable results to the experimental results. The following calibration is carried out using Case 2(d) listed in Table 7.19.

7.7.4.2. West End Interior Girder Stiffness Spring

The fixity at the west end of the interior girder was determined by changing the support to a roller (only vertical translation restrained) and a pin (all three translations restrained). The second modal frequency, the top and bottom strain at the midspan for Girder G8 and the bottom strain at the east end of Girder G8 for the roller support are slightly closer to the test results. Hence, the boundary condition for the west end of the interior girders was found to be closer to the roller support as shown in Table 7.20.

Table 7.20. Effect of West End Interior Girder Boundary Condition on Selected FEM Results

Boundary condition	Modal Frequency (Hz)		Midspan Deflection (in.)		Strain (με)									
					West Top		West Bot		Mid Top	Mid Bot	East Top		East Bot	
	1st	2nd	G4	G8	G4	G8	G4	G8	G8	G8	G4	G8	G4	G8
Test	11.8	16.6	0.04	0.03	-	-3.8	-11.2	-4.8	-33.0	38.3	-3.2	-5.2	-5.7	3.2
Pin	12.3	18.5	0.04	0.06	-1.8	-7.9	-4.1	0.0	-44.3	70.2	-3.0	-7.6	0.0	19.0
Roller	12.5	15.5	0.04	0.06	-3.8	-7.9	0.0	0.0	-42.8	68.7	-3.5	-7.8	0.0	18.6

7.7.4.3. West End Exterior Girder Stiffness Spring

The fixity at the west end of the exterior girder was determined by changing the support to roller (only vertical translation restrained) and pin (all three translations restrained). The first modal

frequency, the second modal frequency, the top and bottom strain at the midspan for Girder G8 and the bottom strain at the east end of Girder G8 for the pin support are slightly closer to the test results. Hence, the boundary condition for the west end of the exterior girders was found to be closer to the pin support as shown in Table 7.21.

Table 7.21. Effect of West End Exterior Girder Boundary Condition on Selected FEM Results

Boundary condition	Modal Frequency (Hz)		Midspan Deflection (in.)		Strain (με)									
					West Top		West Bot		Mid Top	Mid Bot	East Top		East Bot	
	1st	2nd	G4	G8	G4	G8	G4	G8	G8	G8	G4	G8	G4	G8
Test	11.8	16.6	0.04	0.03	-	-3.8	-11.2	-4.8	-33.0	38.3	-3.2	-5.2	-5.7	3.2
Pin	12.3	16.7	0.04	0.06	-3.7	-8.1	0.0	0.0	-43.9	71.3	-3.5	-7.7	0.0	18.8
Roller	12.5	15.5	0.04	0.06	-3.8	-7.9	0.0	0.0	-42.8	68.7	-3.5	-7.8	0.0	18.6

7.7.4.4. East End Interior Girder Stiffness Spring

The fixity at the east end of the interior girder was determined by changing the support to roller (only vertical translation restrained) and pin (all three translations restrained). The second modal frequency, the top and bottom strain at the midspan for Girder G8 and the bottom strain at the east end of Girder G8 for the roller support are slightly closer to the test results. Hence, the boundary condition for the east end of the interior girders was found to be closer to the roller support as shown in Table 7.22.

Table 7.22. Effect of East End Interior Girder Boundary Condition on Selected FEM Results

Boundary condition	Modal Frequency (Hz)		Midspan Deflection (in.)		Strain (με)									
					West Top		West Bot		Mid Top	Mid Bot	East Top		East Bottom	
	1st	2nd	G4	G8	G4	G8	G4	G8	G8	G8	G4	G8	G4	G8
Test	11.8	16.6	0.04	0.03	-	-3.8	-11.2	-4.8	-33.0	38.3	-3.2	-5.2	-5.7	3.2
Pin	12.3	18.5	0.04	0.06	-3.8	-7.9	0.0	0.0	-43.9	71.1	-2.3	-7.4	-4.0	18.4
Roller	12.5	15.5	0.04	0.06	-3.8	-7.9	0.0	0.0	-42.8	68.7	-3.5	-7.8	0.0	18.6

7.7.4.5. East End Exterior Girder Stiffness Spring

The fixity at the east end of the exterior girder was determined by changing the support to roller (only vertical translation restrained) and pin (all three translations restrained). The first modal frequency, the second modal frequency, and the top and bottom strain at the midspan for Girder G8 for the pin support are slightly closer to the test results. Hence, the boundary condition for the east end of the exterior girders was found to be closer to the roller support as shown in Table 7.23.

Table 7.23. Effect of East End Exterior Girder Boundary Condition on Selected FEM Results

Boundary condition	Modal Frequency (Hz)		Midspan Deflection (in.)		Strain (με)									
					West Top		West Bot		Mid Top	Mid Bot	East Top		East Bot	
	1st	2nd	G4	G8	G4	G8	G4	G8	G8	G8	G4	G8	G4	G8
Test	11.8	16.6	0.04	0.03	-	-3.8	-11.2	-4.8	-33.0	38.3	-3.2	-5.2	-5.7	3.2
Pin	12.3	16.7	0.04	0.06	-3.9	-8.0	-0.1	0.0	-43.2	71.5	-3.4	-7.6	0.0	20.1
Roller	12.5	15.5	0.04	0.06	-3.8	-7.9	0.0	0.0	-42.8	68.7	-3.5	-7.8	0.0	18.6

7.7.4.6. Final Calibration

The individual parametric studies suggested that the west end of the exterior girders is similar to a roller support while west end of the interior girders and east end of the exterior girders, and interior girders are similar to a pin support. The final model calibration was initiated with these end fixities. Each input parameter was gradually adjusted till the FEM results were close to the experimental results. During calibration, horizontal stiffness in the transverse direction was also introduced at the supports to ensure better match with the test results. The final calibration model uses a spring stiffness of 500 kip/in./in. for the west end of interior girders, 400 kip/in./in. for the west end of exterior girders, 400 kip/in./in. for the east end of interior girders, and 5000 kip/in./in. for the east end of exterior girders. The final calibrated model parameters are presented in Table 7.24.

Table 7.24. Final Calibrated Model Parameters

Concrete Model	Bottom Longitudinal Stiffness Value (kip/in.)			
	West End Interior Girder	West End Exterior Girder	East End Interior Girder	East End Exterior Girder
Nonlinear Mander Model with $f_t = 0.01f_c'$	500	400	400	5000

The calibrated model for Bridge CM-5 along with the end fixity springs is shown in Figure 7.41. The results obtained from the calibrated FEM model along with the test results are tabulated in Table 7.25. In the following sections, the results from this calibrated model are compared with the experimental results.

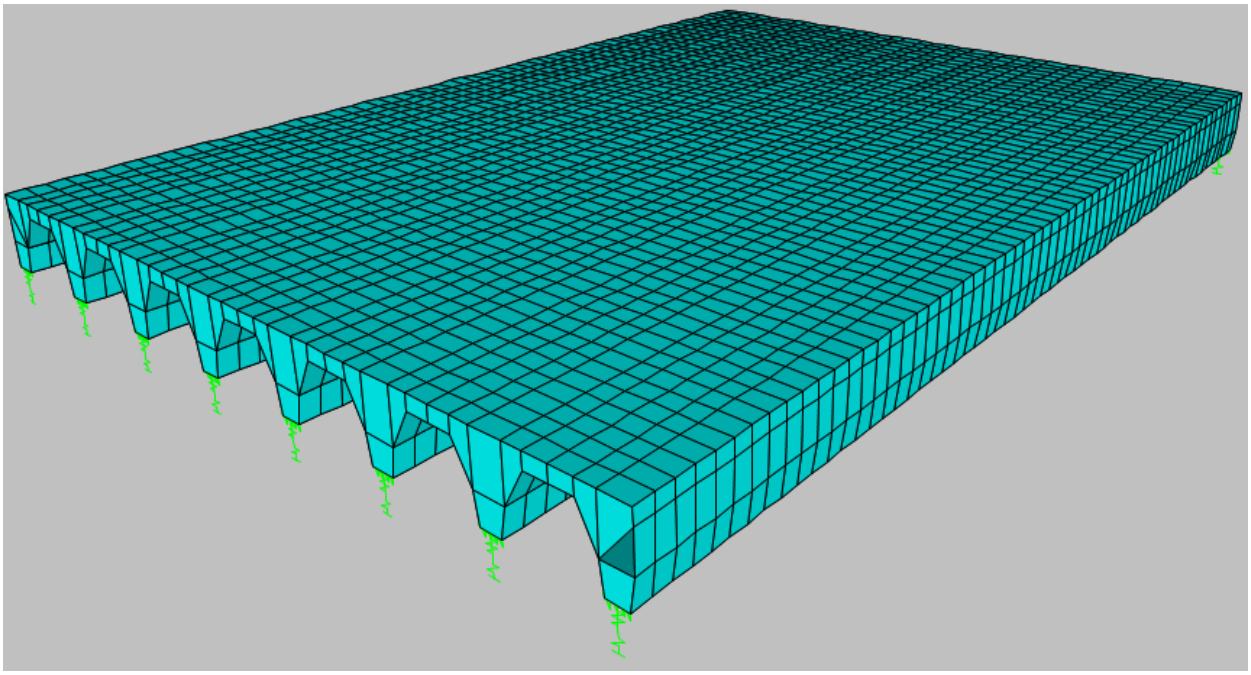

Figure 7.41. Calibrated FEM Model for Bridge CM-5

Table 7.25. Results of CM-5 Model Calibration

Results	Modal Frequency (Hz)		Midspan Deflection (in.)		Strain (με)								
					West Top		West Bot		Mid Bot	East Top		East Bot	
	1st	2nd	G4	G8	G4	G8	G4	G8	G8	G4	G8	G4	G8
Test	11.8	16.6	0.04	0.03	-	-3.8	-11.2	-4.8	38.3	-3.2	-5.2	-5.7	3.2
Calibrated FEM	13.7	16.9	0.04	0.05	-2.3	-6.3	-4.8	-5.5	58.1	-2.8	-5.2	-1.3	7.0

7.8. COMPARISON OF TEST RESULTS AND FEM PREDICTIONS

In the following sections, results obtained from the field test are compared with the FEM results.

7.8.1. Strain Measurements

The strains measured during the field tests are compared with the updated and calibrated FEM results in this section.

7.8.1.1.1. Interior Girder G4

The maximum top and bottom strains for the interior Girder G4 under static test along Path 1 are compared with the calibrated FEM results in Figure 7.42. The strain profile along the west and east ends of G4 is shown in Figure 7.42(a) and that at midspan of Girder G4 is shown in Figure 7.42(b) for stop location test. The strain profile along the west and east ends of Girder G4 is shown in Figure 7.42(c) and that at midspan of Girder G4 is shown in Figure 7.42(d) for stop location test.

The maximum top and bottom strains for the interior Girder G4 under static test along Path 2 are compared with the calibrated FEM results in Figure 7.43. The strain profile along the west and east ends of Girder G4 is shown in Figure 7.43(a) and that at midspan of Girder G4 is shown in Figure 7.43(b) for stop location test. The strain profile along the west and east ends of G4 is

shown in Figure 7.43(c) and that at midspan of Girder G4 is shown in Figure 7.43(d) for stop location test.

The maximum top and bottom strains for the interior Girder G4 under static test along the Middle Path are compared with the calibrated FEM results in Figure 7.44. The strain profile along the west and east ends of Girder G4 is shown in Figure 7.44(a) and that at midspan of Girder G4 is shown in Figure 7.44(b) for stop location test. The strain profile along the west and east ends of Girder G4 is shown in Figure 7.44(c) and that at midspan of Girder G4 is shown in Figure 7.44(d) for stop location test.

It should be noted that the strain values obtained from the bottom strain gauge on Girder G4 were very high compared to both the updated and calibrated FEM model results. Additionally, the top strain gauge for Girder G4 was not attached in line with the bottom strain gauge. The true stain at the top of Girder G4 may be different from the one obtained during testing. However, the updated and calibrated FEM strains at the midspan of Girder G4 were quite similar. The variation in the observed strain values at the ends and midspan of Girder G4 may be attributed to noise in the strain data obtained from testing

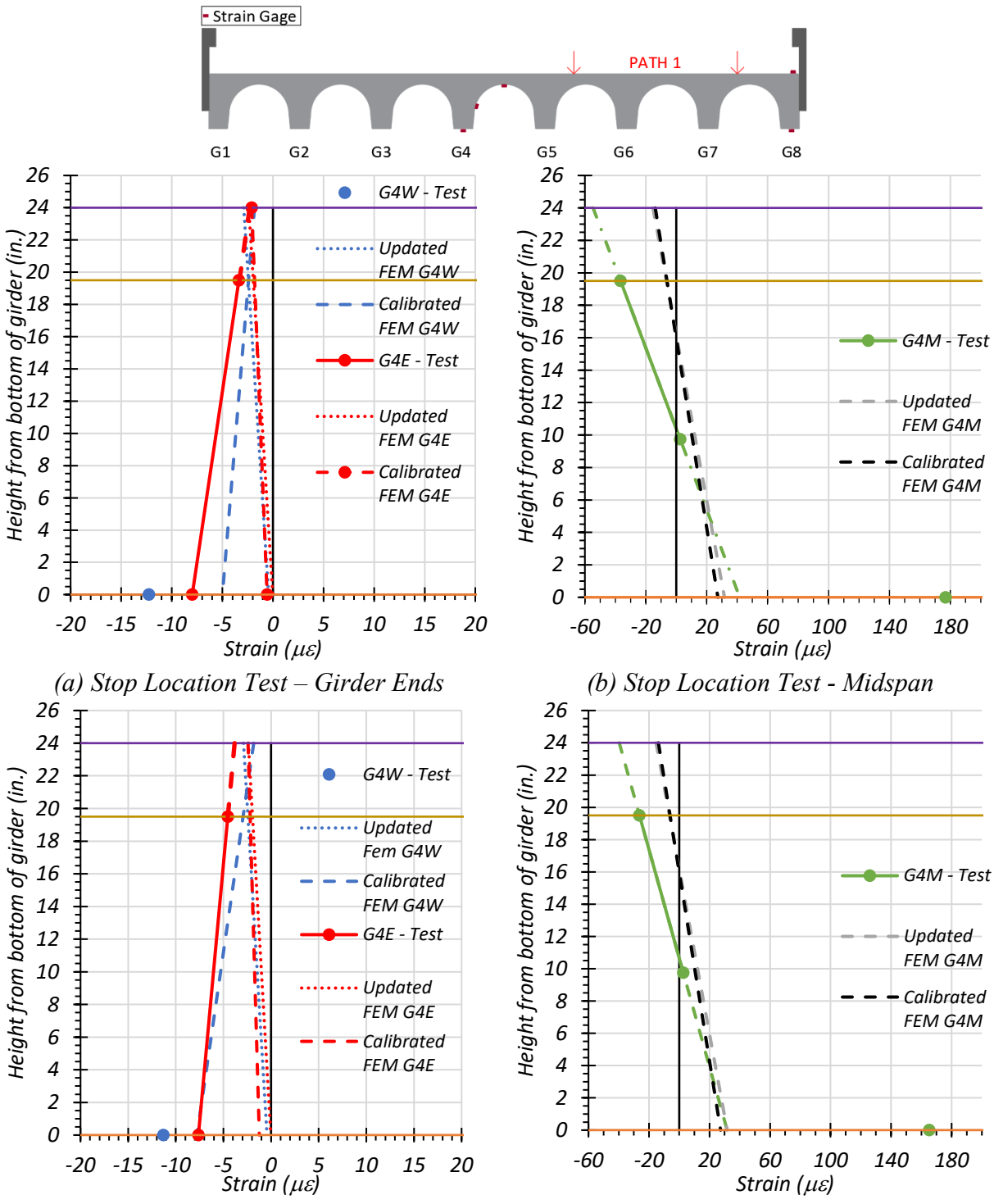

(a) Stop Location Test – Girder Ends

(b) Stop Location Test - Midspan

(c) Crawl Speed Test – Girder Ends

(d) Crawl Speed Test - Midspan

top of slab bottom of slab bottom of girder

Figure 7.42. Comparison of Static Strains for G4 with FEM Results – Path 1

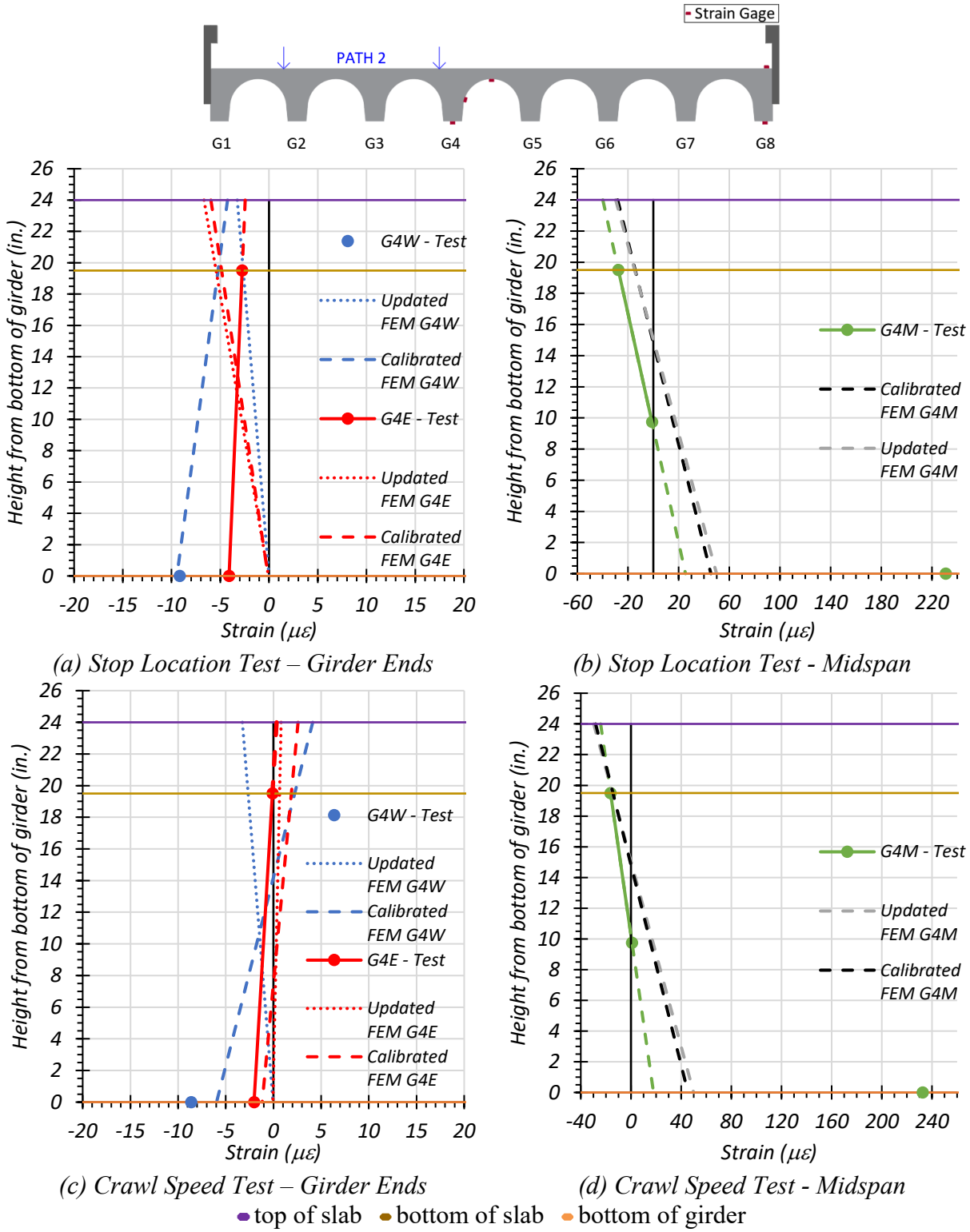

(a) Stop Location Test – Girder Ends

(b) Stop Location Test - Midspan

(c) Crawl Speed Test – Girder Ends

(d) Crawl Speed Test - Midspan

Figure 7.43. Comparison of Static Strains for G4 with FEM Results – Path 2

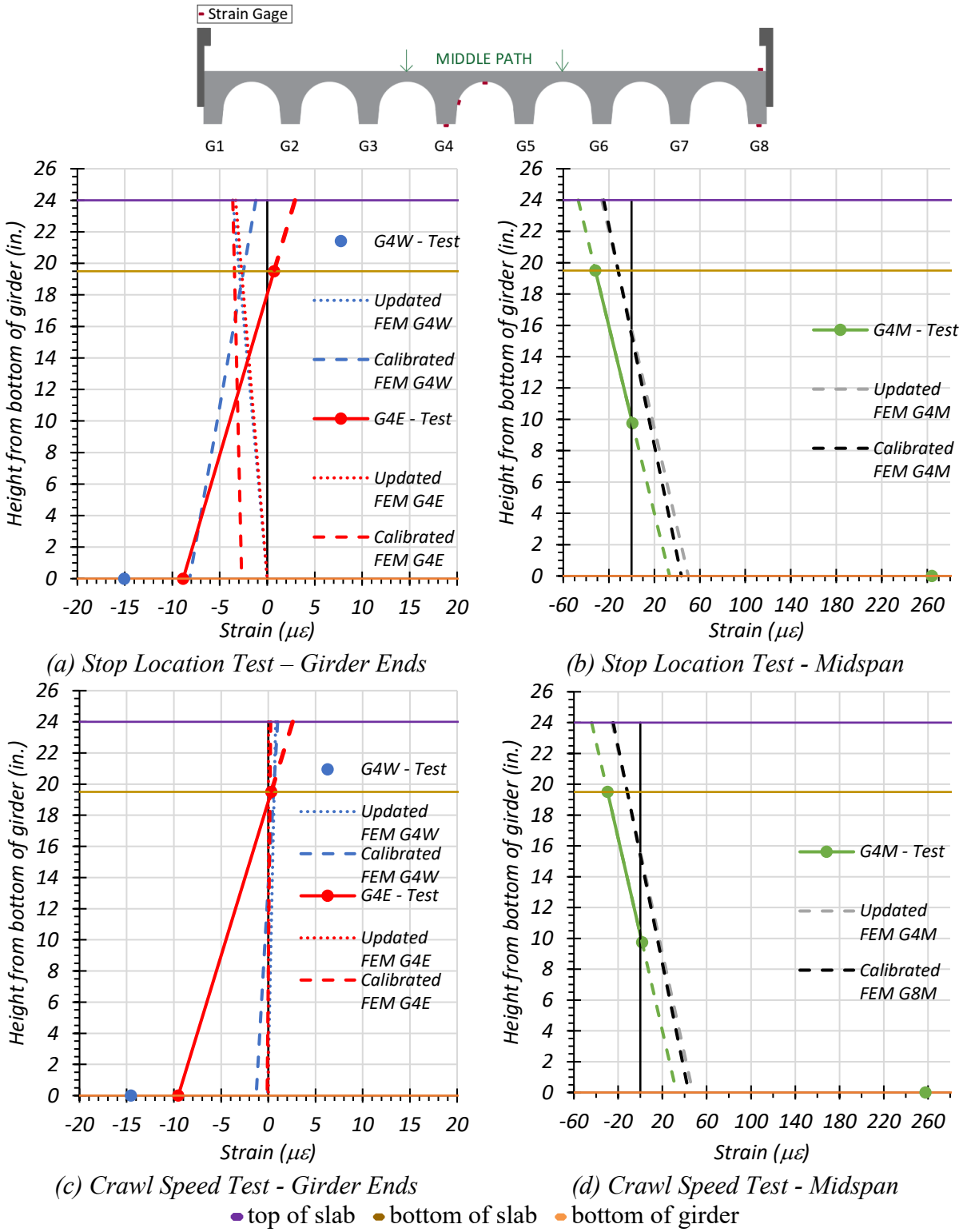

(a) Stop Location Test – Girder Ends

(b) Stop Location Test - Midspan

(c) Crawl Speed Test - Girder Ends

(d) Crawl Speed Test - Midspan

Figure 7.44. Comparison of Static Strains for G4 with FEM Results – Middle Path

7.8.1.1.2. Exterior Girder G8

The maximum top and bottom strains for the exterior Girder G8 under static test along Path 1 are compared with the calibrated FEM results in Figure 7.45. The strain profile along the west and east ends of Girder G8 is shown in Figure 7.45(a) and that at midspan of Girder G8 is shown in Figure 7.45(b) for stop location test. The strain profile along the west and east ends of Girder G8 is shown in Figure 7.45(c) and that at midspan of Girder G8 is shown in Figure 7.45(d) for stop location test.

The maximum top and bottom strains for the exterior Girder G8 under static test along Path 2 are compared with the calibrated FEM results in Figure 7.46. The strain profile along the west and east ends of Girder G8 is shown in Figure 7.46(a) and that at midspan of Girder G8 is shown in Figure 7.46(b) for stop location test. The strain profile along the west and east ends of Girder G8 is shown in Figure 7.46(c) and that at midspan of Girder G8 is shown in Figure 7.46(d) for stop location test.

The maximum top and bottom strains for the exterior Girder G8 under static test along the Middle Path are compared with the calibrated FEM results in Figure 7.47. The strain profile along the west and east ends of Girder G8 is shown in Figure 7.47(a) and that at midspan of Girder G8 is shown in Figure 7.47(b) for stop location test. The strain profile along the west and east ends of Girder G8 is shown in Figure 7.47(c) and that at midspan of Girder G8 is shown in Figure 7.47(d) for stop location test.

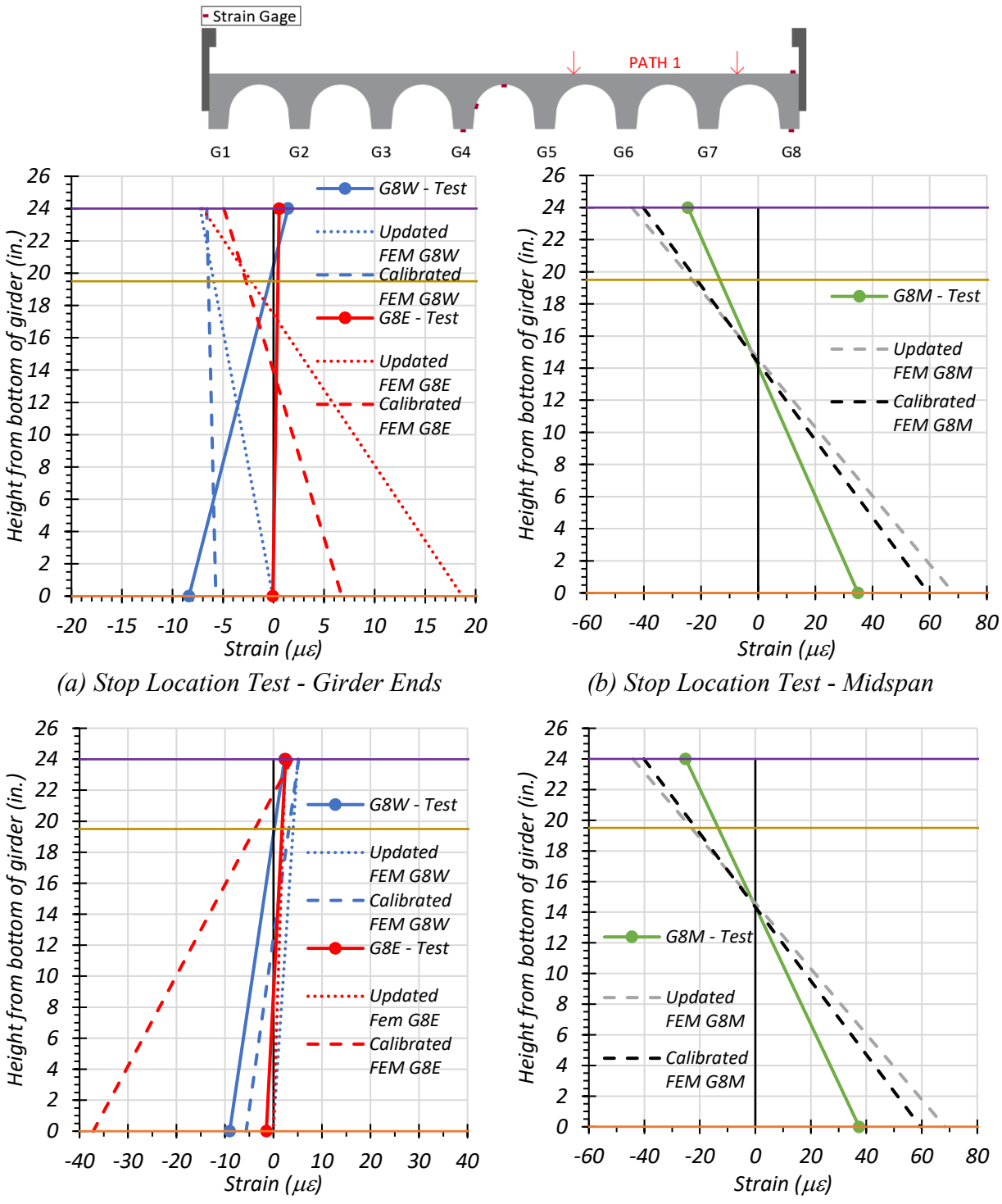

(a) Stop Location Test - Girder Ends

(b) Stop Location Test - Midspan

(c) Crawl Speed Test - Girder Ends

(d) Crawl Speed Test - Midspan

Figure 7.45. Comparison of Static Strains for G8 with FEM Results – Path 1

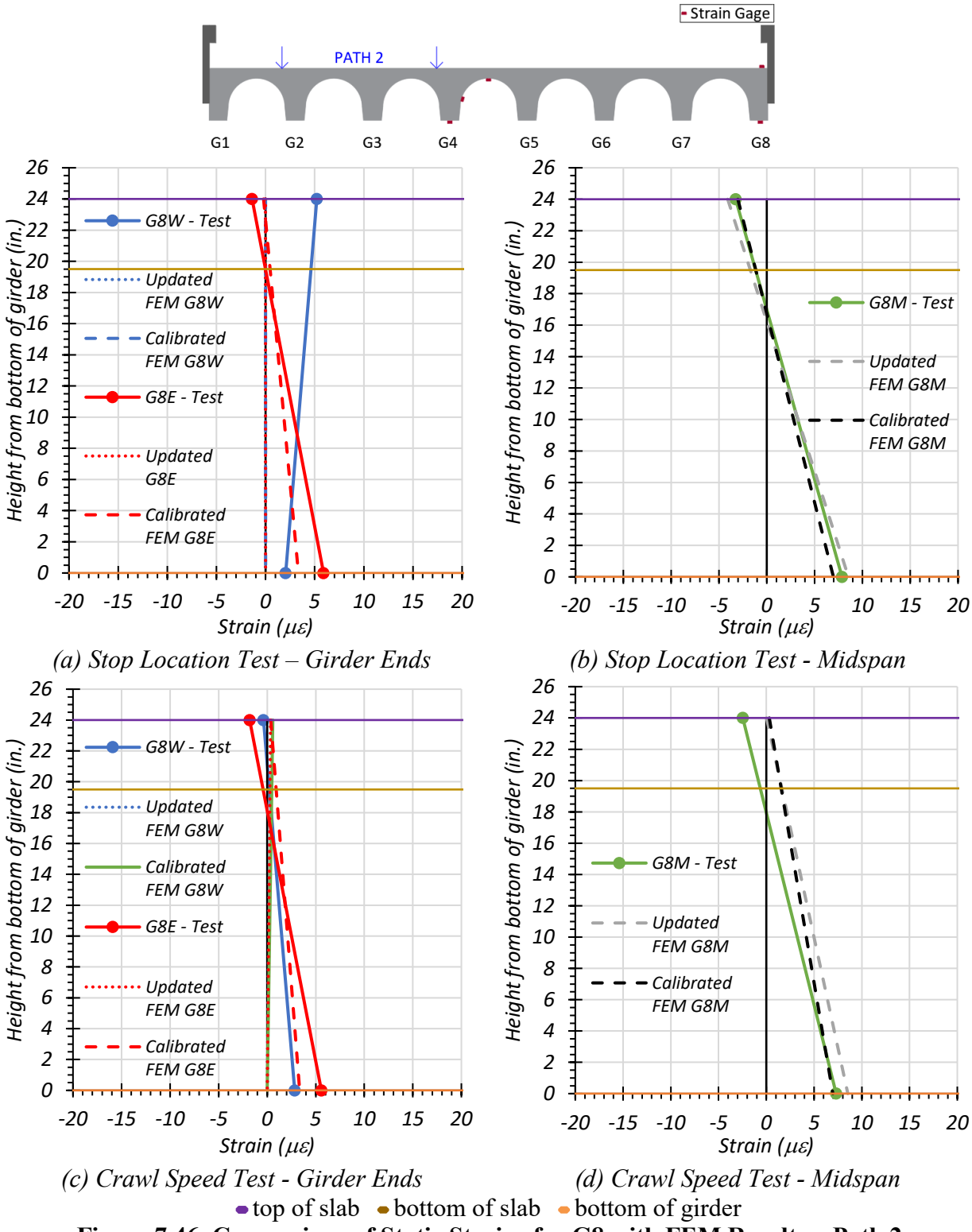

Figure 7.46. Comparison of Static Strains for G8 with FEM Results – Path 2

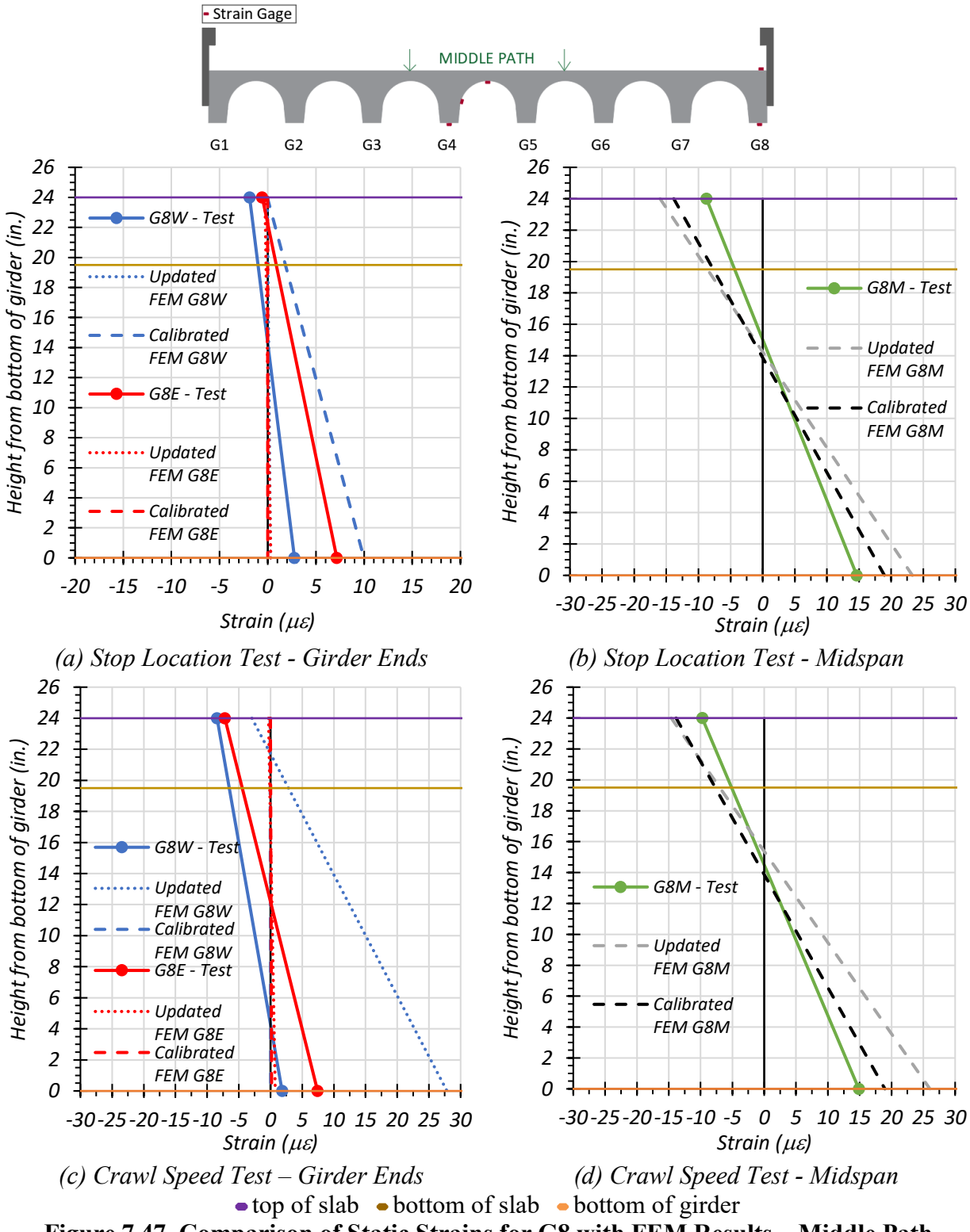

(a) Stop Location Test - Girder Ends

(b) Stop Location Test - Midspan

(c) Crawl Speed Test – Girder Ends

(d) Crawl Speed Test - Midspan

Figure 7.47. Comparison of Static Strains for G8 with FEM Results – Middle Path

7.8.1.1.3. Comparison of Results based on Measured Strains

The neutral axis location for each girder is determined from the strain profile at midspan. The neutral axis positions obtained from Girder G4 was consistently high when compared to those obtained from Girder G8. This may be because of cracks which were noticed in Girder G4.

Table 7.26 lists the neutral axes corresponding to all the different tests. Figure 7.48 compares the neutral axes obtained from the static tests with the FEM neutral axis for both Girder G4 and Girder G8. As previously observed, the neutral axis location is close to the theoretical uncracked section.

Table 7.26 Comparison of Neutral Axis Locations with FEM Results for All Static Load Tests

Test	G4 Neutral Axis Location (in. from bottom of girder)	G8 Neutral Axis Location (in. from bottom of girder)
Path 1 – Stop Location	10.40	15.02
Path 1 – Crawl Speed	10.65	14.37
Path 2 – Stop Location	9.37	19.06
Path 2 – Crawl Speed	10.23	17.96
Middle Path – Stop Location	10.01	14.73
Middle Path – Crawl Speed	10.24	14.50
Updated FEM	15.74	14.24
Calibrated FEM	15.38	13.87
Theoretical Uncracked	14.05	15.21
Theoretical Cracked	19.91	18.87

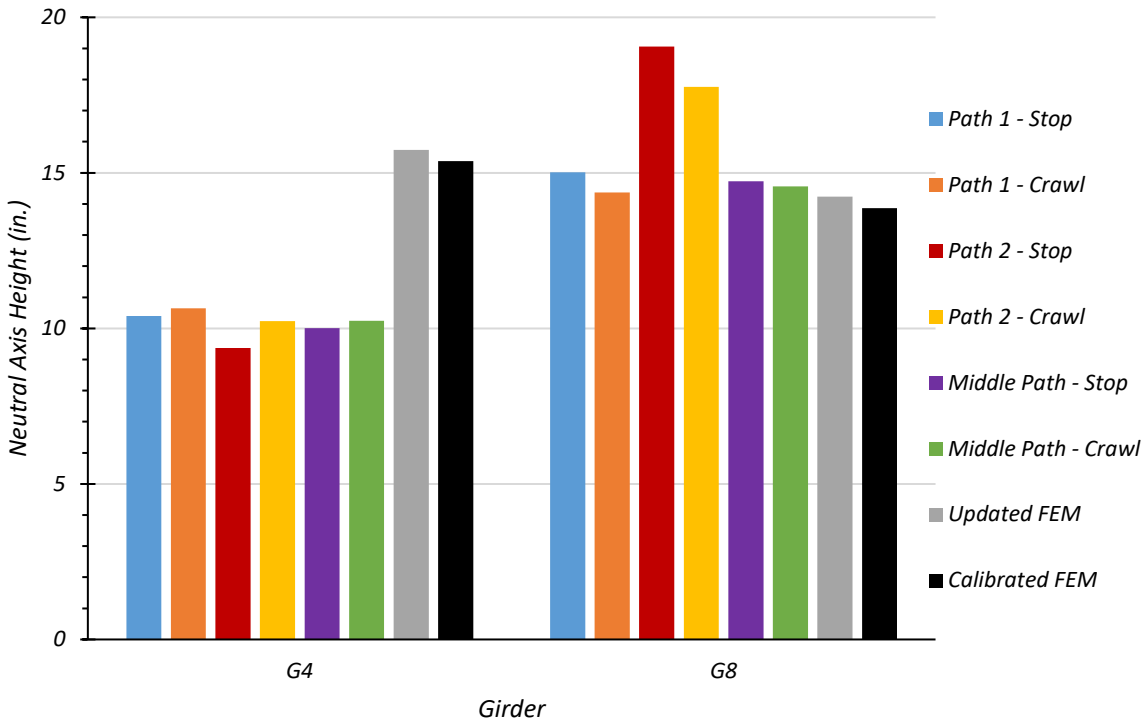

Figure 7.48. Test and Calibrated FEM Neutral Axis Locations

7.8.2. Deflection Measurements

In the following sections, the measured deflections are compared with the FEM results. As noted earlier, the string potentiometers at Girder G2 and Girder G4 show lower displacements for all static tests. Although these results are presented in the following plots, the accuracy of the updated and calibrated FEM models are checked independent of these deflections.

7.8.2.1.1. Path 1 Loading.

The measured maximum downward deflection for each girder under static test and crawl speed test along Path 1 is compared with those obtained from the updated and calibrated FEM models in Figure 7.49(a) and (c) respectively. A comparison of the test LLDFs with those calculated from the AASHTO standard specifications (AASHTO 2002) and updated and calibrated FEM models

are shown in Figure 7.49(b) and (d) for static and crawl tests, respectively. The updated FEM overestimates the deflection by 59 percent for the stop location test and 55 percent for the crawl speed test along Path 1. The calibrated model provided a better estimation of the observed deflections during static tests along Path 1, with a maximum overestimation of 33 percent for the stop location test and 26 percent for the crawl speed test. Correspondingly, the displacement based LLDFs obtained from the calibrated FEM closely model the measured load distribution within the bridge.

Table 7.27 compares the static test deflections for each girder with the update and calibrated FEM deflections. A comparison of the test LLDFs with the FEM displacement LLDFs is provided in Table 7.28. The LLDFs calculated from the test results and calibrated FEM displacements are tabulated along with the LLDFs obtained from the three AASHTO methods in Table 7.29.

Table 7.27. Experimental and FEM Deflections for Path 1 Loading

Girder	G1	G2	G3	G4	G5	G6	G7	G8
Updated FEM	0.005	0.010	0.017	0.027	0.039	0.047	0.053	0.059
Calibrated FEM	0.004	0.008	0.014	0.023	0.033	0.039	0.045	0.048
Stop Location Test Disp. (in.)	0.006	0.002	0.014	0.016	0.034	0.041	0.040	0.037
Crawl Speed Test Disp. (in.)	0.004	0.003	0.014	0.015	0.033	0.041	0.041	0.038
Note: 1 – G = girder, Disp. = Displacement								

Table 7.28. FEM Displacement LLDF Comparison with Test for Path 1 Loading

Test and Girder Type	Updated FEM LLDF (g_{FEM})	Calibrated FEM LLDF (g_{cal})	Test (g_{test})	g_{FEM}/g_{test}	g_{cal}/g_{test}
Stop Location Interior	0.212	0.208	0.218	0.97	0.95
Stop Location Exterior	0.218	0.226	0.184	1.18	1.23
Crawl Speed Interior	0.212	0.208	0.222	0.95	0.94
Crawl Speed Exterior	0.218	0.226	0.191	1.14	1.18

Table 7.29. Experimental, FEM, and AASHTO LLDFs for Path 1 Loading

Girder	G1	G2	G3	G4	G5	G6	G7	G8
Stop Location Test LLDF	0.032	0.012	0.076	0.088	0.180	0.218	0.210	0.184
Crawl Speed Test LLDF	0.019	0.013	0.074	0.079	0.180	0.222	0.221	0.191
Calibrated FEM Disp. LLDF	0.016	0.037	0.066	0.107	0.155	0.185	0.208	0.226
AASHTO Standard LLDF	0.231	0.231	0.231	0.231	0.231	0.231	0.231	0.231
AASHTO LRFD LLDF using simplified stiffness	0.238	0.344	0.344	0.344	0.344	0.344	0.344	0.238
AASHTO LRFD LLDF using analytical stiffness	0.238	0.339	0.339	0.339	0.339	0.339	0.339	0.238

Note: 1 – G = girder, Disp. = Displacement
2 – LLDF values are based on the midspan deflections.

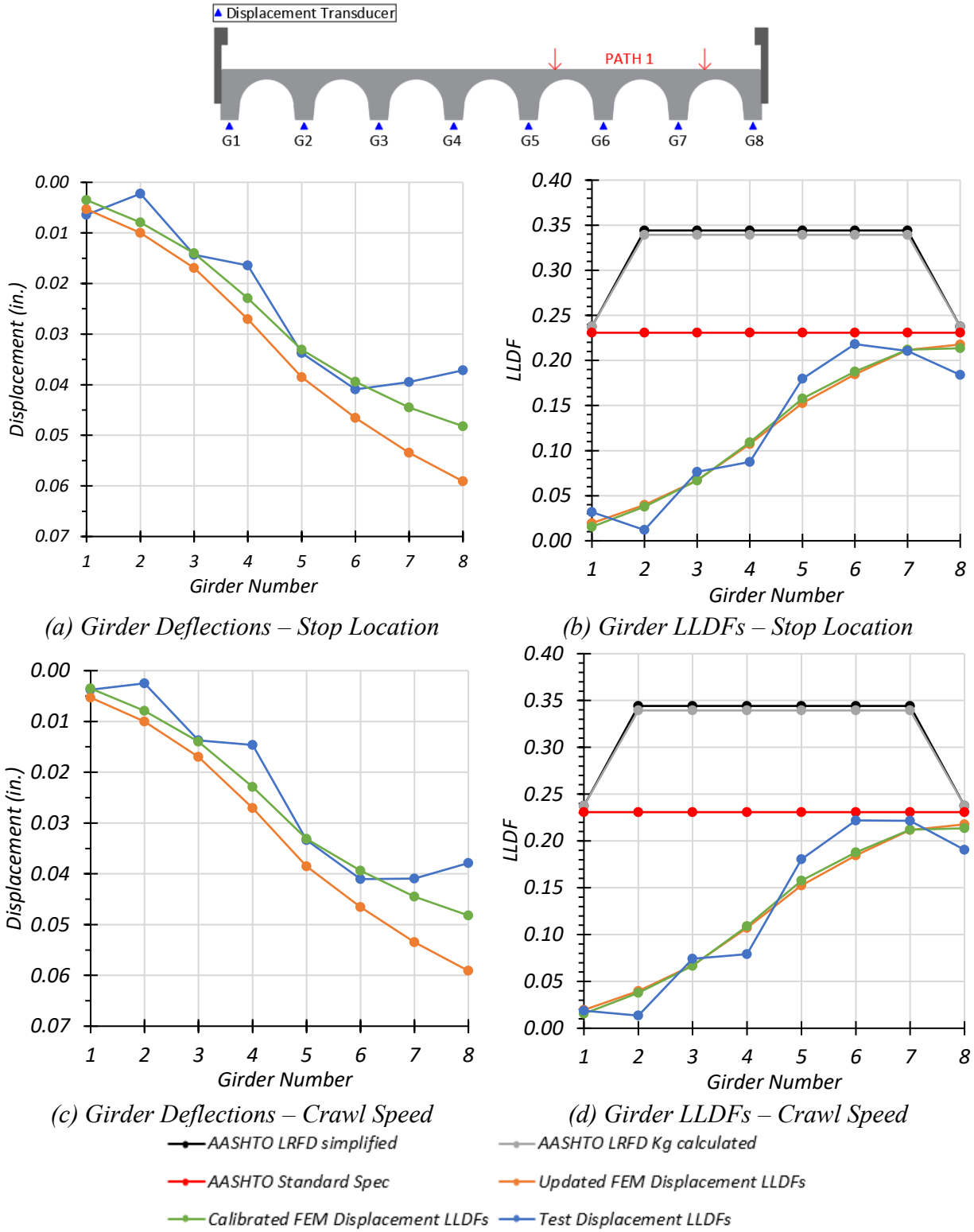

Figure 7.49. Comparison of Static Deflection Results with FEM for Path 1 Loading

7.8.2.1.2. Path 2 Loading

The measured maximum downward deflection for each girder under static test and crawl speed test along Path 2 is compared with those obtained from the updated and calibrated FEM models in Figure 7.50(a) and (c) respectively. A comparison of the test LLDFs with those calculated from the standard specifications and updated and calibrated FEM models are shown in Figure 7.50(b) and (d) for static and crawl tests, respectively. The updated FEM overestimates the deflection by 100 percent for both the stop location test and the crawl speed test along Path 2. The calibrated model provided a better estimation of the observed deflections during static tests along Path 2, with a maximum underestimation of 67 percent for the stop location test and overestimation 80 percent for the crawl speed test. Corresponding the displacement LLDFs obtained from the calibrated FEM closely model the true load distribution within the bridge.

Table 7.30 compares the static test deflections for each girder with the update and calibrated FEM deflections. A comparison of the test LLDFs with the FEM displacement LLDFs is provided in Table 7.31. The LLDFs calculated from the test results and calibrated FEM displacements are tabulated along with the LLDFs obtained from the three AASHTO methods in Table 7.32.

Table 7.30. Experimental and FEM Deflections for Path 2 Loading

Girder	G1	G2	G3	G4	G5	G6	G7	G8
Updated FEM	0.054	0.051	0.046	0.039	0.029	0.019	0.011	0.006
Calibrated FEM	0.044	0.043	0.039	0.034	0.025	0.016	0.009	0.005
Stop Location Test Disp. (in.)	0.030	0.032	0.038	0.024	0.026	0.015	0.006	0.003
Crawl Speed Test Disp. (in.)	0.033	0.031	0.036	0.022	0.023	0.014	0.005	0.003
Note: 1 – G = girder, Disp. = Displacement								

Table 7.31. FEM Displacement LLDF Comparison with Test for Path 2 Loading

Test and Girder Type	Updated FEM LLDF (g_{FEM})	Calibrated FEM LLDF (g_{cal})	Test (g_{test})	g_{FEM}/g_{test}	g_{cal}/g_{test}
Stop Location Interior	0.204	0.200	0.224	0.91	0.89
Stop Location Exterior	0.198	0.204	0.164	1.21	1.24
Crawl Speed Interior	0.204	0.200	0.221	0.92	0.90
Crawl Speed Exterior	0.198	0.204	0.187	1.06	1.09

Table 7.32. Experimental, FEM, and AASHTO LLDFs for Path 2 Loading

Girder	G1	G2	G3	G4	G5	G6	G7	G8
Stop Location Test LLDF	0.174	0.184	0.221	0.139	0.147	0.085	0.034	0.017
Crawl Speed Test LLDF	0.187	0.187	0.221	0.135	0.141	0.083	0.030	0.015
Calibrated FEM Disp. LLDF	0.198	0.204	0.183	0.157	0.115	0.075	0.045	0.024
AASHTO Standard LLDF	0.231	0.231	0.231	0.231	0.231	0.231	0.231	0.231
AASHTO LRFD LLDF using simplified stiffness	0.238	0.344	0.344	0.344	0.344	0.344	0.344	0.238
AASHTO LRFD LLDF using analytical stiffness	0.238	0.339	0.339	0.339	0.339	0.339	0.339	0.238

Note: 1 – G = girder, Disp. = Displacement
2 – LLDF values are based on the midspan deflections.

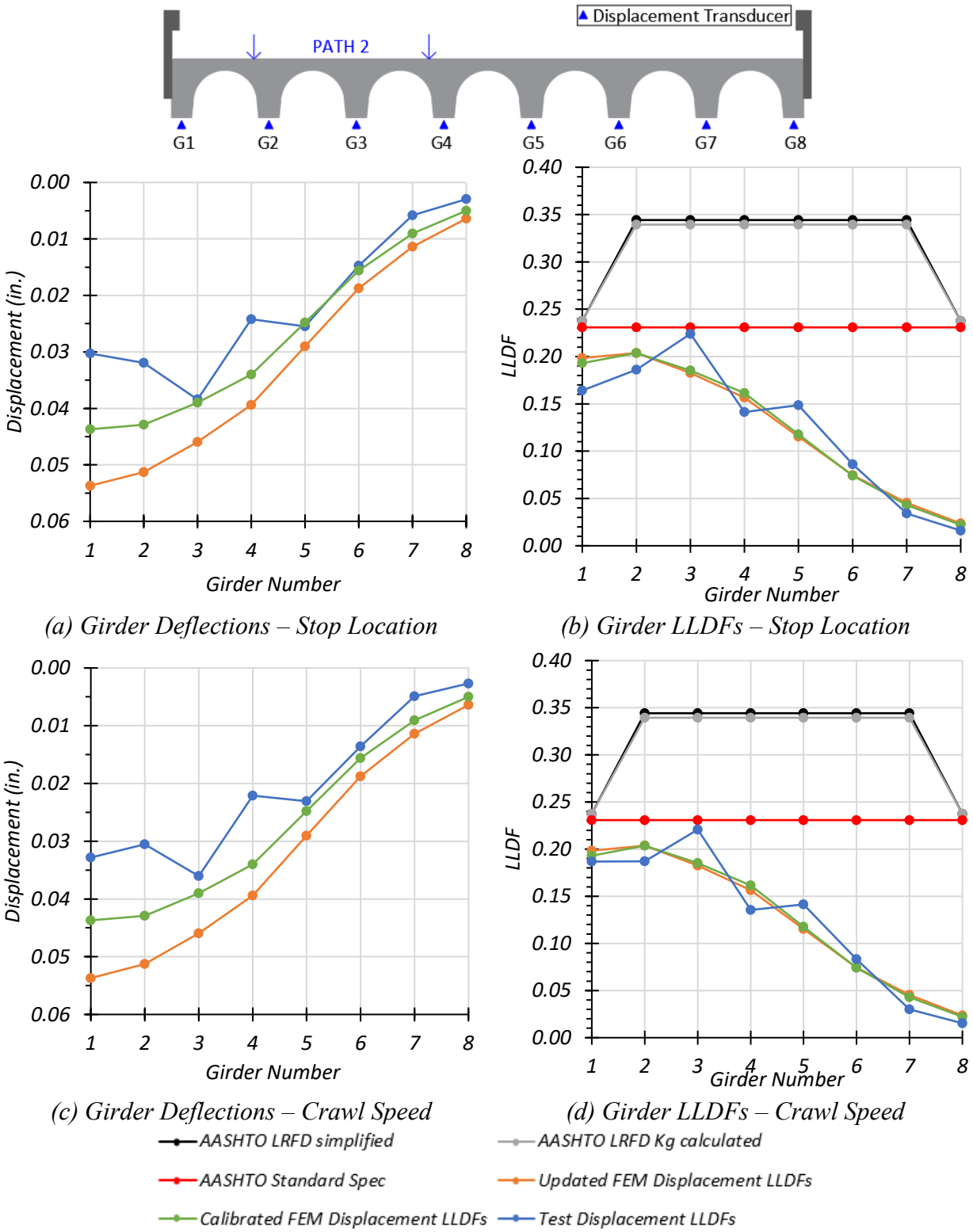

(a) Girder Deflections – Stop Location

(b) Girder LLDFs – Stop Location

(c) Girder Deflections – Crawl Speed

(d) Girder LLDFs – Crawl Speed

Figure 7.50. Comparison of Static Deflection Results with FEM for Path 2 Loading

7.8.2.1.3. Middle Path Loading

The measured maximum downward deflection for each girder under static test and crawl speed test along the Middle Path is compared with those obtained from the calibrated FEM model in Figure 7.51(a) and (c) respectively. A comparison of the test LLDFs with those calculated from the standard specifications and updated and calibrated FEM models are shown in Figure 7.51(b) and (d) for static and crawl tests, respectively. The LLDFs calculated using FEM displacements were found to be similar to that obtained using FEM bending moments. The calibrated model provided a better estimation of the observed deflections during static tests along the Middle Path. Corresponding the displacement LLDFs obtained from the calibrated FEM closely model the true load distribution within the bridge. The updated FEM overestimates the deflection by 62 percent for the stop location test and 75 percent for the crawl speed test along the Middle Path. The calibrated model provided a better estimation of the observed deflections during static tests along the Middle Path, with a maximum underestimation of 33 percent for the stop location test and overestimation of 33 percent for the crawl speed test. Corresponding the displacement LLDFs obtained from the calibrated FEM closely model the true load distribution within the bridge.

Table 7.33 compares the static test deflections for each girder with the update and calibrated FEM deflections. A comparison of the test LLDFs with the FEM displacement LLDFs is provided in Table 7.34. The LLDFs calculated from the test results and calibrated FEM displacements are tabulated along with the LLDFs obtained from the three AASHTO methods in Table 7.35.

Table 7.33. Experimental and FEM Deflections for Middle Path Loading

Girder	G1	G2	G3	G4	G5	G6	G7	G8
Updated FEM	0.021	0.028	0.037	0.040	0.040	0.037	0.028	0.021
Calibrated FEM	0.017	0.024	0.032	0.035	0.035	0.032	0.024	0.016
Stop Location Test Disp. (in.)	0.015	0.016	0.033	0.026	0.036	0.030	0.018	0.013
Crawl Speed Test Disp. (in.)	0.013	0.015	0.030	0.025	0.035	0.028	0.019	0.012
Note: 1 – G = girder, Disp. = Displacement								

Table 7.34. FEM Displacement LLDF Comparison with Test for Middle Path Loading

Test and Girder Type	Updated FEM LLDF (g_{FEM})	Calibrated FEM LLDF (g_{cal})	Test (g_{test})	g_{FEM}/g_{test}	g_{cal}/g_{test}
Stop Location Interior	0.162	0.167	0.195	0.83	0.86
Stop Location Exterior	0.078	0.074	0.076	1.03	0.99
Crawl Speed Interior	0.162	0.167	0.197	0.82	0.85
Crawl Speed Exterior	0.078	0.074	0.069	1.13	1.07

Table 7.35. Experimental, FEM, and AASHTO LLDFs for Middle Path Loading

Girder	G1	G2	G3	G4	G5	G6	G7	G8
Stop Location Test LLDF	0.076	0.085	0.179	0.141	0.195	0.163	0.097	0.064
Crawl Speed Test LLDF	0.069	0.084	0.172	0.143	0.197	0.159	0.109	0.065
Calibrated FEM Disp. LLDF	0.074	0.111	0.150	0.167	0.167	0.150	0.111	0.069
AASHTO Standard LLDF	0.231	0.231	0.231	0.231	0.231	0.231	0.231	0.231
AASHTO LRFD LLDF using simplified stiffness	0.238	0.344	0.344	0.344	0.344	0.344	0.344	0.238
AASHTO LRFD LLDF using analytical stiffness	0.238	0.339	0.339	0.339	0.339	0.339	0.339	0.238

Note: 1 – G = girder, Disp. = Displacement
2 – LLDF values are based on the midspan deflections.

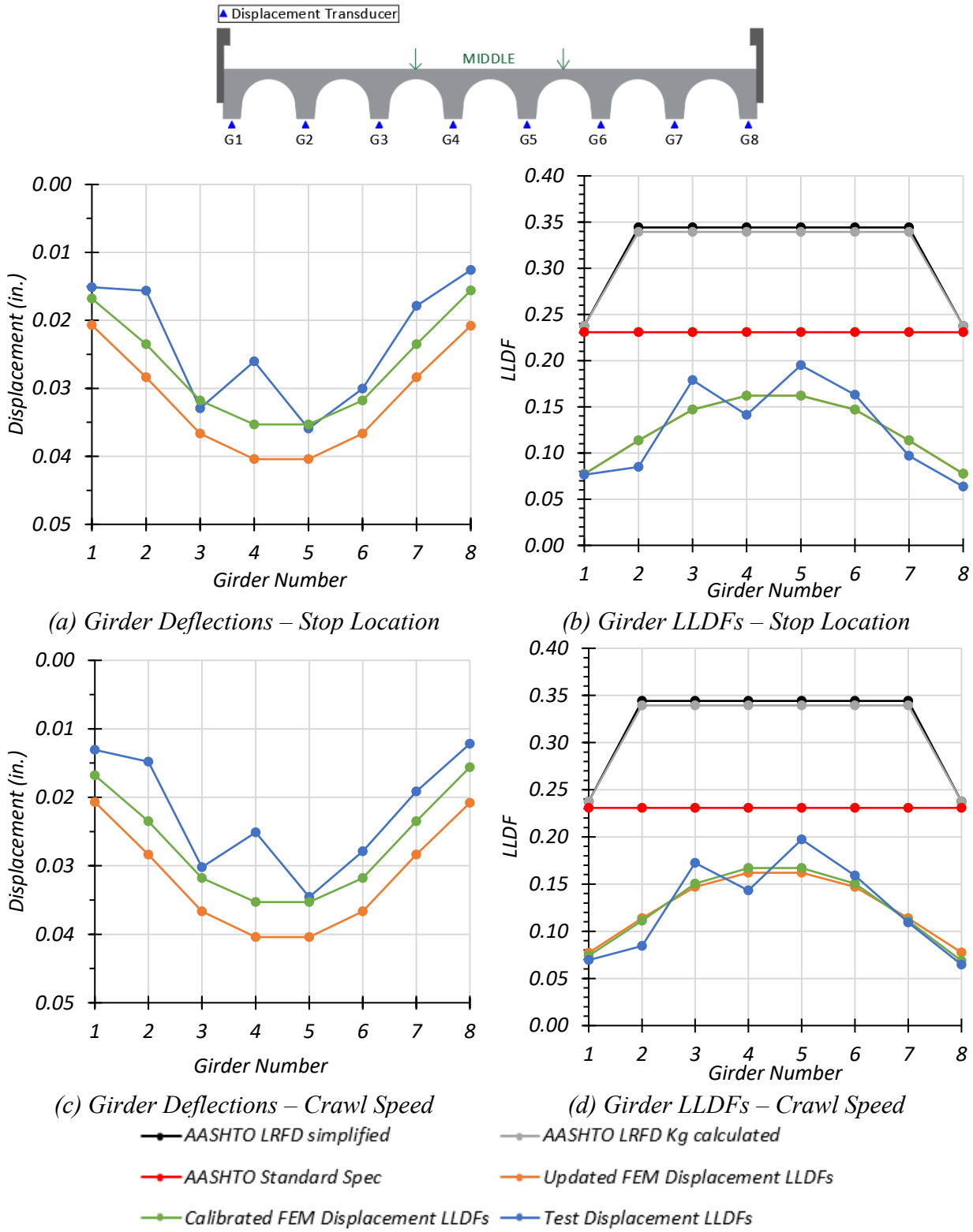

(a) Girder Deflections – Stop Location

(b) Girder LLDFs – Stop Location

(c) Girder Deflections – Crawl Speed

(d) Girder LLDFs – Crawl Speed

Figure 7.51. Comparison of Static Deflection Results with FEM for Middle Path Loading

7.8.3. Dynamic Characteristics of Bridge

The dynamic characteristics of the bridge obtained from the accelerometer data were compared with the updated and calibrated FEM results. The mode shape along the longitudinal section and transverse section for the first natural frequency compared with the updated FEM and calibrated FEM is shown in Figure 7.52. Figure 7.53 provides the mode shape along the longitudinal section and transverse section for the second natural frequency compared with the updated FEM and calibrated FEM. The mode shape along the longitudinal section and transverse section for the third natural frequency compared with the updated FEM and calibrated FEM is shown in Figure 7.54.

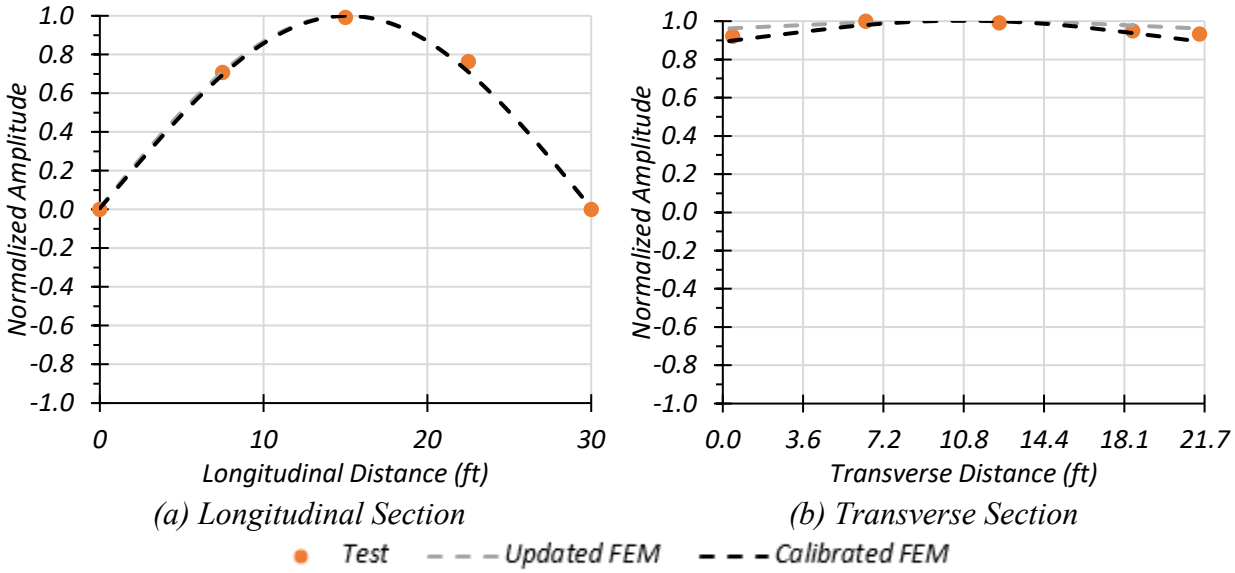

Figure 7.52. Mode Shape 1: Comparison of Experimental and FEM Results

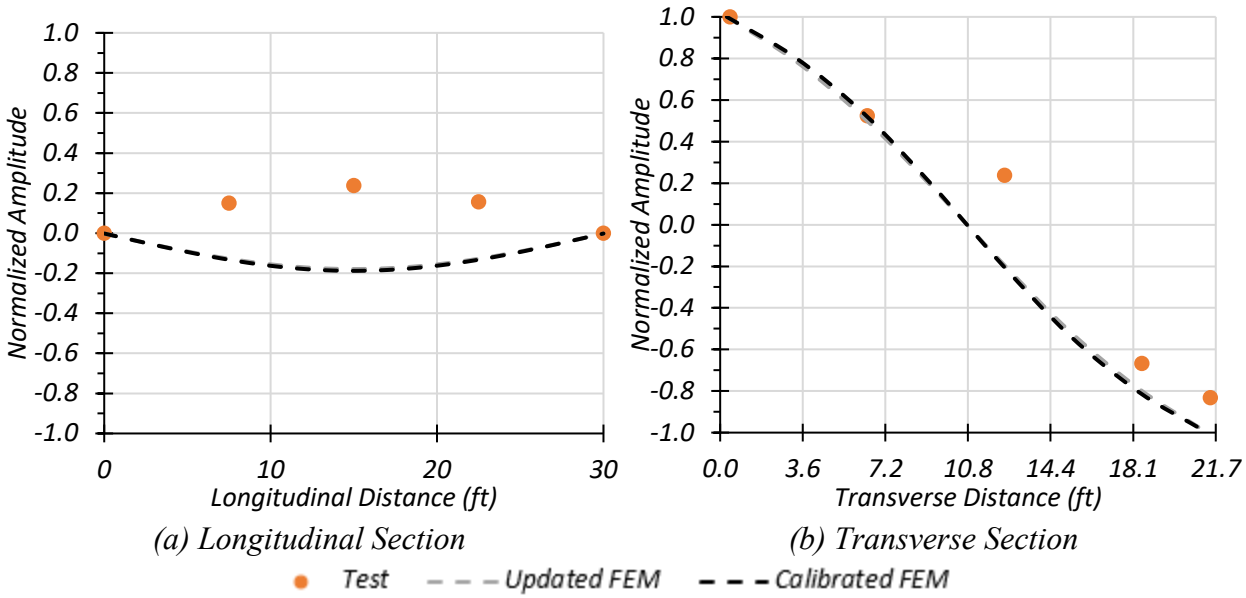

Figure 7.53. Mode Shape 2: Comparison of Experimental and FEM Results

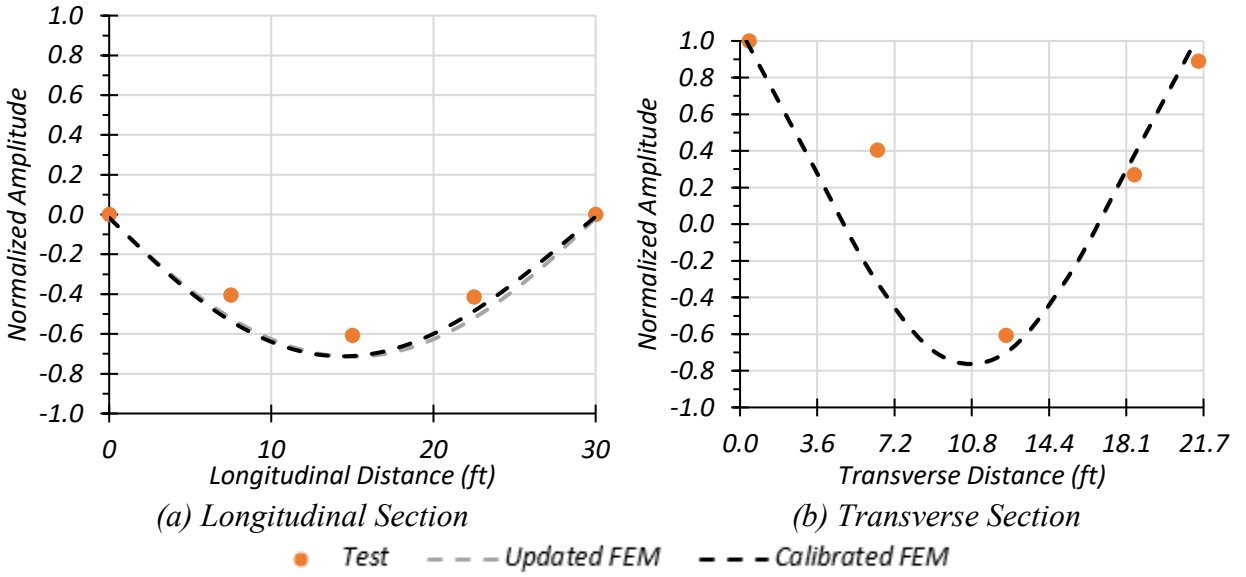

Figure 7.54. Mode Shape 3: Comparison of Experimental and FEM Results

The natural frequencies obtained from the FEM model and those observed during testing of Bridge CM-5 is provided in Table 7.36. The second and third natural frequencies obtained from the calibrated FEM model was closer to those obtained from the tests.

Table 7.36. Bridge CM-5 Test and FEM Natural Frequencies

Frequency	Test (Hz)	Updated FEM (Hz)	Calibrated FEM (Hz)
1st Natural Frequency	11.84	11.95	13.74
2nd Natural Frequency	16.60	14.73	16.94
3rd Natural Frequency	25.15	22.51	24.62

7.9. SUMMARY AND FINDINGS

In the following sections, a summary of the various findings is provided for Bridge CM-5.

7.9.1. Live Load Distribution Factors

The LLDFs calculated based on deflections compared well with those calculated from bending moments obtained from the FEM model. Hence, the experimental LLDFs for each test were calculated from the deflections obtained at midspan of the bridge.

In Section 7.6.1.2, the experimental LLDFs were compared with the FEM LLDFs and those calculated using the approximate equations in the AASTHO Standard Specifications (AASHTO 2002) and AASHTO LRFD Specifications (AASHTO 2017) with the simplified and analytical stiffness parameter. The AASTHO Standard Specifications and AASHTO LRFD Specifications provide conservative LLDFs for all girders. The AASHTO LRFD Specifications provide slightly conservative estimates for the exterior girder but are conservative for the interior girder.

Currently, TxDOT load rates simple-span concrete pan girder bridges using the AASTHO Standard Specifications LLDFs. These were not highly conservative when compared with the experimental LLDFs. Hence, refining the LLDFs would not significantly increase the load limit for such bridge types.

7.9.2. Updated Material Properties

The material strength of concrete comes into play in the calculation of RF. The 28-day concrete compressive strength of concrete for Bridge CM-5 was taken to be 4.0 ksi according to the standard drawing provided on the TxDOT website titled 'CG 30'-4" Spans' (TxDOT 2005). The section also shows a doubly reinforced section. However, NDE tests revealed that the actual concrete compressive strength was 7.0 ksi and that the section is singly-reinforced. Table 7.37 provides a comparison of the updated RFs calculated using the in-situ compressive strength of concrete with the originally calculated RFs. For the LFR approach, increasing the material strength by 75 percent does not significantly increase the RFs. Due to the poor condition rating of the substructure (Item 60 < 6), TxDOT's Off-System Load Rating flowchart (TxDOT 2018a) does not allow the posting to be removed. The bridge should be posted at inventory level with an inspection frequency of less than 2 years.

Table 7.37. Comparison of Bridge CM-5 Material Updated RFs to Original RFs

Rating Factor	Basic Load Rating	Load Rating with Measured Material Properties	Measured Material Properties/Basic Load Rating
Inventory	0.42	0.42	1.00
Operating	0.69	0.71	1.03

7.9.3. Calibrated FEM Model Demands

Calibrating the simply-supported FEM model against experimental results showed that there is some degree of end fixity present. The bending moment corresponding to the HS-20 design truck is obtained from the calibrated FEM model, which includes the effect of updated MOE of concrete, more accurate live load distribution, and updated boundary conditions due to slight end-fixity, and this value is used to determine the updated RF. Table 7.38 provides a comparison of the updated

RFs with the original RFs for a simply-supported bridge. Only the LFR results are shown in the table since this was the method used to load rate Bridge CM-5. Both the inventory RF and operating RF is greater than 1.0. Due to the poor condition rating of the substructure (Item 60 < 6), TxDOT's Off-System Load Rating flowchart (TxDOT 2018b) does not allow the posting to be removed. The bridge should be posted at inventory level with an inspection frequency of less than 2 years. The updated material strength coupled with the slight end fixity reduces the RFs for this bridge.

Table 7.38. Comparison of Bridge CS-9 Calibrated FEM Live Load RFs to Original RFs

Rating Factor	Basic Load Rating	Load Rating with Calibrated FEM Live Load	Calibrated FEM Live Load /Basic Load Rating
Inventory	0.42	0.40	0.95
Operating	0.69	0.67	0.97

8. EXPERIMENTAL TESTING OF BRIDGE CS-9

8.1. INTRODUCTION

In Chapter 4, basic load rating evaluation of 23 simple-span concrete slab (CS) bridges was conducted and an FEM model of a typical load posted bridge was developed using the commercial software package CSiBridge. The selected simple-span concrete slab bridge, CS-9, was load tested in the field. The purpose of the load test was to capture the in-situ behavior of the bridge including the effect of any potential fixity at the bridge ends and the equivalent strip width over which the vehicular loads are distributed. The results from the field tests are used to determine the transverse load distribution between curbs and the slab region. Any observed end fixity was also incorporated into the FEM model to more accurately model the in-situ boundary conditions of the bridge.

Several nondestructive evaluation methods were used to identify the concrete compressive strength and the layout of the reinforcing bars. The results of the NDE tests were used to update the FEM model of the bridge to represent the measured concrete compressive strength, and to confirm that there are no observed differences in reinforcement layout as compared to the reinforcement details provided in the structural drawings.

In addition to conventional measuring devices, such as string potentiometers, strain gauges and accelerometers, two cameras mounted on tripods recorded the bridge response during each load test. An image analysis algorithm was used to determine the displacements from the unloaded bridge image and loaded bridge image. A thorough investigation of the field test results along with the results from the updated and calibrated FEM models are used to determine potential updates to the load posting of the bridge and implications for load postings for similar bridge structures.

8.2. GENERAL DESCRIPTION OF BRIDGE CS-9

Bridge CS-9 has a deck condition rating of 6 (Satisfactory), a superstructure condition rating of 6 (Satisfactory), and a substructure condition rating of 6 (Satisfactory). The flexural resistance of concrete slab controls the rating of the bridge, which has an inventory gross load rating of 16 US tons and an operating gross load rating of 33.7 US tons. The bridge is posted for a 28,000-pound tandem axle. Figure 8.1 shows a transverse section detail and Figure 8.2 shows an elevation view and an underside view of Bridge CS-9.

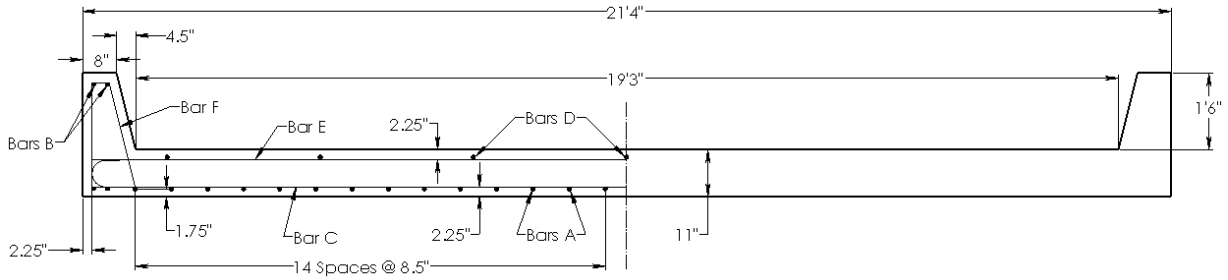

Figure 8.1. Transverse Section of Bridge CS-9 (adapted from TxDOT 2018b)

(a) Elevation View

(b) Underside View

Figure 8.2. Photographs of Bridge CS-9

8.3. IN-SITU MEASUREMENTS AND OBSERVATIONS

The in-situ concrete compressive strength of Bridge CS-9 was determined onsite using nondestructive test methods. The as-built geometric details were also measured to confirm the values provided in the structural drawings. The bridge was measured to be 25 ft in length and the total width was measured to be 21 ft 3 in. wide. The total depth from the top of curb to the bottom of the slab was measured to be 2 ft 5 in. These measurements agreed with the structural drawings of the bridge.

8.3.1. Nondestructive Evaluation Results

The compressive strength of concrete was determined onsite using two different rebound number test instruments – Original Schmidt Hammer and Silver Schmidt Hammer. The surface over which these tests were conducted was first ground smooth using angle grinder with masonry grinding wheel. The surface was further smoothened using a grinding stone. An indicator solution of phenolphthalein in ethanol was applied to the clean surface to check for carbonation of concrete. Concrete carbonation can affect the results obtained from these tests. If the indicator solution did not turn purple, the surface was further ground to reach the non-carbonated layer. Ten rebound number readings were obtained for both Schmidt Hammers by pushing it against the surface. As per the Original Schmidt Hammer operating instructions, the highest and lowest rebound numbers were removed and the average of the remaining eight rebound numbers was calculated. The Silver Schmidt Hammer was developed in accordance with the ASTM C805/C805M-18 (2018) guidelines. This test was carried out at two spots on the bridge: top of curb and side of bridge. The average rebound number for the Original Schmidt Hammer was calculated to be 46.1 at the top of curb and 41.5 at the side of the bridge. This corresponds to a concrete compressive strength of

approximately 7 ksi at the top of curb and 5.2 ksi at the side of the bridge, using the conversion curve in Figure 7.3. In this test, the hammer was pushed vertically down at the top of curb and horizontally onto the surface at the side of the bridge.

The Silver Schmidt Hammer uses the same principle and directly gives the compressive strength of concrete when within the applicable range. This test was carried out two times at the top of the curb and yielded concrete compressive strength values of 7.3 ksi and 5.2 ksi. Another region tested was the side of the bridge where the concrete compressive strength value was observed to be 9 ksi. The average of these values is approximately 7.2 ksi. Figure 7.4 provides the conversion chart used for Silver Schmidt Hammer rebound values.

Table 8.1 summarize the concrete compressive strength results obtained from NDE tests. It should be noted that the Ultrasonic Pulse Velocity (UPV) test could not be performed on this bridge due to the absence of parallel surface for the curbs and the presence of thick asphalt layer on the slab.

Table 8.1. Concrete Compressive Strengths from NDE Tests

Test	**Concrete Compressive Strength (ksi)**	
	Top of Curb	North Side of Bridge
Schmidt Hammer Test	7.0	5.2
Silver Schmidt Hammer Test	6.3	9.0

The lowest concrete compressive strength obtained from the NDEs was noted to be approximately 5.2 ksi. As a result, this strength and the corresponding modulus of elasticity was adopted in the updated FEM models.

8.4. DATA ACQUISITION AND INSTRUMENTATION FOR BRIDGE CS-9

The bridge instrumentation plan was developed to capture the maximum response of the bridge subjected to the different vehicle loading scenarios. The instruments used to measure the response of the bridge included strain gauges, string potentiometers, and accelerometers, which were connected to the data acquisition system for digitally recording the data.

8.4.1. Instrumentation Plan for Bridge CS-9

The instrumentation plan for the bridge was developed to record the response of the bridge subjected to the different loading scenarios. The instrumentation plan for Bridge CS-9 along with the cross-sectional views are shown in Figure 8.3. The labeling system used in the instrumentation plan is explained in Figure 7.6. The instrumentation labels for the data acquisition system are tabulated in Table 8.2.

The measured bridge response is used to identify the actual bridge behavior and live load distribution, and any potential areas of opportunity to increase or remove the load posting. Several goals were identified in determining the instrumentation types and locations, as follows.

- The data collected from the strain gauges are used to determine the neutral axis position and any unintended partial fixity at the supports.
- The midspan deflection data collected by the string potentiometers are used to infer experimental moment LLDFs that can be compared to the effective width values used for design, along with the estimated values from the FEM model of Bridge CS-9 and the AASHTO.
- The accelerometers collect vibration data used to compute the dynamic properties of the bridge.

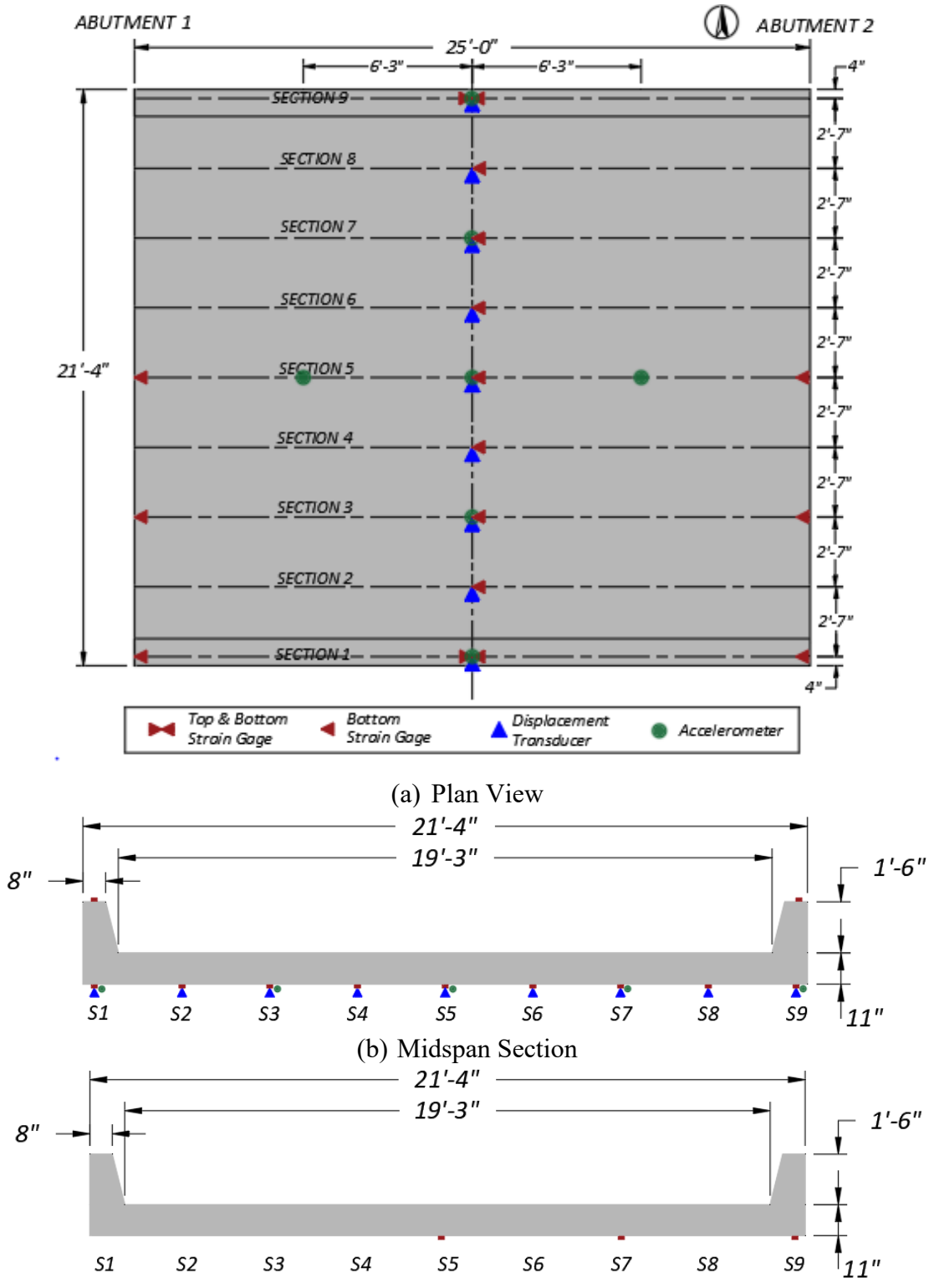

(a) Plan View

(b) Midspan Section

(c) End Section

Figure 8.3. Instrumentation Plan for Bridge CS-9

Table 8.2. Instrumentation Labels for Bridge CS-9

DAQ Box	Channel	Label	Type	DAQ Box	Channel	Label	Type
Strain Book	CH1	SG-9MB	PL-60	WBK 16-3	CH25	SP-3M	SM1-2
	CH2	SG-8MB	PL-60		CH26	SP-2M	SM1-2
	CH3	SG-7MB	PL-60		CH27	SP-1M	SM1-2
	CH4	SG-6MB	PL-60		CH28	-	
	CH5	SG-5MB	PL-60		CH29	-	
	CH6	SG-4MB	PL-60		CH30	-	
	CH7	SG-3MB	PL-60		CH31	-	
	CH8	SG-2MB	PL-60		CH32	-	
WBK 16-1	CH9	SG-1MB	PL-60	WBK 18	CH57	A-9M	4507 IEPE
	CH10	SG-9MT	PL-60		CH58	A-7M	4507 IEPE
	CH11	SG-1MT	PL-60		CH59	A-5M	4507 IEPE
	CH12	SG-9WB	PL-60		CH60	A-3M	4507 IEPE
	CH13	SG-7WB	PL-60		CH61	A-5W	4507 IEPE
	CH14	SG-5WB	PL-60		CH62	A-5E	4507 IEPE
	CH15	SG-9EB	PL-60		CH63	-	
	CH16	SG-7EB	PL-60		CH64	-	
WBK 16-2	CH17	SG-5EB	PL-60				
	CH18	-					
	CH19	SP-9M	SM1-2				
	CH20	SP-8M	SM1-2				
	CH21	SP-7M	SM1-2				
	CH22	SP-6M	SM1-2				
	CH23	SP-5M	SM1-2				
	CH24	SP-4M	SM1-2				

Notes:1 – Refer Figure 7.6 for explanation of the labeling system used

8.4.2. Data Acquisition System and Instrument Details

A total of 34 strain gauges (at 17 measurement locations using half-bridge circuits), nine string potentiometers, and seven accelerometers were installed on Bridge CS-9. Thirty-three channels in the data acquisition system were used. The strain gauges and string potentiometers were connected via cables to the main box (Measurement Computing StrainBook) and WBK16 extension module boxes. The accelerometer data were collected by the additional WBK18 extension module box. The data acquisition system is further described in Section 7.4.2.

8.4.2.1. Strain Gauges

A pair of strain gauges were installed at 17 measurement locations on the bridge to accurately capture the strain profile at the midspan and at the ends of the bridge near the supports. The strain gauge type used in Bridge CS-9 was Tokyo Measuring Instruments Lab PL-60-11-3LT and PL-60-11-3LJCT-F Strain Gauge. The main gauge was installed in the longitudinal direction while the temperature compensation gauge was installed transverse to it. Figure 8.4 shows a close-up of the installation of the concrete strain gauges. Strain gauges were installed along the bottom of the slab at nine different locations. Gauges were also installed on top of the both curbs at midspan. Strain gauges were installed at midspan and at an average of 6 in. from the bearing centerline at each abutment. The strains obtained from these gauges were used to determine the location of neutral axis across the section and identify unintended end fixity at the supports.

Figure 8.4. Close-Up of Strain Gauge Installation

8.4.2.2. String Potentiometers

Nine string potentiometers were installed at the midspan to record the midspan deflections during the vehicular load tests. Celesco SM1-2 string potentiometers having a 2.5 in. stroke were used at all nine locations.

8.4.2.3. Accelerometers

A total of seven Brüel & Kjær IEPE accelerometers were installed: five accelerometers at midspan and two accelerometers at quarter spans along center of the bridge to record the dynamic vibrations of the bridge during the dynamic load tests. The recorded vibrations were used to obtain the frequencies and the mode shapes of the bridge. The piezoelectric accelerometers are light, compact, and sensitive having resonance frequency of 18 kHz, which is much higher than the natural frequency of the bridge.

8.5. LOAD TESTING PROCEDURE FOR BRIDGE CS-9

A comprehensive test program was conducted to evaluate the performance and behavior of Bridge CS-9. The test program consisted of three parts: (1) static load tests, which consisted of stop location tests and crawl speed tests, and (2) dynamic load tests. The vehicular load testing of Bridge CS-9 was conducted on May 22, 2019.

8.5.1. Test Vehicle

The vehicle used in the load testing was a 2006 Sterling dump truck, provided by the TxDOT Bosque Office. The dump truck was loaded with base material to match the rear tandem axle weight to the load posting limit of a 28,000-pound tandem axle. The truck configuration and its empty and loaded weights are shown in Figure 8.5.

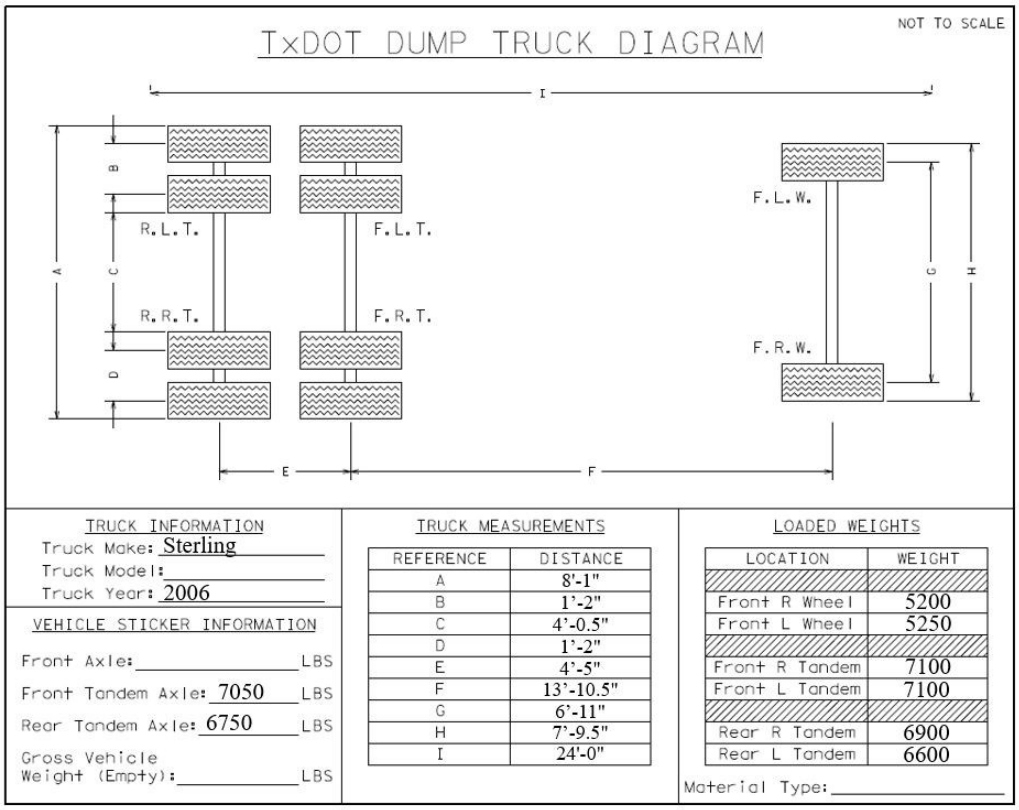

Figure 8.5. Wheel Weights and Spacing of the Loaded Dump Truck

8.5.2. Vehicle Positioning

Three transverse paths were defined across the bridge to create critical transverse loading positions for the bridge. The minimum allowable clearances from the curb and centerline of the bridge, as outlined in AASHTO Standard Specifications (AASHTO 2002) and AASHTO LRFD Specifications (AASHTO 2017), were adhered to when defining the paths. Figure 8.6 shows a schematic of the loading paths across the cross-section of the Bridge CS-9. Path 1 corresponds to the location where the centerline of the adjacent rear wheel of the dump truck is located 2 ft away from the face of the curb. Path 2 is defined along the second lane where the centerline of the adjacent rear wheel is located 1 ft 10 in. from the centerline of the bridge. Due to the narrow width of the bridge, the minimum clearance of 2 ft from the centerline could not be met. A third path

was defined along the centerline of the bridge, called Middle Path, where the dump truck ran along the center of the bridge with the wheel lines equidistant from the bridge centerline.

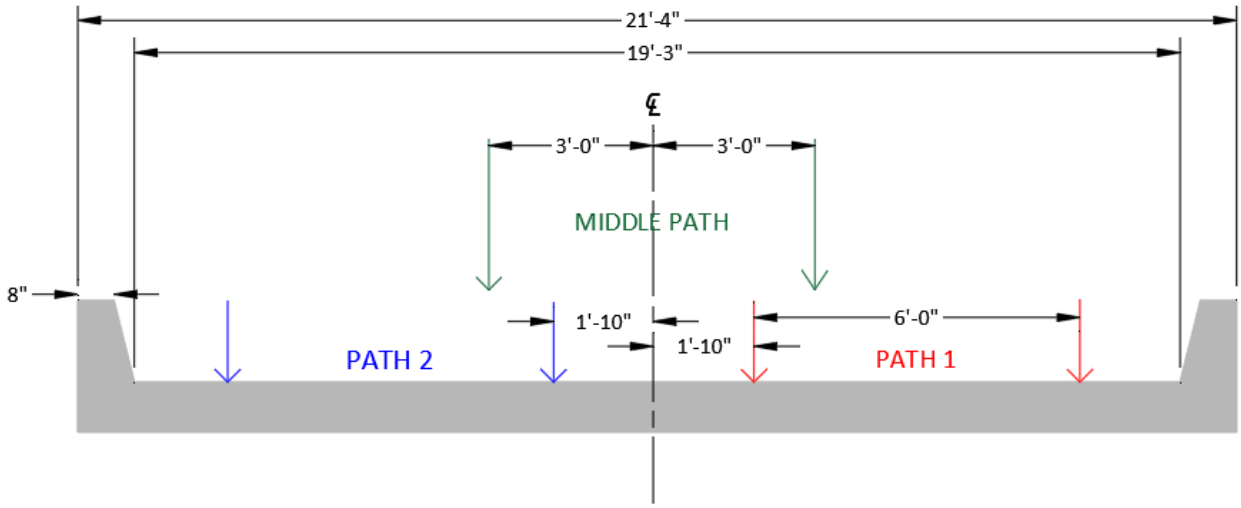

Figure 8.6. Load Test Paths for Bridge CS-9

8.5.3. Test Protocol

Bridge CS-9 was subjected to static, crawl speed, and dynamic tests. Sledge hammer tests were also conducted to capture the dynamic properties of the bridge. In the following sections, details regarding each test are outlined. Table 8.3 lists the test protocol carried out for load testing of Bridge CS-9.

Table 8.3. Test Protocol for Bridge CS-9

Test Number	Load Position	Test Type
1	Path 1	Static – Stop Location (Engine running)
2	Path 1	Static – Crawl Speed
3	Path 1	Dynamic (31 mph)
4	Path 1	Dynamic (41 mph)
5	Path 2	Static – Stop Location (Engine running)
6	Path 2	Static – Crawl Speed
7	Path 2	Dynamic (30 mph)
8	Path 2	Dynamic (40 mph)
9	Middle Path	Static – Stop Location (Engine running)
10	Middle Path	Static – Crawl Speed
11	Middle Path	Dynamic (29 mph)
12	Middle Path	Dynamic (40 mph)
13	Path 1	Static – Stop Location (Engine off)
14	Path 2	Static – Stop Location (Engine off)
15	Middle Path	Static – Stop Location (Engine off)
16	Middle Path	Dynamic (20 mph)
17	Middle Path	Dynamic (59 mph)
18	North	Sledgehammer
19	Middle Path	Sledgehammer
20	South	Sledgehammer
21	North West	Sledgehammer
22	Mid West	Sledgehammer
23	South West	Sledgehammer
24	North East	Sledgehammer
25	Mid East	Sledgehammer
26	South East	Sledgehammer
27	North Curb Middle	Sledgehammer
28	South Curb Middle	Sledgehammer

8.5.3.1. Static Tests

The static load tests conducted on Bridge CS-9 were of two types: (1) Stop Location Test, and (2) Crawl Speed Test. For each static test along Path 1, Path 2, and the Middle Path, reference data were recorded prior to the bridge being loaded. The truck was positioned on the bridge such that

the maximum bending moment would be obtained at midspan of the bridge. This was achieved when the rear tandem and front tandem axles of the truck were located equidistant from the midspan location of the bridge. Due to the short span of Bridge CS-9, the front axle of the truck was off the bridge for each static test. Once the truck was positioned and the engine was turned off, data for the loaded bridge was recorded.

Reference files prior to the truck crawling at a slow speed over the bridge were recorded for each test. Then the data were recorded while the truck passed over the entire span of the bridge at an idle speed of 2-3 mph.

8.5.3.2. Dynamic Tests

Prior to each test, reference files for the unloaded bridge was recorded. The truck picks up a pre-determined speed and passes over the entire span of the bridge while maintaining the speed. The corresponding data were recorded. The dynamic tests were carried out at two different speeds. The first test for each path was conducted for a speed of 30 mph and the second test was carried out for a speed of 45 mph. Additional dynamic tests were conducted along the middle path at 20 mph and 60 mph. The speed limit for the road on which the bridge was located was noted to be 65 mph.

8.5.3.3. Impact Tests

A sledge hammer was used to hit the deck of the bridge three times at eleven different transverse positions to excite different modes of the bridge. The recorded vibration data were used to determine the dynamic properties of Bridge CS-9. The impact tests were carried out at three midspan locations: at north side of the bridge, at transverse center of the bridge, and at south side of the bridge; at the three locations along the west end of the bridge; at the three locations along the east end of the bridge; and at midspans of both curbs.

8.5.4. Test Operations

The testing schedule for Bridge CS-9 spanned over three days from May 20-22, 2019. This includes all instrumentation installation, load testing, and instrumentation removal.

The clearance height to the underside of the bridge was approximately 12 ft. Thus, there was no need for scaffolding. All instrumentation was installed on the underside of the bridge during the first two days with the use of step ladders. The installation locations were marked as per the instrumentation plan. An angle grinder, with masonry grinding wheel, was used to grind an approximately 4 x 4 in. area at locations where the strain gauges were to be installed. The surface was made smooth using 150 and 220 grit sandpapers and then cleaned with acetone. The surface was repeatedly cleaned with acetone applied to paper towels, until a clean tip is no longer discolored by the scrubbing. Liberally applying acetone brings the surface pH back to an optimum alkalinity of 7.0 to 7.5 pH, ideal for bonding of the glue. Any microscopic gaps or cracks on the concrete surface were filled with the application of an epoxy. Once the epoxy cured, the surface was again made smooth with sandpaper and cleaned with acetone as previously described. The strain gauges were installed onto the surface with a suitable adhesive after the surface had dried.

For string potentiometers, nine wooden posts were hammered into the ground and the string potentiometers were screwed onto the posts. Metal hooks were installed on the underside of the slab at midspan and fishing line was attached from the hooks to the string potentiometers. Accelerometers were attached to metal plates glued onto the bottom of slab at selected locations. Figure 8.7 shows the installed instrumentations for Bridge CS-9.

The nondestructive load tests were conducted on May 22, 2019. The designated paths were marked on the bridge with duct tapes. The DAQ system was set up and the cables from all instrumentation attached to the DAQ boxes. The dump truck was loaded approximately to the

posted load limit at the Texas Department of Transportation, Bosque maintenance office. The 28 tests listed in the test protocol were carried out and the corresponding data recorded. Figure 8.8(a) and Figure 8.8(b) shows the set-up for Test 1 and Test 5, respectively. After the completion of all tests, all the instruments were removed.

(a) Installed Strain Gauges

(b) Installed Accelerometer

(c) Installed String Potentiometers

Figure 8.7. Installed Instrumentation for Bridge CS-9

(a) Static Test along Path 1

(b) Dump Truck Positioned for Static Test along Path 2

Figure 8.8. Testing of Bridge CS-9

8.6. TEST RESULTS FOR BRIDGE CS-9

The data recorded during the load test was processed, analyzed, and filtered for noise, if necessary. The slab was divided into nine transverse sections and the corresponding data were recorded. Strain gauge data were used to determine the strain profile within the section depth. String potentiometers recorded the deflections across the bridge width, from which the distribution of load across the bridge was determined. The dynamic properties of the bridge, such as natural frequencies and mode shapes, were obtained from the vibration data recorded by the accelerometers. An image analysis algorithm was used to determine the deflections from the videos recorded during each test. These results are provided in the following sections.

8.6.1. Static Load Tests on Bridge CS-9

Two types of static load tests were performed on Bridge CS-9, stop location tests and crawl speed tests. During the stop location tests, the truck was positioned on the bridge such that the maximum bending moment would be obtained at midspan. This was carried out twice: once with the engine running and a second time with the engine turned off. During crawl speed test, the truck passed over the entire span of the bridge at a crawl speed of approximately 2-3 mph.

8.6.1.1. Strain Measurements

The strain gauge data for each test was compiled. For the stop location test, the maximum strain occurring at each strain gauge location was obtained. For the crawl speed test, the maximum bottom strain in the transverse section and the corresponding time at which this occurs was first obtained. All other strain values were extracted for that specific time. It should be noted that the tensile strains are taken to be positive and the compressive strains are negative. The neutral axis location for each exterior section was determined from the strain profile at midspan. Top strain

gauges could not be installed at the midspan of the bridge for interior slab sections on the roadway due to the thick layer of asphalt. It should be noted that the strain values obtained from the bottom strain gauge attached at the midspan of the transverse section S5 were very high and seem to indicate an issue with the gauge, possibly due to existing cracking in concrete.

8.6.1.1.1. Exterior Sections 1 & 9 - Path 1 Loading

Strain profiles corresponding to the top and bottom strains for the exterior Section S1 and Section S9 under static tests along Path 1 are provided in Figure 8.9. The strain profiles at the midspan of Section S1 are shown in Figure 8.9(a) for the stop location test and Figure 8.9(c) for the crawl speed test. The neutral axis depth at midspan of the curb was found to be 12.55 in. from the bottom face using the strain profile obtained from the stop location test and 14.56 in. from the bottom face using the strain profile obtained from the crawl speed test. The neutral axis depth calculated using the strain profile obtained from the crawl speed test is slightly higher than the one obtained from the stop location test. This could be due to the stop location test being slightly different from the moment critical position for absolute maximum moment. Moreover, the transverse location of truck may be slightly different between the stop location test and crawl speed test.

The strain profiles at the west end, midspan and east end of Section S9 are shown in Figure 8.9(b) for the stop location test and Figure 8.9(d) for the crawl speed test. The strain at the west and east ends of Section S9 are compressive for both the stop location test and crawl speed test, indicating some degree of end fixity present. The neutral axis depth at midspan of the curb was found to be 5.79 in. from the bottom of Section S9 using the strain profile obtained from the stop location test and 4.96 in. from the bottom of Section S9 using the strain profile obtained from the crawl speed test.

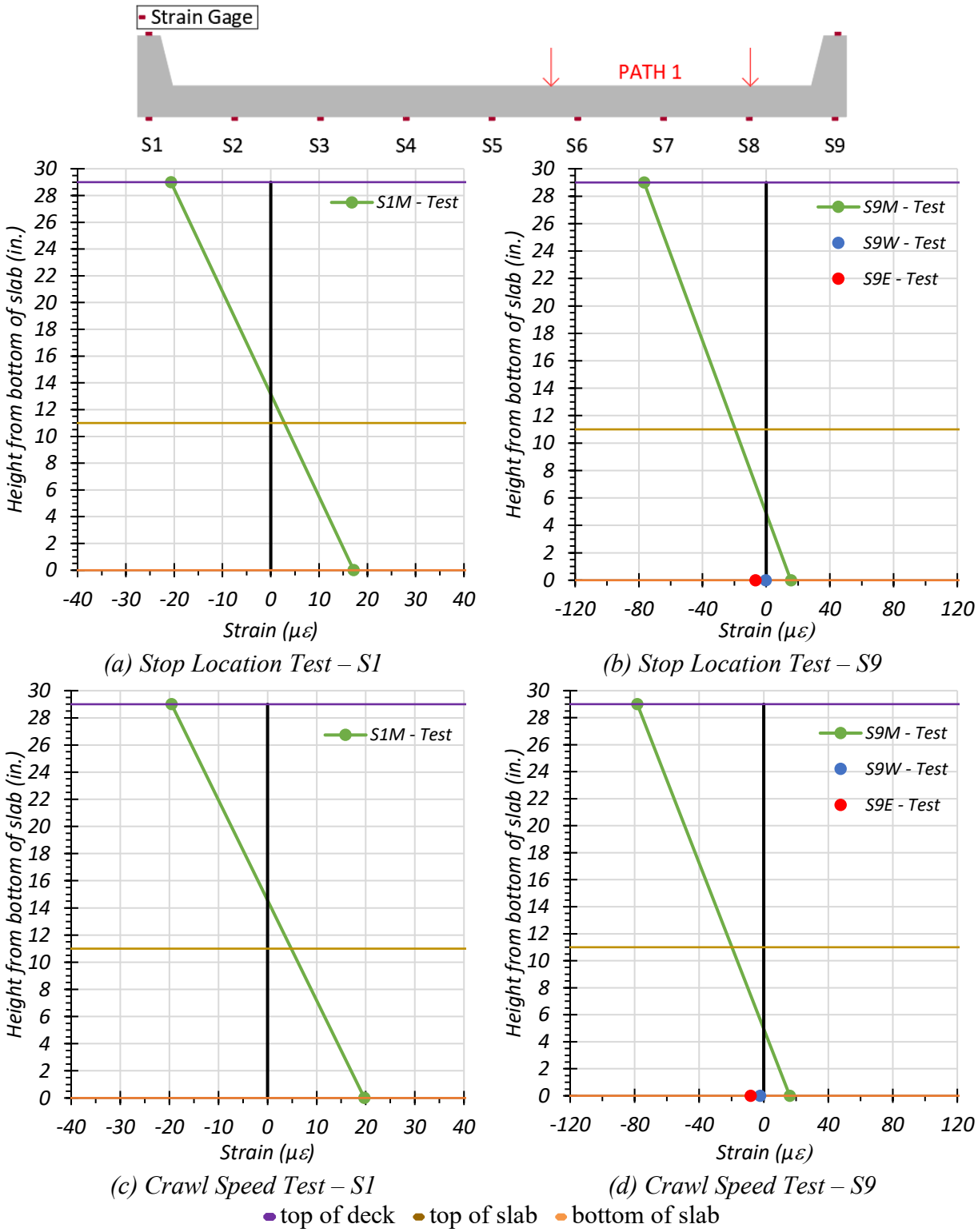

(a) Stop Location Test – S1

(b) Stop Location Test – S9

(c) Crawl Speed Test – S1

(d) Crawl Speed Test – S9

Figure 8.9. Static Strains for Exterior Sections – Path 1

8.6.1.1.2. Exterior Sections 1 & 9 - Path 2 Loading

Strain profiles corresponding to the top and bottom strains for the exterior Section S1 and Section S9 under static tests along Path 2 are provided in Figure 8.10.

The strain profiles at the midspan of Section S1 are shown in Figure 8.10(a) for the stop location test and Figure 8.10(c) for the crawl speed test. The neutral axis depth at midspan of the curb was found to be 13.28 in. from the bottom using the strain profile obtained from the stop location test and 13.50 in. from the bottom using the strain profile obtained from the crawl speed test. The neutral axis depth calculated using the strain profile obtained from the crawl speed test is slightly higher than the one obtained from the stop location test. This also could be due to the stop location test being slightly different from the moment critical position for absolute maximum moment. Moreover, the transverse location of truck may be slightly different between the stop location test and crawl speed test.

The strain profiles at the west end, midspan and east end of Section S9 are shown in Figure 8.10(b) for the stop location test and Figure 8.10(d) for the crawl speed test. The strain at the east ends of Section S9 are compressive for both the stop location test and crawl speed test, indicating some degree of end fixity present. However, the strain at the west end is tensile for the stop location test and compressive for the crawl speed test. The difference at the end strains for both tests may be due to the truck stop location not being exactly at the moment critical position. The neutral axis depth at midspan of the curb was found to be 4.71 in. from the bottom of Section S9 using the strain profile obtained from the stop location test and 4.56 in. from the bottom of Section S9 using the strain profile obtained from the crawl speed test.

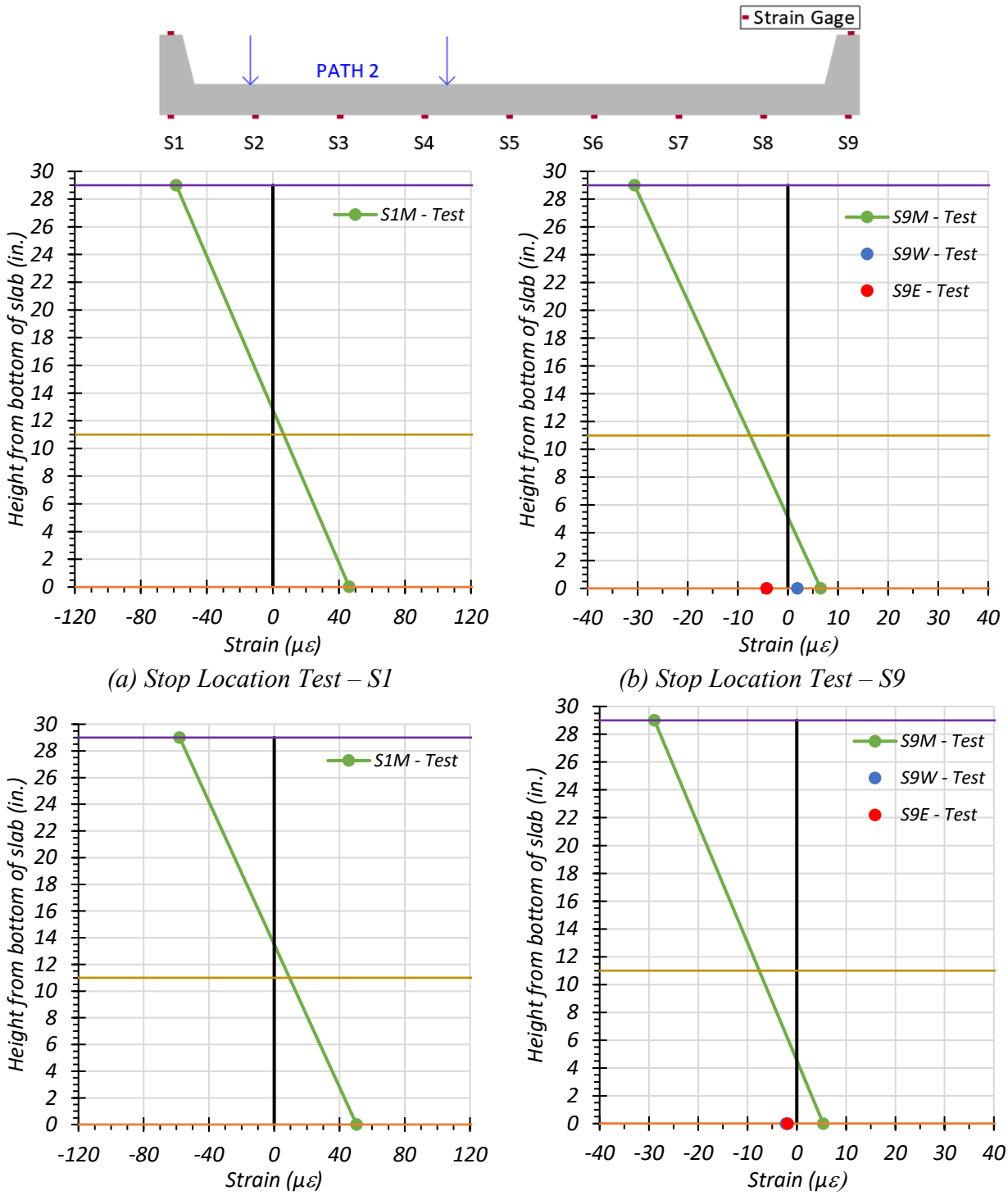

Figure 8.10. Static Strains for Exterior Sections – Path 2

8.6.1.1.3. Exterior Sections 1 & 9 - Middle Path Loading

Strain profiles corresponding to the top and bottom strains for the exterior Section S1 and Section S9 under static tests along the Middle Path are provided in Figure 8.11.

The strain profiles at the midspan of Section S1 are shown in Figure 8.11(a) for the stop location test and Figure 8.11(c) for the crawl speed test. The neutral axis depth at midspan of the curb was found to be 13.57 in. from the bottom of Section S1 using the strain profile obtained from the stop location test and 12.95 in. from the bottom of Section S1 using the strain profile obtained from the crawl speed test. The neutral axis depth calculated using the strain profile obtained from the stop location test is slightly higher than the one obtained from the crawl speed test. This could be due to the stop location test being slightly different from the moment critical position for absolute maximum moment. Moreover, the transverse location of truck may be slightly different between the stop location test and crawl speed test.

The strain profiles at the west end, midspan and east end of Section S9 are shown in Figure 8.11(b) for the stop location test and Figure 8.11(d) for the crawl speed test. The strain at the west end of Section S9 is tensile for both the stop location test and crawl speed test, indicating the absence of any significant end restraint. The bottom strain at the east end of Section S9 are compressive for both the stop location test and crawl speed test, indicating some degree of end fixity present. The difference at the end strains for both tests may be due to the truck stop location not being exactly at the moment critical position. The neutral axis depth at midspan of the curb was found to be 5.23 in. from the bottom of Section S9 using the strain profile obtained from the stop location test and 4.63 in. from the bottom of Section S9 using the strain profile obtained from the crawl speed test.

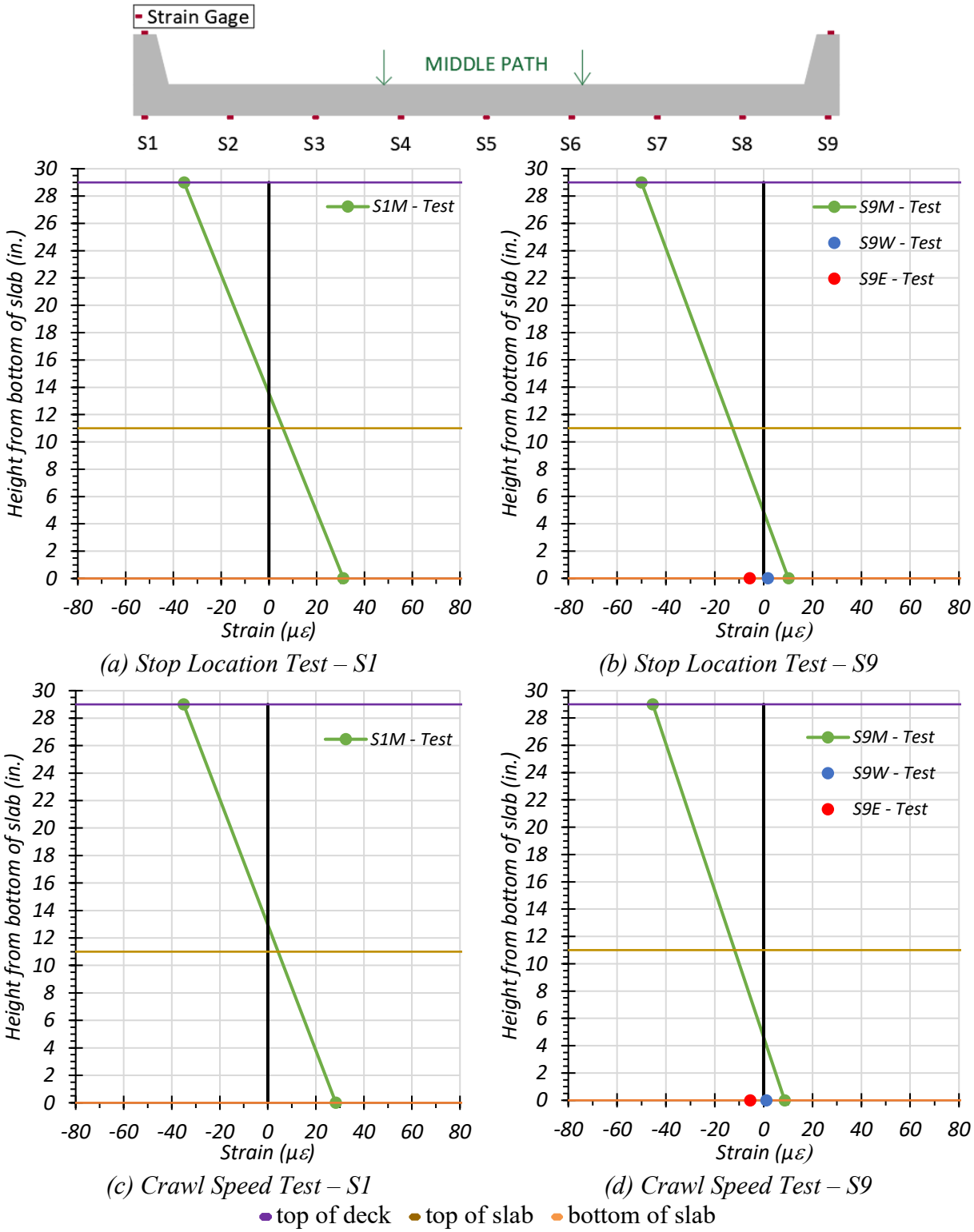

(a) Stop Location Test – S1

(b) Stop Location Test – S9

(c) Crawl Speed Test – S1

(d) Crawl Speed Test – S9

Figure 8.11. Static Strains for Exterior Sections – Middle Path

8.6.1.1.4. Comparison of Measured Strain Results

Theoretical calculations to determine the neutral axis depth for a cracked and uncracked concrete section were carried out for both an exterior and interior transverse section. A typical transverse section, along with the reinforcement information from the structural drawings, is provided in Figure 8.12. The curbs consisted of 2-1.25 in. square bottom reinforcement while the bottom reinforcement in the slab consisted of #8 bars at 8.5 in. centers. The modulus of elasticity for concrete was calculated using the following equation valid for normal weight concrete with unit weights between 0.09 and 0.155 kcf and design compressive strength up to 15.0 ksi as per Article 8.7 in the AASHTO Standard Specifications (AASHTO 2002).

$$E_c = 33{,}000 K_1 w_c^{1.5} \sqrt{f_c'} \tag{8.1}$$

where:

E_c = Elastic modulus of concrete, ksi

K_1 = Correction factor for source of aggregate, to be taken as 1.0 unless determined by physical test

w_c = Unit weight of concrete, kcf

f_c' = Compressive strength of concrete, ksi

The modulus of elasticity for concrete was calculated to be 4809 ksi based on the measured f_c' of 5.2 ksi. The theoretical position of the neutral axis depth was determined to be 13.33 in. from the bottom for the curb and 5.50 in. from the bottom of the slab for an uncracked concrete section. For a cracked concrete section, the neutral axis depth was calculated to be 21.43 in. from the bottom of the curb and 8.29 in. from the bottom of the slab.

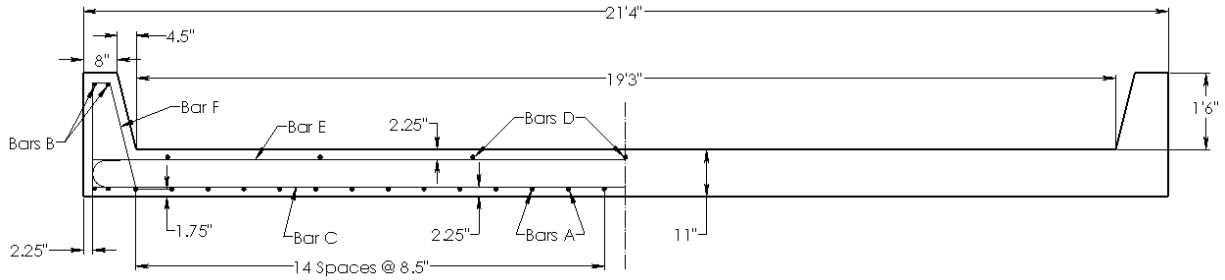

Bill of Reinforcing Steel One Slab					
Bar	**No.**	**Size**	**Space**	**Length**	**Weight**
A	28	1”ϕ	8 ½”	26’-9”	2000 lb.
B	8	1 ¼”□	4”	27’-4”	1162 lb.
C	40	5/8” ϕ	7 ½”	22’-3”	928 lb.
D	7	1/2”ϕ	36”	24’-8”	115 lb.
E	17	1/2”ϕ	18”	21’-1”	239 lb.
F	50	1/2”ϕ	12”	6’-10”	228 lb.

Figure 8.12. Transverse Section of Bridge CS-9 (adapted from TxDOT 2005)

Table 8.4 lists the midspan neutral axes corresponding to all the different tests. Figure 8.13 compares the neutral axes obtained from the static tests with the theoretical neutral axis for both Section S1 and Section S9. The neutral axes determined from the tests are closer to the theoretical uncracked neutral axis for Section S1. However, the neutral axis depth is lower for the transverse Section S9. This may be due to the stiffness of Section S1 being smaller as compared to Section S9.

Table 8.4. Measured Neutral Axis Locations for Exterior Sections - Static Load Tests

Test	S1 Neutral Axis Location (in. from bottom of slab)	S9 Neutral Axis Location (in. from bottom of slab)
Path 1 – Stop Location	15.80	5.79
Path 1 – Crawl Speed	14.56	4.96
Path 2 – Stop Location	12.59	6.17
Path 2 – Crawl Speed	13.50	4.56
Middle Path – Stop Location	13.53	5.78
Middle Path – Crawl Speed	12.95	4.63
Theoretical Uncracked	13.33	
Theoretical Cracked	21.43	

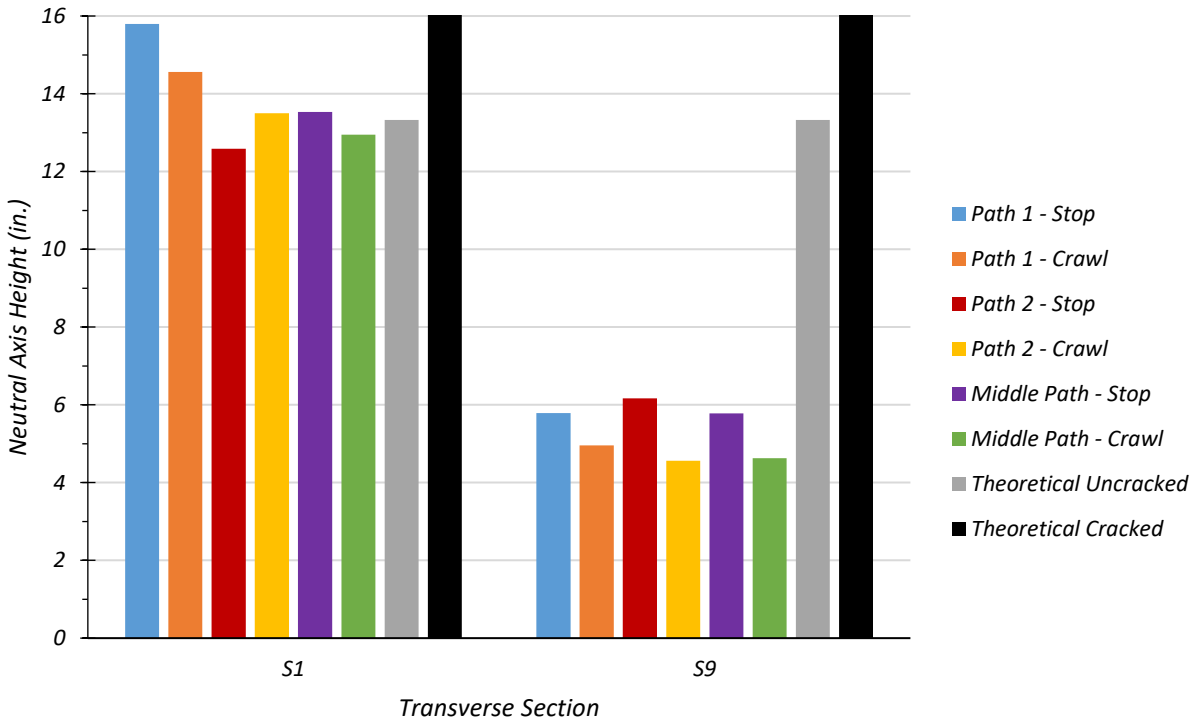

Figure 8.13. Test Neutral Axis Locations

Due to very large compressive strain values (around $-200\ \mu\varepsilon$) obtained from transverse Section S5, which indicates a gauge issue leading to errors in the measured strains, these strain values have not been plotted in the following figures. Figure 8.14 shows the distribution of strain across the bottom of the bridge width for Path 1 loading. The strain distribution across the bottom

of the bridge for Path 2 loading is shown in Figure 8.15. Figure 8.16 shows the bottom strain distribution across the bridge width for Middle Path loading. As anticipated, the strains obtained from the crawl speed test were generally higher that those obtained from the stop location test. However, the strain obtained for the Section S6 is compressive for both the stop location test and crawl speed test for Path 1 and Middle Path loading, an unexpected result. The strains obtained at Section S4 are consistently high for all loading paths. Because the recorded strains for Section S4 are inconclusive, they are presented with black open circles in the following plots.

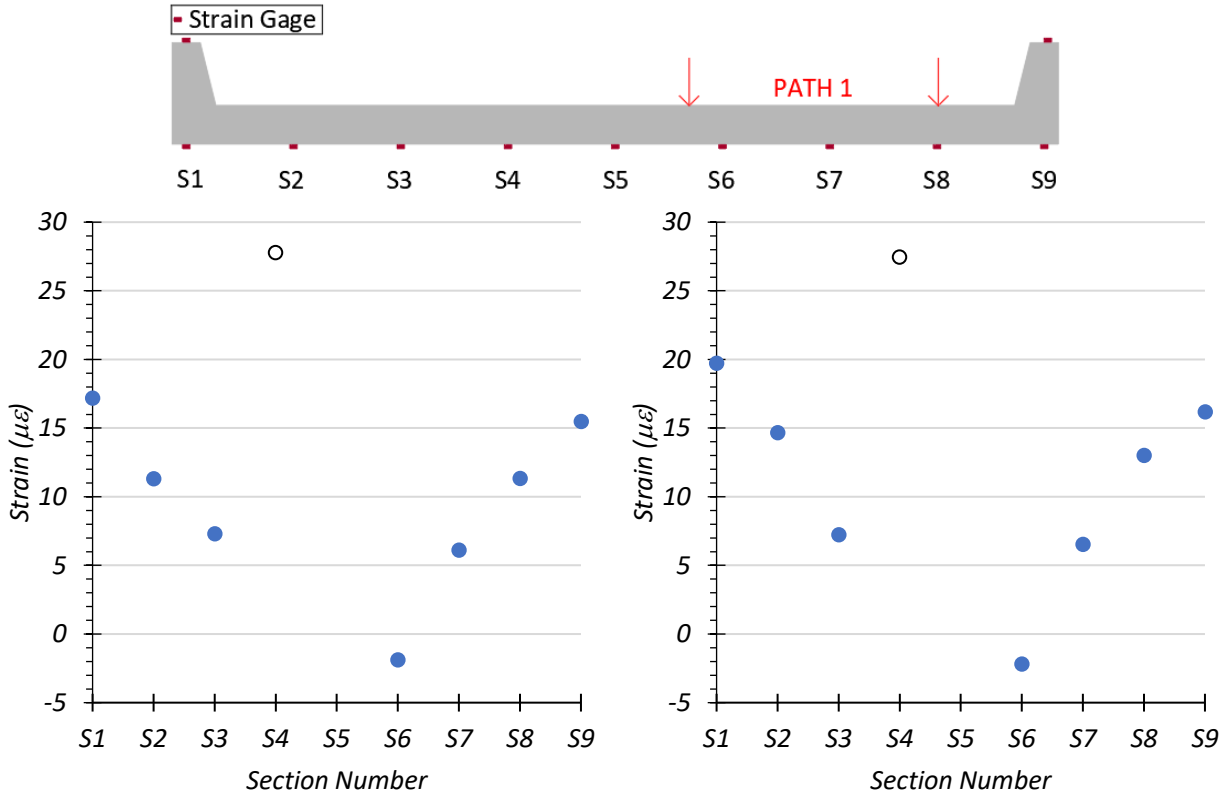

(a) Stop Location Test *(b) Crawl Speed Test*

Figure 8.14. Static Strains across Bridge Width – Path 1

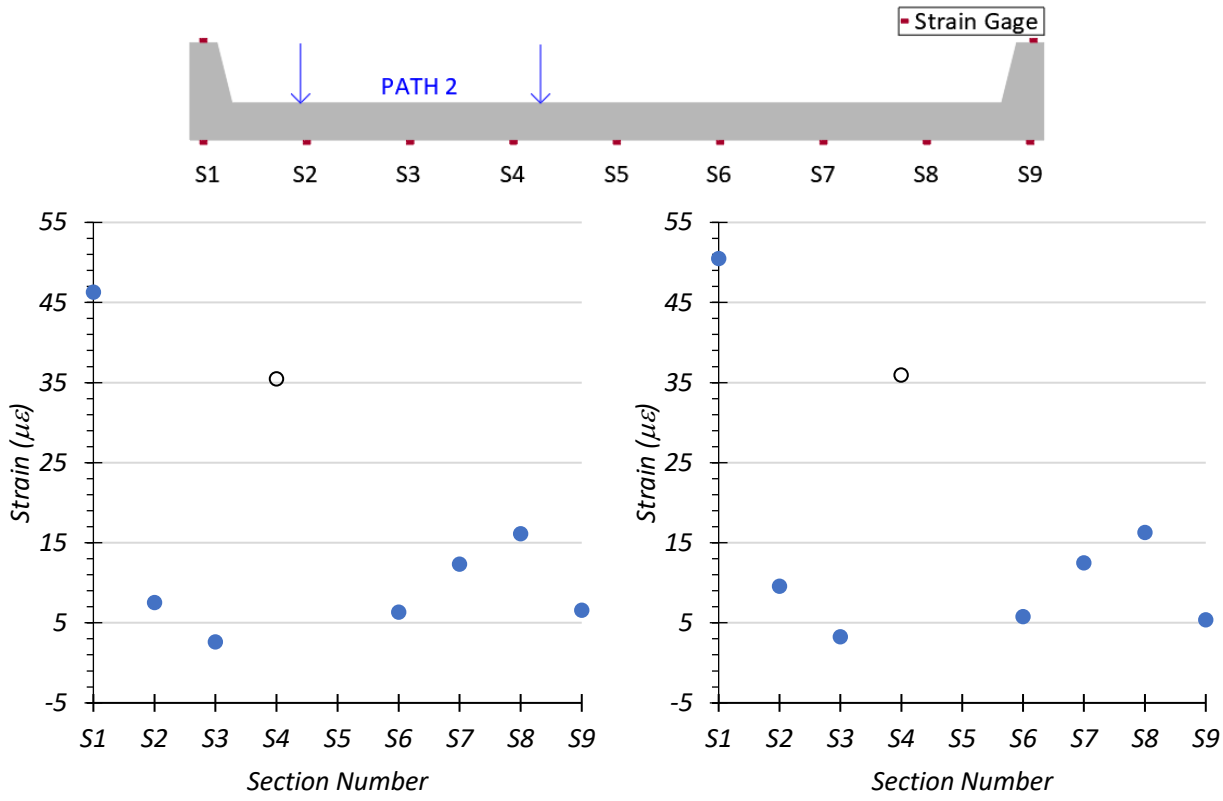

(a) Stop Location Test *(b) Crawl Speed Test*

Figure 8.15. Static Strains across Bridge Width – Path 2

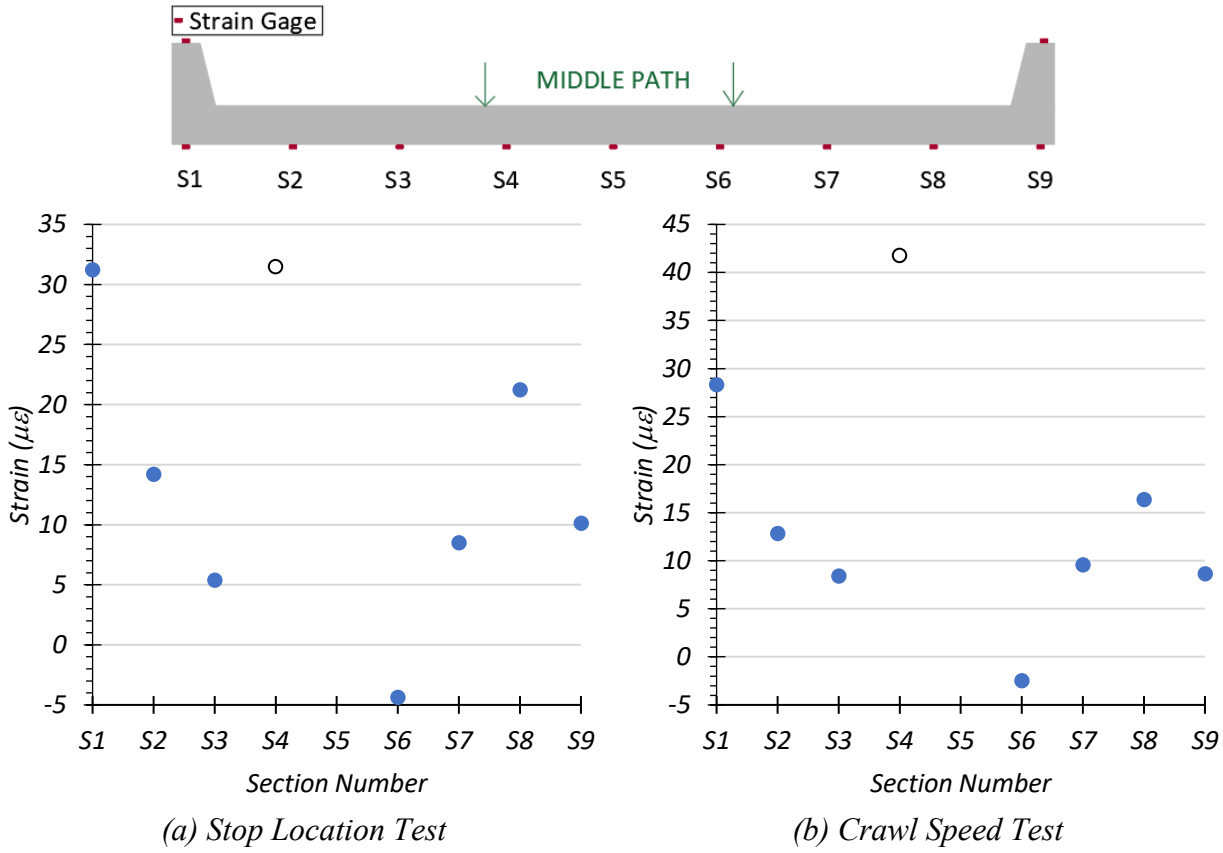

(a) Stop Location Test *(b) Crawl Speed Test*

Figure 8.16. Static Strains across Bridge Width – Middle Path

No significant trends can be observed from the plots of the distribution of strain measured across the bottom of the bridge width at midspan for the different loading scenarios. The measured strains were deemed to provide insufficient information to determine LLDFs with an acceptable level of confidence. In general, the use of bonded gauges can be influenced by cracks at or near a gauge. In the case of an existing bridge, this can be difficult to avoid, particularly when placing gauges in key locations, as for this test. In the following section, LLDFs are calculated using the recorded deflections.

8.6.1.2. Deflection Measurements and LLDFs

The deflection for each transverse section was recorded over a period of time for each test. The maximum downward deflection for each section was obtained. The corresponding LLDF for each section was calculated using Eqn. (8.2). The equivalent width for the slab portion was calculated as the width of the transverse section divided by the maximum LLDF.

$$LLDF = \frac{\Delta_i I_i}{\sum \Delta_i I_i} \tag{8.2}$$

where:

$LLDF$ = Live load distribution factor

Δ_i = Maximum vertical deflection of section *i,* in.

I_i = Cracked moment of inertia of section *i*, in^4

The equivalent width for the slab portion was calculated as the width of the transverse section $W_{Section}$ divided by the maximum LLDF of the slab sections (S3 through S7) as shown in Eqn. (8.3). The interior transverse sections were each 2'-7" wide.

$$E = \frac{W_{Section}}{LLDF_{max}} \tag{8.3}$$

8.6.1.2.1. Path 1 Loading

The measured deflection for all transverse sections along with the LLDFs for the stop location test and crawl speed test along Path 1 are provided in Table 8.5. For both the stop location test and crawl speed test, the maximum exterior section deflection was observed in Section S9 and the maximum interior section deflection was observed in Section S6. This was due to the close

proximity of these sections to the wheel lines. The corresponding LLDF for Section S9 was 0.602 for the stop location test and 0.593 for the crawl speed test. Section S6 had an LLDF of 0.052 for the stop location test and 0.050 for the crawl speed test.

Table 8.5. Experimental Deflections and LLDFs for Path 1 Loading

Section	S1	S2	S3	S4	S5	S6	S7	S8	S9
Stop Location Test Disp. (in.)	0.006	0.011	0.019	0.028	0.035	0.039	0.035	0.036	0.029
Stop Location Test LLDF	0.122	0.015	0.026	0.037	0.048	0.052	0.047	0.049	0.602
Crawl Speed Test Disp. (in.)	0.006	0.012	0.019	0.025	0.032	0.035	0.033	0.034	0.027
Crawl Speed Test LLDF	0.129	0.017	0.028	0.037	0.047	0.050	0.048	0.050	0.593
Note: 1 – S = Section, Disp. = Displacement 2 – LLDF values are based on the midspan deflections.									

The LLDFs computed based on the full bridge width results result in very large equivalent width values (50 - 52 ft). Therefore, the IB346 concept (discussed further in Section 8.6.1.3.1) of defining the L-curb for integral curb and slab bridges is used. Table 8.6 tabulates the step-by-step calculations for the equivalent width of the interior slab section for the stop location test. The IB346 concept of the L-curb (curb section plus 4*h* of the slab) is introduced in this table by considering the combined effect of Sections S1 and S2 and Sections S8 and S9. The bottom width of the curb is 12.5 in. and the thickness of the slab is 11 in. Thus, the total width of the L-curb section is 56.5 in. The deflection for the left L-curb is calculated at the section centroid (23.0 in. from the bridge edge) by linearly interpolating between the deflections for Section S1 and Section S2. This approach is also applied to the right L-curb by interpolating between Section S8 and Section S9. The moment of inertias of the cracked L-curb sections and the interior slab section is presented in the table. The LLDFs are calculated using Eqn. (8.2). The factor *g* refers to the proportion of the total live load taken by each component, the L-curb sections and the mid-slab

section. Eqn. (8.3) is used to calculate the equivalent width for the interior slab portion. For the stop location test, the maximum LLDF for the interior slab portion is 0.153 and the corresponding equivalent width is 16.88 ft. The corresponding results for the crawl speed test are presented in Table 8.7. The maximum LLDF for the crawl speed test for the interior slab portion is 0.145 and the equivalent width is 17.83 ft. The equivalent width calculated from the crawl speed test is higher than that obtained from the stop location test, therefore the stop location result is conservative.

Table 8.6. Experimental Deflections, LLDFs and Equivalent Width for Stop Location Test along Path 1 using L-Curbs

Section	S1+S2 (Left L-curb)		S3	S4	S5	S6	S7	S8+S9 (Right L-curb)	
Width (ft)	4.708		2.083	2.583	2.583	2.583	2.083	4.708	
Δ (in.)	0.006	0.011	0.019	0.028	0.035	0.039	0.035	0.036	0.029
	0.009		0.019	0.028	0.035	0.039	0.035	0.034	
I_i (in^4)	14,925		6682	6682	6682	6682	6682	14,925	
$I_i\Delta$ (in^5)	139.03		127.23	183.85	234.39	257.55	231.90	508.80	
LLDF	0.083		0.076	0.109	0.139	0.153	0.138	0.302	
g	0.083		0.615					0.302	
E (ft)	-		16.88					-	

Table 8.7. Experimental Deflections, LLDFs and Equivalent Width for Crawl Speed Test along Path 1 using L-Curbs

Section	S1+S2 (Left L-curb)		S3	S4	S5	S6	S7	S8+S9 (Right L-curb)	
Width (ft)	4.708		2.083	2.583	2.583	2.583	2.083	4.708	
Δ (in.)	0.006	0.012	0.019	0.025	0.032	0.035	0.033	0.034	0.027
	0.010		0.019	0.025	0.032	0.035	0.033	0.032	
I_i (in^4)	14,925		6682	6682	6682	6682	6682	14,925	
$I_i\Delta$ (in^5)	149.39		128.09	168.89	215.82	230.88	222.47	477.97	
LLDF	0.094		0.080	0.106	0.135	0.145	0.140	0.300	
g	0.094		0.606					0.300	
E (ft)	-		17.83					-	

A comparison of the equivalent widths calculated from the test data for the interior slab portion, based on defining curb sections, and those calculated using the approximate equations in the AASHTO Standard Specifications (AASHTO 2002) and AASHTO LRFD Specifications (AASHTO 2017) are provided in Table 8.8. Comparisons with studies such as Amer et al. (1999) and Jones and Shenton (2012) are also presented. The equivalent width calculated using the approach recommended by Amer et al. (1999) is closer to that determined from the static tests. All other methods provided conservative equivalent widths. It should be noted that the equivalent widths calculated using the approximate equations in the AASHTO Standard Specifications (AASHTO 2002) and AASHTO LRFD Specifications (AASHTO 2017) do not consider slab bridges with integral curbs. Similarly, Jones and Shenton (2012) did not consider bridges with integral curbs. Amer et al. (1999) considered bridges similar to the one tested.

Table 8.8 Equivalent Width (ft) Comparison for Interior Slab for Path 1 Loading

Test	Test (E^m_{Test})	Amer et al. (E^m_{Amer})	Jones and Shenton* ($E^m_{Jones\ \&\ Shenton}$)	AASHTO* (E^m_{AASHTO})	AASHTO LRFD* (E^m_{LRFD})
Stop Location	16.9	14.6	12.0	11.0	10.5
Crawl Speed	17.8	14.6	12.0	11.0	10.5
Note: * Methods do not consider the effect of integral curbs.					

Measured deflections for each section for the stop location test and crawl test are shown in Figure 8.17 (a) and (c), respectively. A comparison of the test equivalent widths with those calculated from the AASHTO Standard Specifications and AASHTO LRFD Specifications (AASHTO 2002), and studies such as Amer et al. (1999) and Jones and Shenton (2012) are shown in Figure 8.17(b) and (d) for the stop location and crawl tests, respectively.

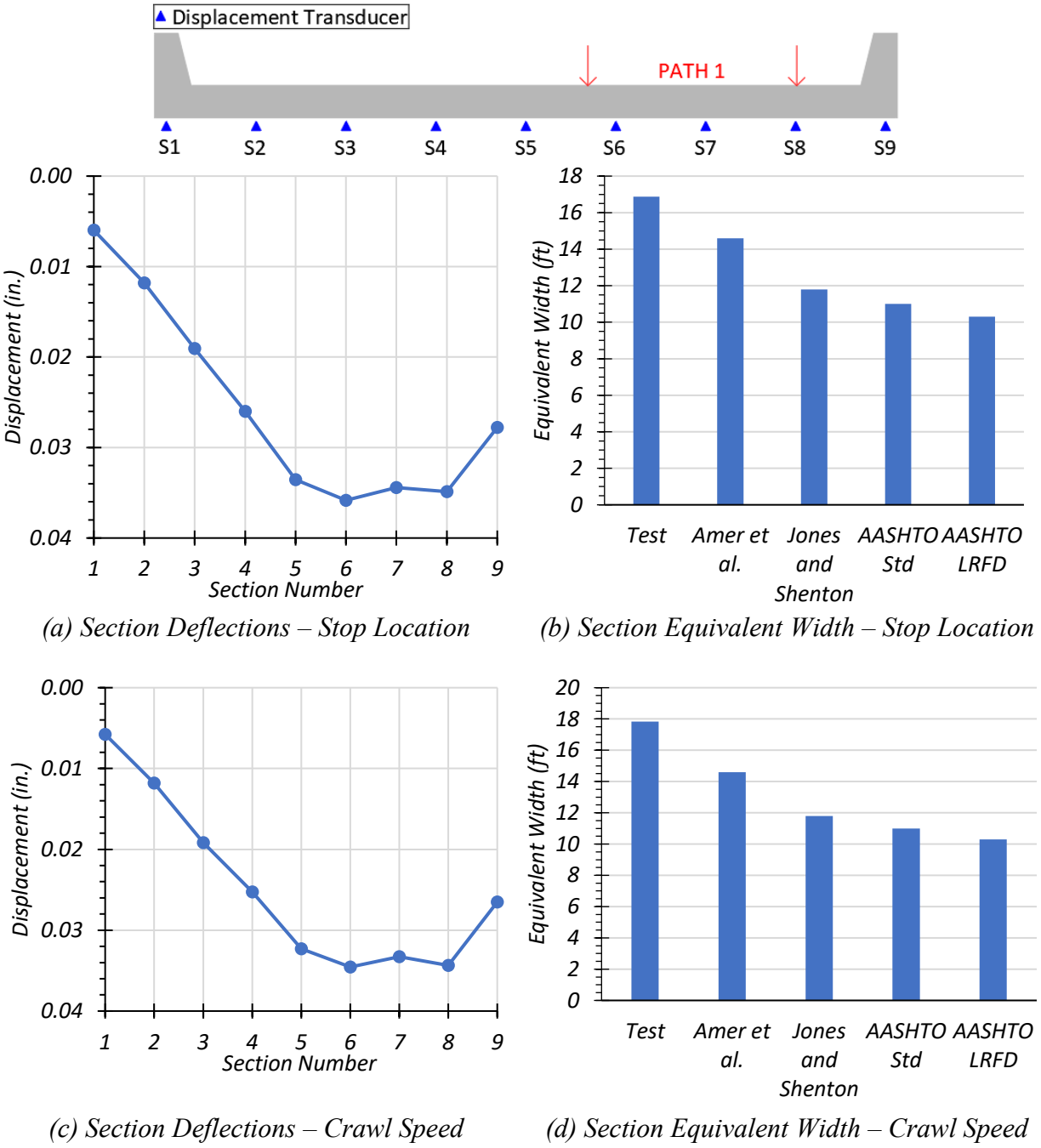

(a) Section Deflections – Stop Location

(b) Section Equivalent Width – Stop Location

(c) Section Deflections – Crawl Speed

(d) Section Equivalent Width – Crawl Speed

Figure 8.17. Static Deflection Results for Path 1 Loading

8.6.1.2.2. Path 2 Loading

The measured deflections for all transverse sections along with the LLDFs for the stop location test and crawl test along Path 2 are provided in Table 8.9. For both the stop location test and crawl

speed test, the maximum exterior section deflection was observed in Section S1 and the maximum interior section deflection was observed in Section S4. This was due to the close proximity of these sections to the wheel lines. The corresponding LLDF for Section S9 was 0.598 for the stop location test and 0.621 for the crawl speed test. Section S4 had an LLDF of 0.053 for the stop location test and 0.054 for the crawl speed test.

Table 8.9. Experimental Deflections and LLDFs for Path 2 Loading

Section	S1	S2	S3	S4	S5	S6	S7	S8	S9
Stop Location Test Disp. (in.)	0.028	0.032	0.038	0.038	0.035	0.027	0.018	0.015	0.006
Stop Location Test LLDF	0.598	0.044	0.052	0.053	0.049	0.038	0.025	0.021	0.120
Crawl Speed Test Disp. (in.)	0.027	0.031	0.035	0.036	0.032	0.024	0.015	0.013	0.004
Crawl Speed Test LLDF	0.621	0.046	0.052	0.054	0.049	0.036	0.022	0.020	0.101
Note: 1 – S = Section, Disp. = Displacement 2 – LLDF values are based on the midspan deflections.									

Table 8.10 tabulates the step-by-step calculations for the equivalent width of the interior slab section for the stop location test using the IB346 definition of L-curbs. The corresponding results for the crawl speed test are presented in Table 8.11. The equivalent width calculated from crawl speed test is smaller than that obtained from the stop location test. This could be due to the stop location test being slightly different from the moment critical position for absolute maximum moment. Moreover, the transverse location of truck may be slightly different between the stop location test and crawl speed test.

Table 8.10. Experimental Deflections, LLDFs and Equivalent Width for Stop Location Test along Path 2 using L-Curbs

Section	S1+S2 (Left L-curb)		S3	S4	S5	S6	S7	S8+S9 (Right L-curb)	
Width (ft)	4.708		2.083	2.583	2.583	2.583	2.083	4.708	
Δ (in.)	0.028	0.032	0.038	0.038	0.035	0.027	0.018	0.015	0.006
	0.031		0.038	0.038	0.035	0.027	0.018	0.013	
I_i (in^4)	14925		6682	6682	6682	6682	6682	14925	
$I_i\Delta$ (in^5)	458.56		252.69	253.90	235.50	182.20	119.50	186.75	
LLDF	0.271		0.150	0.150	0.139	0.108	0.071	0.111	
g	0.271		0.618					0.111	
E (ft)			17.19						

Table 8.11. Experimental Deflections, LLDFs and Equivalent Width for Crawl Speed Test along Path 2 using L-Curbs

Section	S1+S2 (Left L-curb)		S3	S4	S5	S6	S7	S8+S9 (Right L-curb)	
Width (ft)	4.708		2.083	2.583	2.583	2.583	2.083	4.708	
Δ (in.)	0.027	0.031	0.035	0.036	0.032	0.024	0.015	0.013	0.004
	0.029		0.035	0.036	0.032	0.024	0.015	0.011	
I_i (in^4)	14925		6682	6682	6682	6682	6682	14925	
$I_i\Delta$ (in^5)	439.78		231.20	237.51	214.68	158.17	97.17	158.93	
LLDF	0.286		0.150	0.154	0.140	0.103	0.063	0.103	
g	0.286		0.611					0.103	
E (ft)			16.72						

A comparison of the equivalent widths calculated from the test data for the interior slab portion, based on defining curb sections, and those calculated using the approximate equations in the AASHTO Standard Specifications (AASHTO 2002) and AASHTO LRFD Specifications (AASHTO 2017) are provided in Table 8.12. Comparisons with studies such as Amer et al. (1999) and Jones and Shenton (2012) are also presented. The equivalent width calculated using the approach proposed by Amer et al. (1999) was closer to that determined from the static tests. All other approaches provided conservative equivalent widths.

Table 8.12 Equivalent Width (ft) Comparison for Interior Slab for Path 2 Loading

Test	Test (E^m_{Test})	Amer et al. (E^m_{Amer})	Jones and Shenton* ($E^m_{Jones\ \&\ Shenton}$)	AASHTO* (E^m_{AASHTO})	AASHTO LRFD* (E^m_{LRFD})
Stop Location	17.2	14.6	12.0	11.0	10.5
Crawl Speed	16.7	14.6	12.0	11.0	10.5
Note: *Methods do not consider the effect of integral curbs.					

Measured deflections for each section for the stop location test and crawl test are shown in Figure 8.18(a) and (c), respectively. A comparison of the test equivalent widths with those calculated from the in the AASHTO Standard Specifications (AASHTO 2002) and AASHTO LRFD Specifications (AASHTO 2017) and studies such as Amer et al. (1999) and Jones and Shenton (2012) are shown in Figure 8.18(b) and (d) for stop location test and crawl speed test, respectively.

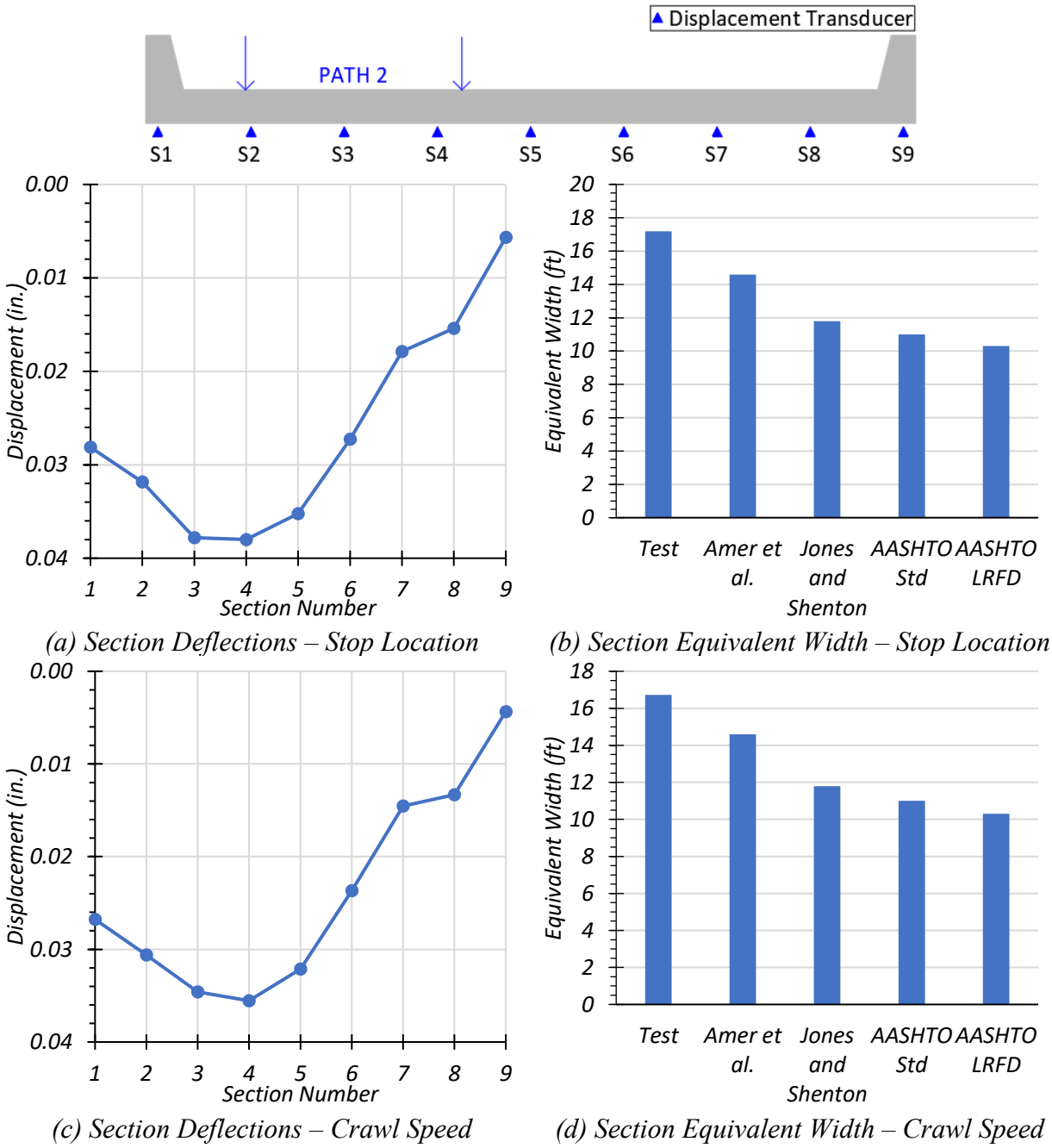

(a) Section Deflections – Stop Location

(b) Section Equivalent Width – Stop Location

(c) Section Deflections – Crawl Speed

(d) Section Equivalent Width – Crawl Speed

Figure 8.18. Static Deflection Results for Path 2 Loading

8.6.1.2.3. Middle Path Loading

The measured deflections for all transverse sections along with the LLDFs for the stop location test and crawl test along the Middle Path are provided in Table 8.13. For both the stop location test and crawl speed test, the maximum exterior section deflection was observed in Section S1 and the

maximum interior section deflection was observed in Section S5. This was due to the close proximity of these sections to the wheel lines. The corresponding LLDF for Section S1 was 0.341 for the stop location test and 0.348 for the crawl speed test. Section S5 had an LLDF of 0.057 for the stop location test and 0.058 for the crawl speed test.

Table 8.13. Experimental Deflections and LLDFs for Middle Path Loading

Section	S1	S2	S3	S4	S5	S6	S7	S8	S9
Stop Location Test Disp. (in.)	0.016	0.022	0.031	0.037	0.040	0.038	0.030	0.027	0.015
Stop Location Test LLDF	0.341	0.031	0.044	0.053	0.057	0.054	0.043	0.038	0.338
Crawl Speed Test Disp. (in.)	0.015	0.022	0.030	0.036	0.038	0.035	0.027	0.024	0.014
Crawl Speed Test LLDF	0.348	0.033	0.045	0.054	0.058	0.053	0.041	0.037	0.331
Note: 1 – S = Section, Disp. = Displacement 2 – LLDF values are based on the midspan deflections.									

Table 8.14 tabulates the step-by-step calculation for the equivalent width of the interior slab section for the stop location test using the IB346 definition of L-curbs. The corresponding results for the crawl speed test are presented in Table 8.15. The equivalent width calculated from crawl speed test is slightly smaller than that obtained from the stop location test.

Table 8.14. Experimental Deflections, LLDFs and Equivalent Width for Stop Location Test along Middle Path using L-Curbs

Section	S1+S2 (Left L-curb)		S3	S4	S5	S6	S7	S8+S9 (Right L-curb)	
Width (ft)	4.708		2.083	2.583	2.583	2.583	2.083	4.708	
Δ (in.)	0.016	0.022	0.031	0.037	0.040	0.038	0.030	0.027	0.015
	0.020		0.0310	0.0375	0.0402	0.0377	0.0303	0.023	
I_i (in^4)	14,925		6682	6682	6682	6682	6682	14,925	
$I_i\Delta$ (in^5)	297.83		207.35	250.42	268.77	251.92	202.78	350.14	
LLDF	0.163		0.113	0.137	0.147	0.138	0.111	0.191	
g	0.163		0.646					0.191	
E (ft)			17.58						

Table 8.15. Experimental Deflections, LLDFs and Equivalent Width for Crawl Speed Test along Middle Path using L-Curbs

Section	S1+S2 (Left L-curb)		S3	S4	S5	S6	S7	S8+S9 (Right L-curb)	
Width (ft)	4.708		2.083	2.583	2.583	2.583	2.083	4.708	
Δ (in.)	0.015	0.022	0.030	0.036	0.038	0.035	0.027	0.024	0.014
	0.020		0.0300	0.0359	0.0383	0.0351	0.0269	0.021	
I_i (in^4)	14,925		6682	6682	6682	6682	6682	14,925	
$I_i\Delta$ (in^5)	297.29		200.64	239.78	256.08	234.23	179.88	320.28	
LLDF	0.172		0.116	0.139	0.148	0.136	0.104	0.185	
g	0.172		0.643					0.185	
E (ft)			17.43						

A comparison of the equivalent widths calculated from the test data for the interior slab portion, based on defining curb sections, and those calculated using the approximate equations in the AASHTO Standard Specifications (AASHTO 2002) and AASHTO LRFD Specifications (AASHTO 2017) are provided in Table 8.16. Comparisons with studies such as Amer et al. (1999) and Jones and Shenton (2012) are also presented. The equivalent width calculated using the approach recommended by Amer et al. (1999) is closer to that determined from the static tests. All other methods provided conservative equivalent widths.

Table 8.16 Equivalent Width (ft) Comparison for Interior Slab for Middle Path Loading

Test	Test (E^m_{Test})	Amer et al. (E^m_{Amer})	Jones and Shenton* ($E^m_{Jones\ \&\ Shenton}$)	AASHTO* (E^m_{AASHTO})	AASHTO LRFD* (E^m_{LRFD})
Stop Location	17.6	14.6	12.0	11.0	10.5
Crawl Speed	17.4	14.6	12.0	11.0	10.5
Note: * Approaches do not consider the effect of integral curbs.					

Measured deflections for each section for the stop location test and crawl test are shown in Figure 8.19(a) and (c), respectively. A comparison of the test equivalent widths with those calculated from the in the AASHTO Standard Specifications (AASHTO 2002) and AASHTO LRFD Specifications (AASHTO 2017) and studies such as Amer et al. (1999) and Jones and

Shenton (2012) are shown in Figure 8.19(b) and (d) for the stop location test and crawl speed test, respectively.

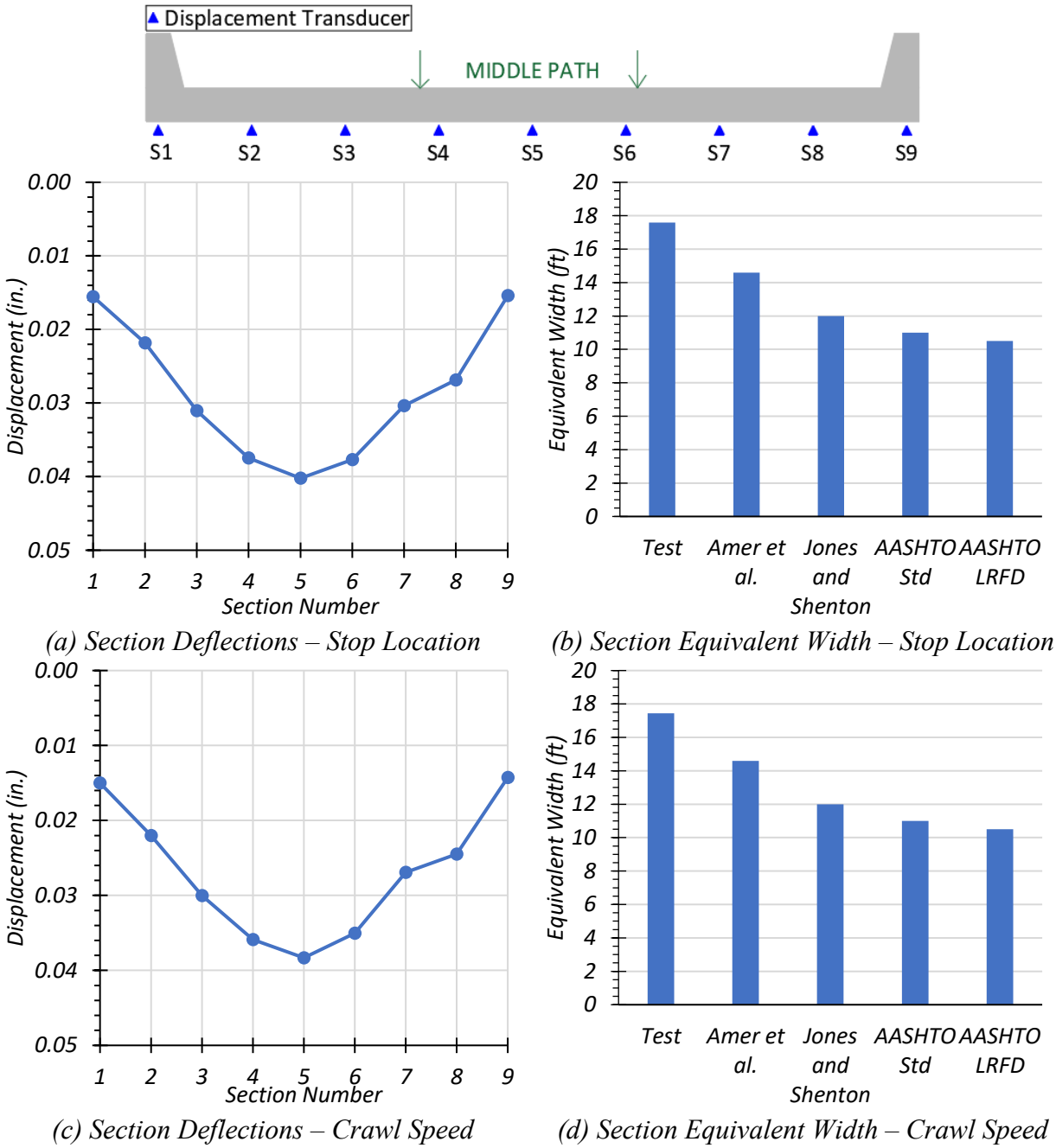

(a) Section Deflections – Stop Location

(b) Section Equivalent Width – Stop Location

(c) Section Deflections – Crawl Speed

(d) Section Equivalent Width – Crawl Speed

Figure 8.19. Static Deflection Results for Middle Path Loading

8.6.1.2.4. Summary of Deflection Results

The string potentiometer at the transverse Section S7 showed consistently low deflections for all static tests along Path 1, Path 2 and the Middle Path. This suggests that there may be an error with the string potentiometer and the corresponding results recorded. This will be further evaluated using the calibrated FEM model.

The measured deflections were similar between the stop location test and crawl speed test along Path 1 loading. The equivalent width calculated for the stop location test was 5 percent smaller than that calculated for the crawl speed test.

For Path 2 loading, the measured deflections were slightly smaller for the crawl speed test when compared with the stop location test. The equivalent width calculated for the static load was 3 percent higher than that calculated for the crawl speed test.

The measured deflections were similar for both the stop location test and crawl speed test for the Middle Path loading. The equivalent width calculated for the static load was less than 2 percent higher than that calculated for the crawl speed test.

The equivalent widths calculated using the approximate equations in the AASTHO Standard Specifications (AASHTO 2002) and AASHTO LRFD Specifications (AASHTO 2017) appear to be quite conservative for integral curb bridges such as Bridge CS-9. Similarly, Jones and Shenton (2012) did not consider bridges with integral curbs and their equivalent widths are conservative. Amer et al. (1999) considered bridges similar to the one tested, having integral curbs, and the equivalent width calculated using their equation was 13 percent more conservative than the Middle Path stop location test equivalent width.

The maximum LLDFs for the different loading scenarios is provided in Table 8.17. The maximum LLDF for the L-curbs is obtained from Path 1 loading and the maximum LLDF for the interior slab portion is obtained from the Middle Path loading.

Table 8.17. Maximum Midspan LLDFs for Stop Location and Crawl Speed Tests

Loading	LLDF						
	S1+S2 (Left L-curb)	**S3**	**S4**	**S5**	**S6**	**S7**	**S8+S9 (Right L-curb)**
Path 1 Stop Location	0.083	0.076	0.109	0.139	0.153	0.138	0.302
Path 1 Crawl Speed	0.094	0.080	0.106	0.135	0.145	0.140	0.300
Max. Path 1 LLDF		0.615					0.302
Path 2 Stop Location	0.271	0.150	0.150	0.139	0.108	0.071	0.111
Path 2 Crawl Speed	0.286	0.150	0.154	0.140	0.103	0.063	0.103
Max. Path 2 LLDF	0.286	0.618					
Middle Path Stop Location	0.163	0.113	0.137	0.147	0.138	0.111	0.191
Middle Path Crawl Speed	0.172	0.116	0.139	0.148	0.136	0.104	0.185
Max. Middle Path LLDF		0.646					0.191

8.6.1.3. Comparison of Experimental Results with Literature

TxDOT currently uses the Illinois Bulletin 346 (IB346) approach to determine the distribution of moment per foot width in the interior slab section and for design of the curbs. This approach is compared to the measured values in the following section.

8.6.1.3.1. Illinois Bulletin 346

TxDOT uses the Illinois Bulletin 346 (IB346) approach to load rate concrete slab bridges with integral curbs and/or beams. IB346 provides equations to determine the bending moment in the curbs and the slab portion of the bridge. The Illinois Bulletin 346 (IB346) suggests that the curb moment reduced by 25 percent to account for the vehicle load being shifted in the transverse

direction. IB346 equations are provided for wheel loads. Therefore, they are converted to total axle (two wheels) distributions in this report to make it consistent with the LLDF definition used throughout the report. In the absence of any distributed live load on the bridge, the moment in the curbs due to the truck load is calculated using to Eqn. (8.4).

$$M_{curb} = \frac{0.75C_1}{2}\frac{Pa}{4} \tag{8.4}$$

where:

$$C_1 = \left(\frac{12}{2.5 + G}\right)\frac{\left(4 - \frac{v}{a}\right)}{\left(4 + 28\left(\frac{v}{a}\right)\right)}$$

$$G = \frac{ah^3}{12I}$$

M_{curb} = Moment shared by a single curb, kip-ft

G = Dimensionless stiffness factor, ratio of slab stiffness to curb stiffness

I = Moment of inertia of curb gross section outside the roadway width, ft^4

h = Slab thickness, ft

v = Axle width, center-to-center of truck tires, ft

P = Magnitude of rear axle load (two wheels), kip

a = Span of bridge from center-to-center of bearing areas, ft

The bending moment applied to the slab region, M_{slab}, (between the curb faces) is calculated according to Eqn. (8.5). The average moment in the slab, $M_{slab,avg.}$, is calculated by

dividing the total slab moment by the width of the slab between the curb faces as shown in Eq. (8.6).

$$M_{slab} = (m - 1.5C_1)\frac{Pa}{4} \tag{8.5}$$

$$M_{slab,avg.} = \frac{M_{slab}}{b} \tag{8.6}$$

where:

b = Width of bridge between curb faces, ft

m = Number of wheel lines (m = 2 for one truck loading)

For the geometry of Bridge CS-9, G was calculated to be 1.49, I was calculated to be 1.03 ft^4, h was 0.92 ft and the truck axle width was 6.92 ft. Thus, C_1 was calculated to be 0.92.

IB346 considers an L-shaped composite section comprising of the curb and adjoining slab of width $4h$ for designing the curbs, where h is the slab thickness, as shown in Figure 8.20. Therefore, the moment demand for the curb is calculated for the L-shaped curb and the slab moment is calculated for the remaining part of the mid-slab portion.

The bending moment applied to the composite curb section (L-shaped) M_{L-curb} is calculated according to Eqn. (8.7) from IB346. The average moment in the slab $M_{slab,avg}$ is calculated by dividing the total slab moment by the width of the slab between the composite curb sections as shown in Eq. (8.8).

$$M_{L-curb} = M_{curb} + 4h\frac{M_{slab}}{b} \tag{8.7}$$

$$M_{mid-slab,avg} = \frac{M_{slab}}{(b - 2(4h))} \tag{8.8}$$

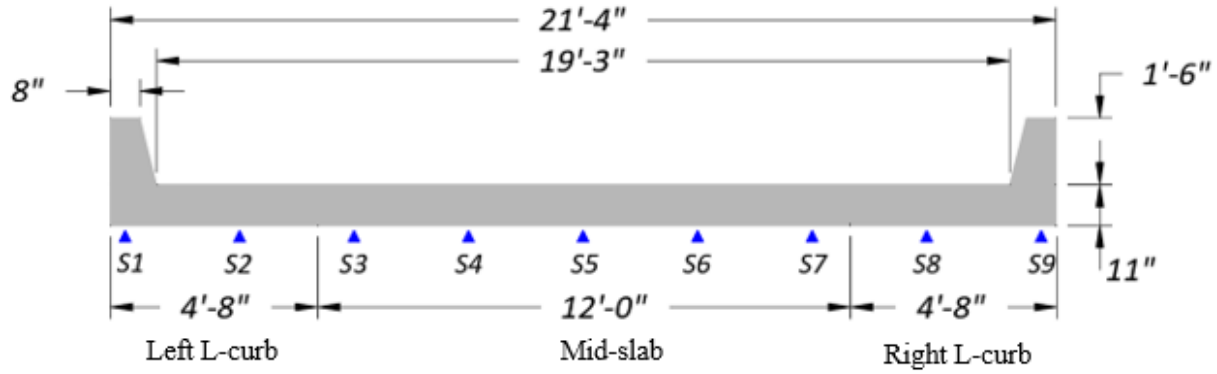

Figure 8.20. Typical Curb Cross-Section for Capacity Calculations

The moment distribution to one of the L-curbs can be calculated as the ratio of the curb moment to the total truck moment as shown in Eqn. (8.9).

$$g_{L-curb} = \frac{M_{L-curb}}{M_{Total}} \tag{8.9}$$

The moment distributed to the slab portion can be calculated as the difference between the total minus the moment share of the two curbs using Equation (8.10).

$$g_{mid-slab} = 1 - 2g_{L-curb} \tag{8.10}$$

The term g may be defined as the distribution of total moment to the bridge components: curbs and slab. It is the ratio of the moment taken by the bridge component to the total moment taken by the bridge. The distribution of the bending moment across Bridge CS-9 is presented in Table 8.18. As expected, the curbs attract a higher moment than the slab. The average moment per unit width of the slab is 1.08 kip-ft/ft.

Table 8.18. Distribution of Bending Moment across Bridge CS-9 using IB346

Component	Left L-Curb	Mid-Slab	Right L-Curb
Moment (kip-ft)	54.94	25.75	54.94
g	0.405	0.190	0.405

Table 8.19 calculates the distribution of bending moment across Bridge CS-9 using cracked section properties of the curb. The use of the cracked section leads to a decreased contribution to the L-curbs and an increased contribution to the mid-slab.

Table 8.19. Distribution of Bending Moment across Bridge CS-9 using IB346 with Cracked Section Properties

Description	Left L-Curb	Mid-Slab	Right L-Curb
Moment (kip-ft)	50.89	33.84	50.89
g	0.375	0.249	0.375

8.6.1.3.2. Experimental LLDFs using Deflections

The maximum LLDFs calculated for the different components for all static test types is shown in Table 8.20. As anticipated, the LLDF is highest in a component when the truck is located nearest to it. For the left L-curb, the truck is running along Path 2 while for the right L-curb the truck is along Path 1.

Table 8.20. Maximum Experimental One-Lane LLDFs for Static Tests

Load Path	***LLDF***		
	Left L-Curb	**Mid-Slab**	**Right L-Curb**
Path 1	0.094	0.615	0.302
Path 2	0.286	0.618	0.111
Middle Path	0.172	0.646	0.191
Max.	0.286	0.646	0.302

Table 8.21 compares the distribution across the slab bridge for the experimental results and IB346 calculations for one-lane loading. The slightly unsymmetric distribution to the two curbs

may be attributed to the test truck not being positioned exactly at the bridge center and/or the two curbs having different amounts of cracking leading to different cracked section moment of inertia values. The results indicate that IB346 underestimates the distribution of moment to the mid-slab region, but gives a conservative estimate of the L-curb moment.

Table 8.21. Comparison of Experimental and IB346 One-Lane LLDFs

Description	g		
	Left L-Curb	**Mid-Slab**	**Right L-Curb**
Test	0.286	0.646	0.302
IB346	0.405	0.190	0.405
IB346 / Test	1.416	0.294	1.341
IB346 (cracked)	0.375	0.249	0.375
IB346 (cracked) / Test	1.311	0.385	1.242

The two-lane loading LLDFs for the experimental tests were determined from the sum of the deflections obtained from Path 1 and Path 2 loading. The IB346 bending moments for the two-lane loaded case is calculated by increasing the number of wheel lines, m used in Eq. (8.8), to 4. The LLDFs for the experimental tests and IB346 method are shown in Table 8.22.

Table 8.22. Two-lane LLDFs for Experimental Tests and IB346

Description	$LLDF$		
	Left L-Curb	**Mid-Slab**	**Right L-Curb**
Stop Location Test	0.354	1.233	0.413
Crawl Speed Test	0.376	1.217	0.407
IB346	0.596	0.808	0.596
IB346 (cracked)	0.566	0.868	0.566

The comparison of the maximum distribution of live load across the slab bridge for the experimental results and IB346 calculations for two-lane loading is shown in Table 8.23. The ratio IB346/Test for the mid-slab component for two-lane LLDF is more than two times higher than the one-lane LLDF. Similar to the one-lane comparison, the results indicate that IB346 underestimates

the distribution of moment to the mid-slab region, but gives a conservative estimate of the L-curb moment.

Table 8.23. Comparison of Experimental and IB346 Two-Lane LLDFs

Description	*g*		
	Left L-Curb	**Mid-Slab**	**Right L-Curb**
Test	0.376	1.233	0.413
IB346	0.596	0.808	0.596
IB346 / Test	1.585	0.655	1.443
IB346 (cracked)	0.566	0.868	0.566
IB346 (cracked) / Test	1.505	0.704	1.370

8.6.1.3.3. Modification to Illinois Bulletin 346 Method

The IB346 approach defines an L-shaped curb section that incorporates a slab length equal to four times the thickness of the slab. Because the measured results indicated that the relative curb stiffness is high, a modification to this approach was considered using a 45-degree projection of the curb height onto the slab portion. This approach is similar to that used for the Equivalent Frame Method outlined in Section 8.11 of ACI 318-14 (ACI Committee 318 2014). The portion of the slab to be included with the beam and/or curb is shown in Figure 8.21.

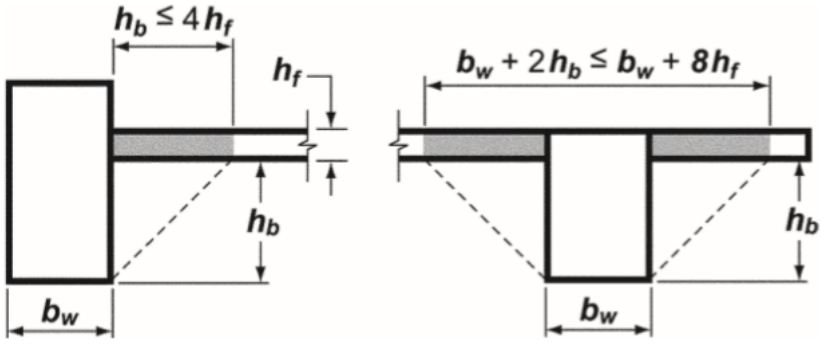

Figure 8.21. Slab Portion to be included with the Beam and/or Curb (ACI Committee 318 2014)

A comparison of the LLDFs calculated using the modified IB346 approach with the experimental values is provided in Table 8.24. The modified approach provides a better estimate of the distribution of moment to the curbs and slab, especially for the two-lane loaded scenario; however, it is still unconservative for the slab region.

Table 8.24. Comparison of Experimental and Modified IB346 LLDFs

Loading	Description	g		
		Left L-Curb	**Mid-Slab**	**Right L-Curb**
One-lane	Test	0.286	0.646	0.302
	Modified IB346	0.364	0.271	0.364
	Modified IB346/Test	1.273	0.420	1.205
Two-lane	Test	0.376	1.233	0.413
	Modified IB346	0.423	1.154	0.423
	Modified IB346/Test	1.125	0.936	1.024

8.6.1.4. Comparison of Experimental Moment LLDFs in Slab Region with Methods from Literature

The test LLDFs and equivalent width values for the concrete slab bridge are compared with the recommended values from the *AASHTO Standard Specifications* (AASHTO 2002) and *AASHTO LRFD Specifications* (AASHTO 2017) and two other methods from the literature. Both AASHTO specifications provide equations for the equivalent width of the slab over which a single truck load is to be distributed for slab bridges. The *AASHTO Standard Specifications* and the *AASHTO LRFD Specifications* expressions are provided in Equation (8.11) and Equation (8.12), respectively. Note that the *AASHTO Standard Specifications* and *AASHTO LRFD Specifications* equations for calculating equivalent slab width do not consider concrete slab bridges with integral curbs.

$$\text{AASHTO Standard:} \quad E = 2(4 + 0.06S) \tag{8.11}$$

AASHTO LRFD: $$E = 10.0 + 5.0\sqrt{L_1 W_1} \quad (8.12)$$

where:

S = Effective span length, ft

L_1 = Modified span length, ft (minimum of actual span or 60 ft)

W_1 = Modified edge-to-edge width of bridge, ft (minimum of actual width or 60 ft for multi-lane loading, or 30 ft for single-lane loading)

Amer et al. (1999) considered both concrete slab bridges without integral curbs and concrete slab bridges with integral curbs in their study. They proposed the following equation for the equivalent width. In the presence of integral edge beams, a factor C_{edge} should be multiplied by the value from Equation (8.14):

$$E = 6.89 + 0.23L \leq \frac{W}{N_L} \quad (8.13)$$

$$C_{edge} = 1.0 + 0.5\left(\frac{d_1}{3.28} - 0.15\right) \geq 1.0 \quad (8.14)$$

where:

E = Equivalent width for a truck load, ft

L = Span length, ft

W = Bridge width, ft

N_L = Number of design lanes

d_1 = Edge beam depth above slab thickness, ft

Jones and Shenton (2012) recommended Equation (8.15) for the determination of the equivalent width for a single-lane bridge. This equation is similar to the equivalent width equation provided in the *AASHTO LRFD Specifications* (AASHTO 2017); however, the coefficient in the second term is 5.8 rather than 5.0. Slab bridges with integral curbs were not considered in this study.

$$E = 10.0 + 5.8\sqrt{L_1 W_1} \tag{8.15}$$

8.6.1.4.1. Path 1 Loading

A comparison of the equivalent widths calculated from the test data for the interior slab portion, based on defining curb sections, to those widths calculated using the approximate equations in the *AASHTO Standard Specifications* (AASHTO 2002) and *AASHTO LRFD Specifications* (AASHTO 2017) is provided in Table 8.25. Comparisons with studies such as Amer et al. (1999) and Jones and Shenton (2012) are also presented. The equivalent width calculated using the approach recommended by Amer et al. (1999) is closer to the width determined from the static tests. All other methods provided conservative equivalent widths. It should be noted that the equivalent widths calculated using the approximate equations in the *AASHTO Standard Specifications* (AASHTO 2002) and *AASHTO LRFD Specifications* (AASHTO 2017) do not consider slab bridges with integral curbs. Similarly, Jones and Shenton (2012) did not consider bridges with integral curbs. Amer et al. (1999) considered bridges similar to the one tested.

Table 8.25. Equivalent Width (ft) Comparison for Interior Slab for Path 1 Loading

Test	Test (E^m_{Test})	Amer et al. (E^m_{Amer})	Jones and Shenton* ($E^m_{Jones\ \&\ Shenton}$)	AASHTO* (E^m_{AASHTO})	AASHTO LRFD* (E^m_{LRFD})
Stop Location	16.9	14.6	12.0	11.0	10.5
Crawl Speed	17.8	14.6	12.0	11.0	10.5
Note: * Methods do not consider the effect of integral curbs.					

A comparison of the test equivalent widths to widths calculated from the *AASHTO Standard Specifications* and *AASHTO LRFD Specifications* (AASHTO 2002) and studies such as Amer et al. (1999) and Jones and Shenton (2012) is shown in Figure 8.22(a) and (b) for the stop location and crawl tests, respectively.

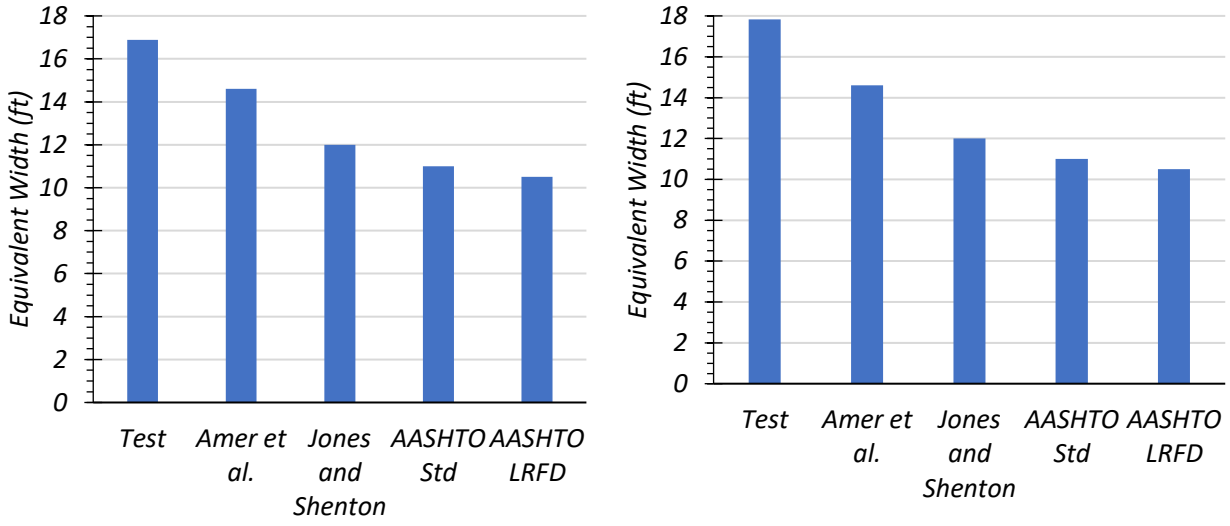

(a) Stop Location Test *(b) Crawl Speed Test*

Figure 8.22. Comparison of Test Equivalent Width with Methods in the Literature for Path 1 Loading

8.6.1.4.2. Path 2 Loading

A comparison of the equivalent widths calculated from the test data for the interior slab portion, based on defining curb sections, to those calculated using the approximate equations in the *AASHTO Standard Specifications* (AASHTO 2002) and *AASHTO LRFD Specifications*

(AASHTO 2017) is provided in Table 8.12. Comparisons with studies such as Amer et al. (1999) and Jones and Shenton (2012) are also presented. The equivalent width calculated using the approach proposed by Amer et al. (1999) was closer to the width determined from the static tests. All other approaches provided conservative equivalent widths.

Table 8.26. Equivalent Width (ft) Comparison for Interior Slab for Path 2 Loading

Test	Test (E^m_{Test})	Amer et al. (E^m_{Amer})	Jones and Shenton* ($E^m_{Jones\ \&\ Shenton}$)	AASHTO* (E^m_{AASHTO})	AASHTO LRFD* (E^m_{LRFD})
Stop Location	17.2	14.6	12.0	11.0	10.5
Crawl Speed	16.7	14.6	12.0	11.0	10.5
Note: * Methods do not consider the effect of integral curbs.					

A comparison of the test equivalent widths to those calculated from the *AASHTO Standard Specifications* (AASHTO 2002) and *AASHTO LRFD Specifications* (AASHTO 2017) and studies such as Amer et al. (1999) and Jones and Shenton (2012) is shown in Figure 8.23(a) and (b) for the stop location test and crawl speed test, respectively.

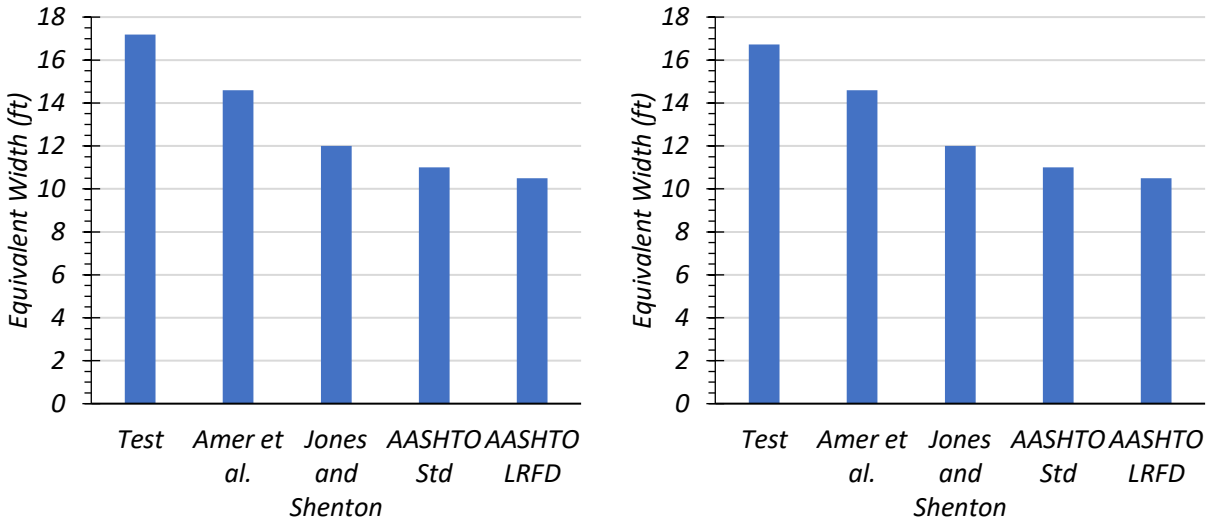

(a) Stop Location Test *(b) Crawl Speed Test*

Figure 8.23. Comparison of Test Equivalent Width with Methods in the Literature for Path 2 Loading

8.6.1.4.3. Middle Path Loading

A comparison of the equivalent widths calculated from the test data for the interior slab portion, based on defining curb sections, to those calculated using the approximate equations in the *AASHTO Standard Specifications* (AASHTO 2002) and *AASHTO LRFD Specifications* (AASHTO 2017) is provided in Table 8.27. Comparisons with studies such as Amer et al. (1999) and Jones and Shenton (2012) are also presented. The equivalent width calculated using the approach recommended by Amer et al. (1999) is closer to the width determined from the static tests. All other methods provided conservative equivalent widths.

Table 8.27. Equivalent Width (ft) Comparison for Interior Slab for Middle Path Loading

Test	Test (E^m_{Test})	Amer et al. (E^m_{Amer})	Jones and Shenton* ($E^m_{Jones\ \&\ Shenton}$)	AASHTO* (E^m_{AASHTO})	AASHTO LRFD* (E^m_{LRFD})
Stop Location	17.6	14.6	12.0	11.0	10.5
Crawl Speed	17.4	14.6	12.0	11.0	10.5
Note: * Methods do not consider the effect of integral curbs.					

A comparison of the test equivalent widths to those calculated from the *AASHTO Standard Specifications* (AASHTO 2002) and *AASHTO LRFD Specifications* (AASHTO 2017) and studies such as Amer et al. (1999) and Jones and Shenton (2012) is shown in Figure 8.24(a) and (b) for the stop location test and crawl speed test, respectively.

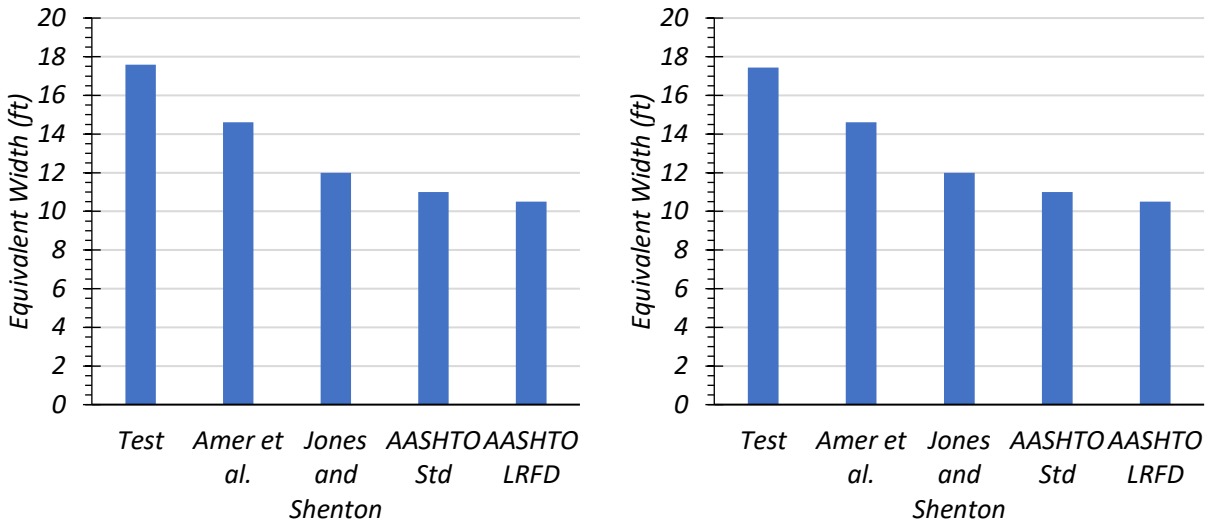

(a) Stop Location Test *(b) Crawl Speed Test*

Figure 8.24. Comparison of Test Equivalent Width with Methods in the Literature for Middle Path Loading

8.6.1.4.4. Summary of Comparisons

The equivalent widths calculated using the approximate equations in the *AASHTO Standard Specifications* (AASHTO 2002) and *AASHTO LRFD Specifications* (AASHTO 2017) appear to be quite conservative for integral curb bridges such as Bridge CS-9. Similarly, Jones and Shenton (2012) did not consider bridges with integral curbs, and their equivalent widths are conservative. Amer et al. (1999) considered bridges similar to the one tested (having integral edge beams), and the equivalent width calculated using their equation was 13 percent more conservative than the width determined for the Middle Path stop location test equivalent width.

TxDOT currently uses the IB346 approach to determine the distribution of moment per ft width in the interior slab section and for design of the curbs. The IB346 methods and other methods from literature are compared to the measured values in the following section.

8.6.1.4.5. Mid-slab Live Load Distribution per foot

The per ft distribution of the live load, $g_{per\ foot}$, is considered for the mid-slab component for both the experimental tests and the IB346 methodology. This distribution is calculated by dividing g for the mid-slab section by the width of the mid-slab component (11.92 ft), as shown in Equation (8.16):

$$g_{per\ foot} = \frac{g}{W_{mid-slab}} \tag{8.16}$$

The g and $g_{per\ foot}$ for the different experimental tests and IB346 for one-lane loading are shown in Table 8.28.

Table 8.28 Experimental and IB346 Moment LLDFs in Slab Region for One-Lane Loaded

Test/Method	g	$g_{per\ foot}$
Stop Location (Path 1)	0.615	0.052
Crawl Speed (Path 1)	0.606	0.051
Stop Location (Path 2)	0.618	0.052
Crawl Speed (Path 2)	0.611	0.051
Stop Location (Middle Path)	0.646	0.054
Crawl Speed (Middle Path)	0.643	0.054
IB346	0.190	0.016
IB346 (cracked)	0.249	0.021

The $g_{per\ foot}$ for the *AASHTO Standard Specifications* (AASHTO 2002), *AASHTO LRFD Specifications* (AASHTO 2017), Amer et al. (1999), and Jones and Shenton (2012) is defined as the inverse of the equivalent width. Table 8.33 provides this information.

Table 8.29. Moment LLDFs in Slab Region with Different Methods for One-Lane-Loaded

Approach	E (ft)	$g_{per\ foot}$
Amer et al.	14.6	0.068
Jones and Shenton*	12.0	0.083
AASHTO*	11.0	0.091
AASHTO LRFD*	10.5	0.096
Note: * Methods do not consider the effect of integral curbs.		

Figure 8.25 *compares the one-lane* $g_{per\ foot}$ factor calculated for the experimental tests and the different methods in the literature. IB346, when considering both uncracked and cracked sections, is highly unconservative for the mid-slab section, while *AASHTO Standard Specifications* (AASHTO 2002), *AASHTO LRFD Specifications* (AASHTO 2017), Amer et al. (1999), and Jones and Shenton (2012) ranges from being conservative to highly conservative for this bridge type.

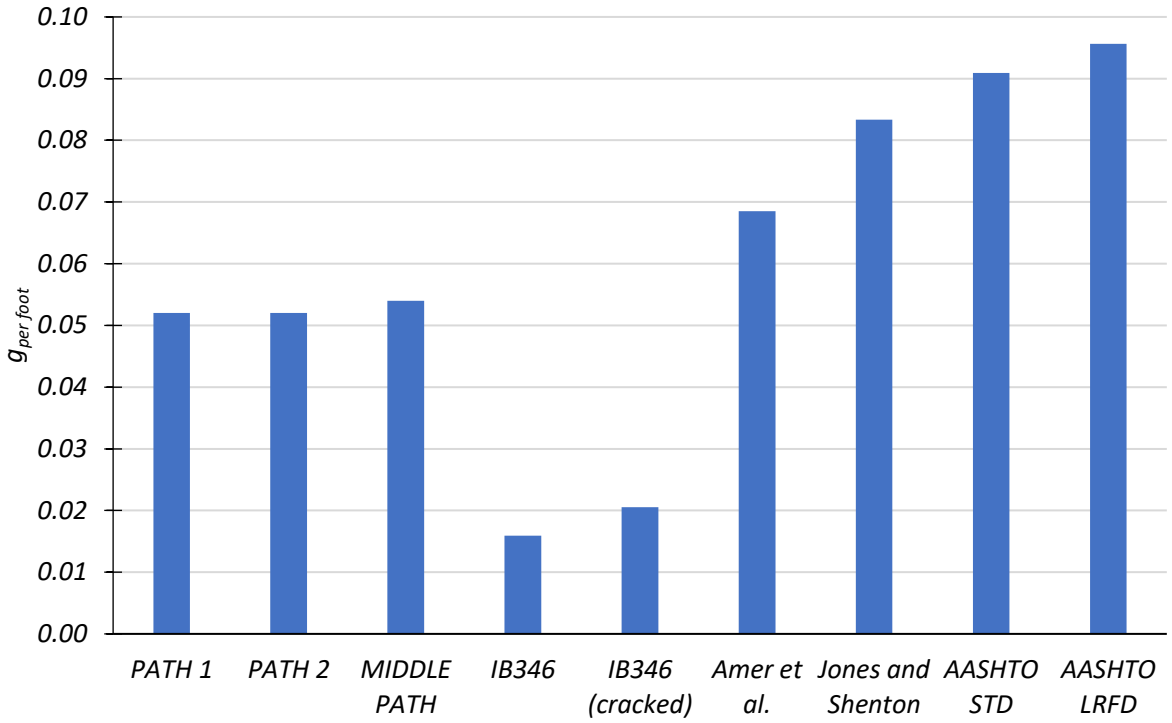

Figure 8.25. Comparison of Experimental Moment LLDFs in Slab Region with Different Methods in the Literature for One-Lane-Loaded

Similar calculations were carried out for the two-lane loading scenario. The two-lane loading LLDFs for the field tests were determined from the sum of the deflections obtained from Path 1 and Path 2 loading. The IB346 bending moments for a two-lane loaded case is calculated by increasing the number of wheel lines, m, used in Equation (8.5), to 4. Table 8.30 provides the g and $g_{per\ foot}$ for the experimental test and IB346 for two-lane loading.

Table 8.30. Experimental and IB346 Moment LLDFs in Slab Region for Two-Lane-Loaded

Test/Method	g	$g_{per\ foot}$
Stop Location (Path 1+2)	1.233	0.104
Crawl Speed (Path 1+2)	1.217	0.102
IB346	0.808	0.068
IB346 (cracked)	0.868	0.073

The equivalent width for two-lane (or more) loading for the *AASHTO LRFD Specifications* (AASHTO 2017) is provided in Equation (8.17). Equation (8.18) provides the corresponding equivalent width recommended by Jones and Shenton (2012). Note that these equations do not consider concrete slab bridges with integral curbs.

$$\text{AASHTO LRFD (AASHTO 2017):} \quad E = 84.0 + 1.44\sqrt{L_1 W_1} \tag{8.17}$$

$$\text{Jones and Shenton (2012):} \quad E = 84.0 + 2.06\sqrt{L_1 W_1} \tag{8.18}$$

where:

L_1 = Modified span length, ft (minimum of actual span or 60 ft)

W_1 = Modified edge-to-edge width of bridge, ft (minimum of actual width or 60 ft for multi-lane loading, or 30 ft for single-lane loading)

Table 8.31 provides the g and $g_{per\ foot}$ for the experimental test and IB346 for two-lane loading. Figure 8.26 compares the two-lane $g_{per\ foot}$ factor calculated for the experimental tests and the different approaches found in the literature. Similar to the one-lane loading, IB346 for uncracked and cracked sections is unconservative for the slab demand, while the approach by Jones and Shenton (2012) is slightly unconservative for this bridge type. In fact, *AASHTO LRFD Specifications* provides a reasonably good estimate of the $g_{per\ foot}$ factor in comparison to the experimental results.

Table 8.31. Moment LLDFs in Slab Region with Different Methods for Two-Lane-Loaded

Test/Method	E (ft)	$g_{per\ foot}$
Amer et al.	14.6	0.068
Jones and Shenton	11.0	0.091
AASHTO Standard Specifications	11.0	0.091
AASHTO LRFD Specifications	9.8	0.102

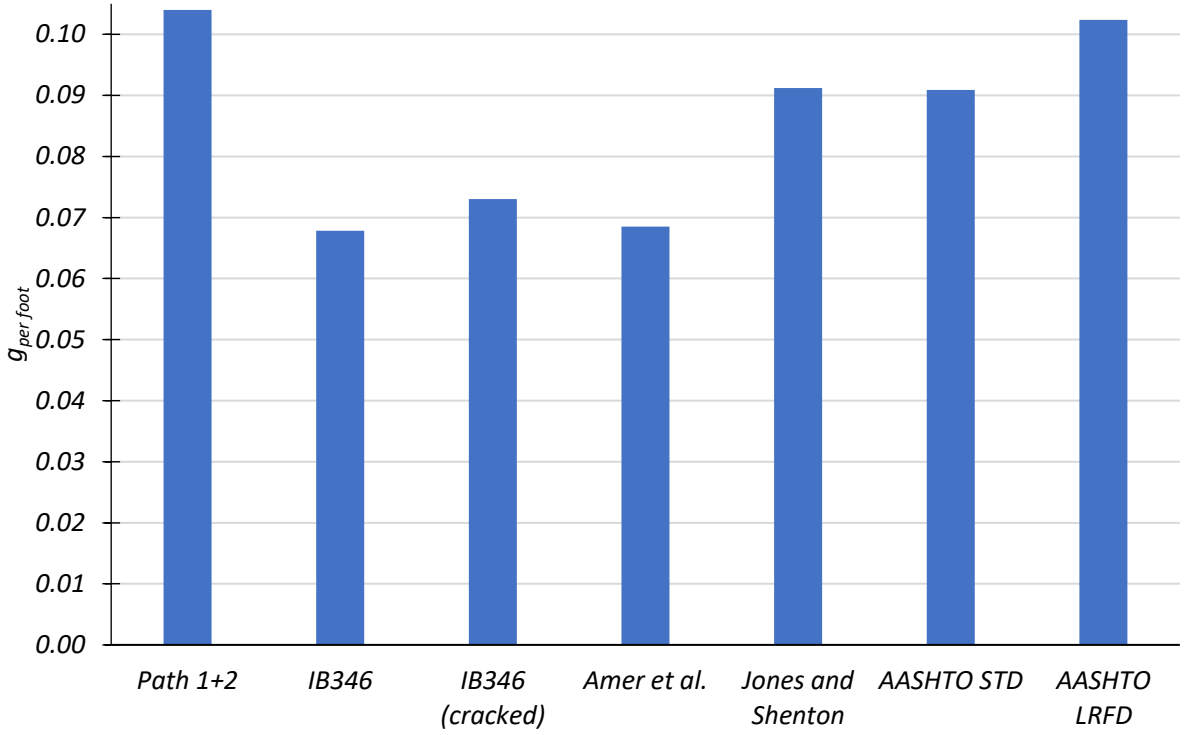

Figure 8.26. Comparison of Experimental Moment LLDFs in Slab Region with Different Methods in the Literature for Two-Lane Loading

8.6.2. Dynamic Load Tests on Bridge CS-9

In this section of the report, results from the dynamic tests undertaken along Path 1, Path 2 and the Middle Path are presented.

8.6.2.1. Dynamic Amplification

The dynamic amplification of the bridge is considered by comparing the magnifications in the strain values and deflections from the stop location test to the dynamic test.

8.6.2.1.1. Maximum Section Strains

The dynamic amplification of strains for the transverse sections, S1 and S9 were obtained by comparing the dynamic test results with the static stop location results. Plots of the strain profiles for S1 and S9 obtained from the stop location tests and dynamic tests for Path 1, Path 2, and Middle Path are shown in Figure 8.27, Figure 8.28, and Figure 8.29, respectively. Figure 8.30 compares the dynamic strains for S1 and S9 with the stop location values.

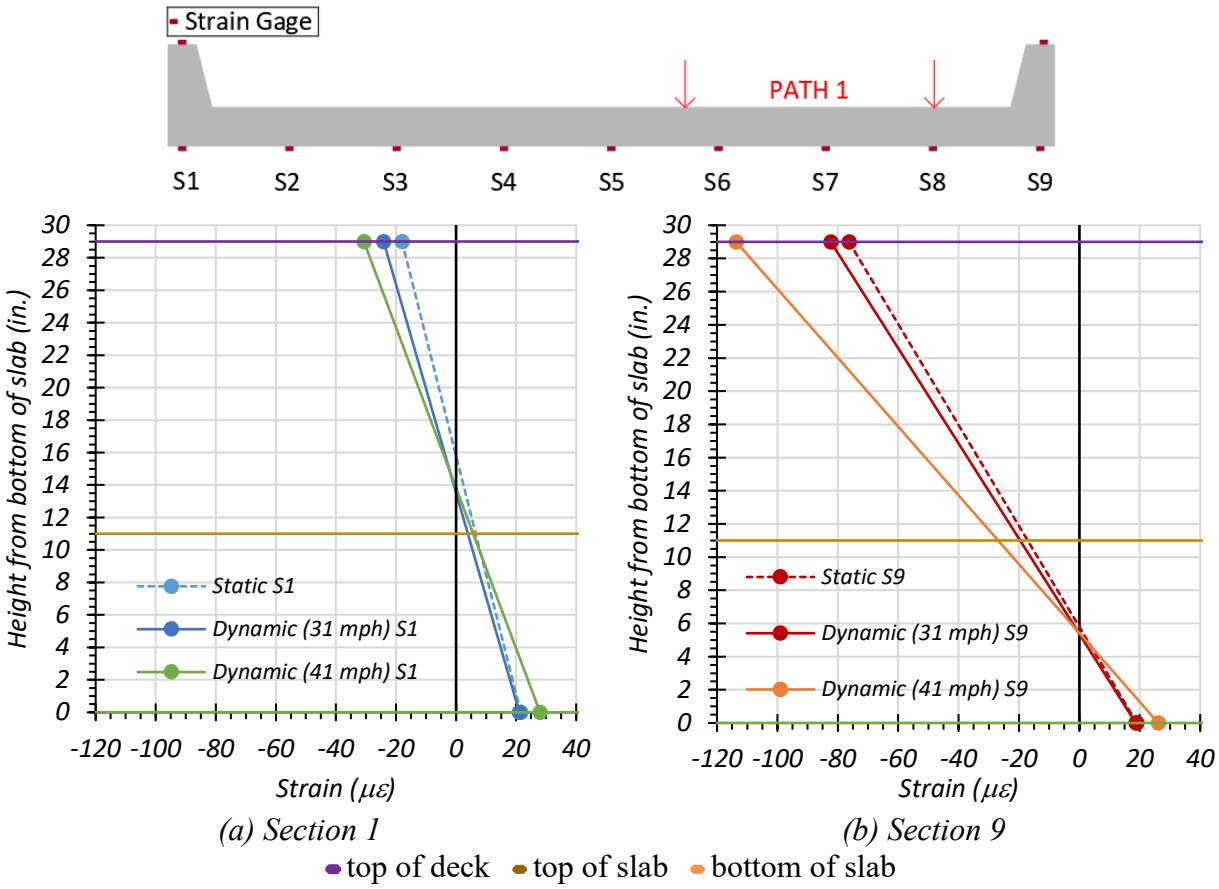

(a) Section 1 *(b) Section 9*

Figure 8.27. Maximum Strains for Static and Dynamic Tests for Path 1 Loading

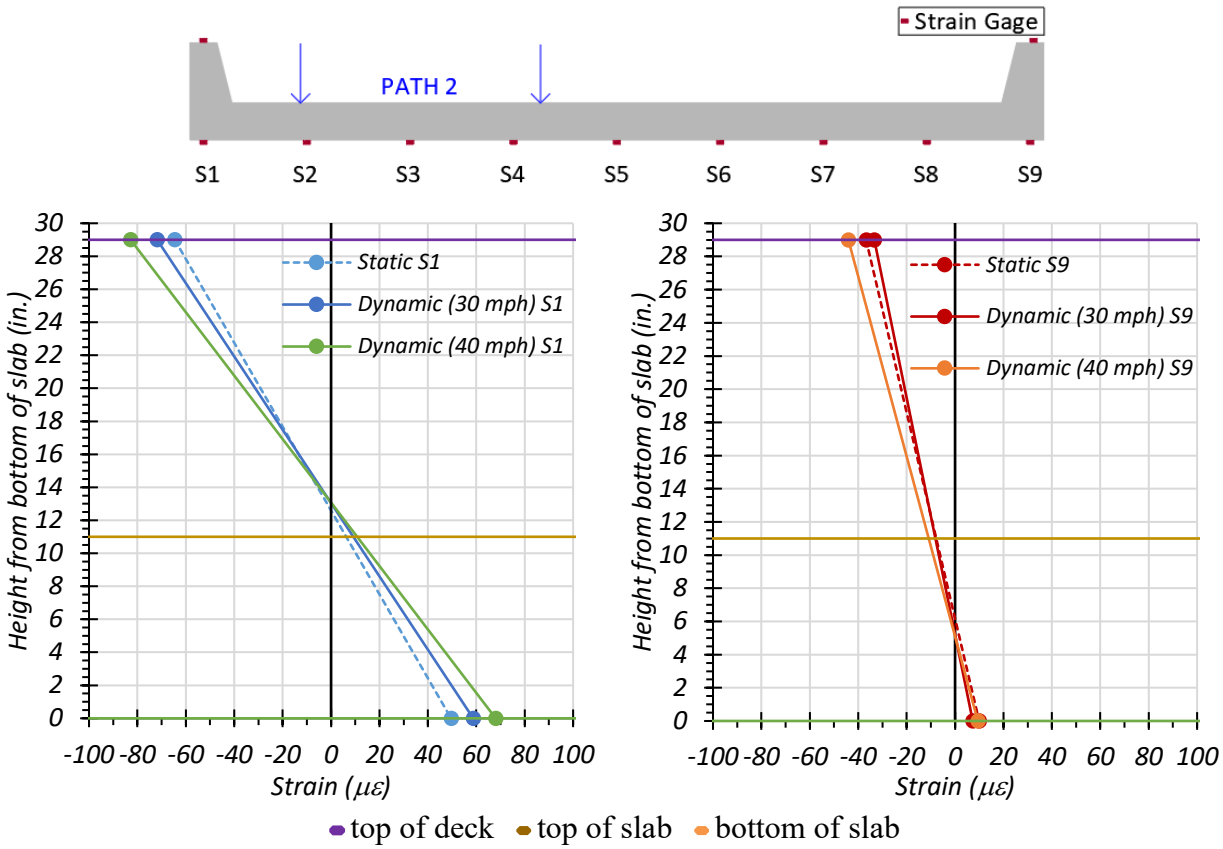

(a) Section 1 *(b) Section 9*

Figure 8.28. Maximum Strains for Static and Dynamic Tests for Path 2 Loading

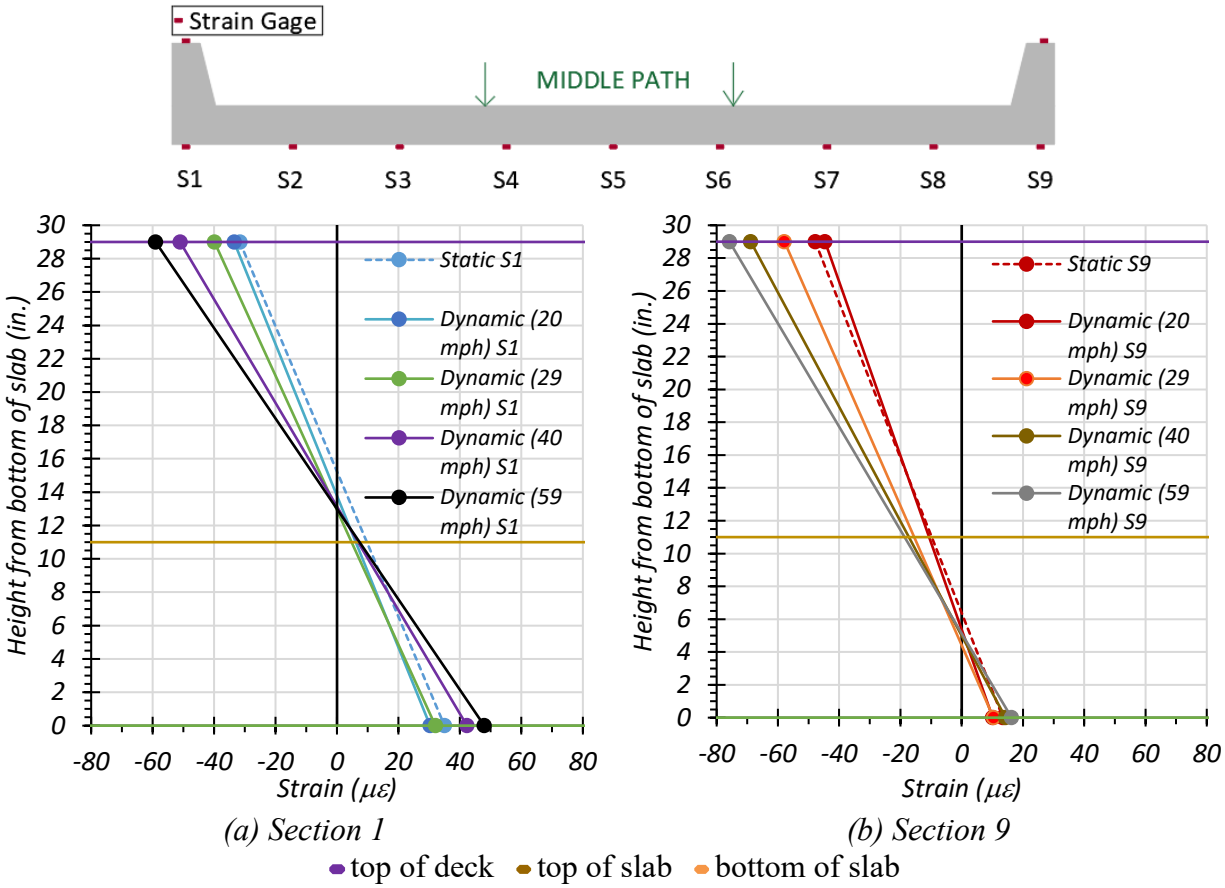

Figure 8.29. Maximum Strains for Static and Dynamic Tests for Middle Path Loading

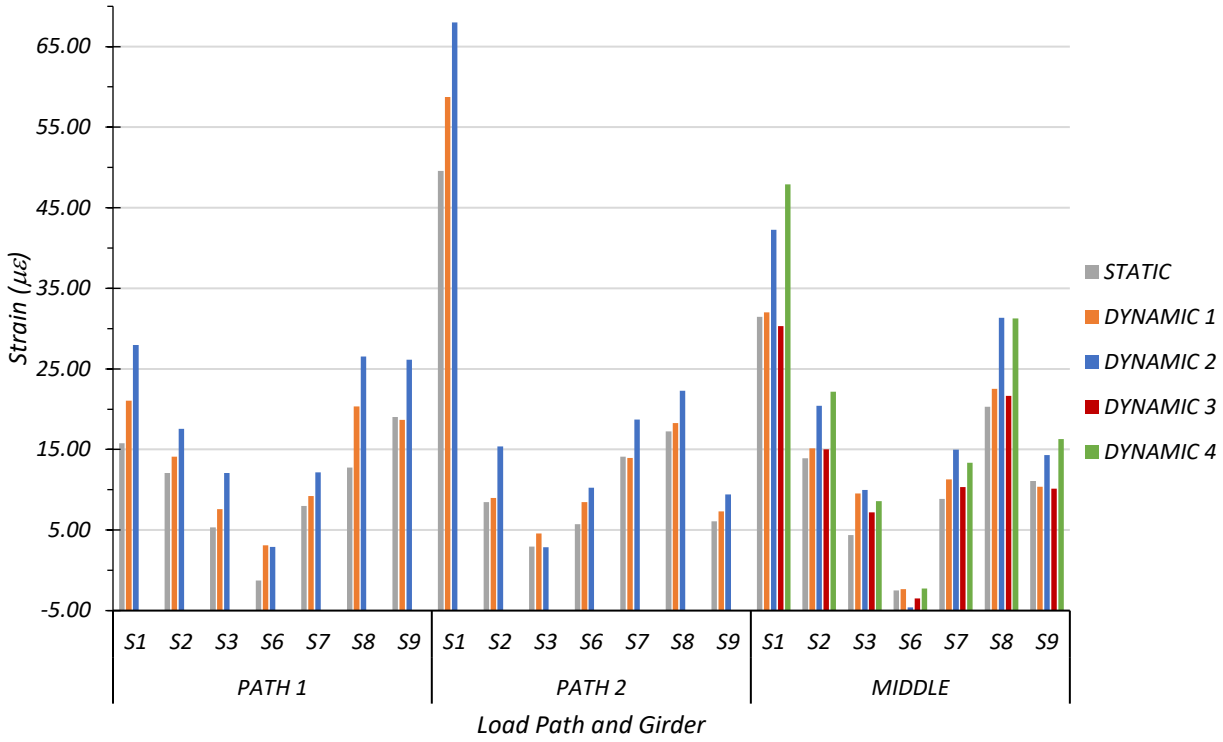

Note:

- *Path 1: Dynamic 1 = 31 mph, Dynamic 2 = 41 mph*
- *Path 2: Dynamic 1 = 30 mph, Dynamic 2 = 40 mph*
- *Middle Path: Dynamic 1 = 20 mph, Dynamic 2 = 29 mph, Dynamic 3 = 40 mph, Dynamic 4 = 59 mph*

Figure 8.30. Comparison of Maximum Bottom Strains for Static and Dynamic Tests

The average dynamic impact factor for the exterior section was found to be 36 percent while that for the interior section was calculated to be 49 percent for Bridge CS-9. These were calculated based on the maximum strains recorded during testing. AASHTO Standard Specifications calls for a dynamic impact factor of 30 percent and AASHTO LRFD Specifications stipulates this to be 33 percent. Thus, for Bridge CS-9 the average dynamic impact factor for the exterior and interior sections is higher than that specified by AASHTO. The maximum impact can be greater than the specified values in AASHTO both in the exterior and interior sections of this integral curb slab bridge.

The maximum strains for each section under static and dynamic tests for Path 1, Path 2, and Middle Path loading is tabulated in Table 8.32. Figure 8.31 compares the dynamic strains for each section with the corresponding static strains. Figure 8.32 shows the measured strains for the controlling dynamic load cases as a ratio to the stop location strain.

The maximum strain obtained for an interior section during the static, Dynamic 1, and Dynamic 2 tests along Path 1 was for Section S3. The strain increased by 43 percent for the Dynamic 1 test and by 126 percent for Dynamic 2 loading when compared to the static test results. The maximum strain obtained for an exterior section during the static, Dynamic 1 and Dynamic 2 tests along Path 1 was for S9. The strain decreased by 2 percent for Dynamic 1 test and increased by 37 percent for the Dynamic 2 loading when compared to the static test results.

The maximum strain obtained for an interior section during the static, Dynamic 1 and Dynamic 2 tests along Path 2 was for Section S2. The strain increased by 7 percent for the Dynamic 1 test and by 82 percent for Dynamic 2 test when compared to the static test results. The maximum strain obtained for an exterior section during the static, Dynamic 1 and Dynamic 2 test along Path 2 was for Section S1. The strain decreased by 3 percent for Dynamic 1 test and increased by 39 percent for Dynamic 2 loading when compared to the static test results.

The maximum strains obtained for an interior section during the static and dynamic tests along the Middle Path were measured for Section S3. The strain increased by 117 percent for the Dynamic 1 test, increased by 127 percent for Dynamic 2 loading, increased by 64 percent for Dynamic 3 test, and increased by 96 percent for Dynamic 4 loading when compared to the static test results. The maximum strains obtained for an exterior section during the static and dynamic tests along the Middle Path were measured for Section S1. The strain increased by 2 percent for the Dynamic 1 test, increased by 34 percent for Dynamic 2 loading, decreased by 4 percent for

Dynamic 3 test, and increased by 52 percent for Dynamic 4 loading when compared to the static test results.

Table 8.32. Maximum Midspan Strains for Static and Dynamic Tests

	Loading	S1	S2	S3	S6	S7	S8	S9
Bottom Strain (με)	Path 1 Static	15.78	12.06	5.33	-1.27	7.99	12.75	19.03
	Path 1 Dynamic (31 mph)	21.07	14.09	7.60	3.11	9.24	20.36	18.68
	Path 1 Dynamic (41 mph)	27.95	17.58	12.06	2.91	12.16	26.54	26.13
	Max. Path 1 Amplification	-	-	126%	-	-	-	37%
Bottom Strain (με)	Path 2 Static	49.58	8.45	2.95	5.73	14.10	17.23	6.09
	Path 2 Dynamic (30 mph)	58.73	9.00	4.56	8.47	13.95	18.29	7.32
	Path 2 Dynamic (40 mph)	68.01	15.37	2.87	10.24	18.69	22.30	9.41
	Max. Path 2 Amplification	37%	82%	-	-	-	-	-
Bottom Strain (με)	Middle Static	31.47	13.91	4.39	-2.51	8.87	20.30	11.10
	Middle Dynamic (20 mph)	32.01	15.13	9.54	-2.36	11.26	22.51	10.37
	Middle Dynamic (29 mph)	42.28	20.43	9.99	-4.62	14.97	31.34	14.32
	Middle Dynamic (40 mph)	30.30	15.01	7.19	-3.48	10.32	21.65	10.12
	Middle Dynamic (59 mph)	47.91	22.16	8.58	-2.27	13.34	31.27	16.28
	Max. Middle Path Amplification	52%	-	127%	-	-	-	-

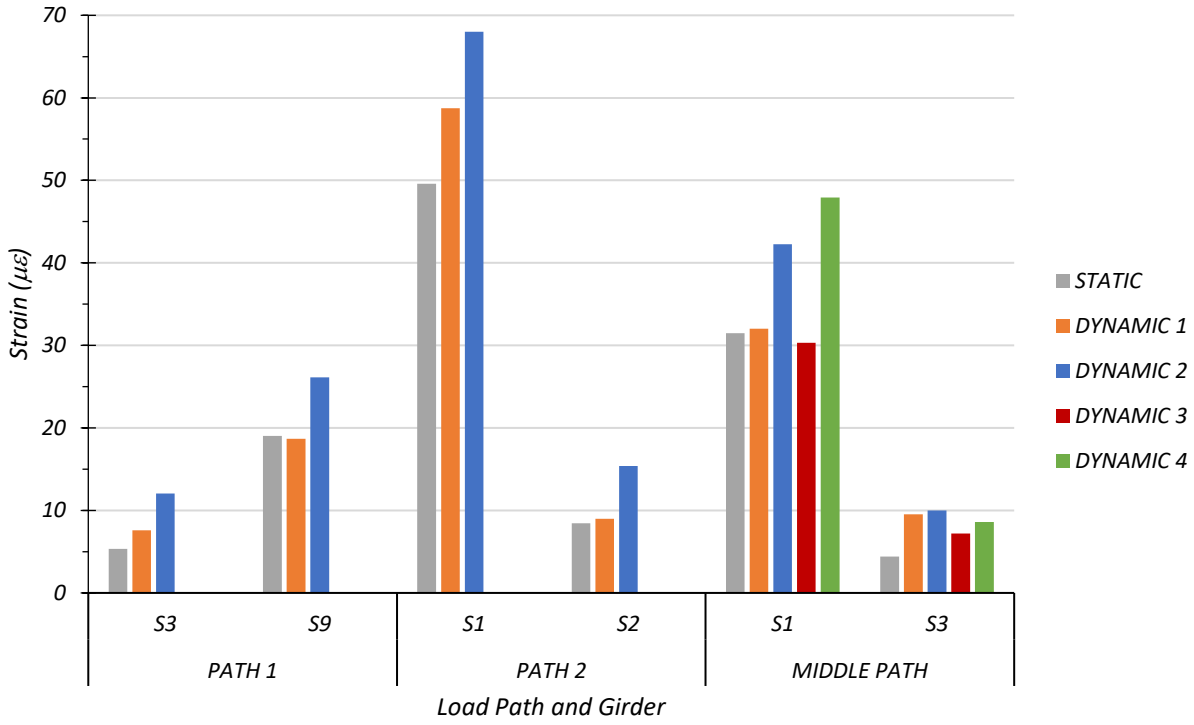

Note:

- *Path 1: Dynamic 1 = 31 mph, Dynamic 2 = 41 mph*
- *Path 2: Dynamic 1 = 30 mph, Dynamic 2 = 40 mph*
- *Middle Path: Dynamic 1 = 20 mph, Dynamic 2 = 29 mph, Dynamic 3 = 40 mph, Dynamic 4 = 59 mph*

Figure 8.31. Static and Dynamic Strain Comparison

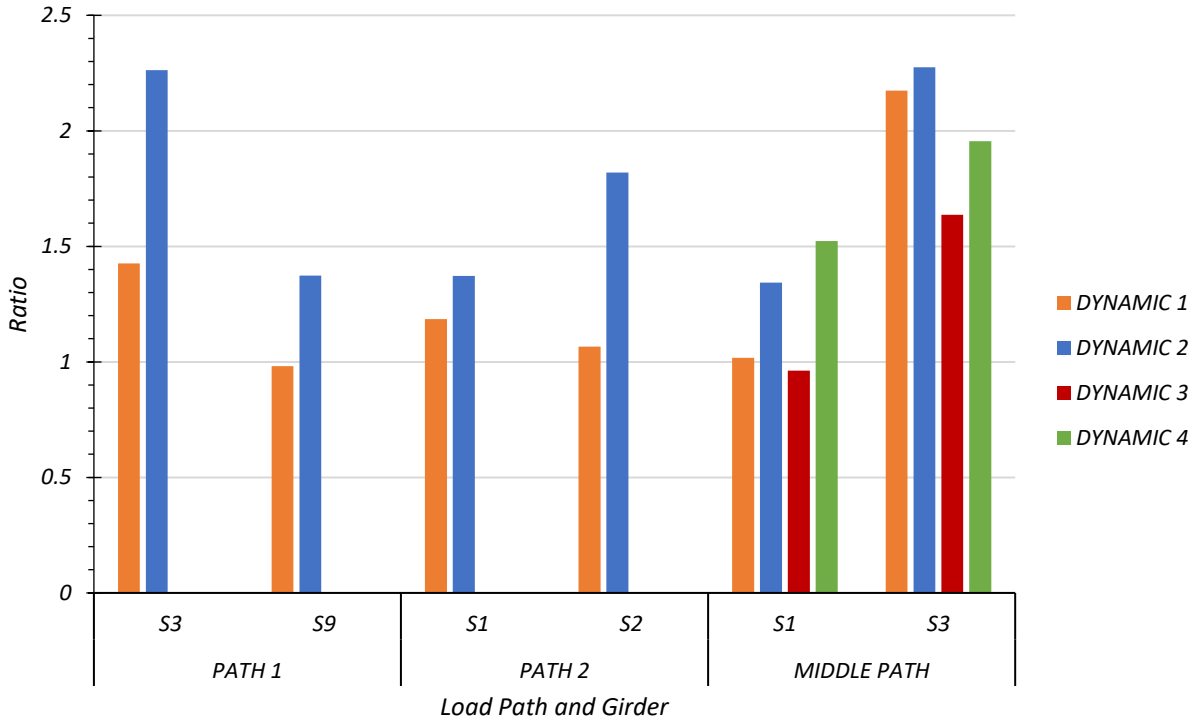

Note:

- *Path 1: Dynamic 1 = 31 mph, Dynamic 2 = 41 mph*
- *Path 2: Dynamic 1 = 30 mph, Dynamic 2 = 40 mph*
- *Middle Path: Dynamic 1 = 20 mph, Dynamic 2 = 29 mph, Dynamic 3 = 40 mph, Dynamic 4 = 59 mph*

Figure 8.32. Maximum Midspan Dynamic Strains to Static Strains Ratios

8.6.2.1.2. Maximum Section Deflections

Dynamic amplification can also be obtained by comparing the dynamic deflections with the static deflections. Deflection time history plots for each section for the Static test and Dynamic 1 and Dynamic 2 tests are provided in Figure 8.33 and Figure 8.34 for Path 1 and Path 2, respectively. Figure 8.35 plots the same for the Middle Path including Dynamic 3 and Dynamic 4 results. The string potentiometer data for statics tests were observed to be noisy. The static data provided in the following graphs were filtered using the moving average approach to remove noise.

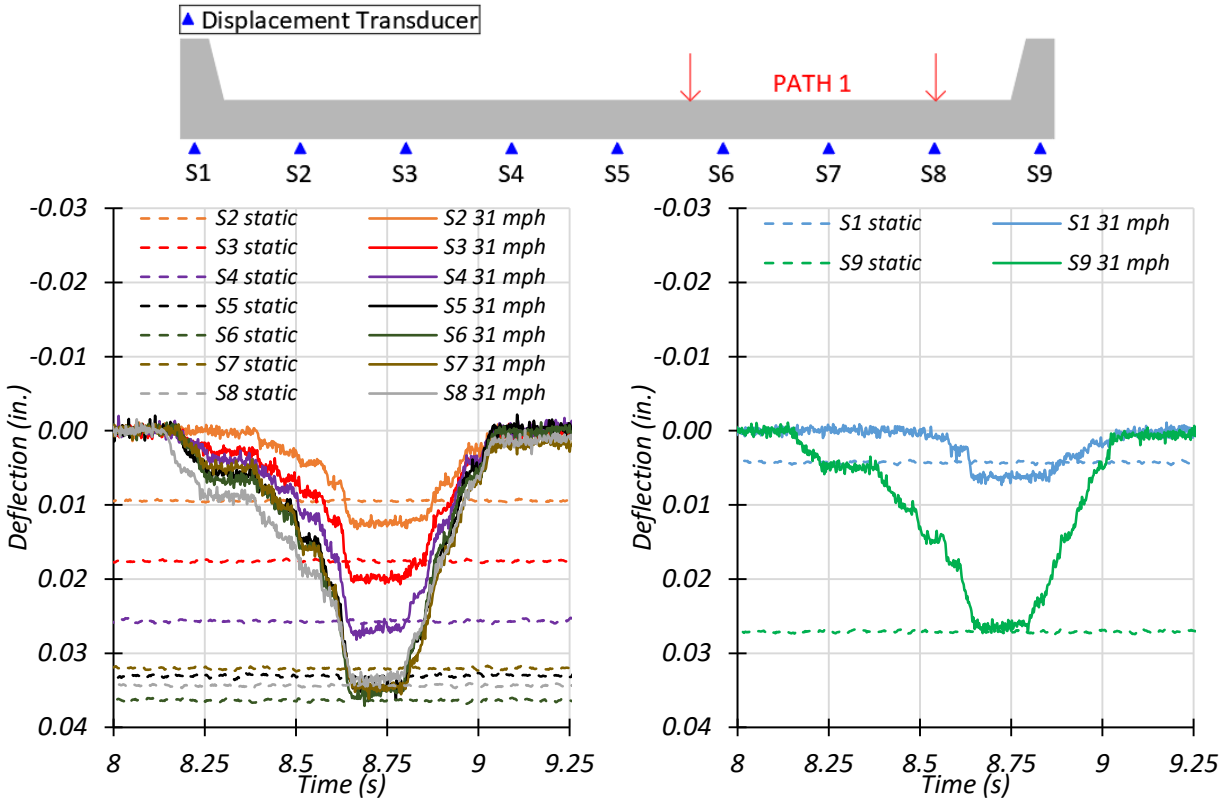

(a) Deflection Time Histories – Dynamic 1 (31 mph)

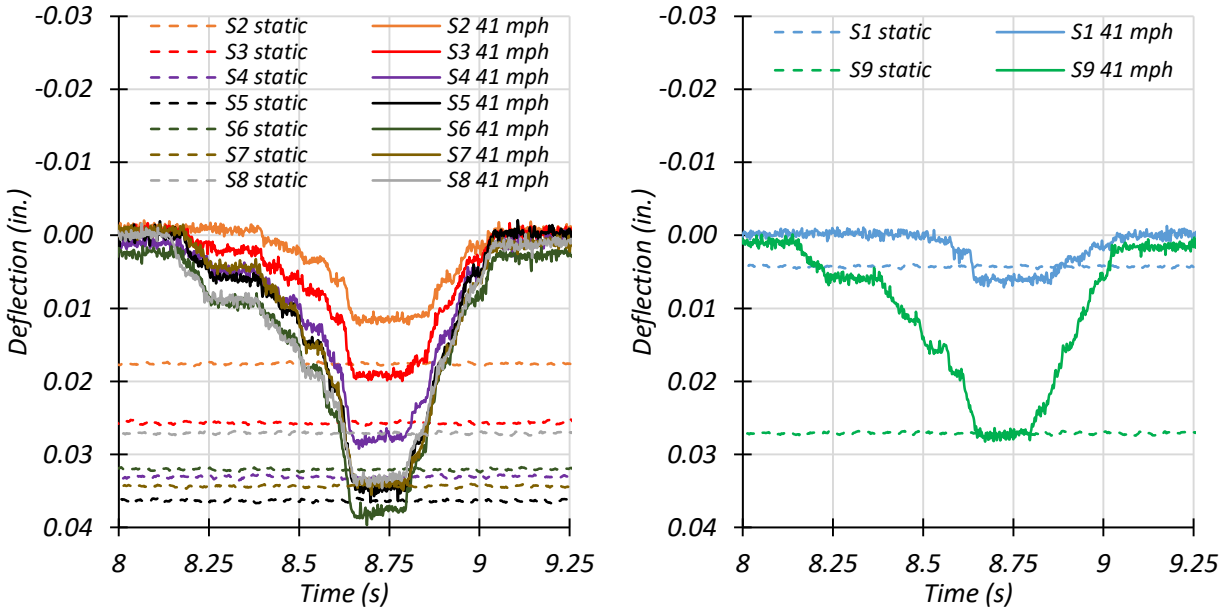

(b) Deflection Time Histories – Dynamic 2 (41 mph)

Figure 8.33. Midspan Deflections for Static and Dynamic Tests for Path 1 Loading

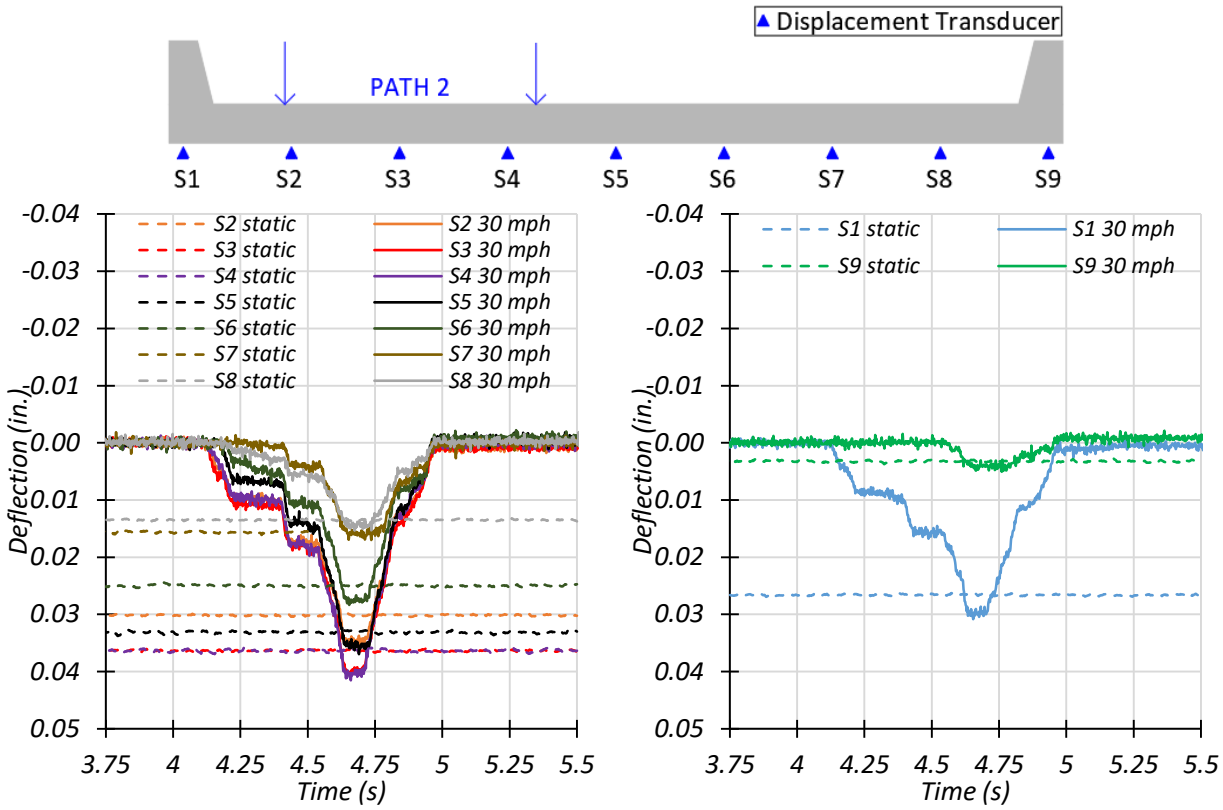

(a) Deflection Time Histories – Dynamic 1 (30 mph)

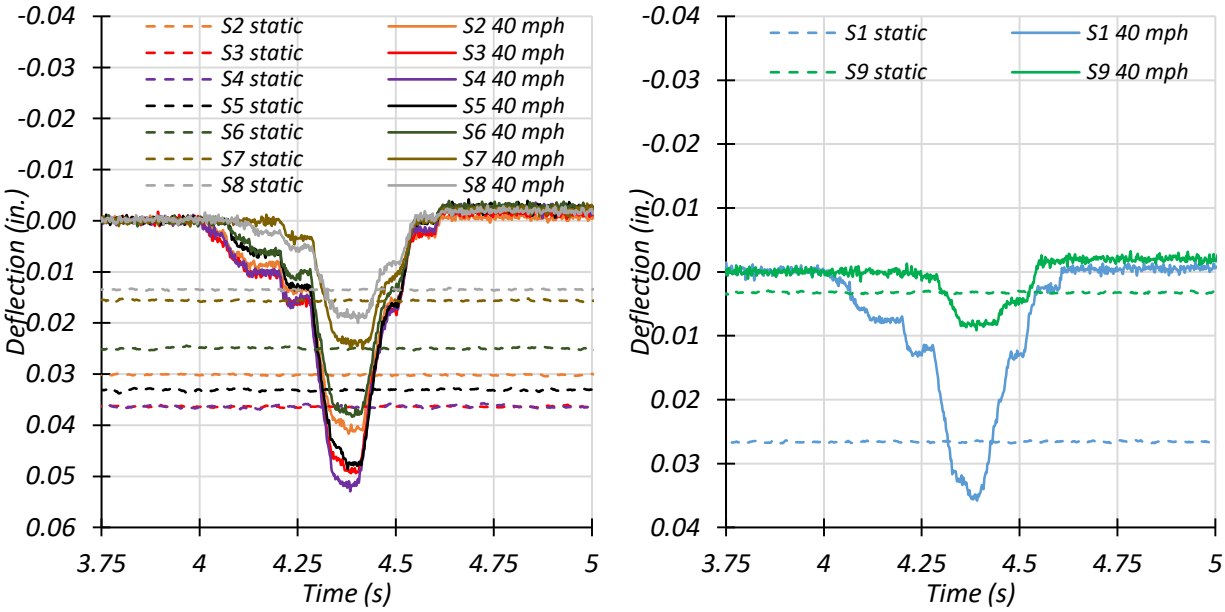

(b) Deflection Time Histories – Dynamic 2 (40 mph)

Figure 8.34. Midspan Deflections for Static and Dynamic Tests for Path 2 Loading

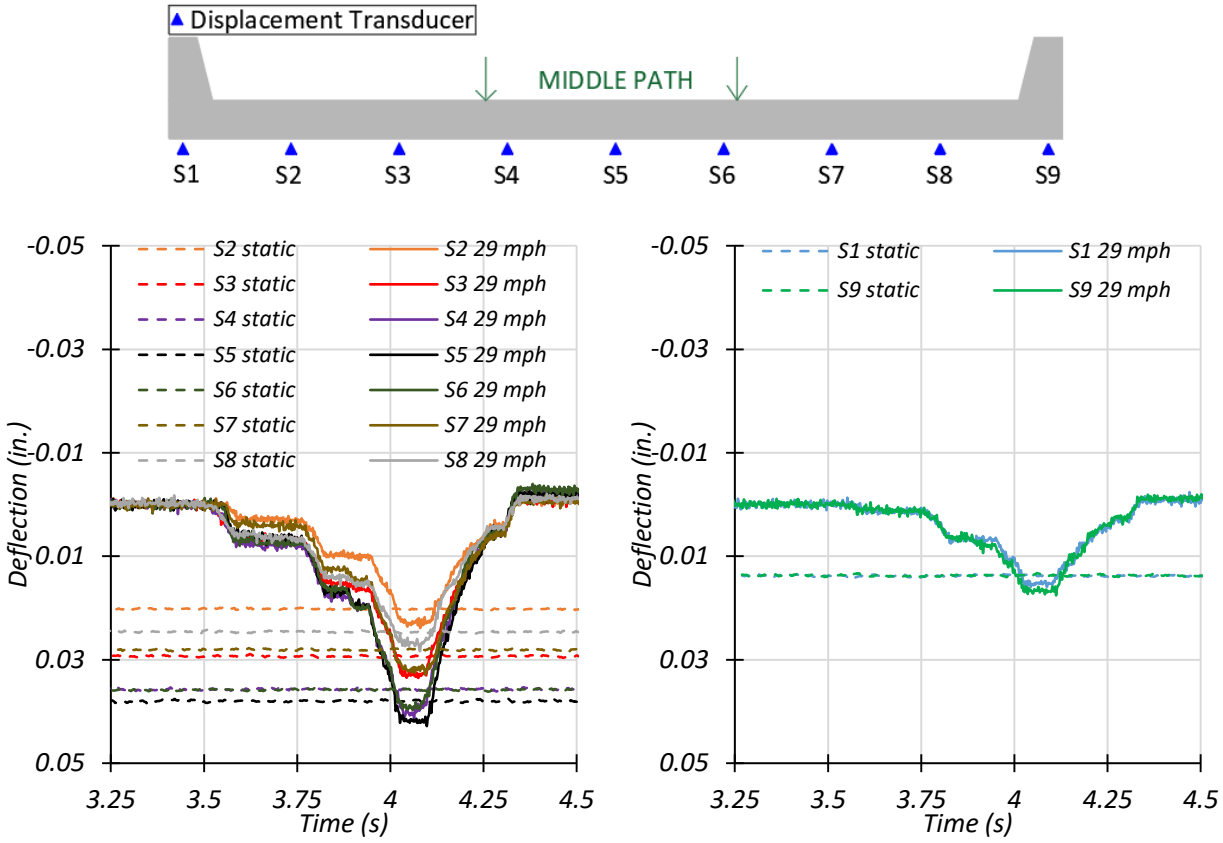

(a) Deflection Time Histories – Dynamic 1 (29 mph)

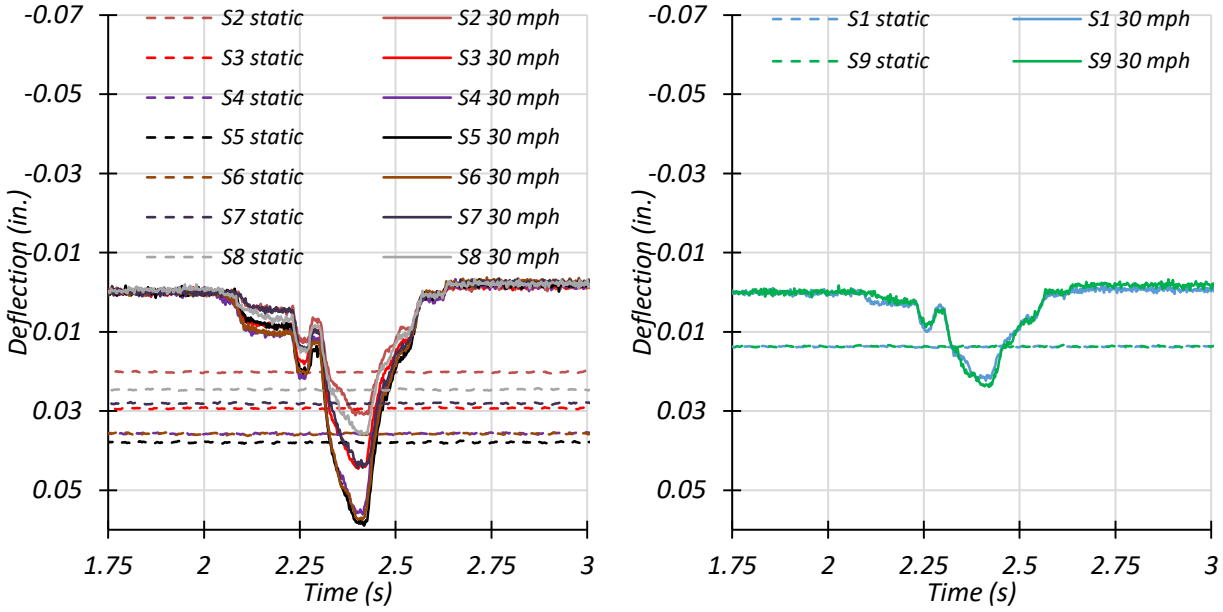

(b) Deflection Time Histories – Dynamic 2 (40 mph)

Figure 8.35. Midspan Deflections for Static and Dynamic Tests for Middle Path Loading

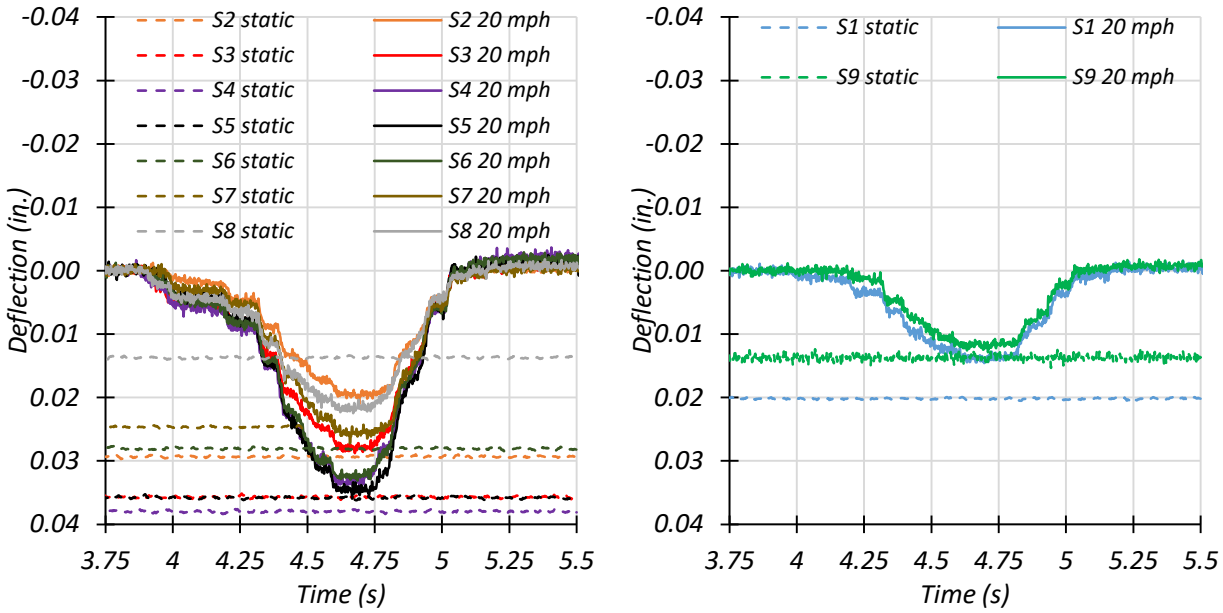

(c) Deflection Time Histories – Dynamic 3 (20 mph)

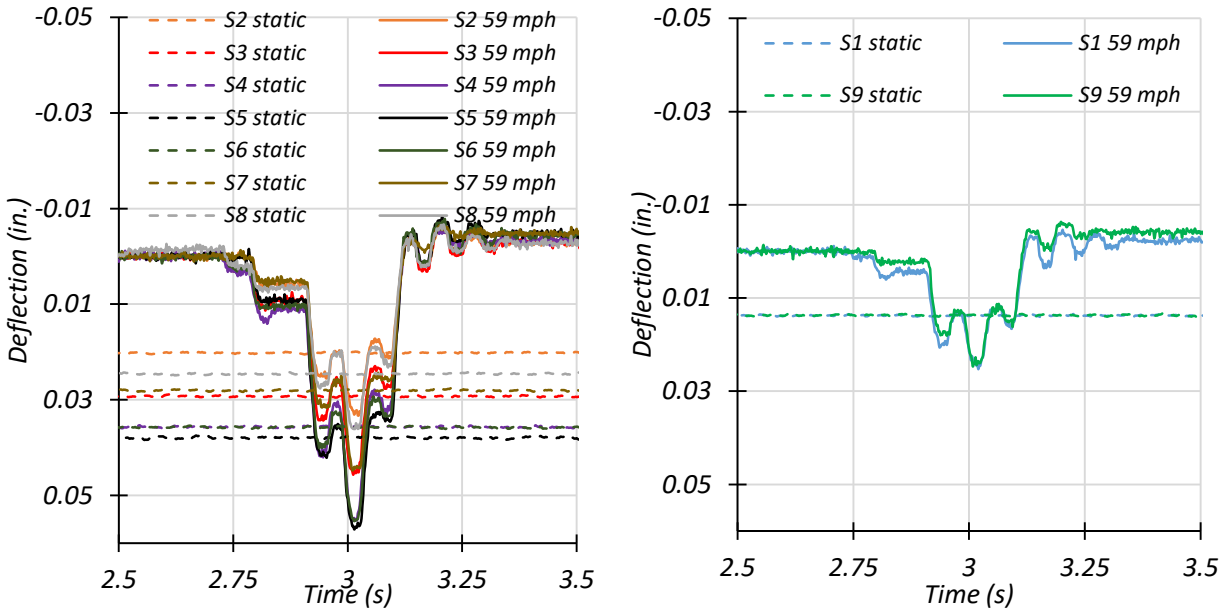

(d) Deflection Time Histories – Dynamic 4 (59 mph)

Figure 8.35 Continued

The maximum deflection for each section under static and dynamic tests for Path 1, Path 2, and Middle Path loading is tabulated in Table 8.33. Figure 8.36 compares the dynamic deflections

for each section with the corresponding static deflections. Figure 8.37 shows the measured deflections for the controlling dynamic load cases as a ratio to the stop location deflection.

Table 8.33. Maximum Midspan Deflections for Static and Dynamic Tests

	Loading	S1	S2	S3	S4	S5	S6	S7	S8	S9
Section Displacement (in.)	Path 1 Static	0.006	0.012	0.019	0.026	0.034	0.036	0.034	0.035	0.028
	Path 1 Dynamic (31 mph)	0.007	0.013	0.021	0.028	0.036	0.037	0.036	0.035	0.027
	Path 1 Dynamic (41 mph)	0.007	0.012	0.020	0.029	0.037	0.040	0.036	0.035	0.028
	Max. Path 1 Amplification	-	-	-	-	-	11%	-	-	0%
Section Displacement (in.)	Path 2 Static	0.028	0.032	0.038	0.038	0.035	0.027	0.018	0.015	0.006
	Path 2 Dynamic (30 mph)	0.031	0.036	0.041	0.042	0.037	0.028	0.017	0.015	0.005
	Path 2 Dynamic (40 mph)	0.036	0.042	0.049	0.053	0.049	0.038	0.025	0.020	0.009
	Max. Path 2 Amplification	29%	-	-	39%	-	-	-	-	-
Section Displacement (in.)	Middle Static	0.016	0.022	0.031	0.037	0.040	0.038	0.030	0.027	0.015
	Middle Dynamic (20 mph)	0.015	0.021	0.029	0.035	0.036	0.033	0.027	0.022	0.013
	Middle Dynamic (29 mph)	0.016	0.024	0.033	0.042	0.043	0.040	0.033	0.028	0.018
	Middle Dynamic (40 mph)	0.022	0.031	0.045	0.056	0.059	0.057	0.044	0.036	0.024
	Middle Dynamic (59 mph)	0.025	0.033	0.046	0.055	0.057	0.055	0.045	0.036	0.025
	Max. Middle Path Amplification	-	-	-	-	48%	-	-	-	67%

The average dynamic impact factor for the exterior section was found to be 32 percent while that for the interior section was calculated to be 33 percent for Bridge CS-9. These were calculated based on the maximum deflections recorded during testing. AASHTO Standard Specifications calls for a dynamic impact factor of 30 percent and AASHTO LRFD Specifications stipulates this to be 33 percent. Thus, for Bridge CS-9 the average dynamic impact factor for the exterior and interior sections is within that specified by AASHTO.

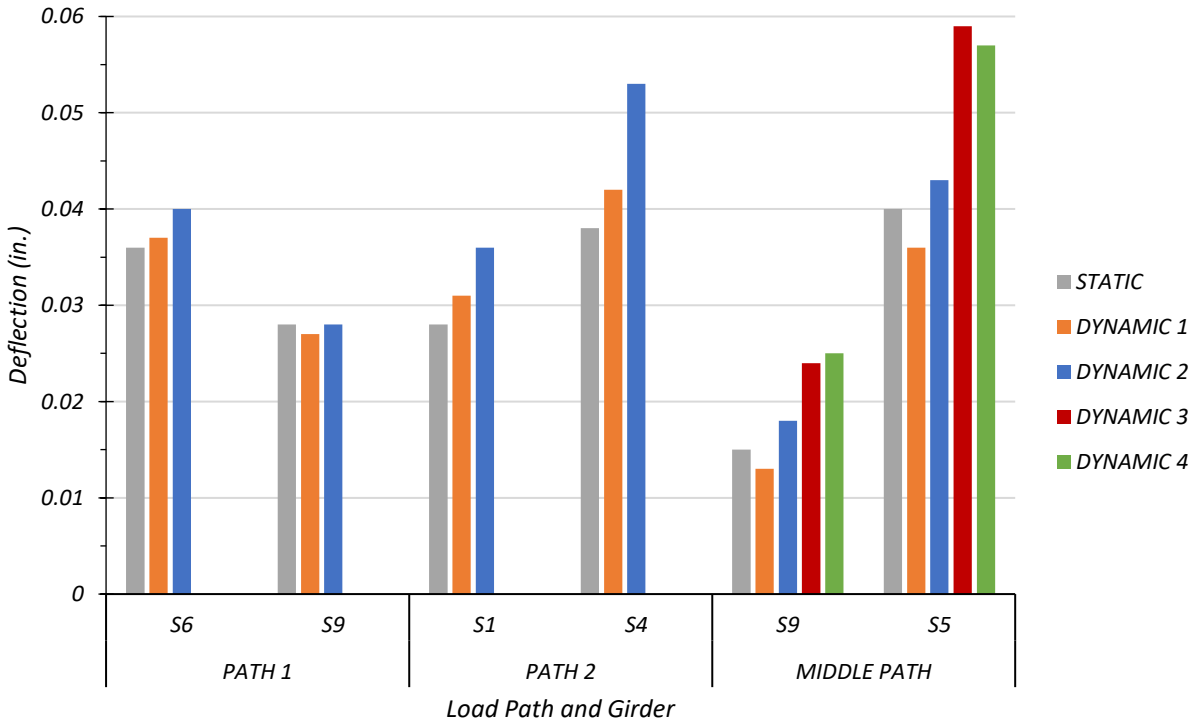

Note:

- *Path 1: Dynamic 1 = 31 mph, Dynamic 2 = 41 mph*
- *Path 2: Dynamic 1 = 30 mph, Dynamic 2 = 40 mph*
- *Middle Path: Dynamic 1 = 20 mph, Dynamic 2 = 29 mph, Dynamic 3 = 40 mph, Dynamic 4 = 59 mph*

Figure 8.36. Static and Dynamic Deflection Comparison

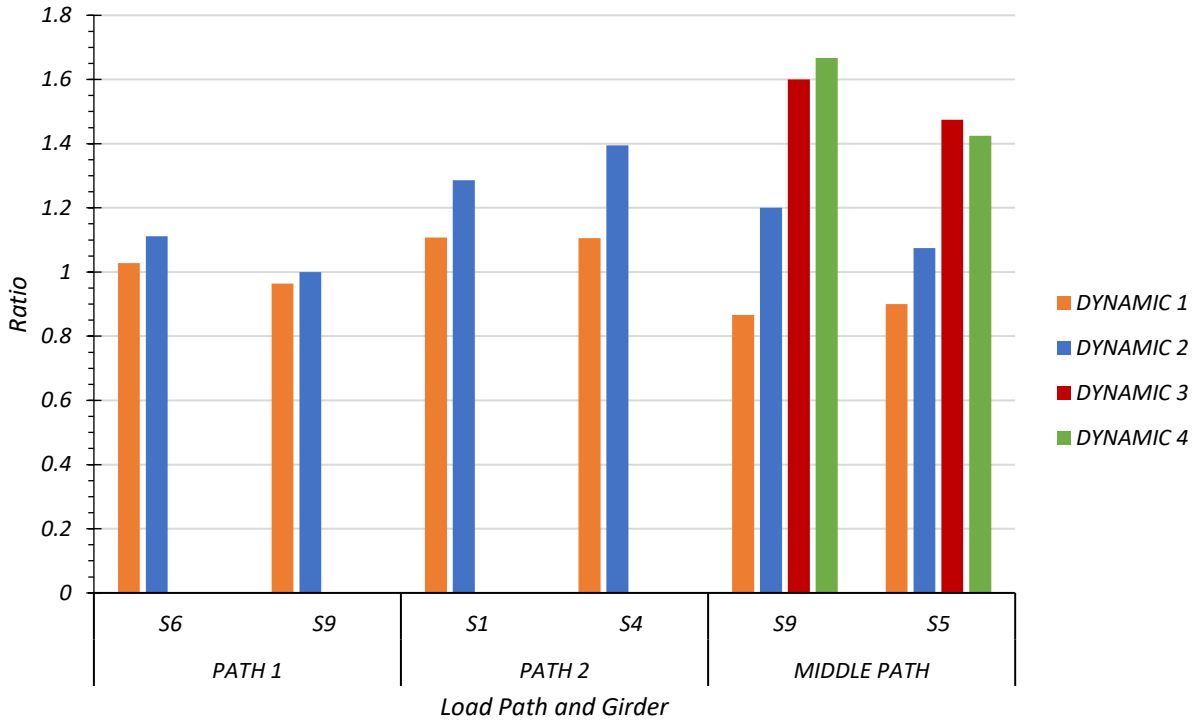

Note:

- *Path 1: Dynamic 1 = 31 mph, Dynamic 2 = 41 mph*
- *Path 2: Dynamic 1 = 30 mph, Dynamic 2 = 40 mph*
- *Middle Path: Dynamic 1 = 20 mph, Dynamic 2 = 29 mph, Dynamic 3 = 40 mph, Dynamic 4 = 59 mph*

Figure 8.37. Maximum Midspan Dynamic Deflections to Static Deflections Ratios

The maximum impact factor for the interior section was calculated to be 48 percent for section S5 during the Middle Path loading scenario. The maximum impact factor for the exterior section was calculated to be 67 percent for Section S9 for the same loading scenario.

The maximum deflection obtained for an interior section during the static, Dynamic 1, and Dynamic 2 tests along Path 1 was for Section S6. The deflection increased by 3 percent for the Dynamic 1 test and by 11 percent for Dynamic 2 loading when compared to the static test results. The maximum deflection obtained for an exterior section during the static, Dynamic 1 and Dynamic 2 tests along Path 1 was for S9. The deflection decreased by 4 percent for Dynamic 1 test and remained unchanged for the Dynamic 2 loading when compared to the static test results.

The maximum deflection obtained for an interior section during the static, Dynamic 1 and Dynamic 2 tests along Path 2 was for S4. The deflection increased by 11 percent for the Dynamic 1 test and by 39 percent for Dynamic 2 test when compared to the static test results. The maximum deflection obtained for an exterior section during the static, Dynamic 1 and Dynamic 2 test along Path 2 was for S1. The deflection increased by 11 percent for Dynamic 1 test and increased by 29 percent for Dynamic 2 loading when compared to the static test results.

The maximum deflection obtained for an interior section during the static, Dynamic 1 (20 mph), Dynamic 2 (29 mph), Dynamic 3 (40 mph) and Dynamic 4 (59 mph) tests along the Middle Path was measured for Section S5. The deflection decreased by 10 percent for the Dynamic 1 test, increased by 7 percent for Dynamic 2 loading, increased by 48 percent for Dynamic 3 test, and increased by 43 percent for Dynamic 4 loading when compared to the static test results. The maximum deflection obtained for an exterior section during the static, Dynamic 1, Dynamic 2, Dynamic 3 and Dynamic 4 tests along the Middle Path was measured for Section S9. The deflection reduced by 13 percent for the Dynamic 1 test, increased by 20 percent for Dynamic 2 loading, increased by 60 percent for Dynamic 3 test, and increased by 67 percent for Dynamic 4 loading when compared to the static test results.

8.6.2.2. Dynamic Characteristics of Bridge

The vibration data recorded by the accelerometers for the dynamic tests and sledge hammer tests were filtered, using a low pass filter (cut-off frequency of 2 Hz) and analyzed to determine the dynamic characteristics of the bridge. Using the Fast Fourier transform (FFT) approach, the first three natural frequencies of the bridge were determined to be 14.65 Hz, 22.46 Hz, and 37.11 Hz. The mode shapes across the longitudinal and transverse section for each natural frequency were

developed using the corresponding amplitude and phase angle for each accelerometer. The accelerometer common to both the longitudinal section and transverse section is at 12.5 ft longitudinally and 10.7 ft transversely. The mode shape along the longitudinal section and transverse section for the first natural frequency is shown in Figure 8.38. Figure 8.39 provides the mode shape along the longitudinal section and transverse section for the second natural frequency. The mode shape along the longitudinal section and transverse section for the third natural frequency is shown in Figure 8.40.

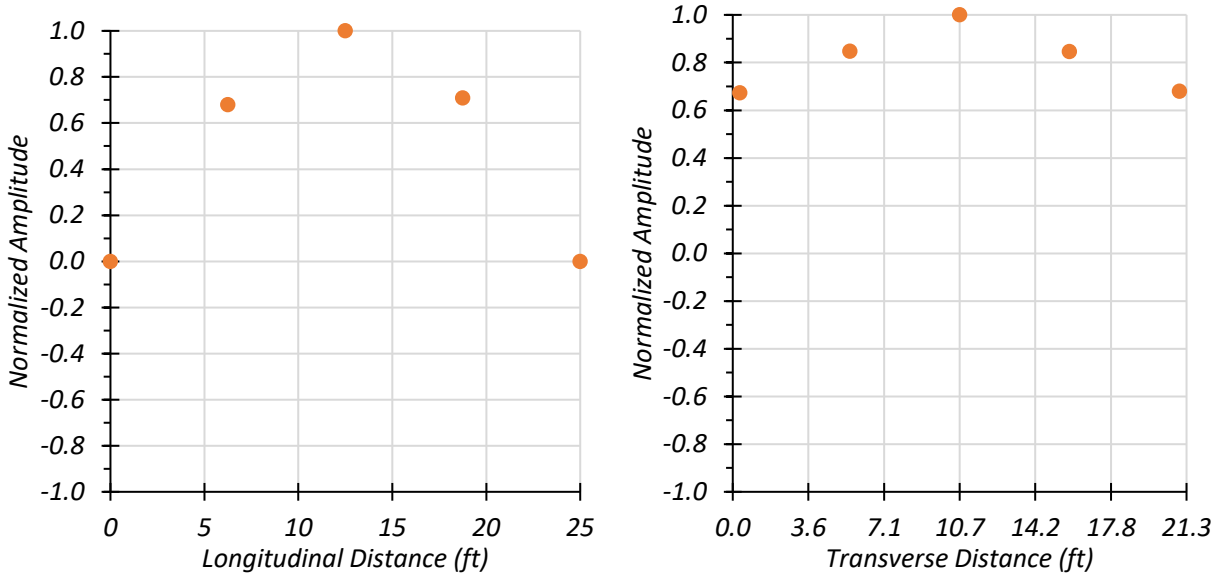

(a) Longitudinal Section *(b) Transverse Section*

Figure 8.38. Measured Mode Shape 1 for Bridge CS-9 (f_1 = 14.65 Hz)

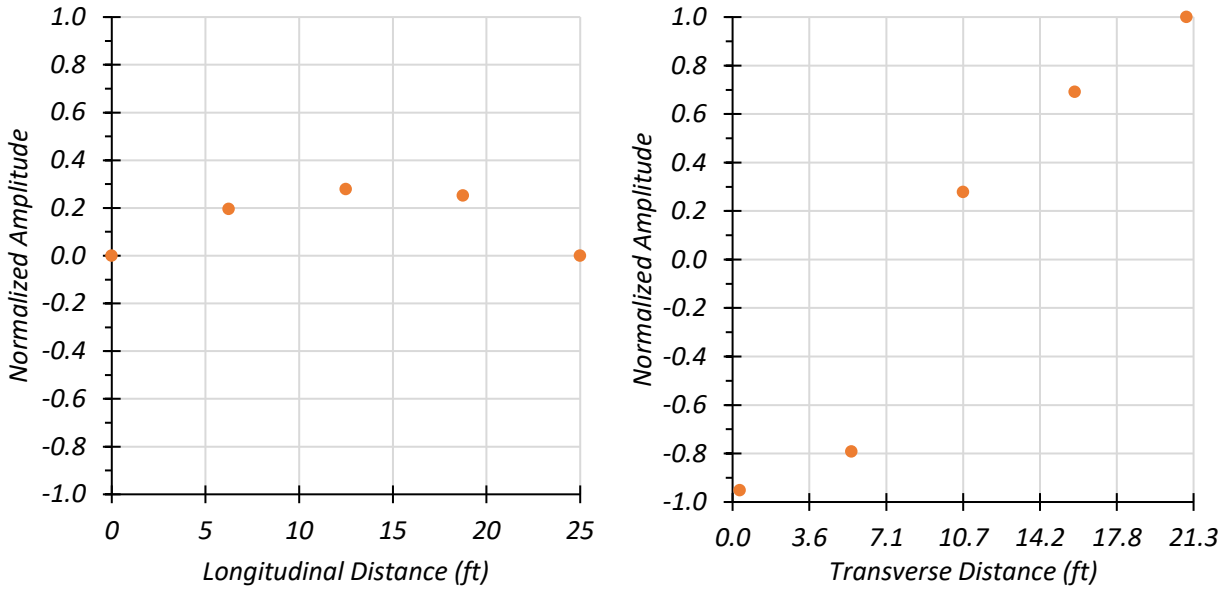

(a) Longitudinal Section *(b) Transverse Section*

Figure 8.39. Measured Mode Shape 2 for Bridge CS-9 (f_2 = 22.46 Hz)

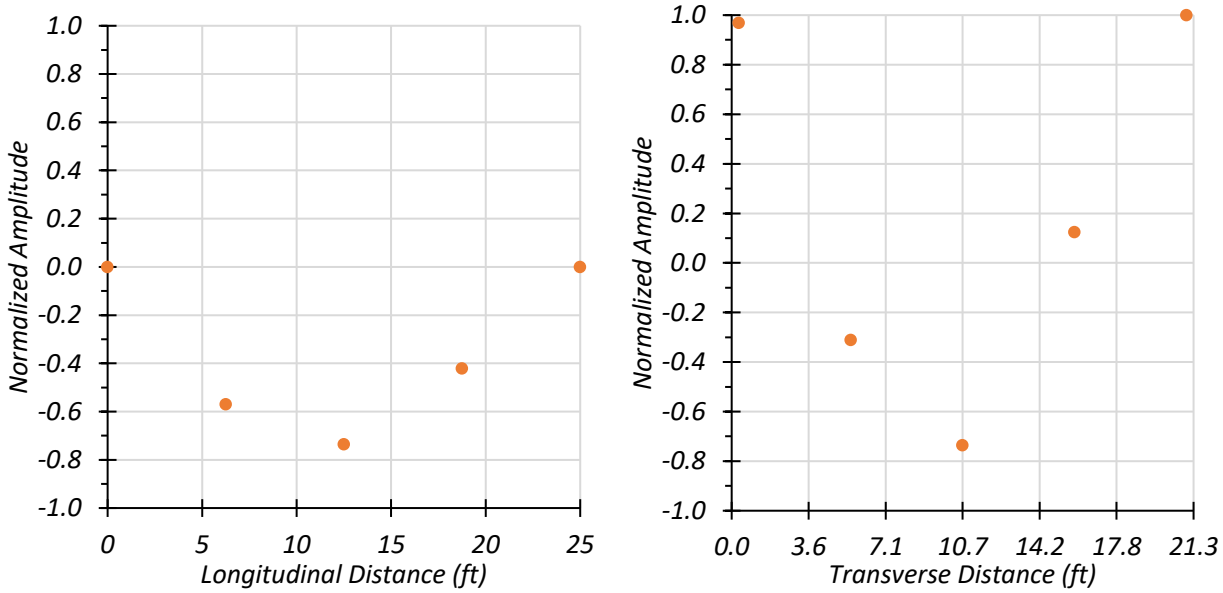

(a) Longitudinal Section *(b) Transverse Section*

Figure 8.40. Measured Mode Shape 3 for Bridge CS-9 (f_3 = 37.11 Hz)

8.6.3. Computer Vision Results

The possibility of determining bridge deflections from video recordings of the bridge during a truck pass was evaluated during the testing of Bridge CS-9. Two cameras, a Sony HDR-CX405 video camera and an iPhone X, were mounted on tripods and set up on either side of the bridge. These were used to record the bridge during each test. The iPhone X was located at the North end of the bridge near Section S1 while the handheld video camera was mounted at the opposite side near Section S9. These were used to record the bridge during each test. The video resolution of the handheld video camera was 1440 pixels by 1080 pixels and it recorded at 30 frames per second (fps). The video resolution of the iPhone was 3840 pixels by 2160 pixels and it recorded at a rate of 60 fps.

A frame-by-frame analysis of the selected sub-window of the area of interest was carried out using an image analysis algorithm written in MATLAB. The location of the sub-window on the bridge was selected such that it covered an area of high contrast. A sensitivity analysis was carried out for different sub-window sizes for the Dynamic Test at 31 mph along Path 1. The results from the different sub-window sizes are presented in Table 8.34. The deflections obtained using a 50 x 50 pixels sub-window was closer to the recorded string potentiometer displacement (0.0267 in.). Thus, this window size was selected for Bridge CS-9.

Table 8.34 Computer Vision Displacement for CS-9 with Different Sub-window Sizes

Window Size (pixels x pixels)	Displacement (in.)
200 x 200	0.0377
100 x 100	0.0392
75 x 75	0.0385
50 x 50	0.0376
100 x 75	0.0382
75 x 100	0.0383

Furthermore, all signals were filtered to remove the noise associated with the data such as unintended vibration of the cameras. Depending on the level of noise, a high pass, a low pass or a band pass filter may be used. However, for this particular bridge all videos were filtered using a lowpass Butterworth filter. A sensitivity analysis was also carried out for this filter by changing the order of the filter and the cut-off frequencies for each load test presented here. A Fast Fourier Transform (FFT) was carried out to plot the magnitude vs. frequency response of the unfiltered computer vision data to determine the range of the cut-off frequency.

The three tests for which computer vision was performed include: (1) Test 2 – Path 1 – Crawl Test, (2) Test 3 – Path 1 – Dynamic at 31 mph, and (3) Test 4 – Path 1 – Dynamic at 41 mph.

The time history plot of deflection obtained from the computer vision analysis was plotted along with the corresponding deflection obtained from the string potentiometer to compare the results. The results from the sensitivity study of the Butterworth Filter for the Crawl Speed Test along Path 1 is presented in Table 8.35. Using a cut-off frequency of 1.5 Hz and a filter of order 5, the results are within 30 percent of the error margin when compared with the string potentiometer result. The image of the bridge taken with the handheld video camera, along with the sub-window used to determine the deflection of the exterior Section S9 during the crawl speed test along Path 1 is shown in Figure 8.41. Figure 8.42 shows the time history plot for the exterior section S9 during the crawl speed test along Path 1. The maximum deflection obtained from the computer vision analysis was found to be 0.0329 in. while the string potentiometer recorded the maximum deflection to be 0.0254 in. The deflection obtained from computer vision was 30 percent higher than that obtained from the string potentiometer. This difference may be due to the associated parallax error.

Table 8.35. Butterworth Filter Sensitivity Study for Path 1 Crawl Speed Test

Order of Butterworth Filter	Cut-off Frequency (Hz)	Computer Vision Deflection (in.)	String Potentiometer Deflection (in.)	% Difference
5	1.0	0.03304	0.02543	2.36
5	1.5	0.03304		2.30
5	2.5	0.03337		2.27
10	1.5	0.03298		2.22
15	1.5	0.03292		2.84

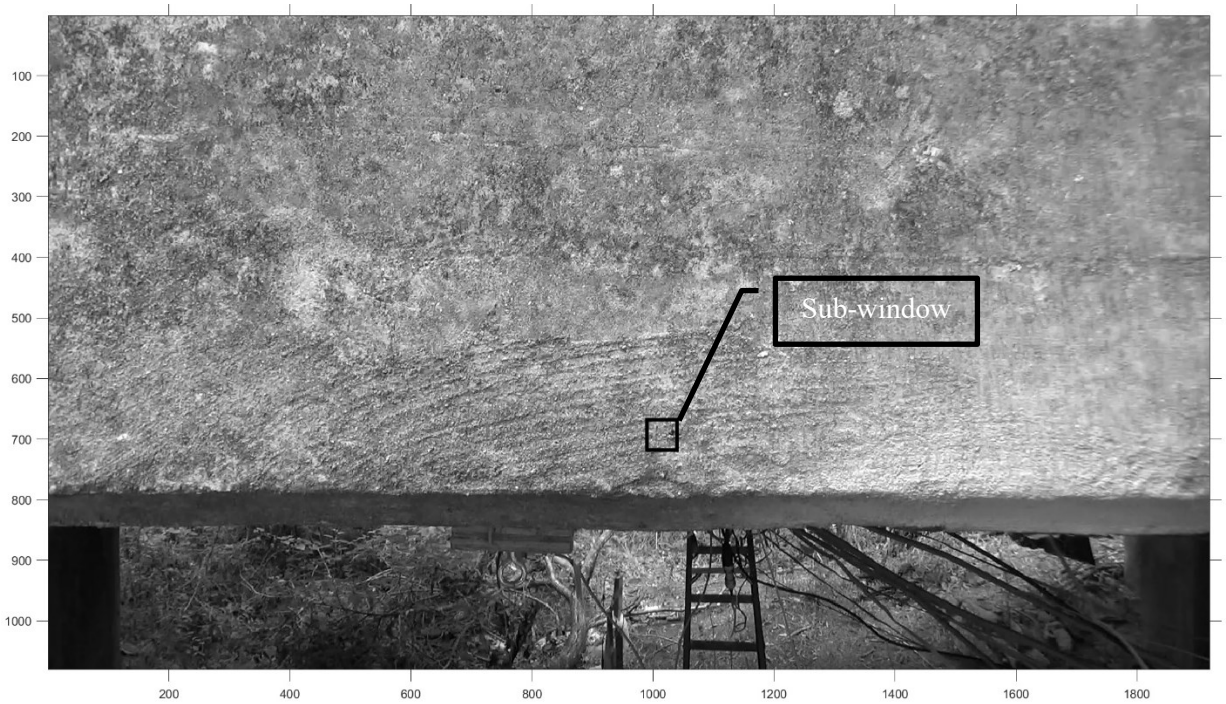

Figure 8.41. Image and Sub-window for Section 9 during Path 1 Crawl Speed Test

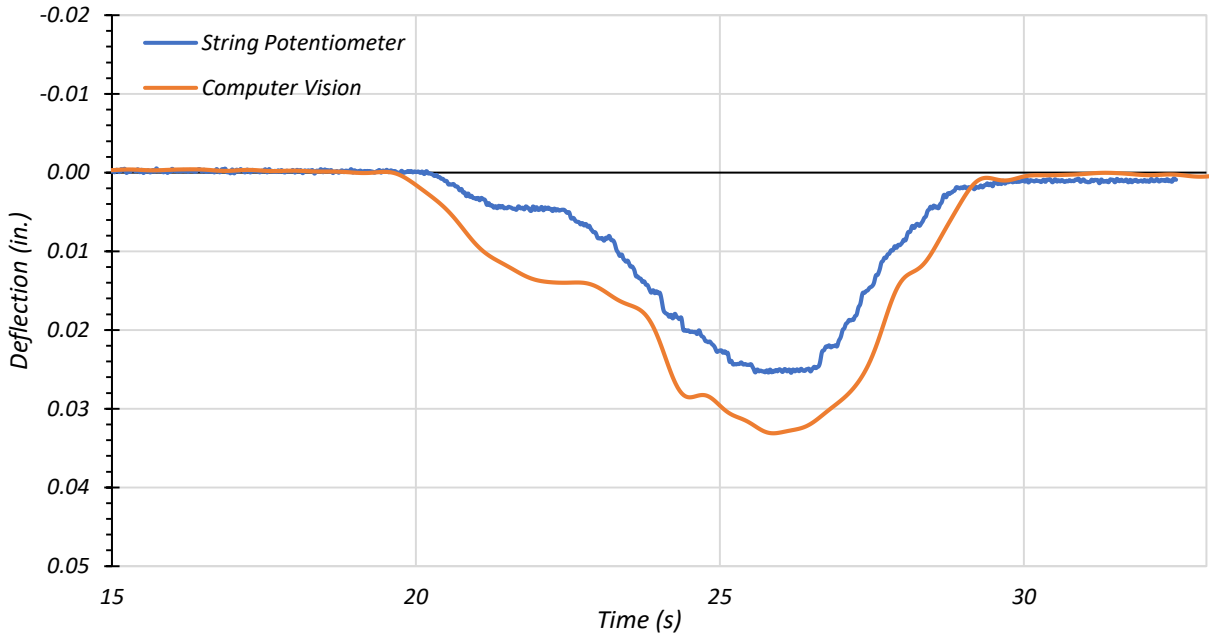

Figure 8.42. Section 9 Midspan Deflections for Path 1 – Crawl Test

A sensitivity study of the Butterworth Filter was also carried out for the Dynamic Test along Path 1 at 31 mph and the results are presented in Table 8.36. Using a cut-off frequency of 1.0 Hz and a filter of order 5 for the image data obtained from the handheld video camera, the results are within 5 percent of the error margin when compared with the string potentiometer result. Although an order of 10 and 15 provided a closer result, the deviation at the end of the time frame associated with these orders were very high. The time history deflection plot for the exterior section S9 during the dynamic test at 31 mph along Path 1 is presented in Figure 8.43. The maximum deflection obtained from the computer vision analysis was found to be 0.0278 in. while the string potentiometer recorded the maximum deflection to be 0.0267 in. The deflection obtained from computer vision was 4.2 percent higher than that obtained from the string potentiometer.

Table 8.36. Butterworth Filter Sensitivity Study for Path 1 Dynamic Test at 31 mph

Order of Butterworth Filter	Cut-off Frequency (Hz)	Computer Vision Deflection (in.)	String Potentiometer Deflection (in.)	% Difference
5	1.0	0.02784	0.02672	4.19
5	1.5	0.03047		14.0
5	2.5	0.03352		25.5
10	1.0	0.02717		1.68
15	1.0	0.02648		-0.90

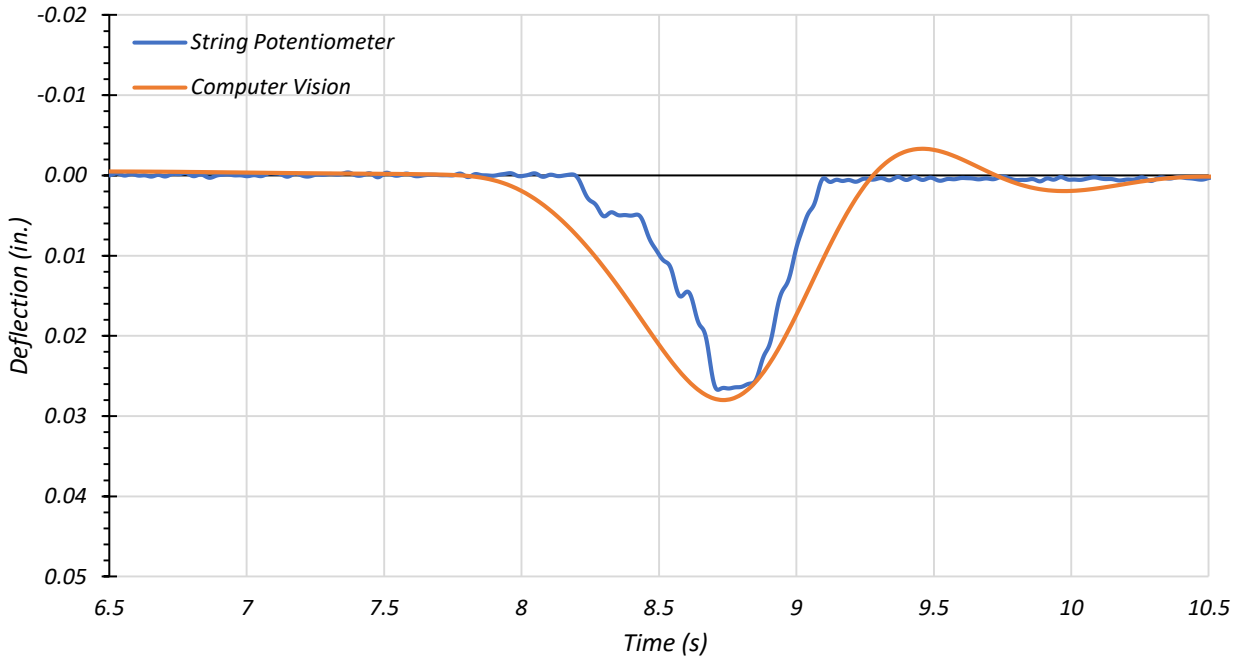

Figure 8.43. Section 9 Midspan Deflections for Path 1 – Dynamic Test at 31 mph

The results from the sensitivity study of the Butterworth Filter for the Dynamic Test at 41 mph along Path 1 are presented in Table 8.37. Using a cut-off frequency of 1.5 Hz and a filter of order 2 for the image data obtained from the handheld video camera, the results are within 10 percent of the error margin when compared with the string potentiometer result. Although an order of 5 and 3 provided a closer result, the deviation at the end of the time frame associated with these orders was very high. The time history deflection plot for the exterior section S9 during the

dynamic test at 31 mph along Path 1 is presented in Figure 8.43. The maximum deflection obtained from the computer vision analysis was found to be 0.0286 in. while the string potentiometer recorded the maximum deflection to be 0.0267 in. The deflection obtained from computer vision was 6.9 percent higher than that obtained from the string potentiometer.

Table 8.37. Butterworth Filter Sensitivity Study for Path 1 Dynamic Test at 41 mph

Order of Butterworth Filter	Cut-off Frequency (Hz)	Computer Vision Deflection (in.)	String Potentiometer Deflection (in.)	% Difference
5	1.0	0.02111	0.02672	-21.0
5	1.5	0.02704		1.20
5	2.5	0.03320		24.3
3	1.5	0.02813		5.28
2	1.5	0.02855		6.85

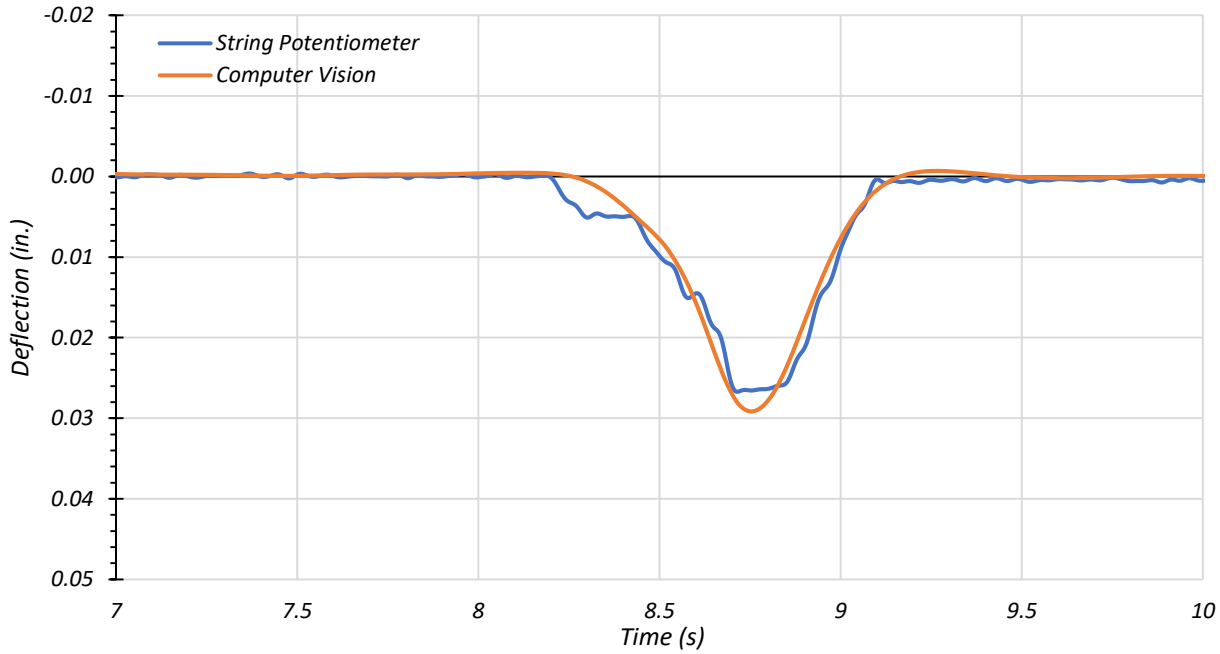

Figure 8.44. Section 9 Midspan Deflections for Path 1 – Dynamic Test at 41 mph

In this section, selected few results obtained from the computer vision analysis are presented. The aim of this analysis was to determine the feasibility of this approach to determine

the true deflection of the bridge under vehicular loading from a video/image. The deflections associated with this bridge are very small (multiple of 1/100 of an inch). This may be the reason for some of the variations observed in the percentage difference. Moreover, the parallax error associated with the position of the camera may also add to the variations observed. However, this approach seems to provide reasonable deflection measurements for this bridge.

8.7. FEM MODEL UPDATE AND CALIBRATION

In the following sections, detailed information regarding updating and calibrating the FEM model based on field measurements.

8.7.1. General

The initial FEM model for Bridge CS-9 was revised to determine appropriate modeling parameters based on comparison to test data. The FEM model update was carried out in two steps: (1) concrete material property update based on NDE tests, and (2) end fixity update based on model calibration.

8.7.2. Updated FEM Model

The concrete compressive strength for Bridge CS-9 was determined to be 5.2 ksi from the NDE tests as explained in Section 8.3.1. This is higher than the initial $f_c{}'$ taken to be 2.5 ksi for the initial FEM model that was created prior to field testing. Therefore, the modulus of elasticity has been updated using $f_c{}' = 5.2$ ksi. In addition, the updated modulus of elasticity (MOE) for Bridge CM-5 was increased by 10 percent for the following reasons: (1) empirical code equations calculate modulus of elasticity (MOE) using secant stiffness, which is smaller than the tangent stiffness; and (2) empirical code equations typically provide lower bound values to be conservative. As a result, the MOE of concrete increased from 3031 ksi to 4809 ksi. The FEM

model was updated to incorporate the MOE based on the measured f_c' and the measured bridge geometries noted in Section 8.3. The end conditions of the updated model were kept the same as the initial FEM model; both ends were modeled with roller supports except one end of one exterior section was modeled as a pin and that of the other exterior section was restrained both vertically and longitudinally. This configuration ensured that the model was structurally restrained in all the degrees of freedom. Table 8.38 provides a few selected results from the updated FEM model and the field test. The results obtained from this updated FEM model are compared with the experimental results in the following sections.

Table 8.38. Selected FEM Results for Updated FEM Model

Model	Modal Frequency (Hz)		Midspan Deflection (in.)		Strain (με)					
					West Bottom		Mid Top	Mid Bottom	East Bottom	
	1st	2nd	S1	S5	S5	S9	S1	S1	S5	S9
Original	11.57	14.30	0.067	0.053	-0.01	23.59	59.15	-111	0.00	-0.03
Updated	11.57	15.38	0.061	0.059	0.00	20.24	53.39	-133	0.00	-0.01
Field Test	14.65	22.46	0.040	0.029	-11.23	3.44	49.58	-64.58	-39.37	-3.33

8.7.3. Model Calibration Process

The updated FEM model for Bridge CS-9 was calibrated for end fixity at the abutments. The model developed from this process could more closely represent the measured behavior of the bridge.

The updated FEM model was calibrated to incorporate cracked concrete properties by using non-linear material properties. This was carried out by considering the cracked behavior of concrete to be the nonlinear Mander model for concrete (Mander et al. 1988). Two different values for concrete tensile strength were considered: 10% of measured concrete compressive strength and 1% of measured concrete compressive strength. These analyses were carried out for simply supported end conditions, pin-pin end conditions and roller-roller end conditions.

Four input parameters were identified for calibrating the above updated FEM model of Bridge CS-9 to determine the appropriate end fixities. These were: (1) west end of all interior sections, (2) west end of both exterior sections, (3) east end of all interior sections, and (4) east end of both exterior sections. The vertical translational degree of freedom was fully restrained for all sections. Horizontal springs were introduced at the bottom nodes of the sections of the concrete slab bridge. The horizontal spring stiffness was modified to provide partial fixities at the ends. The influence of introducing horizontal springs at the top nodes of the concrete slab was also considered. Roller supports were considered to be the lower bound for the horizontal spring stiffness and pin supports were the upper bound. The corresponding upper and lower bound spring stiffness were determined. The effect of each input parameter on the analysis results was studied by gradually varying one parameter at a time. The results from this parametric study are presented in the following sections.

8.7.4. Calibrated FEM Model Results

In this section, the influence of changing each selected input parameter on the analysis results is presented. The calibration of the model was carried out based on experimental results obtained for the static tests carried out on Bridge CS-9, provided in Table 8.39. It should be noted that Section S9 results are obtained from the Path 1 stop location test, Section S1 results from Path 2 stop location, and Section S5 results from the Middle Path stop location test.

Table 8.39. Experimental Results for Calibration of Bridge CS-9

Modal Frequency (Hz)		Midspan Deflection (in.)		Strain (με)					
				West Bottom		Mid Top	Mid Bottom	East Bottom	
1st	2nd	S1	S5	S5	S9	S1	S1	S5	S9
14.65	22.46	0.029	0.040	-11.23	3.44	-64.57	49.58	-39.37	-3.33

8.7.4.1. Modulus of Elasticity

The modulus of elasticity was modified to account for the cracks observed in the slab bridge with integral curbs. The end supports were also modified to study the cumulative effect. These results are summarized and presented in Table 8.40.

Table 8.40. Effect of Modulus of Elasticity Value on Selected FEM Results

Case	West Fixity	East Fixity	Modal Frequency (Hz)		Midspan Deflection (in.)		Strain (με)					
							West Bot		Mid Top	Mid Bot	East Bot	
			1st	2nd	S1	S5	S5	S9	S1	S1	S5	S9
Test	Pin	Roller	14.65	22.46	0.029	0.040	-11.23	3.44	-64.57	49.58	-39.37	-3.33
1(a)	Pin	Pin	14.50	20.75	0.042	0.043	-8.84	0.32	-112	35.29	-9.72	-4.98
1(b)	Pin	Roller	11.64	17.18	0.061	0.059	0.00	18.15	-135	54.67	0.00	-0.01
1(c)	Roller	Roller	11.66	18.15	0.061	0.059	0.00	19.84	-136	55.94	0.00	0.00
1(d)	Roller	Roller	14.50	20.75	0.042	0.043	-5.35	3.16	-112	36.00	-13.06	-18.04
Case 1(a) – 1(c): Nonlinear Mander model for concrete with $f_t = 0.1f_c'$ Case 1(d): Nonlinear Mander model for concrete with $f_t = 0.01f_c'$												

The nonlinear Mander model with $f_t = 1\%f_c'$ for concrete, which was intended to represent the presence of existing cracks, provided agreeable results to the experimental results. The following calibration is carried out using Case 1(d) listed in Table 8.40.

8.7.4.2. West End Interior Section Stiffness Spring

The effect of changing the boundary condition at west end of the interior sections was determined by changing the support to roller (only vertical translation restrained) and pin (all three translations restrained) while keeping the boundary conditions for west end exterior sections and east end as rollers. The second modal frequency and the bottom strain at the midspan for Section S1 for the pin support are close to the test results. Hence, the boundary condition for the west end of the interior sections was found to be closer to the pin support as shown in Table 8.41.

Table 8.41. Effect of West End Interior Section Fixity on Selected FEM Results

West End Interior Sections	Modal Frequency (Hz)		Midspan Deflection (in.)		Strain (με)					
					West Bottom		Mid Top	Mid Bottom	East Bottom	
Support	1st	2nd	S1	S5	S5	S9	S1	S1	S5	S9
Test	14.65	22.46	0.029	0.040	-11.23	3.44	-64.57	49.58	-39.37	-3.33
Pin	12.87	21.20	0.047	0.050	0.00	16.84	-99.1	46.09	0.00	-0.02
Roller	13.03	20.32	0.048	0.050	0.00	16.79	-63.58	27.28	0.00	-0.02

8.7.4.3. West End Exterior Section Stiffness Spring

The effect of changing the boundary condition at west end of the exterior transverse sections was determined by changing the support to roller (only vertical translation restrained) and pin (all three translations restrained) while keeping the boundary conditions for west end interior sections and east end as rollers. The second modal frequency, and the bottom strain at the midspan of Section S1 for the pin support are close to the test results. Hence, the boundary condition for the west end of the exterior sections was found to be closer to the pin support as shown in Table 8.42.

Table 8.42. Effect of West End Exterior Section Fixity on Selected FEM Results

West End Exterior Section	Modal Frequency (Hz)		Midspan Deflection (in.)		Strain (με)					
					West Bottom		Mid Top	Mid Bottom	East Bottom	
Support	1st	2nd	S1	S5	S5	S9	S1	S1	S5	S9
Test	14.65	22.46	0.029	0.040	-11.23	3.44	-64.57	49.58	-39.37	-3.33
Pin	12.82	21.50	0.047	0.050	0.00	16.20	-102	46.58	0.00	-0.02
Roller	13.03	20.32	0.048	0.050	0.00	16.79	-63.58	27.28	0.00	-0.02

8.7.4.4. East End Interior Section Stiffness Spring

The effect of changing the boundary condition at east end of the interior transverse sections was determined by changing the support to roller (only vertical translation restrained) and pin (all three translations restrained) while keeping the boundary conditions for east end exterior sections and west end as rollers. The second modal frequency and the bottom strain at the midspan of Section

S1 for the pin support are close to the test results. Hence, the boundary condition for the east end of the interior sections was found to be closer to the pin support as shown in Table 8.43.

Table 8.43. Effect of East End Interior Section Fixity on Selected FEM Results

East End Interior Section	Modal Frequency (Hz)		Midspan Deflection (in.)		Strain (με)					
					West Bottom		Mid Top	Mid Bottom	East Bottom	
Support	1st	2nd	S1	S5	S5	S9	S1	S1	S5	S9
Test	14.65	22.46	0.029	0.040	-11.23	3.44	-64.57	49.58	-39.37	-3.33
Pin	12.86	21.20	0.047	0.050	0.00	17.07	-102	46.77	0.00	-0.02
Roller	13.03	20.32	0.048	0.050	0.00	16.79	-63.58	27.28	0.00	-0.02

8.7.4.5. East End Exterior Section Stiffness Spring

The fixity at the east end of the exterior section was determined by changing the support to roller (only vertical translation restrained) and pin (all three translations restrained) while keeping the boundary conditions for east end interior sections and west end as rollers. The second modal frequency and the bottom strain at the midspan of Section S1 for the pin support are close to the test results. Hence, the fixity was found to be closer to the pin support as shown in Table 8.44.

Table 8.44. Effect of East End Exterior Section Fixity on Selected FEM Results

East End Exterior Section	Modal Frequency (Hz)		Midspan Deflection (in.)		Strain (με)					
					West Bottom		Mid Top	Mid Bottom	East Bottom	
Support	1st	2nd	S1	S5	S5	S9	S1	S1	S5	S9
Test	14.65	22.46	0.029	0.040	-11.23	3.44	-64.57	49.58	-39.37	-3.33
Pin	12.82	21.50	0.047	0.050	0.00	17.29	-102	47.54	0.00	-0.02
Roller	13.03	20.32	0.048	0.050	0.00	16.79	-63.58	27.28	0.00	-0.02

8.7.4.6. Final Calibration

The individual parametric studies suggested that both ends of the bridge supports are similar to a pin support. The final model calibration was initiated with these end conditions. Each input parameter was gradually adjusted until the FEM results were close to the experimental results. The model was analyzed with different end stiffness values ranging from 50 kip/in. to 15,000 kip/in.

The final calibrated model parameters are presented in Table 8.45. Here pinned indicates an infinitely stiff spring at the support providing restraint in all three translational directions. It should be noted that no horizontal springs were provided to restrain the top nodes of the slab.

Table 8.45. Final Calibrated Model Parameters

Concrete Properties		Stiffness Value (kip/in.)			
f_c' (ksi)	E_c (ksi)	West End Interior Sections	West End Exterior Sections	East End Interior Sections	East End Exterior Sections
5.2	4809	Pinned	Pinned	Pinned	500

The calibrated model for Bridge CS-9 along with the end fixity springs is shown in Figure 8.45. The results obtained from the calibrated FEM model along with the test results are tabulated in Table 8.46. In the following sections, the results from this calibrated model are compared with the experimental results.

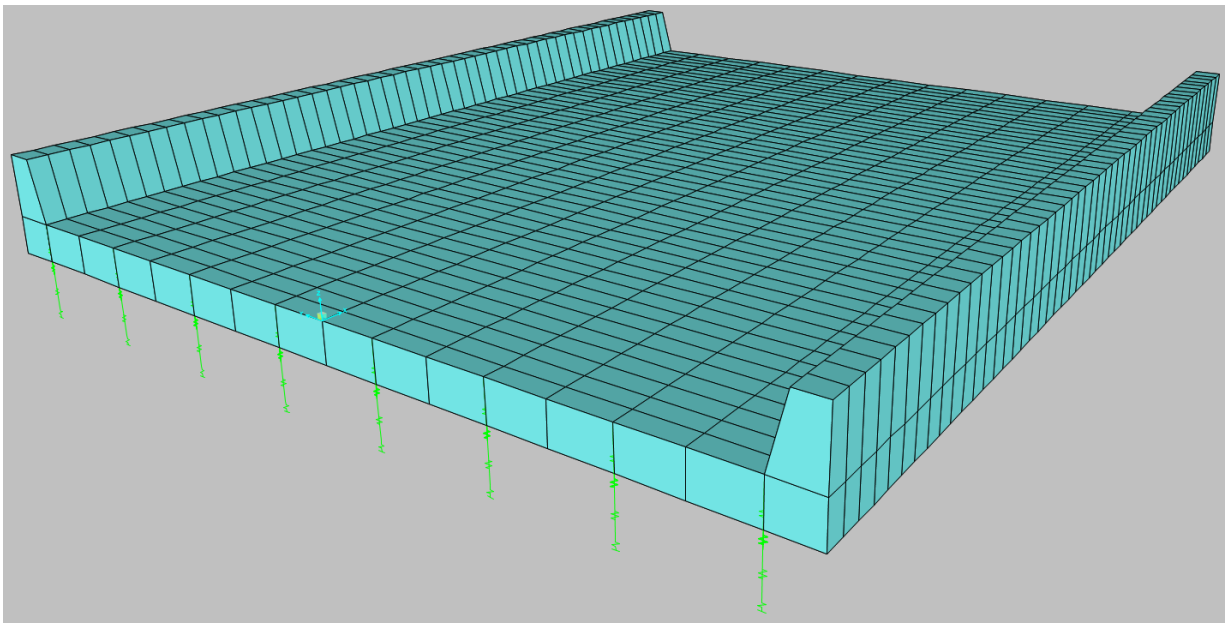

Figure 8.45. Calibrated FEM Model for Bridge CS-9

Table 8.46. Results of CS-9 Model Calibration

Results	Modal Frequency (Hz)		Midspan Deflection (in.)		Strain (με)					
					West Bottom		Mid Top	Mid Bottom	East Bottom	
	1st	2nd	S1	S5	S5	S9	S1	S1	S5	S9
Test	14.65	22.46	0.029	0.040	-11.23	3.44	-64.57	49.58	-39.37	-3.33
Calibrated	16.66	23.11	0.032	0.034	-6.63	3.40	-76.64	31.92	-17.29	-1.89

8.8. COMPARISON OF TEST RESULTS AND FEM PREDICTIONS

In the following sections, results obtained from the field test are compared with the FEM results.

8.8.1. Strain Measurements

The maximum top and bottom strains for the exterior sections S1 and S9 under static tests along Path 1 are compared with the updated and calibrated FEM results in Figure 8.46. Figure 8.46(a) and (c) provide strain profiles for section S1 for stop location test and crawl speed test, respectively. The top strain obtained from the updated FEM model was 107 percent higher and the bottom strain was 25 percent lower than the test values for the static test. The maximum variation obtained from the calibrated FEM model was 16 percent higher for the top strain and 73 percent lower for the bottom strain in comparison to the test results. The corresponding strain profiles for section S9 are provided in Figure 8.46(b) and (d) for static tests. Here, the maximum variation observed in the updated FEM model was 42 percent higher for the top strain and 268 percent higher for the bottom strain when compared to the test results. The calibrated model was 2 percent higher than the recorded top strain and 88 percent higher than the recorded bottom strain. These differences may be due the similar stiffnesses considered for the two curbs, while the experimental measurements indicated significant difference between the stiffnesses of the two curbs.

The maximum top and bottom strains for the exterior sections S1 and S9 under static tests along Path 2 are compared with the updated and calibrated FEM results in Figure 8.47. Figure 8.47(a) and (c) provide strain profiles for section S1 for stop location test and crawl speed test, respectively. The top strain obtained from the updated FEM model was 93 percent higher and the bottom strain was 20 percent higher than the test values for the static test. The maximum variation obtained from the calibrated FEM model was 32 percent higher for the top strain and 36 percent lower for the bottom strain in comparison to the test results. The corresponding strain profiles for section S9 are provided in Figure 8.47(b) and (d) for static tests. The maximum variation observed in the updated FEM model was 21 percent higher for the top strain and 182 percent higher for the bottom strain when compared to the test results. The calibrated model was 49 percent lower than the recorded top strain and 31 percent lower than the recorded bottom strain.

Figure 8.48 compare the strain profiles obtained from sections S1 and S9 during static test along the Middle Path with the updated and calibrated FEM results. Figure 8.48 (a) and (c) provide strain profiles for section S1 for stop location test and crawl speed test, respectively. The top strain obtained from the updated FEM model was 95 percent higher and the bottom strain was 24 percent higher than the test values for the static test. The maximum variation obtained from the calibrated FEM model was 26 percent higher for the top strain and 55 percent lower for the bottom strain in comparison to the test results. The corresponding strain profiles for section S9 are provided in Figure 8.47(b) and (d) for static tests. Here, the maximum variation observed in the updated FEM model was 44 percent higher for the top strain and 318 percent higher for the bottom strain when compared to the test results. The calibrated model was 24 percent lower than the recorded top strain and 92 percent higher than the recorded bottom strain. The calibrated FEM model overall matches better with the test results as compared to the updated FEM model. The calibration was

conducted using test strains obtained from the curb sections. It should be noted that the FEM models consider both the curbs to have similar stiffnesses. However, experimental results indicate otherwise. This may be the reason why the strains obtained from the calibrated FEM models do not match the test values. As highlighted in Section 8.6.1.1, there is lack of confidence in some measured strain values. For this reason, the FEM models were also calibrated against recorded deflections and dynamic characteristics of the bridge.

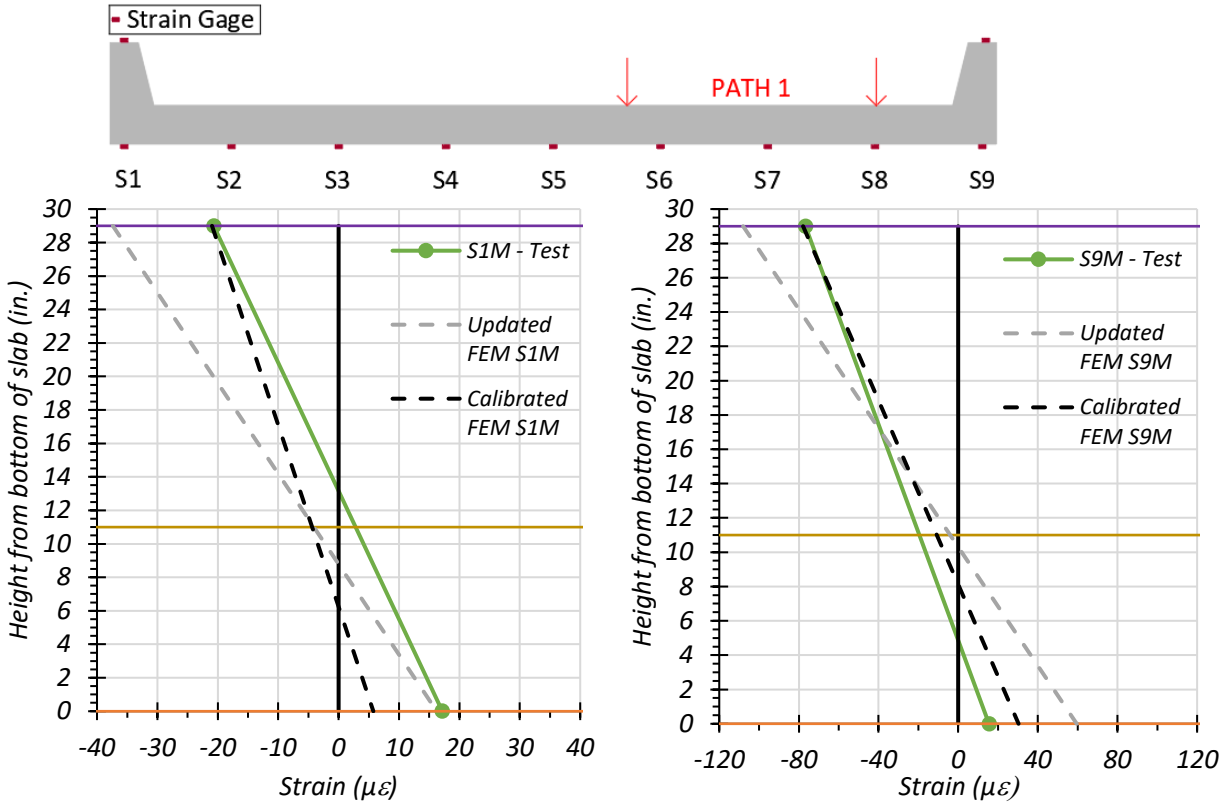

(a) Stop Location Test – S1

(b) Stop Location Test – S9

(c) Crawl Speed Test – S1

(d) Crawl Speed Test – S9

Figure 8.46. Comparison of Static Strains with FEM Results – Path 1

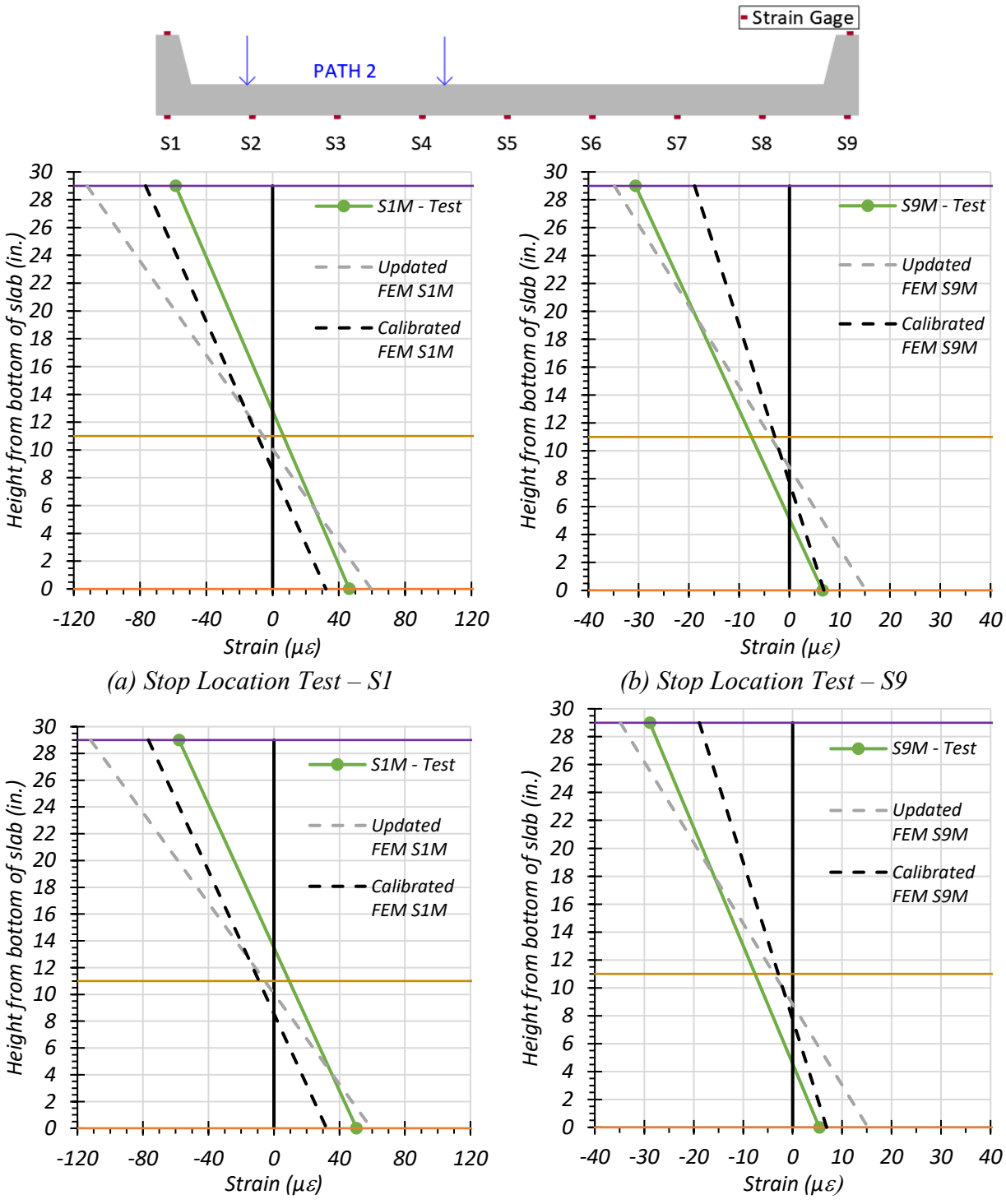

(a) Stop Location Test – S1

(b) Stop Location Test – S9

(c) Crawl Speed Test – S1

(d) Crawl Speed Test – S9

Figure 8.47. Comparison of Static Strains with FEM Results – Path 2

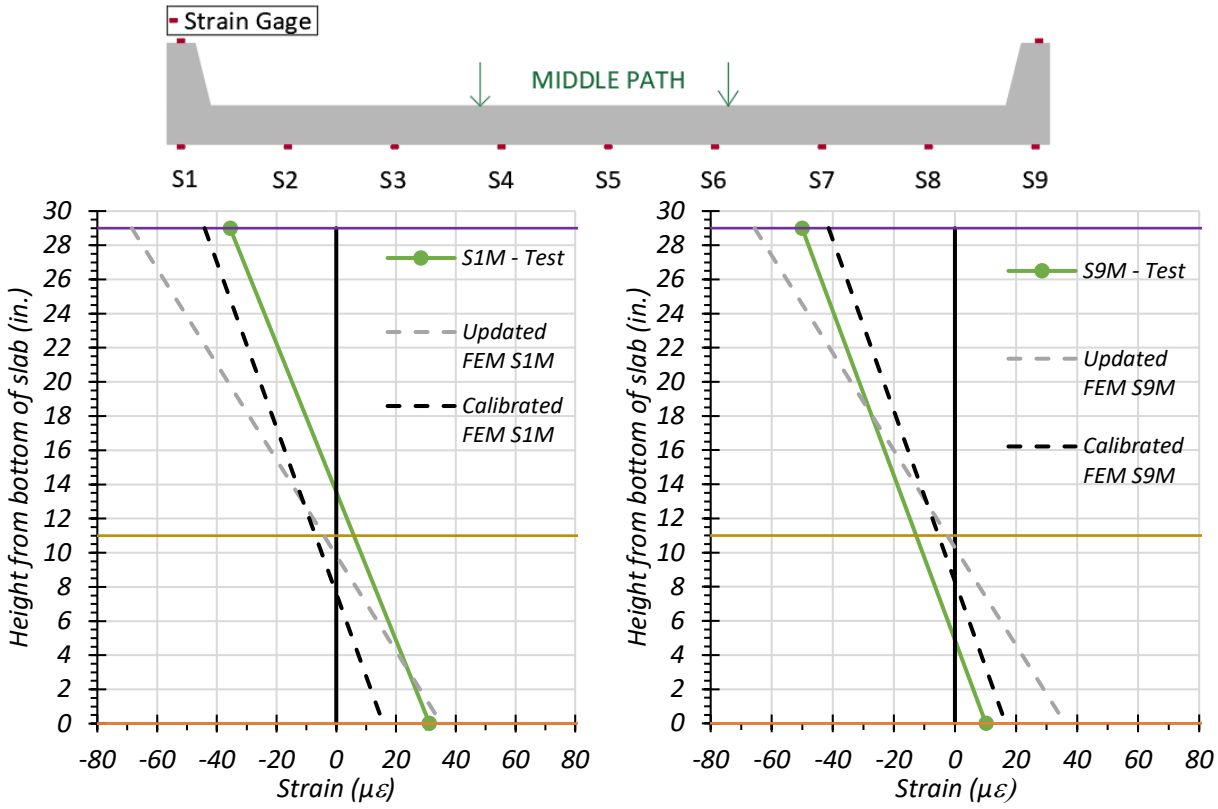

(a) Stop Location Test – S1

(b) Stop Location Test – S9

(c) Crawl Speed Test – S1

(d) Crawl Speed Test – S9

Figure 8.48. Comparison of Static Strains with FEM Results – Middle

8.8.1.1.1. Comparison of Results based on Measured Strains

The neutral axis location for each transverse section is determined from the strain profile at midspan. Table 8.47 lists the neutral axes corresponding to all the different tests. Figure 8.49 compares the neutral axes obtained from the static tests with the FEM neutral axis for both S1 and S9. The test results show that the stiffness of Section S9 may be less than that of Section S1. The FEM models considered the same stiffness for both the sections. Additionally, the calibrated FEM model considers cracked concrete properties for the bridge.

Table 8.47. Measured Neutral Axis Locations for All Static Load Tests

Test	S1 Neutral Axis Location (in. from bottom of slab)	S9 Neutral Axis Location (in. from bottom of slab)
Path 1 – Stop Location	15.80	5.79
Path 1 – Crawl Speed	14.56	4.96
Path 2 – Stop Location	12.59	6.17
Path 2 – Crawl Speed	13.50	4.56
Middle Path – Stop Location	13.53	5.78
Middle Path – Crawl Speed	12.95	4.63
Updated FEM	9.85	10.61
Calibrated FEM	7.62	8.57
Theoretical Uncracked	13.33	
Theoretical Cracked	21.43	

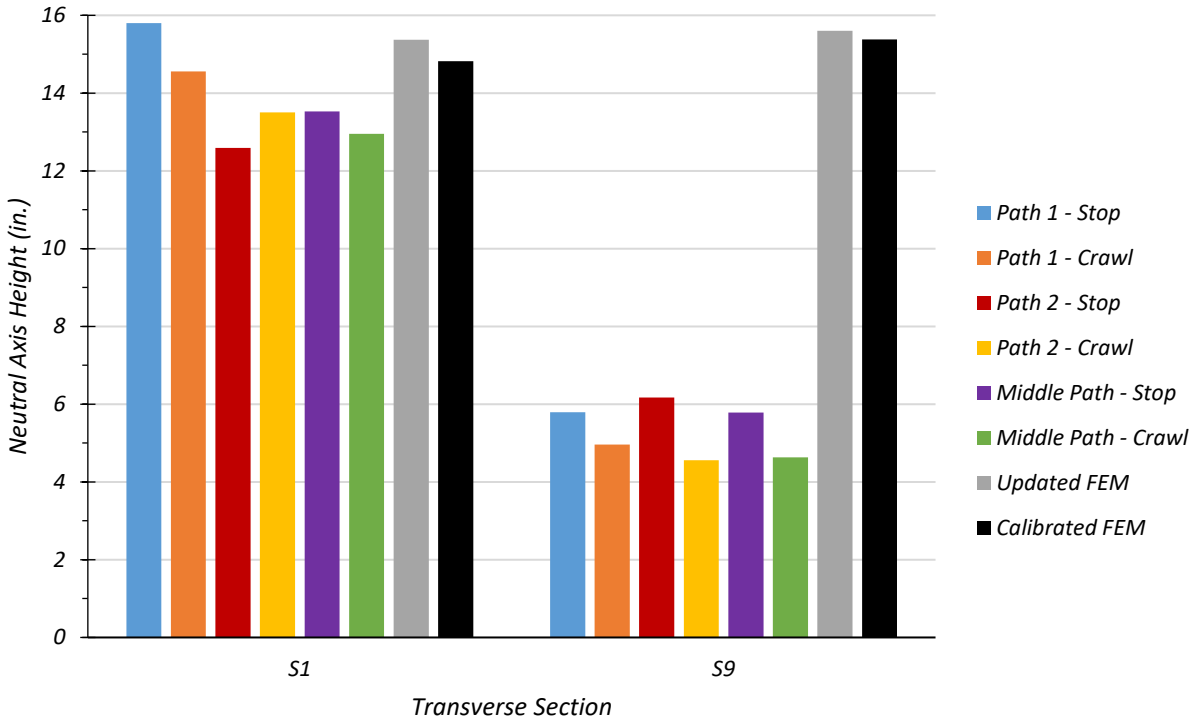

Figure 8.49. Test Neutral Axis Locations

8.8.2. Deflection Measurements

In this section, the deflections measured during the load testing have been compared with the updated and calibrated FEM results.

8.8.2.1.1. Path 1 Loading

The measured maximum downward deflection for each section under static test and crawl speed test along Path 1 is compared with those obtained from the updated and calibrated FEM models in Figure 8.50(a) and (b) respectively. The updated FEM model overestimates the deflection by over 200 percent for both the stop location test and crawl speed test along Path 1. The calibrated FEM model provided a better estimation of the observed deflections during static tests along Path 1,

with a maximum overestimation of 10 percent for the stop location test and 33 percent for the crawl speed test. It should be noted that the FEM models were developed considering similar stiffness for both the curbs. However, the test results showed that the stiffness was smaller for the curb at Section S1 as compared to the one at Section S9.

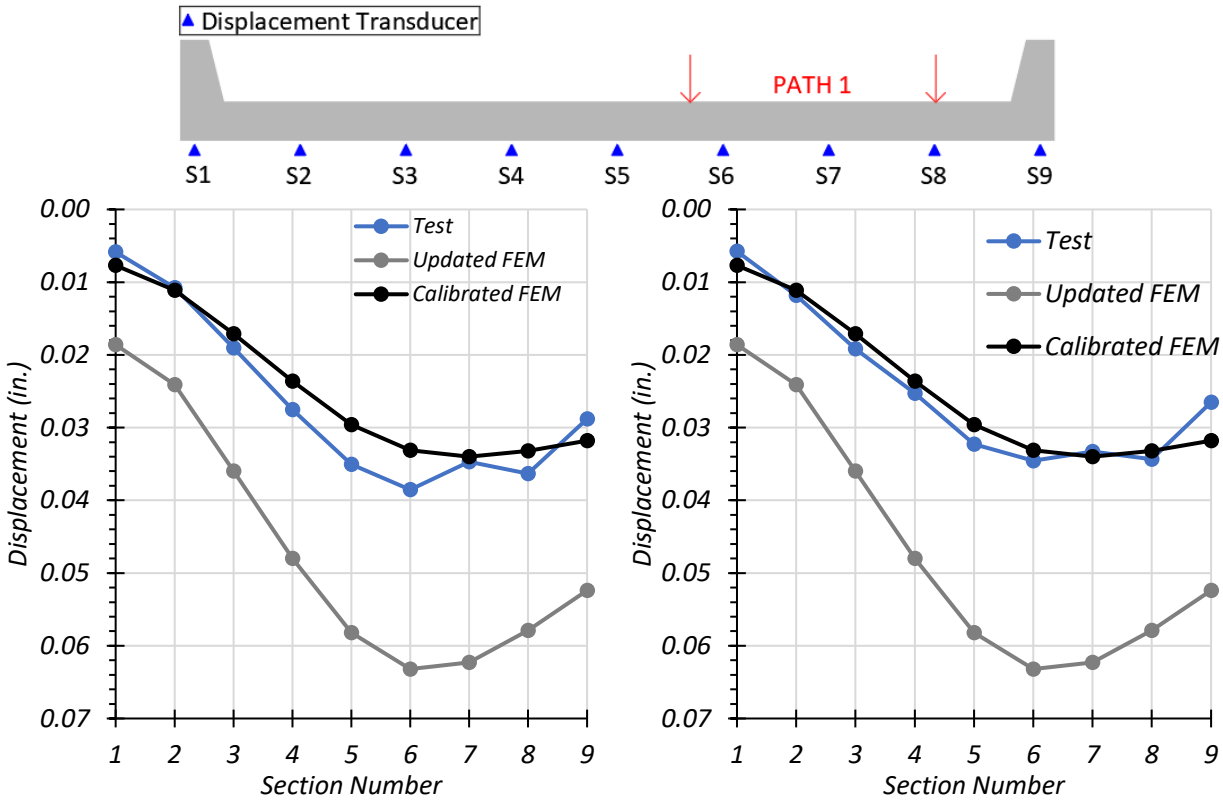

(a) Section Deflections – Stop Location *(b) Section Deflections – Crawl Speed*

Figure 8.50. Comparison of Static Deflection Results with FEM for Path 1 Loading

Similar to the approach used to determine the equivalent width of the slab using the test data (Section 8.6.1.2), the step-by-step calculations for the equivalent width of the interior slab section for the stop location test for the calibrated FEM model are provided in Table 8.48.

Table 8.48. Calibrated FEM Deflections, LLDFs and Equivalent Width for Stop Location Test along Path 1 using L-Curbs

Section	S1+S2 (Left L-curb)		S3	S4	S5	S6	S7	S8+S9 (Right L-curb)	
Width (ft)	4.708		2.083	2.583	2.583	2.583	2.083	4.708	
Δ (in.)	0.008	0.011	0.017	0.024	0.030	0.033	0.034	0.033	0.032
	0.010		0.017	0.024	0.030	0.033	0.034	0.033	
I_i (in^4)	14,925		6682	6682	6682	6682	6682	14,925	
$I_i\Delta$ (in^5)	150.59		114.27	157.70	197.80	221.19	227.20	489.30	
LLDF	0.097		0.073	0.101	0.127	0.142	0.146	0.314	
g	0.097		0.589					0.314	
E (ft)	-		17.72					-	

A comparison of the calibrated FEM results with the Path 1 test results are shown in Table 8.49. The calibrated FEM results provide a $g_{per\ foot}$ value that is 3.8 percent lower than the experimental test value.

Table 8.49. Comparison of Calibrated FEM Results with Test Results for Path 1

Method	Section	S1+S2 (Left L-curb)	Mid-slab	S8+S9 (Right L-curb)
Test	g	0.083	0.615	0.302
	$g_{per\ foot}$	-	0.052	-
	E (ft)	-	16.88	-
Calibrated FEM	g	0.097	0.589	0.314
	$g_{per\ foot}$	-	0.050	-
	E (ft)	-	17.72	-

8.8.2.1.2. Path 2 Loading

The measured maximum downward deflection for each section under static test and crawl speed test along Path 2 is compared with those obtained from the updated and calibrated FEM models in Figure 8.51(a) and (b) respectively. The updated FEM overestimates the deflection by 70 percent for the stop location test and 300 percent for the crawl speed test along Path 2. The calibrated

model provided a better estimation of the observed deflections during static tests along Path 2, with a maximum overestimation of 47 percent for the stop location test and 91 percent for the crawl speed test. It should be noted that these percent differences may seem high due to the low strain values obtained from the bridge testing.

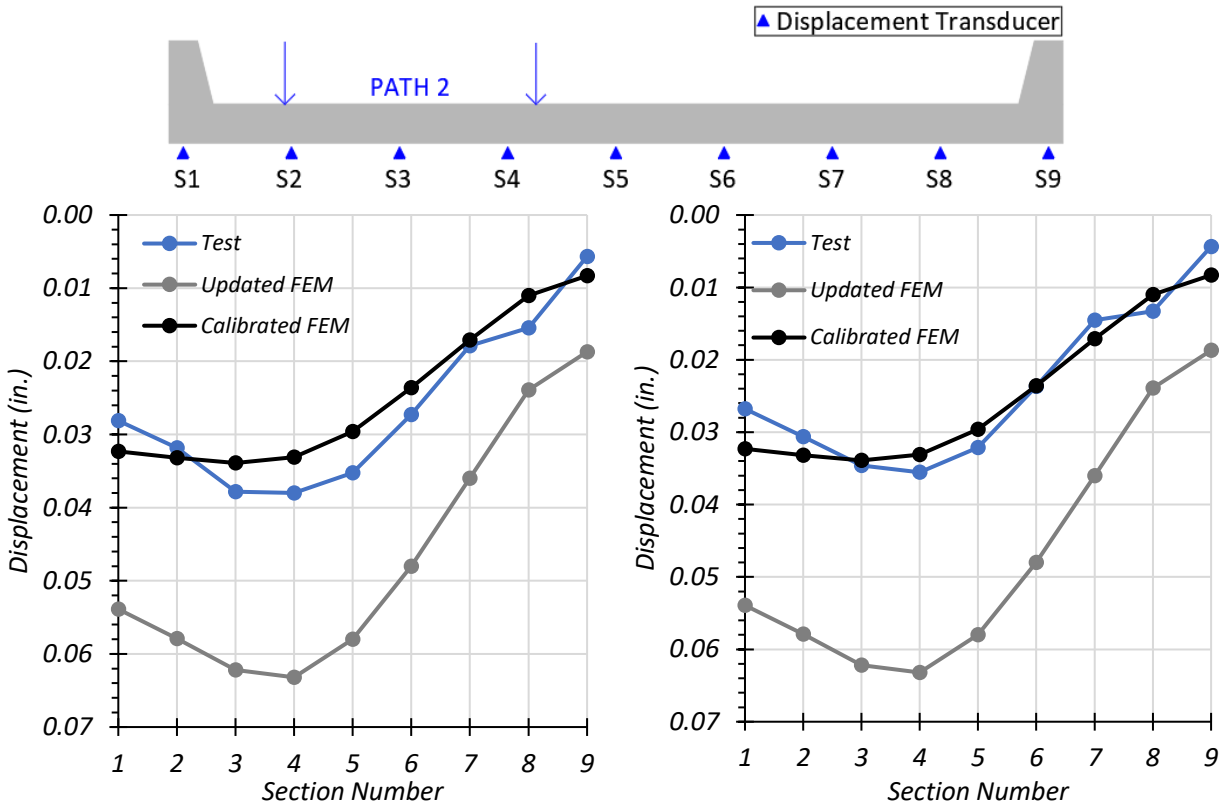

(a) Section Deflections – Stop Location *(b) Section Deflections – Crawl Speed Test*

Figure 8.51. Comparison of Static Deflection Results with FEM for Path 2 Loading

The step-by-step calculations for the equivalent width of the interior slab section for the stop location test for the calibrated FEM model are provided in Table 8.50.

Table 8.50. Calibrated FEM Deflections, LLDFs and Equivalent Width for Stop Location Test along Path 2 using L-Curbs

Section	S1+S2 (Left L-curb)		S3	S4	S5	S6	S7	S8+S9 (Right L-curb)	
Width (ft)	4.708		2.083	2.583	2.583	2.583	2.083	4.708	
Δ (in.)	0.032	0.033	0.034	0.033	0.030	0.024	0.017	0.011	0.008
	0.033		0.034	0.033	0.030	0.024	0.017	0.010	
I_i (in^4)	14,925		6682	6682	6682	6682	6682	14,925	
$I_i\Delta$ (in^5)	491.51		226.53	221.19	197.80	157.70	114.27	152.20	
LLDF	0.315		0.145	0.142	0.127	0.101	0.073	0.097	
g	0.315		0.588					0.097	
E (ft)	-		17.80					-	

A comparison of the calibrated FEM results with the Path 1 test results are shown in Table 8.51. The calibrated FEM results provide a $g_{per\ foot}$ value that is 5.8 percent lower than the experimental test value.

Table 8.51. Comparison of Calibrated FEM Results with Test Results for Path 2

Method	Section	S1+S2 (Left L-curb)	Mid-slab	S8+S9 (Right L-curb)
Test	g	0.271	0.618	0.111
	$g_{per\ foot}$	-	0.052	-
	E (ft)	-	17.19	-
Calibrated FEM	g	0.315	0.588	0.097
	$g_{per\ foot}$	-	0.049	-
	E (ft)	-	17.80	-

8.8.2.1.3. Middle Path Loading

The measured maximum downward deflection for each girder under static test and crawl speed test along the Middle Path is compared with those obtained from the calibrated FEM model in Figure 8.52(a) and (b) respectively. The updated FEM overestimates the deflection by 117 percent for the stop location test and 125 percent for the crawl speed test along the Middle Path. The

calibrated model provided a better estimation of the observed deflections during static tests along the Middle Path, with a maximum overestimation of 20 percent for the stop location test and 28 percent for the crawl speed test.

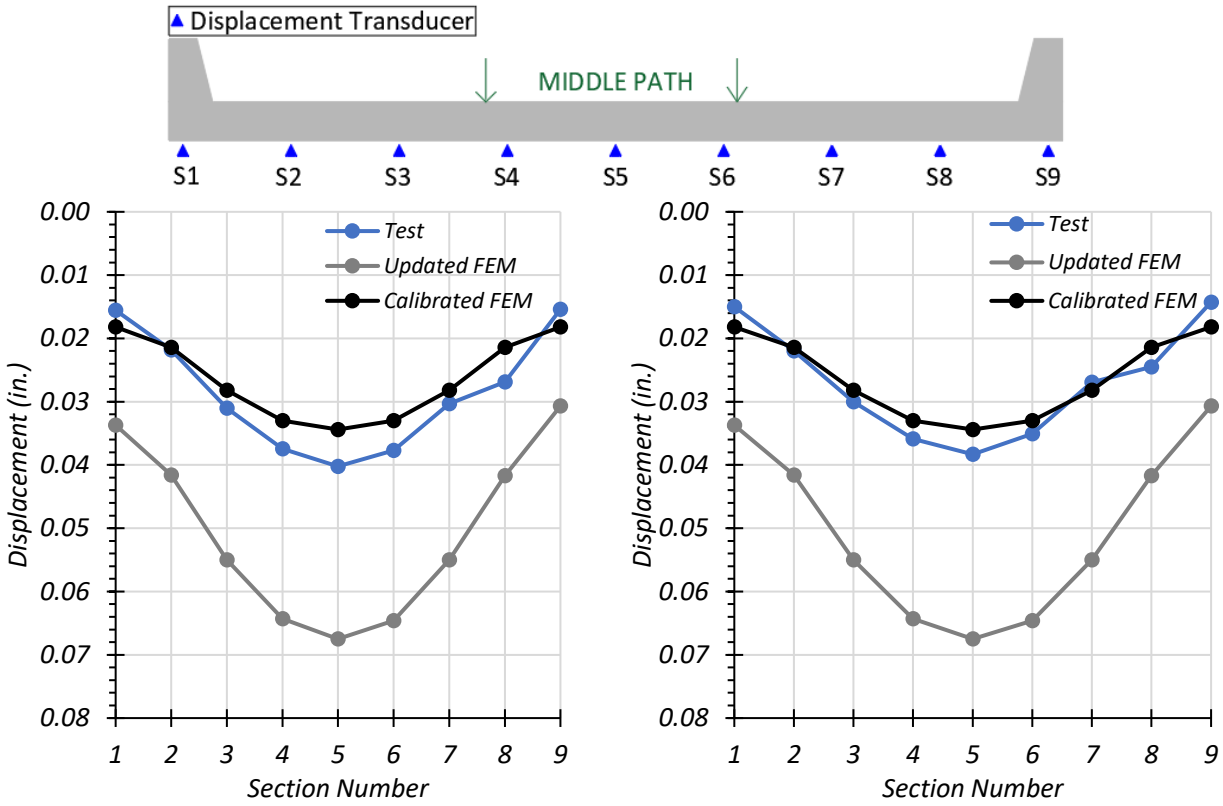

(a) Section Deflections – Stop Location *(b) Section Deflections – Crawl Speed Test*

Figure 8.52. Comparison of Static Deflection Results with FEM for Middle Path Loading

The step-by-step calculations for the equivalent width of the interior slab section for the stop location test for the calibrated FEM model are provided in Table 8.52.

Table 8.52. Calibrated FEM Deflections, LLDFs and Equivalent Width for Stop Location Test along Middle Path using L-Curbs

Section	S1+S2 (Left L-curb)		S3	S4	S5	S6	S7	S8+S9 (Right L-curb)	
Width (ft)	4.708		2.083	2.583	2.583	2.583	2.083	4.708	
Δ (in.)	0.018	0.021	0.028	0.033	0.034	0.033	0.028	0.021	0.018
	0.020		0.028	0.033	0.034	0.033	0.028	0.020	
I_i (in^4)	14,925		6682	6682	6682	6682	6682	14,925	
$I_i\Delta$ (in^5)	305.20		188.44	220.52	229.87	220.52	188.44	305.20	
LLDF	0.184		0.114	0.133	0.139	0.133	0.114	0.184	
g	0.184		0.632					0.184	
E (ft)	-		18.63					-	

A comparison of the calibrated FEM results with the Path 1 test results are shown in Table 8.53. The calibrated FEM results provide a $g_{per\ foot}$ value that is 1.9 percent lower than the experimental test value.

Table 8.53. Comparison of Calibrated FEM Results with Test Results for Middle Path

Method	Section	S1+S2 (Left L-curb)	Mid-slab	S8+S9 (Right L-curb)
Test	g	0.163	0.646	0.191
	$g_{per\ foot}$	-	0.054	-
	E (ft)	-	17.58	-
Calibrated FEM	g	0.184	0.632	0.184
	$g_{per\ foot}$	-	0.053	-
	E (ft)	-	18.63	-

8.8.2.1.4. Comparison with Test and Other Methods

Live load moment distribution across the bridge width was calculated using FEM deflection predictions for the same three paths (path 1, path 2, and middle path) that were used during field testing. The envelope of these three loading paths was used to identify the controlling moment distribution to the left L-curb, middle slab and right L-curb. The calculated FEM displacement-

based LLDF results are compared with the envelope of the LLDF results obtained from the field testing along the same three paths using measured displacements. Table 8.54 provides a comparison of the LLDFs and equivalent width results from the FEM with the test results and other methods in the literature. The calibrated FEM results estimates a $g_{per\ foot}$ value that is 2 percent lower than the test result.

Table 8.54. LLDFs and Equivalent Widths from FEM, Test and Different Methods from the Literature for One-Lane-Loaded Case

Method	Section	S1+S2 (Left L-curb)	Mid-slab	S8+S9 (Right L-curb)
Test	g	0.271	0.646	0.302
	$g_{per\ foot}$	-	0.054	-
	E (ft)	-	17.58	-
Calibrated FEM	g	0.315	0.632	0.314
	$g_{per\ foot}$	-	0.053	-
	E (ft)	-	18.63	-
IB346	g	0.405	0.190	0.405
	$g_{per\ foot}$	-	0.016	-
Amer et al.	$g_{per\ foot}$	-	0.069	-
	E (ft)	-	14.60	-
Jones and Shenton*	$g_{per\ foot}$	-	0.083	-
	E (ft)	-	12.00	-
AASHTO STD*	$g_{per\ foot}$	-	0.091	-
	E (ft)	-	11.00	-
AASHTO LRFD*	$g_{per\ foot}$	-	0.096	-
	E (ft)	-	10.50	-
Note: * Approaches do not consider the effect of integral curbs.				

Table 8.55 provides a comparison of the LLDF and equivalent width results from calibrated FEM results with the two lane-loaded test results and other methods from the literature. The calibrated FEM results provide a $g_{per\ foot}$ value that is 5 percent smaller than the experimental test value.

Table 8.55. Comparison of Calibrated FEM Results with Test Results for Two-lane Loading

Method	Section	S1+S2 (Left L-curb)	Mid-slab	S8+S9 (Right L-curb)
Test	g	0.354	1.233	0.413
	$g_{per\ foot}$	-	0.104	-
	E (ft)	-	9.27	-
Calibrated FEM	g	0.409	1.181	0.409
	$g_{per\ foot}$	-	0.099	-
	E (ft)	-	10.06	-
IB346	g	0.596	0.808	0.596
	$g_{per\ foot}$	-	0.068	-
Amer et al.	$g_{per\ foot}$	-	0.069	-
	E (ft)	-	14.60	-
Jones and Shenton*	$g_{per\ foot}$	-	0.091	-
	E (ft)	-	11.00	-
AASHTO STD*	$g_{per\ foot}$	-	0.091	-
	E (ft)	-	11.00	-
AASHTO LRFD*	$g_{per\ foot}$	-	0.102	-
	E (ft)	-	9.80	-
Note: * Approaches do not consider the effect of integral curbs.				

For the mid-slab region between the L-Curbs, the displacement-based FEM LLDFs are in good agreement with the displacement-based test LLDFs, FEM values only slightly underestimate. The LLDFs for the curbs calculated using the IB346 approach are conservative in comparison to the test measurements and FEM predictions. However, the distribution of live load across the mid-slab portion between L-curbs according to IB346 is unconservative in comparison to the test results for both one-lane and two-lane loading scenario. The Amer et al. (1999) approach for estimating the proportion of moment resisted by the mid-slab portion provides a good moment estimate for one-lane loading, while the *AASHTO LRFD Specifications* provide a better estimate of the proportion of moment demand in the mid-slab portion for two-lane loading. These methods should be adopted if they provide a higher moment estimate in comparison to IB346 method.

8.8.3. Dynamic Characteristics of Bridge

The dynamic characteristics of the bridge obtained from the accelerometer data were compared with the updated and calibrated FEM results. The mode shape along the longitudinal section and transverse section for the first natural frequency compared with the updated FEM and calibrated FEM is shown in Figure 8.53. Figure 8.54 provides the mode shape along the longitudinal section and transverse section for the second natural frequency compared with the updated FEM and calibrated FEM. The mode shape along the longitudinal section and transverse section for the third natural frequency compared with the updated FEM and calibrated FEM is shown in Figure 8.55.

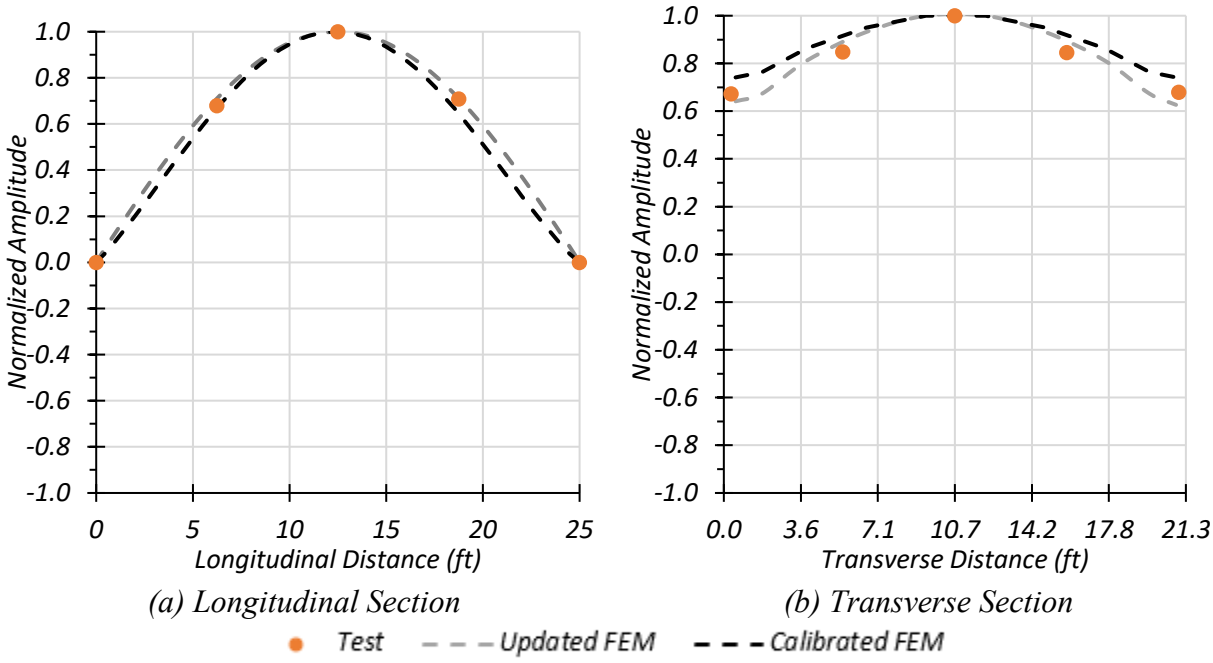

Figure 8.53. Mode Shape 1: Comparison of Experimental and FEM Results

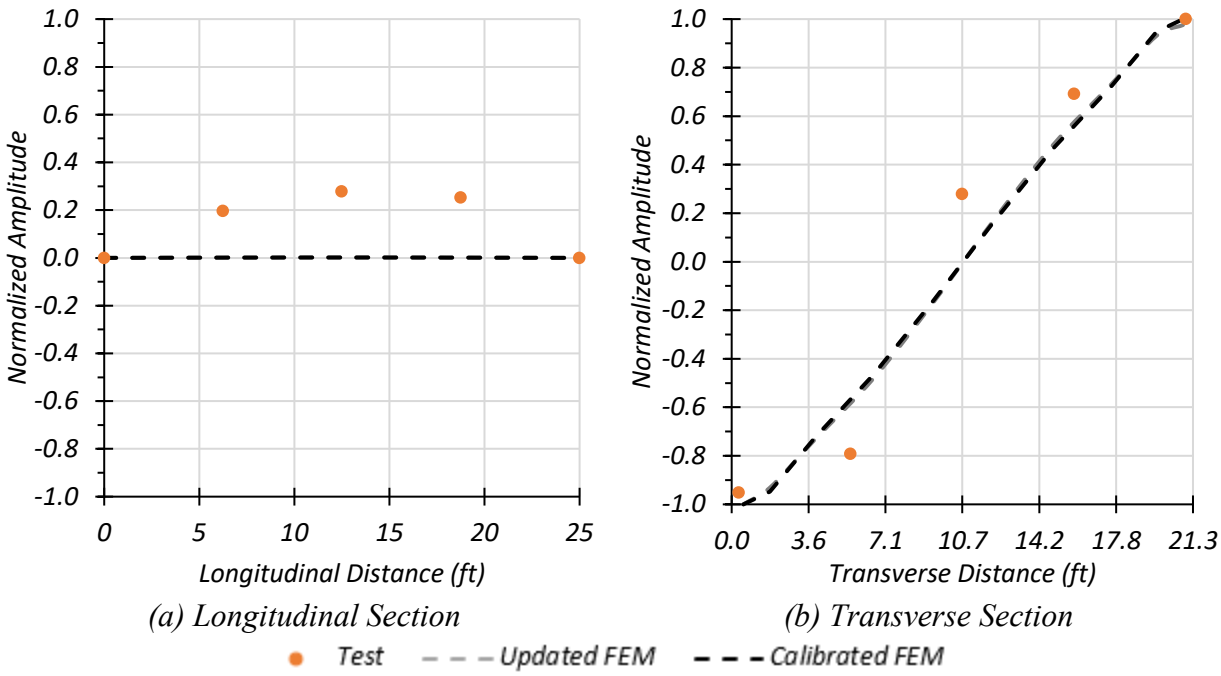

Figure 8.54. Mode Shape 2: Comparison of Experimental and FEM Results

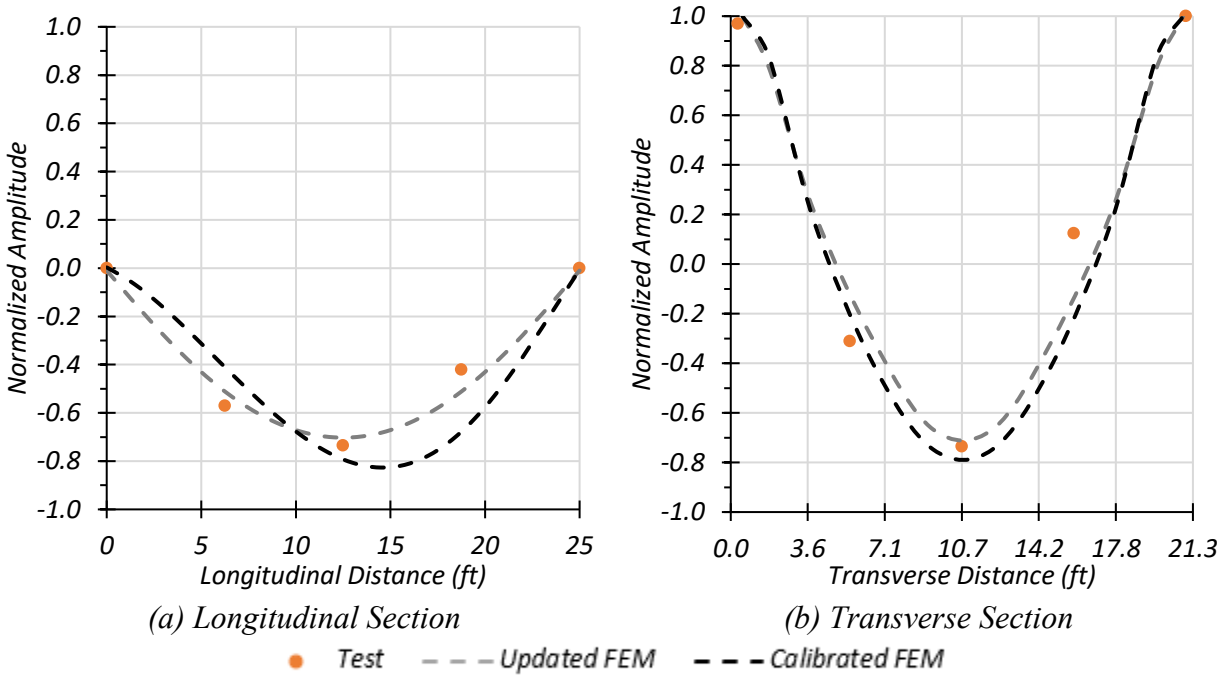

Figure 8.55. Mode Shape 3: Comparison of Experimental and FEM Results

The natural frequencies obtained from the FEM model and those observed during testing of Bridge CS-9 is provided in Table 8.56. The first, second and third natural frequencies obtained from the calibrated FEM model are closer to those obtained from the tests.

Table 8.56. Bridge CS-9 Test and FEM Natural Frequencies

Frequency	Test (Hz)	Updated FEM (Hz)	Calibrated FEM (Hz)
1st Natural Frequency	14.65	13.03	16.66
2nd Natural Frequency	22.46	20.32	23.11
3rd Natural Frequency	37.11	35.83	37.43

8.9. SUMMARY AND FINDINGS

The equivalent width calculated based on deflections were compared with those recommended by AASTHO Standard Specifications (AASHTO 2002) and AASHTO LRFD Specifications (AASHTO 2017). Both the AASHTO Standard Specifications and AASHTO LRFD Specifications provide quite conservative equivalent widths for the interior slab portion. A comparison was conducted of the test equivalent widths with those calculated from studies such as Amer et al. (1999) and Jones and Shenton (2012). The studies were also found to provide conservative equivalent widths.

Currently, TxDOT load rates simple span concrete slab bridges with integral curbs using the Illinois Bulletin 346 (Jenson et al. 1943) recommendations for load distribution. Table 8.57 compares the distribution of live load based on the field measurements with that obtained using the IB346 approach.

Table 8.57. Comparison of Experimental and Selected Literature LLDFs

Loading	Test/Method	g	$g_{per\ foot}$
One-lane	Stop Location (Path 1)	0.615	0.052
	Stop Location (Path 2)	0.618	0.052
	Stop Location (Middle Path)	0.646	0.054
	Calibrated FEM (Path 1)	0.589	0.050
	Calibrated FEM (Path 2)	0.588	0.049
	Calibrated FEM (Middle Path)	0.632	0.053
	IB346	0.190	0.016
	Amer et al.	-	0.068
	AASHTO LRFD	-	0.096
Two-lane	Stop Location (Path 1+2)	1.233	0.104
	Calibrated FEM (Path 1+2)	1.181	0.099
	IB346	0.808	0.068
	Amer et al.	-	0.068
	AASHTO LRFD	-	0.102

The IB346 prediction for the live load distribution to the interior slab region is unconservative when compared to the test results and FEM predictions for both the one-lane and two-lane loading scenario. The approach by Amer et al. (1999) gave a good estimate for the interior slab sections for determining the demand for one-lane loading; however, the *AASHTO LRFD Specifications* provide a better estimate of the moment demand in the interior slab section for two-lane loading.

Table 8.58 shows that the IB346 prediction for the live load distribution to the L-curb sections is conservative when compared to the test results and FEM predictions for both the one-lane and two-lane loading scenario. Therefore, it is recommended to continue using the IB346 approach to determine moment demands in the L-curb sections of concrete slab bridges with integral curbs.

Table 8.58. Comparison of Experimental and IB346 LLDFs

Loading	Load Path	*LLDF*		
		Left L-Curb	**Mid-Slab**	**Right L-Curb**
One-lane	Path 1	0.094	0.615	0.302
	Path 2	0.286	0.618	0.111
	Middle Path	0.172	0.646	0.191
	IB346	0.405	0.190	0.405
Two-lane	Stop Location Test	0.354	1.233	0.413
	Crawl Speed Test	0.376	1.217	0.407
	IB346	0.596	0.808	0.596

Areas of opportunity for this type of bridge include updating the capacity using the actual material strength and by considering any unintended end fixity. The 28-day concrete compressive strength of concrete for Bridge CS-9 was specified to be 2.5 ksi in the structural drawings. However, NDE tests revealed that the actual concrete compressive strength was 5.2 ksi. Table 8.59 provides a comparison of the updated RFs calculated using the in-situ compressive strength of concrete with the originally calculated RFs. As expected, doubling the material strength does not significantly increase the RFs governed by flexure. However, for Bridge CS-9 the increased material strength does provide an operating RF greater than 1.0. Using TxDOT's On-System Load Rating flowchart (TxDOT 2018a), for a bridge with a condition rating greater than 5 for all components and an operating RF less than 1.0, the bridge should be posted at inventory level with an inspection frequency of less than 2 years.

Table 8.59. Comparison of Bridge CS-9 Material Updated RFs to Original RFs

Rating Factor	Basic Load Rating	Load Rating with Measured Material Properties	Measured Material Properties/Basic Load Rating
Inventory	0.45	0.48	1.07
Operating	0.92	0.96	1.04

Calibrating the simply supported FEM model based on load test results in the field showed that there is some degree of end fixity present. The bending moment corresponding to the HS-20 design truck is obtained from the calibrated FEM model, which includes the effect of updated MOE of concrete more accurate live load distribution, and updated boundary conditions due to slight end-fixity, and this value is used to determine the updated RF. Table 8.60 provides a comparison of the updated RFs with the original RFs for a simply supported bridge. Only the LFR results are shown in the table because this was the method used by TxDOT to load rate Bridge CS-9. Using TxDOT's On-System Load Rating flowchart (TxDOT 2018a), for a bridge with a condition rating greater than 5 for all components and an operating RF greater than 1.0, the bridge should be posted at inventory level with an inspection frequency of less than 2 years.

Table 8.60. Comparison of Bridge CS-9 Calibrated FEM Live Load RFs to Original RFs

Rating Factor	Basic Load Rating	Load Rating with Calibrated FEM Live Load	Calibrated FEM Live Load /Basic Load Rating
Inventory	0.45	0.58	1.29
Operating	0.92	1.05	1.14

9. CONCLUSIONS AND FUTURE WORK

In this research, the aim was to investigate the current bridge load rating procedures and provide strategies to TxDOT on how the load posting on existing posted bridges in Texas may be improved. These recommendations were reinforced using refined FEM analysis calibrated with results from proof testing of representative bridges and non-destructive evaluation of its materials.

The state-of-the-practice in load rating existing bridges was explored in the literature review to map the history of the existing procedures and to determine the current practices recommended by AASHTO and adopted by TxDOT. Related research in the field of load rating existing bridges and their key findings were outlined in the state-of-the-art literature. An inventory of the all the load posted bridges in Texas was undertaken using the information provided in the public database, the National Bridge Inventory (NBI). This helped identify the common types of concrete bridges that were load posted. The focus of this research was on simple-span flat slab bridges and simple-span concrete pan girder bridges. A group of concrete bridges from each category were load rated using all three rating methods and the areas of opportunities were identified. From these groups of bridges, a total of two representative bridges typical of concrete slab bridges and concrete pan girder bridges were selected for refined analysis. Three-dimensional FEM models of the bridges were developed based on standard structural drawings, if available. The results obtained from these models were compared with the expected results from the AASHTO guidelines. The selected bridges were instrumented and subjected to the posted load during proof testing. The developed FEM models were verified against these experimental results and calibrated for improved accuracy. In the following sections, conclusions drawn from each

bridge are summarized and recommendations for improved bridge load rating are presented. Suggestions for future work in this field are also outlined.

9.1. CONCLUSIONS AND RECOMMENDATIONS

9.1.1. Bridge CM-5

Bridge CM-5 was one of the representative bridges typical of a simple-span concrete multi-girder bridge. Although the bridge was designed as simply supported, the results from the proof test of the bridge showed the presence of some end restraint. Bottom compressive strains were observed at the ends of the instrumented interior girder while the instrumented exterior girder recorded bottom tensile strains when the truck was located away from it and bottom compressive strains when the truck was close to it. The thick layer of asphalt on top of the slab prevented visually confirming this behavior, because any tensile cracks in the top slab were likely covered by the asphalt layer. The neutral axis locations calculated from the proof testing results were closer to the theoretical uncracked section neutral axes for both the interior and exterior girders. However, during the instrumentation of the bridge it was noted that the bottom section of the pan girders showed signs of cracking, indicating cracked section behavior. The LLDFs calculated using the field test results were compared with the LLDFs calculated using the approximate equations in the AASTHO Standard Specifications (AASHTO 2002) and AASHTO LRFD Specifications (AASHTO 2017). The AASHTO Standard Specification LLDFs were slightly conservative for the controlling girder while the AASHTO LRFD Specification LLDFs were highly conservative. Thus, the AASHTO Standard Specification LLDFs predicted the governing experimentally determined LLDF fairly accurately.

The initial FEM model was calibrated with the field test results. The final FEM model had some degree of end restraint introduced at both ends (refer to Section 7.7.4.6 for details). A cracked concrete model was considered. This model accurately represented the measured behavior of the bridge and was used to determine refined RFs for Bridge CM-5.

9.1.2. Bridge CS-9

Bridge CS-9 was one of the representative bridges typical of a simple-span concrete slab bridge. It should be noted that this bridge had integral concrete curbs on either side. Although the bridge was designed as simply supported, the results from the load test of the bridge showed the presence of slight end restraint. Small bottom compressive strains (< 10 με) were observed at the ends of the instrumented exterior transverse section. The layer of asphalt on top of the slab prevented confirming this visually, because any tensile cracks in the top slab were likely covered by the asphalt layer. The neutral axis locations calculated from the load testing results were closer to the theoretical uncracked section neutral axes for one of the exterior curb sections, while it was much smaller than the theoretical uncracked section neutral axis for the other exterior curb section. However, during the instrumentation of the bridge it was noted that the bottom slab showed signs of cracking indicating cracked section behavior.

The recorded deflections were used to determine the equivalent width of the slab section and the LLDF (g) for each component and these were compared with the approximate equations in the AASTHO Standard Specifications (AASHTO 2002) and AASHTO LRFD Specifications (AASHTO 2017). The AASTHO Standard Specifications provided equivalent width and a corresponding proportional moment demand per foot ($g_{per\ foot}$) that were highly conservative compared to the field test results. However, the AASHTO LRFD Specifications provided

conservative results for one-lane loading but provided reasonable results for two-lane loading. Comparisons with various other approaches in the literature were also carried out. The equivalent width and $g_{per\ foot}$ calculated using the approach by Amer et al. (1999) was closer to the test results for one-lane loading, while Jones and Shenton (2012) provided a conservative estimate. It should be noted that only Amer et al. (1999) considered bridges similar to the tested bridge in their studies. Their study included exterior beams along the slab edges. At present, TxDOT load rates such bridges using the Illinois Bulletin 346 (Jenson et al. 1943) recommendations for load distribution. IB346 provides reasonably accurate bending moments for the curb sections when compared to the experimental results; however, is unconservative for the slab region. Therefore, it is recommended to use the approach of Amer et al. (1999) for determining the moment demand for the interior slab sections for one-lane loading and the approximate equations in the AASHTO LRFD Specifications (AASHTO 2017) for two-lane loading.

The initial FEM model was calibrated with the field test results. The final FEM model had a small amount of end restraint introduced at both ends (refer to Section 8.7.4.6 for details). A cracked concrete model was considered. This model accurately represents the measured behavior of the bridge and can be used to determine the refined RFs for Bridge CS-9.

9.2. RECOMMENDATIONS FOR REFINED LOAD RATING

Based on the findings of this research, the following are a few recommendations that could help to refine the load rating of similar bridge types.

9.2.1. Field Testing and Refined Analysis

Refined analysis provides a tool to more accurately capture the distribution of loads across the bridge width. The exact distribution of the live loads in a bridge can be obtained from field test results. In this study, the bridge was instrumented to record the desired results and these results were used to determine the more precise live load distribution of the bridge. Non-destructive and/or destructive evaluation of the bridge components were carried out at this stage. The material strengths of the bridge components come into play in the capacity calculations. Using the measured material strengths more accurately capture the behavior and strength, allowing refined a RF to be determined for the bridge. Another approach to obtain the in situ distribution of the live loads is through the development of a FEM model. The results obtained from this model can be used to more accurately load rate the bridge.

An advanced approach would be to use the results from the field test to calibrate the initial FEM model. This model would incorporate the in-situ material properties along with any modifications to include end restraint that may be observed on site. As a result, the final FEM model would more accurately capture the in situ behavior of the bridge. The confidence in the RFs calculated from such refined models can be increased relative to basic load rating approaches.

9.2.2. Verification of Number of Lanes

Although a bridge may be classified and striped as two-lanes, this may not functionally be the case. Both Bridge CM-5 and CS-9 were striped as two-lanes but were not wide enough to allow two trucks to pass by at the same time. It was also observed that approaching vehicles would wait for the oncoming vehicle to cross the bridge before getting on the bridge. This essentially meant that the bridge would only be subjected to one-lane traffic. As anticipated, the RF for one-lane bridge

is higher than that for a two-lane bridge. The aforementioned observation could help improve the load rating of a bridge. This could be implemented by installing a one-lane traffic sign near the approach ends of the bridge and removing the two-lane stripes.

9.2.3. Computer Vision

In lieu of field testing and FEM modeling, a non-contact approach for determining the deflection of a bridge during a truck pass is through the use of a targetless computer vision algorithm. In this approach, two images of the bridge as it is unloaded and loaded are provided to the computer vision algorithm. The displacement measurement between the images are obtained using an image analysis algorithm comparing one sub-window of the unloaded bridge image with several sub-windows of the loaded bridge image. This method is efficient and eliminates the need to instrument the bridge, which is a very time-consuming process.

9.3. FUTURE WORK FOR SIMPLE-SPAN CONCRETE BRIDGES

Only two types of concrete bridges were considered in this study and continuous bridges were excluded. The following were identified as possible areas for future work in association with this research.

9.3.1. FEM Model

The three-dimensional FEM model developed in this research only considered brick elements. Other elements such as shells and one-dimensional elements were not considered. These models were limited to the two selected bridges. A parametric study with different bridge characteristics could be undertaken to capture the effect of various parameters on the load distribution.

9.3.2. Material Properties

The material strengths of the various bridge components could be determined with certainty through the use of non-destructive tests (NDT) and destructive tests (DT). The compressive strength of concrete can be determined using NDT such as the Schmidt Hammer Test and the Ultrasonic Pulse Velocity (UPV) test. Destructive testing would require the extraction of concrete cores and steel coupons from bridge components, followed by laboratory testing to determine the material strengths. Mill certificate data, if available, could be used to determine the steel yield strength for the reinforcement.

9.3.3. Computer Vision

The possibility of determining bridge deflections from video recordings of the bridge during a truck pass was evaluated in this research. This was done successfully for a few crawl tests and dynamic tests conducted on both the bridges. Thus, computer vision has the potential to provide a quick and contactless approach to determine the deflections obtained for a truck pass. The algorithm could be automated such that no user input is required other than providing the known characteristics of the bridge. The program could select the sub-windows for analysis itself and average the results over different windows to increase the accuracy of the results.

REFERENCES

AASHO (1970). "Manual for Maintenance Inspection of Bridges, 1970." American Association of State Highway Officials, Washington D.C.

AASHTO (1974). "Manual for Maintenance Inspection of Bridges, 1974." American Association of State Highway and Transportation Officials, Washington D.C.

AASHTO (1978). "Manual for Maintenance Inspection of Bridges, 1978." American Association of State Highway and Transportation Officials, Washington D.C.

AASHTO (1983). "Manual for Maintenance Inspection of Bridges, 1983." American Association of State Highway and Transportation Officials, Washington D.C.

AASHTO (1989). "Standard Specifications for Highway Bridges, 14th Edition." American Association of State Highway and Transportation Officials, Washington, DC.

AASHTO (1994). "Guide Specifications for Distribution of Loads for Highway Bridges." American Association of State Highway and Transportation Officials, Washington, DC.

AASHTO (1994). "Manual for Condition Evaluation of Bridges, 1994." American Association of State Highway and Transportation Officials, Washington D.C.

AASHTO (1996). "Standard Specifications for Highway Bridges, 16th Edition." American Association of State Highway and Transportation Officials, Washington, DC.

AASHTO (2002). "Standard Specifications for Highway Bridges, 17th Edition." American Association of State Highway and Transportation Officials, Washington D.C.

AASHTO (2003). "Manual for Condition Evluation and Load and Resistance Factor Rating (LRFR) of Highway Bridges." American Association of State Highway and Transportation Officials, Washington, DC.

AASHTO (2004). "AASHTO LRFD Bridge Design Specifications, 3rd Edition." American Association of State Highway and Transportation Officials, Washington, DC.

AASHTO (2008). "Manual for Bridge Evaluation, 1st Edition." American Association of State Highway and Transportation Officials, Washngton D.C.

AASHTO (2011). "Manual for Bridge Evaluation, 2nd Edition." American Association of State Highway and Transportation Officials, Washngton D.C.

AASHTO (2014). "AASHTO LRFD Bridge Design Sepcifications, Seventh Edition." American Association of State Highway and Transportation Officials, Washington D.C.

AASHTO (2017). "AASHTO LRFD Bridge Design Specifications, 8th Edition." American Association of State Highway and Transportation Officials, Washington, DC.

AASHTO (2017). "AASHTO LRFD Bridge Design Specifications, Eight Edition." American Association of State Highway and Transportation Officials, Washington D.C.

AASHTO (2017). "AASHTO LRFD Bridge Design Specifications, Eighth Edition." American Association of State Highway and Transportation Officials, Washington D.C.

AASHTO (2018). "Manual for Bridge Evaluation, 3rd Edition." American Association of State Highway and Transportation Officials, Washington, DC.

AASHTO MBE (2018). "Manual for Bridge Evaluation, 3rd Edition." American Association of State Highway and Transportation Officials, Washington, DC.

Amer, A., Arockiasamy, M., and Shahawy, M. (1999). "Load Distribution of Existing Solid Slab Bridges Based on Field Tests." *Journal of Bridge Engineering*, 4(3), 189-193.

American Association of State Highway and Transportation Officials (2014). "AASHTO LRFD Bridge Design Sepcifications, Seventh Edition." AASHTO, Washington D.C.

Arndt, J., Jiang, P., and Robinson, C. (2017). "FHWA Bridge Load Rating Webinar Series." *Topic No. 22: Bridge Load Rating and Posting - States' Practices*, Federal Highway Administration, Washington, DC, 1-78.

ASTM C805/C805M-18 (2018). "Standard Test Method for Rebound Number of Hardened Concrete."

Barth, K. (2015). "Design Example 2A: Two-Span Continuous Straight Composite Steel I-Girder Bridge." *Steel Bridge Design Handbook*, US Department of Transportation, Federal Highway Administration, Washington, DC, 1-114.

Barth, K. E., and Wu, H. (2006). "Efficient nonlinear finite element modeling of slab on steel stringer bridges." *Finite Elements in Analysis and Design*, 42(14), 1304-1313.

Breysse, D. (2012). *Non-Destructive Assessment of Concrete Structures: Reliability and Limits of Single and Combined Techniques*, Springer, Dordrecht, NLD.

Catbas, N., Zaurin, R., Gul, M., and Burak Gokce, H. (2012). *Sensor Networks, Computer Imaging, and Unit Influence Lines for Structural Health Monitoring: Case Study for Bridge Load Rating*.

CEN (2011). "EN1991 Eurocode 1: Actions on Structures – Part 2: Traffic Loads on Bridges, NEN-EN 1991–2/NA:2011." 38.

Chajes, M. J. (1997). "Experimental Load Rating of a Posted Bridge." *Journal of Bridge Engineering*, 2(1).

Computers and Structures, I. 2015. CSiBridge, Integrated 3-D Bridge Analysis, Design and RatingComputers and Structures, Inc., Berkeley, California, USA.

Computers and Structures, I. 2019. CSiBridge, version 20Computers and Structures, Inc, Berkeley, California, USA.

CTC & Associates (2009). "Improved LRFD/LRFR Specifications for Permit and Fatigue Load Trucks." California Department of Transportation, Sacramento, CA, 1-64.

Dassault Systemes, S. A. 2013. Abaqus, version 6. Abaqus, Inc, Providence, RI, USA.

Davids, W. G., Poulin, T. J., and Goslin, K. (2013). "Finite-Element Analysis and Load Rating of Flat Slab Concrete Bridges." *Journal of Bridge Engineering*, 18(10), 946-956.

FHWA (2015). "Bridge Formula Weights." US Department of Transportation, Federal Highway Administration, Washington, DC.

Government, U. (1958). "US Code Title 23 - Highways." United States Government, Washington, DC, 1-389.

Hearn, G. (2014). "State Bridge Load Posting Processes and Practices - A Synthesis of Highway Practice." Transportation Research Board, Washington, DC, 1-144.

Huang, Q., Gardoni, P., and Hurlebaus, S. (2011). *Predicting Concrete Compressive Strength Using Ultrasonic Pulse Velocity and Rebound Number*.

Huang, Q., Gardoni, P., and Hurlebaus, S. (2011). "Predicting Concrete Compressive Strength Using Ultrasonic Pulse Velocity and Rebound Number." *ACI Materials Journal*, 108(4), 403-412.

Hueste, M. B., Mander, J. B., Terzioglu, T., Jiang, D., and Petersen-Gauthier, J. (2015). "Spread Prestressed Concrete Slab Beam Bridges." Texas Department of Transportation, Austin, TX, 237-245.

Hunt, M. (2009). "Historic Context for Texas Bridges, 1945-1965." TXDOT.

IDOT (2012). "Design Guides." *LRFD Slab Bridge Design*, Illinois Department of Transportation, Springfield, IL, 3.2.11-13.

Imbsen, R. A., Liu, W. D., Schamber, R. A., and Nutt, R. V. (1987). "Strength evaluation of existing reinforced concrete bridges." Transportation Research Board, National Research Council, Washington, DC, 1-53.

Jenson, V. P. (1939). "Moments in Simple Span Bridge Slabs with Stiffened Edges." *Bulleting Series No. 315*, University of Illinois, Urbana-Champaign, IL, 11-33.

Jenson, V. P., Kluge, R. W., and Williams, C. B. (1943). "Highway Slab-Bridges with Curbs: Laboratory Tests and Proposed Design Method." *Bulletin Series No. 346*, University of Illinois, Urbana-Champaign, IL, 1-65.

Ji, Y., and Zhang, Q. "A novel image-based approach for structural displacement measurement." *Proc., Bridge Maintenance, Safety, Management, Resilience and Sustainability*, Taylor & Francis, 407-414.

Jones, B. P., and Shenton, H. W. (2012). "Effective Width of Concrete Slab Bridges in Delaware." Delaware Center for Transportation, University of Delaware, Newark, DE, 1-82.

Kulicki, J. M. (1998). "Development of comprehensive bridge specifications and commentary." *Research results digest ; no. 198*, Transportation Research Board, National Research Council, Washington, D.C.

Lantsoght, E. O. L., Yang, Y., van der Veen, C., de Boer, A., and Hordijk, D. A. (2016). "Ruytenschildt Bridge: Field and laboratory testing." *Engineering Structures*, 128(Supplement C), 111-123.

Lichtenstein, A. G. (1993). "The Silver Bridge Collapse Recounted." *Journal of Performance of Constructed Facilities*, 7(4), 249-261.

Lichtenstein Consulting Engineers (2001). "Manual for Condition Evaluation and Load Rating of Highway Bridges Using Load and Resistance Factor Philosophy." *Contractor's Final Report*Paramus, NJ.

Lwin, M. M. (2006). "Bridge Load Ratings for the National Bridge Inventory." F. H. A.-O. o. B. Technology, ed., US Department of Transportation, Washington, DC.

Mander, J. B., Priestley, M. J. N., and Park, R. (1988). "Theoretical Stress-Strain Model for Confined Concrete." *Journal of Structural Engineering*, 114(8)(1804-1826).

MCC (2014). "StrainBook/616." <http://www.mccdaq.com/products/strainbook616.htm>. (July 15, 2014).

Mertz, D. (2015). "Steel Bridge Design Handbook - Load Rating of Steel Bridges." US Department of Transportation, Federal Highway Administration, Washington, DC, 1-25.

Mertz, D. R. (2007). "Simplified Live Load Distribution Factor Equations." Transportation Research Board, National Research Council, Washington, DC, 1-137.

Middleton, C. (2007). "Generalised Collapse Analysis of Concrete Bridges." *ICE Magazine of Concete Research*, 60(8), 575.

Miller, R. A., Aktan, A. E., and Shahrooz, B. M. (1994). "Destructive Testing of Decommissioned Concrete Slab Bridge." *Journal of Structural Engineering*, 120(7), 2176-2198.

Mlynarski, M., Wassef, W. G., and Nowak, A. S. (2011). "A comparison of AASHTO bridge load rating methods." Transportation Research Board, National Research Council, Washington D.C.

Moses, F. (2001). "Calibration of load factors for LRFR bridge evaluation." Transportation Research Board, National Research Council, Washington D.C.

Moses, F., and Verma, D. (1987). "Load capacity evaluation of existing bridges." Transportation Research Board, National Research Council, Washington, D.C.

NBI (2016). "National Bridge Inventory (NBI)." Federal Highway Administration, Washington, DC.

Newmark, N. M. (1938). *A distribution procedure for the analysis of slabs continuous over flexible beams*, The University of Illinois, Urbana, Illinois.

Park, R., and Gamble, W. L. (2000). *Reinforced Concrete Slabs*, John Wiley & Sons, New York, NY.

Pirayeh Gar, S., Mander, J. B., Head, M., and Hurlebaus, S. (2014). "FRP slab capacity using yield line theory." *Journal of Composites for Construction*, 18(6), 04014021.

Proceq (2017). "Original Schmidt Concrete Test Hammer Operating Instructions." *Model N/NR: Conversion Curves Based on the Average Compressive Strength of a Cylinder and the Rebound Value R*, Proceq SA, Schwerzenbach, Switzerlad.

Proceq (2017). "Silver Schmidt Operating Instructions." Proceq SA, Schwerzenbach, Switzerlad.

Pucinotti, R. (2015). "Reinforced concrete structure: Non destructive in situ strength assessment of concrete." *Construction and Building Materials*, 75(Supplement C), 331-341.

Ryan, T. W., Mann, J. E., Chill, Z. M., and Ott, B. T. (2012). "Bridge Inspector's Reference Manual." Federal Highway Administration.

Sanayei, M., Reiff, A. J., Brenner, B. R., and Imbaro, G. R. (2016). "Load Rating of a Fully Instrumented Bridge: Comparison of LRFR Approaches." *Journal of Performance of Constructed Facilities*, 30(2), 04015019.

Santini-Bell, E., J. Lefebvre, P., Sanayei, M., Brenner, B., Sipple, J., and Peddle, J. (2013). *Objective Load Rating of a Steel-Girder Bridge Using Structural Modeling and Health Monitoring*.

Schindler, H.-J. (2005). "On quasi-non-destructive strength and toughness testing of elastic–plastic materials." *International Journal of Solids and Structures*, 42(2), 717-725.

Suksawang, N., and Nassif, H. (2007). "Development of Live Load Distribution Factor Equation for Girder Bridges." *Journal of the Transportation Research Board*, 2028.

Terzioglu, T., Hueste, M. B. D., and Mander, J. B. (2017). "Live Load Distribution Factors for Spread Slab Beam Bridges." *Journal of Bridge Engineering*, 22(10).

Trtnik, G., Kavčič, F., and Turk, G. (2009). "Prediction of concrete strength using ultrasonic pulse velocity and artificial neural networks." *Ultrasonics*, 49(1), 53-60.

TxDOT (2001). "Rate Spreadsheet User Guide." TxDOT.

TxDOT (2001). "RATE Spreadsheet User Guide."

TxDOT (2005). "Bridge Standards." *Concrete Slab and Girder Spans - 24 ft Roadway*, Texas Department of Transportation, Austin, TX.

TxDOT (2005). "CG Spans,24' Rdwy,(All Skews)." <https://www.dot.state.tx.us/insdtdot/orgchart/cmd/cserve/standard/bridge-e.htm>.

TxDOT (2013). "Bridge Inspection Manual." *Ratings and Load Posting*, Texas Department of Transportation.

TxDOT (2018a). "Bridge Inspection Manual." *Ratings and Load Posting*, Texas Department of Transportation, Austin, TX.

TxDOT (2018b). "InspecTech Inspection Records." Bentley Systems and Texas Department of Transportation, Austin, TX.

United States Government (2004). "Federal Register, Rules and Regulations." F. H. A. Department of Transportation, ed.WAshington, DC, 74419-74439.

VDOT (2011). "Simple Span Reinforced Concrete Slab Bridge Input." *Appendix D: LRFD Live Load Distribution Factor Calculations*, Virginia Department of Transportation, Richmond, VA, 109-115.

Washer, G. A. (1998). "Developments for the non-destructive evaluation of highway bridges in the USA." *NDT & E International*, 31(4), 245-249.

WisDOT (2017). "WisDOT Bridge Manual." Wisconsin Department of Transportation, Madison, WI, 1-108.

Yousif, Z., and Hindi, R. (2007). "AASHTO-LRFD Live Load Distribution for Beam-and-Slab Bridges: Limitations and Applicability." *Journal of Bridge Engineering*, 12(6), 765-773.

Zokaie, T., Imbsen, R. A., and Osterkamp, T. A. (1991). "Distribution of Wheel Loads on Highway Bridges." Transportation Research Record, Washington, DC, 119-126.